Investigations of Novel Ordered Bulk and Nano Intermetallic Compounds with Diverse Crystal Structures and Versatile Physicochemical Properties

A Thesis
Submitted for the Degree of

Doctor of Philosophy

By

Subbarao Udumula

New Chemistry Unit

Jawaharlal Nehru Centre for Advanced Scientific Research

BANGALORE-560064, INDIA

November 2015

Dedicated to My Parents, all My Teachers and Friends

DECLARATION

I hereby declare that the matter embodied in the thesis entitled "**Investigations of Novel Ordered Bulk and Nano Intermetallic Compounds with Diverse Crystal Structures and Versatile Physicochemical Properties**" is the result of investigations carried out by me at New Chemistry Unit, Jawaharlal Nehru Centre for Advanced Scientific Research, Bengaluru, India, under the supervision of **Dr. Sebastian C. Peter** and it has not been submitted elsewhere for the award of any degree or diploma.

In keeping with the general practice in reporting scientific observations, due acknowledgment has been made whenever the work described is based on the findings of other investigators.

Udumula Subbarao

Jawaharlal Nehru Centre for Advanced Scientific Research
(A Deemed University)
Department of Science and Technology, Government of India.

CERTIFICATE

I hereby certify that the work described in this thesis entitled "**Investigations of Novel Ordered Bulk and Nano Intermetallic Compounds with Diverse Crystal Structures and Versatile Physicochemical Properties**" has been carried out by **Mr. Subbarao Udumula** at New Chemistry Unit, Jawaharlal Nehru Centre for Advanced Scientific Research, Bangalore, India under my supervision and it has not been submitted elsewhere for the award of any degree or diploma.

Dr. Sebastian C. Peter
(Research Supervisor)

ACKNOWLEDGEMENTS

First and foremost, I would like to express my sincere gratitude to my research supervisor Dr. Sebastian C. Peter, New Chemistry Unit, JNCASR, for his continued support, motivation, infinite patience and guidance throughout my PhD career. He is a person of immense enthusiasm and wisdom. It is a rich and fulfilling experience to work under his guidance. He has taught me the various facts of science, the way of understanding the problem and how to maintain level headed approach when problems do not work. It has been a great privilege and honor to be associated with him.

I would like to express my sincere thanks to Prof. C. N. R. Rao, FRS, the Chairman, New Chemistry Unit for being the source of inspiration, generous support and encouragement throughout myJNC life. . I also thank him for providing the infrastructure and facilities to carry out my research work.

I would like to thank Prof. Mercouri G. Kanatzidis (Northwestern University, U.S.), Dr. Michael Graf (Boston College, U.S.), Prof. Chandrabhas Narayana and, Dr. Ranjan Datta (JNCASR), Dr. M. Gutmann (ISIS Facility, U.K.), Dr. Ashfia Huq (Oak Ridge National laboratory, U.S.), Dr. G. Vaitheeswaran (ACRHEM, University of Hyderabad), Prof. A. Svane (Aarhus University, Denmark), Prof. A. Gupta and Dr. V. R. Reddy (UGC-DAE CSR, Indore) and Dr. S. Rayaprol (UGC-DAE CSR, Mumbai) for collaborative work and various important discussion and help.

I would like to thank Prof. A. Sundaresan, Prof. S. M. Shivaprasad, Prof. M. Eswaramoorthy, Prof. Tapas Kumar Maji and Dr. Sebastian C. Peter for their excellent courses.

I would like to thank JNCASR for providing me all the facilities.

I am thankful to JNCASR Library staff, Comp Lab staff, Hostel staff, and Health Center staff and Doctors for providing and maintaining the various facilities that have helped me immensely.

I would like to thank PETRA-II, DESY, Germany for the XANES and Photon factory, Japan for Synchrotron powder XRD measurements.

I am thankful to the present chairman of the NCU, Prof. C. N. R. Rao, FRS, for providing and maintaining various facilities.

I thank all the office staff of NCU and CPMU, Mrs. Rajani, Mr. Naveen, Ms. Ramya, Sashi madam, Sudha madam, Gowda and Victor for their help.

My sincere thanks to all the technical staff of NCU and CPMU, especially Mr. Sreenivas, Mr. Anil, Mrs. Usha madam, Mrs. Bhavya, Ms. Selvi, Mr. Srinath, Mr. Jagadish, Mr. Alla Sreenivas, Mr. Mahesh and Mr. Vasu for their help with the various characterization techniques.

I am thankful to Prof. A. Sundaresan and his students, especially Mr. Rana, Mr. Bharat and Mr. Somnath for magnetic and resistivity measurement facility.

I am thankful to JNCASR, SSL, DST and CSIR for financial support and fellowship.

I am thankful to present and past hostel staff and wardens Prof, T. K. Maji, Prof. Ranjani Viswanathan, Prof. Subi Jacob George, Dr. Sheeba Vasu, Prof. A. Sundaresan and Prof. S. M. Shivaprasad for their help in various ways.

I am thankful to Gym Instructor Mr. Umesh for his help.

I also thank Mr. Vidyanshu Mishra, Mr. Saurav Ch. Sarma and Dr. Vijaykumar S Marakatti for helping me in different ways while writing the thesis.

I am extremely grateful to all my lab mates, Present Members: Mr. Sumanta Sarkar, Mr. Soumyabrata Roy, Mr. Rajkumar Jana, Mr. Saurav Chandra Sarma, Ms. Shreya Sarkar, Mr. Dundappa Mumbaraddi, Ms. Swetha Ramani, Dr. Vijaykumar S Marakatti, Vamsee, and Mr. Vidyanshu Mishra. Past Members: Mr. Abishek Kannan Iyer, Mr. Mohan Subramanium,

Mr. Pradeep Shanbogh, Ms. Deepti Kalsi, Ms. Swathi N., Mr. Pramod Halappa, Mr. Satyanarayan K.V.V., Mr. Prakrthi N., Dr. Aloke Kumar Ghosh, Dr. Oinam Bijeta Chanu, Dr. Ramesh Siva, and Prof. M. Amshumali. Summer students: Mr. Sourav SekharBera, Mr. Aiswarya Abhisek Mohapatra, Ms. Lahari Balisetty, Ms. Valeen Rashmi Pereira, Ms. Navami Venugopal, Ms. Rohan Borah, Ms. Hiranmayee Vadlamani, Mr. Sthitadhi Maiti, Mr. Anupam Bhim, Ms. Vinita Ahuja, Ms. Juhi Dutta, Mr. Kushagra Gahlot, Ms. Suchi Smita Biswas, Ms. Paramaita Sarkar, Ms. Shikha, Ms. Ekashmi Rathore, Mr. Remesh H, Mr. Niranjan Bhat, Mr. Bibhuti Bhusan Rath, Mr. Samarth Bachkheti, Mr. Ridip Das, Mr. Mahesh Talluri and Mr. Yatish Khulbe for their fruitful discussions, help and co-operation.

My special thanks to the teachers at my school (Govt. High school), and college (M.N.M. Junior College and Sri Nagarjuna Degree College).

I would like to thank my B.Sc chemistry teacher Mr. Ranga Reddy sir who guided me a lot and made it worthwhile for me to pursue a research career in Chemistry.

I would like to thank my school and college friends Tirupathi Reddy, Musala Reddy, Nagarjuna Reddy, Narayana, Venkateswarlu, Vijaya Bhaskar, Sreenu, Ravanaiah, Adaamu, Ysebu, Jasuva, Madhav, Venkata Krishna, Ravindra, Fayaz, Murali, Rajsekhar, Ramana Reddy, Surendhra, Harikrishna, Buchepalli and many more.

.

I would like to thank Gade Nagalakshmi, Sunitha, Neelima, Kaviya, Surya and Pallavi. for their help and co-operation.

My cordial thanks to all my MSc (ANU) seniors, juniors and friends Adi, Gopi, Veeru, Narsing, Santharaju, Santosh, Peethani, Gunja, Katuri, Bharat, Krishna, Kami, Ravi, Suribabu, Ganta, Sreenu, Janbee, Govind, Swetha, Narmada, sanjeevani, Khagesh, Murali, Punnarao, Sreenu, Sivaram, Appalanaidu, Battu, Satish, Santosh, Sreekanth, Viswanath, Dr. Tirumula Prasad and many more for their unforgettable company throughout my academic life. I cannot imagine my life without their support and encouragement.

It is a great privilege to express my heartfelt regards to all my teachers during the entire tenure of my educational career especially all the faculty members of Acharya nagarjuna University College (ANU), Guntur, Prof. Syam Sunder, Prof. Satyanarayana, Dr. Haribabu, Dr. Ramesh Raju, Dr. Anitha, Dr. Balamurgan, Prof. Kesava Rao and Prof. Sunandamma.

I would like to thank all my JNCASR friends Ramakrishna, Saraiah, Anand, Vijay, Yugandhar, Suresh, Dasari, Sarma, Pandu, Ramana Reddy, L.N.Reddy, Sreedhar, Ganga, Karthik, Satyanarayana, Manoj, Gopal, Murthy, Lingampalli, Chandan Kumar Mishra, Ramkumar, Anandroy, Sunitha, Sreekanth, Gurivireddy, Moumita, Ankit, Satyanarayana, chari, Dr. Venkat, Dr. Subbu, Dr. Venki, Dr. Satish setti, Dr. Malli, Dr. Avinash, Dr. Praveen, Dr. Debu, Dr. Pavan, Dr. Tangi, Dr. Naidu, Dr. Barun, Dr. Ashly, Dr. Narendra, Dr. Datta Dr. Sandeep, Dr. Jayaram, Dr. Srinu badram, Dr. Suresh, Dr. Parameswarappa, Dr. Urmi, Dr. Nitesh, Nagarjuna, Sivaprasad, Divakar, Padma, Rajsekahar, Suseela, manjit, Pramod, Uttam, Rana, Somnath, CD, Paramita, Suchismita, Krishnandu, Sasi Kiran, Arpan, Nivedita, Loukya, Rajin sahu, Satya guni, and many more deserve a special mention for providing an wonderful atmosphere in JNCASR which made my stay more comfortable.

Finally and most importantly, I am grateful to my family, especially my parents and sisters for their love, moral support and constant encouragement throughout my life. Their love, blessings and affection have made me what I am today. This thesis is dedicated to my parents, all my teachers and friends for their love and support.

Last but not least, I thank Almighty God for providing me a wonderful Ph.D. life.

Subba

PREFACE

The thesis is divided into seven chapters. **Chapter 1** deals with the brief overview about bulk and nano intermetallics. This chapter describes a few statistics about binary, ternary and quaternary intermetallics followed by the synthesis using different techniques such as arc melting, high frequency induction heating and metal flux techniques. It also discusses about the ordering and disordering concept by selectively choosing a few prototype compounds. The chapter emphasizes the importance of Eu and Yb based compounds due to their ability to exhibit in two energetically similar electronic configurations.

Chapter 2 deals with the synthesis, properties and phase transitions of the compounds in 1-1-3 family. There are 11 different structure types reported within this family. The highlight of this chapter is the discovery of three more new structure types for these compounds. The first part deals with the synthesis, structure and physical properties of $YbCuGa_3$. High quality single crystals of $YbCuGa_3$ were obtained from the reaction of Yb and Cu in excess liquid gallium as solvent at 1173 K. $YbCuGa_3$ crystallizes in a new structure type in the monoclinic space group *C*2/*m*. The magnetic susceptibility was investigated in the temperature range 2-300 K obeying Curie-Weiss law above 130 K and the experimentally measured magnetic moment indicates mixed valent Yb. Electrical conductivity measurements show that the compound exhibits metallic nature. The new structure type in $YbCuGa_3$ motivated us to focus on the compounds *RE*$CuGa_3$ (*RE* = La-Nd, Sm-Gd), which were synthesized by various techniques. A detailed single crystal XRD, neutron diffraction and synchrotron XRD on selected compounds confirmed the non-centrosymmetric $BaNiSn_3$ structure type at room temperature with space group *I*4*mm*. Temperature dependent XRD confirms the structural transition between centro- and non-centro symmetry followed by a phase transition to the Rb_5Hg_{19} type (*I*4/*m* space group) above 400 K and another transition to the Cu_3Au structure type ($Pm\bar{3}m$) above 700 K. Resistivity and magnetization measurements demonstrate that all the compounds undergo magnetic ordering at temperatures between 1.8 and 80 K, apart from the Pr and La compounds: the former remains paramagnetic down to 0.3 K, while superconductivity has been observed in the La compound at T = 1 K. The divalent nature of Eu in $EuCuGa_3$ was confirmed by magnetic and X-ray absorption near edge spectroscopy (XANES), and was further supported by the crystal structure analysis. The complex long-

range magnetic ordering and multiple magnetic phases were studied by using μSR and neutron diffraction studies. The work has extended to the *RE*NiGa$_3$ compounds.

Chapter 3 deals with the ThMn$_{12}$ structure type compounds. High quality single crystals of SmCu$_6$In$_6$, YbCu$_6$In$_6$, EuAg$_4$In$_8$ and YbCu$_4$Ga$_8$ have been grown using the flux method and characterized by means of single crystal X-ray diffraction data. These compounds crystallize in the CeMn$_4$Al$_8$ structure type, which is an ordered superstructure of the ThMn$_{12}$ type, tetragonal space group *I*4/*mmm*. However, a detailed single crystal XRD of YbCu$_4$Ga$_8$ revealed a tripling of the *c*-axis and crystallizing in a new structure type. The structural model was further confirmed by neutron diffraction measurements on high quality single crystal. Solid solutions of SmCu$_{6-x}$In$_{6+x}$ (x = 0, 1, 2) and YbCu$_{6-x}$In$_{6+x}$ (x = 0, 1, 2) compounds were obtained using arc melting and high frequency induction heating and characterized using powder X-ray diffraction. The detailed magnetic susceptibility of these compounds were investigated in the temperature range 2-300 K. Experimentally measured magnetic moment indicates mixed valent ytterbium in YbCu$_6$In$_6$ and YbCu$_4$Ga$_8$ and divalent europium in EuAg$_4$In$_8$, which was confirmed by XANES. Electrical conductivity measurements show that all compounds are metallic in nature.

Chapter 4 deals with the $RE_5M_2X_6$ structure type compounds. A new compound Yb$_5$Ga$_2$Sb$_6$ was synthesized by the metal flux technique. The compounds Eu$_5$In$_2$Sb$_6$ and Yb$_5M_2$Sb$_6$ (*M* = Al, Ga and In) have been synthesized by high frequency induction heating method. Eu$_5$In$_2$Sb$_6$ and Yb$_5$X$_2$Sb$_6$ crystallize respectively in the orthorhombic Ca$_5$Ga$_2$As$_6$ and Ba$_5$Al$_2$Bi$_6$ structure types, space group *Pbam*. These compounds satisfy the classical Zintl-Klemm concept and are a narrow band gap. The oxidation state of the rare earth atom has been deduced from the bond valence sum calculation on the structural data. The deduced values are found to corroborate well with that obtained from the magnetic and XANES measurements, and found Eu atoms in Eu$_5$Ga$_2$Sb$_6$ and Yb atoms in Yb$_5$Ga$_2$Sb$_6$ exist in the mixed valent state.

Chapter 5 deals with ordered crystal structures with rare earth based compounds. We have successfully synthesized high quality single crystals of a few rare earth based ordered intermetallic compounds by using metal flux technique. The powder XRD of EuInGe, Yb$_2$CuGe$_6$, Yb$_{6.6}$Ir$_6$Sn$_{16}$ and EuCu$_2$Ge$_2$ reveals weak superstructure reflections, which leads to a new type structures. We have studied the crystal structure of other compounds Yb$_3$Cu$_4$Ge$_4$, Eu$_3$Ag$_2$In$_9$ and homologous of Sm$_{2n+m}$Ni$_{4n+m}$Al$_{15n+4m}$ series (n = 1 and m = 1). A new

quaternary compound $Yb_7Ni_4InGe_{12}$ was synthesized and compared the crystal structure with ternary compound $Yb_5Co_4Ge_{10}$. The oxidation states of the rare earth atoms all these compounds have been determined by using magnetic and XANES measurements.

Chapter 6 deals with the nanofication and dimensional reduction mediated valence transition as a tool towards air stable materials. One of the biggest challenges in the field of device fabrications for various technological applications is the stability of the materials in aerial conditions. In this work, we have conceptually selected the compounds $REPb_3$ (*RE* = Eu, Yb) crystallizing in the Cu_3Au structure type, which are unstable in ambient conditions, and converted to a stable material by chemical processes "nanofication" and "dimensional reduction". The reduction of the particle size has led to the valence transition of the constituent atom, which was monitored through magnetic susceptibility and XANES measurements and the stability was checked by XRD and thermogravimetric analysis over a period of five months in oxygen and argon atmospheres and confirmed by XANES. The nanoparticles showed outstanding stability towards aerial oxidation compared to the bulk counterpart as the latter one is prone to oxidation within a few days.

Chapter 7 deals with size and morphology controlled NiSe nanoparticles as efficient catalyst for the hydrogenation reactions. Facile and efficient ball milling and polyol methods were employed for the synthesis of NiSe nanoparticle. The particle size of the NiSe nanoparticle was controlled mechanically by varying the ball size in the milling process. The role of the surfactants in the formation of various morphologies was studied. The compounds were characterized by powder XRD, scanning electron microscopy, transmission electron microscopy and X-ray energy dispersive spectroscopy. The efficiency of the NiSe nanoparticle as a catalyst was tested for the hydrogenation of para-nitroaniline to para-phenyldiamine and para-nitrophenol to para-aminophenol using $NaBH_4$ as the reducing agent. Particle size, morphology and the presence of surfactant played a crucial role in the hydrogenation process.

In summary, few novel ordered intermetallic compounds and studied their structure property relationships. Apart the physical properties, a detailed study were performed for the development of air stable materials by using chemical rout and examined a few of our compounds as efficient and stable catalysts for fuel cell applications and hydrogenation reactions.

ABBREVATIONS

RE = Rare earth

T = Transition metal

HFIH = High Frequency Induction Heating

XRD = X-Ray Diffraction

SEM = Scaning Electron Microscope

EDAX = Energy Dispersive X-ray Analyser

QD-PPMS = Quantum Design Physical Property Measurement System

FC = Field Cooled

ZFC = Zero Field Cooled

FP-LAPW = Full-Potential Linear Augmented Plane Wave

LMTO = Linear Muffin-Tin Orbital

LSDA = Local Spin Density Approximation

XANES = X-Ray Absorption Near Edge Spectroscopy

PCD = Pearson Crystal Data

ICSD = Inorganic Crystal Structure Database

EPMA = Electron Probe Micro Analysis

TEM = Transmission Electron Microscopy

HRTEM = High Resolution Transmission electron microscopy

SAED = selected area electron diffraction

XPS = X-ray Photoelectron Spectroscopy

DFT = Density Functional Theory

TGA= Thermogravimetric Analyses

CW = Curie-Weiss law

TABLE OF CONTENTS

Declaration……..……iii

Certificate……..……iv

Acknowledgment…….....v-viii

Preface…….……...…ix-xi

Abbreviations……...….....xii

Table of contents……..…….xiii

Chapter 1

Introduction 1

1.1. About Intermetallics 1

1.2. Rare Earth Intermetallics 2

1.3. Mixed Valent *RE* based Intermetallics 3

1.4. Synthesis of Intermetallics 3

1.4.1. Ceramic method 4

1.4.2. Arc melting 4

1.4.3. High Frequency Induction heating 5

1.4.4. Metal Flux method 6

1.4.5. Synthesis of Nanointermetallics 8

1.4.5.1. Solution Method 8

1.4.5.2. Mechanical Milling 9

1.5. Ordered and Disordered Intermetallic compounds 11

1.5.1. Cu_3Au – Ordered structure of the Cu type 12

1.5.2. $BaNiSn_3$ – Ordered Structure of $BaAl_4$ and $CeAl_2Ga_2$ 13

1.5.3. Ba_2LiSi_3 and Ca_2AgSi_3 – Ordered superstructures of the AlB_2 type 15

1.5.4. YCu_6In_6 $CeMn_4Al_8$ Structures – Ordered superstructure of $ThMn_{12}$ 16

1.5.5. La_2AlGe_6 – Ordered vacant variant of $SmNiGe_3$ Structure type 17

1.6. Physical Properties of Intermetallics 19

1.7. Applications of Intermetallic Compounds 21

1.8. Objectives of the Thesis 22

1.9. References 22

Chapter 2

Structural Diversity, Multiple Phase Transitions and Versatile Physical Properties of the Compounds in the *RETX*$_3$ Family 33

2.1. Crystal Growth and Properties of YbCuGa$_3$: First Monoclinic System in the *RETX*$_3$ Family 35

2.1.1. Introduction 35

2.1.2. Experimental Section 36

2.1.2.1. Synthesis 36

2.1.2.1.1. Reagents 36

2.1.2.1.2. Metal Flux Method 36

2.1.2.1.3. High Frequency Induction Heating 37

2.1.2.1.4. Arc melting method 37

2.1.2.2. Elemental Analysis 38

2.1.2.3. Powder XRD 38

2.1.2.4. Single Crystal XRD 38

2.1.2.5. Magnetic Measurements 39

2.1.2.6. Electrical Resistivity 39

2.1.2.7. X-ray absorption near edge spectroscopy (XANES) 40

2.1.2.8. Neutron diffraction 40

2.1.2.9. Synchrotron XRD 40

2.1.3. Results and Discussions 40

2.1.3.1. Structure Refinement of YbCuGa$_3$ 40

2.1.3.2. Crystal Chemistry of YbCuGa$_3$ 41

2.1.3.3. Physical properties 46

2.1.3.3.1. Magnetism 46

2.1.3.3.2. Electrical Resistivity 48

2.1.4. Conclusion 49

2.2. Swinging Symmetry, Multiple Structural Phase Transitions and Versatile Physical Properties in *RE*CuGa$_3$ (*RE* = La-Nd, Sm-Gd) 50

2.2.1. Introduction 50

2.2.2. Results and Discussion 51

2.2.2.1. Structure Refinement 51

2.2.2.2. Reaction Chemistry 52

2.2.2.3. Crystal Structure 58
2.2.2.4. Neutron diffraction and Synchrotron XRD 68
2.2.2.5. X-ray absorption near edge spectroscopy (XANES) 70
2.2.2.6. Physical Properties 71
2.2.2.6.1. Magnetic studies 71
2.2.2.6.2. Electrical resistivity 73
2.2.3. Conclusion 75
2.3. References 77
Chapter 3
Synthesis, Crystal Structure and Physical Properties of the Compounds Crystallizing as the Ordered Structures of the $ThMn_{12}$ Structure type 83
3.1. Introduction 85
3.2. Experimental Section 86
3.2.1. Reagents 86
3.2.2. Synthesis 86
3.2.2.1. Metal flux synthesis of $YbCu_6In_6$, $SmCu_6In_6$ and $EuAg_4In_8$ 86
3.2.2.2. Metal flux synthesis of $YbCu_4Ga_8$ 86
3.2.2.3. Synthesis of $YbCu6_{-x}In_{6+x}$ (x = 0, 1, 2) by HFIH 87
3.2.2.4. Synthesis of $SmCu_{6-x}In_{6+x}$ (x = 0, 1 and 2) by arc melting 87
3.2.2.5. Direct method synthesis of $YbCu_4Ga_8$ 87
3.2.3. Elemental analysis 88
3.2.4. Powder X-ray diffraction 88
3.2.5. Single crystal X-ray diffraction 88
3.2.6. Magnetic measurements 89
3.2.7. Electrical resistivity 89
3.2.8. Single Crystal Neutron Diffraction (ND) 90
3.2.9. X-ray absorption near edge spectroscopy (XANES) 90
3.3. Crystal Structure of $YbCu_6In_6$ and Mixed Valence Behaviour of Yb in $YbCu_{6-x}In_{6+x}$ (x = 0, 1 and 2) Solid Solution 91
3.3.1. Introduction 91
3.3.2. Results and Discussion 91
3.3.2.1. Reaction chemistry 91
3.3.2.2. Structure refinement of $YbCu_6In_6$ 92

3.3.2.3. Crystal chemistry of $YbCu_6In_6$ 94
3.3.2.4. Physical Properties 97
3.3.2.4.1. Magnetism 97
3.3.2.4.2. Electrical resistivity 100
3.4. Structure and Properties of $SmCu_{6-x}In_{6+x}$ (x = 0, 1, 2) 102
3.4.1. Introduction 102
3.4.2. Results and Discussion 102
3.4.2.1. Structure Refinement 102
3.4.2.2. Crystal chemistry 104
3.4.2.3. Physical Properties 107
3.4.2.3.1. Magnetism 107
3.4.2.3.2. Electrical resistivity 109
3.5. New Structure Type in the Mixed Valent Compound $YbCu_4Ga_8$ 111
3.5.1. Introduction 111
3.5.2. Results and Discussion 112
3.5.2.1. Reaction Chemistry 112
3.5.2.2. Structure refinement of $YbCu_4Ga_8$ 113
3.5.2.3. Crystal chemistry of $YbCu_4Ga_8$ 114
3.5.2.4. Physical Properties 120
3.5.2.4.1. Magnetism 120
3.5.2.4.2. Electrical Resistivity 122
3.6. Crystal Structure and Properties of Tetragonal $EuAg_4In_8$ Grown by Metal Flux Technique 124
3.6.1. Introduction 124
3.6.2. Results and Discussion 124
3.6.2.1. Structure refinement 124
3.6.2.2. Crystal chemistry of $EuAg_4In_8$ 125
3.6.2.3. Physical Properties 131
3.6.2.3.1. Magnetism 131
3.6.2.3.2. Electrical resistivity 133
3.7. Conclusion 134
3.8. References 136

Chapter 4

Mixed Valent and Narrow-Band Gap Zintl Phase Materials in the $RE_5M_2X_6$ (RE = Eu and Yb; M = Al, Ga and In; X = As, Sb and Bi) Family 143

4.1. Introduction 145

4.2. Experimental Section 146

4.2.1. Synthesis 146

4.2.1.1. Metal Flux Method 146

4.2.1.2. High Frequency Induction Heating Method 147

4.2.2. Elemental Analysis 147

4.2.3. Powder XRD 147

4.2.4. Single Crystal XRD 147

4.2.5. Magnetic Measurements 148

4.2.6. Electrical Resistivity 148

4.2.7. Optical Measurements 148

4.2.8. Computational Details 149

4.2.9. XANES 149

4.2.10. Bond Valence Sum (BVS) Calculations 150

4.3. $Yb_5Ga_2Sb_6$: A New Mixed Valent and Narrow-Band Gap Material 151

4.3.1. Results and Discussion 151

4.3.1.1. Structure Refinement 151

4.3.1.2. Crystal Chemistry 151

4.3.1.3. Physical Properties 155

4.3.1.3.1. Magnetism 155

4.3.1.3.2. Electrical Resistivity 156

4.3.1.3.3. Optical Properties 157

4.3.1.3.4. Band Structure and Density of States 158

4.4. Magnetic and XANES Studies on $RE_5M_2Sb_6$ 160

4.4.1. Results and Discussion 160

4.4.1.1. Crystal chemistry 160

4.4.1.2. Physical Properties 163

4.5. Conclusion 167

4.6. References 168

Chapter 5

Ordered Crystal Structures of the Compounds with Mixed Valent Rare Earths 171

5. 1. Introduction 173

5.2. Experimental Section 174

5.2.1. Synthesis 174

5.2.1.1. Metal flux synthesis 174

5.2.1.2. High frequency induction heating 174

5.2.1.3. Arc Melting 175

5.2.2. Elemental analysis 175

5.2.3. Powder PXRD 175

5.2.4. Single-Crystal XRD 175

5.2.5. Magnetic Measurements 176

5.2.6. Electrical Resistivity 176

5.2.7. XANES 176

5.2.8. Mössbauer Spectroscopy 177

5.2.9. Theoretical calculations 177

5.3. Metal flux Crystal Growth Technique in the Determination of Ordered Superstructure in EuInGe 179

5.3.1. Introduction 179

5.3.2. Results and Discussion 179

5.3.2.1. Structure Refinement 179

5.3.2.2. Reaction Chemistry 180

5.3.2.3. Crystal Chemistry 181

5.3.2.4. Mössbauer Spectroscopy 185

5.3.2.5. Physical Properties 186

5.3.2.6. Band Structure Calculations 189

5.4. Crystal Structure of Yb_2CuGe_6 and $Yb_3Cu_4Ge_4$ and the Valency of Ytterbium ... 191

5.4.1. Introduction 191

5.4.2. Results and Discussion 191

5.4.2.1. Structure Refinement 191

5.4.2.2. Reaction Chemistry 192

5.4.2.3. Crystal Structure 192

5.4.2.3.1. Yb_2CuGe_6 192

5.4.2.3.2. $Yb_3Cu_4Ge_4$ 198
5.4.2.4. XANES 199
5.4.2.5. Calculations 200
5.5. Flux Growth of $Yb_{6.6}Ir_6Sn_{16}$ Having Mixed Valent Ytterbium 202
5.5.1. Introduction 202
5.5.2. Results and Discussion 202
5.5.2.1. Structure Refinement 202
5.5.2.2. Reaction Chemistry 203
5.5.2.3. Crystal Chemistry 205
5.5.2.4. Magnetism 210
5.5.2.5. XANES 211
5.5.2.6. Electrical resistivity and heat capacity 212
5.6. Crystal Growth, Structure and Magnetic Properties of $Sm_3Ni_5Al_{19}$: A Compound in the $Sm_{2n+m}Ni_{4n+m}Al_{15n+4m}$ Homologous Series 213
5.6.1. Introduction 213
5.6.2. Results and Discussion 213
5.6.2.1. Reaction Chemistry 213
5.6.2.2. Structure Refinement 214
5.6.2.3. Crystal Chemistry 215
5.6.2.4. Magnetic Properties 221
5.7. $Yb_7Ni_4InGe_{12}$: A Quaternary Compound Having Mixed Valent Yb atoms Grown from Indium Flux 223
5.7.1. Introduction 223
5.7.2. Results and Discussion 223
5.7.2.1. Reaction Chemistry 223
5.7.2.2. Structure refinement 224
5.7.2.3. Crystal chemistry 226
5.7.2.4. Physical Properties 230
5.7.2.4.1. XANES 231
5.8. The Structural Evolution of the Compounds $Eu_3T_2In_9$ (T = Cu and Ag) through the Superstructure of $EuCu_2Ge_2$ and their Physical Properties 233
5.8.1. Introduction 233
5.8.2. Results and Discussion 233

5.8.2.1. Reaction Chemistry 233
5.8.2.2. Structure Refinement of $Eu_3Ag_2In_9$ and $EuCu_2Ge_2$ 234
5.8.2.3. Crystal Chemistry of $Eu_3Ag_2In_9$ and $EuCu_2Ge_2$ 238
5.8.2.4. Magnetism 242
5.8.2.5. XANES 243
5.9. Conclusion 244
5.10. References 245
Chapter 6
Nanofication and Dimensional Reduction Mediated Valence Transition as a Tool towards Air Stable Material 253
6.1. Introduction 255
6.2. Experimental Section 257
6.2.1. Chemicals 257
6.2.2. Solvothermal method 257
6.2.3. High Frequency Induction Heating (HFIH) 257
6.2.4. Characterization 258
6.3. Results and Discussions 260
6.3.1. Reaction Chemistry 260
6.3.2. Magnetism 266
6.4. Conclusion 277
6.5. Nano Intermetallic *RE*Pd_3 (*RE* = Eu and Yb) Compounds for Electrochemical Studies 278
6.5.1. Introduction 278
6.5.2. Structure analysis 278
6.5.3. TEM Analysis 279
6.5.4. XANES Analysis 280
6.5.5. Electrochemical Studies 281
6.6. References 284
Chapter 7
Size and Morphology Controlled Synthesis of Ordered Nanoparticles in the NiAs Structure type as efficient Catalysts for the Hydrogenation Reactions 289
7.1. Introduction 291
7.2. Experimental Section 293

7.2.1. Synthesis 293
7.2.1.1. Chemicals 293
7.2.1.2. Direct Method 293
7.2.1.3. Ball Milling Method 293
7.2.1.4. Polyol Method 294
7.2.1.5. Elemental analysis 294
7.2.1.6. Powder XRD 295
7.2.1.7. TEM 296
7.2.1.8. UV-Vis spectroscopy 296
7.2.1.9. Catalytic studies 296
7.3. Results and Discussions 297
7.3.1. Structure analysis 297
7.3.2. Hydrogenation of PNA and PNP 300
7.4. Conclusion 308
7.5. References 309

Summary and Conclusions …...……313

List of Publications ……317

Chapter 1

Introduction

1.1. About Intermetallics

Intermetallics are compounds composed of two or more metallic elements or with optionally one or more semi-metallic elements that adopt a different crystal structure than their constituent elements. Intermetallics are also unique compared to the metals in terms of their bonding features. The bonding electrons are more delocalized in metals and distribute themselves throughout the material resulting in predominantly nondirectional bonding in the solid. On the other hand, the atomic bonding in intermetallic compounds is more directional, which means the electrons are more localized having slight ionic and covalent character. Based on some statistics, intermetallic compounds are divided in to three categories, which are (a) binary systems (A_xB_y) with around 20,000 members known, which is about 80% of all possible combinations, (b) ternary systems ($A_xB_yC_z$) with only 5% of the compounds have been discovered among 100,000 possible combinations and (c) quaternary systems ($A_xB_yC_zQ_m$), with only a few representative compounds were reported.[1] Chemists often find difficulty in understanding some very basic characteristics of intermetallic compounds mostly their compositions, bonding, and assignment of oxidation states for individual atoms. Because of this, the synthetic solid state chemistry community has given more attention to the growth of the materials such as oxides, ceramics, carbides, borides, pnictides, chalcogenides, or halides. Even then, intermetallics are considered to be an important class of materials with wide range of applications in modern functional, constructional and technological industries. The focus of this work is to discover and design intermetallics, which may find various applications in field of condensed material physics which includes ferromagnetism,[2, 3] superconductivity,[4, 5] Kondo behaviour,[6] heavy fermions,[7] magneto resistance,[8-10] shape-memory effects[11] and other applications such as solid state hydrogen storage capacity,[12] structural hardness,[13] catalysis [14] and corrosion resistance.[15, 16]

1.2. Rare Earth Intermetallics

The studies on rare earth (*RE*) based intermetallic compounds have been active research area for the past several decades and currently is one of the prime research focuses due to the remarkable potential of these materials to show various interesting properties such as superconductivity, Kondo behaviour, heavy fermion, zero thermal expansion and so on.[17-23] The term rare earth and the abbreviation *RE* in this thesis refer to the lanthanide elements from La (atomic number 57) to Lu (atomic number 71) along with the element yttrium Y.

Among these elements La, Lu, and Y have no magnetic moment. The other *RE* elements exhibits a variety of magnetic behaviour in the solid state both as pure metals and as their alloys or intermetallics. For example, Gd is ferromagnetic with a Curie temperature (Tc) of 293 K, whereas Eu is antiferromagnetic with a Neel temperature (T_N) of 90 K. However, the compound GdPtBi shows antiferromagnetic ordering at 3 K[24] and EuAgMg shows ferromagnetic ordering at 22 K[25] in their intermetallic form. The other pure *RE* metals show diverse magnetic behaviour including low temperature ferromagnetism followed by antiferromagnetism at higher temperatures and also canted magnetic structures. One would therefore expect *RE* based intermetallic compounds to show a similar variety of magnetic behaviour. *RE* elements form intermetallic compounds with non-transition metals or transition metals exist in a variety of crystalline structures which were described in detail by Taylor[26] and Wallace.[27] The review articles of Buschow[28, 29] and Iandelli and Palenzona[30] contain more information about the crystalline structure of several *RE* based intermetallics.

Because of the large number of possible and already investigated intermetallic compounds based on *RE* metals and strange as well as unique magnetic properties, these compounds have been in the focus of interest. Still there are more detailed investigations of these compounds required, especially with respect to the magnetic properties, more possible applications of these properties in science and technology will appear within the near future. Nevertheless only a few really large scale technical applications are seen on the horizon today, especially in future oriented fields like the computer industry, electronics, design of intricate devices etc. Some possible applications of these hard and soft magnetic materials are based on very unique properties of *RE* intermetallic compounds.

1.3. Mixed Valent *RE* based Intermetallics

Among the *RE*s, the special attention has given to the synthesis and design of the compounds with Ce, Eu and Yb because of their ability to show multiple oxidation states.[31, 32] Literature showed that the Ce based compounds are well studied because these compounds can be easily synthesized by simple conventional techniques such as arc melting and induction furnace.[33] On the other hand, high vapour pressure of Eu and Yb limited their synthesis by these techniques. In fact, many compounds based on Eu and Yb are not yet extensively explored. However, in the recent past, several groups have put tremendous effort in synthesizing new Eu and Yb based compounds by metal flux technique, which often leads to the formation of new compounds with novel structure types and unique properties.[34] It is a well-established fact that Eu and Yb can exist in divalent and trivalent states due to the presence of unstable electronic 4*f*-shell, as they show two electronic configurations that are closely spaced in energy: for Eu, the magnetic $Eu^{2+}(4f^7)$ and nonmagnetic $Eu^{3+}(4f^6)$ and for Yb, the magnetic $Yb^{3+}(4f^{13})$ and nonmagnetic $Yb^{2+}(4f^{14})$. In this case, the roles of the 4*f* electron and 4*f* hole can be interchanged and Eu and Yb based compounds often crystallize in new structure types. Interest also originates from the ability of Eu and Yb to exhibit various peculiar properties such as intermediate valence, heavy fermions, Kondo behaviour, unusual magnetism[35-37] and superconductivity at low temperature.[38] The examples are $YbNi_{0.8}Al_{4.2}$,[39] $EuIr_2Si_2$,[40] $Yb_7Co_4InGe_{12}$,[41] shows intermediate valence which contains mixed-valent of divalent of Yb^{2+}, Eu^{2+} and trivalent of Yb^{3+}, Eu^{3+}, $YbRh_2Si_2$ shows heavy fermion behaviour,[42] $EuCu_2Si_2$ shows Kondo behaviour,[43] $TbMn_6Ge_6$ shows unusual magnetism[44] and $PuRhGa_5$ shows superconductivity at low temperature.[45] These properties are generally believed to arise from the strong hybridization (interaction) between the localized 4*f* electrons and the delocalized *s*, *p*, *d* conduction electrons.[46-48] Since Eu and Yb can also show divalent oxidation state, the compounds of these metals show chemical and physical nature similar to alkaline earth metals based compounds, which is unique feature of these metals compared to other *RE*s.

1.4. Synthesis of Intermetallics

There is great interest in developing methodologies for synthesis of materials with intended functionalities. Several synthetic tools have been developed in the past for achieving this approach. However, one of the biggest challenges in the field of solid state

chemistry is the synthesis and crystal growth of the novel compounds. This has become even more complicated in intermetallics because the composition of most compounds does not yield to the type of electron counting and oxidation number analysis typically applied to more familiar solid-state compounds such as halides, oxides, and chalcogenides. It is very difficult to predict the type of composition that would be stable in a given system of metallic elements. Some exceptional cases are in the case of Zintl, Laves, or Hume–Rothery phases. Non-intermetallic compounds display more ionic character in their bonding, extensive charge transfer between different atoms, and as a result can be explained easily, whereas this is difficult for intermetallic compounds. Since majority of the binary compounds are already been reported, the focus of this work is to the synthesis of either ternary or quaternary compounds. In going from binary to ternary and then to quaternary compounds, complexity of the crystal structures proportionate. Traditional solid state synthesis is combining metals in stoichiometric ratios and heat to high temperature but structural aspects of many intermetallic compounds interestingly depend on the way the compound is synthesized, which in most of the cases may indirectly affect the physical properties of the material as structure and property are intriguingly related to each other. Therefore the synthesis and growth of single crystals are crucial to understand the precise structures before establishing the correct structure-property relations.

1.4.1. Ceramic method

Bulk intermetallics are traditionally synthesized mostly by metallurgical technique, which involves the heating of constituent elements taken in a quartz tube or any other ampoules at high temperature followed by annealing for long periods of time (often days or weeks) to get the desired structures.

1.4.2. Arc melting

Although it is highly successful for the synthesis of many important intermetallic compounds by ceramic method, this traditional method of preparation does have some limitations. In this regard, Arc melting, one of important conventional methods has been used often for the synthesis of intermetallic compounds. The advantage of this method is that the compounds can be synthesized in short period of time even sometimes within a minute and it can achieve the temperature above 3000 K. So, in principle, any metal can melt and lead into

the fast diffusion to the formation of intermetallic compounds. A typical arc melter MAM-1 constructed by Edmund Bühler GmbH is shown in Figure 1.1.

The main problem for this synthesis method arises from the low boiling temperature of the metals being used. For examples Eu (b. p. 1099 K) and Yb (b. p. 1802 K) are having lowest boiling point in the *RE* series, which lead into the high vapour pressure during the synthesis. In a quasi-open system like an arc-melting furnace,[49] significant evaporation can irreversibly affect the synthesis conditions.[49] To give an example: for the synthesis of YbPtSn[50] by arc melting, ytterbium would evaporate (b.p. 1469 K) before platinum melts (m.p. 2045 K).

1.4.3. High Frequency Induction heating

Such difficulties can be overcome by using high-frequency furnace (Figure 1.1).[51] In this method, the elements are reacted in sealed inert, refractory metal tubes, e.g. niobium, tantalum or molybdenum. The details about the container based synthesis can be available in a review by Corbett.[52] An effective method is the reaction of pre-reacted transition metal alloys with ytterbium. This technique was recently utilized for the synthesis of YbPtSn.[50] In a first step, a relatively low-melting PtSn alloy was prepared by arc melting and subsequently this alloy was reacted with ytterbium in a sealed tantalum tube resulting in a single phase YbPtSn sample.

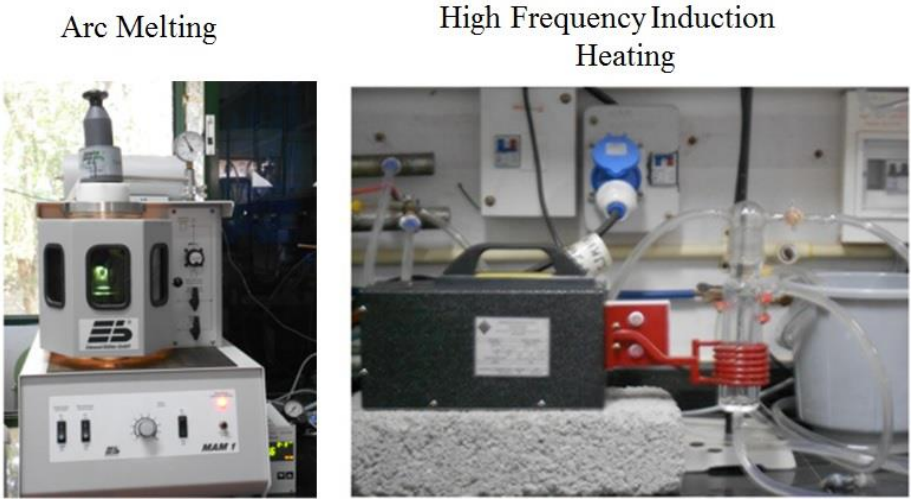

Figure 1.1. Arc melter designed by Edmund Bühler GmbH and high frequency induction furnace designed by Ambrell company, U.S.

In some cases it is also possible to react the elements in glassy carbon crucibles in a water-cooled sample chamber of the high-frequency furnace. This method has been described

in detail by Kußmann et al.[53] An advantage of this preparative technique is the direct observability of the reaction through an observation window. The techniques described above have mainly been used for compounds with the element from the third and fourth main group. For the synthesis of pnictides some other techniques can also be applied. Phosphides[54] arsenides and bismuthides can be synthesized directly from the elemental components in evacuated sealed silica tubes. In order to avoid side reactions with the silica tube, an aluminium oxide container can be used as inner crucible material. In this way YbPtP[55] was prepared. This solid-state synthesis can sometimes lead to inhomogeneous products, if reaction layers form an unreacted material and prevent diffusion. In such cases, repeated grinding, pressing and reannealing is necessary.

1.4.4. Metal Flux method

Although conventional techniques such as arc melting and high frequency induction heating can be used for the synthesis majority of the compounds within short period of time, they are limited only for the synthesis of thermodynamically stable products, so it is difficult to access the metastable phases or the structures that are stable at low temperatures. Apart from, these traditional methods are limited in the synthesis of and crystal growth of well-shaped single crystals. High temperature methods favour grain growth and the formation of large crystallites of micrometre scale due to the difficulty in controlling the crystallite size and morphology. Growing high quality single crystals is of utmost importance not only for proper structural characterization but also for the better physical property measurement as it is well known that pellets made up of polycrystalline compound contain microscopic grain boundaries which may affect the transport properties of the system. Moreover, synthesis of a high quality single crystal is the only way for the measurement of asymmetric physical property. In such case metal flux method has been proved to be a tremendous tool to grow single crystals and effective way to explore completely new phases. Metal flux method has not only been proved to be a tremendous tool to grow single crystals of already known polycrystalline compounds for studying detailed physical properties but also been an effective way to explore completely new phases.[56-64] There are several key characteristics must be mentioned for a metal to be a viable flux for reaction chemistry: 1) the metal should form a flux (i.e. a melt) at reasonably low temperatures so that normal heating equipment and containers can be used, 2) the metal should have a large difference between its melting point

and boiling point temperatures, 3) it should be possible to separate the metal from the products, by chemical dissolution, filtration during its liquid state, or if necessary mechanical removal, 4) the metal flux should not form highly stable binary compounds with any of the reactants.

In general, aluminium, gallium indium, tin and lead metal fluxes have been exploited widely as a synthetic medium for the synthesis of new intermetallic compounds.[65-93] The melting and boiling point of different elements are: aluminium (m. p. 933 K and b. p. 2792 K), gallium (m.p. 303 K and b. p. 2478 K), indium (m. p. 429 K and b. p. 2345 K), tin (m.p. 504 K and 2876 K) and lead (m.p. 600 K and b. p. 2023 K). The molten metal-flux technique is proving to be an outstanding tool for preparation. The advantages of this method lie in the enhanced diffusion of the elements facilitated by the solvent and the lower reaction temperatures that can be tolerated. For the synthesis of intermetallic tetrelide (mainly Si and Ge containing) compounds, the option of molten metal fluxes presents a promising approach, particularly with the use of low melting metals of Group 13 (Al, Ga, and In). These metals have low melting points, large solubility limits for tetrelides at moderate temperatures, do not form binary compounds with tetrelides, and are easily isolable from the final products through either chemical or physical means. Even within the flux growth scenario, variation of the reaction time and temperature can influence the product outcome within a system just as in any conventional solution-based process.

Interestingly, these metal fluxes can be used as both active and non-active solvents. For examples aluminium has been used as the active flux in the crystal growth of $Ho_6Mo_4Al_{43}$[94], gallium has been used as the active flux for the synthesis of RE_3Ga_9Ge (*RE*= Y, Ce, Sm, Gd and Yb)[38] and inactive flux for the crystal growth of the silicides $RE_2Ni_{3+x}Si_{5-x}$ (*RE* = Sm, Gd, and Tb),[95] indium has been used as active flux in the case of $Dy_2Pt_7In_{16}$[96] and inactive flux for the synthesis of $CeCu_2Si_2$,[97] tin has been used as the active flux for the synthesis of $Ca_7Ni_4Sn_{13}$[98] and inactive flux for the synthesis of $EuCo_2P_2$.[99] One of the interesting features of the metal flux synthesis method is in the reduction of melting point and vapor pressure of the starting materials, which resulted in the formation of new compounds. A good review about the concept and use of metal flux technique for the formation of new compounds was reported by Kanatzidis and co-workers has been demonstrated that molten metal fluxes represent an excellent alternative to the conventional

synthetic methods for the exploratory synthesis of new *RE* intermetallic compounds, as well as single crystal growth of already reported compounds.[100] The schematic representation for the synthesis of intermetallic compounds by using metal flux technique is shown in Figure 1.2. Every new compound discovered by metal flux method displayed a novel situation in the physical properties. Some notable examples of the unique properties of Eu and Yb based compounds are: zero thermal expansion behaviour in YbGaGe,[101] metamagnetism in Eu_2AuGe_3[102] structural phase transition in RE_2AuGe_3 (*RE* = Eu and Yb),[102, 103] valence fluctuations in Yb_4TGe_8,[104] low temperature Fermi-liquid behaviour in $Yb_3Ga_7Ge_3$,[105] non Fermi-liquid behaviour in $Yb_5Ni_4Ge_{10}$[106] and heavy fermion behaviour in $YbRh_2Si_2$.[42]

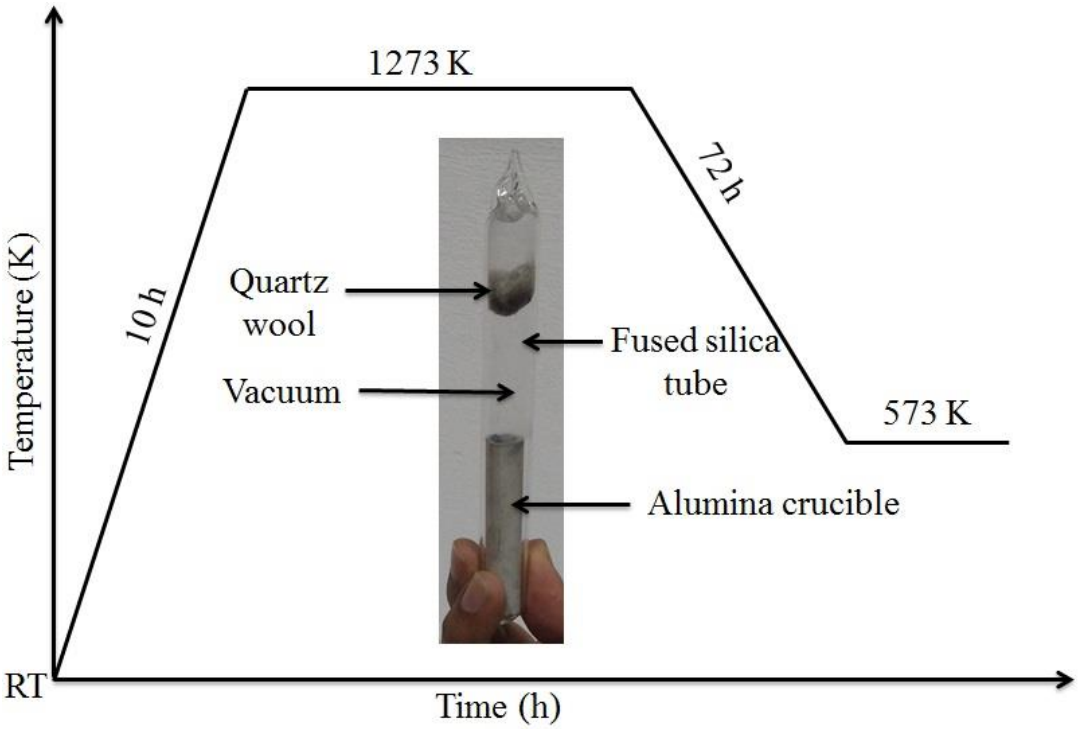

Figure 1.2. Schematic representation for synthesis of intermetallic compounds by using metal flux technique of quartz ampoule with simple temperature profile.

1.4.5. Synthesis of Nanointermetallics

1.4.5.1. Solution Method

The nanocompounds can be synthesized mainly by two methods bottom-up approach (solution methods) and top-down approach (mechanical milling or grinding). A large variety of intermetallic nanoparticles are synthesized through solution phase methods which involve sol-gel, solvothermal/hydrothermal and colloidal/polyol methods etc., Intermetallics in general have been overlooked as synthetic targets of solution-based synthetic strategies. This

is a significant shortcoming because the availability of general low-temperature solution routes for synthesizing nanocrystalline intermetallic compounds would likely open the door to many new and metastable phases as well as increased utilization in emerging nanotechnological applications. Solution-based synthetic strategies offer several important advantages over traditional high-temperature methods.[107] For example, solution routes can precipitate nanocrystalline powders at low temperatures where bulk-phase solid-state reaction kinetics are typically too slow to facilitate reactivity.[108] Also, solution methods often allow control over nanostructure and morphology, providing a convenient method and processing them into thin films[109] and nanotemplated materials.[110] Colloidal/polyol methods exploits high-boiling polyalcohol solvents that also act as mild reducing agents when heated, was originally developed for the synthesis of nanocrystalline powders of Pd and other late transition elements.[111] For metal and metal alloys the precursor salts are typically dissolved in aqueous or organic solvent. Formation of nanoparticles is triggered by the reduction of salts using reducing agent or through the controlled decomposition of organometallic compounds. Reaction time, temperature, concentration of surfactant and concentration of reagents plays a crucial role in controlling the size and shape of the nanoparticle. Surfactants are generally used to control the growth and aggregation of the nanoparticles. Most of the growth mechanism has been attributed to the 'Oswald ripening' process where large particle continues to increase in size with time. Since then, it has been modified to produce size and shape controlled nanocrystals of a variety of elements and alloys[112] and has yielded important magnetic, catalytic, and optical nanomaterials.

1.4.5.2. Mechanical Milling

Mechanical milling is another method can be used to obtain the product from micro level to nano level within short period. In general, pure intermetallic compounds obtained from the direct method is subsequently loaded into a planetary ball miller (Fritsch Planetary Micro Mill Pulverisette-7 premium line) having two steel bowls of 25 mL capacity with tungsten carbide balls. Mostly, tungsten carbide balls, zirconium oxide balls, agate balls of various sizes are used for the synthesis of intermetallic nanoparticle of different sizes (Figure 1.3). While converting from bulk material to nano material by using mechanical milling method, there are many factors are need to be monitored to get nano material such as milling speed, milling time, milling atmosphere, milling temperature etc. (Figure 1.4).[113] Now a days

ball milling is used for the synthesis of many intermetallics compounds. For example, Ivanov et al. reported NiAl, TiAl and NbAl can be considered as the first attempt of producing nano intermetallics systems.[114] In another works, Co_2Si, MnBi has been synthesized in nanocrystalline form through mechanically milling in a high-energy ball mill.[115, 116] The stability and properties of such structures have not been studied systematically. However, ball milling should be a practical method of producing large quantities of nanocrystalline materials.

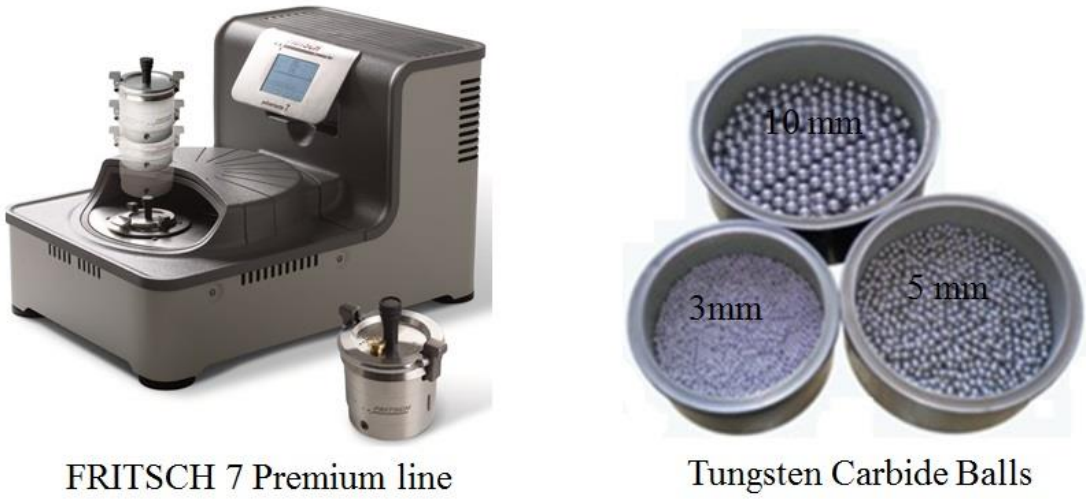

Figure 1.3. Synthesis of intermetallic compounds from micro to nano size by using mechanical milling

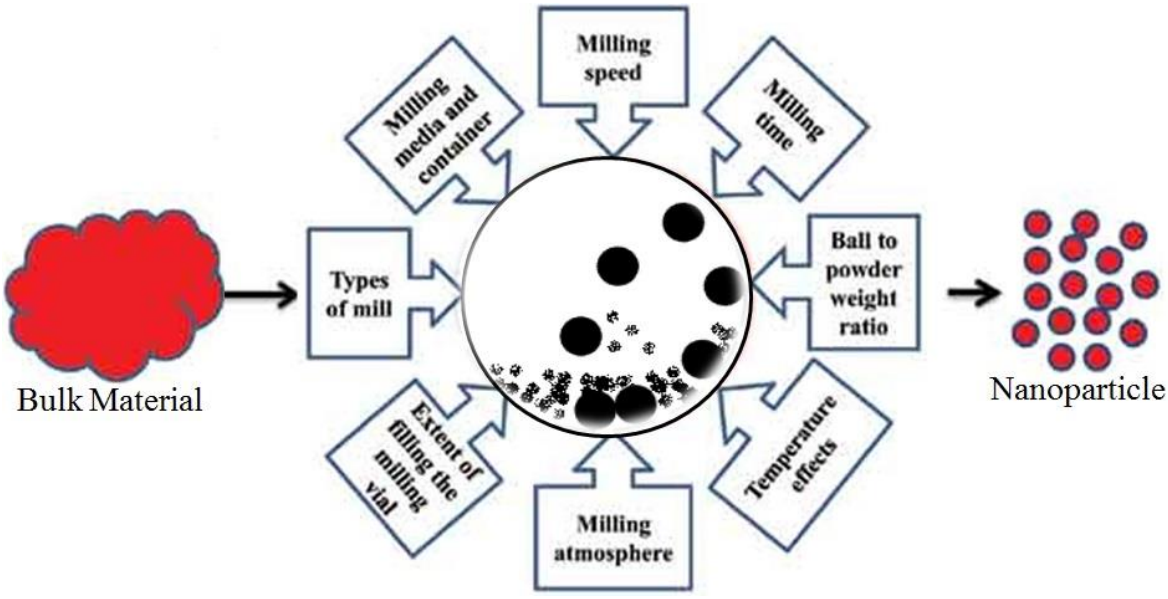

Figure 1.4. Synthesis process of intermetallic compounds from micro to nano size by using mechanical milling (with permission from Bentham Science Publisher, ref. [113]).

1.5. Ordered and Disordered Intermetallic compounds

The main focus of this thesis is to synthesize ordered intermetallic compounds, which is basically aimed to alter the structure and properties of these materials compared to the disordered parent compounds. The thesis also focused to develop new structures or superstructures of the existing ones. The new structures often find a close relation with known compounds, which has been discussed in detail in the respective chapters.

In general, all crystalline compounds can be classified as ordered and disordered compounds based on the fact that whether each crystallographic site is occupied solely by a single constituent atom or have mixed positions shared statistically between two atoms respectively. Both of these arrangements are crucial in generating novel ternary and quaternary structure types from the corresponding binary structure, which effectively acts as a structural template for those compounds. Majority of the intermetallics reported are binary compounds as they are relatively easier to synthesize and holding simple structural analysis. Most of these compounds are reported in the crystal structure types of the constituent metals or ordered types of the same. The crystallographic details of all these compounds are available in Inorganic Crystal Structure Database[117] and Pearson's crystal data[118] and the well-established phase diagrams accessible via Pauling phase diagram databases. It is a well-known fact that many of the metals are known to exist in different modifications at high temperature and high pressure leading to a wide variety of structures, chemical bonding and physical properties, which motivated the chemists to focus on the binary compounds for their diversity in structure and physical properties. This has been exemplified with a plethora of literature reports available for several decades. In going from binary to ternary and quaternary compounds one ends up with incredible number of new phases and sometime new structure types. During last two decades, plenty of new ternary ordered structure types were reported.[37, 102, 119-124] Ordering and disordering factors will play crucial role in tuning their structural and physical properties. The assignment of atoms in disordered compounds is quite difficult as they are statistically distributed. Most of the conventional techniques such as ceramic, arc melting and HFIH mostly led into the formation of the disordered compounds. On the other hand, metal flux technique favoured the formation of the ordered compounds. A few examples shown below explain the relation between ordered and disordered compounds.

1.5.1. Cu_3Au – Ordered structure of the Cu type

The relation between ordering and disordering can be explained by taking the example Ag_3In published by Sarkar et al.[125] Silver metal has face-centered cubic crystal structure ($Fm\bar{3}m$) where all the corners and faces are occupied by the Ag atoms (Wyckoff no. 4*a*) with the lattice parameter 4.09 Å (Figure 1.5a).[126]

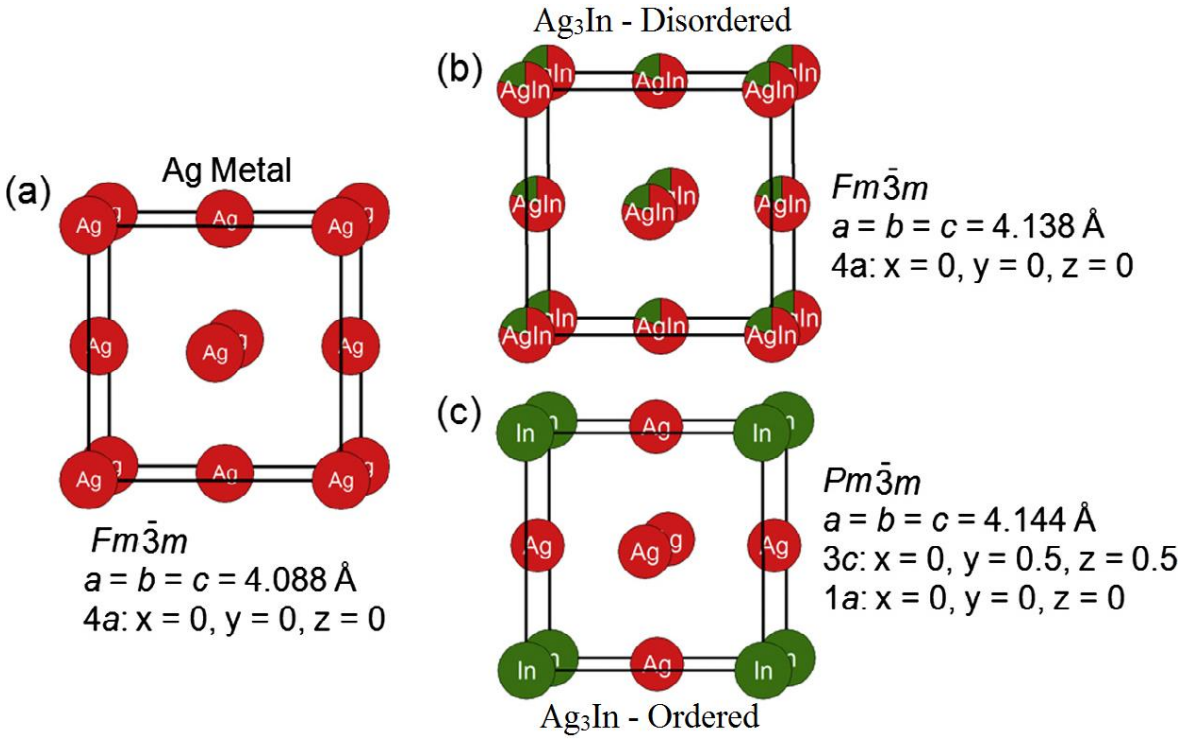

Figure. 1.5. The unit cell representation of (a) Ag, (b) Disordered $Ag_{0.75}In_{0.25}$ and (c) Ordered Ag_3In (ref. [125]).

The disordered phase of Ag_3In ($Ag_{0.75}In_{0.25}$) can be obtained by statistical mixing 25% In position with 75% of the Ag site (Wyckoff no. 4*a*) without any change in the lattice symmetry. As the covalent radii of In is higher than Ag (1.44 and 1.37 Å for In and Ag, respectively), the lattice parameter of the disordered phase increases slightly to 4.14 Å (Figure 1.5b).[127] Both Ag and disordered $Ag_{0.75}In_{0.25}$ crystallizes in the Cu structure type. With an increase in the reaction temperature, the thermal vibration of the atoms increases proportionally. As a result, the Ag and In sites tend to order in different positions. The ordered structure of Ag_3In belongs to the Cu_3Au structure type with ($Pm\bar{3}m$) space group. The In atoms occupy the corner positions (Wyckoff no. 1*a*) forming a primitive lattice and the Ag atoms occupy half of the octahedral holes (Wyckoff no. 3*c*), and hence, a change in

the Bravais lattice occurs from *F* to *P* due to the lowering of the lattice symmetry (Figure1.5c).[128] The lowering in symmetry generates several extra low intensity peaks in the PXRD patterns of the samples synthesized at higher reaction times.

1.5.2. $BaNiSn_3$ – Ordered Structure of $BaAl_4$ and $CeAl_2Ga_2$

The compounds crystallize in the $BaNiSn_3$ structure type have ordered arrangement of atoms in the crystal structure.[129] This structure type is related to the disordered $BaAl_4$[130] and its ternary derivative disordered centrosymmetric $CeAl_2Ga_2$ [131] and $BaNiSn_3$ crystallize in the non-centrosymmetric *I*4*mm* space group.[129] On the other hand the disordered variant crystallizes in the centrosymmteric *I*4/*mmm* space group. The compounds belongs to $RETX_3$ (*RE* = rare earths *T* = transition metal and *X* = Al, Ga, Si, Ge, Sb) family, crystallize in these three structure types and the relation between them is shown in Figure 1.6. These compounds crystallize either in centrosymmteric or non-centrosymmteric systems depend on the synthetic strategies adopted. As per Inorganic Crystal Structure Database[117] and Pearson's crystal data,[118] more than 100 $RETX_3$ compounds have been reported. The $BaAl_4$ and $CeAl_2Ga_2$ structures contains three atomic positions; one 2*a* Wyckoff site occupied by a *RE* atom and the remaining two positions (4*d*, 4*e* Wyckoff sites) are occupied by a mixture of Cu and Ga (in the case of $BaAl_4$ type) with either one Ga atom occupying 4*d* Wyckoff site or Cu/Ga mixing occurs at a 4*e* Wyckoff site (in the case of $CeAl_2Ga_2$ type).

The ordering of Cu and Ga plays a crucial role in crystallizing the compound in a particular structure. The ordered non-centrosymmetric $BaNiSn_3$ contains four atomic coordinates, consisting of one *RE* atom (2*a* Wyckoff site), one Cu atom (2*a* Wyckoff site) and two Ga atoms (4*b* and 2*a* Wyckoff sites). The dotted line shown in Figure 1.6 represents the inversion symmetry, which remains absent for the $BaNiSn_3$ structure type and leads to the non-centrosymmetric *I*4*mm* space group. In both ternary structure types, the *RE* layers are separated by zig-zag type Cu-Ga layers. Overall, the amount of disorderness is less in $BaNiSn_3$ structure type compounds compared to the other compounds in $RETX_3$ series, which leads them to crystallize in the ordered $BaNiSn_3$ structure type.

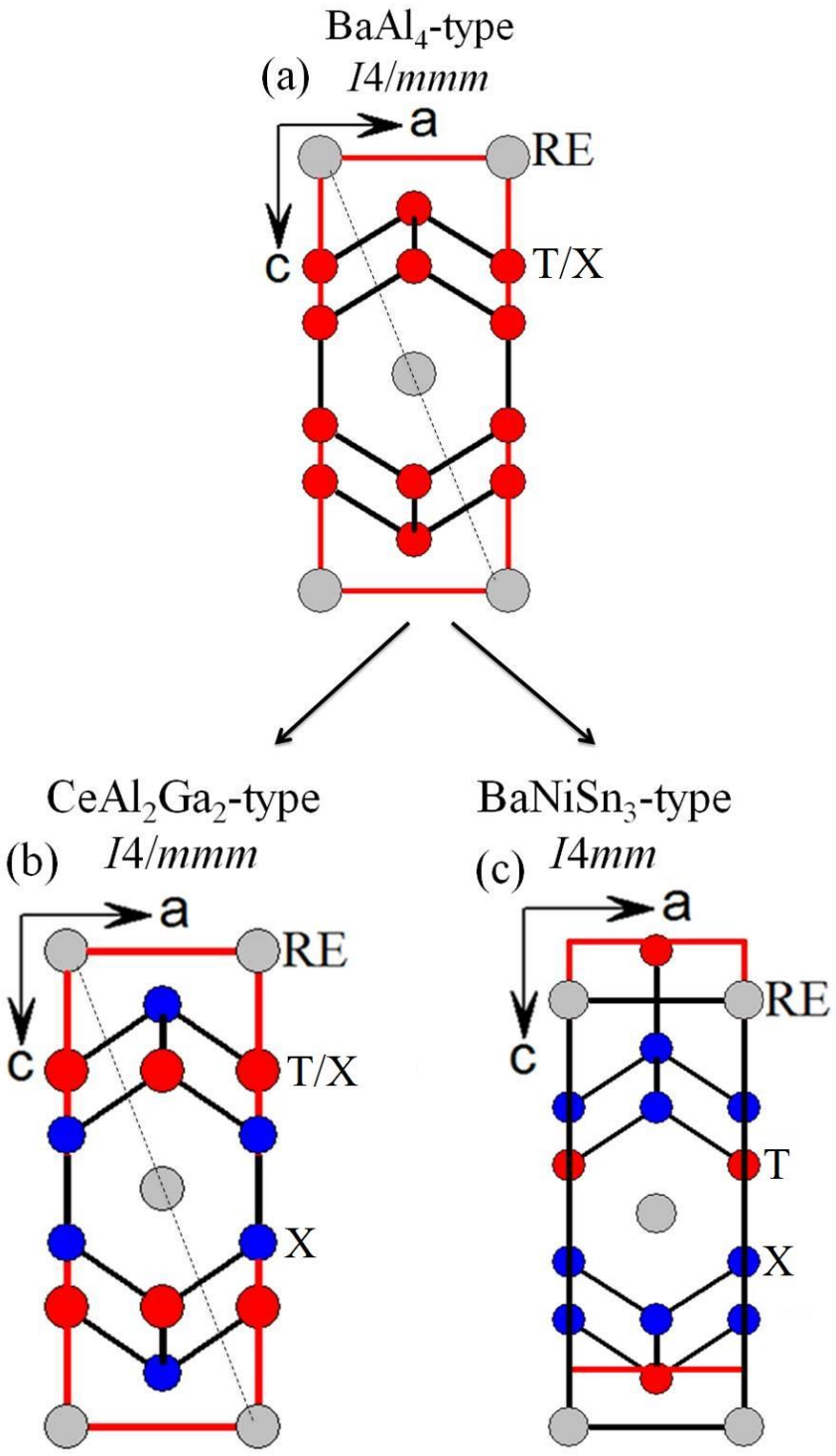

Figure 1.6. Comparison of three possible tetragonal crystal structures of $RETX_3$ (*RE* = rare earths *T* = transition metal and *X* = Al, Ga, Si, Ge, Sb) are shown along the *b*-axis which crystallizes in (a) centrosymmetric $BaAl_4$ structure type, (b) centrosymmetric $CeAl_2Ga_2$ structure type and (c) non-centrosymmetric $BaNiSn_3$ structure type. The unit cells are outlined as redlines. Dotted line shows the inversion symmetry presents in the $BaAl_4$ and $CeAl_2Ga_2$ structure types.

1.5.3. Ba_2LiSi_3 and Ca_2AgSi_3 – Ordered superstructures of the AlB_2 type

The structural relation between AlB_2 and the ordered compounds Ba_2LiSi_3 and Ca_2AgSi_3 is shown in Figure 1.7.

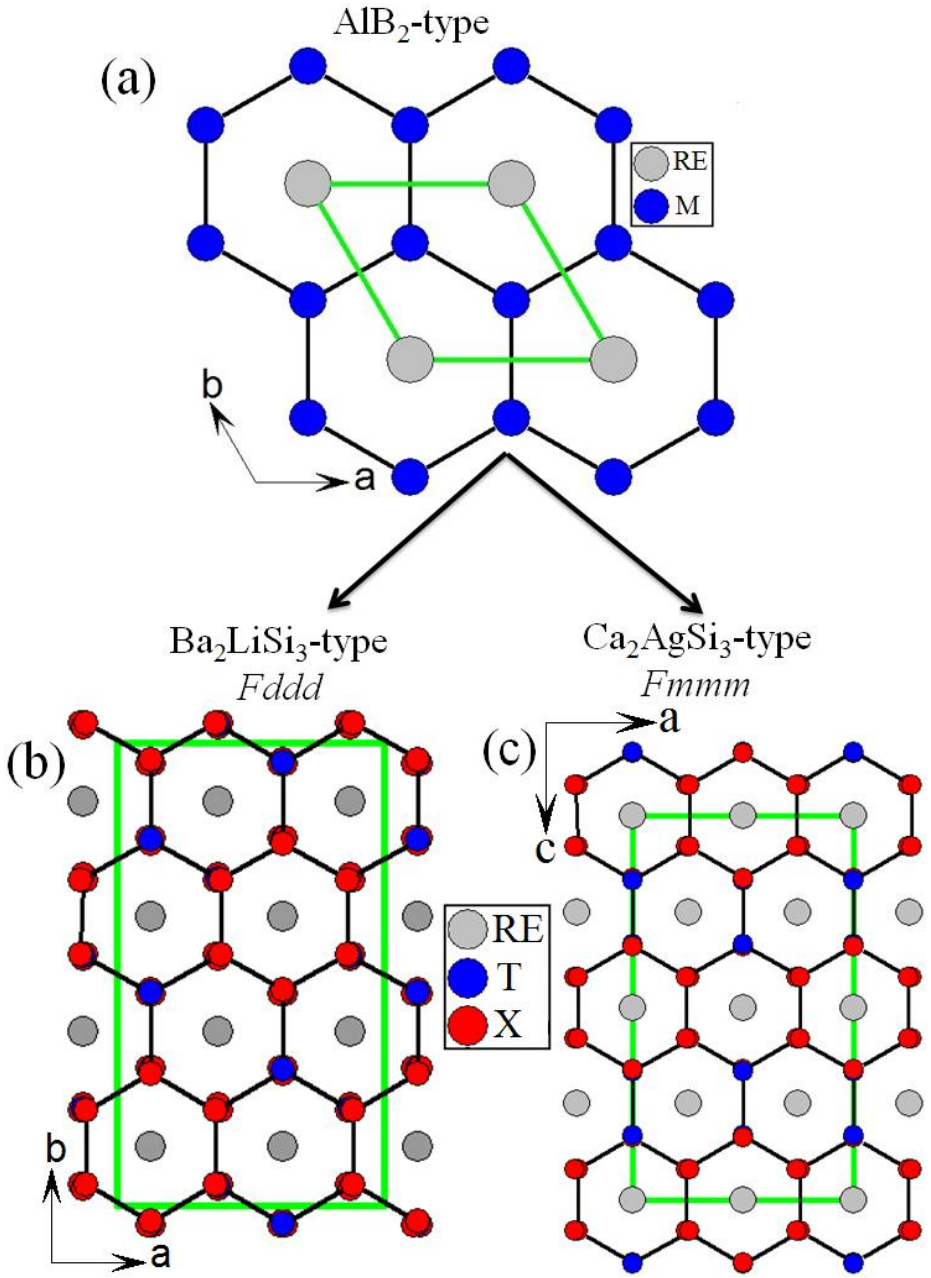

Figure 1.7. Crystal structure of (a) AlB_2 along the *c*-axis, (b) ordered Ba_2LiSi_3 along the *c*-axis and (c) ordered Ca_2AgSi_3 along the *b*-axis. The unit cell is outlined as solid green lines.

The crystal structure of disorder RE_2TX_3 (X = Si and Ge) crystallizing in the AlB_2 structure type in hexagonal crystal system with the space group of *P*6/*mmm*, shown along the *c*-direction in Figure 1.7a. *RE* atoms occupy the Al position while *T* and *X* atoms are

statistically distributed on the boron positions of the AlB_2 structures, respectively.[132] It resulted in the formation of the disorder RE_2TX_3 compounds. The hexagonal system is composed of infinite arrays of planar hexagonal [TX_3] units stacked along the [001] direction and the *RE* sites are sandwiched between these parallel hexagonal networks. The TX_3 layers in hexagonal AlB_2 phase where layers are planar. When *T* and *X* occupy in their own atomic positions, resulted in the formation of new ordered orthorhombic superstructures Ba_2LiSi_3[133] with the space group of *Fddd* (Figure 1.7b) and Ca_2AgSi_3[134] with the space group of *Fmmm* (Figure 1.7c).

1.5.4. YCu_6In_6 $CeMn_4Al_8$ Structures – Ordered superstructure of $ThMn_{12}$

The structural relation between $ThMn_{12}$, disordered RET_xX_{12-x}, ordered $CeMn_4Al_8$ and ordered YCu_6In_6 is shown in Figure 1.8. The compounds RET_xX_{12-x} (*X* = Al and In) crystallizes in the tetragonal $ThMn_{12}$ type and $CeMn_4Al_8$ crystallizes in ordered superstructure $ThMn_{12}$ type (space group *I*4/*mmm*). An interesting feature of $CeMn_4Al_8$ is that Mn and Al atoms are not distributed at random over the three atomic positions available for these elements in $ThMn_{12}$-type structure. By further substitution of Cu and In atoms in RET_4X_8 completely occupy the Mn and Al2 positions, respectively, in the $CeMn_4Al_8$ structure and Al1 position is occupied with both *T* (52%) and *X* (48%) atoms (denoted as *M*). This mixed position could be one of probable reasons for the enhanced distortions observed in the crystal structure of RET_4X_8 and resultant disorder (Figure 1.8a). The *RE* atoms occupy the 2*a* site of point symmetry (4/*mmm*), the *T* atom occupy the 8*f* site of point symmetry (2/*m*), the In atom occupy the 8*i* site of point symmetry (*m*2*m*) and 8*j* site occupied by mixture of *T* and *X* atoms of point symmetry (*m*2*m*).

RECu_6In_6 (*RE* = Y, Ce, Pr, Nd, Gd, Tb, Dy) also crystallizes in the tetragonal system (defined as YCu_6In_6 type structure) within space group *I*4/*mmm*.[135] The cigar-like shape of $Cu_{0.5}In_{0.5}$ positions resolved by the split model keeping inner square uniquely occupied by copper and an outer one uniquely occupied by indium atoms as shown in Figure 1.8b, it resultant forming a ordered srystal structure. Crystal structure of all these compounds is composed of pseudo Frank-Kasper cages made up of *T* and *X* atoms occupying one *RE* atom in each ring to form a stable structure. These pseudo Frank-Kasper cages are shared through the corner atoms (mostly transition metals) atoms along *ab*-plane resulted in a stable three dimensional network.

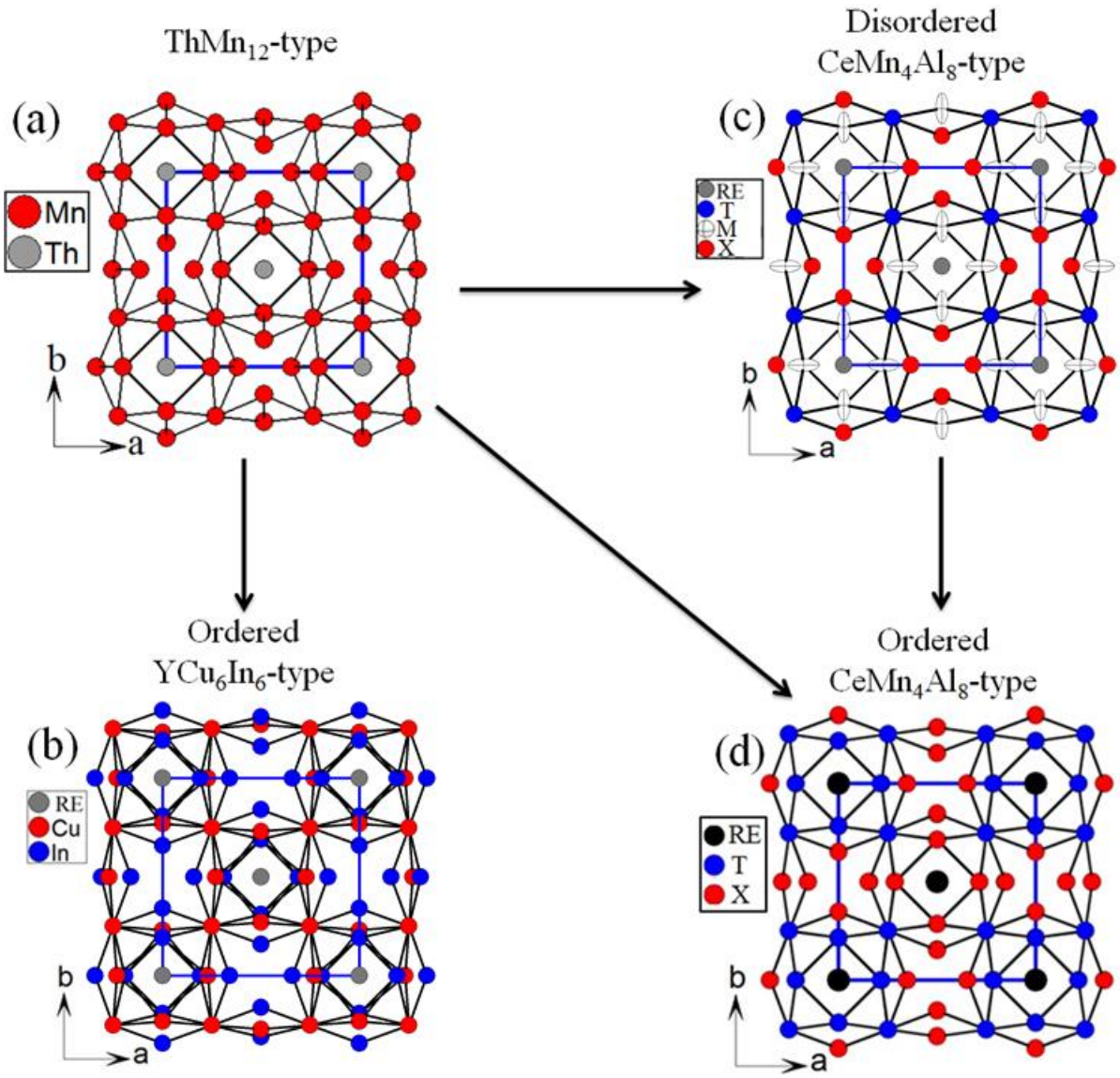

Figure 1.8. The relation between the crystal structures of (a) $ThMn_{12}$ type, (b) YCu_6In_6, (c) doisordred $CeMn_4Al_8$ and (d) ordered $CeMn_4Al_8$ viewed along the *c*-axis. The unit cell is outlined as solid blue lines. The cigar-like shape of $Cu_{0.5}In_{0.5}$ positions in YCu_6In_6 is resolved by the split model keeping inner square uniquely occupied by copper and an outer one uniquely occupied by indium atoms for order system. Mixed atomic positions (M) of *T* and *X* at 8*j* position in disorder $CeMn_4Al_8$ are elongated along the *b*-axis. *T* and *X* uniquely occupied for order system in $CeMn_4Al_8$ structure type.

1.5.5. La_2AlGe_6 – Ordered vacant variant of $SmNiGe_3$ Structure type

The crystal structure of RE_2TGe_6 was first determined from powder diffraction[136, 137] to be of Ce_2CuGe_6 type with the orthorhombic crystal system with the space group of *Amm*2 (Figure 1.9b). an disordered variant of the $SmNiGe_3$ structure type (Figure 1.9a),.[138] Later with detailed analysis Parthé et al. reported ordered RE_2TX_6 compounds are crystallizing

La_2AlGe_6 structure type in monoclinic crystal system with the space group of *C*2/*m* (Figure 1.9c).[139] The single crystal XRD refinement of RE_2TX_6 revealed a larger unit cell with doubled *a* and *b* lattice parameters, crystallizing in the La_2AlGe_6 structure (Figure 1.9c), which is the ordered derivative of the $SmNiGe_3$ type. On the other hand, La_2AlGe_6 structure can be defined as the vacant variant of the $SmNiGe_3$ type.

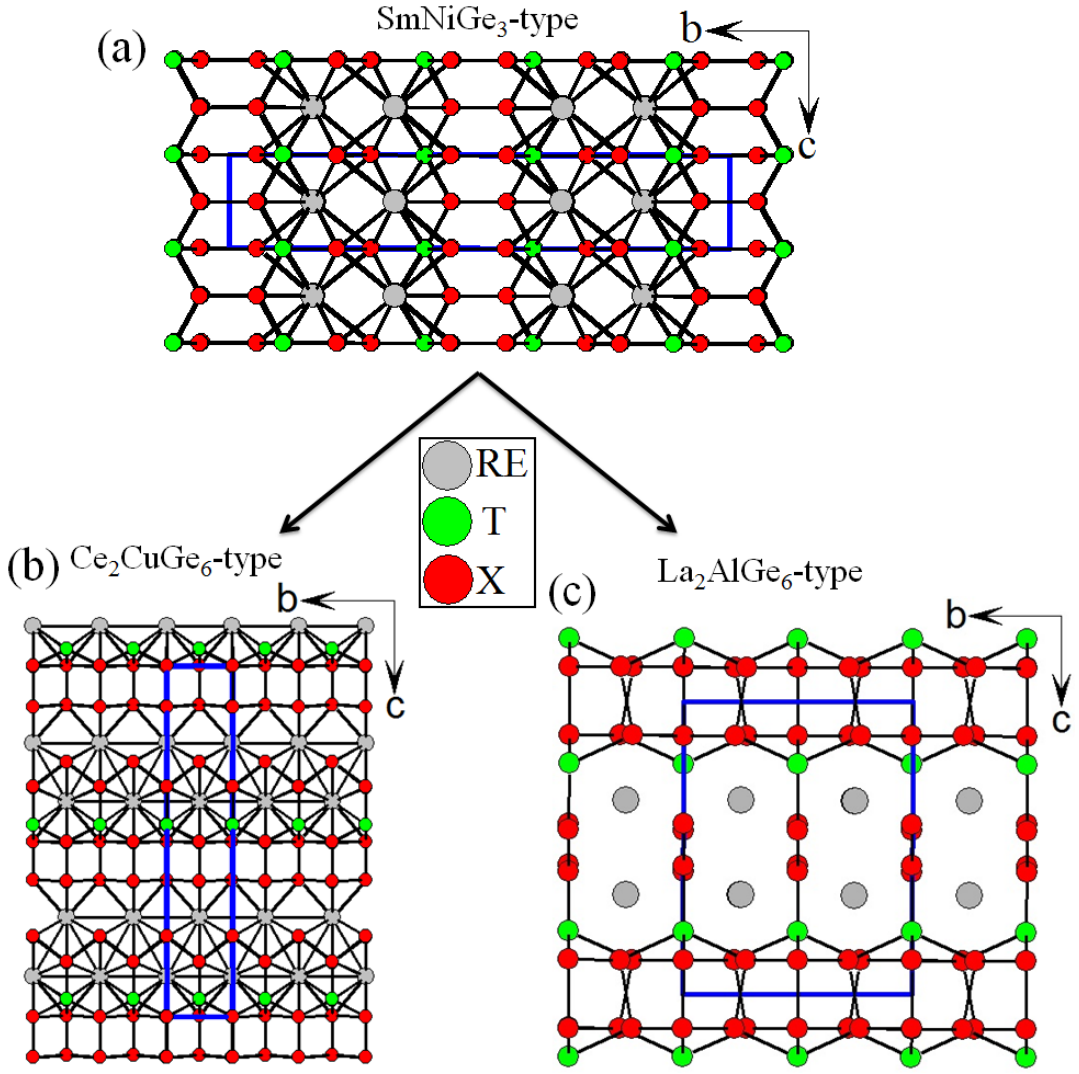

Figure 1.9. The relation between the crystal structures of (a) orthorhombic $SmNiGe_3$ type, (b) orthorhombic Ce_2CuGe_6 type and (c) monoclinic La_2AlGe_6 type, emphasized along the *a* axis. The unit cell is marked as solid blue lines.

There are seven crystallographically distinct atomic positions in the RE_2TX_6 structure – one for *RE*, one for *T* and five for the *X* atoms. The crystal structure of RE_2TX_6 is similar to that of $RETX_3$.[140] The difference between $MNiSi_3$ and RE_2TX_6 structures are in the nature and arrangement of the fragments. The crystal structure of RE_2TX_6 can be described as the

intergrowth of fragments *X* dimmers and zig–zag *X* chains. In RE_2TX_6, the *X* dimers are collinear with the *c*-axis direction compared to *b*-axis in the case of $RETX_3$ structure. These dimers in RE_2TX_6 are arranged side by side in a rectangular array which extends over the *ab*-plane.

1.6. Physical Properties of Intermetallics

During the last 3-4 decades, research in magnetic and transport properties have characterized by a boom in the field of *RE* based intermetallic compounds. Currently, *RE* intermetallics are in a prominent situation not only from a fundamental point of view but also for the large number of technological applications, in particular in the field of permanent magnets, superconductors, catalysis, etc. The properties of the intermetallics can be divided into two based on the classification of the compounds: *RE* based and transition metal based compounds.

RE based intermetallics play important role in a large range of current research fields, in particular those devoted to heavy fermions, valence fluctuations, Kondo lattices, magnetostrictive materials, permanent-magnet materials, spin glasses, random anisotropy systems, topological insulators, zero thermal expansion and so on. Within the series of the *RE*s, the *f* shells become progressively filled and most of the *RE* elements with partly filled 4*f* shells are in the trivalent state, with stable magnetic moments. However, there are exceptions among them (e.g. Ce, Sm, Eu or Yb). There exist two additional variables in the *RE* intermetallic compounds: namely, the variation of the interatomic distances, depending on the partner elements, and the environment of the *RE* and atoms inside the lattice. It is generally observed that the 4*f* electron states of the *RE* ions are hardly influenced when these elements are alloyed with a non-transition metal. Even in compounds with transition metals, like manganese, iron, cobalt or nickel, the influence on the 4*f* electron states is weak. So, most of the magnetic properties are originated from *RE*s. However the strong hybridization between the 4*f* orbitals of the *RE* and *d* orbitals of second and third row of the transition metals, particularly Ru, Pd, Rh, Ag, Os, Ir, Pt and Au can lead into unique electronic structure and interesting physical properties. The interesting example is the recently reported $EuIr_4In_2Ge_4$ with strong spin splitting described by the Dresselhaus term.[141] This was observed at both the conduction and valence band edges due to spin–orbit coupling among

the Ir atoms as well as lack of inversion symmetry, which is generated mainly from hybridization of the Ir 5*d* orbitals.[141]

A few other examples having different physical properties are spin density wave ordering observed in $ErPd_2Si_2$,[142] thermoelectricity behaviour in YNiSb,[143] topological insulating properties topological surface state, which can be lead into topological insulator observed in ,[144, 145] Kondo insulator observed in SmB_6,[144, 145] first-order phase transitions observed in$(Gd_{1-x}Y_x)Mn_2Ge_2$,[146] metamagnetic transitions in Lu_2Fe_{17},[147] high magnetic anisotropy in $SmFe_7$,[148] high magnetic moments and Curie temperature in YCo compounds,[149] high spin polarization in Tm*X* (*X* = Cu, Ag) and various semiconducting properties $R_3Cu_3Sb_4$ (*R* = Y, La, Ce, Pr, Nd, Sm, Gd, Tb, Dy, Ho, Er),[150] zero thermal exapnsion in RE_4TGe_8 (*RE* = Gd, Yb, *T* = Mn-Ni, Ag).[151-155] A physical property of intermetallic compounds mainly depends on the crystal structure. The parameters such as local structure, structural transition, defects, substitutions and disorder play key role in tuning the physical properties.[156-158] For example, $CeCuGa_3$ crystallize in both ordered are disordered structures within $CeAl_2Ga_2$ (space gorup *I*4/*mmm*) and $BaNiSn_3$ structure types (space group *I*4*mm*), respectively. The disordered structure in the single crystals of $CeCuGa_3$ exhibit a ferromagnetic ordering below 4 K with a strong anisotropy,[156, 157] while ordered $CeCuGa_3$ showed anti ferromagnetic ordering below 3 K.[158]

Among the *RE*s, Ce, Eu and Yb have particular scientific interest because they can exhibit two energetically similar electronic configurations: the magnetic $Ce^{3+}(4f^1)$, $Eu^{2+}(4f^6)$, $Yb^{3+}(4f^{13})$ and the nonmagnetic $Ce^{4+}(4f^0)$, $Eu^{3+}(4f^7)$, $Yb^{2+}(4f^{14})$ ones. Due to this feature many phenomena, such as intermediate valence, Kondo effect or heavy-fermion behaviour, are observed in Ce and Yb analogues. [159, 160 42] Yb is usually considered as the "*f*-hole" analogue of Ce. In this case, the roles of the 4*f* electron and 4*f* hole can be interchanged and resulted in unique properties. There are plenty non *RE* based intermetallics compounds are also well known for various other properties such as catalysis, [161] sensors,[162] hydrogen storage,[163, 164] and shape memory etc.[165, 166]

It is worth to metion that the magnetic and catalytic properties of these materials mostly depend on the size and morphology of the particles. For example, the polycrystalline $YbAl_3$ has been reported with intermediate valence of Yb.[159] However, the valency of of Yb changes from trivalent to divalent when the particle size reduces.[167] In this compound the

valence of Yb changes from 3+ to 2+ with decrease in grain size. Such a reduction leads to the existence of a large number of Yb^{2+} atoms at the surface with respect to the bulk affecting the overall electronic state and reduction in the magnetic moment.

The diversity of chemical and physical properties of intermetallics renders as attractive materials not only for exploring fundamental aspects of matter but also raises interest for the versatile modern technological applications. The electronic ground state can be tuned or modified by making them in complex structures. For example, several intermetallic compounds contain group 13 and/or group 14 elements as one of the constituents. The key tool in the rational design of intermetallic compounds is the knowledge and control of the properties, and whether they are dominated by intrinsic factors (e.g. electronic structure and anisotropic properties) or by extrinsic factors (e.g. structural order, phase dynamics). These two parameters become complicated but more interesting when these classes of materials are made up of constituents with diverse chemical characteristics.

1.7. Applications of Intermetallic Compounds

Intermetallic compounds have been widely used for many technological applications in various fields including industrial, medical, consumer, and military products etc. One classical example is Nb_3Sn, which shows superconductivity at 18 K and used in NMR spectrometer.[168, 169] The compounds REX_5 (*RE* = La, Ce, Ne, Pr; *T* = Ni, Co, Mn, Al) intermetallic compounds have been used for hydrogen storage,[170] Nitinol (NiTi) has been using as shape memory alloys and[171] $SmCo_5$ is the one of the best example for permanent magnetism.[172] Intermetallic compounds also being used as aircraft engines due to the ability to withstand at high temperatures have the promise of higher strength and elastic stiffness while hot condition. $MoSi_2$ is a classic example used in wide range of applications such as turbine hardware, vanes, combustor liners, flame holders, diesel engine glow plugs, ignites, electronic devices, heating elements, glass melting and energy conversion devices.[173]

Nano intermetallic compounds also have been used in various applications with a particular focus in electrochemical conversion of chemical energy and catalysis.[174] A few notable technological applications of these materials recently developed tin and tin-based intermetallics being used in Li ion battery,[174] amorphous and nanocrystalline FeTi intermetallic compound are known in field of hydrogen storage,[163, 164] Pd_5Ge, Pd_2Ge reported as catalysts for oxidative acetoxylation,[175, 176] PdGa reported for highly selective semi

hydrogenation catalysts,[177] $AuAl_2$ used as sensors,[162] AuCu nano wires used for glucose detection[178, 179] and Pt*X* (*X* = Bi, Pb, Pd, Ru) reported in fuel cell applications as electrode materials.[180]

1.8. Objectives of the Thesis

In concise, the main objective of this thesis is the continued development of the novel ordered intermetallic compounds based on rare earths and transition metals with diverse crystals structures and interesting physical properties [19, 20] A particular focus in *RE* based compounds is given to Sm, Eu and Yb as they are known to exhibit multiple oxidations states, which may lead into new structure types and interesting physical properties. Sine only 5% of the compounds have been discovered among 100,000 possible combinations of the ternary compounds, the thesis mainly focussed to discover novel ternary compounds with some exceptions to binary and quaternary. The synthesis and crystal growth of novel compounds have been designed with the help of metal flux technique. The other main objective of the thesis is to develop ordered compounds of known disordered materials by using different synthetic strategies to understand the changes in the structure and related physical properties. The compositions of the novel system are aimed with the help of single crystal XRD and EDAX studies. After establishing the crystal structure of unknown (novel) compounds with the help of high quality single crystal data, the yield of the compounds will be scaled up with the help of traditional and conventional technique. The structural relations between disordered, ordered and superstructure are discussed using advanced crystallographic tool. Since the thesis aimed in the synthesis of mixed valent *RE*s, the oxidation state of these are studied by XANES measurements using the various synchtrotron beamline facilities at PETRA III, DESY and APS in ANL. The other focus of the thesis is to study the physical properties of the interesting systems and establishing structure property relationship. Finally, the other important objective of the thesis is to develop ordered compounds in nanodimension for their application in catalysis and electrochemical energy conversion. The focus also extends in discussion with the variation of the chemical properties associated with the size reduction, which may find applications towards future technologies.

1.9. References

1. DiSalvo, F. J., *Solid State Commun.* **1997,** *102,* 79-85.

2. Sun, S. H.; Murray, C. B.; Weller, D.; Folks, L.; Moser, A., *Science* **2000,** *287*, 1989-1992.

3. Sun, S. H.; Anders, S.; Thomson, T.; Baglin, J. E. E.; Toney, M. F.; Hamann, H. F.; Murray, C. B.; Terris, B. D., *J. Phys. Chem. B* **2003,** *107*, 5419-5425.

4. Cava, R. J.; Takagi, H.; Batlogg, B.; Zandbergen, H. W.; Krajewski, J. J.; Peck, W. F.; Vandover, R. B.; Felder, R. J.; Siegrist, T.; Mizuhashi, K.; Lee, J. O.; Eisaki, H.; Carter, S. A.; Uchida, S., *Nature* **1994,** *367*, 146-148.

5. He, T.; Huang, Q.; Ramirez, A. P.; Wang, Y.; Regan, K. A.; Rogado, N.; Hayward, M. A.; Haas, M. K.; Slusky, J. S.; Inumara, K.; Zandbergen, H. W.; Ong, N. P.; Cava, R. J., *Nature* **2001,** *411*, 54-56.

6. Van daal, H. J.; Buschow, K. H., *Phys. Status Solidi A* **1970,** *3*, 853-871.

7. Adroja, D. T.; Malik, S. K., *J. Magn. Magn. Mater.* **1991,** *100*, 126-138.

8. Francisco, M. C.; Malliakas, C. D.; Piccoli, P. M. B.; Gutmann, M. J.; Schultz, A. J.; Kanatzidis, M. G., *J. Am. Chem. Soc.* **2010,** *132*, 8998-9006.

9. Szytula, A., *Phys. Scripta* **1993,** *T49*, 284-288.

10. Singh, N. K.; Pecharsky, V. K.; Gschneidner, K. A., *Phys. Rev. B* **2008,** *77*, 054414-054424.

11. Ullakko, K.; Huang, J. K.; Kantner, C.; OHandley, R. C.; Kokorin, V. V., *Appl. Phys. Lett.* **1996,** *69*, 1966-1968.

12. Kamakoti, P.; Sholl, D. S., *J. Membrane Sci.* **2003,** *225*, 145-154.

13. Liu, C. T., *Mater. Chem. Phys.* **1995,** *42*, 77-86.

14. Xu, Y.; Ruban, A. V.; Mavrikakis, M., *J. Am. Chem. Soc.* **2004,** *126*, 4717-4725.

15. Sauthoff, G., *Intermetallics*. Wiley: New York, 1995.

16. Cahn, R. W., *Contemp. Phys.* **2001,** *42*, 365-375.

17. Bauer, E., *Adv. Phys.* **1991,** *40*, 417-534.

18. Wachter, P., *Handbook on the Physics and Chemistry of Rare Earths*. Elsevier Science: Amsterdam, 1994; p 177.

19. Matsumoto, Y.; Nakatsuji, S.; Kuga, K.; Karaki, Y.; Horie, N.; Shimura, Y.; Sakakibara, T.; Nevidomskyy, A. H.; Coleman, P., *Science* **2011,** *331*, 316-319.

20. Ernst, S.; Kirchner, S.; Krellner, C.; Geibel, C.; Zwicknagl, G.; Steglich, F.; Wirth, S., *Nature* **2011,** *474*, 362-366.

21. Stockert, O.; Arndt, J.; Faulhaber, E.; Geibel, C.; Jeevan, H. S.; Kirchner, S.; Loewenhaupt, M.; Schmalzl, K.; Schmidt, W.; Si, Q.; Steglich, F., *Nat. Phys.* **2011,** *7*, 119-124.

22. Peter, S. C.; Chondroudi, M.; Malliakas, C. D.; Balasubramanian, M.; Kanatzidis, M. G., *J. Am. Chem. Soc.* **2011,** *133*, 13840-13843.

23. Kindler, B.; Finsterbusch, D.; Graf, R.; Ritter, F.; Assmus, W.; Luthi, B., *Phys. Rev. B* **1994,** *50*, 704-707.

24. Khmelevskyi, S., *Phys. Rev. B* **2012,** *86*, 104429-104434.

25. Johrendt, D.; Kotzyba, G.; Trill, H.; Mosel, B. D.; Eckert, H.; Fickenscher, T.; Pöttgen, R., *J. Solid State Chem.* **2002,** *164*, 201-209.

26. Taylor, K. N. R., *Adv. Phys.* **1971,** *20*, 551-555.

27. Wallace, W. E., Rare earth intermetallics. In *academic Press*, academic Press: New York, 1973.

28. Buschow, K. H. J., *Rep. Prog. Phys.* **1979,** *42*, 1373-1378.

29. Buschow, K. H. J., *Rep. Prog. Phys.* **1977,** *40*, 1179-1184.

30. Iandelli, A.; Palenzona, A., *Handbook on the Physics and Chemistry of Rare Earths*. North-Holland, Amsterdam, 1979; Vol. 2.

31. SAINT 6.02; Bruker AXS Inc.: Madison, Wisconsin, USA, 2000.

32. Peter, S. C.; Disseler, S. M.; Svensson, J. N.; Carretta, P.; Graf, M. J., *J. Alloy Compd.* **2012,** *516*, 126-133.

33. Peter, S. C.; Kanatzidis, M. G., *J. Solid State Chem.* **2010,** *183*, 878-882.

34. Zhuravleva, M. A.; Bilc, D.; Pcionek, R. J.; Mahanti, S. D.; Kanatzidis, M. G., *Inorg. Chem.* **2005,** *44*, 2177-2188.

35. Stockert, O.; Arndt, J.; Faulhaber, E.; Geibel, C.; Jeevan, H. S.; Kirchner, S.; Loewenhaupt, M.; Schmalzl, K.; Schmidt, W.; Si, Q.; Steglich, F., *Nat. Phys.* **2011,** *7*, 119-124.

36. Chondroudi, M.; Balasubramanian, M.; Welp, U.; Kwok, W. K.; Kanatzidis, M. G., *Chem. Mater.* **2007,** *19*, 4769-4775.

37. Peter, S. C.; Salvador, J.; Martin, J. B.; Kanatzidis, M. G., *Inorg. Chem.* **2010,** *49*, 10468-10474.

38. Zhuravleva, M. A.; Kanatzidis, M. G., *J. Solid State Chem.* **2003,** *173*, 280-292.

39. Tran, V. H.; Miller, W.; Kowalczyk, A.; Tolinski, T.; Chelkowska, G., *J. Phys-Condens Mat.* **2006,** *18*, 10353-10363.

40. Patil, S.; Nagarajan, R.; Gupta, L. C.; Vijayaraghavan, R.; Padalia, B. D., *Solid State Commun.* **1987,** *63*, 955-958.

41. Chondroudi, M.; Balasubramanian, M.; Welp, U.; Kwok, W. K.; Kanatzidis, M. G., *Chem. Mater.* **2007,** *19*, 4769-4775.

42. Gegenwart, P.; Tokiwa, Y.; Westerkamp, T.; Weickert, F.; Custers, J.; Ferstl, J.; Krellner, C.; Geibel, C.; Kerschl, P.; Muller, K. H.; Steglich, F., *New J. Phys.* **2006,** *8*, 1-12.

43. Cao, C. D.; Klingeler, R.; Leps, N.; Vinzelberg, H.; Kataev, V.; Muranyi, F.; Tristan, N.; Teresiak, A.; Zhou, S. Q.; Loser, W.; Behr, G.; Buchner, B., *Phys. Rev. B* **2008,** *78*.

44. Venturini, G.; Elidrissi, B. C.; Ressouche, E.; Malaman, B., *J. Alloy Compd.* **1995,** *216*, 243-250.

45. Sakai, H.; Tokunaga, Y.; Fujimoto, T.; Kambe, S.; Walstedt, R. E.; Yasuoka, H.; Aoki, D.; Homma, Y.; Yamamoto, E.; Nakamura, A.; Shiokawa, Y.; Nakajima, K.; Arai, Y.; Matsuda, T. D.; Haga, Y.; Onuki, Y., *Physica B* **2006,** *378-80*, 1005-1006.

46. Disseler, S. M.; Svensson, J. N.; Peter, S. C.; Byers, C. P.; Baines, C.; Amato, A.; Giblin, S. R.; Carretta, P.; Graf, M. J., *Phys. Rev. B* **2011,** *84*.

47. Lawrence, J. M.; Riseborough, P. S.; Park, R. D., *Rep. Prog. Phys.* **1981,** *44*, 1-84.

48. Fisk, Z.; Hess, D. W.; Pethick, C. J.; Pines, D.; Smith, J. L.; Thompson, J. D.; Willis, J. O., *Science* **1988,** *239*, 33-42.

49. Pöttgen, R.; Gulden, T.; Simon, A., **1999,** *43*, 133.

50. Andraka, B.; Pietri, R.; Kaczorowski, D.; Leithe-Jasper, A.; Rogl, P., *J. Appl. Phys.* **2000,** *87*, 5149-5151.

51. Pöttgen, R.; Lang, A.; Hoffmann, R. D.; Kunnen, B.; Kotzyba, G.; Mullmann, R.; Mosel, B. D.; Rosenhahn, C., *Z. Kristallogr.* **1999,** *214*, 143-150.

52. Corbett, J. D., *Inorg. Synth.* **1983,** *22*, 15-22.

53. Kußmann, D.; Hoffmann, R. D.; Pöttgen, R., *Z. Anorg. Allg. Chem.* **1998,** *624*, 1727-1735.

54. von Schnering, H. G.; Hönle, W., *Phosphides: solid state chemistry, in: Encyclopedia of Inorganic Chemistry*. Wiley: London, 1994.

55. Wenski, G.; Mewis, A., *Z. Kristallogr.* **1986,** *176*, 125-129.

56. Sarkar, S.; Peter, S. C., *J. Chem. Sci.* **2012,** *124*, 1385-1390.

57. Kanatzidis, M. G.; Pöttgen, R.; Jeitschko, W., *Angew. Chem. Int. Edit.* **2005,** *44*, 6996-7023.

58. Peter, S. C.; Sarkar, S.; Kanatzidis, M. G., *Inorg. Chem.* **2012,** *51*, 10793-10799.

59. Peter, S. C.; Rayaprol, S.; Francisco, M. C.; Kanatzidis, M. G., *Eur. J. Inorg. Chem.* **2011**, 3963-3968.

60. Peter, S. C.; Malliakas, C. D.; Kanatzidis, M. G., *Inorg. Chem.* **2013,** *52*, 4909-4915.

61. Peter, S. C.; Kanatzidis, M. G., *Z. Anorg. Allg. Chem.* **2012,** *638*, 287-293.

62. Chondroudi, M.; Peter, S. C.; Malliakas, C. D.; Balasubramanian, M.; Li, Q. A.; Kanatzidis, M. G., *Inorg. Chem.* **2011,** *50*, 1184-1193.

63. Peter, S. C.; Chondroudi, M.; Malliakas, C. D.; Balasubramanian, M.; Kanatzidis, M. G., *J. Am. Chem. Soc.* **2011,** *133*, 13840-13843.

64. Peter, S. C.; Kanatzidis, M. G., *J. Solid State Chem.* **2010,** *183*, 2077-2081.

65. Chen, X. Z.; Sportouch, S.; Sieve, B.; Brazis, P.; Kannewurf, C. R.; Cowen, J. A.; Patschke, R.; Kanatzidis, M. G., *Chem. Mater.* **1998,** *10*, 3202-3211.

66. B. Sieve; X. Z. Chen; R. Henning; P. Brazis; C. R. Kannewurf; J. A. Cowen; A. J. Schultz; Kanatzidis, M. G., *J. Am. Chem. Soc.* **2001,** *123*, 7040.

67. Chen, X. Z.; Larson, P.; Sportouch, S.; Brazis, P.; Mahanti, S. D.; Kannewurf, C. R.; Kanatzidis, M. G., *Chem. Mater.* **1999,** *11*, 75-83.

68. Zhuravleva, M. A.; Kanatzidis, M. G., *Z. Naturforch B : Sec. B* **2003,** *58*, 649-657.

69. Zhuravleva, M. A.; Pcionek, R. J.; Wang, X. P.; Schultz, A. J.; Kanatzidis, M. G., *Inorg. Chem.* **2003,** *42*, 6412-6424.

70. Zhuravleva, M. A.; Evain, M.; Petricek, V.; Kanatzidis, M. G., *J. Am. Chem. Soc.* **2007,** *129*, 3082-3083.

71. Chen, X. Z.; Small, P.; Sportouch, S.; Zhuravleva, M.; Brazis, P.; Kannewurf, C. R.; Kanatzidis, M. G., *Chem. Mater.* **2000,** *12*, 2520-2522.

72. Latturner, S. E.; Bilc, D.; Mahanti, S. D.; Kanatzidis, M. G., *Inorg. Chem.* **2003,** *42*, 7959-7966.

73. Wu, X. U.; Latturner, S. E.; Kanatzidis, M. G., *Inorg. Chem.* **2006,** *45*, 5358-5366.

74. Latturner, S. E.; Kanatzidis, M. G., *Inorg. Chem.* **2008,** *47*, 2089-2097.

75. Latturner, S. E.; Bilc, D.; Mahanti, S. D.; Kanatzidis, M. G., *Chem. Mater.* **2002,** *14*, 1695-1705.

76. Salvador, J. R.; Gour, J. R.; Bilc, D.; Mahanti, S. D.; Kanatzidis, M. G., *Inorg. Chem.* **2004,** *43*, 1403-1410.

77. Salvador, J. R.; Bilc, D.; Gour, J. R.; Mahanti, S. D.; Kanatzidis, M. G., *Inorg. Chem.* **2005,** *44*, 8670-8679

78. Salvador, J. R.; Kanatzidis, M. G., *Inorg. Chem.* **2006,** *45*, 7091-7099.

79. Chondroudi, M.; Balasubramanian, M.; Welp, U.; Kwok, W.-K.; Kanatzidis, M. G., *Chem. Mater.* **2007,** *19*, 4769-4775.

80. Salvador, J. R.; Hoang, K.; Mahanti, S. D.; Kanatzidis, M. G., *Inorg. Chem.* **2007,** *46*, 6933

81. Kanatzidis, M. G.; Pöttgen, R.; Jeitschko, W., *Angew. Chem. Int. Edit.* **2005,** *44*, 6996-7023.

82. Canfield, P. C.; Fisk, Z., *Z. Philos. Mag. B* **1992,** *65*, 1117-1123.

83. Bud'ko, S. l.; Islam, Z.; Wiener, T. A.; Fisher, I. R.; Lacerda, A. H.; Canfield, P. C., *J. Magn. Magn. Mater.* **1999,** *205*, 53-78.

84. Fisher, I. R.; Islam, Z.; Canfield, P. C., *J. Magn. Magn. Mater.* **1999,** *202*, 1-10.

85. Nicklas, M.; Sidorov, V. A.; Borges, H. A.; Pagliuso, P. G.; Petrovic, C.; Fisk, Z.; Sarrao, J. L.; Thompson, a. J. D., *Phys. Rev. B* **2004,** *67*, 020506.

86. Hundley, M. F.; Sarrao, J. L.; Thompson, J. D.; Movshovich, R.; Jaime, M.; Petrovic, C.; Fisk, a. Z., *Phys. Rev. B* **2001,** *65*, 024401.

87. Macaluso, R. T.; Sarrao, J. L.; Moreno, N. O.; Pagliuso, P. G.; Thompson, J. D.; Fronczek, F. R.; Hundley, M. F.; Malinowski, A.; Chan, J. Y., *Chem. Mater.* **2003,** *15*, 1394-1398.

88. Bailey, M. S.; McCuire, M. A.; DiSalvo, a. F. J., *J. Solid Sate Chem.* **2005,** *178*, 3494-3499.

89. Benbow, E. M.; Latturner, S. E., *Inorg. Chem.* **2006,** *179*, 3989-3996.

90. Klunter, W.; Jung, W., *J. Solid Sate Chem.* **2006,** *179*, 2880-2888.

91. Lukachuk, M.; Galadzhun, Y. V.; Zaremba, R. I.; Dzevenko, M. V.; Kalychak, Y. M.; Zaremba, V. I.; Rodewald, U. C.; Pöttgen, R., *J. Solid State Chem.* **2005,** *178*, 2724-2733.

92. Macaluso, R. T.; Sarrao, J. L.; Pagliuso, P. G.; Moreno, N. O.; Goodrich, R. G.; Browne, D. A.; Fronczek, F. R.; Chan, J. Y., *J. Solid Sate Chem.* **2002,** *166*, 245-250.

93. Zaremba, V. I.; Dubenskiy, V. P.; Rodewald, U. C.; Heying, B.; Pöttgen, R., *J. Solid State Chem.* **2006,** *179*, 891-897.

94. Niemann, S.; Jeitschko, W., *Z. Metallkd.* **1994,** *85*, 345-349.

95. Zhuravleva, M. A.; Kanatzidis, M. G., *Z. Naturforsch B* **2003,** *58*, 649-657.

96. Zaremba, V. I.; Kalychak, Y. M.; Dubenskiy, V. P.; Hoffmann, R. D.; Rodewald, U. C.; Pöttgen, R., *J. Solid State Chem.* **2002,** *169*, 118-124.

97. Salvador, J. R.; Gour, J. R.; Bilc, D.; Mahanti, S. D.; Kanatzidis, M. G., *Inorg. Chem.* **2004,** *43*, 1403-1410.

98. Vennos, D. A.; Badding, M. E.; Disalvo, F. J., *J. Less-Common Met.* **1991,** *175*, 339-346.

99. Reehuis, M.; Jeitschko, W.; Moller, M. H.; Brown, P. J., *J. Phys. Chem. Solids* **1992,** *53*, 687-690.

100. Kanatzidis, M. G.; Pöttgen, R.; Jeitschko, W., *Angew. Chem. Int. Ed.* **2005,** *44*, 6996-7023.

101. Salvador, J. R.; Gu, F.; Hogan, T.; Kanatzidis, M. G., *Nature* **2003,** *425*, 702-705.

102. Peter, S. C.; Malliakas, C. D.; Chondroudi, M.; Schellenberg, I.; Rayaprol, S.; Höffmann, R. D.; Pöttgen, R.; Kanatzidis, M. G., *Inorg. Chem.* **2010,** *49*, 9574-9580.

103. Peter, S. C.; Sarkar, S.; Kanatzidis, M. G., *Inorg. Chem.* **2012,** *51*, 10793-10799.

104. Peter, S. C.; Chondroudi, M.; Malliakas, C. D.; Balasubramanian, M.; Kanatzidis, M. G., *J. Am. Chem. Soc.* **2011,** *133*, 13840-13843.

105. Peter, S. C.; Malliakas, C. D.; Nakotte, H.; Kothapilli, K.; Rayaprol, S.; Schultz, A. J.; Kanatzidis, M. G., *J. Solid State Chem.* **2012,** *187*, 200-207.

106. Peter, S. C.; Rayaprol, S.; Francisco, M. C.; Kanatzidis, M. G., *Eur. J. Inorg. Chem.* **2011**, 3963-3968.

107. Stein, A.; Keller, S. W.; Mallouk, T. E., *Science* **1993,** *259*, 1558-1564.

108. Leonard, B. M.; Bhuvanesh, N. S. P.; Schaak, R. E., *J. Am. Chem. Soc.* **2005,** *127*, 7326-7327.

109. Kurihara, L. K.; Chow, G. M.; Schoen, P. E., *Nanostruct. Mater.* **1995,** *5*, 607-613.

110. Schaak, R. E.; Sra, A. K.; Leonard, B. M.; Cable, R. E.; Bauer, J. C.; Han, Y. F.; Means, J.; Teizer, W.; Vasquez, Y.; Funck, E. S., *J. Am. Chem. Soc.* **2005,** *127*, 3506-3515.

111. Murray, C. B.; Kagan, C. R.; Bawendi, M. G., *Annu. Rev. Mater. Sci.* **2000,** *30*, 545-610.

112. Sun, Y. G.; Mayers, B.; Herricks, T.; Xia, Y. N., *Nano Lett.* **2003,** *3*, 955-960.

113. Ullah, M.; Ali, M. E.; Abd Hamid, S. B., *Curr. Nanosci.* **2014,** *10*, 344-354.

114. Ivanov, E.; Grigorieva, T.; Golubkova, G.; Boldyriev, V.; Fasman, A. B., *Mater. Lett.* **1988,** *1*, 51-55.

115. Zhou, G. F.; Bakker, H., *J. Phys-Condens Mat.* **1994,** *6*, 4043-4052.

116. Davis, R. M.; McDermott, B.; Koch, C. C., *Metall. Trans. A* **1988,** *19*, 2867-2869.

117. Fachinformationszentrum Karlsruhe GmbH Inorganic Crystal Structure Database. In Eggenstein-Leopoldshafen, Germany, 2012.

118. Villars, P.; Cenzual, K., Pearson's Crystal Data - Crystal Structure Database for Inorganic Compounds. In ASM International, M. P., Ed. Ohio, USA, 2010-11.

119. Solokha, P.; De Negri, S.; Skrobanska, M.; Saccone, A.; Pavlyuk, V.; Proserpio, D. M., *Inorg. Chem.* **2012,** *51*, 207-214.

120. Treadwell, L. J.; Watkins-Curry, P.; McAlpin, J. D.; Rebar, D. J.; Hebert, J. K.; DiTusa, J. F.; Chan, J. Y., *Inorg. Chem.* **2015,** *54*, 963-968.

121. Sarkar, S.; Peter, S. C., *Inorg. Chem.* **2013,** *52*, 9741-9748.

122. Gumeniuk, R.; Akselrud, L.; Kvashnina, K. O.; Schnelle, W.; Tsirlin, A. A.; Curfs, C.; Rosner, H.; Schoneich, M.; Burkhardt, U.; Schwarz, U.; Grin, Y.; Leithe-Jasper, A., *Dalton T.* **2012,** *41*, 6299-6309.

123. Sarkar, S.; Gutmann, M. J.; Peter, S. C., *Dalton T.* **2014,** *43*, 15879-15886.

124. Zhang, X.; Yi, W.; Feng, K.; Wu, D. S.; Yang, Y. F.; Zheng, P.; Yao, J. Y.; Matsushita, Y.; Sato, A.; Jiang, H. W.; Wang, H.; Shi, Y. G.; Yamaura, K.; Wang, N. L., *Inorg. Chem.* **2014,** *53*, 4387-4393.

125. Sarkar, S.; Balisetty, L.; Shanbogh, P. P.; Peter, S. C., *J. Catal.* **2014,** *318*, 143-150.

126. Dai, X. D.; Kong, Y.; Li, J. H.; Liu, B. X., *J. Phys-Condens Mat.* **2006,** *18*, 4527-4542.

127. Ning, Y. T.; Zhou, X. M., *J. Alloy Compd.* **1992,** *182*, 131-144.

128. Hoffmann, R. D.; Pöttgen, R., *Z. Kristallogr.* **2001,** *216*, 127-145.

129. Dörrscheidt, W.; Schäfer, H., *J. Less-Common Met.* **1978,** *58*, 209-216.

130. Andress, K. R.; Alberti, E., *Z. Metallkd.* **1935,** *27*, 126-128.

131. Zarechnyuk, O. S.; Krypyakevych, P. I.; Gladyshevskii, E. I., *Sov. Phys. Crystallogr.* **1965,** *9*, 706-708.

132. Chevalier, B.; Pöttgen, R.; Darriet, B.; Gravereau, P.; Etourneau, J., *J. Alloy Compd.* **1996,** *233*, 150-160.

133. vonSchnering, H. G.; Bolle, U.; Curda, J.; Peters, K.; CarrilloCabrera, W.; Somer, M.; Schultheiss, M.; Wedig, U., *Angew. Chem. Int. Edit.* **1996,** *35*, 984-986.

134. Gil, R. C.; Carrillo-Cabrera, W.; Schultheiss, M.; Peters, K.; von Schnering, H. G.; Grin, Y., *Z. Anorg. Allg. Chem.* **1999,** *625*, 285-293.

135. Zaremba, R.; Muts, I.; Hoffmann, R. D.; Kalychak, Y. M.; Zaremba, V. I.; Pöttgen, R., *J. Solid State Chem.* **2007,** *180*, 2534-2540.

136. Konyk, M. B.; Romaka, L. P.; Gorelenko, Y. K.; Bodak, O. I., *J. Alloy Compd.* **2000,** *311*, 120-123.

137. Salamakha, P. S.; Konyk, M. B.; Dzyanyi, R.; Sologub, O. L.; Bodak, O. I., *Pol J. Chem.* **1996,** *70*, 270-274.

138. Bodak, O. I.; Pecharsky, V. K.; Mruz, O. Y.; Zavodnik, V. E.; Vitvitskaya, G. M.; Salamakha, P. S., *Dopov. Akad. Nauk Ukr. RSR (Ser. B)* **1985,** *2*, 36-38.

139. Zhao, J. T.; Cenzual, K.; Parthé, E., *Acta Crystallogr. C* **1991,** *47*, 1777-1781.

140. Chen, X. Z.; Small, P.; Sportouch, S.; Zhuravleva, M.; Brazis, P.; Kannewurf, C. R.; Kanatzidis, M. G., *Chem. Mater.* **2000,** *12*, 2520-2522.

141. Calta, N. P.; Im, J.; Rodriguez, A. P.; Fang, L.; Bugaris, D. E.; Chasapis, T. C.; Freeman, A. J.; Kanatzidis, M. G., *Angew. Chem. Int. Edit.* **2015,** *54*, 9186-+.

142. Li, H. F.; Cao, C. D.; Wildes, A.; Schmidt, W.; Schmalzl, K.; Hou, B. Y.; Regnault, L. P.; Zhang, C.; Meuffels, P.; Loser, W.; Roth, G., *Sci. Rep-Uk* **2015,** *5*, 7968-7975.

143. Larson, P.; Mahanti, S. D.; Sportouch, S.; Kanatzidis, M. G., *Phys. Rev. B* **1999,** *59*, 15660-15668.

144. Kim, D. J.; Xia, J.; Fisk, Z., *Nature Mater.* **2014**, doi:10.1038/ncomms3991.

145. Neupane, M.; Alidoust, N.; Xu, S. Y.; Kondo, T.; Ishida, Y.; Kim, D. J.; Liu, C.; Belopolski, I.; Jo, Y. J.; Chang, T. R.; Jeng, H. T.; Durakiewicz, T.; Balicas, L.; Lin, H.; Bansil, A.; Shin, S.; Fisk, Z.; Hasan, M. Z., *Nat. Commun.* **2013,** *4*, 1-7.

146. Sokolov, A. Y.; Guo, G. H.; Granovskii, S. A.; Levitin, R. Z.; Wada, H.; Shiga, M.; Goto, T., *J. Exp. Theor. Phys.* **1999,** *89*, 723-733.

147. Tereshina, E. A.; Andreev, A. V., *Intermetallics* **2010,** *18*, 1205-1210.

148. Samata, H.; Fujiwara, N.; Nagata, Y.; Uchida, T.; Lan, M. D., *Jpn. J. Appl. Phys. 1* **1998,** *37*, 3290-3294.

149. Kashyap, A.; Skomski, R.; Sabiryanov, R. F.; Jaswal, S. S.; Sellmyer, D. J., *Ieee T. Magn.* **2003,** *39*, 2908-2910.

150. Skolozdra, R. V.; Salamakha, P. S.; Ganzyuk, A. L.; Bodak, O. I., *Inorg. Mater.* **1993,** *29*, 26-29.

151. Singh, D. K.; Thamizhavel, A.; Chang, S.; Lynn, J. W.; Joshi, D. A.; Dhar, S. K.; Chi, S., *Phys. Rev. B* **2011,** *84*, 052401-052409.

152. Zlatic, V.; Monnier, R., *Phys. Rev. B* **2005,** *71*, 165109-165117.

153. Martin, K. N.; de Groot, P. A. J.; Rainford, B. D.; Wang, K.; Bowden, G. J.; Zimmermann, J. P.; Fangohr, H., *J. Phys-Condens Mat.* **2006,** *18*, 459-478.

154. Moulas, G.; Lehnert, A.; Rusponi, S.; Zabloudil, J.; Etz, C.; Ouazi, S.; Etzkorn, M.; Bencok, P.; Gambardella, P.; Weinberger, P.; Brune, H., *Phys. Rev. B* **2008,** *78*.

155. Zhao, Y. H.; Liu, B. G., *Chinese Phys. B* **2008,** *17*, 3417-3421.

156. Joshi, D. A.; Burger, P.; Adelmann, P.; Ernst, D.; Wolf, T.; Sparta, K.; Roth, G.; Grube, K.; Meingast, C.; von Lohneysen, H., *Phys. Rev. B* **2012,** *86*, 035144-035150.

157. Sampathkumaran, E. V.; Das, I., *Solid State Commun.* **1992,** *81*, 901-904.

158. Mentink, S. A. M.; Bos, N. M.; Vanrossum, B. J.; Nieuwenhuys, G. J.; Mydosh, J. A.; Buschow, K. H. J., *J. Appl. Phys.* **1993,** *73*, 6625-6627.

159. Wei, B. W.; Zhang, J. H.; Sun, P. J.; Wang, W. Q.; Wang, N. L.; Steglich, F., *J. Phys-Condens Mat.* **2015,** *27*.

160. Custers, J.; Lorenzer, K. A.; Muller, M.; Prokofiev, A.; Sidorenko, A.; Winkler, H.; Strydom, A. M.; Shimura, Y.; Sakakibara, T.; Yu, R.; Si, Q.; Paschen, S., *Nat. Mater.* **2012,** *11*, 189-194.

161. Osswald, J.; Kovnir, K.; Armbruster, M.; Giedigleit, R.; Jentoft, R. E.; Wild, U.; Grin, Y.; Schlogl, R., *J. Catal.* **2008,** *258*, 219-227.

162. Cortie, M.; Maaroof, A.; Mortari, A.; Wuhrer, R., *2006 International Conference on Nanoscience and Nanotechnology, Vols 1 and 2* **2006**, 95-98.

163. Zaluski, L.; Zaluska, A.; Tessier, P.; StromOlsen, J. A.; Schulz, R., *J. Mater Sci.* **1996,** *31*, 695-698.

164. Zaluski, L.; Tessier, P.; Ryan, D. H.; Doner, C. B.; Zaluska, A.; Stromolsen, J. O.; Trudeau, M. L.; Schulz, R., *J. Mater Res.* **1993,** *8*, 3059-3068.

165. Meng, X. L.; Cai, W.; Fu, Y. D.; Li, Q. F.; Zhang, J. X.; Zhao, L. C., *Intermetallics* **2008,** *16*, 698-705.

166. Otsuka, K.; Ren, X. B., *Intermetallics* **1999,** *7*, 511-528.

167. Rojas, D. P.; Barquin, L. F.; Espeso, J. I.; Fernandez, J. R., *Phys. Rev. B* **2008,** *78*, 094412-094420.

168. Mcintyre, P.; Wu, Y.; Liang, G.; Meitzler, C. R., *Ieee. T. Appl. Supercon.* **1995,** *5*, 238-241.

169. Kunzler, J. E.; Buehler, E.; Hsu, F. S. L.; Wernick, J. H., *Phys. Rev. Lett.* **1961,** *6*, 89-91.

170. Kopera, J. Inside the Nickel Metal Hydride Battery. 2004.

171. Funakubo, H., *Shape Memory Alloys*. New York, 1987.

172. Doane, D. A., *J. Appl. Phys.* **1977,** *48*, 2591-2596.

173. Stoloff, N. S.; Liu, C. T.; Deevi, S. C., *Intermetallics* **2000,** *8*, 1313-1320.

174. Winter, M.; Besenhard, J. O., *Electrochim. Acta* **1999,** *45*, 31-50.

175. Cui, C. H.; Gan, L.; Heggen, M.; Rudi, S.; Strasser, P., *Nat. Mater.* **2013,** *12*, 765-771.

176. Komatsu, T.; Inaba, K.; Uezono, T.; Onda, A.; Yashima, T., *Appl. Catal. a-Gen.* **2003,** *251*, 315-326.

177. Armbruster, M.; Kovnir, K.; Behrens, M.; Teschner, D.; Grin, Y.; Schlogl, R., *J. Am. Chem. Soc.* **2010,** *132*, 14745-14747.

178. Liu, X.; Gu, L. L.; Zhang, Q. P.; Wu, J. Y.; Long, Y. Z.; Fan, Z. Y., *Nat. Commun.* **2014,** *5*, 4007.

179. Kim, S. I.; Eom, G.; Kang, M.; Kang, T.; Lee, H.; Hwang, A.; Yang, H.; Kim, B., *Nanotechnology* **2015,** *26*.

180. Ji, X. L.; Lee, K. T.; Holden, R.; Zhang, L.; Zhang, J. J.; Botton, G. A.; Couillard, M.; Nazar, L. F., *Nat. Chem.* **2010,** *2*, 286-293.

Chapter 2

Structural Diversity, Multiple Phase Transitions and Versatile Physical Properties of the Compounds in the $RETX_3$ Family

Chapter 2.1: Crystal Growth and Physical Properties of $YbCuGa_3$: First Monoclinic System in the $RETX_3$ Family

Chapter 2.2: Swinging Symmetry, Multiple Structural Phase Transitions and Versatile Physical Properties in $RECuGa_3$ (RE = La-Nd, Sm-Gd)

Papers published on this work have appeared in

[1] *Cryst. Growth Des.*, **2013**, *13*, 953-959.

[2] *Inorg. Chem.*, **2015**, Press.

2.1. Crystal Growth and Properties of $YbCuGa_3$: First Monoclinic System in the $RETX_3$ Family

2.1.1. Introduction

$RETX_3$ (*RE* = Ce, Eu, Yb, *T* = transition metal and *X* = Al, Ga, Si, Ge, Sb) class of compounds show interesting physical phenomena arising from the competition associated with different structure types[1-12] and mixed valence behaviour of *RE* atoms. As per the inorganic crystal structure database[13] and Pearson's crystal data,[1] approximately 100 compounds were reported within the $RETX_3$ family till. It is interesting to note that all of them were reported in higher symmetry systems such as orthorhombic and above.

There are eleven different crystal structure types reported in the $RETX_3$ family. $BaNiSn_3$ is one of the most important among them, having the highest number of $RETX_3$ compounds crystallizing in the tetragonal space group $I4mm$.[14] $CeRhGe_3$,[2] $CeCoSi_3$,[15] $EuNiGe_3$,[16] $CeRuSi_3$[3] and $CeTGe_3$ (*T* = Rh and Ir)[4] are a few interesting examples which crystallize in the $BaNiSn_3$ structure type. $CeRhGe_3$ shows heavy fermion behaviour, $CeCoSi_3$ is a superconductor at 1 K[15] and $CeTGe_3$ (*T* = Rh and Ir) compounds show Kondo lattice behaviour.[4] A few $RETGa_3$ compounds, for example $CeCuGa_3$,[17] are also reported in the $BaNiSn_3$ structure type and studied for their interesting physical phenomena.

$CeAl_2Ga_2$[18], the second most important structure type, includes the examples of $EuNiSi_3$,[19] $CeNiGa_3$,[5] and $CeCuAl_3$.[20] $CeAl_2Ga_2$ crystallizing in the centrosymmteric tetragonal space group $I4/mmm$. $CeCuAl_3$ is a classic example exhibiting heavy fermion antiferromagnetic behaviour.[20]

$BaNiO_3$ is another type that adopts the hexagonal perovskite structure.[7] The crystal structure of the compounds crystallizing in this structure type consists of one-dimensional chains of face-sharing octahedra that are common for chalcogenides and halides. $RETiGe_3$ (*RE* = La, Ce, Pr)[6] and $RECrGe_3$ (*RE* = La-Nd, Sm)[8] are the examples which adopt the $BaNiO_3$ structure type. $CeTiGe_3$ orders ferromagnetically at 14 K and was proposed to be a dense Kondo lattice compound.[6]

There are a few $RETX_3$ intermetallic compounds that crystallize in various other structure types. $CePtGa_3$ crystallizes in the $BaAl_4$ type tetragonal structure (space group $I4/mmm$), showing anti-ferromagnetic ordering at 0.5 K.[21] CeT_xGa_{4-x} (*T* = Ni, Cu; x = 0.4 to 0.7)[9] is another interesting series which also crystallizes in the $BaAl_4$ type structure.

$CeNi_xGa_{4-x}$ (x = 0.5, 0.625, 0.75, 0.875 and 1.1) and $CeCu_xGa_{4-x}$ (x = 0.5, 1.0, 1.25 and 1.5) are two important members in this series, showing ferromagnetically dense Kondo behaviour.[10] $GdNiSi_3$ crystallizes in the orthorhombic[22] (space group *Amm*2) $ScNiSi_3$ structure type.[23] $CeRuGe_3$ crystallizes in two different structure types;[24] one is in the cubic (space group $Pm\bar{3}n$) $LaRuSn_3$ structure type[25] and the other one is in the orthorhombic (space group *Cmmm*) $SmNiGe_3$ structure type.[26] $CePtGe_3$ is another orthorhombic system (space group *Cmmm*)[27] crystallizing in its own structure type, while $CeTiGe_3$[12] crystallizes in its own structure type within the more symmetric tetragonal space group *P*4. While looking at the structural diversity of the compounds in the $RETX_3$ family, it was found that none of the compounds were reported in symmetry lower than the orthorhombic system.

Among the large numbers of $RETX_3$ compounds, only five Yb-based compounds were reported in the $RETX_3$ family. $YbCrSb_3$[28] crystallizes in the orthorhombic $CeCrSb_3$[29] structure type (*Pbcm* space group) having the highest magnetic ordering transition at T_c = 280 K. $YbBaSn_3$ crystallizes in the orthorhombic system in its own structure type (*Cmce* space group),[30] $YbNiGe_3$[31] and $YbNiSi_3$[32] crystallize in the orthorhombic $SmNiGe_3$ structure type having *Cmmm* space group.$YbCuAl_3$ crystallizes in the tetragonal $BaAl_4$ structure type with space group *I*4/*mmm*.[33]

This chapter discusses the synthesis, crystal structure and properties of a new compound $YbCuGa_3$. $YbCuGa_3$ is the sixth compound in the Yb based 1-1-3 series and the first $RETX_3$ compound crystallizing in the monoclinic system.

2.1.2. Experimental Section

2.1.2.1. Synthesis

2.1.2.1.1. Reagents

Rare earths (La-Nd, Sm-Gd, Yb)) (in the form of pieces cut from metal chunks, 99.99%), Cu (ingots, 99.99%) and Ga (pieces 99.99%) were used as purchased from Alfa Aesar without further purification.

2.1.2.1.2. Metal Flux Method

High quality single crystals of $YbCuGa_3$ were obtained by combining ytterbium metal (0.3 g), copper powder (0.14 g) and gallium pieces (1.5 g) in an alumina crucible. The crucible was placed in a 13-mm fused silica tube which was flame-sealed under a vacuum of

10^{-3} Torr to prevent oxidation during heating. The reactants were then heated to 1273 K over 10 h, maintained at that temperature for 10 h to allow proper homogenization, then cooled to 1173 K in 2 h and kept at this temperature for 120 h. Finally, the sample was allowed to cool slowly to 303 K over 96 h. No reaction with the alumina crucible material could be detected. The reaction product was isolated from excess gallium flux by heating at 673 K and subsequently centrifuging through a coarse frit. Any remaining gallium flux was removed by immersion and sonication in 2-3 molar solution of iodine in dimethylformamide (DMF) over 12-24 h at room temperature. The final crystalline product was rinsed with hot water and DMF then dried with acetone and ether. This method produced the target compound with ca. 99% purity up to the level of powder XRD limits and 60% yield on the basis of the initial amount of Yb metal used in the reaction. The shiny gray coloured plate-shaped single crystals of $YbCuGa_3$ up to 0.5 mm length were carefully selected for elemental analysis and single crystal XRD data collection. The compound was found to be stable in moist air for several months.

2.1.2.1.3. High Frequency Induction Heating

For the synthesis of $EuCuGa_3$ and $YbCuGa_3$, the elements europium, ytterbium, copper and gallium were mixed in the ideal 1:1:3 atomic ratio and sealed in tantalum ampoules under argon atmosphere in an arc-melting apparatus. The tantalum ampoules were subsequently placed in a water-cooled sample chamber of an induction furnace (Easy Heat induction heating system, Model 7590), rapidly heated to 180 Amperes (ca. 1200-1350 K) and kept at that temperature for 20 min. Finally, the reaction was rapidly cooled to room temperature by switching off the power supply. All compounds could be easily removed from the tantalum tubes. No reactions with the crucible material could be detected. All the compounds were found to be stable in moist air for several months. They were obtained in polycrystalline form having light gray in colour. The weight losses of the final material were found to be less than 1%. The samples obtained from the high frequency induction heating method were used for the property studies.

2.1.2.1.4. Arc melting method

The compounds *RE*$CuGa_3$ were prepared by using an Edmund Buhler GmbH MAM-1 arc melter in an Ar atmosphere. The starting metals were taken in 1:1:3 stoichiometric ratios and melted repeatedly (four times) in the same atmosphere to ensure homogeneity. The

weight losses of the final materials were found to be less than 1%. The polycrystalline ingot samples obtained from this method were used for the single crystal XRD study as well as magnetic and resistivity studies.

2.1.2.2. Elemental Analysis

Semi-quantitative microprobe analyses of the single crystals obtained from the flux techniques were performed with a SEM equipped with Bruker 129 eV EDAX instrument. Data were acquired with an accelerating voltage of 20 kV in 90 s accumulation time. The typical SEM image of a plate-like crystal of *RE*$CuGa_3$ (*RE* = La-Nd, Sm-Gd, Yb) grown from the flux synthesis is shown in Figure 2.1.1. The EDAX analysis performed on visibly clean surfaces of the single crystal (obtained from the flux method) indicated that the atomic composition is close to 1:1:3 which is in good agreement with the single crystal XRD data.

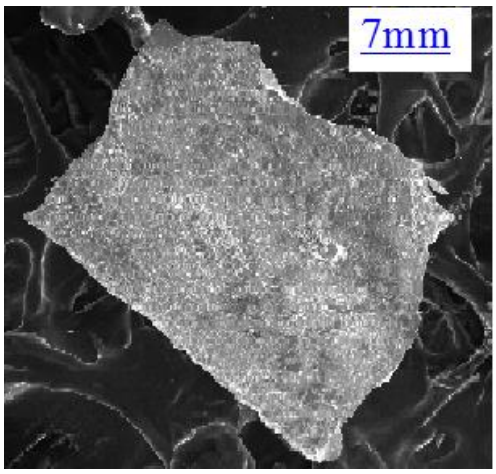

Figure 2.1.1. Typical SEM image of $YbCuGa_3$ single crystal grown from Ga flux.

2.1.2.3. Powder XRD

Phase identity and purity of the *RE*$CuGa_3$ (*RE* = La-Nd, Sm-Gd, Yb) samples were determined by powder XRD experiments with a Bruker D8 Discover diffractometer using Cu-*K*α radiation (λ = 1.5406 Å) over the angular range $15^0 \leq 2\theta \leq 60^0$, with a step size of 0.070864^0 at room temperature calibrated against corundum standards.

2.1.2.4. Single Crystal XRD

Single crystal XRD data of *RE*$CuGa_3$ (*RE* = La-Nd, Sm-Gd, Yb) were collected at room temperature on selected plate-shaped single crystals using a Bruker Smart–CCD diffractometer equipped with a normal focus, 2.4 kW sealed tube X-ray source with graphite monochromatic Mo-*K*α radiation (λ = 0.7107 Å) operating at 50 kV and 30 mA, with the ω

scan mode. A crystal of suitable size (0.5 x 0.05 x 0.05 mm) was cut from a plate-shape crystal and mounted on a thin glass (~0.1 mm) fiber with commercially available super glue. A full sphere of 60 frames was acquired up to 73.28˚ in 2θ. The individual frames were measured with steps of 0.50˚ and an exposure time of 10 s per frame. The programs SAINT[34] was used for integration of diffraction profiles while absorption correction were made with the SADABS program.[35] The systematic absences were leading to the centrosymmetric space group *C*2/*m*. The Platon program within the WinGx system, ver. 1.80.05[36] was used to check the additional symmetry which did not suggest any additional symmetry. The structure was solved by SHELXS 97[37] and refined by a full matrix least-squares method using SHELXL[38] with anisotropic atomic displacement parameters for all atoms. Packing diagrams were generated with Diamond.[39] As a check for the correct composition, the occupancy parameters were refined in a separate series of least-squares cycles.

2.1.2.5. Magnetic Measurements

Magnetic measurements were carried out using a Quantum Design MPMS-SQUID magnetometer. Measurements were performed on poly crystals, which were ground and screened by powder XRD to verify phase identity and purity. Temperature dependent data were collected for FC mode between 2 and 300 K in an applied field (H) of 1000 Oe. Magnetization data were also collected for $YbCuGa_3$ at 2 K and 300 K with field sweeping from -55000 Oe to 55000 Oe. For *RE*$CuGa_3$ (*RE* = La-Nd, Sm-Gd,) the DC magnetization was measured over the temperature range 1.8 K < *T* < 340 K and in fields up to 7 *T* via the extraction method in a Quantum Design MPMS3 system. Pressed plates (≈ 10 mg) were mounted on quartz rods with the plate surface parallel to the applied field; no demagnetization correction was applied to the measured susceptibility. For comparison, measurements also were made on unpressed powders using the VSM mode, and no significant quantitative differences were observed in the data.

2.1.2.6. Electrical Resistivity

The resistivity measurements were performed in 1*T* field on $YbCuGa_3$ with a conventional AC four probe setup. Four very thin copper wires were glued to the pellet using a strongly conducting silver epoxy paste. The data were collected in the range from 3-300 K using a commercial QD-PPMS. The results were reproducible for several batches. For *RE*$CuGa_3$ (*RE* = La-Nd, Sm-Gd), the resistivity of the pressed plates was measured using a 4-

terminal AC resistance bridge down to 0.3 K in a ^{3}He refrigerator, with high temperature data being taken on a very slow warm-up to room temperature. The excitation amplitude dependence was measured at the lowest temperature to ensure that the samples were not self-heating. It is expected that the absolute values of the resistivity cannot be accurately determined due to the tortuosity, intergrannular scattering and uncertainty in the geometric parameters of the porous pressed samples.

2.1.2.7. X-ray absorption near edge spectroscopy (XANES)

XANES experiments at 300 K on $EuCuGa_3$ was performed at PETRA III, P06 beamline of DESY, Germany. Measurements at the Eu L_{III}-edge and at ambient pressure were performed in transmission mode using gas ionization chambers to monitor the incident and transmitted X-ray intensities. Monochromatic X-rays were obtained using a Si [111] double crystal monochromator which was calibrated by defining the inflection point (first derivative maxima) of Cu foil as 8980.5 eV. The beam was focused employing a Kirkpatrick–Baez (K–B) mirror optic. A rhodium coated X-ray mirror was used to suppress higher order harmonics. A CCD detector was used to record the transmitted signals. The sample was prepared by mixing an appropriate amount of finely ground powder with cellulose and cold pressing them to a pellet.

2.1.2.8. Neutron diffraction

Neutron diffraction was carried out using the PXD instrument at the ISIS spallation neutron source (Oxfordshire, England). The samples were loaded in V-can which is sealed by an Al lid with a Cu gasket in an Ar gas environment.

2.1.2.9. Synchrotron XRD

The temperature dependent XRD measurements were performed on $CeCuGa_3$ in the range of room temperature to 800 K by using synchrotron (λ = 1.0287 Å) beamline at the Photon Factory, KEK, Japan.

2.1.3. Results and Discussions

2.1.3.1. Structure Refinement of $YbCuGa_3$

The crystal data of $YbCuGa_3$ suggested the C-centered monoclinic lattice and the structure was successfully refined in the *C*2/*m* space group. There are six crystallographic positions in the $YbCuGa_3$ crystal structure, of which two Yb atoms occupy the 2*c* and 2*a*

Wyckoff sites of point symmetry 2/*m*, one Cu atom and three Ga atoms occupy four different 4*i* Wyckoff sites of point symmetry *m*. The overall stoichiometry obtained from the refinement is $YbCuGa_3$.

The crystal structure refinement of $YbCuGa_3$ produced Cu-Ga3 bond distance of 2.422(8) Å which is shorter than the Cu-Ga1 (2.576(4) Å) and Cu-Ga2 (2.580(7) Å) distances and the theoretical distance of Cu-Ga (2.54 Å).[40] In order to verify the correct structure, the Ga3 position was substituted by Cu atom in the refinement process which resulted in higher thermal parameters. An attempt to mix the Ga3 position with Cu also did not help in lowering the isotropic displacement parameters, confirming the validity of the structural model. The data collection details and structure refinement parameters for $YbCuGa_3$ are listed in Table 2.1.1. The standard atomic positions and isotropic atomic displacement parameters of this compound are given in Table 2.1.2. The anisotropic displacement parameters and important bond lengths are listed in Tables 2.1.3 and 2.1.4, respectively. Further information on the structure refinement is available from: Fachinformationszentrum Karlsruhe, D-76344 Eggenstein-Leopoldshafen (Germany), by quoting the Registry No. CCDC–425031.

2.1.3.2. Crystal Chemistry of $YbCuGa_3$

The crystal structure of $YbCuGa_3$ along [010] direction is shown in Figure 2.1.2. $YbCuGa_3$ crystallizes as a new structure type in the monoclinic space group *C*2/*m*. Crystal structure of $YbCuGa_3$ is composed of complex $[CuGa]^{(2+\delta)-}$ polyanionic network in which the Yb ions are embedded. These polyanionic networks are shared through the edges of Cu and Ga atoms along [110] plane resulting in a three-dimensional network. The overall substructure of $YbCuGa_3$ as viewed down the *c*-axis is illustrated in Figure 2.1.3. The bonds to the Yb atoms were omitted to emphasize the three-dimensional (3D) $[CuGa_3]$ framework and its channels. For simplicity, the structure can also be described as an intergrowth of distorted PbO-type layers (Figure 2.1.3b) with the Yb atoms residing within the channels formed by the connection of the two layers. The distorted PbO-type slab contains Cu and all three Ga atoms. In this, the tetrahedrally coordinated Ga1 and Ga2 atoms form a 2-dimensional (2D) quadratic sheet that extends in the *bc*-plane (Figure 2.1.3a) and is capped by Cu and Ga1 atoms alternatively above and below the plane, thus forming a puckered layer as shown in Figure 2.1.3c.

Table 2.1.1. Crystal data and structure refinement for $YbCuGa_3$ at 296 (2) K.

Empirical formula	$YbCuGa_3$
Formula weight	454.85
Wavelength	0.71073 Å
Crystal system	Monoclinic
Space group	*C*2/*m*
Unit cell dimensions	a = 11.6891(8) Å, c = 8.3196(7) Å b = 4.1620(4) Å, β = 110.834(5)°
Volume	378.28(6) $Å^3$
Z	4
Density (calculated)	7.82612 g/cm^3
Absorption coefficient	50.840 mm^{-1}
F(000)	768
Crystal size	0.5 x 0.05 x 0.05 mm^3
θ range for data collection	2.62 to 23.46°
Index ranges	-13=<*h*=<13, -4=<*k*=<4, -9=<*l*=<9
Reflections collected	1367
Independent reflections	322 [R_{int} = 0.0749]
Completeness to θ = 23.46°	100%
Refinement method	Full-matrix least-squares on F^2
Data / restraints / parameters	322 / 0 / 34
Goodness-of-fit	1.237
Final *R* indices [>2σ(I)]	R_{obs} = 0.0689, wR_{obs} = 0.2345
Extinction coefficient	0.0043(1)
Largest diff. peak and hole	4.083 and -3.717 e·$Å^{-3}$

$R = \Sigma||F_o|-|F_c|| / \Sigma|F_o|$, $wR = \{\Sigma[w(|F_o|^2 - |F_c|^2)^2] / \Sigma[w(|F_o|^4)]\}^{1/2}$ and calcw=$1/[\sigma^2(Fo^2)+(0.0359P)^2+6.1794P]$ where $P = (Fo^2+2Fc^2)/3$

Table 2.1.2. Atomic coordinates (x10^4) and equivalent isotropic displacement parameters ($Å^2$x10^3) for $YbCuGa_3$ at 296(2) K with estimated standard deviations in parentheses.

Label	Wyckoff site	*x*	*y*	*z*	Occupancy	U_{eq}*
Yb1	2*c*	0	0	0.5	1	13(1)
Yb2	2*a*	0	0	0	1	13(1)
Cu	4*i*	8893(5)	0.5	1942(7)	1	23(1)
Ga1	4*i*	7504(4)	0	1250(6)	1	15(1)
Ga2	4*i*	2500(4)	0	3751(6)	1	14(1)
Ga3	4*i*	8890(4)	0.5	6947(6)	1	11(1)

*U_{eq} is defined as one third of the trace of the orthogonalized U_{ij} tensor.

Table 2.1.3. Anisotropic displacement parameters ($Å^2x10^3$) for $YbCuGa_3$ at 296(2) K with estimated standard deviations in parentheses.

Label	U_{11}	U_{22}	U_{33}	U_{12}	U_{13}	U_{23}
Yb1	17(2)	3(1)	19(2)	0	6(1)	0
Yb2	17(2)	3(1)	19(2)	0	6(1)	0
Cu	13(3)	7(3)	20(3)	0	5(2)	0
Ga1	16(3)	7(3)	23(3)	0	6(2)	0
Ga2	17(3)	4(3)	22(3)	0	6(2)	0
Ga3	12(3)	6(3)	18(3)	0	5(1)	0

The anisotropic displacement factor exponent takes the form: $-2\pi^2[h^2a^{*2}U_{11} + ... + 2hka^*b^*U_{12}]$.

Table 2.1.4. Selected bond lengths [Å] for $YbCuGa_3$ at 296(2) K with estimated standard deviations in parentheses.

Label	Distances	Label	Distances
Cu—Ga1	2.576(4)	Ga2—Ga3	2.576(4)
Cu—Ga2	2.580(7)	Ga1—Yb2	3.437(3)
Cu—Ga3	2.422(8)	Yb1—Ga1	3.431(5)
Cu—Yb1	3.184(4)	Yb1—Ga2	3.432(4)
Cu—Yb2	3.179(4)	Yb1—Ga3	3.183(3)
Ga1—Ga1	2.940(7)	Yb2—Ga1	3.428(4)
Ga1—Ga2	2.944(5)	Yb2—Ga2	3.434(4)
Ga1—Ga3	2.577(6)	Yb2—Ga3	3.181(3)
Ga2—Ga2	2.941(7)		

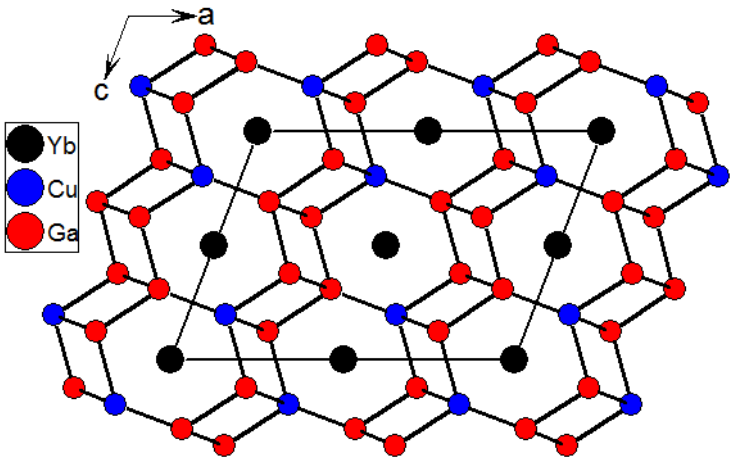

Figure 2.1.2. The structure of $YbCuGa_3$ as viewed along the *b*-axis; the unit cell is outlined with black solid line.

The connection between the distorted layers creates channels that extend down the *a*-axis, and each of them accommodates one Yb atoms. The connection of the two layers with

Cu–Ga3 bonds makes a penta coordination (2 Ga1, 2 Ga2 and 1 Ga3) and (1 Ga1, 3 Ga2 and 1 Cu atom) distorted square pyramidal geometry for Cu and Ga3 atoms, respectively. Ga1 atom is tetrahedrally coordinated by 3 Cu and 1 Ga3 atoms while Ga2 is tetrahedrally coordinated by 1 Cu and 3 Ga3 atoms. This is a common geometry in intermetallic compounds when one neglects the *RE* contacts.

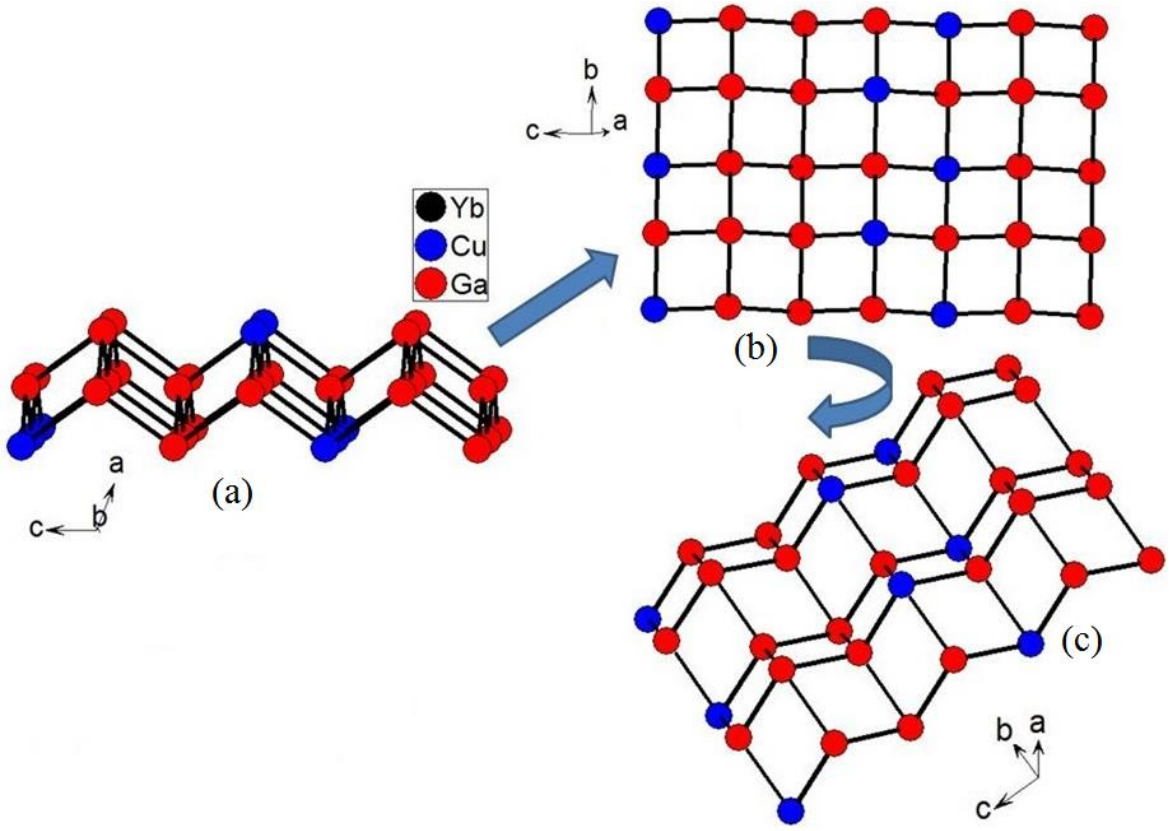

Figure 2.1.3. (a) $CuGa_3$ layer of PbO-type in the crystal structure of $YbCuGa_3$. (b) Projection of a $CuGa_3$ layer onto the *b*,*c*-plane (c) a rotated view of the $CuGa_3$ slab where the puckered form of the layer is emphasized.

The local coordination environments of all atoms are presented in Figure 2.1.4. The coordination environment of Yb1 and Yb2 atoms are similar and formed as cages of 20 atoms [$Yb_4Cu_4Ga_{12}$] (Figure 2.1.4a). Coordination environments of Cu and Ga3 are formed as capped square antiprismatic, (Figure 2.1.4a) composed of 9 atoms of which four are Yb atoms and the remaining five atoms are Ga atoms [Yb_4Ga_5] for Cu, and four Ga atoms and one Cu atom [Yb_4CuGa_4] for Ga3 atom. The coordination environment of Ga1 and Ga2 atoms (Figure 2.1.4c) are formed as cuboctahedron, composed of [$Yb_4Cu_3Ga_5$] and [Yb_4CuGa_7], respectively.

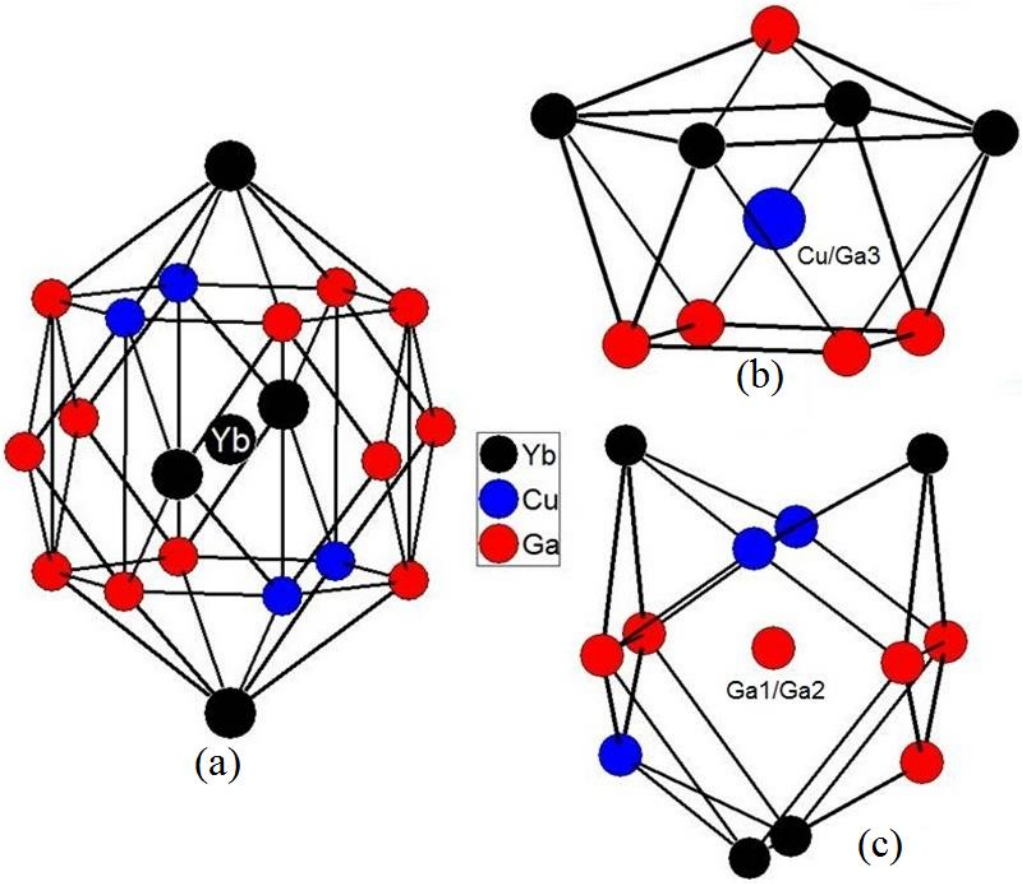

Figure 2.1.4. The coordination environment of Yb (a), Cu/Ga3 atoms (b) and Ga1/Ga2 atoms (c) in the crystal structure of $YbCuGa_3$.

Yb-Yb distance in $YbCuGa_3$ (4.1598(3) Å) is close to the calculated atomic radii of 3.84 Å[41]. This suggests the presence of divalent ytterbium in the compound which was later confirmed from the magnetic data showing the presence of 80% Yb^{2+}. The shortest distance of Yb-Cu is 3.179(4) Å, which is slightly shorter than the calculated distances of Yb^{2+}-Cu (3.19 Å)[42] and the Yb-Cu distance (3.176 Å) reported in $YbCu_2Si_2$[43]. This further confirmed the higher percentage of Yb^{2+} in $YbCuGa_3$. The shortest distance of Yb-Ga3 (3.183(3) Å) is very close to the calculated distance of Yb-Ga (3.20 Å)[44] suggesting a strong covalent interaction between them. However, Yb and Ga1 have weaker interactions as it has a distance of 3.431(5) Å, which is higher than that of the theoretically calculated values. The shortest distance of Cu-Ga1 (2.576(4) Å) and Cu-Ga2 (2.580(7) Å) are very close to the calculated distance of 2.54 Å.[40] The shortest distance of Cu-Ga3 2.422(8) Å is not common in *RE* based intermetallics but such small values were reported in other compounds such as $Mg_{17.53}Cu_{12}Ga_{26.33}$ (2.441 Å).[45]

2.1.3.3. Physical properties

2.1.3.3.1. Magnetism

Magnetic susceptibility measurements were done on polycrystalline sample of $YbCuGa_3$ obtained from the HFIH. The temperature dependent molar magnetic susceptibility (χ_m) of $YbCuGa_3$ and inverse susceptibility ($1/\chi_m$) at an applied field of 1000 Oe are shown in Figure 2.1.5.

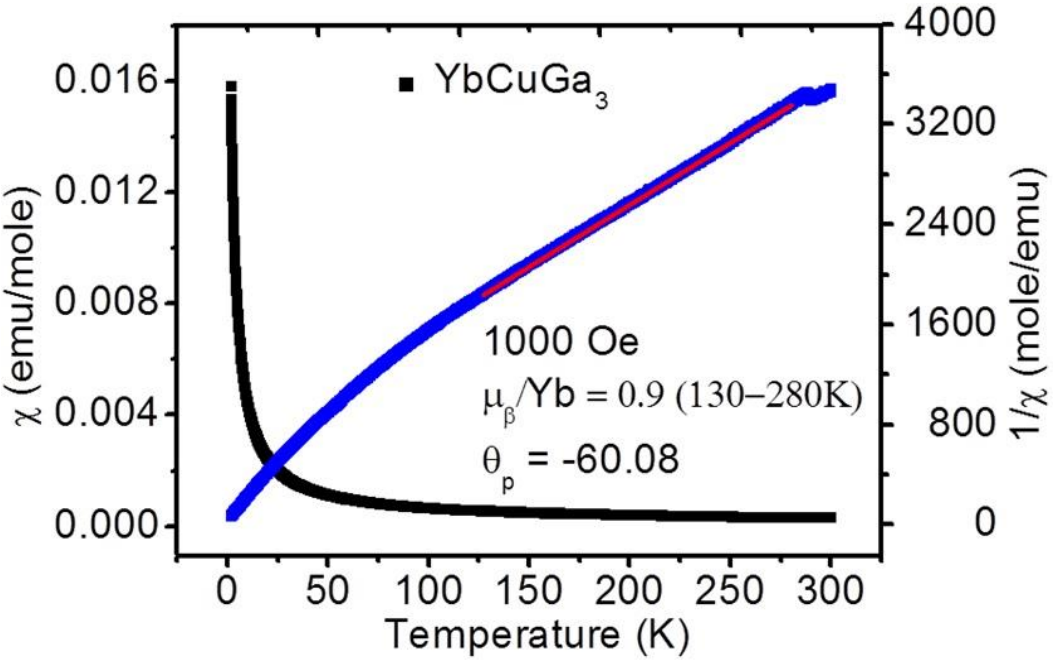

Figure 2.1.5. Temperature dependent magnetic susceptibility (χ_m) and inverse magnetic susceptibility ($1/\chi_m$) of $YbCuGa_3$ at 1000 Oe. The solid red line shows the fitting range.

The magnetic transition observed at temperature around 291 K is shown in Figure 2.1.6. At a higher field around 5000 Oe, the magnetic ordering at 291 K is clearly visible both in susceptibility and inverse susceptibility data (Figure 2.1.6). The inverse susceptibility curve above 130 K for $YbCuGa_3$ obeys Curie-Weiss law, $\chi(T) = C/(T-\theta_p)$,[46] where C is the Curie-Weiss constant ($N_A\mu_{eff}^2/3K_bT$) and θ_p is the Weiss temperature. A fit to the curve above 130 K resulted in an effective magnetic moment of 0.9 μ_B/Yb atom suggesting the existence of mixed valent Yb atoms in $YbCuGa_3$. The estimated experimental μ_{eff} value is about 20% of that expected for a free Yb^{3+} ion moment (4.56 μ_B/Yb). Magnetic susceptibility of $YbCuGa_3$ shows no magnetic ordering down to 2 K but the susceptibility slightly increases at lower temperature with increasing field, which is normal for *RE* based intermetallics.[47, 48] This deviation can be attributed to the crystal field contributions and/or magnetic impurities.

Another possible explanation for this behaviour is that the Yb ion is undergoing a valence transition from the diamagnetic Yb^{2+} state with a filled *f* shell to an intermediate valence state with an oxidation state between 2+ and 3+, therefore becoming paramagnetic. First order valence fluctuations of this type was previously observed in compounds like $YbCu_4In$, where the Yb undergoes an Yb^{3+} to Yb^{2+} transition at 20 K.[49]

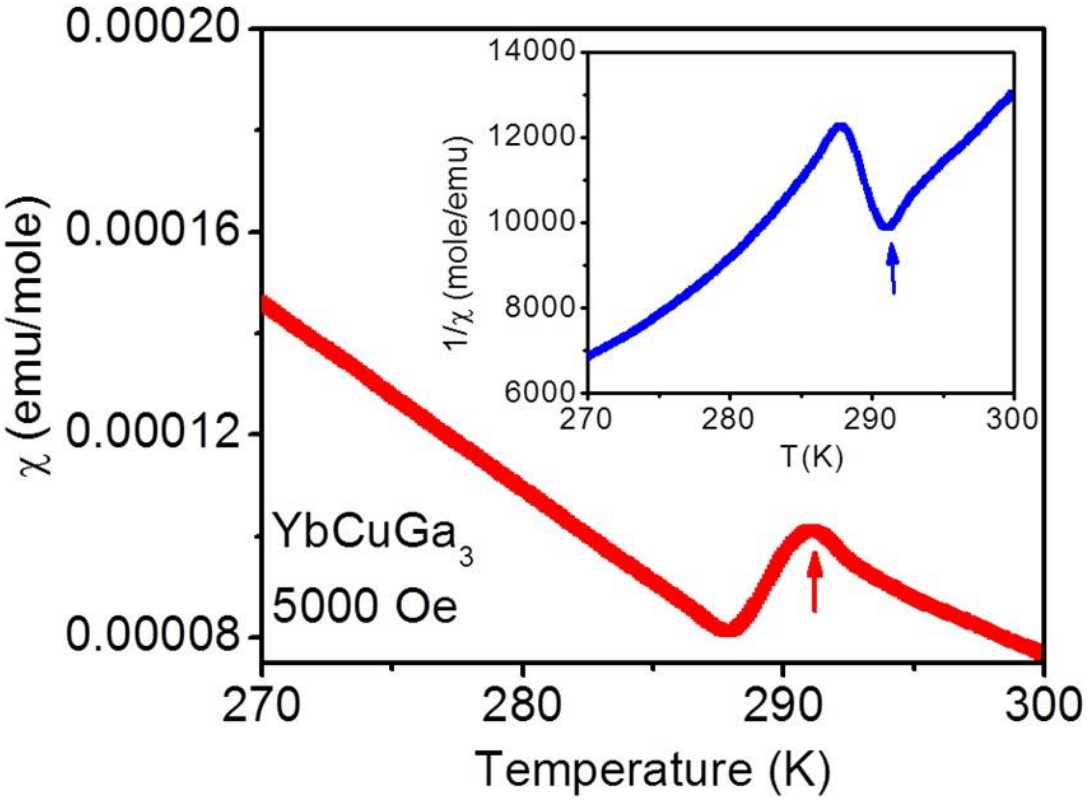

Figure 2.1.6. Magnetic susceptibility (χ_m) and inverse magnetic susceptibility ($1/\chi_m$) of $YbCuGa_3$ within the range 270-300 K. The magnetic ordering at 291 K is marked with arrow.

The field dependence of the magnetization *M*(*H*) for ground samples of $YbCuGa_3$,measured at 2 K and 300 K, can be seen in Figure 2.1.7. The paramagnetic nature observed at 2 K shows a slight field dependent response up to ~ 30 kOe, continues to rise slowly up to the highest obtainable field (50000 Oe) and then almost saturates at ~50 kOe with magnetic moment of ~0.017 emu/mol. The data measured at 300 K show paramagnetism at lower fields close to zero and interestingly shows the classical diamagnetic nature at higher field up to 50 kG. This clearly indicates a possible unstable valence of Yb atoms in $YbCuGa_3$ and/or strong crystal field contributions.

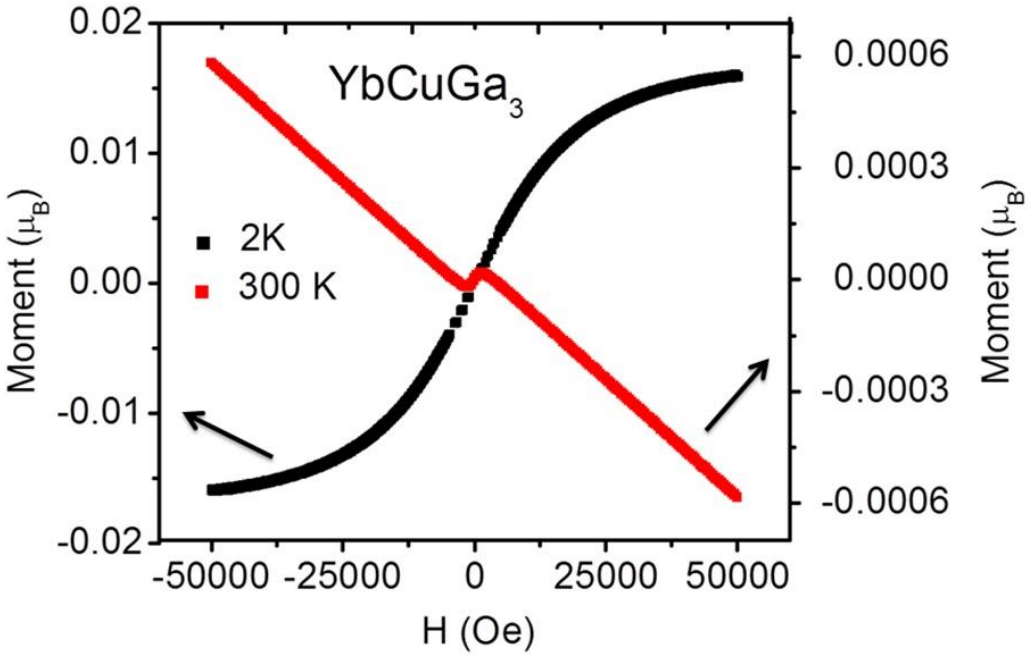

Figure 2.1.7. Magnetization as a function of applied magnetic field at 2 K and 300 K for the polycrystalline sample of $YbCuGa_3$.

2.1.3.3.2. Electrical Resistivity

Electrical resistivity (ρ) of $YbCuGa_3$ measured as a function of temperature in the range of 10-300 K and applied magnetic field of 0*T*, 1*T*, 2*T*, and 3*T* are shown in Figure 2.1.8a. The resistivity of the sample continuously decreases linearly with decreasing temperature, typical for metallic systems.[50] The absolute resistivity value of $YbCuGa_3$ is 18 $\mu\Omega$cm at room temperature that is comparable to the resistivity values of many copper based intermetallic compounds such as 30 $\mu\Omega$cm in $CeCuGa_3$,[17] and 26 $\mu\Omega$cm in $Ho_3Cu_4Si_4$.[51] While increasing the field from 0 to 3 *T*, the resistivity value is slightly increased at the high temperature region then a slight drop at around 291 K in consistent with the magnetic measurement studies. The linear dependence of the resistivity of $YbCuGa_3$ at temperatures below and above 291 K can be attributed to electron-phonon scattering. This is more clearly seen in the plot of $d\rho/dT$ shown in Figure 2.1.8b. Assuming the systems undergoing second order structural transitions, the effect of spin-fluctuations in the paramagnetic region becomes important (below 291 K), and this can be clearly seen as a peak in the plot of $d\rho/dT$ vs. T.[52] Therefore, the anomaly around 291 K in the plot of $\rho(T)$ can be assumed as a slight change in the crystal structure.

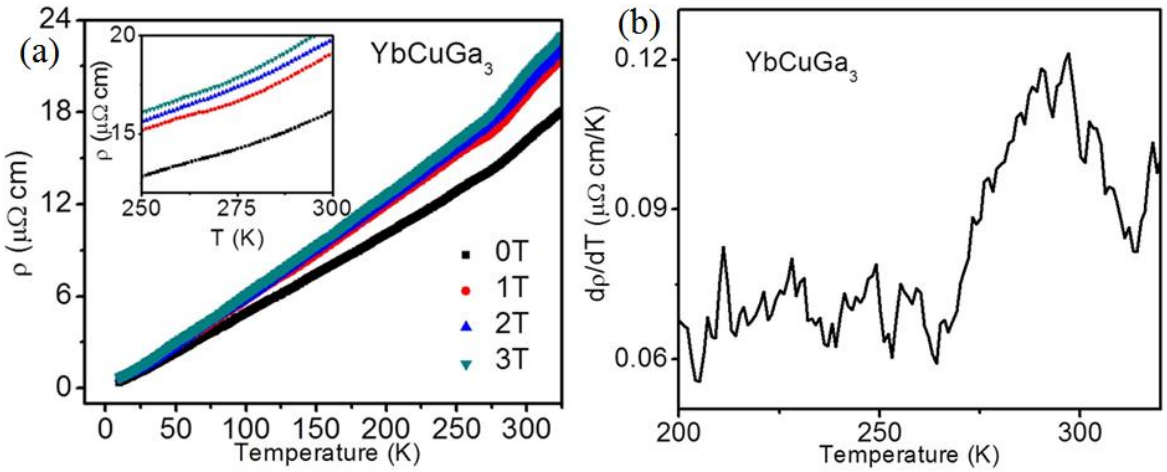

Figure 2.1.8. (a) Resistivity (ρ) measured as a function of temperature plots, measured at 0*T*, 1*T*, 2*T* and 3*T*. Inset figure shows the high temperature range, (b) the derivative plot of resistivity (ρ) at higher temperature clearly indicates transition at 291 K.

2.1.4. Conclusion

High quality single crystals of $YbCuGa_3$ were obtained from the metal flux technique which was studied using single crystal XRD. $YbCuGa_3$ is the first monoclinic system reported within the *RETX*$_3$ family that crystallizes in a new structure type. One might expect the existence of many other Yb-based new compounds within the same family because of the mixed valent nature of ytterbium. The magnetic susceptibility of $YbCuGa_3$ obeys Curie-Weiss law in the temperature range of 130 to 300 K, with an effective magnetic moment of 0.9 μ_B/Yb atom. The estimated experimental μ_{eff} value is 20 % of Yb^{3+} compared to the theoretical value of 4.56 μ_B/Yb atom. A systematic temperature and magnetic field dependent structural and physical property measurements on these compounds will bring out the interesting structure-property relations.

2.2. Swinging Symmetry, Multiple Structural Phase Transitions and Versatile Physical Properties in *RE*$CuGa_3$ (*RE* = La-Nd, Sm-Gd)

2.2.1. Introduction

As per Inorganic Crystal Structure Database[53] and Pearson's crystal data,[54] more than 100 compounds were reported within the $RETX_3$ (*RE* = rare earths *T* = transition metal and *X* = Al, Ga, Si, Ge, Sb) family. These compounds show interesting structural diversity with thirteen different structure types and wide range of physical properties. All the observed structure types are listed in the recent work and a new structure type observed for $YbCuGa_3$.[55] $SrPdGa_3$ is the latest new structure type crystallizing in the orthorhombic space group *Cmcm* which was recently reported by Pöttgen et al.[56]

The majority of these compounds crystallize either in the $BaNiSn_3$ structure type having *I*4*mm* space group or in the $BaAl_4$ structure type having *I*4/*mmm* space group. A few compounds crystallize in the $CeAl_2Ga_2$[57] structure type (*I*4/*mmm* space group), which is a ternary variant of the $BaAl_4$ structure. $CeRhGe_3$,[58] $CeCoGe_3$,[59] $EuNiGe_3$,[60] $CeRuSi_3$,[61] and Ce*T*Ge_3 (*T* = Rh and Ir)[62] are a few examples of materials which crystallize in the $BaNiSn_3$ type, while $SmRuSi_3$,[63] $NdAg_{0.88}Al_{3.12}$,[64] $CeCoSi_3$,[65] $LaCuAl_3$[66] and $SmCuAl_3$[67] are examples of materials which crystallize in the $BaAl_4$ type. On the other hand, $CeCuAl_3$,[68] YbT_xGa_{3-x} (*T* = Ag, Au, Pd and Pt),[69] $CeNiGa_3$,[70] *RE*Ni_xGa_{4-x} (*RE* = La-Nd, Sm, Gd and Tb),[71] *RE*Pt_xGa_{4-x} (*RE* = La-Nd, Sm)[72] and *RE*Pd_xGa_{4-x} (*RE* = La-Nd, Sm)[73] compounds have been reported to crystallize in the $CeAl_2Ga_2$ structure. These three crystal structures are closely related to one another in atomic arrangement and coordination environments, which in fact can cause symmetry fluctuation induced phase transitions under the influence of external factors such as temperature and pressure. $BaAl_4$ and $CeAl_2Ga_2$ are centrosymmetric structures with one Ba (Ce) and two different Al atoms (Al and Ga in the latter case) occupying tetrahedral and pyramidal sites. The non-centrosymmetric compound $BaNiSn_3$ is the ordered ternary derivative with distinct occupation sites for Ni and Sn atoms. Due to this, the structure loses centrosymmetry and crystallizes in the *I*4*mm* space group. It is expected that the presence of a transition metal can lead to strong spin-orbit interactions with the rare earths yielding interesting properties. This is in fact observed in a few $RETX_3$ compounds reported in the $BaNiSn_3$ type structure. For example, μSR and neutron diffraction studies clearly reveal

complex long-range magnetic ordering and multiple magnetic phases below 14.5 K for $CeRhGe_3$[58] and below 21 K for $CeCoGe_3$.[59] Despite this, the physical properties of most of the tetragonal $RETX_3$ compounds have not been studied in detail.

With this motivation, detailed studies of the *RE*$CuGa_3$ family have been performed, which is often reported either in centrosymmetric or non-centrosymmetric space groups. Initially, Markiv et al. reported *RE*Cu_xGa_{4-x} within the $BaAl_4$ type, based on the powder XRD data.[74] Later Grin et al. studied the compounds *RE*Cu_xGa_{4-x} (*RE* = La-Nd, Sm and Gd),[75] and $YbCu_{0.35}Ga_{3.65}$[69] in the $CeAl_2Ga_2$ structure type. Among them, $CeCuGa_3$[76] was reported in the $BaNiSn_3$ structure type, which is the only compound of this family having a non-centrosymmetric (*I*4*mm*) space group. However, this was based on preliminary powder XRD data. Among these compounds, only limited physical properties have been reported for $CeCuGa_3$. Polycrystalline $CeCuGa_3$ shows the onset of a magnetic transition at approximately 1.9 K,[77] and the single crystals have been reported to exhibit a ferromagnetic ordering below 4 K with a strong anisotropy.[78] In another report, Martin et al. reported the existence of long-range incommensurate magnetic ordering in $CeCuGa_3$ below an ordering temperature of 1.25 K.[79]

This chapter discusses the synthesis, crystal structure and physical properties of the compounds *RE*$CuGa_3$ (*RE* = La-Nd, Sm-Gd).

2.2.2. Results and Discussion

2.2.2.1. Structure Refinement

The crystal structure of the compounds *RE*$CuGa_3$ was solved by SHELXS 97[80] and refined by a full matrix least-squares method using SHELXL[81] with anisotropic atomic displacement parameters for all atoms. to check the correct composition, the occupancy parameters were refined in a separate series of least-squares cycles. Single crystals of *RE*$CuGa_3$ from different synthesis batches were used for the data collection. The crystallographic details of the reported centrosymmetric space group (*I*4/*mmm*) of $CeCuGa_3$[75, 82] were taken at the initial step of the refinement, but the refinement was unsuccessful. The refinement value (>10%) and thermal parameters are quite high. To overcome these problems, the atomic coordinates of the non-centrosymmetric $BaNiSn_3$ structure were used in the next step to successfully refine the crystal structure of all *RE*$CuGa_3$

compounds. All bond lengths are within an acceptable range. Packing diagrams were generated with Diamond.[83] The data collection and structure refinement are listed in Tables 2.2.1a and 2.2.1b. The standard atomic positions and isotropic atomic displacement parameters of all compounds are listed in Table 2.2.2. The anisotropic displacement parameters and important bond lengths are listed in Tables 2.2.3 and 2.2.4, respectively. Further information on the structure refinements is available from Cambridge Crystallographic Data Centre by quoting the Registry Nos. CCDC 1047127 (LaCuGa$_3$_300 K), 1047124 (CeCuGa$_3$_300K), 1047129 (PrCuGa$_3$_300 K), 1419076 (PrCuGa$_3$_400 K), 1419074 (NdCuGa$_3$_200 K) 1047128 (NdCuGa$_3$_300 K), 1419075 (NdCuGa$_3$_400 K), 1047130 SmCuGa$_3$_300 K), 1047125 (EuCuGa$_3$_300 K) and 1047126 (GdCuGa$_3$_300 K).

2.2.2.2. Reaction Chemistry

All the compounds except EuCuGa$_3$ were obtained from the arc-melting technique. Since Eu has low boiling point and high vapour pressure, EuCuGa$_3$ was synthesized by high frequency induction furnace similar to previous reports.[84, 85] Irregularly shaped grey crystals were obtained from the reaction and are shown in Figure 2.2.1. Gallium acted as the self-flux for the synthesis of the *RE*CuGa$_3$ compounds, which has already been reported for the synthesis of many intermetallic compounds.[86, 87] The compounds are stable in air and no decomposition were observed even after several weeks.

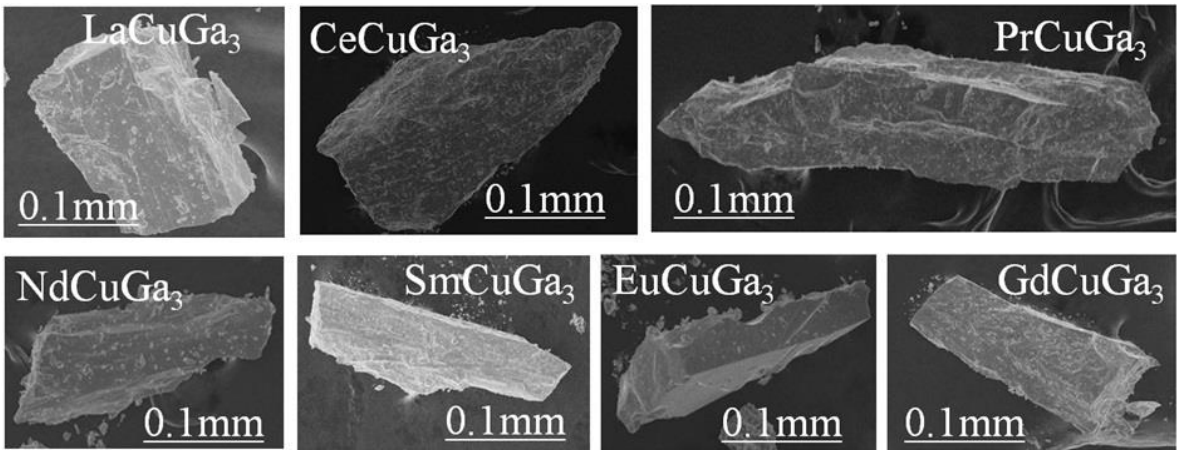

Figure 2.2.1. SEM images of irregularly shaped crystals of *RE*CuGa$_3$ synthesized by arc-melting technique and EuCuGa$_3$ by HFIH method.

Table 2.2.1a. Crystal data and structure refinement for *RE*$CuGa_3$ (*RE* = La-Nd). Wavelength = 0.71073 Å, crystal system = tetragonal, space group = *I*4*mm*, z = 2.

Empirical formula	$LaCuGa_3$	$CeCuGa_3$	$PrCuGa_3$	$NdCuGa_3$
Formula weight	411.61	412.82	413.61	416.94
Temperature	296 K	296 K	296 K	200 K
Unit cell dimensions	$a = b$ = 4.2837(1) Å c = 10.4482(5) Å	$a = b$ = 4.2487(1) Å c = 10.4372(4) Å	$a = b$ = 4.2090(1) Å c = 10.4885(4) Å	$a = b$ = 4.1913(8) Å c = 10.409(2) Å
Volume	191.73(1) $Å^3$	188.41(1) $Å^3$	185.81(1) $Å^3$	182.85(6) $Å^3$
Density (calculated)	7.12951 g/cm^3	7.27642 g/cm^3	7.39219 g/cm^3	7.573 g/cm^3
Absorption coefficient	36.907 mm^{-1}	38.300 mm^{-1}	39.696 mm^{-1}	41.214 mm^{-1}
F(000)	357.8	359.8	361.8	364
Crystal size	0.1 x 0.05 x 0.05 mm^3	0.1 x 0.05 x 0.05 mm^3	0.1 x 0.05 x 0.05 mm^3	0.10 x 0.05 x 0.05
θ range for data collection	3.9 to 41.2°	3.9 to 49.2°	3.9 to 43.1°	3.92 to 29.91°
Index ranges	-5=<h=<7, -7=<k=<4, -18=<l=<18	-8=<h=<6, -8=<k=<9, -22=<l=<13	-5=<h=<6, -8=<k=<8, -18=<l=<20	-5<=h<=5, -5<=k<=5, -14<=l<=12
Reflections collected	1226	1151	1362	646
Independent reflections	387 [R_{int} = 0.051]	445 [R_{int} = 0.0393]	442 [R_{int} = 0.0341]	163 [R_{int} = 0.0728]
Completeness to θ = 30.55°	100%	100%	100%	100%
Refinement method	Full-matrix least-squares on F^2			
Data / restraints / parameters	387 / 0 / 15	445 / 0 / 15	442 / 0 / 15	163 / 1 / 15
Goodness-of-fit	1.102	1.131	1.082	1.339
Final R indices [>2σ(I)]	R_{obs} = 0.046, wR_{obs} = 0.117	R_{obs} = 0.034, wR_{obs} = 0.092	R_{obs} = 0.024, wR_{obs} = 0.058	R_{obs} = 0.044, wR_{obs} = 0.120
Extinction coefficient	0.00484	0.03134	0.004988	0.016(6)
Largest diff. peak and hole	4.348 and -3.453 e·$Å^{-3}$	3.472 and -4.665 e·$Å^{-3}$	3.044 and -2.385 e·$Å^{-3}$	3.333 and -2.610 e·$Å^{-3}$

$R = \Sigma||F_o|-|F_c|| / \Sigma|F_o|$, w$R$ = $\{\Sigma[w(|F_o|^2 - |F_c|^2)^2] / \Sigma[w(|F_o|^4)]\}^{1/2}$ and calcw=$1/[\sigma^2(Fo^2)+(0.0359P)^2+6.1794P]$ where P = $(Fo^2+2Fc^2)/3$

Table 2.2.1b. Crystal data and structure refinement for *RE*$CuGa_3$ (*RE* = Sm, Eu and Gd). Wavelength = 0.71073 Å, crystal system = tetragonal, space group = *I*4*mm*, z = 2.

Empirical formula	$SmCuGa_3$	$EuCuGa_3$	$GdCuGa_3$
Formula weight	423.05	424.66	429.95
Temperature	296 K	296 K	296 K
Unit cell dimensions	$a = b$ = 4.1441(3) Å c = 10.5568(11) Å	$a = b$ = 4.2589(2) Å c = 10.6898(4) Å	$a = b$ = 4.1190(1) Å c = 10.5327(4) Å
Volume	181.30(3) $Å^3$	193.89(2) $Å^3$	178.70(1) $Å^3$
Density (calculated)	7.74911 g/cm^3	7.27328 g/cm^3	7.999002 g/cm^3
Absorption coefficient	43.442 mm^{-1}	41.652 mm^{-1}	46.200 mm^{-1}
F(000)	367.8	369.8	371.8
Crystal size	0.1 x 0.05 x 0.05 mm^3	0.1 x 0.05 x 0.05 mm^3	0.1 x 0.05 x 0.05 mm^3
θ range for data collection	3.9 to 43.8°	3.8 to 35.4°	3.9 to 37.8°
Index ranges	-7=<h=<8, -7=<k=<3, -20=<l=<20	-3=<h=<6, -6=<k=<4, -12=<l=<16	-5=<h=<7, -7=<k=<3, -17=<l=<17
Reflections collected	1237	831	879
Independent reflections	446 [R_{int} = 0.0558]	273 [R_{int} = 0.0670]	310 [R_{int} = 0.0498]
Completeness to θ = 30.55°	100%	100%	100%
Refinement method	Full-matrix least-squares on F^2		
Data / restraints / parameters	446 / 0 / 15	273 / 0 / 15	310 / 0 / 15
Goodness-of-fit	1.067	1.095	1.118
Final R indices [>2σ(I)]	R_{obs} = 0.047, wR_{obs} = 0.118	R_{obs} = 0.031, wR_{obs} = 0.072	R_{obs} = 0.025, wR_{obs} = 0.065
Extinction coefficient	0.00241	0.008896	0.00115
Largest diff. peak and hole	7.703 and -5.069 e·$Å^{-3}$	2.168 and -2.602 e·$Å^{-3}$	3.000 and -1.588 e·$Å^{-3}$

$R = \Sigma||F_o|-|F_c|| / \Sigma|F_o|$, w$R = \{\Sigma[w(|F_o|^2 - |F_c|^2)^2] / \Sigma[w(|F_o|^4)]\}^{1/2}$ and calcw=$1/[\sigma^2(Fo^2)+(0.0359P)^2+6.1794P]$ where P = $(Fo^2+2Fc^2)/3$

Table 2.2.2. Atomic coordinates ($x10^4$) and equivalent isotropic displacement parameters ($Å^2x10^3$) for *RE*$CuGa_3$ (*RE* = La-Nd, Sm-Gd) at 296(2) K with estimated standard deviations in parentheses.

	Label	Wyckoff site	*x*	*y*	*z*	Occupancy	U_{eq}*
$LaCuGa_3$	La	2*a*	0	0	5791(2)	1	11(2)
	Cu	2*a*	0	0	1922(3)	1	19(1)
	Ga1	4*b*	0	0	0	1	15(1)
	Ga2	2*a*	0	5000	3287(3)	1	18(1)
$CeCuGa_3$	Ce	2*a*	0	0	5769(4)	1	5(1)
	Cu	2*a*	0	0	1912(6)	1	14(1)
	Ga1	4*b*	0	0	0	1	8(1)
	Ga2	2*a*	0	5000	3279(5)	1	13(1)
$PrCuGa_3$	Pr	2*a*	0	0	5751(1)	1	4(1)
	Cu	2*a*	0	0	2056(12)	1	8(1)
	Ga1	4*b*	0	0	0	1	8(1)
	Ga2	2*a*	0	5000	3251(11)	1	7(1)
$NdCuGa_3$	Nd	2*a*	0	0	5776(1)	1	2(1)
	Cu	2*a*	0	0	1925(7)	1	8(1)
	Ga1	4*b*	0	0	0	1	5(1)
	Ga2	2*a*	0	5000	3295(6)	1	15(1)
$SmCuGa_3$	Sm	2*a*	0	0	5751(1)	1	5(1)
	Cu	2*a*	0	0	2029(19)	1	8(1)
	Ga1	4*b*	0	0	0	1	8(1)
	Ga2	2*a*	0	5000	3254(19)	1	7(1)
$EuCuGa_3$	Eu	2*a*	0	0	5781(4)	1	11(1)
	Cu	2*a*	0	0	1938(19)	1	14(1)
	Ga1	4*b*	0	0	0	1	15(1)
	Ga2	2*a*	0	5000	3288(18)	1	19(1)
$GdCuGa_3$	Gd	2*a*	0	0	5524(1)	1	8(1)
	Cu	2*a*	0	0	1722(2)	1	13(1)
	Ga1	4*b*	0	0	0	1	11(2)
	Ga2	2*a*	0	5000	3027(2)	1	16(4)

Table 2.2.3. Anisotropic displacement parameters (Å^{2}x10^3) for *RE*CuGa$_3$ (*RE* = La-Nd, Sm-Gd) at 296(2) K with estimated standard deviations in parentheses.

Compound	Label	U_{11}	U_{22}	U_{33}	U_{12}	U_{13}	U_{23}
LaCuGa$_3$	La	10(2)	10(2)	13(3)	0	0	0
	Cu	17(8)	17(1)	26(3)	0	0	0
	Ga1	14(1)	16(1)	14(4)	0	0	0
	Ga2	13(1)	13(1)	30(3)	0	0	0
CeCuGa$_3$	Ce	5(1)	5(1)	6(1)	0	0	0
	Cu	9(1)	9(1)	26(2)	0	0	0
	Ga1	5(1)	13(1)	7(3)	0	0	0
	Ga2	7(1)	7(1)	25(2)	0	0	0
PrCuGa$_3$	Pr	3(1)	4(1)	6(1)	0	0	0
	Cu	7(1)	7(1)	8(4)	0	0	0
	Ga1	7(1)	8(1)	8(3)	0	0	0
	Ga2	7(1)	7(1)	9(4)	0	0	0
NdCuGa$_3$	Nd	7(1)	7(1)	9(1)	0	0	0
	Cu	11(1)	11(1)	29(12)	0	0	0
	Ga1	12(1)	11(1)	36(3)	0	0	0
	Ga2	12(1)	12(5)	9(10)	0	0	0
SmCuGa$_3$	Sm	7(1)	7(1)	3(1)	0	0	0
	Cu	11(1)	11(1)	1(1)	0	0	0
	Ga1	10(1)	10(1)	3(1)	0	0	0
	Ga2	10(4)	10(4)	2(1)	0	0	0
EuCuGa$_3$	Eu	11(1)	11(1)	12(1)	0	0	0
	Cu	8(1)	8(1)	26(3)	0	0	0
	Ga1	18(4)	16(3)	13(3)	0	0	0
	Ga2	21(1)	21(1)	15(2)	0	0	0
GdCuGa$_3$	Gd	7(1)	7(1)	11(1)	0	0	0
	Cu	10(1)	10(1)	17(2)	0	0	0
	Ga1	10(1)	10(1)	12(4)	0	0	0
	Ga2	11(1)	11(1)	25(10)	0	0	0

The anisotropic displacement factor exponent takes the form: $-2\pi^2[h^2a^{*2}U_{11} + ... + 2hka^*b^*U_{12}]$.

Table 2.2.4. Selected bond lengths [Å] for *RE*CuGa$_3$ (*RE* = La-Nd, Sm-Gd) at 296(2) K with estimated standard deviations in parentheses.

Label	Distances	Label	Distances
LaCuGa$_3$		Cu—Ga1	2.532(5)
La—Cu	3.251(1)	Cu—Ga2	2.363(3)
La—Ga1	3.371(2)	Ga1—Ga1	2.971(2)
La—Ga1	3.385(2)	Ga1—Ga2	2.542(4)
La—Ga2	3.269(2)	**SmCuGa$_3$**	
Cu—Ga1	2.580(3)	Sm—Cu	3.226(9)
Cu—Ga2	2.415(3)	Sm—Ga1	3.353(10)
Ga1—Ga2	2.543(3)	Sm—Ga2	3.098(7)
CeCuGa$_3$		Cu—Ga1	2.441(14)
Ce—Cu	3.233(4)	Cu—Ga2	2.356(3)
Ce—Ga1	3.359(3)	Ga1—Ga1	2.930(2)
Ce—Ga1	3.370(3)	Ga1—Ga2	2.637(14)
Ce—Ga2	3.231(4)	**EuCuGa$_3$**	
Cu—Ga1	2.556(8)	Eu—Cu	3.246(2)
Cu—Ga2	2.383(3)	Eu—Ga1	3.407(3)
Ga1—Ga1	3.0043(1)	Eu—Ga1	3.427(3)
Ga1—Ga2	2.552(7)	Eu—Ga2	3.256(2)
PrCuGa$_3$		Cu—Ga1	2.589(5)
Pr—Cu	3.275(5)	Cu—Ga2	2.449(1)
Pr—Ga1	3.361(6)	Ga1—Ga1	3.011(1)
Pr—Ga1	3.363(3)	Ga1—Ga2	2.561(5)
Pr—Ga2	3.141(4)	**GdCuGa$_3$**	
Cu—Ga1	2.451(8)	Gd—Cu	3.104(7)
Cu—Ga2	2.373(3)	Gd—Ga1	3.341(1)
Ga1—Ga1	2.976(1)	Gd—Ga1	3.344(1)
Ga1—Ga2	2.653(9)	Gd—Ga2	3.174(9)
NdCuGa$_3$		Cu—Ga1	2.582(2)
Nd—Cu	3.193(3)	Cu—Ga2	2.336(2)
Nd—Ga1	3.329(1)	Ga1—Ga1	2.912(1)
Nd—Ga1	3.361(3)	Ga1—Ga2	2.475(2)
Nd—Ga2	3.202(2)		

High quality single crystals were used to collect the XRD data. Since the centrosymmetric (*I*4/*mmm*) and non-centrosymmetric (*I*4*mm*) models are very similar and the Cu and Ga X-ray scattering powers are comparable, CeCuGa$_3$ was chosen for neutron diffraction studies to confirm the correct structure as the neutron absorption cross-section of Ce is very low. On comparing the PXRD simulated from both centro- and non-

centrosymmetric refinements with the experimental patterns, it was found that they match more closely with the non-cetrosymmteric $BaNiSn_3$ structure type.

2.2.2.3. Crystal Structure

The crystal structure of *RE*CuGa$_3$ along the [010] direction is shown in Figure 2.2.2. Crystal structures of *RE*CuGa$_3$ compounds are composed of a complex $[CuGa]^{(2+\delta)-}$ polyanionic network in which the *RE* ions are embedded. These polyanionic networks are shared through the edges of Cu and Ga atoms along the [101] plane resulting in a three dimensional network. *RE*CuGa$_3$ compounds have been reported as three different structure types: centrosymmetric $BaAl_4$,[88] its ternary derivative disordered centrosymmetric $CeAl_2Ga_2$,[57] and ordered non-centrosymmetric $BaNiSn_3$.[89] The relation between these three structures is shown in Figure 2.2.3 and the corresponding atomic coordinates are listed in Table 2.2.5.

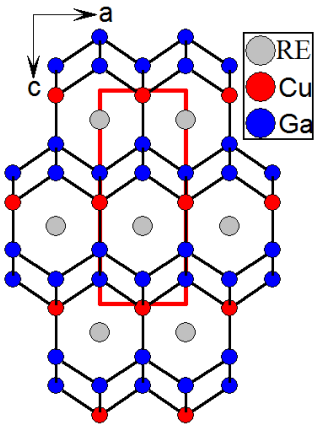

Figure 2.2.2. The crystal structures of *RE*CuGa$_3$ are shown along the *b*-axis. The unit cell is outlined with red.

The $BaAl_4$ and $CeAl_2Ga_2$ structures contains three atomic positions; one 2*a* Wyckoff site occupied by a *RE* atom and the remaining two positions (4*d*, 4*e* Wyckoff sites) are occupied by a mixture of Cu and Ga (in the case of $BaAl_4$ type) with either one Ga atom occupying 4*d* Wyckoff site or Cu/Ga mixing occurs at a 4*e* Wyckoff site (in the case of $CeAl_2Ga_2$ type). The ordering of Cu and Ga plays a crucial role in crystallizing the compound in a particular structure. However, Cu-Ga ordering as obtained from powder XRD data is not conclusive due to the close X-ray scattering powers due to which the occupancy of Cu or Ga at certain positions cannot be determined with precision. In this work, the Cu and Ga positions have been assigned based on the bond distance analysis and it was found that the

compounds *RE*CuGa$_3$ crystallize in the BaNiSn$_3$ structure type. The ordered non-centrosymmetric BaNiSn$_3$ contains four atomic coordinates, consisting of one *RE* atom (2*a* Wyckoff site), one Cu atom (2*a* Wyckoff site) and two Ga atoms (4*b* and 2*a* Wyckoff sites). The dotted line shown in Figure 2.2.3 represents the inversion symmetry, which is absent for the BaNiSn$_3$ structure type leading it to the non-centrosymmetric *I*4*mm* space group. In both ternary structure types, the *RE* layers are separated by zigzag type Cu-Ga layers. Overall, the amount of disorder is less in *RE*CuGa$_3$ compared to the other centrosymmetric compounds in 1-1-3 series, which leads them to crystallize in the ordered BaNiSn$_3$ structure type.

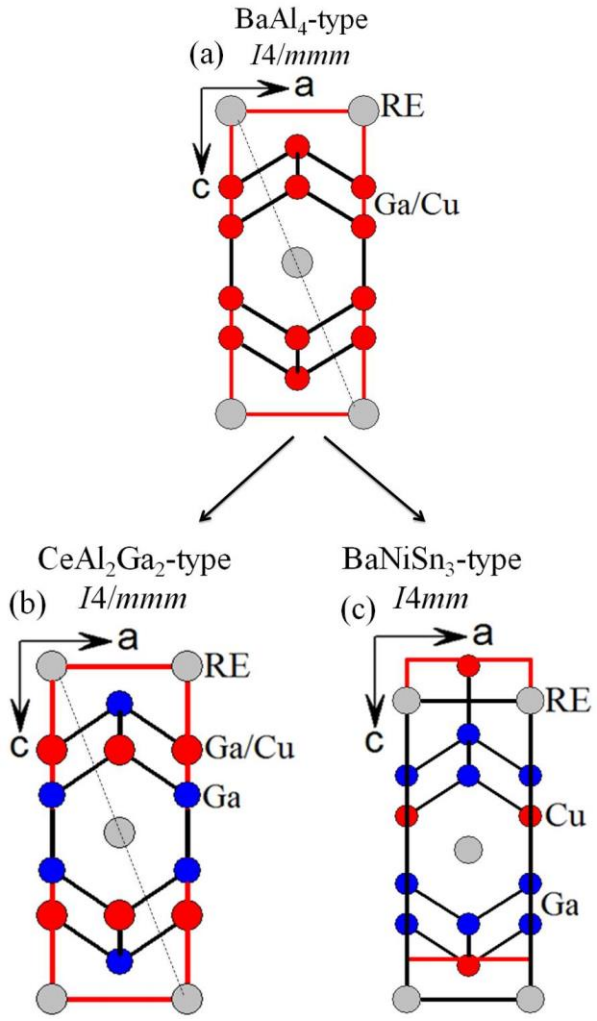

Figure 2.2.3. Comparison of three possible tetragonal crystal structures of *RE*CuGa$_3$ are shown along the *b*-axis which crystallizes in (a) centrosymmetric BaAl$_4$ structure type, (b) centrosymmetric CeAl$_2$Ga$_2$ structure type and (c) non-centrosymmetric BaNiSn$_3$ structure type (unit cell outlined with red). Dotted line shows the inversion symmetry presents in the BaAl$_4$ and CeAl$_2$Ga$_2$ structure types.

Table 2.2.5. Atomic coordinates (x10^4) of *RE*CuGa$_3$ crystallizes in three different BaAl$_4$, CeAl$_2$Ga$_2$ and BaNiSn$_3$ structure types.

Structure type	Atom name	Wyckoff site	*x*	*y*	*z*
BaAl$_4$	*RE*	2*a*	0	0	0
	Cu1/Ga1	4*d*	0	0	3800
	Cu2/Ga2	4*e*	0	5000	2500
CeAl$_2$Ga$_2$	*RE*	2*a*	0	0	0
	Ga	4*d*	0	0	3700
	Cu/Ga	4*e*	0	5000	2500
BaNiSn$_3$	*RE*	2*a*	0	0	5759
	Cu	2*a*	0	0	2313
	Ga1	4*b*	0	0	0
	Ga2	2*a*	0	5000	3494

The coordination environments of *RE*, Cu and Ga atoms in the centrosymmetric and non-centrosymmetric structures are shown in Figure 2.2.4. The overall morphology of the coordination environments is the same except the Ga position is split into two in the ordered structure. The average bond distance between *RE* and Cu atoms within the first coordination sphere was calculated as 3.218 Å. The shortest individual bond distances of *RE*-Cu are 3.251 Å, 3.233 Å, 3.275 Å, 3.193 Å, 3.226 Å, 3.246 Å and 3.104 Å for *RE* = La, Ce, Pr, Nd, Sm, Eu and Gd, respectively, close to the calculated bond distances from the atomic radii. Interestingly, the Eu-Cu (3.246 Å) bond distance is greater than the Sm-Cu bond distance (3.226 Å), indicating that Eu is mostly in the divalent Eu^{2+} state, which was confirmed by magnetic susceptibility and XANES measurements (described below). The average bond distance of *RE*-Ga1 and *RE*-Ga2 for all compounds is in the range 3.195-3.375 Å.

The unit cell volume of the *RE*CuGa$_3$ compounds have been compared in Figure 2.2.5a. The cell volume of the compounds decreases with the decreasing covalent radii of the *RE* metals, which is consistent with the well-known lanthanide contraction. The exception is in the case of Eu where there is a sharp increase in the cell volume due to the presence of divalent europium atom. The c/a ratio versus *RE* atom for *RE*CuGa$_3$ has also been plotted in Figure 2.2.5b. As expected the deviation from the linearity for EuCuGa$_3$ is due to the divalent nature of Eu, but surprisingly NdCuGa$_3$ also deviates from the linearity due to large drop in the *c* lattice parameters, which suggests a structural instability of this compound. In addition,

high values of largest peak and deepest hole (6.385 and -14.264 e·Å^{-3}) at 300 K indicate the structure is highly unstable. Assuming that the structural instability is temperature dependent, the SCXRD data at various temperatures have been collected and refined. The data obtained at 200 K and 400 K resulted in better refinements (Table 2.2.6 and 2.2.7) and the high values of largest peak and deepest hole substantially reduced to the normal range (~3 and -2 e·Å^{-3}).

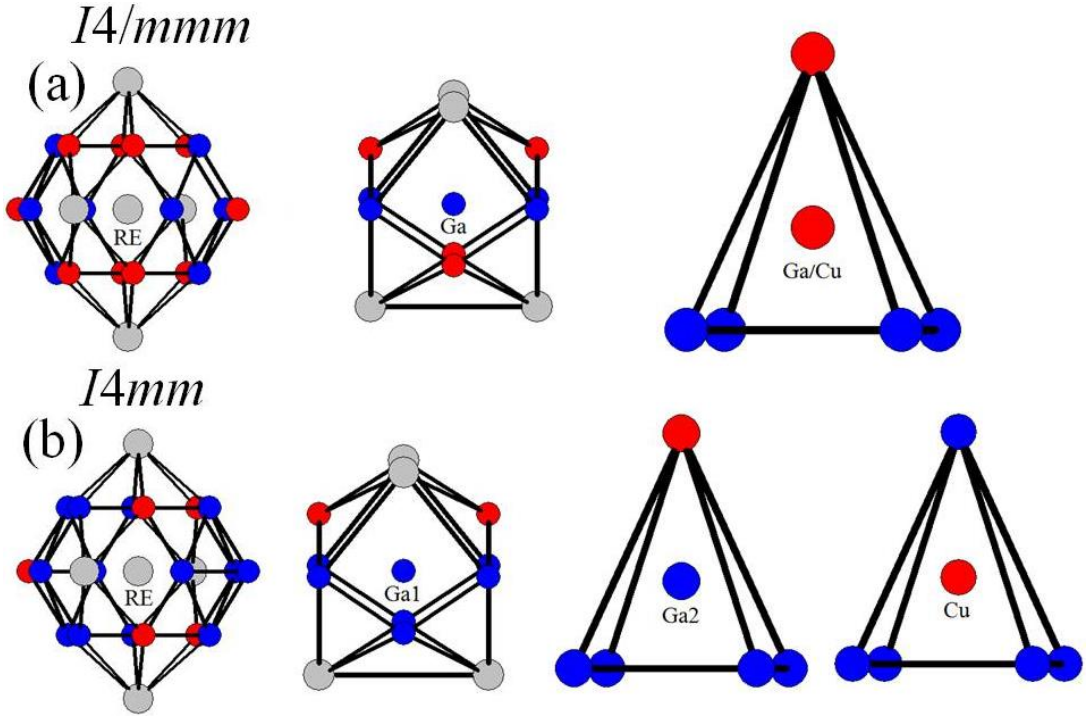

Figure 2.2.4. Coordination environment of *RE* (La-Nd, Sm-Gd), Cu, Ga1 and Ga2 atoms (a) centrosymmetric (*I*4/*mmm*) $CeAl_2Ga_2$ structure type and (c) non-centrosymmetric (*I*4*mm*) $BaNiSn_3$ structure type in *RE*CuGa$_3$.

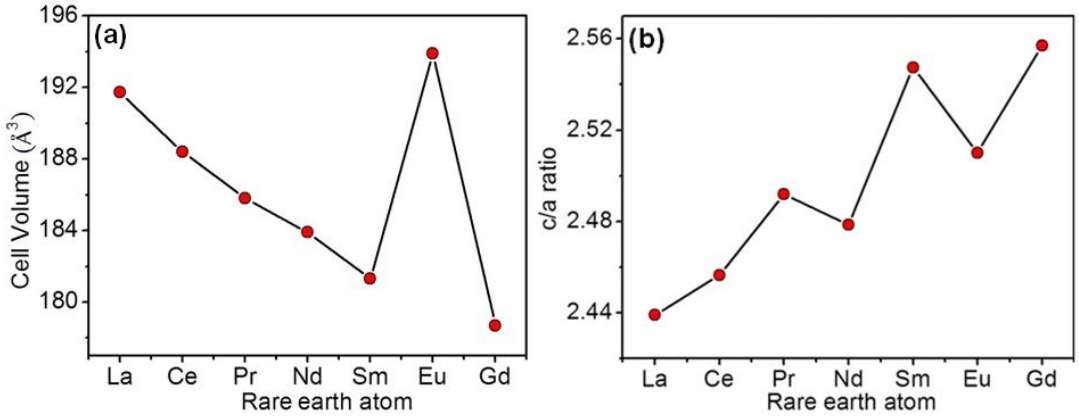

Figure 2.2.5. (a) Unit cell volume and (b) *c*/*a* ratio versus *RE* atom in the compounds *RE*CuGa$_3$

Table 2.2.6. Crystal data and structure refinement for NdCuGa$_3$ at 200 K, 300 K and 400 K.

	200 K	300 K	400 K
Empirical formula	NdCuGa$_3$	NdCuGa$_3$	NdCuGa$_3$
Formula weight	416.94	416.94	416.94
Temperature	293(2) K	293(2) K	293(2) K
Wavelength	0.71073 Å	0.71073 Å	0.71073 Å
Crystal system	Tetragonal	Tetragonal	Tetragonal
Space group, *Z*	*I*4*mm*, 2	*I*4*mm*, 2	*I*4*mm*, 2
Unit cell dimensions	$a = b$ = 4.1913(8) Å c = 10.409(2) Å	$a = b$ = 4.2020(3) Å c = 10.4151(8) Å	$a = b$ = 4.2194(8) Å c = 10.449(2) Å
Volume	182.85(6) Å^3	183.90(2) Å^3	186.02(6) Å^3
Density (calculated)	7.573 g/cm^3	7.530 g/cm^3	7.444 g/cm^3
Absorption coefficient	41.214 mm^{-1}	40.979 mm^{-1}	40.512 mm^{-1}
F(000)	364	364	364
Crystal size (mm^3)	0.10 x 0.05 x 0.05	0.10 x 0.05 x 0.05	0.10 x 0.05 x 0.05
θ range for data collection	3.92 to 29.91°	3.91 to 62.73°	3.90 to 29.41°
Index ranges	-5<=h<=5, -5<=k<=5, -14<=l<=12	-8<=h<=10, -10<=k<=10, -26<=l<=26	-5<=h<=5, -5<=k<=5, -13<=l<=13
Reflections collected	646	5395	825
Independent reflections	163 [R_{int} = 0.0728]	929 [R_{int} = 0.0544]	167 [R_{int} = 0.0615]
Completeness to θ = 62.73°	100%	100%	100%
Refinement method	Full-matrix least-squares on F^2		
Data / restraints / parameters	163 / 1 / 15	929 / 1 / 15	167 / 1 / 15
Goodness-of-fit	1.339	1.269	1.201
Final R indices [>2σ(I)]	R_{obs} = 0.0440, wR_{obs} = 0.1198	R_{obs} = 0.0429, wR_{obs} = 0.1130	R_{obs} = 0.0335, wR_{obs} = 0.0765
R indices [all data]	R_{all} = 0.0440, wR_{all} = 0.1198	R_{all} = 0.0504, wR_{all} = 0.1334	R_{all} = 0.0336, wR_{all} = 0.0766
Extinction coefficient	0.016(6)	0.073(9)	0.012(3)
Largest diff. peak and hole	3.333 and -2.610 e·Å^{-3}	6.385 and -14.264 e·Å^{-3}	2.543 and -1.265 e·Å^{-3}

$R = \Sigma||F_o|-|F_c|| / \Sigma|F_o|$, $wR = \{\Sigma[w(|F_o|^2 - |F_c|^2)^2] / \Sigma[w(|F_o|^4)]\}^{1/2}$ and calcw=1/[$\sigma^2(Fo^2)$+(0.0359P)^2+6.1794P] where P = (Fo^2+2Fc^2)/3

Table 2.2.7. Anisotropic displacement parameters (Å^{2}x10^3) for NdCuGa$_3$ at different temperatures with estimated standard deviations in parentheses.

Label	U_{11}	U_{22}	U_{33}	U_{12}	U_{13}	U_{23}
At 200K						
Nd	6(1)	6(1)	6(1)	0	0	0
Cu	14(2)	14(2)	36(7)	0	0	0
Ga(1)	5(2)	5(2)	19(4)	0	0	0
Ga(2)	8(2)	8(2)	8(2)	0	0	0
At 300K						
Nd	8(1)	8(1)	9(1)	0	0	0
Cu	10(1)	10(1)	29(1)	0	0	0
Ga(1)	14(1)	14(1)	37(2)	0	0	0
Ga(2)	11(1)	12(1)	9(1)	0	0	0
At 400K						
Nd	9(1)	9(1)	7(1)	0	0	0
Cu	5(2)	5(2)	26(4)	0	0	0
Ga(1)	25(2)	25(2)	22(3)	0	0	0
Ga(2)	16(2)	14(2)	9(1)	0	0	0

The anisotropic displacement factor exponent takes the form: $-2\pi^2[h^2a^{*2}U_{11} + ... + 2hka^*b^*U_{12}]$.

Because of the diversity in crystal structure of 1-1-3 series (with twelve different structure types including YbCuGa$_3$ discussed in last section) and the structural instability observed in NdCuGa$_3$ compound, temperature dependent SCXRD studies have performed in the temperature range 100-400 K for all compounds to check for any phase transitions. As expected, an increase in the lattice parameters and cell volume of the structure with increasing temperature has been observed (Figure 2.2.6). In general, no phase transitions were observed within this temperature range for all compounds except PrCuGa$_3$. Interestingly, the single crystal data of PrCuGa$_3$ at 400 K suggests tetragonal crystal system crystallizing in the Rb$_5$Hg$_{19}$ having centrosymmetric space group (*I*4/*m*). This is another indication that PrCuGa$_3$ is unstable at room temperature and tries to stabilize in a more symmetric structure at higher temperature. The parameters obtained from the refinement are higher than the accepted values (Table 2.2.8, 2.2.9 and 2.2.10) due to low quality or insufficient data. The superstructure of PrCuGa$_3$ observed at 400 K is shown in Figure 2.2.7.

Table 2.2.8. Crystal data and structure refinement for $PrCuGa_3$ at 400(2) K

Empirical formula	$PrCuGa_3$
Formula weight	521.65
Wavelength	0.71073 Å
Crystal system	Tetragonal
Space group, *Z*	*I*4/*m*, 2
Unit cell dimensions	$a = b = 9.4158(14)$ Å, $c = 10.4817(19)$ Å
Volume	929.3(3) Å^3
Density (calculated)	7.457 g/cm^3
Absorption coefficient	40.604 mm^{-1}
F(000)	1822
Crystal size	0.10 x 0.05 x 0.05 mm^3
θ range for data collection	2.91 to 29.96°
Index ranges	-10<=*h*<=13, -11<=*k*<=12, -14<=*l*<=13
Reflections collected	3491
Completeness to $\theta = 29.96°$	99.4%
Refinement method	Full-matrix least-squares on F^2
Data / restraints / parameters	711 / 0 / 33
Goodness-of-fit	1.077
Final *R* indices [>2σ(I)]	$R_{obs} = 0.1048$, $wR_{obs} = 0.2863$
Extinction coefficient	0.0035(9)
Largest diff. peak and hole	8.242 and -5.267 e·Å^{-3}

$R = \Sigma||F_o|-|F_c|| / \Sigma|F_o|$, $wR = \{\Sigma[w(|F_o|^2 - |F_c|^2)^2] / \Sigma[w(|F_o|^4)]\}^{1/2}$ and calcw=1/[$\sigma^2(Fo^2)$+(0.0359P)^2+6.1794P] where P = (Fo^2+2Fc^2)/3

Table 2.2.9. Atomic coordinates (x10^4) and equivalent isotropic displacement parameters (Å^{2}x10^3) for $PrCuGa_3$ at 400(2) K with estimated standard deviations in parentheses.

Label	*x*	*y*	*z*	Occupancy	U_{eq}*
Pr(1)	0	0	5000	1	8(2)
Pr(2)	3000(3)	1002(3)	0	1	7(2)
Cu	0	0	1112(15)	1	26(3)
Ga(1)	0	5000	2500	1	12(2)
Ga(2)	1998(4)	4003(5)	1117(6)	1	30(2)
Ga(3)	998(4)	2001(4)	2499(5)	1	14(2)

*U_{eq} is defined as one third of the trace of the orthogonalized U_{ij} tensor.

Table 2.2.10. Anisotropic displacement parameters (Å^{2}x10^3) for PrCuGa$_3$ at 400(2) K with estimated standard deviations in parentheses.

Label	U_{11}	U_{22}	U_{33}	U_{12}	U_{13}	U_{23}
Pr(1)	5(2)	5(2)	14(3)	0	0	0
Pr(2)	5(2)	5(2)	12(2)	0(1)	0	0
Cu	1(2)	1(2)	76(9)	0	0	0
Ga(1)	6(2)	6(2)	26(6)	0	0	0
Ga(2)	8(2)	10(2)	71(4)	-1(2)	1(3)	0(3)
Ga(3)	7(2)	4(2)	31(3)	-1(2)	1(2)	0(2)

The anisotropic displacement factor exponent takes the form: $-2\pi^2[h^2a^{*2}U_{11} + ... + 2hka^*b^*U_{12}]$.

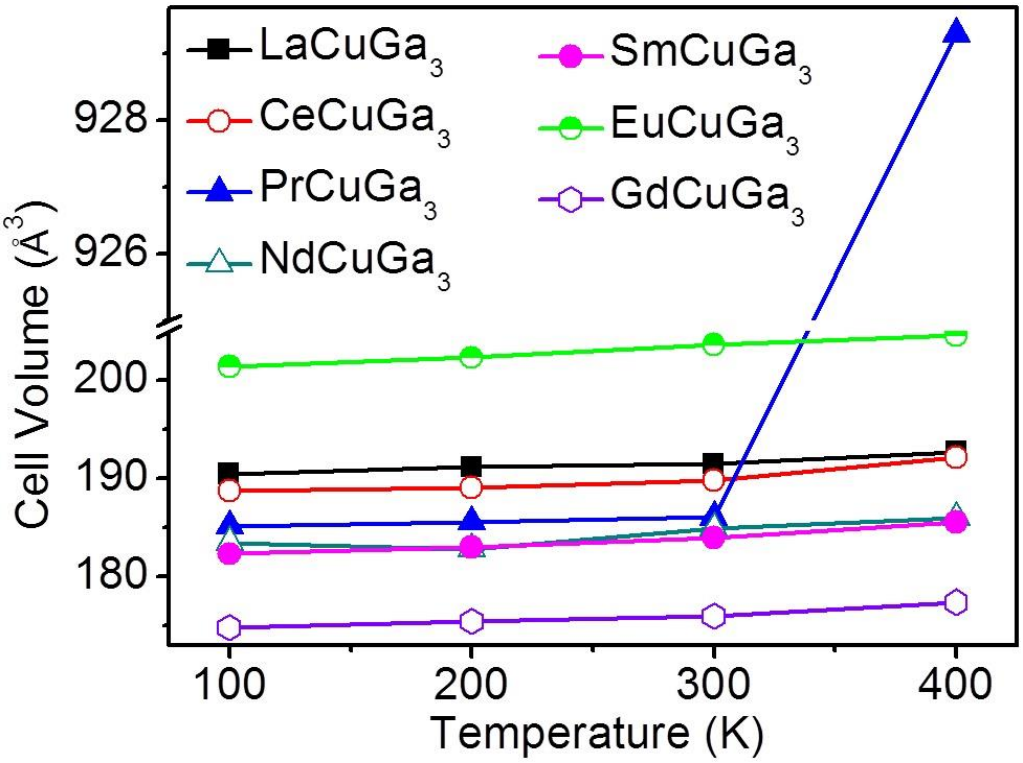

Figure 2.2.6. Temperature dependence of the unit cell volume obtained from the single crystal data of *RE*CuGa$_3$ over the range of 100 to 400 K.

This could probably indicate that the system has not completely transformed into another phase and data at higher temperature is required for better refinement. This probable phase transition was further checked with the *E***E*-1 values obtained for all the compounds from the single crystal XRD data. The values are in the range 0.587-0.734 K, which is close

to the expected value for a non-centrosymmetric system (Figure 2.2.8.) except for PrCuGa$_3$ at 400 K (*E*E*-1 = 1.5406), which clearly predicts a centrosymmetric structure.

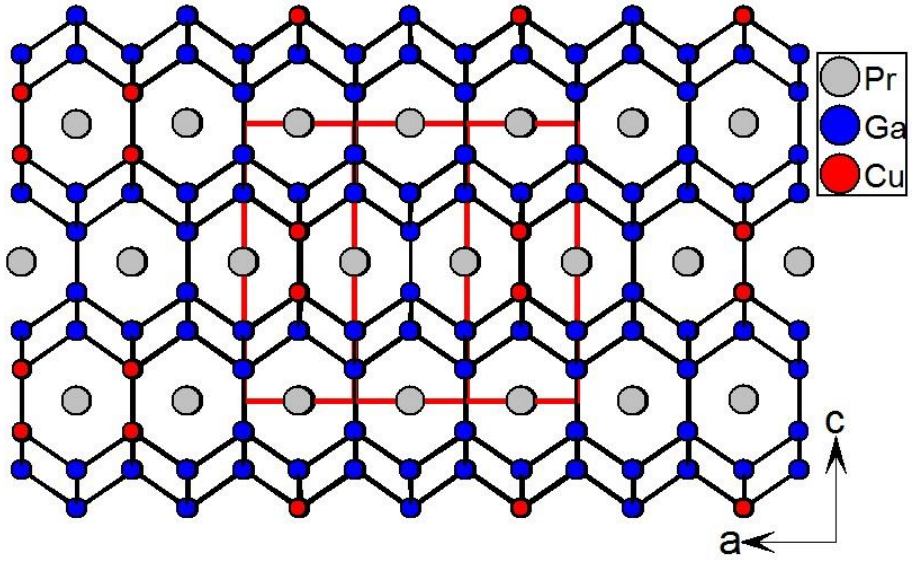

Figure 2.2.7. The crystal structures of PrCuGa$_3$ shown along the *b*-axis, at 400 K with the space group of *I*4/*m*. The unit cell outlined with solid red.

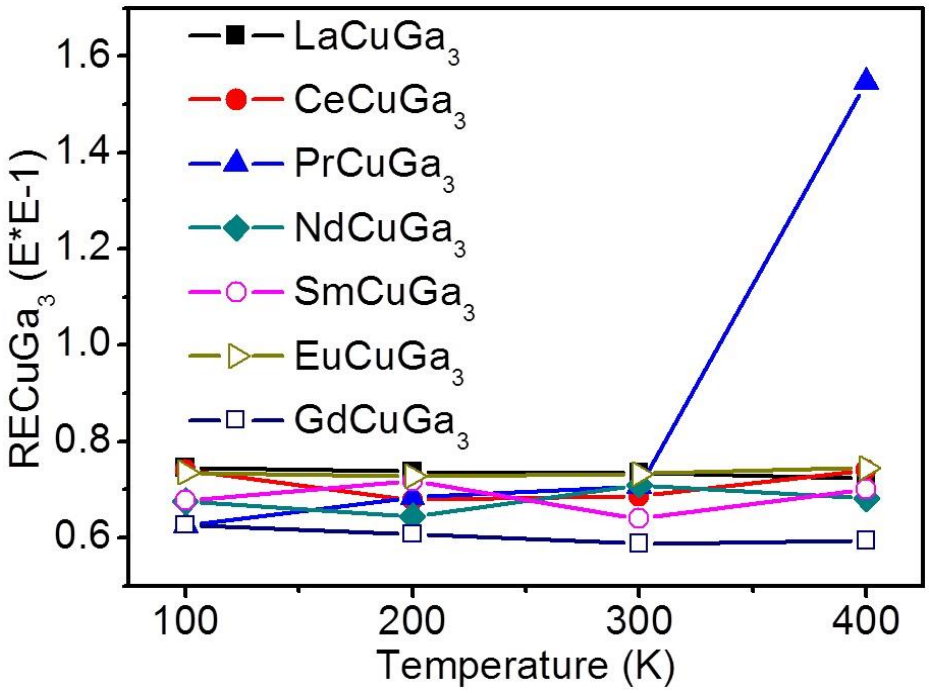

Figure 2.2.8. The *E*E*-1 values of *RE*CuGa$_3$ vs temperature with different temperature ranges.

To probe this, high temperature synchrotron powder XRD measurements have performed (Figure 2.2.9) on PrCuGa$_3$. The material undergoes a structural phase transition at

800 K to more symmetrical primitive cubic system with Cu_3Au structure type ($Pm\bar{3}m$). However, the phase transition at 400 K could not be traced in the case of single crystal XRD of $PrCuGa_3$, because the PXRD patterns of $BaNiSn_3$, $BaAl_4$ and Rb_5Hg_{19} are very similar in nature. The structural swinging close to room temperature and structural phase transitions observed at higher temperatures through single crystal and powder XRD are represented in Figure 2.2.10. All these controlled measurements indicate that the crystal structures in these compounds are highly unstable. This instability could be due to electronic, steric and other factors which suggest the ability to tune the physical properties significantly via pressure or other external probes.

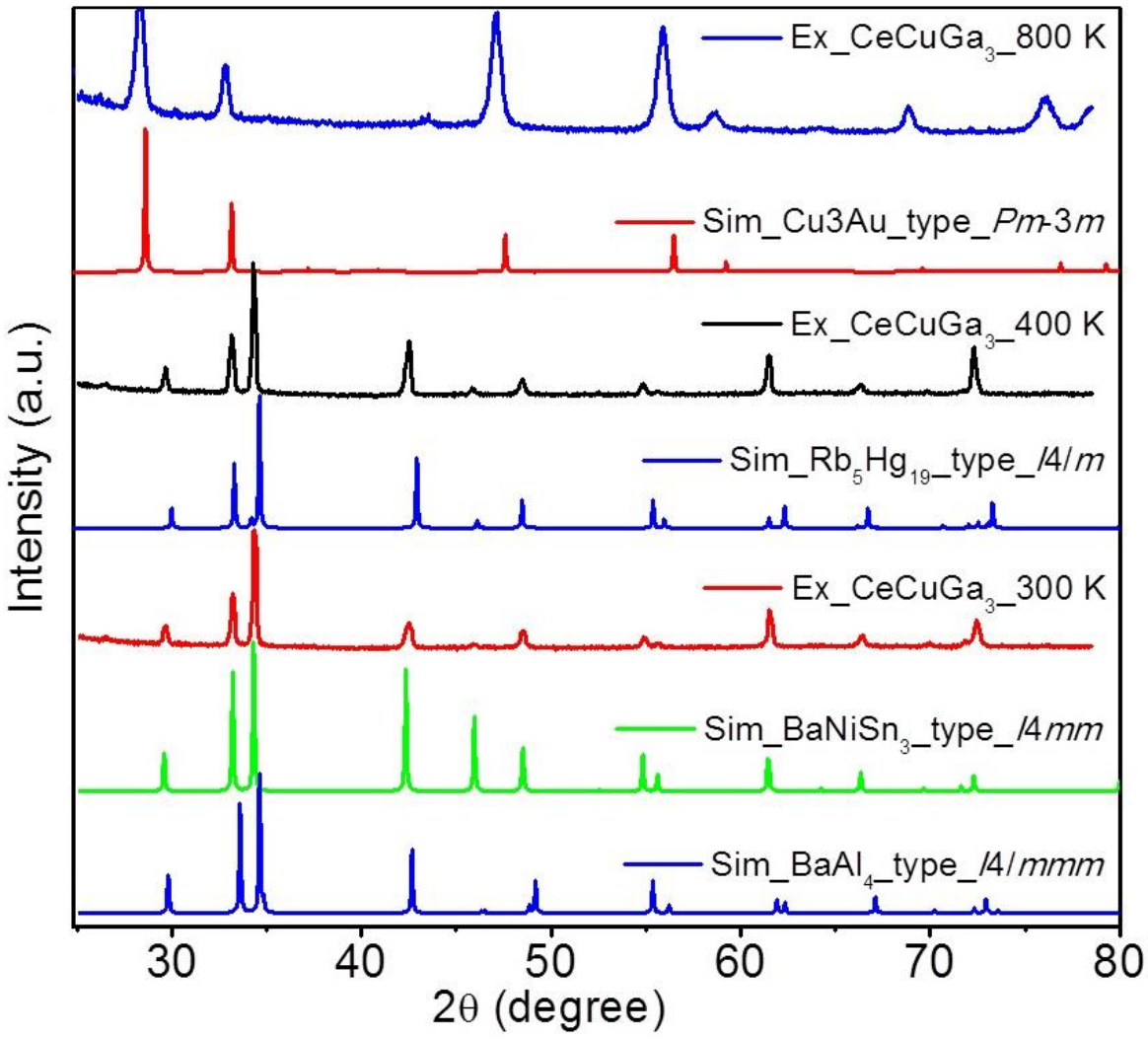

Figure 2.2.9. PXRD patterns of $CeCuGa_3$ at 300 K, 400 K and 800 K using synchrotron XRD collected at Indian beamline, KEK, photon fctory, Japan. The powder patterns are compared with simulated patterns of $BaAl_4$, $BaNiSn_3$, Rb_5Hg_{19} and Cu_3Au structure types.

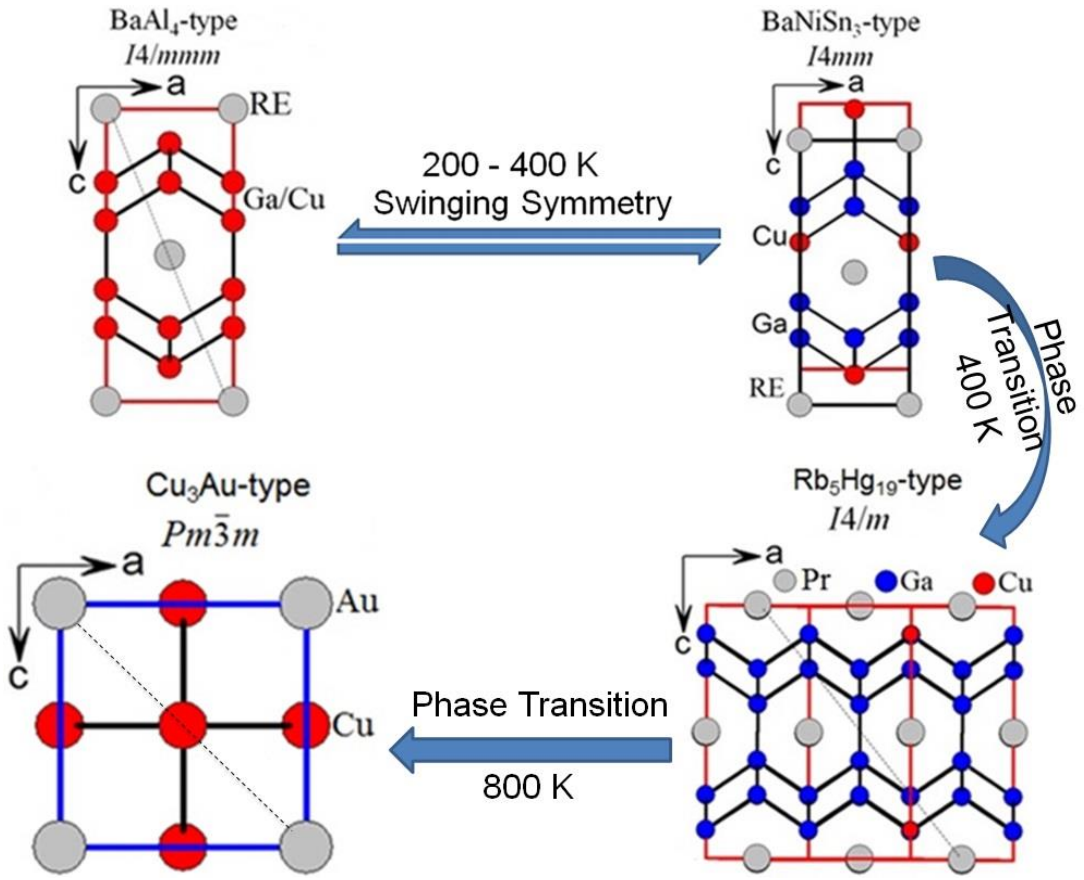

Figure 2.2.10. Unit cell representation of the temperature dependant evolution of the different structure types as observed in *RE*CuGa$_3$ compounds.

2.2.2.4. Neutron diffraction and Synchrotron XRD

Neutron diffraction experiment on the powdered sample of $CeCuGe_3$ was carried out at 10 K and 300 K (Figure 2.2.11). The data for both the temperatures were analyzed by Rietveld refinement method using the structural models of the *I*4/*mmm* and *I*4*mm* space groups. As far as diffraction peaks and profile matching is concerned, both space groups gave reasonably good fit and it is very difficult to precisely point out the appropriate space group this compound. In addition to the neutron data, synchrotron XRD data was also used to refine the structure at 300 K (Figure 2.2.12). The combined analysis of neutron and XRD data at 300 K gives a better profile fitting for the *I*4*mm* space group. The best probable solution for structure at room temperature appears to be *I*4*mm*, as it provides a better fit to the XRD data (at 300 K); the fit is not so different from the original ND data refinements for both the space groups.

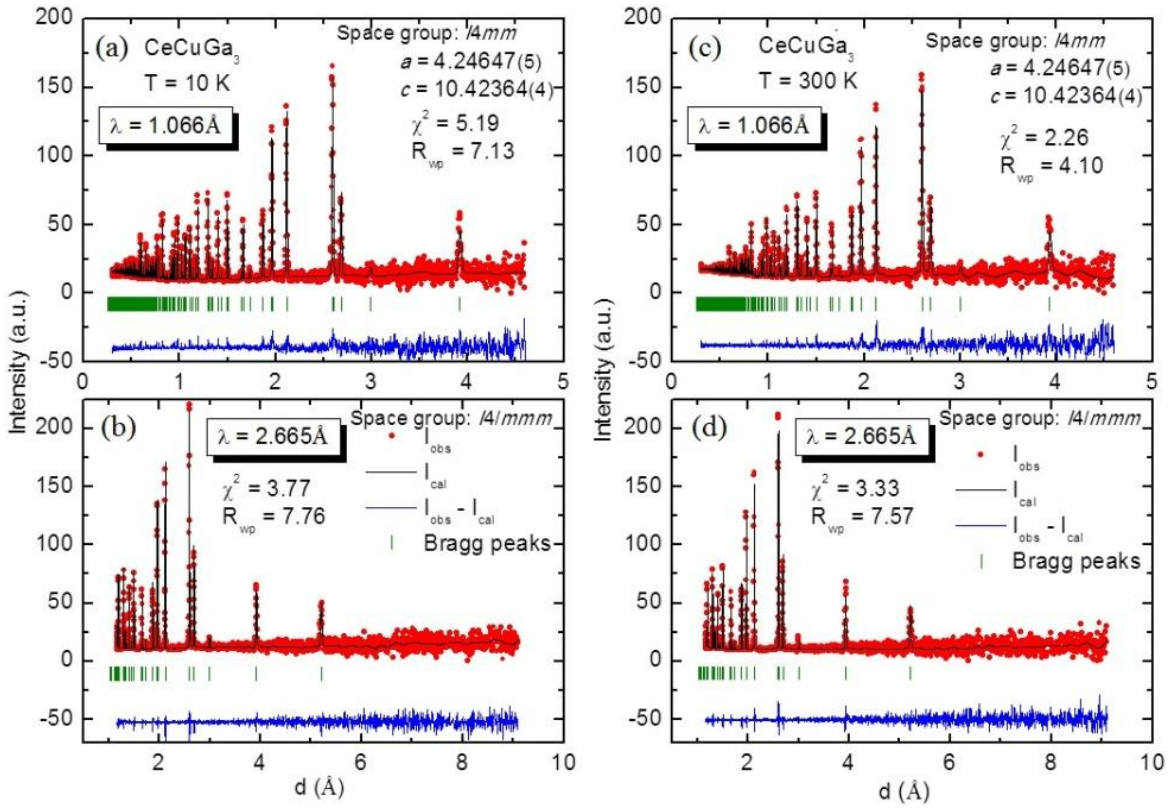

Figure 2.2.11. Rietveld refinement plots of the neutron diffraction patterns of CeCuGa$_3$ at (a) and (b) 10 K, (c) and (d) 100 K, with the space groups of *I*4*mm* and *I*4/*mmm*.

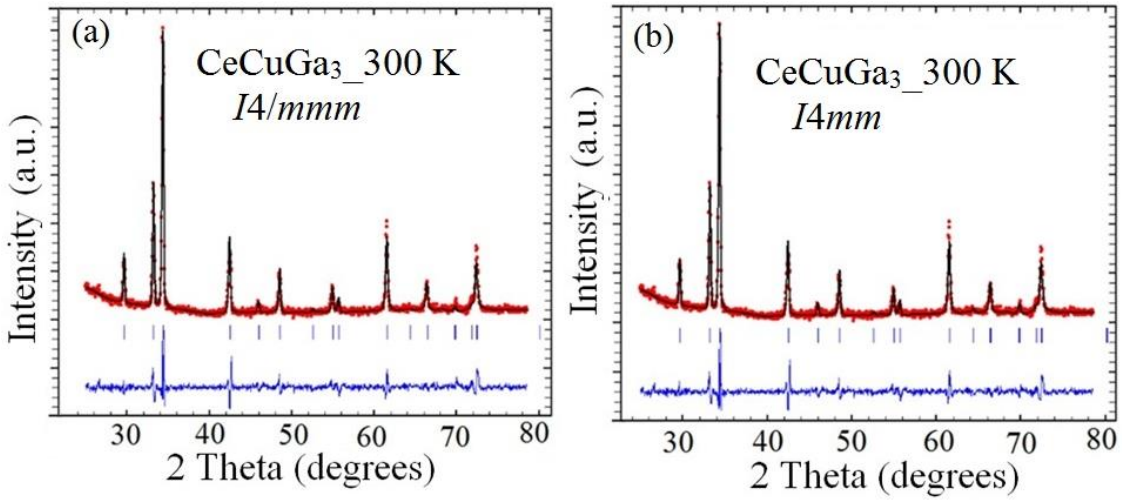

Figure 2.2.12. Rietveld refinement plots of CeCuGa$_3$ at 300 K with the space groups of *I*4/*mmm* (a) and *I*4*mm* (b), using synchrotron XRD collected at the Indian beamline at KEK Photon Factory, Japan.

Up to 300 K, *I*4*mm* fits slightly better than *I*4/*mmm* however, at 500 K and 800 K, it appears that either there is a transformation of the structure, or amorphization, or loss of Ga

from the structure as significant changes in the XRD patterns are clearly visible. The phase transition at 500 K may be related to the formation of ordered *RE*CuGa$_3$ within Rb_5Hg_{19} structure type as observed in the single crystal XRD refinement for PrCuGa$_3$ and phase transition at 800 K to the Cu_3Au structure type which is observed in synchrotron XRD studies. These two high temperature phases are in fact reported here for the first time in 1-1-3 family compounds.

2.2.2.5. X-ray absorption near edge spectroscopy (XANES)

Because of the deviation of the unit cell volume for EuCuGa$_3$ from the trend of the remaining compounds, the oxidation state of the Eu atom was studied. To confirm the oxidation state of Eu, the XANES measurements were performed, which is a strong experimental tool to firmly establish the valence state of an element in a compound. A sharp signal at 6973 eV was observed in the Eu L_{III} X-ray absorption spectrum of EuCuGa$_3$ (Figure 2.2.13). This value is characteristic of the $4f^7$ (Eu^{2+}) configuration and arises due to a $2p_{3/2}$ to 5d transition.[90] This result directly proves that the Eu is in its divalent state, as inferred from the unit cell volume (Figure 2.2.5a) and the magnetic susceptibility data (discussed below).

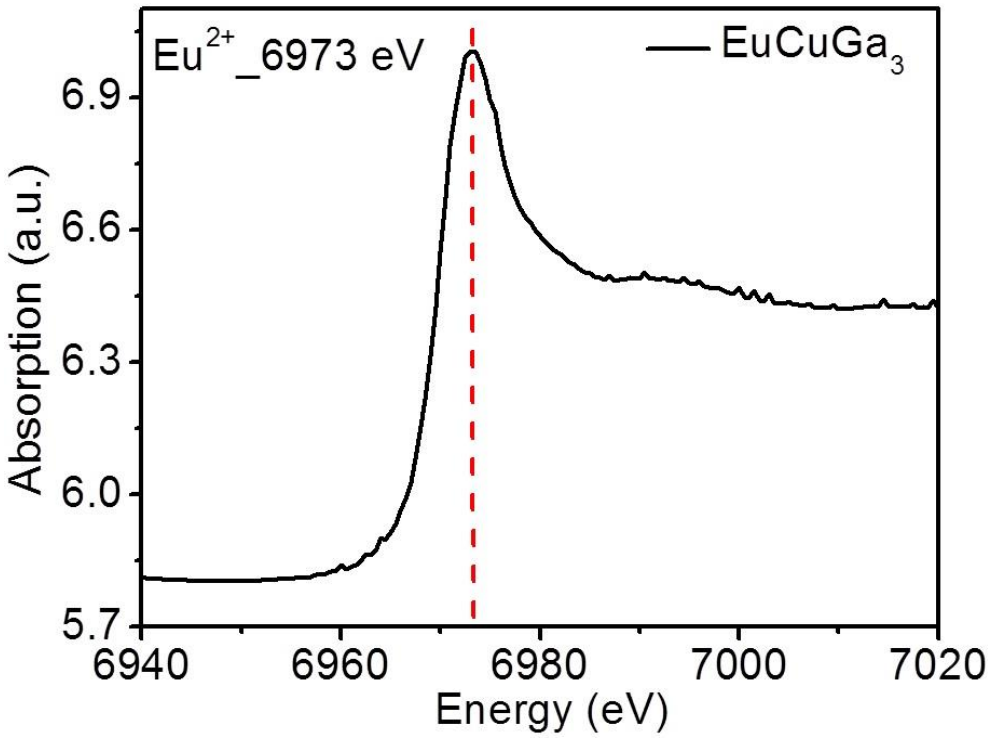

Figure 2.2.13. Eu L_{III} absorption edge spectrum for EuCuGa$_3$. The dotted line represents the energy characteristic of divalent Eu absorption.

2.2.2.6. Physical Properties

2.2.2.6.1. Magnetic studies

The temperature dependent DC susceptibility at high temperatures for all the *RE*CuGa$_3$ compounds (excluding non-magnetic LaCuGa$_3$) were studied and are shown in Figure 2.2.14. In the high temperature limit the data for all materials, except for non-magnetic LaCuGa$_3$, were fitted to the modified Curie-Weiss form, including a temperature independent contribution[75]

$$c(T) = \frac{C}{T - q_{CW}} + c_0 \quad .$$

The values for χ_0 are much smaller than the Curie-Weiss contribution, as evidenced by the linear behaviour seen in Figure 2.2.14, except for the case of SmCuGa$_3$ (inset of Figure 2.2.14), where the Curie-Weiss contribution itself is quite small. χ_0 corrects for both intrinsic (*e.g.*, Pauli contribution) and extrinsic (impurity phase) contributions. The values of the Curie-Weiss temperature θ_{CW} and effective moment μ_{eff} (in Bohr magneton μ_B) extracted from *C* are listed in Table 2.2.11.

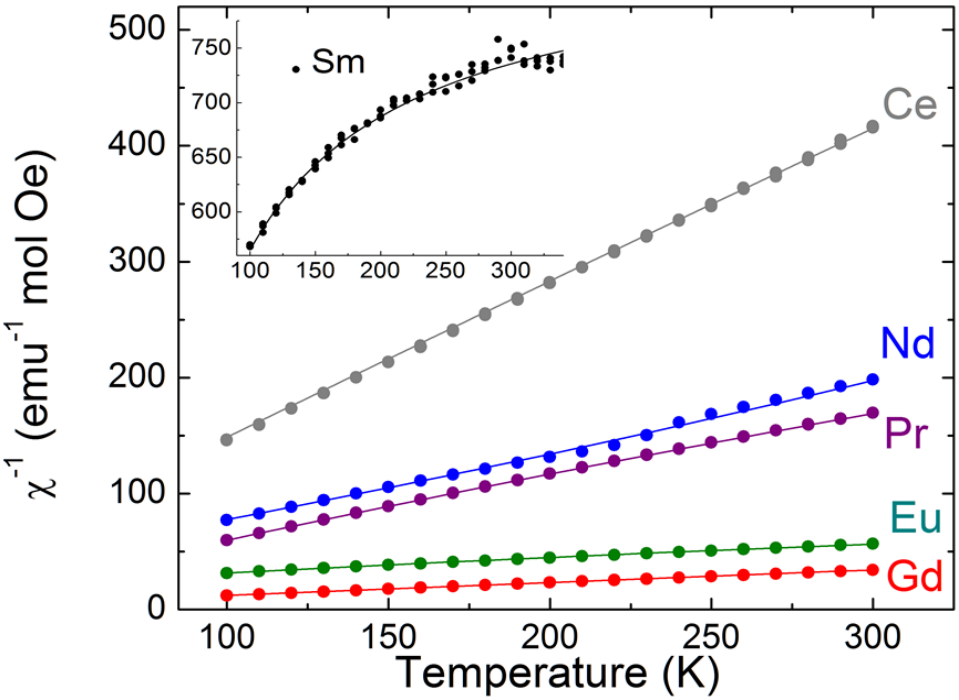

Figure 2.2.14. DC susceptibility for the *RE*CuGa$_3$ materials at high temperature. Solid lines are fits as described in the text; the curves for NdCuGa$_3$ and EuCuGa$_3$ have been offset by +20 emu^{-1} mol Oe for clarity.

Table 2.2.11. Magnetic properties of *RE*CuGa$_3$. $T_{N,C}$ denotes magnetic transition temperature.

	CeCuGa$_3$	PrCuGa$_3$	NdCuGa$_3$	SmCuGa$_3$	EuCuGa$_3$	GdCuGa$_3$
θ_{CW} (K)	-8.1	4.3	5.1	12.4	25.2	-6.1
μ_{eff} (μ_B)	2.4	3.5	4.1	0.6	7.0	8.3
$T_{N,C}$ (K)	1.9	< 0.3	2.8	17	24	8.3

The experimental values for μ_{eff} are in good agreement with those expected from Hund's rules for trivalent lanthanides, apart from EuCuGa$_3$ and SmCuGa$_3$. For EuCuGa$_3$, the large moment is due to the predominance of the Eu^{2+} valence state, and the observed $\mu_{eff,Eu}$ = 7.0 μ_B is reasonably close to the expected divalent value of 7.94 μ_B; the deviation may be due to a small fraction of (non-magnetic) Eu^{3+} formation. For SmCuGa$_3$, it must be noted that Sm^{3+} is often observed to have a reduced moment due to mixing of the lowest lying and excited crystal field levels. Apart from the La and Pr compounds, all the materials exhibit a peak in the DC susceptibility transition above 1.8 K (see Figure 2.2.15) which can be attributed to the onset of magnetic order.

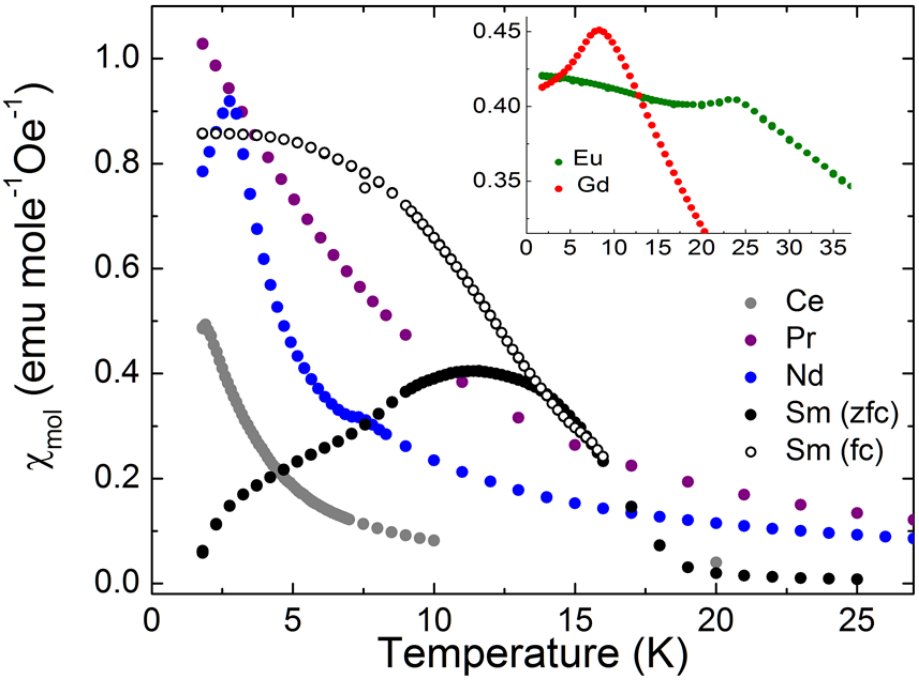

Figure 2.2.15. DC susceptibility versus temperature at low temperatures for the *RE*CuGa$_3$ materials. Data were taken in magnetic fields of 100 Oe (Sm 'fc' = field cooled and 'zfc' = zero field cooled).

Field-cooled and zero-field cooled curves were nearly identical, except for the Sm compound, suggesting that ordering is antiferromagnetic in all the ordered materials except SmCuGa$_3$. These transition temperatures are in agreement with earlier observations on GdCuGa$_3$, CeCuGa$_3$, and SmCuGa$_3$.[23] Close inspection of the curves for SmCuGa$_3$ shows an inflection near 5 K, suggesting that a second magnetic transition may occur. Magnetic measurements are underway on these systems for better understanding of their magnetic order. Measurements of the magnetization in over five quadrants cycles confirmed that only the Sm compound showed any significant hysteresis consistent with all the other materials undergoing antiferromagnetic transitions, while the SmCuGa$_3$ undergoes a ferri- or ferromagnetic transition. The magnetization data is shown in Figure 2.2.16, with the full hysteresis loop for SmCuGa$_3$ shown in the inset.

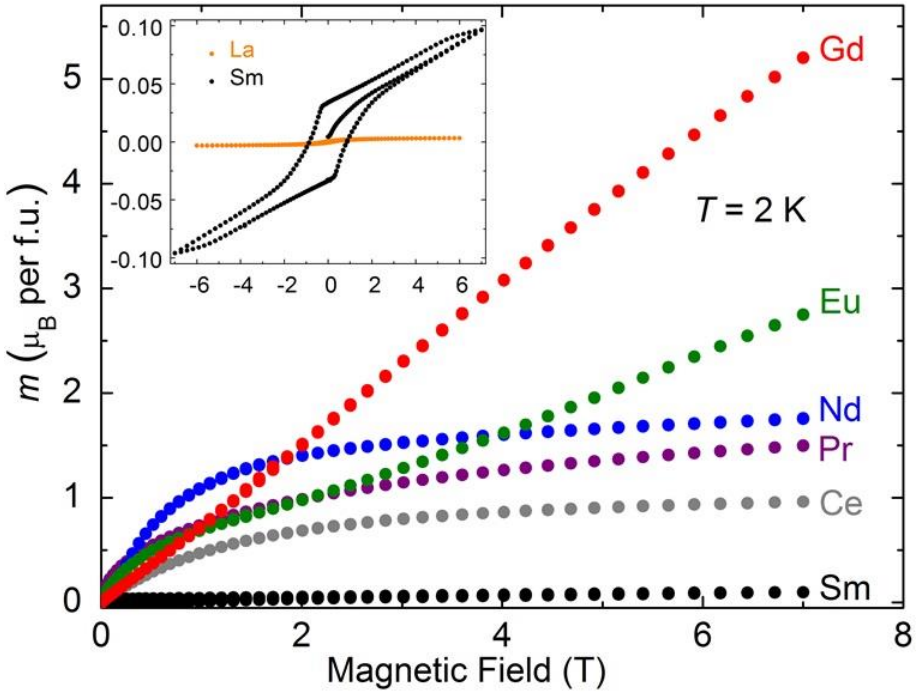

Figure 2.2.16. DC magnetization vs magnetic field taken at T = 2 K. Each curve in the figure includes data for both increasing and decreasing magnetic field. Inset: Full hysteresis loop on an expanded scale for SmCuGa$_3$ and LaCuGa$_3$.

2.2.2.6.2. Electrical resistivity

The temperature dependent resistivity (normalized to the room temperature resistivity) is shown in Figure 2.2.17. As expected, all samples are metallic and those that order magnetically exhibit resistive anomalies at the ordering temperatures determined from

the temperature dependent magnetization; the anomaly is very weak for NdCuGa$_3$ and is shown in the inset of Figure 2.2.18. The room temperature resistivity's range from 0.4 (LaCuGa$_3$) to 2.5 $\mu\Omega$cm (EuCuGa$_3$). As mentioned earlier, the tortuosity and intergrain scattering causes the measured resistivity to be much larger than the intrinsic resistivity, which explains why the room temperature resistivity measured for the CeCuGa$_3$ sample is approximately twenty-five times larger than that reported for single crystal samples.[78]

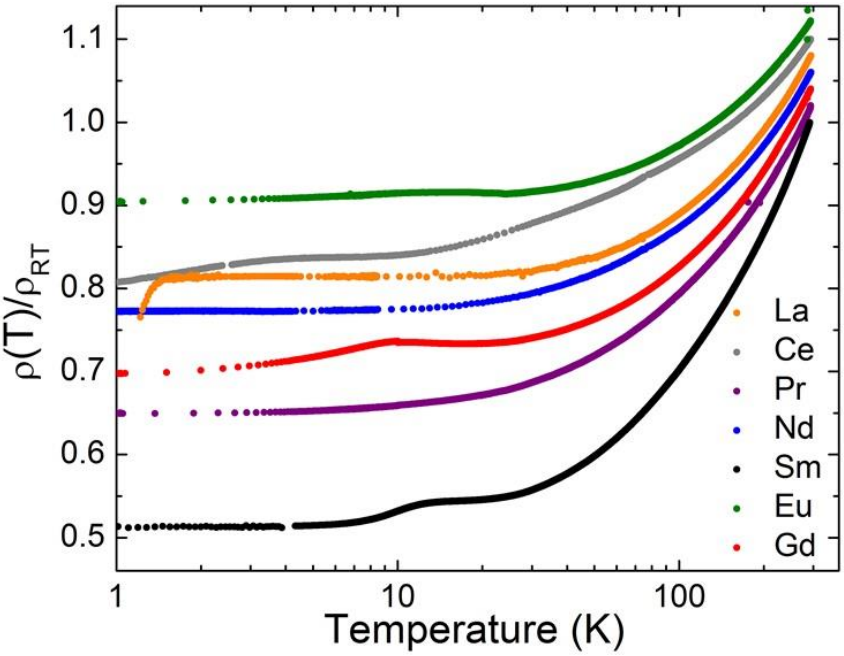

Figure 2.2.17. Normalized resistivity vs temperature for *RE*CuGa$_3$. Curves have been offset by equal increments of 0.02 for clarity.

The resistivity measurements taken for the samples PrCuGa$_3$ and LaCuGa$_3$ below 1.8 K (Figure 2.2.18) showed two important features. First, within the experimental resolution PrCuGa$_3$ has no resistive anomaly down to 0.3 K, so it remains paramagnetic. Second, the LaCuGa$_3$ sample shows incomplete superconductivity below 1 K which was observed for two different samples. These two features suggest granular superconductivity, where individual grains become superconducting at a critical temperature T_{C1}, but phase coherence between grains is achieved at some lower temperature T_{C2}.[91] The transition temperature of 1 K is very close to that for bulk superconducting Ga and so superconductivity could be due to Ga filaments at grain boundaries. XRD and SEM microprobe analysis showed no signs of significant amounts of isolated Ga. Moreover, the low temperature critical field to be well over 0.1 *T* have measured an order of magnitude larger than that for bulk Ga, The occurrence

of bulk superconductivity originating from the non-centrosymmetric structure of the material would be of great interest.[92] Experiments to confirm the bulk nature of superconductivity in $LaCuGa_3$ are currently underway.

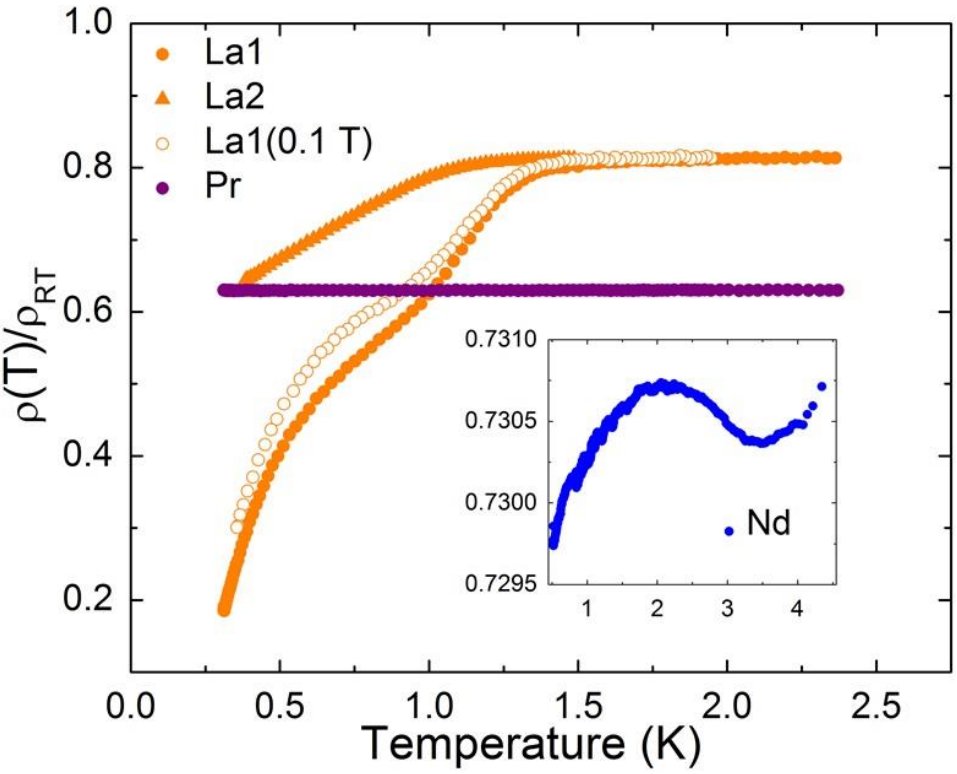

Figure 2.2.18. Low temperature normalized resistivity for $PrCuGa_3$ and two samples of $LaCuGa_3$; also shown for $LaCuGa_3$ sample 1 is the temperature dependent normalized resistivity in a field of 1000 Oe. Inset: expanded view of the weak resistive anomaly at the magnetic ordering temperature of $NdCuGa_3$.

2.2.3. Conclusion

One of the biggest challenges in the field of intermetallic chemistry is the synthesis and crystal growth of pure compounds. Since there are difficulties in predicting the chemical bonding nature in these compounds, a systematic synthesis method cannot be employed. Quite often these compounds are synthesized by conventional techniques such as arc melting and high frequency induction furnaces. Without proper single crystal growth, the actual structure of the compounds, in most cases, cannot be realized. The close relationship between the structural models and the similar scattering power of constituent atoms further adds to the difficulty of using X-rays to determine the actual structure. However, a proper understanding of the crystal structure is needed to characterize the structure property relationships. With all

these issues in mind, irregularly shaped single crystals of the compounds *RE*$CuGa_3$ have been synthesized using the arc-melting technique and high frequency induction heating with Ga as the self flux. There are several factors limiting the correct prediction of the crystal structures of these compounds, the most important being the 12 different crystal types (one more structure type $SrPdGa_3$ was reported by Pöttgen et al. during this work)[56] in the 1:1:3 family of intermetallics and the centrosymmetric $BaAl_4$ and non-centrosymmetric $BaNiSn_3$ structures are closely related. In addition, it is very hard to find the ordering of Cu and Ga due to their very similar scattering power of X-rays. All these issues have been circumvented by using the combined study of powder and single crystal XRD, neutron diffraction and synchrotron XRD. The temperature dependent measurements on XRD suggest the large instability of these systems, which cause multiple structural transitions and allows the tuning of interesting physical properties. The transition at high temperatures of $PrCuGa_3$ into the Rb_5Hg_{19} and Cu_3Au structures are reported for the first time in the 1-1-3 family, extending the number of probable structure types to 15. The unique nature of Eu in terms of valency has been studied by bond analysis, magnetism and XANES measurements. Complex magnetic phases and possible bulk superconductivity are indicated by the preliminary magnetic and electronic transport measurements.

2.3. References

1. Villars, P.; Cenzual, K. *Pearson's Crystal Data-Crystal Structure Database for Inorganic Compounds*, ASM International: Materials Park: Ohio, USA, 2010.

2. Hillier, A. D.; Adroja, D. T.; Manuel, P.; Anand, V. K.; Taylor, J. W.; McEwen, K. A.; Rainford, B. D.; Koza, M. M., *Phys. Rev. B* **2012,** *85*, 134405−13441.

3. Seropegin, Y. D.; Shapiev, B. I.; Gribanov, A. V.; Bodak, O. I., *J. Alloy Compd.* **1999,** *288*, 147-150.

4. Muro, Y.; Eom, D.; Takeda, N.; Ishikawa, M., *J. Phys. Soc. Jpn.* **1998,** *67*, 3601-3604.

5. Cava, R. J.; Ramirez, A. P.; Takagi, H.; Krajewski, J. J.; Peck, W. F., *J. Magn. Magn. Mater.* **1993,** *128*, 124-128.

6. Muller, U., *Inorganic Structural Chemistry*. Wiley: Chichester, U.K., 1993.

7. Bie, H. Y.; Zelinska, O. Y.; Tkachuk, A. V.; Mar, A., *Chem. Mater.* **2007,** *19*, 4613-4620.

8. Manfrinetti, P.; Dhar, S. K.; Kulkarni, R.; Morozkin, A. V., *Solid State Commun.* **2005,** *135*, 444-448.

9. Grin, Y. N.; Hiebl, K.; Rogl, P.; Noel, H., *J. Less-Common Met.* **1990,** *162*, 371-377.

10. Sampathkumaran, E. V.; Das, I., *Solid State Commun.* **1992,** *81*, 901-904.

11. Ghosh, K.; Ramakrishnan, S.; Dhar, S. K.; Malik, S. K.; Chandra, G.; Pecharsky, V. K.; Gschneidner, K. A.; Hu, Z.; Yelon, W. B., *Phys. Rev. B* **1995,** *52*, 7267-7277.

12. Morozkin, A., *J. Alloy Compd.* **2004,** *370*, L1-L3.

13. Bergerhoff, G.; Brown, I. D. *Inorganic Crystal Structure Database*, International Union of Crystallography: Chester, 1987.

14. Dörrscheidt, W.; Schäfer, H., *J. Less-Common Met.* **1978,** *58*, 209−216.

15. Iwamoto, Y.; Ueda, K.; Kohara, T.; Yamada, Y., *Physica B* **1995,** *206–207*, 276-278.

16. Oniskovets, B. D.; Bodak, O. I.; Goral, O. E., *Dopov. Akad. Nauk Ukr. RSR (Ser. B)* **1987,** *8*, 46-48.

17. Mentink, S. A. M.; Bos, N. M.; Vanrossum, B. J.; Nieuwenhuys, G. J.; Mydosh, J. A.; Buschow, K. H. J., *J. Appl. Phys.* **1993,** *73*, 6625-6627.

18. Zarechnyuk, O. S.; Krypyakevych, P. I.; Gladyshevskii, E. I., *Sov. Phys. Crystallogr.* **1965,** *9*, 706−708.

19. Mayer, I.; Felner, I., *J. Phys. Chem. Solids* **1977,** *38*, 1031-1034.

20. Kontani, M.; Ido, H.; Ando, H.; Nishioka, T.; Yamaguchi, Y., *J. Phys. Soc. Jpn.* **1994,** *63*, 1652-1655.

21. Tang, J.; Gschneidner, K. A.; Caspary, R.; Steglich, F., *Physica B* **1990,** *163*, 201-204.

22. Bodak, O. I.; Shvets, A. F., *Inorg. Mater.* **1983,** *19*, 1188−1190.

23. Bodak, O. I.; Kotur, B. Y.; Gladyshevskii, E. I., *Dopov. Akad. Nauk Ukr. RSR (Ser. A)* **1976,** *7*, 655−657.

24. Seropegin, Y. D.; Shapiev, B. I.; Gribanov, A. V.; Bodak, O. I., *J. Alloy Compd.* **1999,** *288*, 155-158.

25. Eisenmann, B.; Schäfer, H., *J. Less-Common Met.* **1986,** *123*, 89−94.

26. Bodak, O. I.; Pecharskii, V. K.; Mrooz, O. Y.; Zavodnik, V. E.; Vitvitskaya, G. M.; Salamakha, P. S., *Dopov. Akad. Nauk Ukr. RSR (Ser. B)* **1985,** *2*, 36−38.

27. Bodak, O. I.; Seropegin, Y. D.; Sologub, O. L.; Pecharskii, V. K.; Gribanov, A. V. In *Coll. Abs. Eur. Crystallogr. Meet. (12th)*, Moscow, 1989; Moscow, 1989; p 155−156.

28. Crerar, S. J.; Deakin, L.; Mar, A., *Chem. Mater.* **2005,** *17*, 2780-2784.

29. Ferguson, M. J.; Hushagen, R. W.; Mar, A., *J. Alloy Compd.* **1997,** *249*, 191-198.

30. Ge, M. H.; Corbett, J. D., *Inorg. Chem.* **2007,** *46*, 4138-4144.

31. Grube, K.; Wolf, T.; Adelmann, P.; Meingast, C.; Von Lohneysen, H., *Physica B* **2006,** *378-80*, 750-751.

32. Braun, H. F.; Segre, C. U., *Solid State Commun.* **1980,** *35*, 735−738.

33. Kuzma, Y. B.; Stelmakhovych, B. M., *Dopov. Akad. Nauk Ukr. RSR (Ser. B)* **1988,** *3*, 11−38.

34. SAINT, 6.02 ed.; Bruker AXS Inc.: Madison, Wisconsin, USA, 2000.

35. Sheldrick, G. M. *SADABS, Empirical Absorption Correction Program*, Göttingen, Germany, 1997.

36. Farrugia, L. J., *J. Appl. Crystallogr.* **1999,** *32*, 837−838.

37. Sheldrick, G. M., *Acta Crystallogr. A* **2008,** *64*, 112-122.

38. Sheldrick, G. M. *Bruker Analytical X-ray Systems Inc.*, Madison, WI, 1997.

39. *CRYSTAL IMPACT*, Rathausgasse 30, 53111, Bonn, Germany, 2010.

40. Fornasini, M. L.; Merlo, F. J., *J. Less-Common Met.* **1988,** *142*, 289−294.

41. Fornasini, M. L.; Manfrinetti, P.; Mazzone, D.; Riani, P.; Zanicchi, G., *J. Solid State Chem.* **2004,** *177*, 1919-1924.

42. Merlo, F.; Pani, M.; Fornasini, M. L., *J. Less-Common Met.* **1990,** *166*, 319-327.

43. Rieger, W.; Parthé, E., *Monatsh. Chem.* **1969,** *100*, 444−454.

44. Sampathkumaran, E. V.; Gupta, L. C.; Vijayaraghavan, P. R.; Hatwar, T. K.; Ghatikar, M. N.; Padalia, B. D., *Mater. Res. Bull.* **1980,** *15*, 939−943.

45. Lin, Q. S.; Corbett, J. D., *Inorg. Chem.* **2005,** *44*, 512-518.

46. Smart, J. S., *Effective Field Theories of Magnetism*. Philadelphia, PA, 1966.

47. Chondroudi, M.; Peter, S. C.; Malliakas, C. D.; Balasubramanian, M.; Li, Q. A.; Kanatzidis, M. G., *Inorg. Chem.* **2011,** *50*, 1184-1193.

48. Peter, S. C.; Eckert, H.; Fehse, C.; Wright, J. P.; Attfield, J. P.; Johrendt, D.; Rayaprol, S.; Hoffmann, R. D.; Pöttgen, R., *J. Solid State Chem.* **2006,** *179*, 2376-2385.

49. Felner, I.; Nowik, I.; Vaknin, D.; Potzel, U.; Moser, J.; Kalvius, G. M.; Wortmann, G.; Schmiester, G.; Hilscher, G.; Gratz, E.; Schmitzer, C.; Pillmayr, N.; Prasad, K. G.; Dewaard, H.; Pinto, H., *Phys. Rev. B* **1987,** *35*, 6956−6963.

50. Dremov, R. V.; Koblyuk, N.; Mudryk, Y.; Romaka, L.; Sechovsky, V., *J. Alloy Compd.* **2001,** *317*, 293-296.

51. Gondek, L.; Szytula, A.; Kaczorowski, D.; Prokhnenko, O.; Nenkov, K., *Phase Transit* **2007,** *80*, 563-573.

52. Pecharsky, V. K.; Gschneidner, K. A., *Adv. Mater.* **2001,** *13*, 683-686.

53. Fachinformationszentrum Karlsruhe GmbH Inorganic crystal structure database. In Eggenstein-Leopoldshafen, Germany, 2012.

54. Villars, P.; Cenzual, K., Pearson's crystal data - crystal structure database for inorganic compounds. In ASM International, M. P., Ed. Ohio, USA, 2010-11.

55. Subbarao, U.; Peter, S. C., *Cryst. Growth Des.* **2013,** *13*, 953-959.

56. Seidel, S.; Hoffmann, R. D.; Pöttgen, R., *Z. Kristallogr.* **2014,** *229*, 421-426.

57. Zarechnyuk, O. S.; Krypyakevych, P. I.; Gladyshevskii, E. I., *Sov. Phys. Crystallogr.* **1965,** *9*, 706-708.

58. Hillier, A. D.; Adroja, D. T.; Manuel, P.; Anand, V. K.; Taylor, J. W.; McEwen, K. A.; Rainford, B. D.; Koza, M. M., *Phys. Rev. B* **2012,** *85*, 134405−13441.

59. Smidman, M.; Adroja, D. T.; Hillier, A. D.; Chapon, L. C.; Taylor, J. W.; Anand, V. K.; Singh, R. P.; Lees, M. R.; Goremychkin, E. A.; Koza, M. M.; Krishnamurthy, V. V.; Paul, D. M.; Balakrishnan, G., *Phys. Rev. B* **2013,** *88*, 134416-134427.

60. Oniskovets, B. D.; Bodak, O. I.; Goral, O. E., *Dopov. Akad. Nauk. Ukr. RSR (Ser. B)* **1987,** *8*, 46-48.

61. Seropegin, Y. D.; Shapiev, B. I.; Gribanov, A. V.; Bodak, O. I., *J. Alloy Compd.* **1999,** *288*, 147-150.

62. Muro, Y.; Eom, D.; Takeda, N.; Ishikawa, M., *J. Phys. Soc. Jpn.* **1998,** *67*, 3601-3604.

63. Morozkin, A. V.; Seropegin, Y. D.; Bodak, O. I., *J. Alloy. Compd.* **1996,** *234*, 143-150.

64. Denysyuk, O. V.; Stelmakhovych, B. M.; Kuzma, Y. B., *J. Solid State Chem.* **1994,** *109*, 172-174.

65. Levin, E. M.; Bodak, O. I.; Zhipa, Y. V., *Dopov. Akad. Nauk Ukr. RSR (Ser. A)* **1986,** *5*, 77-79.

66. Zarechnyuk, O. S.; Emes Misenko, E. I.; Malinkovich, A. N.; Gabrusevich, V. V., *Russ. Metall.* **1969,** *3*, 133-135.

67. Prevarskii, A. P.; Kuz'ma, Y. B.; Zarechnyuk, O. S., *Dopov. Akad. Nauk Ukr. RSR (Ser. B)* **1983,** *8*, 53-56.

68. Kontani, M.; Ido, H.; Ando, H.; Nishioka, T.; Yamaguchi, Y., *J. Phys. Soc. Jpn.* **1994,** *63*, 1652-1655.

69. Grin, Y. N.; Ellner, M.; Hiebl, K.; Rogl, P., *J. Alloy Compd.* **1993,** *196*, 207-212.

70. Cava, R. J.; Ramirez, A. P.; Takagi, H.; Krajewski, J. J.; Peck, W. F., *J. Magn. Magn. Mater.* **1993,** *128*, 124-128.

71. Grin, Y. N.; Hiebl, K.; Rogl, P.; Noel, H., *J. Less-Common Met.* **1990,** *162*, 361-369.

72. Grin, Y. N.; Rogl, P.; Hiebl, K., *J. Less-Common Met.* **1988,** *136*, 329-338.

73. Grin, Y.; Rogl, P.; Hiebl, K.; Eibler, R., *J. Less-Common Met.* **1986,** *118*, 335-342.

74. Markiv, V. Y.; Chevchenko, I. P.; Belyavina, N. N.; Kuzmenko, P. P., *Dokl. Akcd. Nauk U.S.S.R., Ser. A,* **1985,** *7*, 76-81.

75. Grin, Y. N.; Hiebl, K.; Rogl, P.; Noel, H., *J. Less-Common Met.* **1990,** *162*, 371-377.

76. Mentink, S. A. M.; Bos, N. M.; Vanrossum, B. J.; Nieuwenhuys, G. J.; Mydosh, J. A.; Buschow, K. H. J., *J. Appl. Phys.* **1993,** *73*, 6625-6627.

77. Martin, J. M.; Paul, D. M.; Lees, M. R.; Werner, D.; Bauer, E., *J. Magn. Magn. Mater.* **1996,** *159*, 223-226.

78. Joshi, D. A.; Burger, P.; Adelmann, P.; Ernst, D.; Wolf, T.; Sparta, K.; Roth, G.; Grube, K.; Meingast, C.; von Lohneysen, H., *Phys. Rev. B* **2012,** *86*, 035144-035150.

79. Martin, J. M.; Lees, M. R.; Paul, D. M.; Dai, P.; Ritter, C.; Bi, Y. J., *Phys. Rev. B* **1998,** *57*, 7419-7422.

80. Sheldrick, G. M., *Acta Crystallogr. A* **2008,** *64*, 112-122.

81. Sheldrick, G. M. 5.10; University of Göttingen: Göttingen, Germany, 1997.

82. Sampathkumaran, E. V.; Das, I., *Solid State Commun.* **1992,** *81*, 901-904.

83. Diamond version 3.0g; Rathausgasse: Bonn, Germany, 2011.

84. Peter, S. C.; Subbarao, U.; Sarkar, S.; Vaitheeswaran, G.; Svane, A.; Kanatzidis, M. G., *J. Alloy Compd.* **2014,** *589*, 405-411.

85. Subbarao, U.; Sebastian, A.; Rayaprol, S.; Yadav, C. S.; Svane, A.; Vaitheeswaran, G.; Peter, S. C., *Cryst. Growth Des.* **2013,** *13*, 352-359.

86. Kanatzidis, M. G.; Pöttgen, R.; Jeitschko, W., *Angew. Chem. Int. Edit.* **2005,** *44*, 6996-7023.

87. Peter, S. C.; Malliakas, C. D.; Nakotte, H.; Kothapilli, K.; Rayaprol, S.; Schultz, A. J.; Kanatzidis, M. G., *J. Solid State Chem.* **2012,** *187*, 200-207.

88. Andress, K. R.; Alberti, E., *Z. Metallkd.* **1935,** *27*, 126-128.

89. Dörrscheidt, W.; Schäfer, H., *J. Less-Common Met.* **1978,** *58*, 209-216.

90. Inoue, T.; Kubozono, Y.; Kashino, S.; Takabayashi, Y.; Fujitaka, K.; Hida, M.; Inoue, M.; Kanbara, T.; Emura, S.; Uruga, T., *Chem. Phys. Lett.* **2000,** *316*, 381-386.

91. Abeles, B., *Phys. Rev. B* **1977,** *15*, 2828-2829.

92. Bauer, E.; Sigrist, M., *Non-centrosymmetric superconductors: Introduction and overview*. Springer: Berlin, 2012; Vol. 847.

Chapter 3

Synthesis, Crystal Structure and Physical Properties of the Compounds Crystallizing as the Ordered Structures of the $ThMn_{12}$ Structure type

---

Papers published on this work have appeared in

[1] *Inorg. Chem.*, **2012**, *51*, 6326−6332.

[2] *J. Chem. Sci.*, **2013**, *125*, 1315–1323.

[3] *Inorg. Chem.*, **2013**, *52*, 2219- 2227.

[4] *J. Solid State Chem.*, **2015**, *226*, 126–132.

3.1. Introduction

$ThMn_{12}$ type compounds crystallizing tetragonal structure type with the space group of *I*4/*mmm*, with the lattice parameters of $a = b = 8.74(1)$ Å and $c = 4.95(1)$ Å.[1] The crystal structure of $ThMn_{12}$ along *c*-axis is shown in Figure 3.1a. The $ThMn_{12}$ crystal structure consists of four atomic positions, which are one Th and three Mn atoms. The Th atom occupies the 2*a* site of point symmetry (4/*mmm*), while the Mn1, Mn2 and Mn3 atoms occupy the 8*f*, 8*i* and 8*i* sites of point symmetry (2/*m*, *m*2*m* and *m*2*m*). The crystal structure of $ThMn_{12}$ is composed of pseudo Frank-Kasper cages [Mn_{20}] occupying one thorium atom in each ring to form a stable structure. These pseudo Frank-Kasper cages are shared through the corner Mn atoms along *ab*-plane resulted in a three dimensional network (Figure 3.1a). Compounds of *RE*Fe_6Al_6 and *REM*$_4Al_8$ (*M* = Cr, Mn, Fe and Cu) [2, 3] series crystallizing in the same structure type show interesting magnetic properties and hyperfine interactions. $CeMn_4Al_8$ is one of the ordered structures of the $ThMn_{12}$ structure type reported.[1] An interesting feature of $CeMn_4Al_8$ compound is that Mn and Al atoms are not distributed at random over the three atomic positions available for these elements in $ThMn_{12}$ type structure. YCu_6In_6 is another ordered structure of $ThMn_{12}$ structure type, revealed a copper-indium ordering. The split positions of copper and indium at 8*j* position has observed in this type which led into the formation of a new structure type.[4] The coordination environment of Th and Mn atoms are shown in Figure 3.1b. The substitution of *T* and *X* atoms cause structural distortion and lead into the formation of new ordered structures of the $ThMn_{12}$ type, which inevitably alter the electronic structure and result in new physical properties. This chapter discusses about the synthesis of a few ordered structures of$ThMn_{12}$ structure type, structure relations and physical properties.

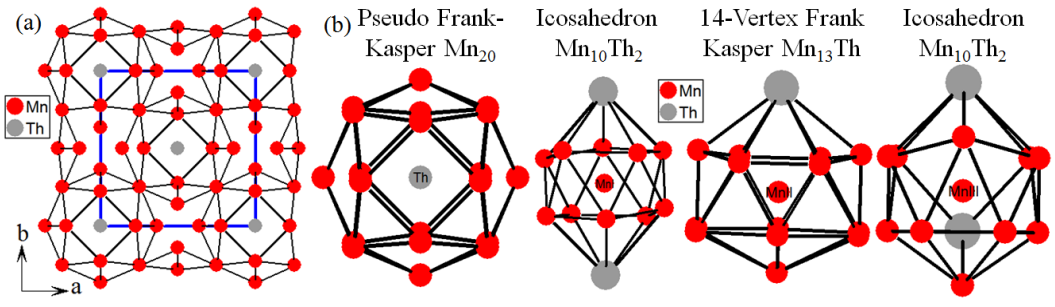

Figure 3.1. (a) Crystal structure of $ThMn_{12}$ as viewed along the *c*-axis; the unit cell is outlined as blue solid lines, (b) the coordination environment of Th and Mn atoms in $ThMn_{12}$ atoms.

3.2. Experimental Section

3.2.1. Reagents

Rare earths (Yb, Eu, Sm (ingots, 99.99%)), Cu (ingots, 99.99%), Ag (ingots, 99.99%), In (shots, 99.99%) and Ga (pieces 99.999%) were purchased from Alfa Aesar and used without further purification

3.2.2. Synthesis

3.2.2.1. Metal flux synthesis of $YbCu_6In_6$, $SmCu_6In_6$ and $EuAg_4In_8$

High quality single crystals of $YbCu_6In_6$, $SmCu_6In_6$, $YbCu_4Ga_8$ and $EuAg_4In_8$ were obtained by combining respective weights of metals in an alumina (Al_2O_3) crucible under an inert gas atmosphere inside the glove box. The crucible was placed in a 13 mm fused silica tube, which was flame sealed under a vacuum of 10^{-3} torr, to prevent oxidation during heating. The reactants were then heated to 1000 °C over 10 h, and maintained at that temperature for 10 h to allow proper homogenization. The reaction was then cooled to 850 °C in 5 h and kept at that temperature for 96 h. Finally, the sample was allowed to cool slowly to 30 °C over 72 h. The reaction product was isolated from excess indium flux by heating at 450 °C and subsequently centrifuging through a coarse frit. Any remaining flux was removed by immersion and sonication in glacial acetic acid for 24 h. The final crystalline product was rinsed with water and dried with acetone. This method produced the target compound with ca. 99% purity and low yield on the basis of the initial amount of Yb metal used in the reaction. Small rod-shaped crystals of $YbCu_6In_6$, $SmCu_6In_6$, $YbCu_4Ga_8$ and $EuAg_4In_8$ were carefully selected for elemental analysis and single crystal XRD data collection.

3.2.2.2. Metal flux synthesis of $YbCu_4Ga_8$

High quality single crystals of $YbCu_4Ga_8$ were obtained by combining 0.1757 g of ytterbium, 0.2581 g of copper and 0.5663 g of gallium metals in a 9 mm dia quartz tube under an inert (argon) atmosphere inside a glove box which was flame-sealed under vacuum of 10^{-3} torr to prevent oxidation during heating. The tube was then placed in a vertically aligned tube furnace and heated to 1000 ^{o}C over a period of 5 h and maintained at that temperature for 5 h to allow proper homogenization followed by cooling to 900 ^{o}C in 10 h and kept isothermally for 6 days. Finally, the system was allowed to cool to room

temperature in 10 h. Unreacted gallium was removed by immersion and sonication in 2-4 molar solution of iodine in dimethylformamide (DMF) over 12-24 h at room temperature. The product was rinsed with hot water and DMF then dried with acetone and ether. Large (3-4 mm), rod-like crystals of $YbCu_4Ga_8$, were obtained with high yield (>90%). Very small amount of Ga metal was present in the product that was quite unavoidable (detected in powder XRD). Several crystals, which grow as metallic silver rods, were carefully selected for elemental analysis and structure characterization.

3.2.2.3. Synthesis of $YbCu6_{-x}In_{6+x}$ (x = 0, 1, 2) by HFIH

Ytterbium, copper and indium elements were mixed in the ideal 1:6:6, 1:5:7 and 1:4:8 atomic ratios and sealed in tantalum ampoules under argon atmosphere in an arc-melting apparatus. The tantalum ampoules were subsequently placed in a water-cooled sample chamber of an induction furnace (Easy Heat induction heating system, Model 7590), first rapidly heated to 180 Amperes (850-950 ˚C) and kept at that temperature for 15 min. Finally the reaction was rapidly cooled to room temperature by switching off the power supply. All the compounds could easily be removed from the tantalum tubes. No reactions with the crucible material could be detected. All the compounds were found to be stable in moist air for several days. They were in polycrystalline form and light grey in colour. The weight losses of the final material were found to be less than 1%. The samples obtained from HFIH method were used for the property studies. Synthesis of $EuAg_4In_8$ compound in bulk polycrystalline form using HFIH also resulted in the formation of $EuAg_4In_8$ as major product along with unreacted indium and $AgIn_2$ phases.

3.2.2.4. Synthesis of $SmCu_{6-x}In_{6+x}$ (x = 0, 1 and 2) by arc melting

Single phases of $SmCu_{6-x}In_{6+x}$ (x = 0, 1, 2) were prepared by arc melting in Ar-atmosphere. The samples were melted repeatedly in the same atmosphere to ensure homogeneity. The weight losses of the final material were found to be less than 1%. Powder XRD measurements showed that all compounds are single phases with the expected structure type. The samples obtained via arc melting method were used for the physical property studies.

3.2.2.5. Direct method synthesis of $YbCu_4Ga_8$

Ytterbium, copper and gallium elements were mixed in the ideal 1:4:8 atomic ratios and sealed in tantalum ampoules under argon atmosphere in an arc-melting apparatus. The tantalum ampoules were subsequently placed in a water-cooled sample chamber of an induction furnace (Easy Heat induction heating system, Model 7590), first rapidly heated to 180 Amperes (ca. 1300-1450 ˚C) and kept at that temperature for 20 min. Finally, the reaction was rapidly cooled to room temperature by switching off the power supply. All compounds could easily be removed from the tantalum tubes. No reactions with the crucible material could be detected. All compounds were found to be stable in moist air for several months. The compounds were polycrystalline and light grey in colour. The weight losses of the final material were found to be less than 1%. The samples obtained from the high frequency induction heating method were used for the property studies.

3.2.3. Elemental analysis

Semiquantitative microprobe analyses of the single crystals obtained from the flux techniques were performed with a SEM equipped with Bruker 129 eV EDAX. EDAX analyses were done using P/B-ZAF standardless analysis. Data were acquired with an accelerating voltage of 20 kV and in 90 s of accumulation time. The EDAX analysis performed on visibly clean surfaces of the single crystal obtained from the flux method indicated that the atomic composition was close to target composition.

3.2.4. Powder X-ray diffraction

Phase identity and purity of the $YbCu_{6-x}In_{6+x}$ (x = 0, 1, 2), $SmCu_{6-x}In_{6+x}$ (x = 0, 1 and 2), $YbCu_4Ga_8$ and $EuAg_4In_8$ sample were determined by powder XRD experiments by a Bruker D8 Discover diffractometer using Cu-*K*α radiation (λ = 1.5406 Å). The experimental powder patterns of $YbCu_{6-x}In_{6+x}$ (x = 0, 1, 2), $SmCu_{6-x}In_{6+x}$ (x = 0, 1 and 2), $YbCu_4Ga_8$ and $EuAg_4In_8$ were compared to the pattern calculated from the single-crystal X-ray structure refinement of the $YbCu_6In_6$, $SmCu_6In_6$, $YbCu_4Ga_8$ and $EuAg_4In_8$ and were found to be in good agreement**.**

3.2.5. Single crystal X-ray diffraction

X-ray diffraction data were collected on selected single crystals of $YbCu_6In_6$, $SmCu_6In_6$, $YbCu_4Ga_8$ and $EuAg_4In_8$ at room temperature using a Bruker Smart-CCD

diffractometer equipped with a normal focus 2.4 kW sealed tube X-ray source with graphite monochromatic Mo-*Kα* radiation (λ = 0.7107 Å) operating at 50 kV and 30 mA with ω scan mode. A crystal of suitable size (0.05 x 0.05 x 0.1 mm^3) was cut from a rod shaped crystal and mounted on a thin glass (~0.1 mm) fiber with commercially available super glue. A full sphere of 60 frames was acquired. The individual frames were measured with steps of 0.5˚ and an exposure time of 10 s per frame. The programme SAINT[5] was used for integration of diffraction profiles and absorption correction was made with SADABS programme.[6] The systematic absences led to the centrosymmetric space group *I*4/*mmm*. However, the Platon program with WinGx system, ver. 1.80.05[7] was used to check the additional symmetry, which confirms the final structure refinement. The structure was solved by SHELXS 97[8] and refined by a full matrix least-squares method using SHELXL with anisotropic atomic displacement parameters for all atoms. Packing diagrams were generated with Diamond.[9] As a check for the correct composition, the occupancy parameters were refined in a separate series of least-squares cycles. All bond lengths are within the acceptable ranges compared to their theoretical values.

3.2.6. Magnetic measurements

Magnetic measurements of $YbCu_{6-x}In_{6+x}$ (x = 0, 1, 2), $SmCu_{6-x}In_{6+x}$ (x = 0, 1 and 2), $YbCu_4Ga_8$ and $EuAg_4In_8$ were carried out on a Quantum Design MPMS-SQUID magnetometer. Measurements were performed on poly crystals, which were ground and screened by powder XRD to verify phase identity and purity. Temperature dependent data were collected for FC mode) between 2 and 300 K with an applied field of 1 kG. Magnetization data were also collected for $YbCu_{6-x}In_{6+x}$ (x = 0, 1, 2), $SmCu_{6-x}In_{6+x}$ (x = 0, 1 and 2), $YbCu_4Ga_8$ and $EuAg_4In_8$ at 2 K and 300 K with field sweeping from -55 kOe to 55 kOe.

3.2.7. Electrical resistivity

The resistivity measurements at 1T were performed on $YbCu_{6-x}In_{6+x}$ (x = 0, 1, 2), $SmCu_{6-x}In_{6+x}$ (x = 0, 1 and 2), $YbCu_4Ga_8$ and $EuAg_4In_8$ with a conventional AC four probe setup. Four thin copper wires were glued to the pellet using a highly conducting silver epoxy paste. The data were collected in the range 3−300 K using a commercial QD-PPMS. The results were reproducible for several batches.

3.2.8. Single Crystal Neutron Diffraction (ND)

ND was carried out using the SXD instrument at the ISIS spallation neutron source (Oxfordshire, England).[10] A large crystal of dimensions 1x1x3 mm^3 was mounted on an aluminium pin with adhesive Al tape inside a top-loading closed-cycle refrigerator in He exchange gas environment. Five crystal settings were recorded at 50 K with exposure times of the order of 9 h per orientation and data reduced to structure factors using the locally available program SXD2001.[11] Sample absorption was found negligible and did not influence the final result. The structure was solved by SHELXS 97[12] and refined by a full matrix least-squares method using SHELXL.[13]

3.2.9. X-ray absorption near edge spectroscopy (XANES)

XANES experiments at 300 K on $EuAg_4In_8$ were performed at PETRA III, P06 beam line of DESY, Germany. Measurements at the Eu L_{III}-edge and at ambient pressure were performed in transmission mode using gas ionization chambers to monitor the incident and transmitted X-ray intensities. Monochromatic X-rays were obtained using a Si [111] double crystal monochromator which was calibrated by defining the inflection point (first derivative maxima) of Cu foil as 8980.5 eV. The beam was focused employing a Kirkpatrick–Baez (K–B) mirror optic. A rhodium coated X-ray mirror was used to suppress higher order harmonics. A CCD detector was used to record the transmitted signals. The sample was prepared by mixing an appropriate amount of finely ground powder with cellulose and cold pressing them to a pellet.

3.3. Crystal Structure of $YbCu_6In_6$ and Mixed Valence Behaviour of Yb in $YbCu_{6-x}In_{6+x}$ (x = 0, 1 and 2) Solid Solution

3.3.1. Introduction

The compounds in the Yb-Cu-In ternary system was investigated over the whole concentration range at 400 °C and the isothermal section was reported by Kalychak et al.[14, 15] So far, only a few compounds have been reported within the Yb-Cu-In system. The temperature dependent lattice parameters for the $YbCu_4In$ compound was reported by Kojima et al.[16] The valency of Yb in $YbCu_4In$ was studied by neutron and X-ray diffraction methods. This compound showed a first order temperature induced valence transition in the range 40-60 K from the Yb^{2+} non-magnetic ground state to the Yb^{3+} magnetic high temperature state.[17, 18] $Yb_{0.4}Cu_2In_{0.6}$ is another compound in this family which exhibits characteristic properties associated with a heavy-fermion system was reported by Felner et al.[19, 20]

Another compound $YbCu_{5.1}In_{6.9}$ was reported, which was characterized only by powder XRD.[21, 22] This compound crystallizes in the $CeMn_4Al_8$ type structure[23, 24] which is a modified structure of $ThMn_{12}$ type[1] with space group *I4/mmm*. Compounds of *RE*Fe_6Al_6[2] and *RET*$_4Al_8$ (*T* = Cr, Mn, Fe and Cu)[3] series crystallizing in the same structure type show interesting magnetic properties and hyperfine interactions. However, the physical properties of Yb$T_{6-x}In_{6+x}$ series have not been studied yet.

This chapter discusses about the synthesis of $YbCu_6In_6$ using indium flux and the synthesis of solid solution $YbCu_{6-x}In_{6+x}$ (x = 0, 1, 2) using HFIH method. The crystal structure of $YbCu_6In_6$ solved using single crystal XRD. Magnetic susceptibility and electrical resistivity studies were performed on compounds obtained by high frequency induction heating.

3.3.2. Results and Discussion

3.3.2.1. Reaction chemistry

$YbCu_6In_6$ was obtained from Yb-Cu-In reaction in liquid indium as flux in high purity. The shiny grey colour rod-shaped single crystals up to 1 mm in length were stable in

air, and no decomposition was observed even after several months. Typical SEM image of a rod-like crystal of $YbCu_6In_6$ as grown from the flux synthesis is shown in Figure 3.3.1.

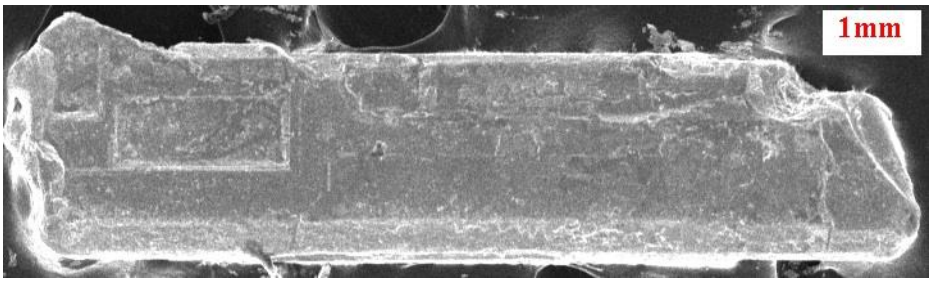

Figure 3.3.1. Typical SEM image of a $YbCu_6In_6$ single crystal grown from In flux

After establishing the crystal structure of the compound, to find out the solubility range for $YbCu_{6-x}In_{6+x}$ and succeeded in the synthesis of $YbCu_6In_6$, $YbCu_5In_7$ and $YbCu_4In_8$ compounds using HFIH. These products form only microcrystals of $YbCu_{6-x}In_{6+x}$ (x = 0, 1, 2) instead of large single crystals. Synthesis of $YbCu_7In_5$ and $YbCu_3In_9$ in pure single phase were not successful.

3.3.2.2. Structure refinement of $YbCu_6In_6$

The atomic parameters of $YbCu_{5.9}In_{6.1}$[19] were taken as starting parameters and the structure was refined using Shelxl-97 (full-matrix least-squares on F^2) with anisotropic atomic displacement parameters for all atoms. As a check for the correct composition, the occupancy parameters were refined in a separate series of least-squares cycles. The data confirms the previous X-ray powder data,[20, 21] but the atomic positions have been refined with higher precision. $YbCu_6In_6$ crystallizes in a body centered tetragonal lattice (*I*4/*mmm*) of $CeMn_4Al_8$ type structure. There are four crystallographic positions in $YbCu_6In_6$ structure in which one ytterbium atom occupies 2*a* cerium site, while copper and indium atoms are distributed over the manganese and aluminium sites 8*f*, 8*i* and 8*j*. To check the refinement initially crystal structure with one ytterbium, two copper and one indium atoms were tried. During isotropic refinement of $YbCu_6In_6$, it was observed that the thermal parameters of Cu atom at 8*j* was largely unsatisfactory marked with relatively high residuals (R_1 > 15%), and large electron density residuals (30 eÅ^{-3}) around copper atoms. The anomalous thermal parameters were not resolved by subsequent refinement of the occupancy parameters. While substitution of the Cu position with In could not also solve the large refinement values. All these facts indicated a crystallographic disorder associated at 8*j* position, consequently Cu and In atoms were mixed and refined successfully with reasonably good thermal parameters,

but slightly large U_{11} and electron density residuals (~8 e $Å^{-3}$) probably due to a certain degree of disorder in $YbCu_6In_6$. This could be due to the strong distortions happened because of mixed position. The overall stoichiometry obtained from the refinement is $YbCu_{6.08}In_{5.92}$ and rounded to the nearest integers as $YbCu_6In_6$.

The data collection and structure refinement for $YbCu_6In_6$ are listed in Table 3.3.1. The standard atomic positions and isotopic atomic displacement parameters of this compound are collected in Table 3.3.2. The Anisotropic displacement parameters and important bond lengths are listed in Tables 3.3.3 and 3.3.4, respectively. Further information on the structure refinement is available from: Fachinformationszentrum Karlsruhe, D-76344 Eggenstein-Leopoldshafen (Germany), by quoting the Registry No. CSD– 424351.

Table 3.3.1. Crystal data and structure refinement for $YbCu_{6.08}In_{5.92}$ at 296(2) K.

Empirical formula	$YbCu_{6.08}In_{5.92}$
Formula weight	1239.13
Wavelength	0.71073 Å
Crystal system	Tetragonal
Space group, *Z*	*I*4/*mmm*, 2
Unit cell dimensions	$a = b = 9.2200(2)$ Å $c = 5.3976(2)$ Å
Volume	458.84(2) $Å^3$
Density (calculated)	8.972 g/cm^3
Absorption coefficient	38.326 mm^{-1}
F(000)	1073
Crystal size	0.1 x 0.06 x 0.06 mm^3
θ range for data collection	3.12 to 30.55°
Index ranges	-12<=*h*<=7, -13<=*k*<=13, -7<=*l*<=7
Reflections collected	2745
Completeness to $\theta = 30.55°$	100%
Refinement method	Full-matrix least-squares on F^2
Data / restraints / parameters	232 / 0 / 17
Goodness-of-fit	1.114
Final *R* indices [>2σ(I)]	$R_{obs} = 0.0415$, $wR_{obs} = 0.0998$
Extinction coefficient	0.0181(16)
Largest diff. peak and hole	7.328 and -8.237 e·$Å^{-3}$

$R = \Sigma||F_o|-|F_c|| / \Sigma|F_o|$, $wR = \{\Sigma[w(|F_o|^2 - |F_c|^2)^2] / \Sigma[w(|F_o|^4)]\}^{1/2}$ and calcw=$1/[\sigma^2(Fo^2)+(0.0359P)^2+6.1794P]$ where $P = (Fo^2+2Fc^2)/3$

Table 3.3.2. Atomic coordinates ($x10^4$) and equivalent isotropic displacement parameters ($Å^2x10^3$) for $YbCu_{6.08}In_{5.92}$ at 296(2) K with estimated standard deviations in parentheses.

Label	Wyckoff site	*x*	*y*	*z*	Occupancy	U_{eq}*
Yb	2*a*	0	0	0	1	3(1)
Cu	8*f*	2500	2500	2500	1	6(1)
In	8*i*	3398(2)	0	0	1	6(1)
M(Cu+In)	8*j*	2996(4)	5000	0	(0.52+0.48)	21(2)

*U_{eq} is defined as one third of the trace of the orthogonalized U_{ij} tensor.

Table 3.3.3. Anisotropic displacement parameters ($Å^2x10^3$) for $YbCu_{6.08}In_{5.92}$ at 296(2) K with estimated standard deviations in parentheses.

Label	U_{11}	U_{22}	U_{33}	U_{12}	U_{13}	U_{23}
Yb	3(1)	3(1)	3(1)	0	0	0
Cu	7(1)	7(1)	4(2)	1(1)	2(1)	2(1)
In	4(1)	5(1)	8(1)	0	0	0
M(Cu+In)	60(2)	2(2)	2(2)	0	0	0

The anisotropic displacement factor exponent takes the form: $-2\pi^2[h^2a^{*2}U_{11} + ... + 2hka^*b^*U_{12}]$.

Table 3.3.4. Selected bond lengths [Å] for $YbCu_{6.08}In_{5.92}$ at 296(2) K with estimated standard deviations in parentheses.

Label	Distances	Label	Distances
M–*M*	2.613(5)	In-In	2.954(3)
Cu-Cu	2.6988	In-*M*	2.9893(16)
Cu-*M*	2.7098(6)	Yb-In	3.1329(14)
In-Cu	2.7963(4)	Yb-*M*	3.2706(19)

3.3.2.3. Crystal chemistry of $YbCu_6In_6$

The crystal structure of $YbCu_6In_6$ along *c*-axis is shown in Figure 3.3.2. $YbCu_6In_6$ crystallizes in the tetragonal $CeMn_4Al_8$ type structure (space group *I4/mmm*), which is an ordered superstructure of $ThMn_{12}$ type. $YbCu_6In_6$ is slightly more distorted compared to the parent compound. An interesting feature of $CeMn_4Al_8$ compound is that Mn and Al atoms are randomly not distributed over the three atomic positions available for these elements in the $ThMn_{12}$ type structure. By further substitution of Cu and In atoms in $YbCu_6In_6$ completely occupy the Mn and Al2 positions respectively, in the $CeMn_4Al_8$ structure and Al1 position is occupied with both Cu (52%) and In (48%) atoms (denoted as *M*). This mixed

position could be one of probable reasons for the enhanced distortions observed in the crystal structure of $YbCu_6In_6$. The Yb atoms occupy the 2*a* site of point symmetry (4/*mmm*), the Cu atom occupy the 8*f* site of point symmetry (2/*m*), the In atom occupy the 8*i* site of point symmetry (*m*2*m*) and 8*j* site occupied by mixture of Cu and In atoms of point symmetry (*m*2*m*). Crystal structure of $YbCu_6In_6$ is composed of pseudo Frank-Kasper cages [$Cu_8In_4M_8$] occupying one ytterbium atom in each ring to form a stable structure. These pseudo Frank-Kasper cages are shared through the corner *M* atoms along *ab*-plane resulted in a three dimensional network (Figure 3.3.3). The local coordination environments of Cu and In atoms within a radius of 3.6 Å are presented in Figure 3.3.4 and 3.3.5. The slight distortion of $YbCu_6In_6$ is clearly evident in the comparison of Mn ($CeMn_4Al_8$ structure) and Cu ($YbCu_6In_6$ structure) coordination environments (Figure 3.3.4) which in fact develop mixed valence behaviour of Yb atom in $YbCu_6In_6$. Considering the fact that Cu can exist as both monovalent and divalent, assume a slight electron transfer from Cu to Yb cause mixed valency at Yb, probably in Cu atom as well, and enhanced Yb-Cu bond distances (3.528(1) Å) compared to the theoretical value.

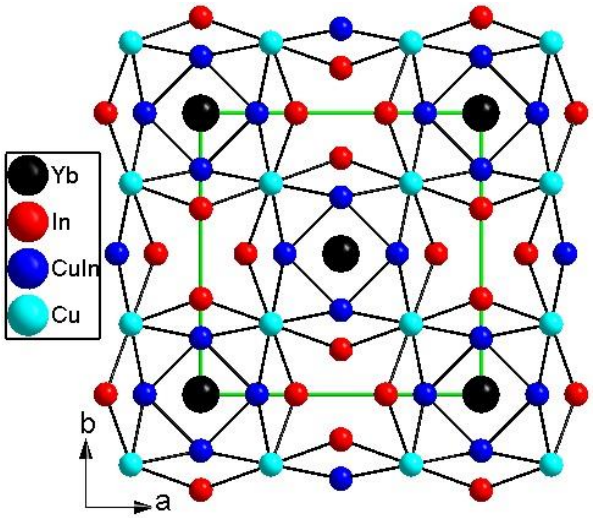

Figure 3.3.2. The structure of $YbCu_{6.08}In_{5.92}$ as viewed along the *c*-axis; the unit cell is outlined as green solid lines.

This is further confirmed in the magnetic measurements (discussed below) as the magnetic moments of Yb were enhanced upon adding more Cu atom at the In position. The contribution of trivalent Yb is more in $YbCu_6In_6$ (88%) compared to $YbCu_4In_8$ sample (13%). The coordination environment of In atoms is formed as 14-vertex Frank-Kasper cage.

M atoms are in the distorted icosahedrons geometry composed of 12 atoms of which two are Yb atoms and the remaining ten atoms are shared by Cu and In atoms. All icosahedrons and Frank-Kasper cages are slightly distorted compared to the parent compounds

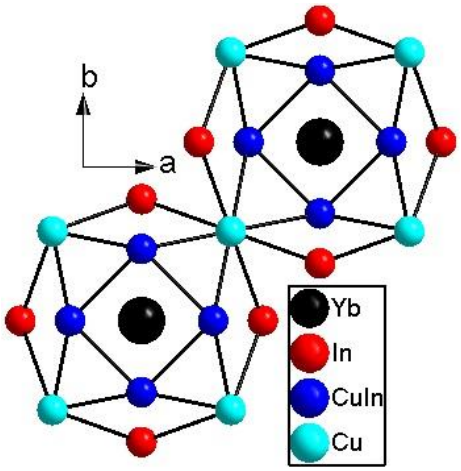

Figure 3.3.3. Pseudo Frank-Kasper cages in $YbCu_6In_6$ are shared through the corner M atoms along *ab*-plane.

This is further confirmed in the magnetic measurements (discussed below) as the magnetic moments of Yb were enhanced upon adding more Cu atom at the In position. The contribution of trivalent Yb is more in $YbCu_6In_6$ (88%) compared to $YbCu_4In_8$ sample (13%). The coordination environment of In atoms is formed as 14-vertex Frank-Kasper cage. *M* atoms are in the distorted icosahedrons geometry composed of 12 atoms of which two are Yb atoms and the remaining ten atoms are shared by Cu and In atoms. All icosahedrons and Frank-Kasper cages are slightly distorted compared to the parent compounds.

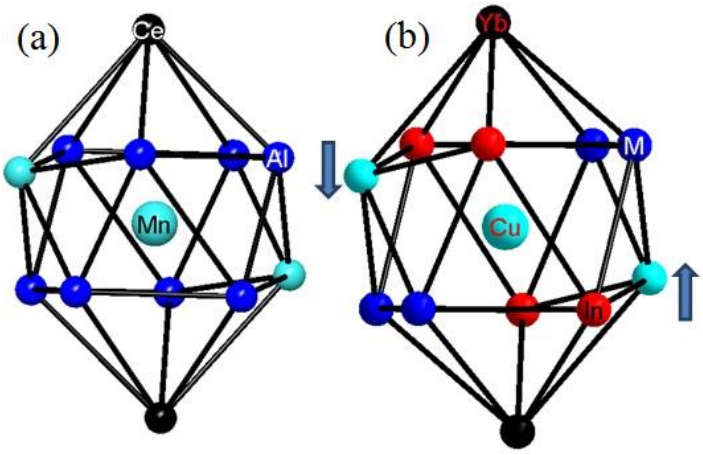

Figure 3.3.4. Comparison of the icosahedron polyhedra of Mn in $CeMn_4Al_8$ and Cu in $YbCu_{6-x}In_{6+x}$. The distortion at the Cu atom is marked as blue arrows.

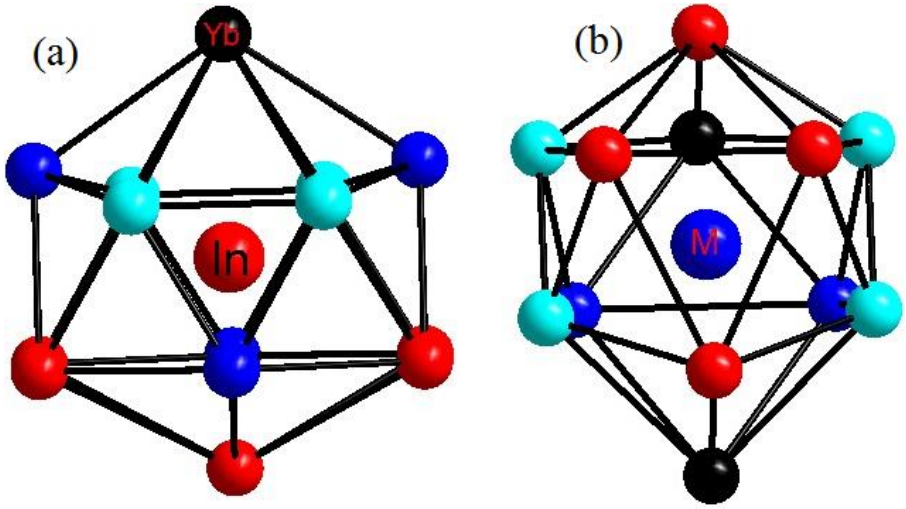

Figure 3.3.5. The coordination environment of In (a) and mixed atomic position (b) in $YbCu_{6.08}In_{5.92}$

M-M distance is the shortest bond distance (2.613(5) Å) in $YbCu_6In_6$ which is close to the atomic radii of Cu-Cu distance (2.560 Å) observed in $YbCuAl_8$.[34] The shortest distance of Yb-In is 3.1329(14) Å smaller than the calculated distances of 3.38 Å[25] probably because of strong covalent bond between the Yb and In atoms, however the shortest distance between Yb and Cu atoms is 3.528(1) Å substantially larger than the theoretical value of 3.22 Å[25] suggest a weak interaction between them. Yb-*M* bond distance 3.271(2) Å is lying in the between Yb-Cu and Yb-In distances. The Cu-sites along *c*-axis are connected with as bond distance of 2.6988(5) Å which is little higher than the normal Cu-Cu distance which is 2.560 Å comparable in $Cu_2Y_{0.1}Yb_{0.3}In_{0.6,}$[20] $YbCuIn_4$[26] etc. Yb−Cu bond distances of 3.5280(3) Å for Yb−Cu and 3.2707(5) Å for Yb−*M* are very close to the bond distance of $Yb-Cu^+$ (3.19 Å) compared to $Yb-Cu^{2+}$ (3.06 Å), indicating that the copper atoms present in $YbCu_6In_6$ are in a monovalent nonmagnetic state.

3.3.2.4. Physical Properties

3.3.2.4.1. Magnetism

Magnetic susceptibility measurements were performed on polycrystalline sample of $YbCu_{6-x}In_{6+x}$ (x = 0, 1, 2) obtained from HFIH synthesis. The temperature dependent molar magnetic susceptibility (χ_m) and inverse susceptibility ($1/\chi_m$) of $YbCu_{6-x}In_{6+x}$ (x = 0, 1, 2) at an applied field of 1 kOe are shown in Figure 3.3.6 and 3.3.7, respectively.

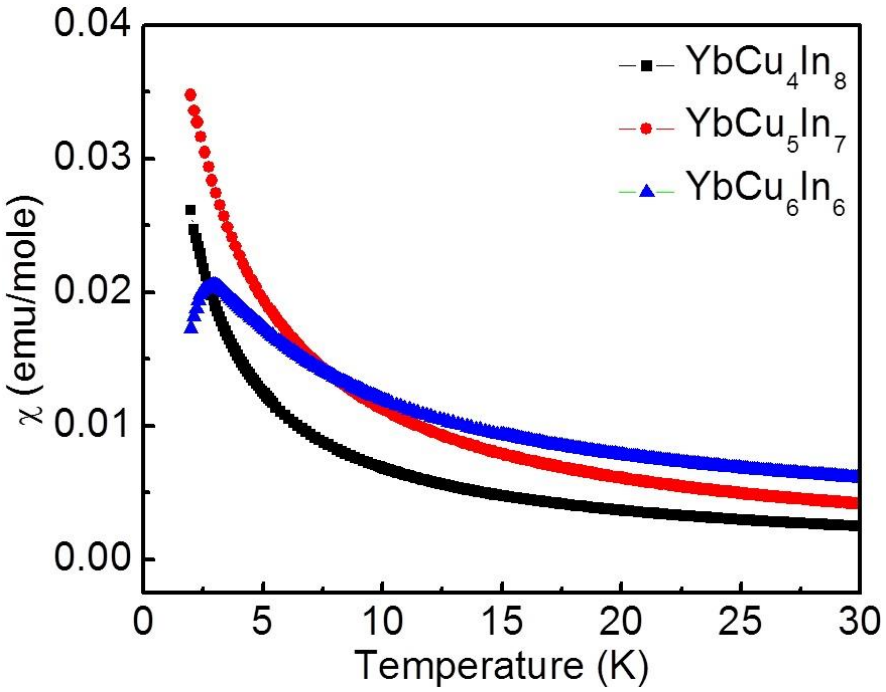

Figure 3.3.6. Temperature dependent magnetic susceptibility (χ_m) of $YbCu_4In_8$, $YbCu_5In_7$ and $YbCu_6In_6$.

The susceptibility curve obeys modified Curie-Weiss law, $\chi = C/(T-\theta) + \chi_0$, above 50 K in $YbCu_4In_8$ and $YbCu_5In_7$ and above 150 K in $YbCu_6In_6$. Magnetic susceptibility of $YbCu_6In_6$ shows a transition around 3 K. No magnetic ordering was observed in $YbCu_4In_8$ and $YbCu_5In_7$ compounds down to 2 K, but the susceptibility slightly increases at lower temperature which is normal for *RE* based intermetallics.[27] In $YbCu_6In_6$, the susceptibility data begin to follow a modified Curie-Weiss law only in the temperature region above 150 K. At lower temperature the deviation can be attributed to crystal field contributions and/ or to a possible onset of valence fluctuations. Above 150 K $YbCu_6In_6$ exhibits paramagnetic behaviour with an effective magnetic moment of 4.024 μ_B/Yb atom. The estimated experimental μ_{eff} value is about 88% of that expected for a free ion Yb^{3+} moment (4.56 μ_B/Yb). However, the inverse magnetic susceptibility curves for $YbCu_4In_8$ and $YbCu_5In_7$ compounds are completely different from $YbCu_6In_6$ and present two linear regions in the temperature ranges 50-200 K and 200-300 K. The magnetic susceptibility in these two temperature ranges fits the modified Curie-Weiss law and the effective magnetic moments obtained in the high temperature range region (200-300 K) are 0.61 and 0.9 μ_B/Yb for

$YbCu_4In_8$ and $YbCu_5In_7$, respectively. These values are less than a quarter of the value expected for an Yb^{3+} ion.

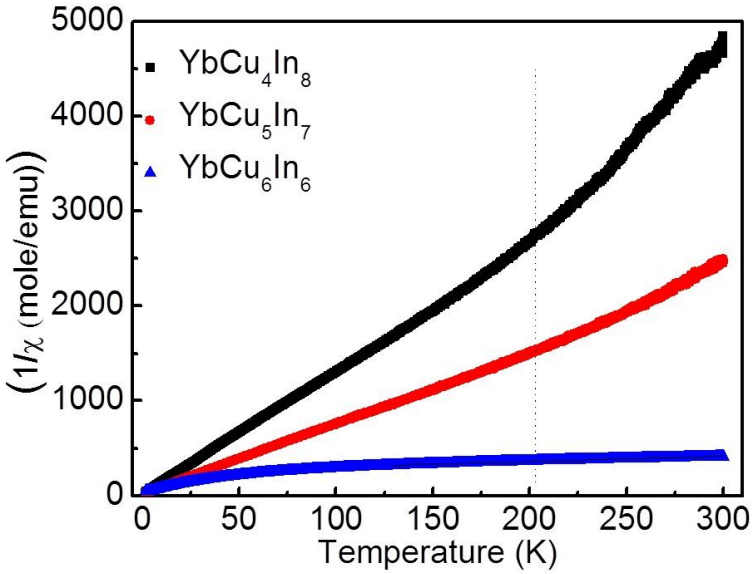

Figure 3.3.7. Temperature dependence of the modified reciprocal magnetic susceptibility ($1/\chi_m$) of the $YbCu_4In_8$, $YbCu_5In_7$ and $YbCu_6In_6$.

The calculated magnetic moment for Yb in $YbCu_4In_8$ (13% Yb^{2+}) is pretty close to the value observed for Yb in $YbCr_4Al_8$ compound (10 % Yb^{2+}).[34] This indicates that both compounds are in the same structure type and assuming both Cu and Cr elements are nonmagnetic, the observed magnetic moments are due to the mixed valent nature of Yb atoms. A fit to the low temperature range (50-200 K) produced magnetic moments of 0.79 and 1.02 μ_B/Yb for $YbCu_4In_8$ and $YbCu_5In_7$; respectively suggest these systems have a valence fluctuation of Yb^{2+} to Yb^{3+} below 200 K. It was observed that the compounds crystallize in the $CeMn_4Al_8$ type structure create disorder at the Mn and Al sites. Such disorders affect the magnetic behaviour in the solid solution and it was previously reported for $LaMn_{4+x}Al_8$.[28] In $YbCu_{6-x}In_{6+x}$ (x = 0, 1, 2) a small change in Cu to In ratio reduces the magnetic moment substantially and valence fluctuations of Yb atom. Assuming Cu and In are nonmagnetic elements in the systems,[29] this large difference in the magnetic moment could be associated with the structural behaviour. Much more detailed structural studies such as neutron diffraction could give an insight to the structure-property relations in these compounds.

The field dependence of the magnetization $M(H)$ for ground samples of $YbCu_{6-x}In_{6+x}$ (x = 0, 1, 2) were measured at 2 K and 300 K can be seen in Figure 3.3.8. The data measured

at 300 K exhibit linear behaviour and no signs of saturation up to highest attainable field of 60 kOe. The magnetization curve taken at 2 K (within the magnetic ordering) shows a slight field dependent response up to ~ 30 kOe, continues to rise slowly up to the highest obtainable field (60 Oe). However, the saturation behaviour is different for each system at highest field. $YbCu_4In_8$ system almost saturates at ~30 kOe with magnetic moment of ~0.5 emu/mol. $YbCu_5In_7$ saturate at high value with higher saturation magnetic moments and $YbCu_6In_6$ does not saturate even at the highest applied magnetic field.

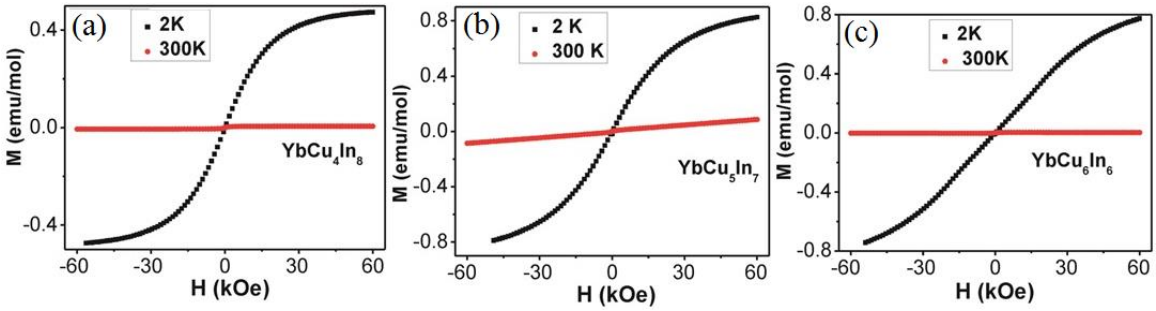

Figure 3.3.8. Magnetization as a function of applied magnetic field at 2 K and 300 K for a polycrystalline sample of (a) $YbCu_4In_8$, (b) $YbCu_5In_7$ and (c) $YbCu_6In_6$.

3.3.2.4.2. Electrical resistivity

The normal state temperature dependent resistivity of $YbCu_{6-x}In_{6+x}$ (x = 0, 1, 2) in Figure 3.3.9 decreases linearly with decreasing temperature, typical for metallic systems [30, 31] but without any long range magnetic ordering. The resistivity values of $YbCu_4In_8$, $YbCu_5In_7$ and $YbCu_6In_6$ are 24 $\mu\Omega$cm, 22 $\mu\Omega$cm and 92 $\mu\Omega$cm, respectively at room temperature. At low temperature range of 0-50 K, the $\rho(T)$ data can be fitted to the power law function, $\rho = \rho_0 + AT^n$, where ρ_0 is the residual resistivity expressed in units of Ωcm, A and n are the fitting parameters. The values obtained from the fit are shown in Figure 3.3.9. According to Fermi-liquid theory, at low temperatures the resistivity varies as $\rho = \rho_0 + AT^2$. Experimentally it has been observed that when electron-electron scattering dominates over electron-phonon scattering, $\rho \alpha T^2$. The value obtained from the fit power is close to 2 in $YbCu_6In_6$, which is the case for systems exhibiting Fermi liquid state.[32, 33] But in $YbCu_4In_8$ and $YbCu_5In_7$the values obtained from the fit power are 1.28 and 1.19, respectively, characteristic for Non-Fermi liquid state.[34] In order to verify Fermi liquid and non-Fermi liquid behaviour, the resistivity data is plotted as $(\rho - \rho_0)$ vs. T^2 (as shown in inset to Figure 3.3.9). For $YbCu_6In_6$,

linearity in the data confirms Fermi-liquid behaviour in this compound at low temperatures, while other two compounds show a deviation in the curve.

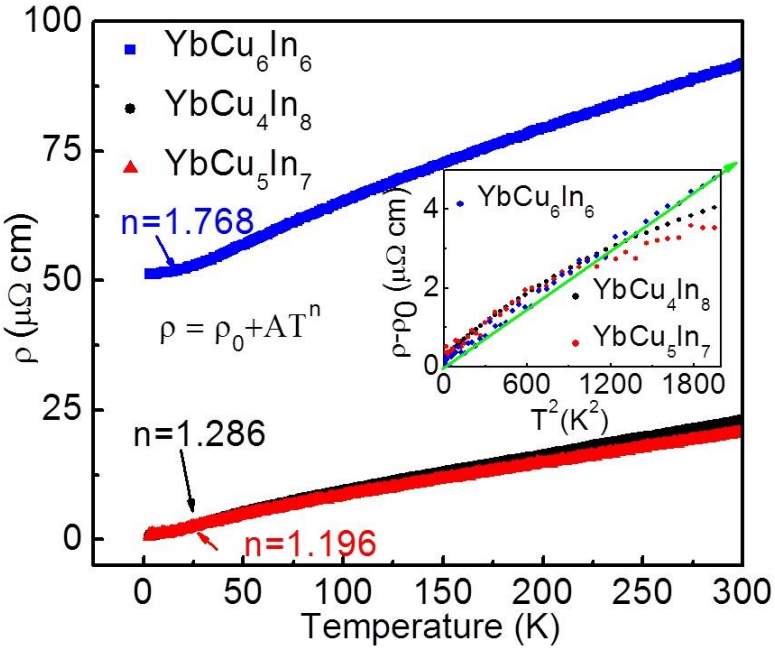

Figure 3.3.9. Resistivity (ρ) measured as a function of temperature. The low temperature data has been fitted to the power law, $\rho = \rho_0 + AT^n$. The values obtained from the fit are shown in the figure.

3.4. Structure and Properties of $SmCu_{6-x}In_{6+x}$ (x = 0, 1, 2)

3.4.1. Introduction

During the course of studies on *RE*-Cu-In phase based on the overview on the chemistry and physical properties of the many $RE_xCu_yIn_z$ phases is given in the review by Kalychak et al.[35] rod shaped single crystal of $SmCu_6In_6$ has observed from the excess indium metal. A recent work on $RECu_6In_6$ (*RE* = Y, Ce, Pr, Nd, Gd, Tb, Dy) by Pöttgen et al. revealed the copper-indium ordering in this family using split positions of copper and indium at 8*j* position.[4] Among these only the compound $SmCu_6In_6$ was missing. Apart that there are a few compounds were reported within the Sm-Cu-In family. $SmCu_2In$ crystallizes in the $MnCu_2Al$ structure type has two antiferromagnetic phase transitions observed at 2.0 and 3.7 K.[36] The other compounds are $SmCu_{0.5}In_{1.5}$ and Sm_2Cu_2In briefly studied using powder XRD.[37, 38] However, so far only powder XRD studies of $SmCu_{5.1}In_{6.9}$ was reported,[21, 39] which shows that it crystallizes in the $CeMn_4Al_8$ type structure[40] with space group *I*4/*mmm*.

This section reports the metal flux synthesis of $SmCu_6In_6$ and its crystal structure elucidation using single crystal XRD data. After establishing the crystal structure, the existence of $SmCu_{6-x}In_{6+x}$ solid solution checked by changing the Cu to In ratio. Three compounds of $SmCu_{6-x}In_{6+x}$ (x = 0, 1 and 2) were successfully synthesized using arc melting technique. The phase purity of these compounds was checked by powder XRD and SEM /EDAX. This work also report physical properties such as magnetic susceptibility and electrical resistivity of all compounds.

3.4.2. Results and Discussion

3.4.2.1. Structure Refinement

The atomic parameters of $SmCu_{5.1}In_{6.9}$ were taken as starting parameters and the structure was refined using SHELXL-97 (full-matrix least-squares on F^2) with anisotropic atomic displacement parameters for all atoms. As a check for the correct composition, the occupancy parameters were refined in a separate series of least-squares cycles. There are four crystallographically positions in $SmCu_6In_6$ structure one for Sm and other three (Wyckoff positions 8*f*, 8*i*, 8*j*) are shared by In and Cu atoms. The refinement of the occupancy parameters revealed full occupancy of the 8*f* and 8*i* sites with copper and indium,

respectively. However, 8*j* sites revealed occupancy by approximately 50% copper and 50% indium and huge anisotropic displacement parameters U_{11} which is seven times larger than U_{22}. Further, the split model for 8*j* sites similar to the refinement of *RE*Cu_6In_6 and refined the structure occupying Cu and In fully occupied in one site each. Sm atoms occupy the 2*a* site of 4/*mmm* point symmetry, Cu1 atom occupy the 8*f* site of 2/*m* point symmetry, In1 atom occupy the 8*i* site of *m*2*m* point symmetry and 8*j* site split for Cu and In atoms of *m*2*m* point symmetry. The refinement then smoothly converged to the normal residuals. The data collection and refinement parameters are summarized in Table 3.4.1. The atomic coordinates and equivalent thermal parameters, anisotropic displacement parameters and important bond lengths are listed in Tables 3.4.2, 3.4.3 and 3.4.4, respectively. Further information on the structure refinement is available from: Fachinformationszentrum Karlsruhe, D-76344 Eggenstein-Leopoldshafen (Germany), by quoting the Registry No. CSD–424639.

Table 3.4.1. Crystal data and structure refinement for $SmCu_6In_6$ at 293(2) K.

Empirical formula	$SmCu_6In_6$
Formula weight	1220.51
Wavelength	0.71073 Å
Crystal system	Tetragonal
Space group, *Z*	*I*4/*mmm*, 2
Unit cell dimensions	$a = b = 9.2036(3)$ Å, $c = 5.4232(3)$ Å
Volume	459.38(3) $Å^3$
Absorption coefficient	34.507 mm^{-1}
F(000)	1060
Crystal size	0.10 x 0.05 x 0.05 mm^3
θ range for data collection	3.13 to 32.06°
Index ranges	-13<=*h*<=13,-13<=*k*<=10,-8<=*l*<=7
Reflections collected	2164
Refinement method	Full-matrix least-squares on F^2
Data / restraints / parameters	264 / 0 / 17
Goodness-of-fit	1.112
R indices [all data]	$R_{all} = 0.0283$, $wR_{all} = 0.0653$
Extinction coefficient	0.0117(14)
Largest diff. peak and hole	2.265 and -3.339 e·$Å^{-3}$

$R = \Sigma||F_o|-|F_c|| / \Sigma|F_o|$, $wR = \{\Sigma[w(|F_o|^2 - |F_c|^2)^2] / \Sigma[w(|F_o|^4)]\}^{1/2}$ and calcw=$1/[\sigma^2(Fo^2)+(0.0359P)^2+6.1794P]$ where $P = (Fo^2+2Fc^2)/3$

Table 3.4.2. Atomic coordinates ($x10^4$) and equivalent isotropic displacement parameters ($Å^2x10^3$) for $SmCu_6In_6$ at 293(2) K with estimated standard deviations in parentheses.

Label	Wyckoff Site	*x*	*y*	*z*	occupancy	U_{eq}*
Sm	2*a*	0	0	0	1	6(1)
Cu1	8*f*	2500	2500	2500	1	10(1)
Cu2	8*j*	2697(5)	5000	0	0.3	10(2)
In1	8*i*	3409(2)	0	0	1	8(1)
In2	8*j*	3123(3)	5000	0	0.2	10(1)

*U_{eq} is defined as one third of the trace of the orthogonalized U_{ij} tensor.

Table 3.4.3. Anisotropic displacement parameters ($Å^2x10^3$) for $SmCu_6In_6$ at 293(2) K with estimated standard deviations in parentheses.

Label	U_{11}	U_{22}	U_{33}	U_{12}	U_{13}	U_{23}
Sm	6(1)	6(1)	4(1)	0	0	0
Cu1	11(1)	11(1)	7(1)	2(1)	2(1)	2(1)
Cu2	23(3)	8(2)	5(2)	0	0	0
In1	8(1)	9(1)	14(1)	0	0	0
In2	8(2)	6(1)	2(1)	0	0	0

The anisotropic displacement factor exponent takes the form: $-2\pi^2[h^2a^{*2}U_{11} + ... + 2hka^*b^*U_{12}]$.

Table 3.4.4. Selected bond lengths [Å] for $SmCu_6In_6$ at 293(2) K with estimated standard deviations in parentheses.

Label	Distances	Label	Distances
Sm-In1	3.1378(7)	Cu2-In1	2.93(3)
Sm-In2	3.215(7)	Cu1-In1	2.798(4)
Cu2-Cu2	2.918(7)	Cu1-Cu1	2.7116(5)
In2-In2	2.444(19)	Cu1-Cu2	2.682(5)
Cu2-In2	2.69(4)	In1-In1	2.9279(12)
Cu1-In2	2.731(3)		

3.4.2.2. Crystal chemistry

$SmCu_6In_6$ crystallizes in the tetragonal YCu_6In_6 type structure (space group *I*4/*mmm*),[4] which is an ordered structure of $CeMn_4Al_8$ type. SEM image of a typical rod-like crystal of $SmCu_6In_6$ as grown from the flux synthesis is shown in Figure 3.4.1. The crystal structure of $SmCu_6In_6$ along [001] direction is shown in Figure 3.4.2. The view of $SmCu_6In_6$ unit cell with the parameters obtained from the refinement using mixed atomic position at 8*j* is shown in Figure 3.4.2a. The cigar-like shape of $Cu_{0.5}In_{0.5}$ positions

resolved by the split model keeping inner square uniquely occupied by copper and an outer one uniquely occupied by indium atoms as shown in Figure 3.4.2b.

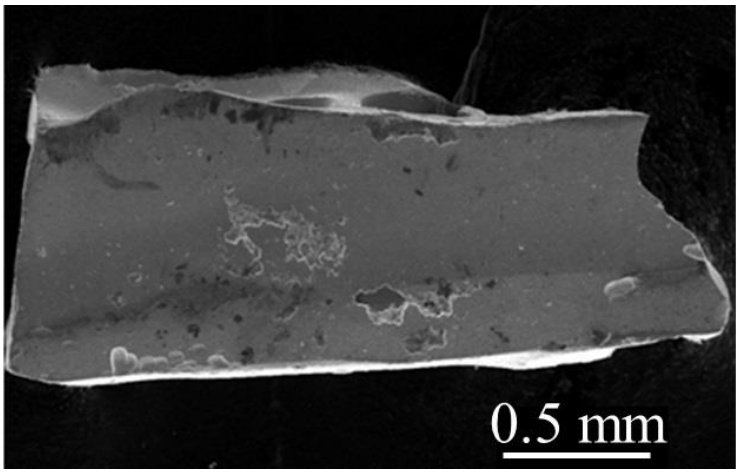

Figure 3.4.1. SEM image of a typical single crystal of $SmCu_6In_6$.

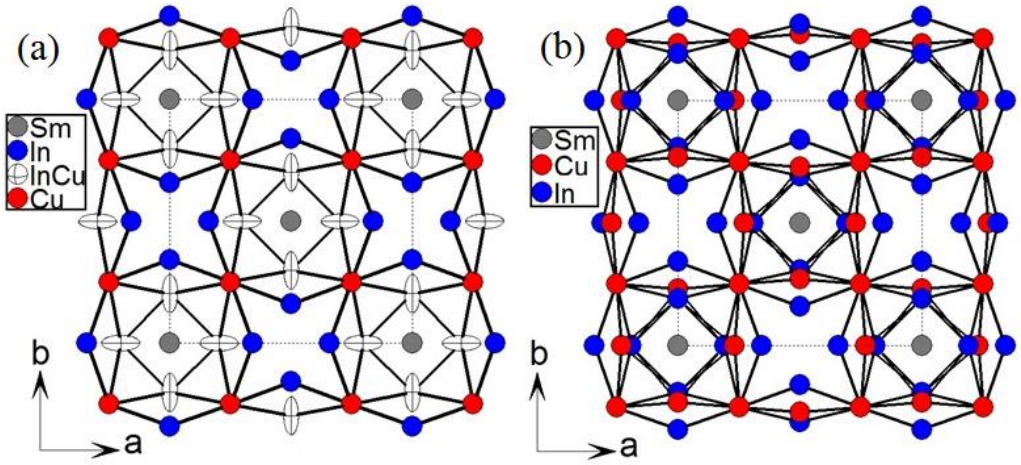

Figure 3.4.2. The structure of $SmCu_6In_6$ as viewed along the *c*-axis; the unit cell is outlined as dot lines. (a) The parameters obtained from the refinement using mixed atomic positions of Cu and In at 8*j* and (b) The cigar-like shape of $Cu_{0.5}In_{0.5}$ positions resolved by the split model keeping inner square uniquely occupied by copper and an outer one uniquely occupied by indium atoms.

Crystal structure of $SmCu_6In_6$ is composed of pseudo Frank-Kasper cages $[Cu_8In_8]$ occupying one samarium atom in each ring to form a stable structure (Figure 3.4.3). These pseudo Frank-Kasper cages are shared through the corner coppers atoms along *ab*-plane resulted in a three dimensional network. A slight distortion in $SmCu_6In_6$ is clearly evident in comparison of the coordination environments of Mn in $CeMn_4Al_8$ structure and Cu in $SmCu_6In_6$ structure (Figure 3.4.4).

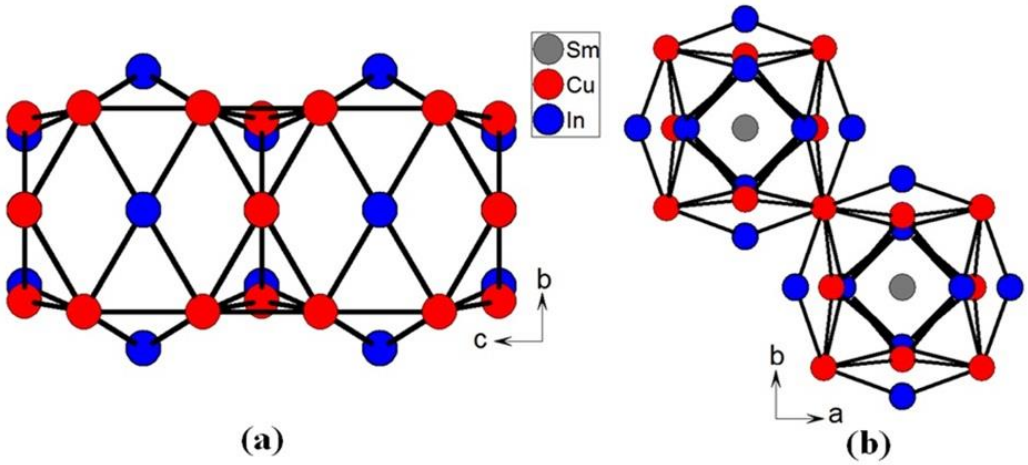

Figure 3.4.3. Pseudo Frank-Kasper cages in $SmCu_6In_6$ are shared through the (a) Bridged with split atoms and (b) corner Cu atoms along *ab*-plane.

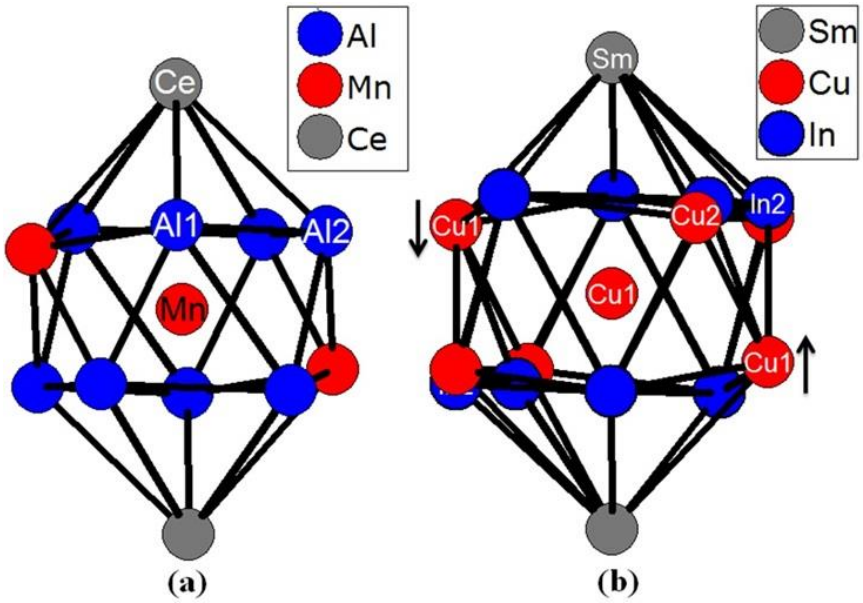

Figure 3.4.4. Comparison of the icosahedron polyhedra of (a) Mn in $CeMn_4Al_8$ and (b) Cu in $SmCu_6In_6$.

The coordination environment of indium atoms is formed as 14-vertex Frank-Kasper cage (not shown in figure). Split atoms in the distorted icosahedrons geometry composed of 12 atoms of which two are Sm atoms and the remaining ten are shared by Cu and In atoms. All icosahedrons and Frank-Kasper cages are slightly distorted compared to the $CeMn_4Al_8$ compound. The shortest distance of Sm-In (3.1378(7) Å) is smaller than the calculated distances of 3.263 Å[41] suggest a strong covalent bond between Sm and In atoms, however the shortest distance Sm-Cu atom (3.5251(3) Å) is

substantially larger than the theoretical value of 3.084 Å[42] indicates weak interaction between them. The shortest Cu-In distance in $SmCu_6In_6$ is 2.753(4) Å close to the distances observed in other *RE*Cu_6In_6 compounds.[4] Relatively small In-In distances (2.483(4) Å) are due to the split model refinement which allows to the formation of suitable bond lengths between the copper and indium atoms.

3.4.2.3. Physical Properties

3.4.2.3.1. Magnetism

Magnetic susceptibility measurements were made on polycrystalline sample of $SmCu_{6-x}In_{6+x}$ (x = 0, 1 and 2) obtained from arc melting. The temperature dependent magnetic susceptibility at an applied field of 1 kOe is shown in Figure 3.4.5 and inverse molar magnetic susceptibility data versus temperature is shown in Figure 3.4.6. All compounds show weak temperature dependent paramagnetism in the temperature range 50-300 K (Figure 3.4.5) which is typical for samarium based intermetallics.

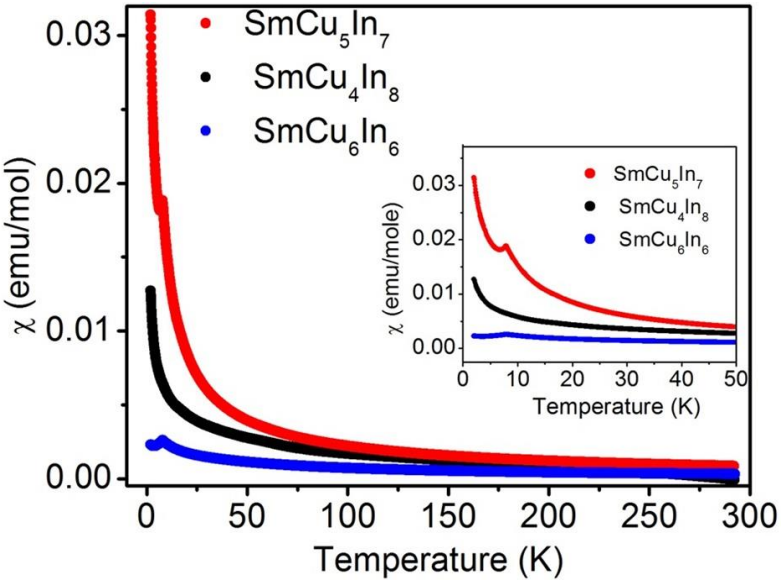

Figure 3.4.5. Temperature dependent magnetic susceptibility, χ, of $SmCu_4In_8$, $SmCu_5In_7$ and $SmCu_6In_6$. Inset figure shows the low temperature behaviour.

The temperature dependent molar susceptibility (χ_m) of all compounds obeys modified Curie-Weiss law, $\chi = C/(T-\theta) + \chi_0$ above 50 K and an antiferromagnetic ordering found at 7.8 K for $SmCu_6In_6$ and $SmCu_5In_7$. There is no long range magnetic ordering found down to 2 K in $SmCu_4In_8$. In all compounds the susceptibility rises with decreasing temperature as seen in paramagnets but $SmCu_5In_7$ and $SmCu_4In_8$ have a

sudden increase over a very low temperature in the range of 2-10 K. In contrast, $SmCu_4In_8$ magnetic susceptibility data shows two regions, i.e 50-120 K (1.13 μ_B) and 170-220 K (0.85 μ_B).

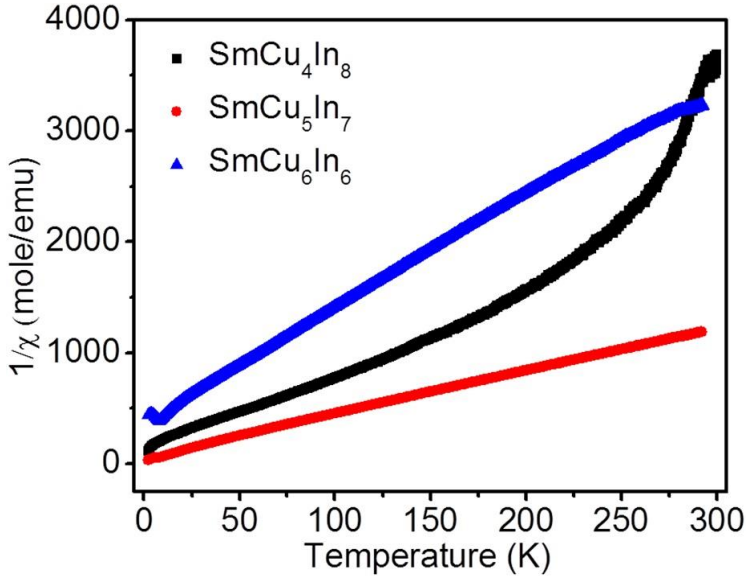

Figure 3.4.6. Temperature dependence of the modified reciprocal magnetic susceptibility, $1/\chi$, of the $SmCu_4In_8$, $SmCu_5In_7$ and $SmCu_6In_6$ samples.

A significant deviation at the lower temperature can be attributed to crystal field effects. Interesting point to notice here is the effective Bohr magneton number (μ_{eff}) observed from the linear fit using modified Curie-Weiss equation are 0.83 μ_B and 0.90 μ_B (in the range 170-220 K) per Sm atom for $SmCu_4In_8$ and $SmCu_6In_6$, respectively close to the calculated magnetic moment of 0.84 μ_B for a free trivalent samarium ion.[43] The magnetic moment 0.84 μ_B of free samarium ion was calculated using Hund's rule using antiparallel spin (S = 5/2) and orbital (L = 5) angular momenta. In contrast the magnetic moment for Sm in $SmCu_5In_7$ obtained as 1.45 μ_B/Sm atom. Here, Hund's rules are expected to be unreliable in this system because another *J* multiplet lies just above this free-ion ground state of samarium, and crystalline electric field effects frequently lead to different ground states and in pure Sm metal, the paramagnetic moment is observed to be 1.5 μ_B, instead of the 0.84 μ_B expected.

The calculated values of paramagnetic Curie temperature (θ_p) are 64.038 K, -21.53 K and -52.08 K for $SmCu_4In_8$, $SmCu_5In_7$ and $SmCu_6In_6$, respectively suggests a strong ferromagnetic interactions in $SmCu_4In_8$ and antiferromagnetic interactions in other two

compounds. In general, compounds crystallizing in the $CeMn_4Al_8$ structure type, show disorder at the Mn and Al sites which affects the magnetic behaviour in the solid solution and it was previously reported for $LaMn_4Al_8$[28] and very recently for $YbCu_{6-x}In_{6+x}$ (x = 0, 1, 2). Assuming Cu and In are non-magnetic elements in the systems, this large difference in the magnetic moment could be possibly associated with the structural behaviour. Much more detailed structural studies such as neutron diffraction and magnetic compton scattering measurement could give an insight to the structure-property relations in these compounds.

The field dependence of the magnetization, *M(H)* for $SmCu_{6-x}In_{6+x}$ (x = 0, 1, 2) ground samples were measured at 2 K and 20 K shown in Figure 3.4.7. The data measured at 20 K exhibits linear behaviour and no signs of saturation up to highest attainable field of 60 kOe. The magnetization curve taken at 2 K (within the magnetic ordering) shows a slight field dependent response up to ~ 30 kOe, continues to rise slowly up to the highest obtainable field (60 kOe). However, the saturation behaviour is different for each system at highest field. $SmCu_4In_8$ system almost saturates at ~30 kOe with magnetic moment of ~0.2 emu/mol. $SmCu_5In_7$ saturate at high value with higher saturation magnetic moments and $SmCu_6In_6$ does not saturate even at the highest applied magnetic field up to (60 kOe).

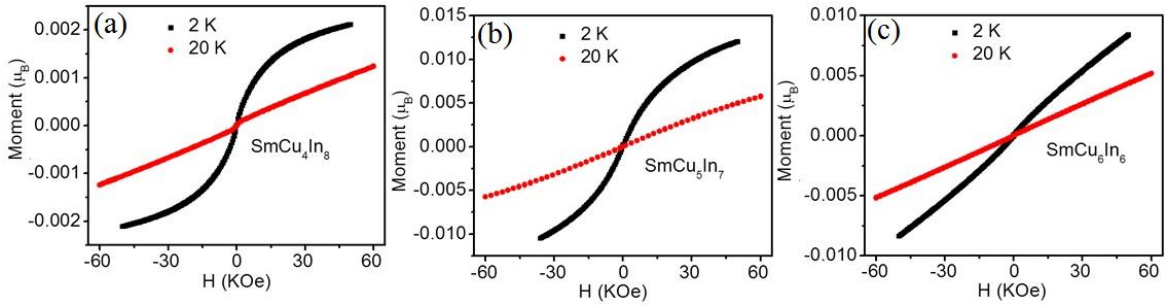

Figure 3.4.7. Magnetization as a function of applied magnetic field at 2 K and 20 K for a polycrystalline sample of (a) $SmCu_4In_8$ (b) $SmCu_5In_7$ and (c) $SmCu_6In_6$.

3.4.2.3.2. Electrical resistivity

The normal state temperature dependent reduced elctrical resistivities of $SmCu_{6-x}In_{6+x}$ (x = 0, 1, 2) are shown in Figure 3.4.8. Because the sample contained several micro cracks and were irregularly shaped, only the reduced resisitivity (ρ/ρ_{300}) are plotted here. The ρ/ρ_{300} continuously decreases linearly with decreasing temperature, typical for

metallic systems[30, 31] but without any long range magnetic ordering. At low temperature, in the range of 0-50 K, the $\rho(T)$ data can be fitted to the power law function, $\rho = \rho_0 + AT^n$, where ρ_0 is the residual resistivity expressed in units of Ωcm, A and n are the fitting parameters. The values obtained from the fit are shown in Figure 3.4.8. According to the Fermi-liquid theory, at low temperatures, the resistivity varies as $\rho = \rho_0 + AT^2$. Experimentally it has been observed that when electron-electron scattering dominates over electron-phonon scattering, $\rho \alpha T^2$. The value obtained from the fit power is close to 2 in $SmCu_6In_6$ which is the case for systems exhibiting Fermi liquid state.[32, 44] But in $SmCu_4In_8$ and $SmCu_5In_7$ the value obtained from the fit power is 0.9299 and 0.8684, respectively, characteristic for non-Fermi liquid state.[34] In order to verify Fermi liquid and non-Fermi liquid behaviour, the resistivity data is plotted as $(\rho - \rho_0)$ vs. T^2 as inset to Figure 3.4.8. For $SmCu_6In_6$, linearity in the data confirms a possible Fermi-liquid behaviour at low temperatures, while other two compounds show a deviation from the linearity. Similar kind of behaviour have observed in $YbCu_{6-x}In_{6+x}$ (x = 0, 1 and 2).

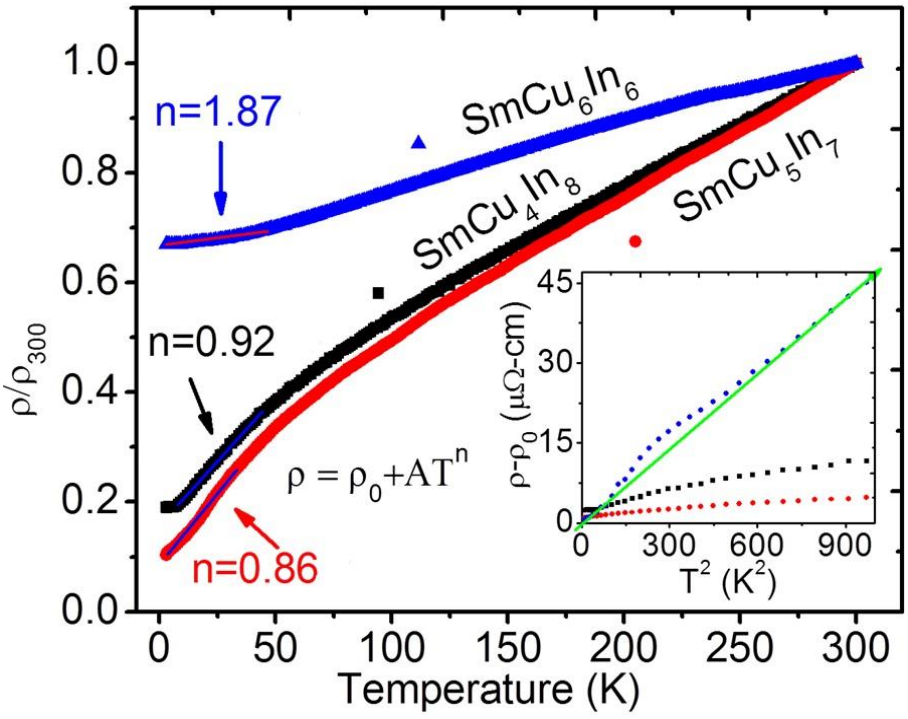

Figure 3.4.8. Temperature dependent electrical resistivity $\rho(T)$ of $SmCu_4In_8$, $SmCu_5In_7$ and $SmCu_6In_6$. The inset figure shows the low temperature data fit using the Power law $\rho = \rho_0 + AT^n$.

3.5. New Structure Type in the Mixed Valent Compound $YbCu_4Ga_8$

3.5.1. Introduction

Compounds having general formula RET_4X_8 (*RE* = La-Nd, Sm-Lu and U; *T* = Cr, Mn, Fe, Co, Cu and Ag; *X* = Al, Ga and In) have been reported for their interesting physical properties.[45-49] For example, high-temperature antiferromagnetic ordering (T_N) observed in $GdFe_4Al_8$[45] (T_N = 155 K), in addition to the two low-temperature magnetic transitions at T_1 = 21 K and T_2 = 27 K, high temperature magnetic ordering (163.5 K) in $TbFe_4Al_8$,[50] anisotropic magnetic properties on the single crystals of UFe_4Al_8[46] and some more compounds are reported in $REFe_4Al_8$ family.[47, 49, 51] The antiferromagnetic–paramagnetic transitions observed in $GdCr_xAl_{12-x}$ at T_N = 6.50 and 6.75 K for x = 3.5 and 4.0, respectively.[48]

As per inorganic crystal structure database[52] and Pearson's crystal data,[53] despite a large (ca.200) number of RET_4X_8 compounds, only a few Yb based compounds are reported in the 1-4-8 family. Interesting examples are $YbCr_4Al_8$,[3] $YbFe_4Al_8$,[54] $YbMn_4Al_8$[55] and $YbCu_4Al_8$.[3] All these compounds crystallize in the tetragonal $ThMn_{12}$ structure type (space group *I*4/*mmm*). Two gallides, $YbCo_{5.4}Ga_{6.6}$[56] and $YbMn_{4.7}Ga_{7.3}$,[57], were reported in the same structure type for their phase studies using powder XRD and this motivated to look for more compounds with first row transition metals.

Though Cu-based compounds are relatively easy to synthesize using conventional synthesis techniques, only YbCuGa,[58] $YbCu_{5-x}Ga_x$ ($0 \leq x \leq 2$),[59] $YbCu_xGa_{4-x}$ (x = 1.2 and 0.35),[60] $YbCu_{0.8}Ga_{1.2}$,[61] and $YbCuGa_3$[62] were reported in the Yb-Cu-Ga family. This motivated to focus on the synthesis of the Ga rich compounds in the same family. Chan et al. reported[63] the crystal structure and properties of $ThMn_{12}$ structure type $RE(CuGa)_{12}$ (*RE* = Y, Gd-Er and Yb), where the antiferromagnetic transition were observed at 12.5 K in $Gd(CuGa)_{12}$, 13.5 K in $Tb(CuGa)_{12}$, 6.7 K in $Dy(CuGa)_{12}$ and 3.4 K in $Er(CuGa)_{12}$. But in $Yb(CuGa)_{12}$ observed Pauli paramagnetism.[63] This section discusses about the synthesis of a new compound $YbCu_4Ga_8$ for the first time which crystallizes in a new structure type, a superstructure derived from the $CeMn_4Al_8$ and $ThMn_{12}$ types. High quality single crystals of $YbCu_4Ga_8$ were grown using Ga as metal flux. Use of gallium flux has been proved as an excellent tool to produce many novel ternary and quaternary intermetallic phases.[64-66] Several new pollygallides with an impressive set of diverse structures and compositions have been

synthesized using Ga as solvent.[67-72] The crystal structure of $YbCu_4Ga_8$ was studied using single crystal XRD data and the Cu/Ga atomic site differentiation was investigated with single crystal neutron diffraction measurements on a large single crystal. Magnetic susceptibility and electrical resistivity studies were performed on sample obtained by HFIH.

3.5.2. Results and Discussion

3.5.2.1. Reaction Chemistry

Compound $YbCu_4Ga_8$ was obtained from reactions of Yb/Cu/Ga in liquid gallium which acted as reactive solvent and formed a new compound $YbCu_4Ga_8$. The grey rod shaped single crystal of $YbCu_4Ga_8$ obtained from the flux reaction is shown in Figure 3.3.5.1.

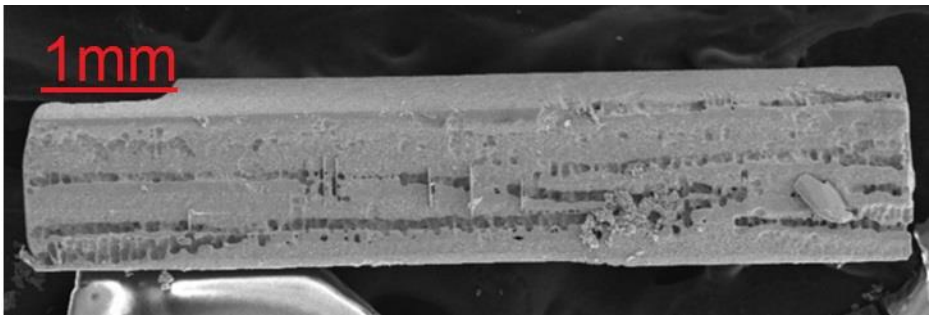

Figure 3.5.1. The SEM image of a typical $YbCu_4Ga_8$ single crystal grown from Ga flux.

$YbCu_4Ga_8$ is stable in air and no decomposition was observed even after several months. A high quality single crystal was used to collect the XRD data and refined the crystal structure within the $CeMn_4Al_8$ type and different lattice parameters are $a = b =$ 8.649(4) Å and c = 5.1484(3) Å. The elemental analysis of this compound with SEM/EDAX gave the atomic composition (1:4:8) which is in excellent agreement with the results obtained from the single crystal refinement.

The XRD pattern of the powdered sample is in good agreement with the simulated pattern obtained from single crystal data. However, a close look at the powder data (Figure 3.5.2) showed additional peaks indicating a possible superstructure reflection or minor impurity phase. Then the data was refined within a new structure type, a superstructure of the $CeMn_4Al_8$ type and the lattice parameters obtained are $a = b$ = 8.6529(4) Å and c = 15.465(1) Å. The superstructure reflections are clearly visible in the experimental powder XRD pattern of $YbCu_4Ga_8$ as shown in the Figure 3.5.2a and 3.5.2b. After a synthesis method was established for $YbCu_4Ga_8$ other first row transition metals also employed in similar reaction

condition in order to produce more members in the YbT_4Ga_8 (T = Ni, Co, Cu and Ag) family but was not successful.

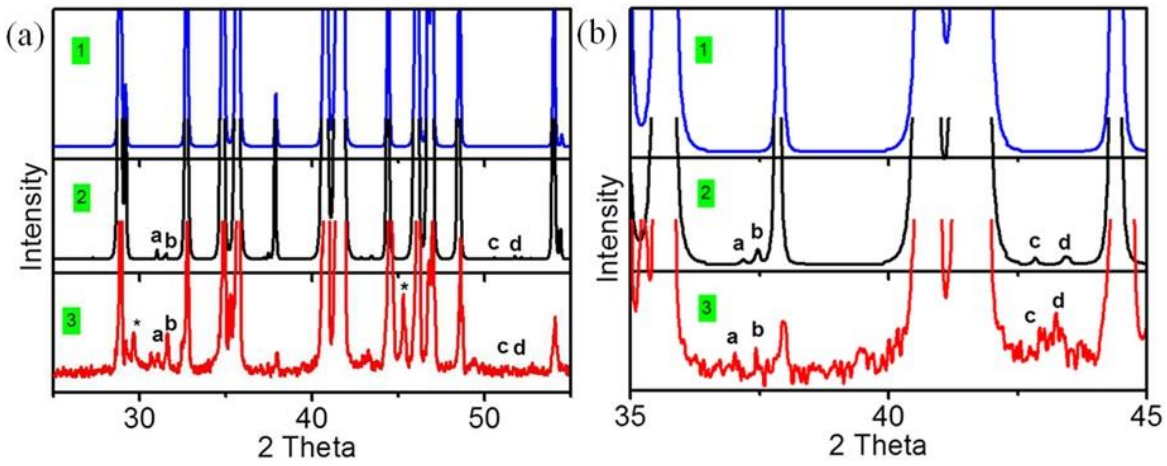

Figure 3.5.2. (a) The experimental powder pattern of $YbCu_4Ga_8$ (3) was compared to the single crystal X-ray structure refinement of the superstructure $YbCu_4Ga_8$ (2) and substructure of $YbCu_4Ga_8$ (1). Superstructure reflections are marked as a, b, c and d, which are comparable with experimental pattern (marked as a, b, c and d). * represents unreacted Ga-metal peak. (b) Expanded view of the Figure 3.20a showing the superstructure reflections more clearly.

3.5.2.2. Structure refinement of $YbCu_4Ga_8$

The crystal structure of $YbCu_4Ga_8$ was refined using SHELXL-97 (full-matrix least-squares on F^2) [12] with anisotropic atomic displacement parameters for all atoms. As a check for the correct composition, the occupancy parameters were refined in a separate series of least-squares cycles. Single crystals of $YbCu_4Ga_8$ from different synthesis batches were used for the data collection. The data collected in the first step of refinement shows that $YbCu_4Ga_8$ crystallizes in a body centered tetragonal lattice ($I4/mmm$) within the $CeMn_4Al_8$ type structure and lattice constants are $a = b = 8.6529(4)$ Å and $c = 5.155(3)$ Å. This refinement resulted in four crystallographic positions with one ytterbium atom occupies 2*a* site, one copper atom occupies at 8*f* site and two gallium atoms occupy at 8*i* and 8*j* sites. During isotropic refinement of $YbCu_4Ga_8$, it was observed that the highest difference peak and deepest hole are 12 and -3.6, respectively. The attempts to refine the mixed positions of Cu and Ga were also not solved the highest difference peak and deepest hole. In addition, the anisotropic displacement parameter U_{33} of all four positions was slightly larger. All these facts indicated that the $YbCu_4Ga_8$ compound crystallizes in the superstructure and the refinement indeed confirm this with a stable refinement with a tripling of *c*-axis. The second

step considered the superstructure reflections and refined the structure in the same space group *I*4/*mmm* within the superstructure of the $CeMn_4Al_8$ type structure and the lattice parameters are $a = b = 8.6529(4)$ Å and $c = 15.465(1)$ Å. In this refinement, there are eight crystallographic positions in the $YbCu_4Ga_8$ superstructure of which two ytterbium atoms occupy 2*a* and 4*e* sites, two copper atoms occupy 8*i* and 16*m* and four gallium atoms occupy two 16*n*, 8*j* and 8*f* sites. The final refinement is quite stable and the overall stoichiometry obtained from the refinement is $YbCu_4Ga_8$. Owing to the small contrast between Cu and Ga, the assignment of the sites was further checked using single crystal neutron diffraction. The sites were initially assigned to be of type Ga and the occupancy refined one site at a time to decide whether it was occupied by Ga or Cu.

The data collection and structure refinement for $YbCu_4Ga_8$ using X-ray and neutron are listed in Table 3.5.1. The standard atomic positions and isotropic atomic displacement parameters of this compound are collected in Table 3.5.2. The anisotropic displacement parameters and important bond lengths are listed in Tables 3.5.3 and 3.5.4, respectively. Group-subgroup scheme in the Bärnighausen formalism[73-75] for the subcell and the superstructure of $YbCu_4Ga_8$ is given in Figure 3.5.3. Further information on the structure refinements is available from: Fachinformationszentrum Karlsruhe, D-76344 Eggenstein-Leopoldshafen (Germany), by quoting the Registry Nos. CSD–424999 (Substructure), CSD-425503 (Superstructure XRD) and CSD-425502 (ND).

3.5.2.3. Crystal chemistry of $YbCu_4Ga_8$

The crystal structure of $YbCu_4Ga_8$ along the *c*-axis is shown in Figure 3.5.4a. $YbCu_4Ga_8$ crystallizes in the tetragonal superstructure of the $CeMn_4Al_8$ type (space group *I*4/*mmm*), which is an ordered superstructure of the $ThMn_{12}$ type. Crystal structure of $YbCu_4Ga_8$ is composed of 8 Cu atoms and 12 Ga atoms forming $[Cu_8Ga_{12}]$ cages occupying one ytterbium atom in each ring to form a stable structure. These cages are shared through the corner Cu-linkage along *ab*-plane resulted in a three dimensional network. Bonds to the Yb atoms have been omitted to emphasize the 3D $[Cu_4Ga_8]$ framework and its channels (Figure 3.5.4b). The tripling of *c*-axis in the subcell of $YbCu_4Ga_8$ structure ($CeMn_4Al_8$ type) is shown in Figure 3.5.5a. The compound contains two layers: one distorted slab contains Cu and Ga atoms (Figure 3.5.5b) and a planar layer contains all three elements (Figure 3.5.5d). These two layers are interconnected through the bonds between Cu and Ga atoms form a

stable three dimensional structure. In the distorted layer, Cu and Ga atoms forming a 2-dimensional sheet that extends in the *bc*-plane (Figure 3.5.5a) and is capped by Cu and Ga atoms alternatively above and below this plane, thus forming a puckered overall layer (Figure 3.5.5c). The planar layer on the other hand, form one dimensional (1D) cis and trans infinite zigzag chains of Cu and Ga atoms propagating along the *c*-axis as shown in Figure 3.5.4d.

Table 3.5.1. Crystal data and structure refinement for $YbCu_4Ga_8$ at 296(2) K (XRD) and 50 K (ND)

Empirical formula		$YbCu_4Ga_8$	
Formula weight		984.96	
Crystal system		Tetragonal	
Space group		*I*4/*mmm*	
Diffraction Method	*X*-Ray		Neutron
Volume	385.93(3) Å^3	1157.91(11) Å^3	1134.7(7) Å^3
Z	2	6	6
a (Å)	8.6529(4)	8.6529(4)	8.600(3)
c (Å)	8.600(3)	15.465(1)	15.342(6)
Density (calculated)	8.474 g/cm^3	8.473 g/cm^3	8.647 g/cm^3
Absorption coefficient	50.071 mm^{-1}	50.066 mm^{-1}	51.221 mm^{-1}
F(000)	867.4	2602.3	610
Crystal size (mm^3)	1 x 0.05 x 0.05	0.5 x 0.05 x 0.05	3.00 x 1.00 x 1.00
θ range for data collection	3.3 to 32.1°	2.6 to 32.1°	9.69 to 88.00°
Index ranges	-12=<*h*=<4, -12=<*k*=<12, -7=<*l*=<7	-12=<*h*=<4, -12=<*k*=<12, -23=<*l*=<23	-23=<*h*=<22, -22=<*k*=<18, -33=<*l*=<36
Reflections collected	1226	3730	3537
Independent reflections	218 [R_{int} = 0.0344]	628 [R_{int} = 0.0403]	3537
Completeness to θ = 30.55°	100%	99.95%	99%
Refinement method	Full-matrix least-squares on F^2		
Data / restraints / parameters	218 / 0 / 16	628 / 48 / 37	3537 / 48 / 41
Goodness-of-fit	1.191	1.083	1.049
Final *R* indices [>2σ(I)]	R_{obs} = 0.024, wR_{obs} = 0.064	R_{obs} = 0.042, wR_{obs} = 0.136	R_{obs} = 0.0591, wR_{obs} = 0.1419
Extinction coefficient	0.0077	0.00081(13)	0.000080(11)
Largest diff. peak and hole (e·Å^{-3})	2.35 and -2.541	5.951 and -3.578	6.352 and -6.143

$R = \Sigma||F_o|-|F_c|| / \Sigma|F_o|$, $wR = \{\Sigma[w(|F_o|^2 - |F_c|^2)^2] / \Sigma[w(|F_o|^4)]\}^{1/2}$ and calcw=$1/[\sigma^2(Fo^2)+(0.0359P)^2+6.1794P]$ where $P = (Fo^2+2Fc^2)/3$

Table 3.5.2. Atomic coordinates ($x10^4$) and equivalent isotropic displacement parameters ($Å^2x10^3$) for sub-structure and super-structure of $YbCu_4Ga_8$ at 296(2) K with estimated standard deviations in parentheses.

Label	Wyckoff site	*x*	*y*	*z*	Occupancy	U_{eq}*
Substructure						
Yb	2*a*	0	0	0	1	10(3)
Cu	8*f*	2500	2500	2500	1	12(3)
Ga1	8*i*	3463(1)	0	0	1	14(3)
Ga2	8*j*	2847(1)	5000	0	1	23(3)
Superstructure						
Yb1	2*a*	0	0	0	1	3(1)
Yb2	4*e*	5000	5000	1664(1)	1	3(1)
Cu1	16*m*	2504(4)	2504(4)	828(2)	1	8(1)
Cu2	8*j*	2840(7)	5000	0	1	6(1)
Ga1	16*n*	5000	1537(3)	1669(2)	1	8(1)
Ga2	8*f*	2500	2500	2500	1	10(1)
Ga3	8*i*	0	3462(6)	0	1	8(1)
Ga4	16*n*	2151(4)	0	1670(2)	1	13(1)
ND data						
Yb1	2*a*	0	0	0	1	1(1)
Yb2	4*e*	5000	5000	1685(7)	1	1(1)
Cu1	16*m*	2534(9)	2534(9)	830(2)	1	3(1)
Cu2	8*j*	3046(2)	5000	0	1	2(1)
Ga1	16*n*	5000	1546(5)	1628(4)	1	4(1)
Ga2	8*f*	2500	2500	2500	1	2(1)
Ga3	8*i*	0	3484(9)	0	1	4(2)
Ga4	16*n*	2259(2)	0	1659(5)	1	4(1)

*U_{eq} is defined as one third of the trace of the orthogonalized U_{ij} tensor.

These cis and trans chains are interconnected through the Ga-Ga bonds, forming one dimensional hexagons which are separated by ordered Yb atoms. The average Cu-Cu bond distance in the $YbCu_4Ga_8$ crystal structure 2.563(3) Å is close to the atomic radii of Cu-Cu distance (2.560 Å) observed in $YbCu_4Al_8$[3] and exactly matching with the theoretical distance of 2.56 Å.[76] The shortest distance of Yb-Ga is 2.996(7) Å is smaller than the calculated distances of Yb^{2+}-Ga (3.09 Å)[77, 78] and larger than Yb^{3+}-Ga (2.92 Å)[77, 78] suggesting mixed

valency or intermediate valency of Yb atoms in $YbCu_4Ga_8$. However, both Yb1-Ga and Yb2-Ga short distances are similar rule out the mixed valency instead $YbCu_4Ga_8$ is an intermediate valent compound. The shortest distance between Yb and Cu atoms 3.178(2) Å is close to the radii of Yb-Cu distance (3.176 Å) observed in $YbCu_2Si_2$[79] but slightly shorter to the theoretical distance of 3.19 Å of Yb^{2+}-Cu.

Table 3.5.3. Anisotropic displacement parameters ($Å^2x10^3$) for $YbCu_4Ga_8$ at 296(2) K with estimated standard deviations in parentheses.

Label	U_{11}	U_{22}	U_{33}	U_{12}	U_{13}	U_{23}
Substructure						
Yb	3(3)	3(3)	3(3)	0	0	0
Cu	8(4)	8(4)	2(1)	1(1)	1(1)	0
Ga1	5(1)	6(1)	11(5)	0	0	0
Ga2	29(7)	6(1)	5(1)	0	0	0
Super structure						
Yb1	3(1)	3(1)	4(1)	0	0	0
Yb2	2(1)	2(1)	4(1)	0	0	0
Cu1	8(1)	5(1)	4(1)	0	0	0
Cu2	13(2)	5(2)	4(1)	0	2(1)	2(1)
Ga1	6(1)	6(1)	11(1)	0	0	0
Ga2	10(1)	10(1)	9(1)	0	-1(1)	-1(1)
Ga3	7(2)	6(2)	10(2)	0	0	0
Ga4	22(2)	8(1)	8(1)	0	0	0
ND data						
Yb1	1(1)	1(1)	1(1)	0	0	0
Yb2	1(1)	1(1)	1(1)	0	0	0
Cu1	3(1)	3(1)	2(1)	-1(1)	0	0
Cu2	4(1)	2(1)	1(1)	0	0	0
Ga1	3(1)	2(1)	6(1)	0	0	0
Ga2	2(1)	2(1)	2(1)	-1(1)	0	0
Ga3	5(1)	4(2)	4(2)	0	0	0
Ga4	6(1)	2(3)	3(1)	0	2(1)	0

The anisotropic displacement factor exponent takes the form: $-2\pi^2[h^2a^{*2}U_{11} + ... + 2hka^*b^*U_{12}]$.

Table 3.5.4. Selected bond lengths [Å] for $YbCu_4Ga_8$ at 296(2) K with estimated standard deviations in parentheses.

Label	Distances	Label	Distances
Cu1—Cu1	2.589(3)	Ga2—Ga2	2.643(7)
Cu1—Cu2	2.537(3)	Ga3—Ga3	2.659(7)
Cu2—Cu2	2.636(6)	Ga3—Ga4	2.811(3)
Cu1—Ga2	2.571(16)	Ga4—Ga4	2.634(4)
Cu1—Ga3	2.656(2)	Ga4—Ga3	2.797(4)
Cu1—Ga1	2.646(2)	Ga4—Ga2	2.539(12)
Cu2—Ga2	2.535(13)	Yb1—Cu2	3.180(2)
Cu2—Ga3	2.798(4)	Yb2—Cu2	3.183(3)
Cu1—Ga4	2.531(3)	Yb2—Ga1	2.995(19)
Cu2—Ga1	2.809(3)	Yb1—Ga3	2.997(4)
Ga1—Ga1	2.661(4)	Yb2—Ga2	3.318(7)
Ga1—Ga2	2.655(14)	Yb2—Ga4	3.182(3)
Ga1—Ga4	2.800(2)	Yb1—Ga4	3.175(2)
Ga1—Ga4	2.827(3)		

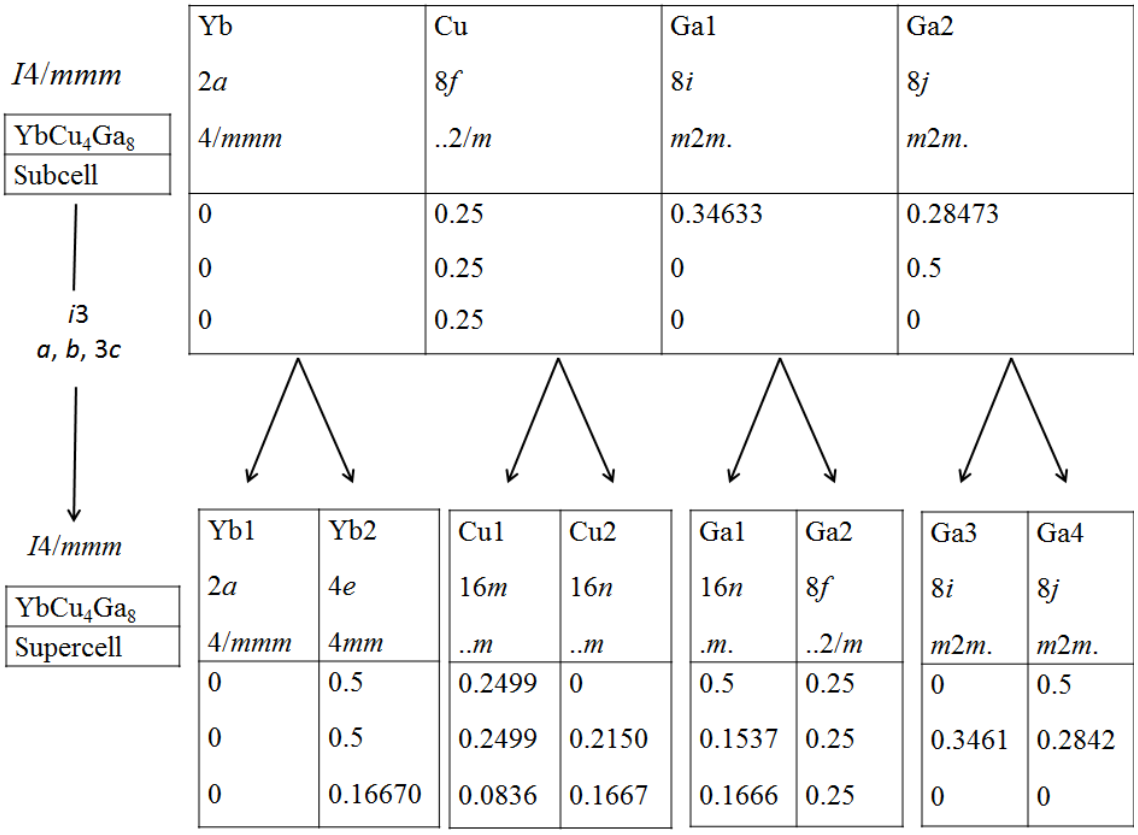

Figure 3.5.3. Group-subgroup scheme in the Bärnighausen formalism, for the subcell and the superstructure of $YbCu_4Ga_8$. The indices for the isomorphic (i) transition and the unit cell transformations are given. The evolution of the atomic parameters is shown at the right.

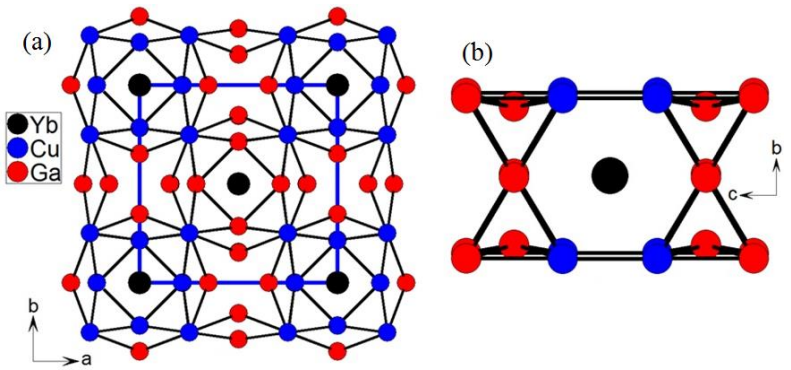

Figure 3.5.4. (a) Crystal structure of $YbCu_4Ga_8$ as viewed along the *c*-axis; the unit cell is outlined as blue solid lines. (b) Cu_4Ga_8 framework shown along [010] direction with an Yb atom sandwich in between them.

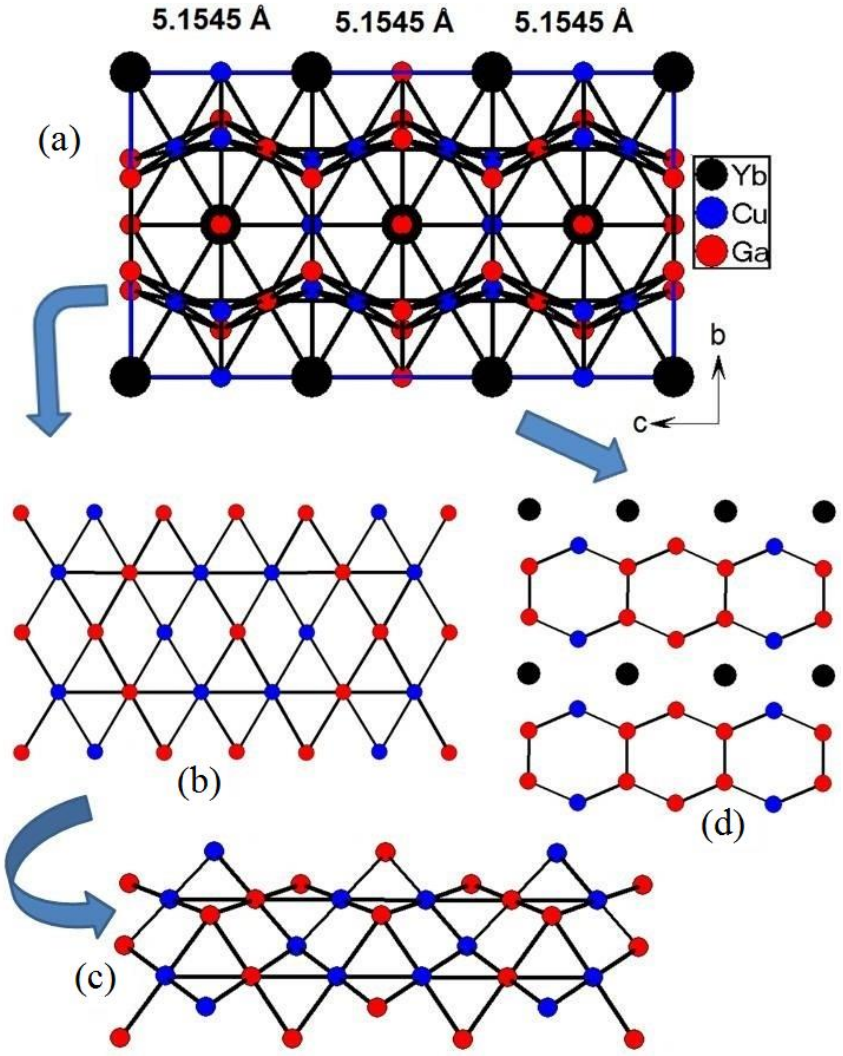

Figure 3.5.5. (a) Crystal structure of $YbCu_4Ga_8$ as viewed along the *a*-axis; (b) Projection of the fragment $[Cu_xGa_y]$, (c) A rotated view of the $[Cu_xGa_y]$ slab where the puckered form of the layer is emphasized and (d) Projection of the planar layer of $YbCu_{4-x}Ga_{8-y}$.

The local coordination environments of all atoms in the crystal structure of $YbCu_4Ga_8$ are presented in Figure 3.5.6. The coordination environments Yb1 and Yb2 atoms are similar and formed as cages of 20 atoms $Cu_{16}Ga_4$ and Cu_8Ga_{12}, respectively. The coordination environments for Cu1 and Cu2 atoms are similar composed as cuboctahedran of $[Yb_2Cu_3Ga_7]$ and $[Yb_2Cu_4Ga_6]$, respectively. Ga1 and Ga3 are having similar sphere composed of 14-vertex Frank-Kasper cage of $[YbCu_5Ga_8]$ and $[YbCu_6Ga_7]$, respectively. Ga2 and Ga4 atoms also have similar coordination environments composed as icosahedron of $[Yb_2Cu_6Ga_4]$ and $[Yb_2Cu_4Ga_6]$, respectively.

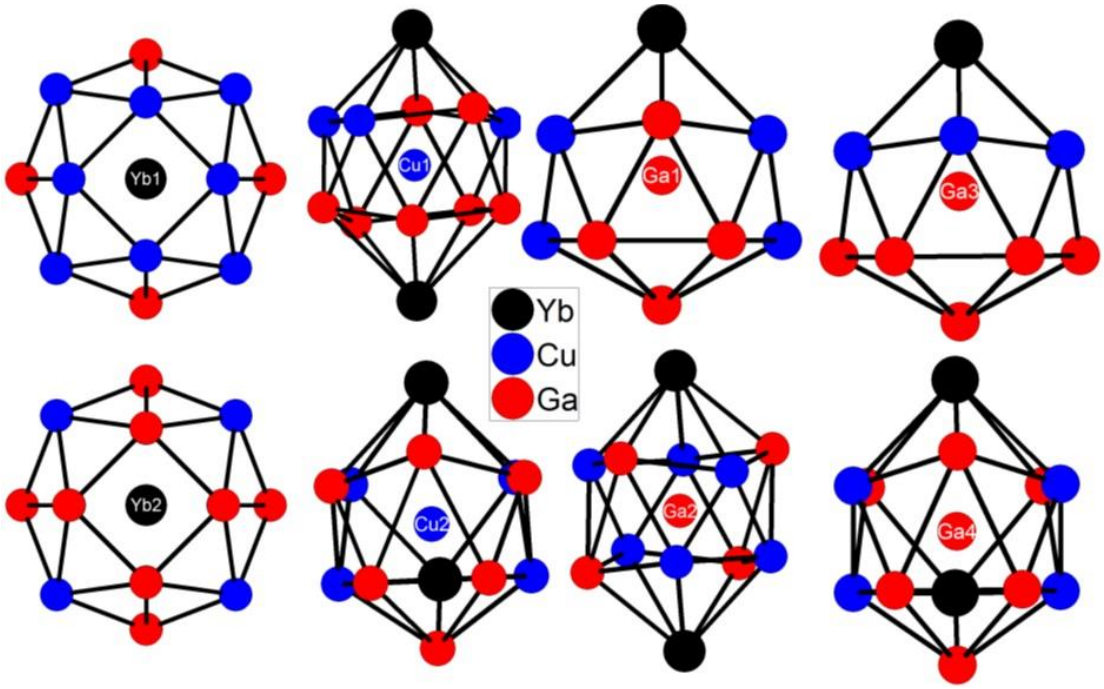

Figure 3.5.6. Coordination sphere of all atoms in the crystal structure of $YbCu_4Ga_8$.

3.5.2.4. Physical Properties

3.5.2.4.1. Magnetism

Magnetic susceptibility measurements were made on a polycrystalline sample of $YbCu_4Ga_8$ obtained from high frequency induction heating synthesis. The temperature dependent molar magnetic susceptibility (χ_m) and inverse susceptibility ($1/\chi_m$) of $YbCu_4Ga_8$ at an applied field of 10000 Oe are shown in Figure 3.5.7. The magnetic susceptibility, also measured on single crystals in two orientations, one being parallel to the applied magnetic field (marked as $H \parallel c$-axis) and other being perpendicular to the field (marked as $H \perp c$-axis) as shown in, Figure 3.5.8.

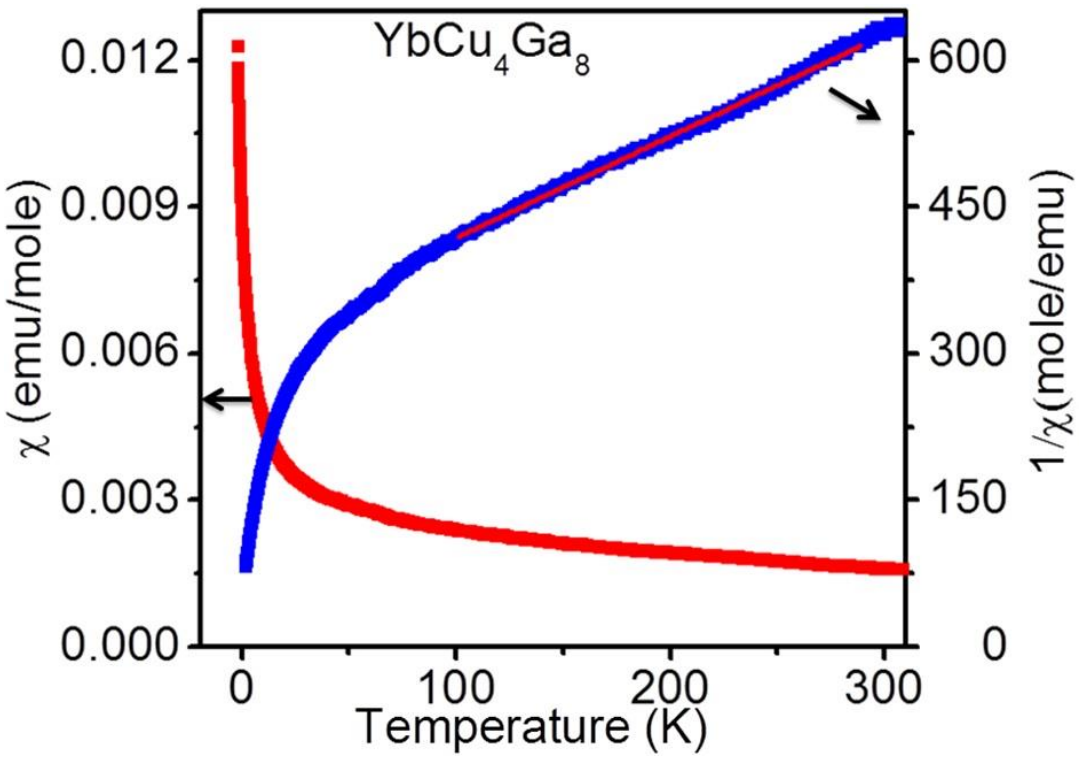

Figure 3.5.7. Temperature dependence of the modified magnetic susceptibility (χ_m) and reciprocal magnetic susceptibility ($1/\chi_m$) of the $YbCu_4Ga_8$. The red straight line shows the temperature range where the modified Curie-Weiss law was applied to calculate the magnetic moment.

In all measurements, χ increases gradually with increasing temperature and no magnetic ordering down to 2 K but the susceptibility slightly increases at lower temperature with increasing field, which is normal for *RE* based intermetallics.[27, 80] The inverse susceptibility curve obeys modified Curie-Weiss law, $\chi = C/(T-\theta) + \chi_0$ (χ_0 = 0.00519 emu/mole), in the range of 100-290 K with an effective magnetic moment of 2.77 μ_B/Yb atom suggesting the mixed valent or intermediate valent nature of Yb atoms. The estimated experimental μ_{eff} value is about 60% of that expected for a free ion Yb^{3+} moment (4.56 μ_B/Yb). However, the calculated magnetic moment for Yb in $YbCu_4Ga_8$ (40% Yb^{2+}) is close to the value observed for Yb in $YbLiGe_2$[81] and Yb_5Ge_4[82] compounds. Drake et al. already pointed out the negligible temperature dependence of the magnetic susceptibility and speculated the mixed valence of Yb in $Yb(CuGa)_{12}$.[63] Felner and Nowik studied the magnetic properties of other prototypes YbT_4Al_8 (*T* = Cr, Mn, Fe and Cu) in detail and observed the mixed valent behaviour of Yb in the $YbCr_4Al_8$ and $YbCu_4Al_8$ compounds as they exhibit temperature independent paramgnetism and positive Curie-Weiss temperature and later it

was confirmed by ^{170}Yb Mössbauer spectroscopy.[83] On the other hand, in $YbMn_4Al_8$ and $YbFe_4Al_8$ the Yb ion exists as divalent and trivalent, respectively.

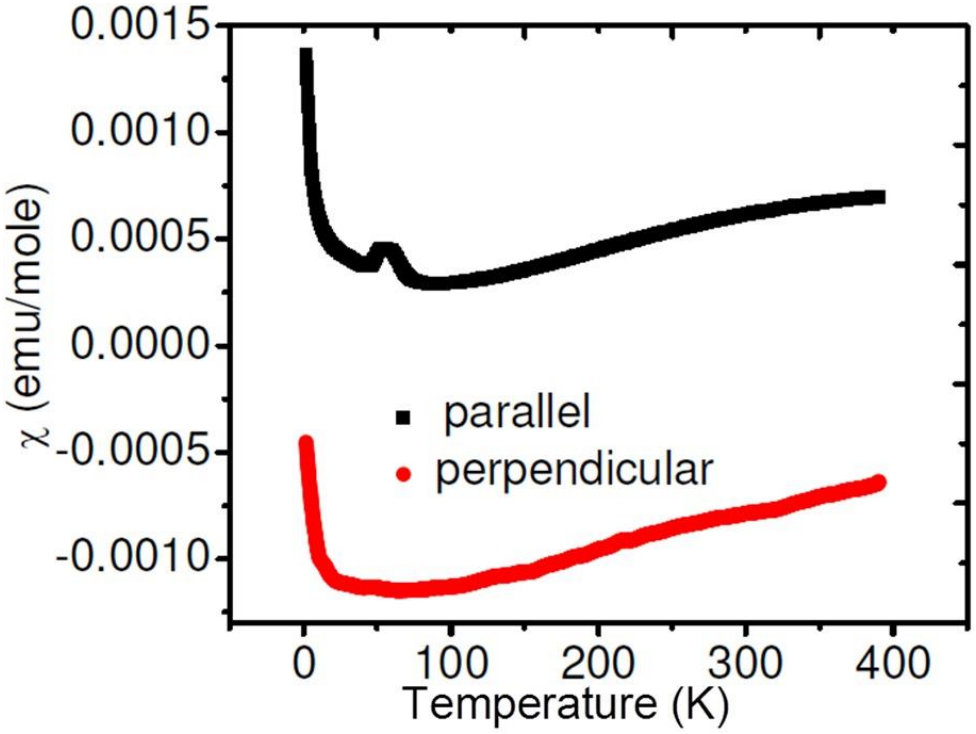

Figure 3.5.8. Magnetic susceptibility measured on a single crystal of $YbCu_4Ga_8$ in two different orientations, magnetic field along the *c*-axis ($H \parallel c$) and magnetic field perpendicular to the *c*-axis ($H \perp c$).

3.5.2.4.2. Electrical Resistivity

The normal state temperature dependent resistivity of $YbCu_4Ga_8$ is shown in Figure 3.5.9 decreases linearly with temperature, typical for metallic systems[30, 31] but without any long range magnetic ordering. The resistivity value of $YbCu_4Ga_8$ is 220 $\mu\Omega$cm at room temperature is comparable to the resistivity of $Yb_5Ir_4Ge_{10}$ (220 $\mu\Omega$cm).[84] At low temperature in the range of 3-30 K, the $\rho(T)$ data can be fitted to the power law function, $\rho = \rho_0 + AT^n$, where ρ_0 is the residual resistivity expressed in units of Ωcm (ρ_0 is 131 $\mu\Omega$cm), A and n are the fitting parameters. According to Fermi-liquid theory, at low temperatures, the resistivity varies as $\rho = \rho_0 + AT^2$. Experimentally it has been observed that when electron-electron scattering dominates over electron-phonon scattering, $\rho \alpha T^2$. The value obtained from the fit is slightly larger than 2 in $YbCu_4Ga_8$, which is the case for systems exhibiting Fermi liquid state.[32, 85] In order to verify Fermi liquid behaviour, the resistivity data is plotted as ($\rho - \rho_0$)

vs. T^2 as inset to Figure 3.5.9. For $YbCu_4Ga_8$, linearity in the data indicates a probable Fermi-liquid behaviour in this compound at low temperatures.

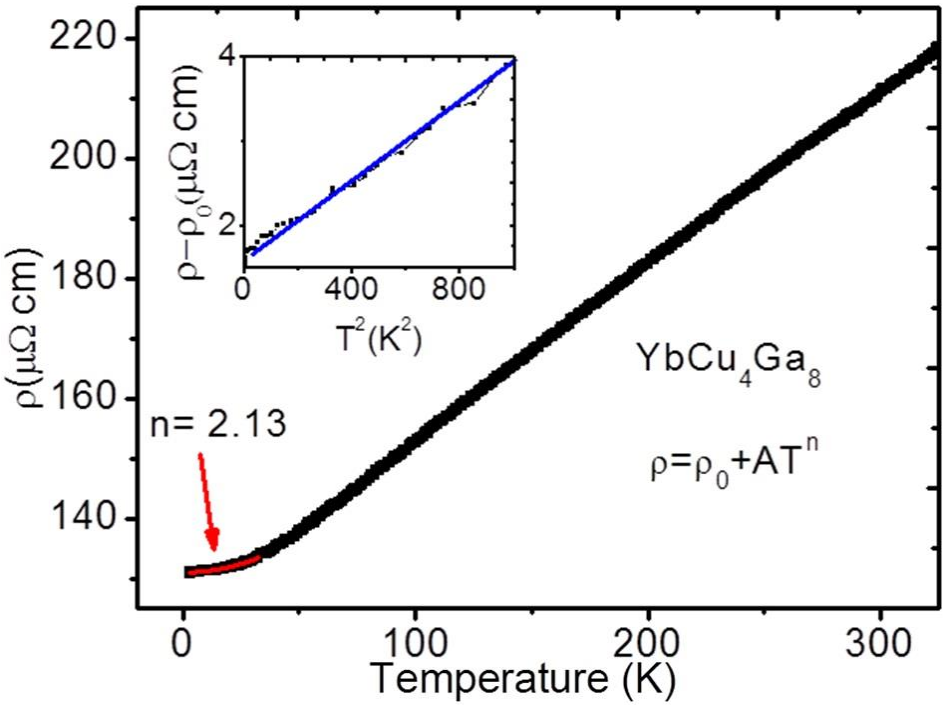

Figure 3.5.9. Resistivity (ρ) measured as a function of temperature. Low temperature data have been fitted to the Power law $\rho = \rho_0 + AT^n$. The values obtained from the fit are shown in inset.

3.6. Crystal Structure and Properties of Tetragonal $EuAg_4In_8$ Grown by Metal Flux Technique

3.6.1. Introduction

This chapter discusses about the compound $EuAg_4In_8$ which was previously reported by Sysa et al.[86] as a hexagonal crystal system with space group *P*6/*mmm,* which is unusual in the RET_4X_8 family. Based on literature and previous reports on $YbCu_4Ga_8$,[87] $YbCu_6In_6$[88] and $SmCu_6In_6$,[89] it was known that the family of these compounds crystalizes mostly in the tetragonal crystal system with space group *I*4/*mmm*. Sysa et al. have synthesized the compound by arc melting, which is not an efficient technique for the synthesis of Eu based compounds due to high vapor pressure of Eu. They have reported the divalent state of Eu in $EuAg_4In_8$ with the help of XANES. In continuation to the studies in the RET_4X_8 family and related compounds in this series, it was found that $EuAg_4In_8$ exists in tetragonal phase as well.

As per ICSD[90] and PCD[91] $EuAg_4In_8$ is the only compound so far reported in the Eu-Ag-In system.[86] In addition, among the large number of RET_4X_8 compounds, only a few Eu based compounds were reported so far. The examples are $EuCu_4Al_8$,[92, 93] $EuFe_4Al_8$[94] and $EuMn_4Al_8$.[93] All these compounds crystallize in the tetragonal $ThMn_{12}$ structure type (space group *I*4/*mmm*). Though there is a slight variation in composition, $EuFe_6Al_6$[95, 96] is another compound reported in the same structure type.

The single crystals of $EuAg_4In_8$ were grown using In as the active metal flux. The crystal structure of $EuAg_4In_8$ was studied using single crystal XRD data. Magnetic susceptibility and electrical resistivity studies were performed on the single crystals obtained by metal flux method.

3.6.2. Results and Discussion

3.6.2.1. Structure refinement

The crystal structure of $EuAg_4In_8$ was refined using Shelxl-97 (full-matrix least-squares on F^2)[8] with anisotropic atomic displacement parameters for all atoms. As a check for the correct composition, the occupancy parameters were refined in a separate series of least-squares cycles. The first step of refinement showed that $EuAg_4In_8$ crystallizes in a body centered tetragonal lattice (*I*4/*mmm*) within the $CeMn_4Al_8$ structure type with lattice

constants $a = b = 9.7937(2)$ Å and $c = 5.7492(2)$ Å. This refinement resulted in four crystallographic positions where one europium atom occupies 2*a* site, one silver atom occupies 8*f* site and two indium atoms occupy 8*i* and 8*j* sites. During the isotropic refinement of $EuAg_4In_8$, it was observed with unacceptable highest difference peak and deepest hole is little bit high (>12 and -11 $eÅ^3$). The refinement residual value (*R*1) also was found to be slightly high (8%). Since the scattering power of Ag and In are very close due to only two electron difference, the attempts was to refine the structure with Ag and In mixing; however, it did not improve the refinement parameters. To overcome all these problems observed in the refinement $EuAg_4In_8$, the data was recollected with long exposure time (60 s) and more number of frames (120). This revised data collection overcame the problems associated with the initial data collection (10 s and within 30 frames).

Since the structure was previously reported in the hexagonal system, the next intention was to collect the single crystal XRD data on available temperature range in the instrument. For this, the temperature dependent single crystal XRD studies were carried out using Bruker Photon 100 CMOS detector in shutter less mode equipped with a micro focus, 5 kW sealed tube X-ray source with graphite monochromatic Mo-*Kα* radiation ($\lambda = 0.71073$ Å) operating at 50 kV and 1 mA, with ω scan mode at various temperatures 100 K, 200 K, 350 K and 450 K.

The details of the data collection and structure refinement are listed in Table 3.6.1. The standard atomic positions and isotopic atomic displacement parameters of this compound are given in Table 3.6.2. The anisotropic displacement parameters and important bond lengths are listed in Tables 3.6.3 and 3.6.4, respectively. Further information on the structure refinements is available from: by quoting the Registry No. CCDC 1002249.

3.6.2.2. Crystal chemistry of $EuAg_4In_8$

SEM image of a typical single crystal of $EuAg_4In_8$ is shown in Figure 3.6.1. The powder XRD of $EuAg_4In_8$ on crushed single crystals is compared with the simulated data obtained from the single crystal structure refinement on the tetragonal and hexagonal systems (shown in figure 3.6.2). It is well evident that the pattern is perfectly matching with simulated tetragonal crystal system. There are a few additional peaks observed in the hexagonal pattern (marked with *), which are absent in the powder XRD of the sample synthesized.

Table 3.6.1. Crystal data and structure refinement for $EuAg_4In_8$ at 296(2) K.

Empirical formula	$EuAg_4In_8$
Formula weight	1502
Wavelength	0.71073 Å
Crystal system	Tetragonal
Space group	*I*4/*mmm*
Unit cell dimensions	$a = b$= 9.7937(2) Å, c = 5.7492(2) Å
Volume	551.44(3) $Å^3$
Z	2
Density (calculated)	9.04528 g/cm^3
Absorption coefficient	28.826 mm^{-1}
F(000)	1285.9
Crystal size	0.05 x 0.05 x 0.10 mm^3
θ range for data collection	2.94 to 45.35°
Index ranges	-19<=*h*<=19, -15<=*k*<=17, -8<=*l*<=11
Reflections collected	3286
Independent reflections	686 [R_{int} = 0.0485]
Completeness to θ = 45.35°	100%
Refinement method	Full-matrix least-squares on F^2
Data / restraints / parameters	686/ 0 / 16
Goodness-of-fit	1.181
Final *R* indices [>2σ(I)]	R_{obs} = 0.036, wR_{obs} = 0.086
Extinction coefficient	0.012793
Largest diff. peak and hole	2.728 and -4.887 e·$Å^{-3}$

$R = \Sigma||F_o|-|F_c|| / \Sigma|F_o|$, $wR = \{\Sigma[w(|F_o|^2 - |F_c|^2)^2] / \Sigma[w(|F_o|^4)]\}^{1/2}$ and calcw=$1/[\sigma^2(Fo^2)+(0.0359P)^2+6.1794P]$ where $P = (Fo^2+2Fc^2)/3$

Table 3.6.2. Atomic coordinates ($x10^4$) and equivalent isotropic displacement parameters ($Å^2x10^3$) for $EuAg_4In_8$ at 296(2) K with estimated standard deviations in parentheses.

Label	Wyckoff site	*X*	*y*	*z*	Occupancy	U_{eq}*
Eu	2*a*	0	0	0	1	8(1)
Ag	8*f*	2500	2500	2500	1	12(1)
In1	8*i*	3471(5)	0	0	1	12(1)
In2	8*j*	2880(9)	5000	0	1	20(1)

*U_{eq} is defined as one third of the trace of the orthogonalized U_{ij} tensor.

Table 3.6.3. Anisotropic displacement parameters ($Å^2x10^3$) for $EuAg_4In_8$ at 296(2) K with estimated standard deviations in parentheses.

Label	U_{11}	U_{22}	U_{33}	U_{12}	U_{13}	U_{23}
Eu	8(1)	8(1)	9(1)	0	0	0
Ag	14(2)	14(2)	8(1)	1(1)	3(1)	3(1)
In1	11(2)	10(2)	15(2)	0	0	0
In2	42(2)	7(1)	11(2)	0	0	0

The anisotropic displacement factor exponent takes the form: $-2\pi^2[h^2a^{*2}U_{11} + ... + 2hka^*b^*U_{12}]$.

Table 3.6.4. Selected bond lengths [Å] for $EuAg_4In_8$ at 296(2) K with estimated standard deviations in parentheses.

Label	Distances	Label	Distances
Eu—In1	3.4001(5)	In1—In1	2.9935(10)
Eu—In2	3.5458(5)	In1—In1	3.5699(3)
Eu—Ag	3.7491(1)	In1—In2	3.1649(4)
Ag—Ag	2.8746(1)	In1—In2	3.1934(8)
Ag—In1	2.9944(2)	In1—In2	4.9310(2)
Ag—In2	2.8635(1)	In2—In2	2.9359(9)

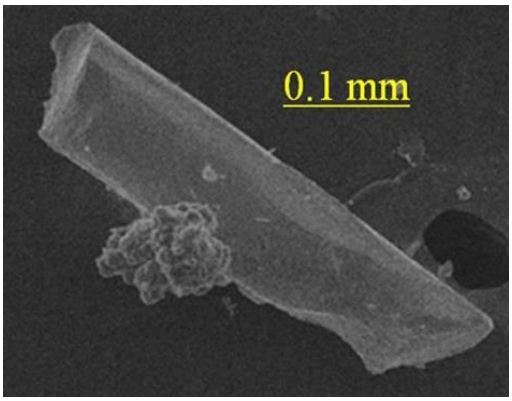

Figure 3.6.1. The SEM image of typical $EuAg_4In_8$ single crystal grown from In flux.

The absence of a couple of prominent peaks (103) and (203) expected in the hexagonal system (shown in inset of Figure 3.6.2) clearly suggests that above compound crystallizes in the stable tetragonal phase. The hexagonal phase reported by Sysa et al. was formed probably due to the difference in the synthesis methods. However, it was unable to repeat their synthesis method due to the non-technical way of dealing Eu in the arc-melting chamber, which may lead into the Eu deficiency in the resulted product. Another possibility is formation of the hexagonal phase as a metastable phase, which resulted probably due to the

rapid quenching of sample from high temperature. These attempts to synthesize the compound, by HFIH also led to the formation of the mixed phases of tetragonal and hexagonal systems along with In and an unknown phase. The crystal structure of $EuAg_4In_8$ along *c*-axis is shown in Figure 3.6.3. $EuAg_4In_8$ crystallizes in the $CeMn_4Al_8$ structure type (space group *I*4/*mmm*), which is an ordered superstructure of the $ThMn_{12}$ type. Crystal structure of $EuAg_4In_8$ is composed with pseudo Frank-Kasper cages of 8 Ag atoms and 12 In atoms, which form $[Ag_8In_{12}]$ cages with one europium atom occupied in each ring. These cages are shared through the corner Ag-linkage along *ab*-plane resulting in a 3D network. Since the compound was reported in different structure, it is worth comparing the structures in details to understand the relations between them. The tetragonal structure consists of only four atomic positions, while hexagonal system is packed with eight atomic coordinates. The crystal structures of tetragonal and hexagonal systems are compared in Figure 3.6.3a (along *c*-axis) and 3.6.3b (along *a*-axis), respectively.

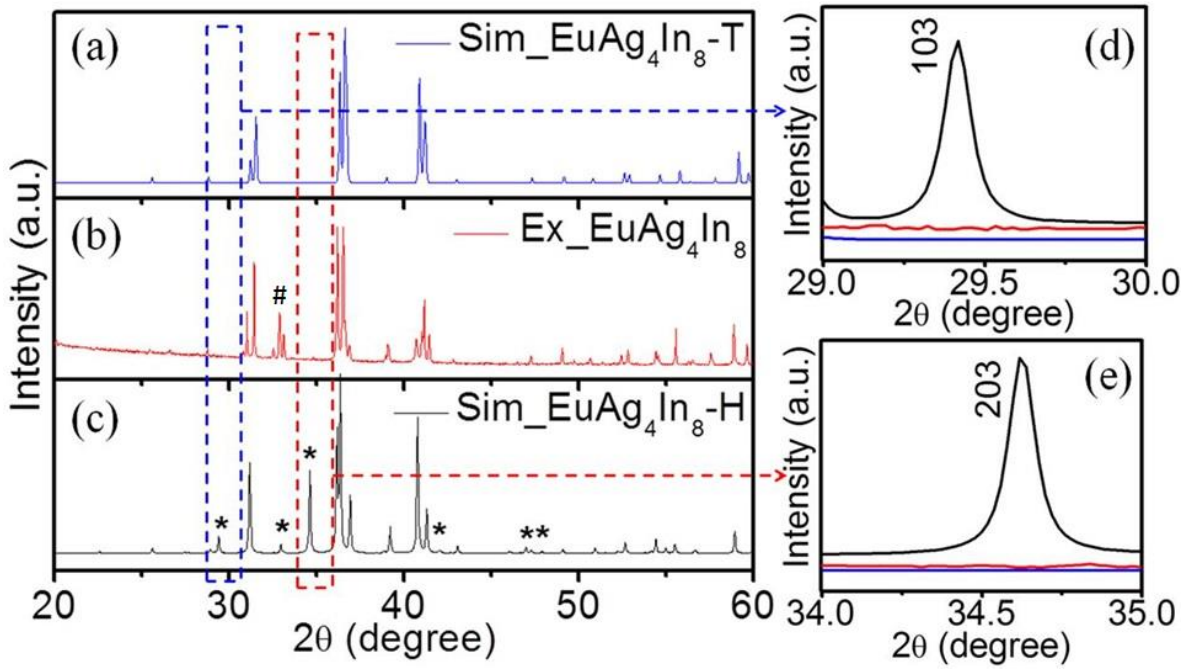

Figure 3.6.2. PXRD comparison of simulated tetragonal (a) and hexagonal (c) with experimental (c) $EuAg_4In_8$. The # mark in Figure (b) corresponds to unreacted indium peak and * peaks in (c) correspond to the additional peaks in the hexagonal crystal system compared to the tetragonal system and (d and e) show two extra peaks ([103] and [203] planes), which are highlighted from the hexagonal system.

In order to understand the detailed relations, the structure should be checked in layer by layer as drawn in Figures 3.6.3c-g. The tetragonal system is composed of two different

types of layers, [$EuIn_4$] and [Ag_4In_4], while the hexagonal system is composed of three different layers, [$EuIn_6$], [Eu_2In_6] and [$Ag_{12}In_{12}$]. The layers are arranged in ABABAB and ABCBAB fashion in tetragonal (along *c*-direction) and hexagonal (along *a*-direction) systems, respectively. The layer [$EuIn_4$] in the tetragonal phase and layers [$EuIn_6$] and [Eu_2In_6] in hexagonal phase are compared in Figure 3.6.3c, 3.6.3d and 3.6.3e. In all these layers, the Ag and In atoms form hexagons and Eu atoms are statistically distributed at the center.

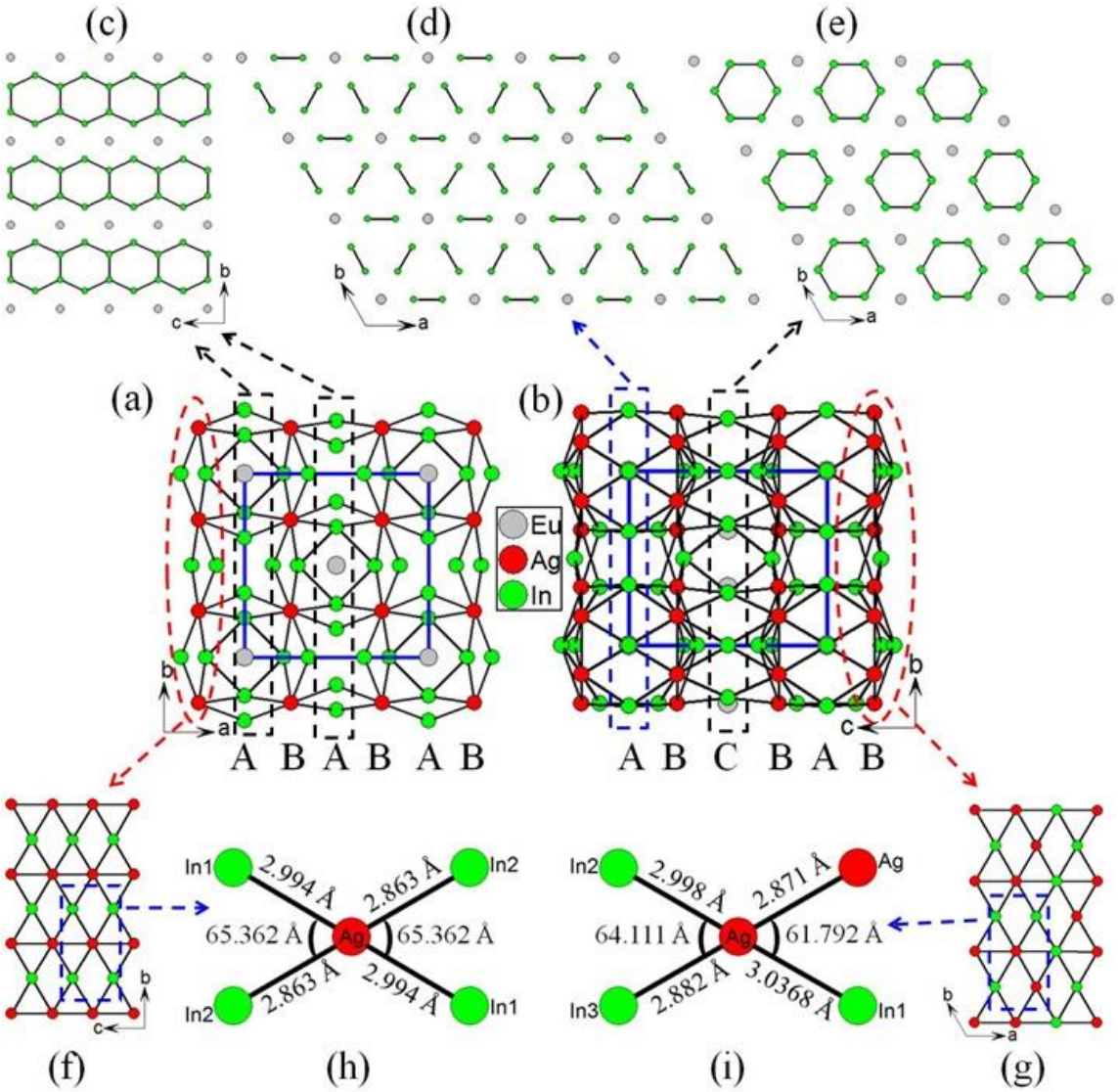

Figure 3.6.3. Crystal structure of $EuAg_4In_8$ (a) tetragonal system along the *c*-axis (b) hexagonal system along the *a*-axis, unit cell outlined as blue solid lines, (c and f) $EuIn_4$ and Ag_4In_4 two layers are present in tetragonal system, (d, e and g) $EuIn_6$, Eu_2In_6 and $Ag_{12}In_{12}$ three layers are present in hexagonal system and (*h* and *i*) coordination environment of Ag atoms in the layers of tetragonal and hexagonal crystal systems.

The notable difference between the structures is in the arrangement of hexagon rings. In the case of the tetragonal systems, the hexagons are edge shared and propagated along the *c*-direction (Figure 3.6.3c). These layers are well separated with the bond distances of 4.15 Å of In2-In2 atoms and one layer of Eu atoms is sandwiched between them. On the other hand, in the hexagonal system, the hexagons are discrete in one layer C (Figure 3.6.3e) with the bond distance of 3.954 Å of In4-In4 atoms and only dimers in layer A (Figure 3.6.3d).

In layer C of the hexagonal system, the Eu atoms are occupied in a triangle trap of three hexagon rings. The appearance of the layers $[Ag_4In_4]$ and $[Ag_{12}In_{12}]$ in the tetragonal and hexagonal systems, respectively shown in Figure 3.6.3f and 3.6.3g are similar with the formation of 4 membered rings of Ag and In atoms. However, a close look at the coordination environments of Ag atoms in the layers suggests that they are substantially different (Figure 3.6.3h and 3.6.3i). In the case of tetragonal system, there is presence of inversion symmetry with equal bond distances of Ag-In1 (2.994 Å) and Ag-In2 (2.863 Å) along with similar In1-Ag-In2 bond angle (65.362 Å). On the other hand, in the case of hexagonal, the inversion symmetry lost due to the slight distortion of Ag-In bonds (Figure 3.6.3i) angle from 61.792 Å (Ag-Ag-In1) to 64.111 Å (In2-Ag-In3). Overall, the structures are closely related, but as mentioned earlier, the different synthesis parameters lead into different crystal systems. In order to check the phase transition from tetragonal to hexagonal, temperature dependent SCXRD studies were done in the temperature range 100-450 K. Even though there is no visible phase transition in the temperature range 100-450 K, an increment in the lattice parameters and cell volume of the structure was observed (Figure 3.6.4). The local coordination environments of all atoms in the crystal structure of $EuAg_4In_8$ are presented in Figure 3.6.5. The coordination environment of Eu atom is formed as cages of 20 atoms composed of 8 Ag and 12 In. The coordination environment of Ag atom is made up of a cuboctahedron of $[Eu_2Ag_2In_8]$. Coordination environments of In1 and In2 are composed of $[EuAg_4In_3]$ and $[Eu_2Ag_4In_6]$. The average Ag-Ag bond distance in the $EuAg_4In_8$ crystal structure is 2.8746(1) Å, which is close to the sum of the atomic radii of two Ag atoms (2.871 Å) and is close to value observed in the previously reported hexagonal $EuAg_4In_8$ structure as well.[86] The average bond distance of Eu-In (3.4729(5) Å) is close to the theoretical distance of 3.44 Å.[97] The bond distance between Eu and Ag atoms is 3.7491(1) Å, which is also close to the radii sum of Eu-Ag atoms (3.75 Å) observed in $EuAg_4In_8$.[86]

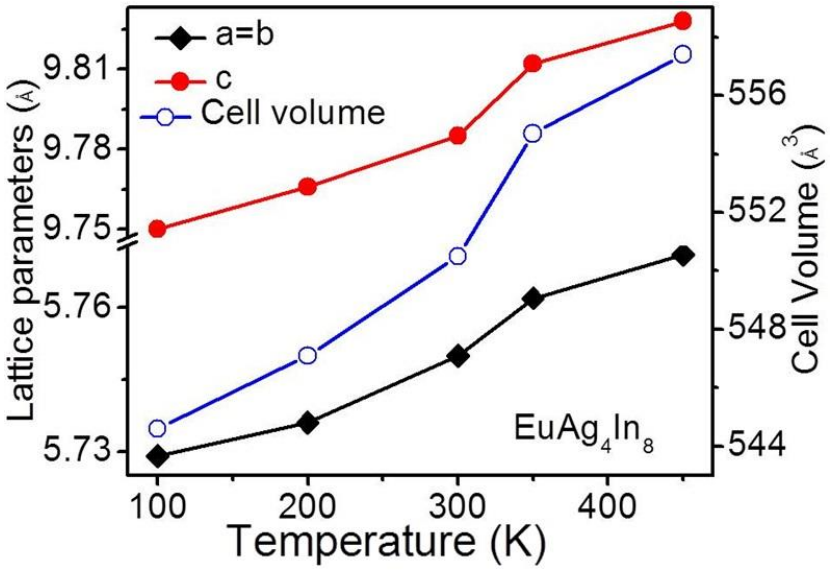

Figure 3.6.4. Temperature dependent single crystal data of $EuAg_4In_8$, lattice parameters and cell volume.

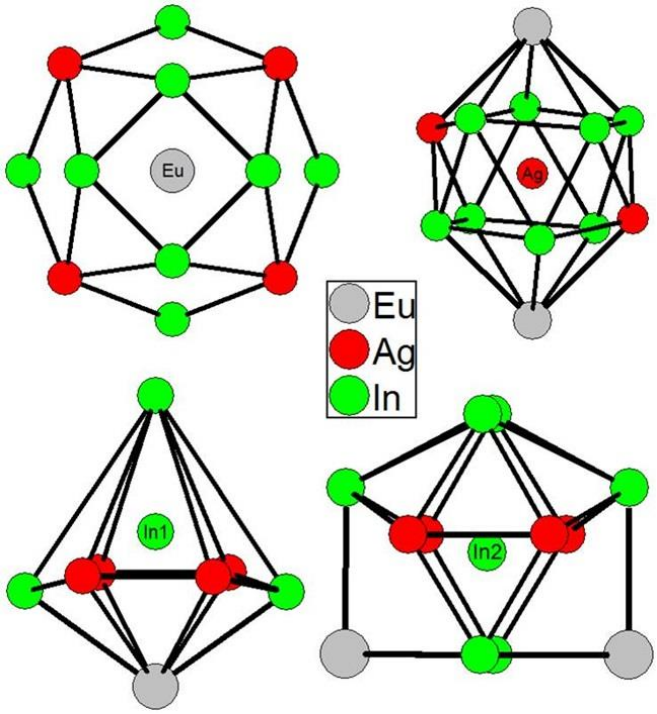

Figure 3.6.5. Coordination sphere of all atoms in the crystal structure of $EuAg_4In_8$ is presented.

3.6.2.3. Physical Properties

3.6.2.3.1. Magnetism

The temperature dependent molar magnetic susceptibility (χ_m) and inverse susceptibility ($1/\chi_m$) of $EuAg_4In_8$ at an applied field of 1000 Oe are shown in Figure 3.6.6.

The inverse susceptibility curve obeys Curie-Weiss law, $\chi = C/(T-\theta)$, above 50 K with an effective magnetic moment of 8.26 μ_B/Eu atom, which suggests the existence of divalent nature of Eu atoms. The estimated experimental μ_{eff} value is slightly larger than the expected for a free Eu^{2+} ion moment (7.96 μ_B/Eu), which can be attributed due to the conduction electron polarization.[98] However, it is not uncommon as the slight higher values are reported in many *RE* based intermetallic compounds, for example in $EuIrIn_4$,[99] the magnetic moment of Eu ions shows 8.45 μ_B/Eu and Tb_2CuGe_3 the magnetic moment of Tb ions shows 9.72 μ_B/Tb.[98]

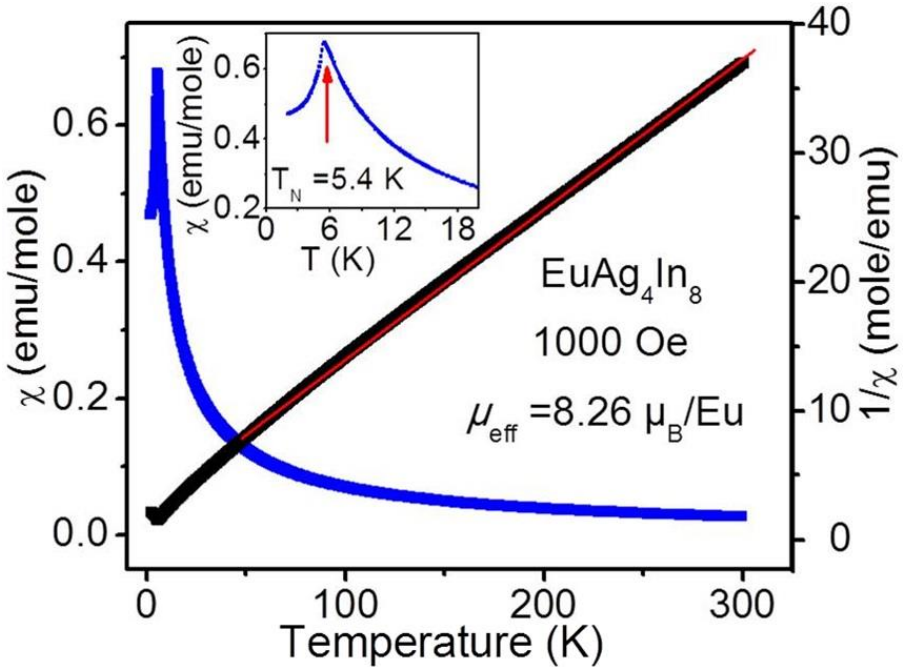

Figure 3.6.6. Temperature dependence of magnetic susceptibility (χ_m) and inverse magnetic susceptibility ($1/\chi_m$) of $EuAg_4In_8$ measured at 1000 Oe.

The divalent nature of Eu was further confirmed by XANES at Eu L_{III}-edge (Figure 3.6.7), which is again in corroboration with the hexagonal phase.[86] Magnetic susceptibility curve of $EuAg_4In_8$ shows an antiferromagnetic ordering around 5.4 K (T_N) (showed in inset figure 3.6.6). The field dependence of the magnetization $M(H)$ for ground sample of $EuAg_4In_8$ measured at 2 K and 300 K have been shown in Figure 3.6.8. The data measured at 300 K exhibits linear behaviour up to higher magnetic moment obtained at 0.02 emu/mole. The magnetization curve taken at 2 K shows a slight field dependent response up to ~ 10 kOe and continues to rise slowly up to the highest obtainable field (60 kOe) without any further saturation.

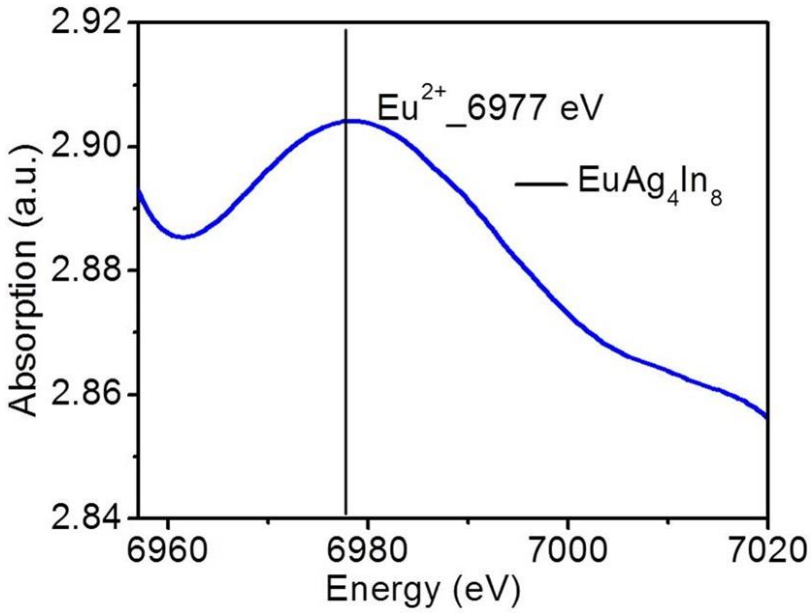

Figure 3.6.7. Eu L_{III} absorption edge spectra of $EuAg_4In_8$ measured at 300 K.

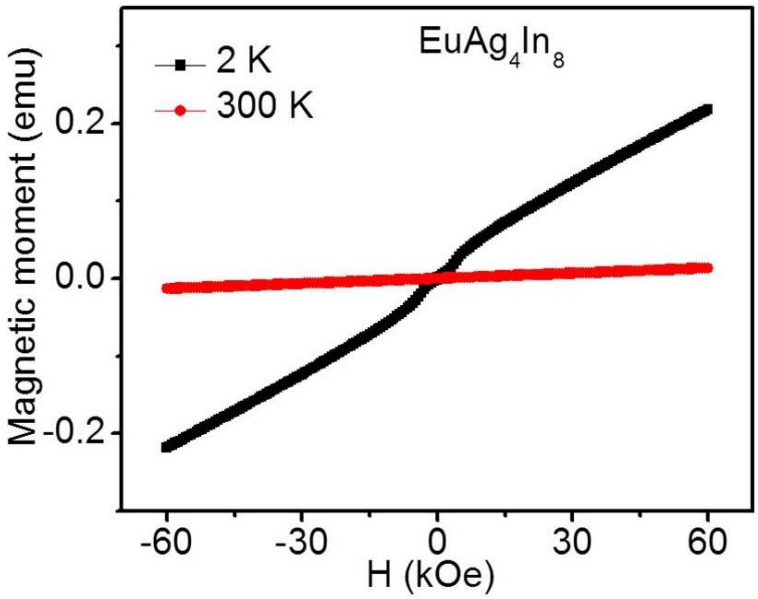

Figure 3.6.8. Magnetization as a function of applied magnetic field at 2 K and 300 K for a single crystal of $EuAg_4In_8$.

3.6.2.3.2. Electrical resistivity

The normal state temperature dependent resistivity (ρ) of $EuAg_4In_8$ decreases linearly with temperature (shown in Figure 3.6.9), which is typical for metallic systems.[31, 100] A weak dip at 4.5 K in the resistivity data shown in inset is in corroboration with the magnetic susceptibility data. The low temperature data (5-10 K) was fitted with power law equation, $\rho = \rho_0 + AT^n$ (ρ_0 is the residual resistivity and A and n are the fitting parameters),[101] which

yielded a residual resistivity of 1.0 $\mu\Omega$cm and n value of 2.11. Thus for this compound at very low temperature ρ varies with T^2 which establishes the fact that this compound shows Fermi-liquid behaviour at low temperature.[102, 103]

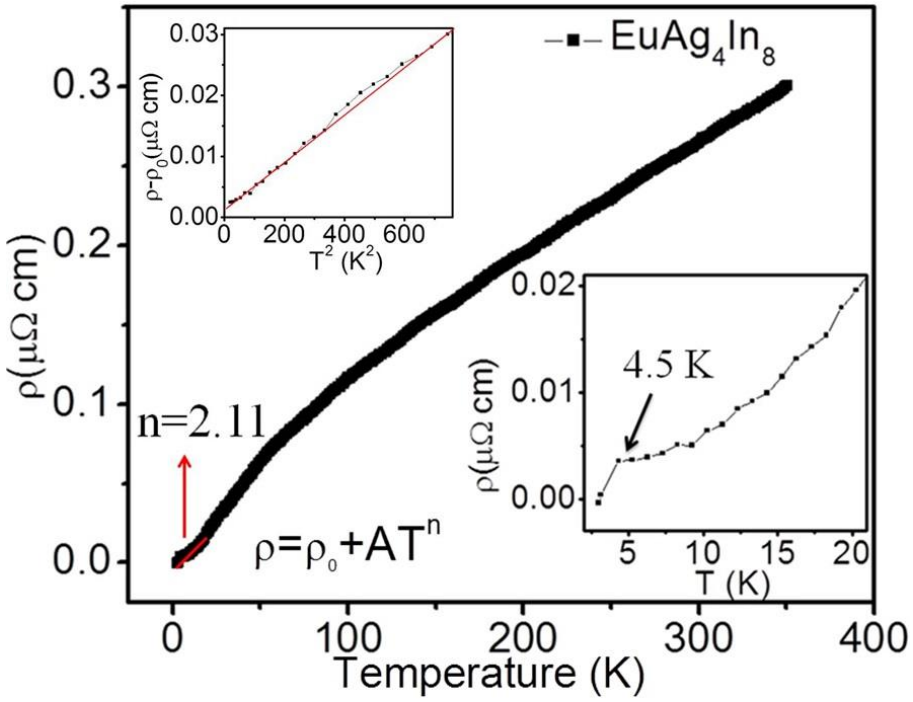

Figure 3.6.9. Temperature dependence of the electrical resistivity (ρ) of $EuAg_4In_8$ with zero applied magnetic field. Inset shows low temperature resistivity data on an expanded scale showing the peaks at close to 4.5 K which corresponds to antiferromagnetic ordering.

3.7. Conclusion

High quality single crystals of $YbCu_6In_6$, $SmCu_6In_6$, $YbCu_4Ga_8$ and $EuAg_4In_8$ were obtained from the metal flux technique and the crystal structure of $YbCu_6In_6$, $SmCu_6In_6$, $YbCu_4Ga_8$ and $EuAg_4In_8$ were studied using single crystal XRD. The solid solution, $YbCu_{6-x}In_{6+x}$ (x = 0, 1 and 2) and $SmCu_{6-x}In_{6+x}$ (x = 0, 1 and 2) obtained from the HFIH treatment were studied by powder XRD. $YbCu_4Ga_8$ crystallizes in a new structure type, a superstructure of $CeMn_4Al_8$. At room temperature $EuAg_4In_8$ structure was refined from single crystal diffractometer data revealing tetragonal structure type, which is in contrast to the hexagonal system previously reported. The argument on the existence of the hexagonal phase might have been due to the metastable or superstructure of the well-known tetragonal *I*4/*mmm* space group, which in fact may be associated with the different synthesis method. The metal flux technique has been proved as a vital synthesis method to obtain novel compounds within new structure types. The magnetic susceptibility of $YbCu_6In_6$ following

modified Curie-Weiss law in the temperature range of 155 to 300 K, with an effective magnetic moment of 4.024 μ_B/Yb atom. The estimated experimental μ_{eff} value is 88 % of Yb^{3+} compared to the theoretical value of 4.56. A significant difference in the magnetic moment of $YbCu_4In_8$ and $YbCu_5In_7$ could be associated with strong structural disorder in these systems and a change in the linearity in modified inverse magnetic susceptibility curves suggest a valance transition from the diamagnetic Yb^{2+} state to Yb^{3+}. The physical properties of $YbCu_{6-x}In_{6+x}$ (x = 0, 1, and 2) exhibit that there exists a Fermi-liquid regime at low temperature as $\rho\alpha T^2$, $SmCu_{6-x}In_{6+x}$ (x = 0, 1 and 2) obeys modified Curie-Weiss law above 50 K and a substantial difference in the magnetic behaviour of each compounds, $YbCu_4Ga_8$ also following modified Curie-Weiss law in the temperature range of 100-300 K and the estimated experimental μ_{eff} value is 60 % of Yb^{3+} compared to the theoretical value of 4.56 μ_B/Yb. The detailed bond analysis confirmed that Yb atoms of $YbCu_4Ga_8$ are in the intermediate valent state. The electrical resistivity physical measurements of $YbCu_4Ga_8$ suggest a possible Fermi-liquid ground state at low temperature as $\rho\alpha T^2$. The compound $EuAg_4In_8$ features divalent Eu confirmed by magnetic and XANES measurements. Since Eu is expected to show the valence fluctuation, attempt was to see any phase transitions within the probable window of temperature range 100-400 K, but it resulted in stable phase. A systematic temperature and magnetic field dependent structural and physical property measurements on these compounds will bring out the interesting physical phenomena.

3.8. References

1. Florio, J. V.; Rundle, R. E.; Snow, A. I., *Acta Crystallogr.* **1952,** *5*, 449−457.
2. Felner, I.; She, M.; Rakavy, M.; Nowik, I., *J. Phys. Chem. Solids* **1981,** *42*, 369−377.
3. Felner, I.; Nowik, I., *J. Phys. Chem. Solids* **1979,** *40*, 1035−1044.
4. Zaremba, R.; Muts, I.; Hoffmann, R. D.; Kalychak, Y. M.; Zaremba, V. I.; Pöttgen, R., *J. Solid State Chem.* **2007,** *180*, 2534-2540.
5. SAINT 6.02; Bruker AXS Inc.: Madison, Wisconsin, USA, 2000.
6. Sheldrick, G. M. SADABS: Göttingen, Germany, 1997.
7. WinGX. A Windows Program for Crystal Structure Analysis: Farrugia, L. J., *J. Appl. Cryst.* **1999,** *32*, 837-838.
8. Sheldrick, G. M., *Acta Crystallogr. A* **2008,** *64*, 112-122.
9. Diamond 3.0g; Crystal Impact: Rathausgasse, Bonn, Germany, 2011.
10. Keen, D. A.; Gutmann, M. J.; Wilson, C. C., *J. Appl. Crystallogr.* **2006,** *39*, 714-722.
11. Gutmann, M. J. *SXD2001; ISIS Facility, Rutherford Appleton Laboratory: Oxfordshire, England*, 2005.
12. Sheldrick, G. M., *Acta Crystallogr. A* **2008,** *64*, 112-122.
13. Sheldrick, G. M. *Bruker Analytical X-ray Systems Inc.*, Madison, WI, 1997.
14. Kalychak, Y. M., *Russ. Metall.* **1998,** *4*, 138-148.
15. Kalychak, Y. M.; Zaremba, V. I.; Pöttgen, R.; Lukachuk, M.; Hoffmann, R., *Crys. Structure Phys. Prop., Phase Relations, Phase Diagram, Review, 402* **2005,** *34*, 1-133.
16. Kojima, K.; Nakai, Y.; Suzuki, T.; Asano, H.; Izumi, F.; Fujita, T.; Hihara, T., *J. Phys. Soc. Jpn.* **1990,** *59*, 792-795.
17. Kojima, K.; Hayashi, H.; Minami, A.; Kasamatsu, Y.; Hihara, T., *J. Magn. Magn. Mater.* **1989,** *81*, 267−272.
18. Severing, A.; Gratz, E.; Rainford, B. D.; Yoshimura, K., *Physica B* **1990,** *163*, 409-411.
19. Felner, I.; Nowik, I.; Vaknin, D.; Potzel, U.; Moser, J.; Kalvius, G., M.; Wortmann, G.; Schmiester, G.; Hilscher, G.; Gratz, E.; Schmitzer, C.; Pillmayr, N.; Prasad, K. G.; De Waard, H.; Pinto, H., *Phys. Rev. B* **1987,** *35*, 6956−6963.
20. Felner, I.; Nowik, I., *J. Magn. Magn. Mater.* **1987,** *63*, 615−617.

21. Suski, W.; Wochowski, K.; Bodak, O. I.; Kalychak, Y. M.; Zaremba, V. I.; Mydlarz, T., *J. Alloy Compd.* **1997,** *250*, 642-645.

22. Zaved, I. V. U., *Tsvetn. Metall.* **1990,** *1*, 1-99.

23. Buschow, K. H. J.; Van Vucht, J. H. H.; Van Den Haagenhof, W., *J. Less-Common Met.* **1976,** *50*, 145−150.

24. Zarechnyuk, O. S.; Krypyakevych, P. I., *Sov. Phys. Crystallogr.* **1962,** *7*, 436−446.

25. Donohue, J., *The Structures of the Elements*. Wiley: New York, 1974.

26. Adroja, D. T.; Malik, S. K.; Padalia, B. D.; Vijayaraghavan, P. R., *J. Phys. C: Solid State Phys.* **1987,** *20*, L307−L310.

27. Peter, S. C.; Rayaprol, S.; Francisco, M. C.; Kanatzidis, M. G., *Eur. J. Inorg. Chem.* **2011**, 3963-3968.

28. Yamasaki, T.; Matsui, K.; Nakamura, H.; Shiga, M., *Solid State Commun.* **2001,** *119*, 415-418.

29. Bauer, E.; Hauser, R.; Gratz, E.; Gignoux, D.; Schmitt, D.; Sereni, J., *J. Phys-Condens Mat.* **1992,** *4*, 7829-7838.

30. Dremov, R. V.; Koblyuk, N.; Mudryk, Y.; Romaka, L.; Sechovsky, V., *J. Alloy Compd.* **2001,** *317*, 293-296.

31. He, J.; Ling, G.; Jiao, Z., *Physica B* **2001,** *301*, 196-202.

32. Peter, S. C.; Malliakas, C. D.; Nakotte, H.; Kothapilli, K.; Rayaprol, S.; Schultz, A. J.; Kanatzidis, M. G., *J. Solid State Chem.* **2012,** *187*, 200-207.

33. Varma, C. M., *Rev. Mod. Phys.* **1976,** *48*, 219-238.

34. Maple, M. B.; Seaman, C. L.; Gajewski, D. A.; Dalichaouch, Y.; Barbetta, V. B.; Deandrade, M. C.; Mook, H. A.; Lukefahr, H. G.; Bernal, O. O.; Maclaughlin, D. E., *J. Low Temp. Phys.* **1994,** *95*, 225-243.

35. Kalychak, Y. M.; Zaremba, V.; Pöttgen, R.; Lukachuk, M.; Hoffmann, R. D.; Gschneidner, J. K. A.; Pecharsky, V. K.; Bünzli, J. C., *Handbook on the Physics and Chemistry of Rare Earths*. Elsevier: Amsterdam, 2005; Vol. 34.

36. Sato, K.; Isikawa, Y.; Mori, K., *J. Magn. Magn. Mater.* **1992,** *104*, 1435-1436.

37. Baranyak, V. M.; Dmytrakh, O. V.; Kalychak, Y. M.; Zavalii, P. Y., *Inorg. Mater.* **1988,** *24*, 739-741.

38. Kalychak, Y. M.; Zaremba, V. I.; Baranyak, V. M.; Zavalii, P. Y.; Bruskov, V. A.; Sysa, L. V.; Dmytrakh, O. V., *Inorg. Mater.* **1990,** *26*, 74-76.

39. Sysa, L. V.; Kalichak, Y. M.; Akhmad, B.; Baranyak, V. M., *Sov. Phys. Crystallogr.* **1989,** *34*, 443-444.

40. Buschow, K. H. J.; Van Vucht, J. H. N.; Van Den Hoogenhof, W. W., *J. Less-Common Met.* **1976,** *50*, 145-150.

41. Galadzhun, Y. V.; Hoffmann, R. D.; Pöttgen, R.; Adam, M., *J. Solid State Chem.* **1999,** *148*, 425-432.

42. Iandelli, A., *J. Less-Common Met.* **1983** *90*, 121-126.

43. McCarthy, J. E.; Duffy, J. A.; Detlefs, C.; Cooper, M. J.; Canfield, P. C., *Phys. Rev. B* **2000,** *62*, R6073-R6076.

44. Varma, C. M., *Rev. Mod. Phys.* **1976,** *48*, 219-223.

45. Angst, M.; Kreyssig, A.; Janssen, Y.; Kim, J. W.; Tan, L.; Wermeille, D.; Mozharivskyij, Y.; Kracher, A.; Goldman, A. I.; Canfield, P. C., *Phys. Rev. B* **2005,** *72*, 174407−174420.

46. Godinho, M.; Bonfait, G.; Goncalves, A. P.; Almeida, M.; Spirlet, J. C., *J. Magn. Magn. Mater.* **1995,** *140*, 1417-1418.

47. Klesnar, H.; Rogl, P., *J. Mater. Res.* **1991,** *6*, 53-56.

48. Verbovytsky, Y.; Latka, K.; Pacyna, A. W.; Tomala, K., *J. Alloy Compd.* **2007,** *438*, L12-L15.

49. Yanson, T. I.; Manyako, M. B.; Bodak, O. I.; Cerny, R.; Pacheco, J. V.; Yvon, K., *Z. Krist-New Cryst. St.* **1997,** *212*, 505-507.

50. Buschow, K. H. J.; Van der Kraan, A. M., *J. Phys. (Paris)* **1978,** *F8*, 921-924.

51. Felner, I., *J. Less-Common Met.* **1980,** *72*, 241−249.

52. Bergerhoff, G.; Brown, I. D. *Inorganic Crystal Structure Database*, International Union of Crystallography: Chester, 1987.

53. Villars, P.; Cenzual, K. *Pearson's Crystal Data-Crystal Structure Database for Inorganic Compounds*, ASM International: Materials Park: Ohio, USA, 2010.

54. Drulis, H.; Gaczynski, P.; Iwasieczko, W.; Suski, W.; Kotur, B. Y., *Solid State Commun.* **2002,** *123*, 391-394.

55. Buschow, K. H. J.; Van Vucht, J. H. N.; Van Den Hoogenhof, W. W., *J. Less-Common Met.* **1976,** *50*, 145−150.

56. Chernyak, B. I.; Gladyshevskii, R. E., *Tezizy Dokl. Vses. Konf. Kristallokhim. Intermet. Soeden. 4th (Lvov)* **1983,** *47*, 48-50.

57. Markiv, V. Y.; Belyavina, N. N.; Karpenko, V. A.; Karpenko, A., *Dopov. Akad. Nauk Ukr. RSR (Ser. A)* **1985,** *7*, 76-81.

58. Adroja, D. T.; Malik, S. K.; Padalia, B. D.; Bhatia, S. N.; Walia, R., *Phys. Rev. B* **1990,** *42*, 2700-2703.

59. Adroja, D. T.; Malik, S. K.; Padalia, B. D.; Vijayaraghavan, R., *J. Phys. C: Solid State Phys.* **1987,** *20*, L307−L310.

60. Grin, Y. N.; Ellner, M.; Hiebl, K.; Rogl, P., *J. Alloy Compd.* **1993,** *196*, 207-212.

61. Markiv, V. Y.; Belyavina, N. N.; Zhunkovskaya, T. I., *Dopov. Akad. Nauk Ukr. RSR (Ser. A)* **1982,** *2*, 80-82.

62. Subbarao, U.; Peter, S. C., *Cryst. Growth Des.* **2013,** *13*, 953-959.

63. Drake, B. L.; Capan, C.; Cho, J. Y.; Nambu, Y.; Kuga, K.; Xiong, Y. M.; Karki, A. B.; Nakatsuji, S.; Adams, P. W.; Young, D. P.; Chan, J. Y., *J. Phys-Condens Mat.* **2010,** *22*, 066001−066014.

64. Kanatzidis, M. G.; Pöttgen, R.; Jeitschko, W., *Angew. Chem. Int. Edit.* **2005,** *44*, 6996-7023.

65. Tobash, P. H.; Bobev, S.; Thompson, J. D.; Sarrao, J. L., *J. Alloy Compd.* **2009,** *488*, 533-537.

66. Bobev, S.; Hullmann, J.; Harmening, T.; Pöttgen, R., *Dalton T.* **2010,** *39*, 6049-6055.

67. Chen, X. Z.; Small, P.; Sportouch, S.; Zhuravleva, M.; Brazis, P.; Kannewurf, C. R.; Kanatzidis, M. G., *Chem. Mater.* **2000,** *12*, 2520-2522.

68. Zhuravleva, M. A.; Bilc, D.; Pcionek, R. J.; Mahanti, S. D.; Kanatzidis, M. G., *Inorg. Chem.* **2005,** *44*, 2177-2188.

69. Schluter, M.; Jeitschko, W., *Inorg. Chem.* **2001,** *40*, 6362-6368.

70. Zhuravleva, M. A.; Kanatzidis, M. G., *Inorg. Chem.* **2008,** *47*, 9471-9477.

71. Menard, M. C.; Drake, B. L.; McCandless, G. T.; Thomas, K. R.; Hembree, R. D.; Haldolaarachchige, N.; DiTusa, J. F.; Young, D. P.; Chan, J. Y., *Eur. J. Inorg. Chem.* **2011**, 3909-3919.

72. Gray, D. L.; Francisco, M. C.; Kanatzidis, M. G., *Inorg. Chem.* **2008,** *47*, 7243-7248.

73. Bärnighausen, H., *Commun. Math. Chem.* **1980,** *9*, 139−175.

74. Bärnighausen, H.; Müller, U., Symmetriebeziehungen zwischen den Raumgruppen als Hilfsmittel zur straffen Darstellung Von Strukturzusammenha ñgen in der Kristallchemie. In University of Karlsruhe and University/GH Kassel: Karlsruhe, Germany, 1996.

75. Muller, U., *Z. Anorg. Allg. Chem.* **2004,** *630*, 1519-1537.

76. Vanýsek, P. In *Electrochemical Science and Technology of Copper*, Proceedings of the International Symposium; The Electrochemical Society, 2002.

77. Sanderson, R. T., *J. Am. Chem. Soc.* **1983,** *105*, 2259−2261.

78. Allen, F. H.; Kennard, O.; Watson, D. G.; Brammer, L.; Orpen, A. G.; Taylor, R. J., *Chem. Soc., Perkin Trans.* **1987,** *2*, S1−S19.

79. Rieger, W.; Parthé, E., *Monatsh. Chem.* **1969,** *100*, 444−454.

80. Chondroudi, M.; Peter, S. C.; Malliakas, C. D.; Balasubramanian, M.; Li, Q. A.; Kanatzidis, M. G., *Inorg. Chem.* **2011,** *50*, 1184-1193.

81. Iyer, A. K.; Peter, S. C., *Eur. J. Inorg. Chem.* **2012**, 1790-1794.

82. Ahn, K.; Tsokol, A. O.; Mozharivskyj, Y.; Gschneidner, K. A.; Pecharsky, V. K., *Phys. Rev. B* **2005,** *72*, 054404−054415.

83. Lawrence, J. M.; Riseborough, P. S.; Park, R. D., *Rep. Prog. Phys.* **1981,** *44*, 1−84.

84. Katoh, K.; Tsutsumi, T.; Yamada, K.; Terui, G.; Niide, Y.; Ochiai, A., *Physica B-Condensed Matter* **2006,** *373*, 111-119.

85. Varma, C. M., *Rev. Mod. Phys.* **1976,** *48*, 219−238.

86. Sysa, L. V.; Kalychak, Y. M.; Ctets, I. N.; Galadzhun, Y. V., *Kristallografiya.* **1994,** *39*, 821-824.

87. Subbarao, U.; Gutmann, M. J.; Peter, S. C., *Inorg. Chem.* **2013,** *52*, 2219-2227.

88. Subbarao, U.; Peter, S. C., *Inorg. Chem.* **2012,** *51*, 6326-6332.

89. Subbarao, U.; Peter, S. C., *J. Chem. Sci.* **2013,** *125*, 1315-1323.

90. Bergerhoff, G.; Brown, I. D. *International Union of Crystallography*, In Crystallographic Databases: Chester, 1987.

91. Villars, P.; Cenzual, K. ASM International, Materials Park: Ohio, USA, 2011.

92. Yamson, T. I.; Manyako, M. B.; Zarechnyuk, O. S., *Russ. Metall.* **1992,** *6*, 161-165.

93. Felner, I.; Nowik, I., *J. Phys. Chem. Solids* **1979,** *40*, 1035-1044.

94. Felner, I.; Nowik, I., *J. Phys. Chem. Solids* **1978,** *39*, 951-956.

95. Felner, I.; Seh, M.; Rakavy, M.; Nowik, I., *J. Phys. Chem. Solids* **1981,** *42*, 369-377.

96. Felner, I., *J. Less-Common Met.* **1980,** *72*, 241-249.

97. Sampathkumaran, E. V.; Gupta, L. C.; Vijayaraghavan, P. R.; Hatwar, T. K.; Ghatikar, M. N.; Padalia, B. D., *Mater. Res. Bull.* **1980,** *15*, 939-943.

98. Majumdar, S.; Sampathkumaran, E. V., *Solid State Commun.* **2001,** *117*, 645-648.

99. Sarkar, S.; Gutmann, M. J.; Peter, S. C., *Dalton T.* **2014,** *43*, 15879-15886.

100. Dremov, R. V.; Koblyuk, N.; Mudryk, Y.; Romaka, L.; Sechovsky, V., *J. Alloy Compd.* **2001,** *317*, 293-296.

101. Kambe, S.; Suderow, H.; Fukuhara, T.; Flouquet, J.; Takimoto, T., *J. Low. Temp. Phys.* **1999,** *117*, 101-112.

102. Li, S. Y.; Taillefer, L.; Hawthorn, D. G.; Tanatar, M. A.; Paglione, J.; Sutherland, M.; Hill, R. W.; Wang, C. H.; Chen, X. H., *Phys. Rev. Lett.* **2004,** *93*.

103. Peter, S. C.; Malliakas, C. D.; Nakotte, H.; Kothapilli, K.; Rayaprol, S.; Schultz, A. J.; Kanatzidis, M. G., *J. Solid State Chem.* **2012,** *187*, 200-207.

Chapter 4

Mixed Valent and Narrow-Band Gap Zintl Phase Materials in the $RE_5M_2X_6$ (*RE* = Eu and Yb; *M* = Al, Ga and In; *X* = As, Sb and Bi) Family

---

Papers published on this work have appeared in

[1] *Inorg. Chem.,* **2013,** *52,* 13631−13638.

[2] *J. Alloy Compd.,* **2016**, *658,* 395-401.

4.1. Introduction

Zintl phases are special class of intermetallic compounds comprised of a highly electropositive metal ion and a polyanionic network.[1] These compounds have drawn much attention because of their applications in the field of thermoelectrics. The reason behind this fascinating behaviour stems from their "dual nature", i.e. they can act as both crystal and glass. Because of this ability, Zintl phases generally show high electrical conductivity (like crystal) and low thermal conductivity (like glass).[2] Zintl phases containing heavier *p*-block elements usually exhibit a narrow band gap; *e.g.*, $Ba_8In_4Sb_{16}$[3] and $BaGa_2Sb_2$[4] are found to be narrow band gap *p*-type semiconductors. This in turn facilitates the transfer of electrons from the valence band to the conduction band. The presence of heavier elements (e.g., Sb, Bi, and *AE*/*RE* elements) also enhances the phonon scattering due to soft binding[5] and hence the lattice contribution (k_{Lattice}) toward overall thermal conductivity decreases which effectively results in a higher *ZT* value.

Compounds with general formula $AE_5M_2X_6$ (*AE* = Ca, Sr, Ba; *M* = Al, Ga, In; *X* = As, Sb, Bi) are classified as the Zintl phase. Though these compounds were studied for their structural and basic physical properties for decades,[6] their potential ability as thermoelectric materials was understood very recently.[6, 7] These compounds crystallize in two different types of structures, *viz.* $Ca_5Ga_2As_6$[8] and $Ba_5Al_2Bi_6$.[9] Both structures contain basic MX_4 tetrahedra sharing their corners and are bridged by X_2 dumbbells forming infinite parallel ladders, however, the orientation of these ladders like geometries differ in these two structures. $Ca_5Al_2Sb_6$ was the first member to be investigated as thermoelectric material by Toberer et al.[10] Their report spurred a series of studies in the succeeding years dealing with the thermoelectric properties and other related studies like transport, optical properties, and band structure calculations on the analogous compounds.[11-13] Yan et al. reported the first-principle calculations of the electronic structure and the transport coefficient of $Ca_5Al_2Sb_6$ at different temperatures. The carrier concentrations[14] and the anisotropic one-dimensional structure of $Ca_5Ga_2As_6$ are favourable for a good thermoelectric material with thermoelectric figure of merit *ZT* of 0.7 at 930 K.[11] Later, the compounds Zn-doped $Ca_5Al_2Sb_6$,[15] Mn doped $Ca_5Al_2Sb_6$ and $Ca_5M_2Sb_6$ (*M* = Al, Ga, and In),[12] and $Ca_5M_2Sb_6$ (*M* = Al, Ga, and In)[13, 16] were also studied for the thermoelectric properties.

Interestingly, only three *RE* based compounds in the $RE_5M_2X_6$ family were reported: one Eu based compound, $Eu_5In_2Sb_6$ and two Yb based compounds, $Yb_5Al_2Sb_6$[17, 18] and $Yb_5In_2Sb_6$.[6] The compound $Eu_5In_2Sb_6$[7] crystallizes in the $Ca_5Ga_2As_6$ type structure, while the two Yb compounds crystallize in the $Ba_5Al_2Bi_6$ type structure. The three compounds were studied for detailed crystallography, electrical conductivity, thermo power, and thermal conductivity. Band structure calculations performed on these three compounds confirmed the presence of the narrow/zero band gap. However, in all three compounds the *RE*s were assigned as divalent according to the Zintl-Klemm concept.

This chapter discusses about a new compound $Yb_5Ga_2Sb_6$, obtained from the metal flux method. This compound is the first Ga containing member in the $RE_5M_2X_6$ family. $Yb_5Ga_2Sb_6$ crystallizes in the orthorhombic $Ba_5Al_2Bi_6$ structure type with the space group of *Pbam*. This chapter also discusses about the valency of *RE* atoms in $Eu_5In_2Sb_6$ and $Yb_5M_2Sb_6$ using magnetic and XANES measurements along with valency bond sum calculations.

4.2. Experimental Section

4.2.1. Synthesis

The following reagents were used as purchased without further purification: Yb and Eu (in the form of metal pieces cut from metal chunk, 99.99%, Alfa Aesar), Al, Ga and In (pieces, 99.999%, Alfa Aesar) and Sb (shots, 99.99%, Alfa-Aesar).

4.2.1.1. Metal Flux Method

Well shaped single crystals of $Yb_5Ga_2Sb_6$ were obtained by combining ytterbium metal (0.3 g), gallium pieces (2 g) and antimony shots (0.4 g) in an alumina crucible. The crucible was placed in a 13 mm fused silica tube which was flame-sealed under a vacuum of 10^{-5} Torr, to prevent oxidation during heating. The reactants were then heated to 1273 K over 10 h, maintained at that temperature for 5 h to allow proper homogenization, then cooled down to 1123 K in 2 h, and kept at this temperature for 72 h. Finally, the sample was allowed to cool slowly to 303 K over 48 h. No side-reaction with the alumina crucible material was detected. The reaction product was isolated from the excess gallium flux by heating at 673 K and subsequently centrifuging through a coarse frit. Extra gallium was removed by immersion and sonication in 2-4 M solution of iodine in dimethylformamide (DMF) over 12-24 h at room temperature. The product was rinsed with hot water and DMF and dried with

acetone and ether. The large (1mm) and rod-like grey crystals of $Yb_5Ga_2Sb_6$ are obtained in high yield (>90%). A very small amount of Ga metal present in the product was quite unavoidable (detected in powder XRD). $Yb_5Ga_2Sb_6$ is stable in air and no decomposition was observed even after several months. Several crystals, which grow as metallic silver rods, were carefully selected for the elemental analysis.

4.2.1.2. High Frequency Induction Heating Method

Rare earth (Yb and Eu), trielide (Al, Ga, In) and antimony were mixed in the ideal 5:2:6 atomic ratio and sealed in a tantalum crucible under argon atmosphere in an arc-melting apparatus. The tantalum crucible was subsequently placed in a water-cooled sample chamber of an induction furnace (Easy Heat induction heating system, Model 7590), rapidly heated to approximately 1200-1350 K and kept at that temperature for 30 min. Finally the reaction was rapidly cooled to room temperature by switching off the power supply. All the compounds could easily be removed from the tantalum crucible. No side-reactions with the crucible could be detected. The samples were in polycrystalline form and light grey in colour. The weight loss of the final material was found to be less than 1%. The samples obtained from the high frequency induction heating method were used for the magnetic and XANES studies.

4.2.2. Elemental Analysis

Semiquantitative microanalyses were performed on the single crystals obtained from the flux techniques using a Leica 220i SEM equipped with a Bruker 129 eV EDAX. Data were acquired with an accelerating voltage of 20 kV and 90 s accumulation time. The EDAX analyses were performed on visibly clean surfaces of the single crystals obtained from the flux method and indicated that the atomic composition was close to 5:2:6, which is in good agreement with the composition obtained from the single crystal X-ray data refinement.

4.2.3. Powder XRD

Phase identities and purities of the $Eu_5In_2Sb_6$ and $Yb_5M_2Sb_6$ (*M* = Al, Ga and In) sample were determined by powder XRD measurements that were carried out with a Bruker D8 Discover diffractometer using Cu-*K*α radiation (λ = 1.5406 Å).

4.2.4. Single Crystal XRD

XRD data was collected on a selected single crystal of $Yb_5Ga_2Sb_6$ at room temperature using a Bruker Smart Apex 2–CCD diffractometer equipped with a normal

focus, 2.4 kW sealed tube X-ray source with graphite monochromatic Mo-*K*α radiation (λ = 0.7107 Å) operating at 50 kV and 30 mA, with ω scan mode. A crystal of suitable size (0.1 x 0.05 x 0.05 mm^3) was cut from a plate shaped crystal and mounted on a thin glass (~0.1 mm) fibre with commercially available super glue. A full sphere of 60 frames was acquired up to 73.28˚ in 2θ. The individual frames were measured with steps of 0.50˚ and an exposure time of 10 s per frame. The program SAINT[19] was used for integration of diffraction profiles and absorption correction were made with SADABS program.[20] The systematic absences led to the non-centrosymmetric space group *Pbam*. However, the Platon program with WinGX system, ver. 1.80.05[21] was used to check the additional symmetry and confirms the final structure refinement. The structure was solved by SHELXS 97[22] and refined by a full matrix least-squares method using SHELXL[23] with anisotropic atomic displacement parameters for all atoms. Packing diagrams were generated with Diamond.[24] As a check for the correct composition, the occupancy parameters were refined in a separate series of least-squares cycles. All bond lengths are within the acceptable range compared to the theoretical values.

4.2.5. Magnetic Measurements

Magnetic measurements were carried out using a Quantum Design MPMS-SQUID magnetometer. Measurements were performed on polycrystalline sample, which were ground and screened by powder XRD to verify phase identity and purity. Temperature dependent data were collected in FC between 2 and 300 K in an applied field (H) of 1 tesla (T). Magnetization data were also collected for $Eu_5In_2Sb_6$ and $Yb_5M_2Sb_6$ at 2 and 300 K with field sweeping from -60000 Oe to 60000 Oe.

4.2.6. Electrical Resistivity

The resistivity measurements were performed under an applied field of 1 T, on $Yb_5Ga_2Sb_6$ with a conventional ac four probe setup. Four very thin copper wires were glued to the pellet using a strongly conducting silver epoxy paste. The data were collected in the range 3-300 K using commercial QD-PPMS.

4.2.7. Optical Measurements

Diffuse reflectance measurement on the $Yb_5Ga_2Sb_6$ compound was performed with a Bruker IFS 66v/s instrument by the KBr pellet method in the mid-IR and nearIR spectral

ranges. The polycrystalline sample obtained from the high frequency induction heating was used for the measurement.

4.2.8. Computational Details

The electronic properties of $Yb_5Ga_2Sb_6$ have been studied by using the full-potential linear augmented plane wave (FP-LAPW) method based on first-principle density functional theory calculations as implemented in the WIEN2k program which yield reliable results for the electronic and structural properties of crystalline solids.[25] The calculations were carried out by solving the Kohn-Sham equations self consistently based on the Generalized Gradient Approximation of Perdew-Burke-Ernzerhof (GGA-PBE) scheme for the exchange-correlation potential.[26] The muffin-tin radii were chosen as 2.5 *a.u.* for Yb and 2.3 *a.u.* for both Ga and Sb atoms. To achieve the convergence of energy eigenvalues, the wave functions in the interstitial region were expanded using plane waves with a cut-off of $R_{MT}K_{max} = 11$, where K_{max} is the plane wave cut-off, and R_{MT} is the smallest of all atomic sphere radii. The charge density was Fourier expanded up to $G_{max} = 12$. The maximum value for the wave function expansion inside the atomic spheres was confined to $l_{max} = 10$. Convergence tests were carried out using higher G_{max} and $R_{MT}K_{max}$ values, giving no significant changes in the calculated properties. Here, 1000 *k*-points were used for $Yb_5Ga_2Sb_6$ k-mesh in the Monkhorst-Pack scheme,[27] resulting in 154 *k*-points in the irreducible part of the Brillouin zone for the self-consistent calculation with the inclusion of spin-orbit coupling. All the calculations were performed with the experimental parameters with an energy convergence up to 10^{-6} Ry between the successive iterations per unit cell.

4.2.9. XANES

XANES experiments were performed at PETRA III, P06 beamline of DESY, Germany. Measurements at the L_{III}-edges of Eu and Yb and ambient pressure were performed in transmission mode using gas ionization chambers to monitor the incident and transmitted X-ray intensities. The beam size was 10 X 10 μm^2. Monochromatic X-rays were obtained using a Si [111] double-crystal monochromator which was calibrated by defining the inflection point (first derivative maxima) of Cu foil as 8980.5 eV. The beam was focused employing a Kirkpatrick−Baez (K−B) mirror optic. A rhodium-coated X-ray mirror was utilized to suppress higher order harmonics. Sample was prepared by mixing an appropriate

amount of finely ground powder, thoroughly mixed with cellulose and cold pressed to form a homogenous pellet of diameter 13 mm.

4.2.10. Bond Valence Sum (BVS) Calculations

Based on the Pauling's concept,[28] the BVS surrounding the europium and ytterbium atom is equal to the oxidation state Z_x (x = Eu and Yb), as shown below

$$Z_x = \sum S_{Eu5In2Sb6 \text{ and } Yb5M2Sb6 (M = Al, Ga \text{ and } In)} \qquad (4.1)$$

The valences of the individual bonds, $S_{Eu5In2Sb6 \text{ and } Yb5M2Sb6 (M = Al, Ga \text{ and } In)}$ in Eq.(4.1), can be calculated from the observed bond lengths using

$$S_{Eu5In2Sb6 \text{ and } Yb5M2Sb6} = \exp[R_0 - R_{Eu5In2Sb6 \text{ and } Yb5M2Sb6}]/b \qquad (4.2)$$

Where $R_{Eu5In2Sb6 \text{ and } Yb5M2Sb6}$ is the observed bond length in $Eu_5In_2Sb_6$ and $Yb_5M_2Sb_6$, and R_0 is the constant dependent on the nature of $Eu_5In_2Sb_6$ and $Yb_5M_2Sb_6$ pair. The constant b was determined to be 0.37,[29] which is a generally accepted value.[30] The R_0 value can be viewed as a bond length of unit valence. The usual procedure was to assume an oxidation state and to use a previously determined R_0 value appropriate to the bond being considered. The R_0 value was calculated using the software VALENCE.[31] The valences of Eu1, Eu2 and Eu3 in $Eu_5In_2Sb_6$ and Yb1, Yb2 and Yb3 in $Yb_5M_2Sb_6$ (*M* = Al, Ga and In) were calculated using the program CIFTOOL.[32]

4.3. $Yb_5Ga_2Sb_6$: A New Mixed Valent and Narrow-Band Gap Material

4.3.1. Results and Discussion

4.3.1.1. Structure Refinement

The crystal structure of $Yb_5Ga_2Sb_6$ was refined using SHELXL-97 (full-matrix least-squares on F^2) with anisotropic atomic displacement parameters for all atoms. As a check for the correct composition, the occupancy parameters were refined in a separate series of least-squares cycles. Single crystals of $Yb_5Ga_2Sb_6$ from different syntheses batches were used for the data collection. The lattice parameters of the $Ca_5Al_2Bi_6$ structure were taken at the initial step and the refinement resulted in seven crystallographic positions in the $Yb_5Ga_2Sb_6$ structure; one ytterbium atom occupies the 2*a* site, two ytterbium atoms occupy the 4*g* sites, one gallium atom occupies the 4*h* site, and three antimony atoms occupy the 4*h*, 4*h*, and 4*g* sites. Further information on the structure refinements is available from: Fachinformationszentrum Karlsruhe, D-76344 Eggenstein-Leopoldshafen (Germany), by quoting the Registry No. CSD–426568.

The data collection and structure refinement for $Yb_5Ga_2Sb_6$ are listed in Table 4.3.1. The standard atomic positions and isotropic atomic displacement parameters of this compound are collected in Table 4.3.2. The anisotropic displacement parameters and important bond lengths are listed in Tables 4.3.3 and 4.3.4, respectively.

4.3.1.2. Crystal Chemistry

The compound $Yb_5Ga_2Sb_6$ crystallizes in the orthorhombic the $Ba_5Al_2Bi_6$[9] structure type, *Pbam* space group, lattice parameters a = 7.2769 (2) Å, b = 22.9102 (5) Å and c = 4.3984 (1) Å. $Yb_5Al_2Sb_6$[17, 18] and $Yb_5In_2Sb_6$[6] are the two other Yb based compounds reported in the $Ba_5Al_2Bi_6$ type structure and a detailed crystal structure description is reported elsewhere.[6,9] SEM image of a typical single crystal of $Yb_5Ga_2Sb_6$ is shown in Figure 4.3.1. The crystal structure of $Yb_5Ga_2Sb_6$ along the [001] direction is shown in Figure 4.3.2. As reported, the crystal structure of $Yb_5Ga_2Sb_6$ can be explained as composition of infinite one dimensional $[Ga_2Sb_6]^{10-}$ double chains arranged in parallel fashion in the [110] plane resulting in the formation of a stable crystal structure. These double chains are interconnected by $GaSb_4$ tetrahedral single chains bridged by Sb_2 dumb-bell groups shown in Figures 4.3.2 and 4.3.3.

Table 4.3.1. Crystal data and structure refinement for $Yb_5Ga_2Sb_6$ at 296(2) K.

Empirical formula	$Yb_5Ga_2Sb_6$
Formula weight	1735.14
Wavelength	0.71073 Å
Crystal system	Orthorhombic
Space group, *Z*	*Pbam*, 2
Unit cell dimensions	a = 7.2769(2) Å, b = 22.9102(5) Å, c = 4.39840(10) Å
Volume	733.28(3) $Å^3$
Absorption coefficient	45.936 mm^{-1}
F(000)	1436
Crystal size	0.10 x 0.05 x 0.05 mm^3
θ range for data collection	1.78 to 48.01°
Index ranges	-15<=h<=15, -47<=k<=47, -4<=l<=9
Reflections collected	24672
Completeness to θ = 48.01°	99.9%
Refinement method	Full-matrix least-squares on F^2
Data / restraints / parameters	3799 / 0 / 42
Goodness-of-fit	1.062
Final R indices [>2σ(I)]	R_{obs} = 0.0329, wR_{obs} = 0.0796
Extinction coefficient	0.0013(1)
Largest diff. peak and hole	8.208 and -3.461 e·$Å^{-3}$

$R = \Sigma||F_o|-|F_c|| / \Sigma|F_o|$, w$R = \{\Sigma[w(|F_o|^2 - |F_c|^2)^2] / \Sigma[w(|F_o|^4)]\}^{1/2}$ and calcw=$1/[\sigma^2(Fo^2)+(0.0359P)^2+6.1794P]$ where $P = (Fo^2+2Fc^2)/3$

Table 4.3.2. Atomic coordinates ($x10^4$) and equivalent isotropic displacement parameters ($Å^2x10^3$) for $Yb_5Ga_2Sb_6$ at 296(2) K with estimated standard deviations in parentheses.

Label	Wyckoff site	x	y	z	Occupancy	U_{eq}*
Yb1	2*a*	9578(1)	884(1)	5000	1	11(1)
Yb2	4*g*	2663(1)	2465(1)	5000	1	10(1)
Yb3	4*g*	5000	0	5000	1	10(1)
Ga	4*h*	3163(1)	1218(1)	0	1	12(1)
Sb1	4*h*	5288(1)	1358(1)	5000	1	9(1)
Sb2	4*h*	90(1)	1880(1)	0	1	9(1)
Sb3	4*g*	2004(1)	10046(1)	0	1	10(1)

*U_{eq} is defined as one third of the trace of the orthogonalized U_{ij} tensor.

Table 4.3.3. Anisotropic displacement parameters ($Å^2x10^3$) for $Yb_5Ga_2Sb_6$ at 296(2) K with estimated standard deviations in parentheses.

Label	U_{11}	U_{22}	U_{33}	U_{12}	U_{13}	U_{23}
Yb1	12(1)	9(1)	12(1)	-1(1)	0	0
Yb2	5(1)	10(1)	14(1)	0(1)	0	0
Yb3	6(1)	10(1)	14(1)	-1(1)	0	0
Ga	8(1)	14(1)	13(1)	0(1)	0	0
Sb1	6(1)	7(1)	14(1)	0(1)	0	0
Sb2	8(1)	11(1)	9(1)	2(1)	0	0
Sb3	7(1)	12(1)	11(1)	-1(1)	0	0

The anisotropic displacement factor exponent takes the form: $-2\pi^2[h^2a^{*2}U_{11} + ... + 2hka^*b^*U_{12}]$.

Table 4.3.4. Selected bond lengths [Å] for $Yb_5Ga_2Sb_6$ at 296(2) K with estimated standard deviations in parentheses.

Label	Distances	Label	Distances	Label	Distances
Yb1-Yb1	4.0953(5)	Yb1-Sb3	3.2711(3)	Yb3-Sb3	3.0988(2)
Yb1-Yb2	4.0319(3)	Yb1-Sb3	3.4106(3)	Yb1-Ga	3.4968(5)
Yb1-Yb2	4.2619(3)	Yb2-Sb1	3.1751(4)	Yb2-Ga	3.6236(6)
Yb1-Yb3	3.8982(3)	Yb2-Sb1	3.2036(4)	Sb1-Ga	2.7074(4)
Yb2-Yb2	3.6420(1)	Yb2-Sb2	3.1845(4)	Sb2-Ga	2.7017(7)
Yb1-Sb1	3.3056(4)	Yb2-Sb2	3.1953(3)	Sb3-Ga	2.8136(8)
Yb1-Sb2	3.1909(3)	Yb3-Sb1	3.1178(3)	Sb3-Sb3	2.9235(7)

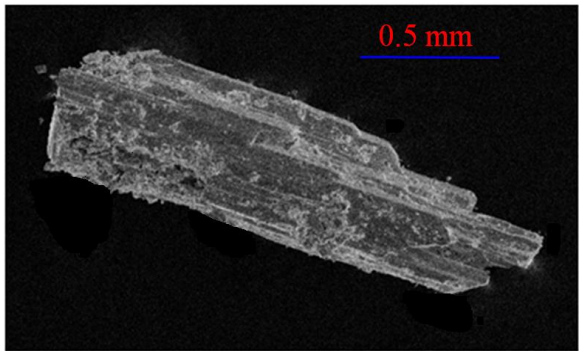

Figure 4.3.1. Typical SEM image of $Yb_5Ga_2Sb_6$ single crystal grown from the active Ga flux.

The next layer of double chains, below the *ab*-plane, is crystallographically equivalent and related by *b*-glide and *a*-glide symmetry operations perpendicular to the *a* and *b* directions and are separated by Yb cations, respectively (Figure 4.3.2). The Yb atoms

situated between the rows of infinite $[Ga_2Sb_6]^{10-}$ play crucial roles in providing charge balance and effective Coulomb screening. On the basis of the Zintl-Klemm concept, the formula for the compounds $Yb_5Al_2Sb_6$[17, 18] and $Yb_5In_2Sb_6$[6] have been proposed as $(Yb^{2+})_5[(\{Al/In^{3+}\})_2(Sb_2^{4-})(Sb^{3-})_4]$.[6, 17]

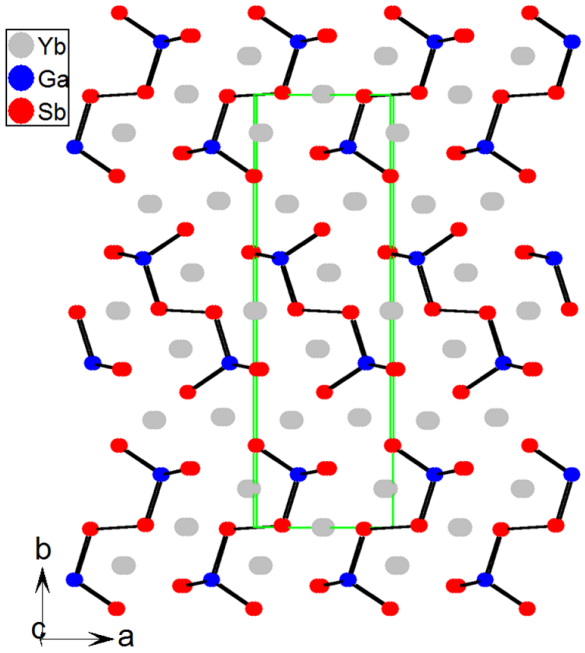

Figure 4.3.2. Crystal structure of $Yb_5Ga_2Sb_6$ as viewed along the [001] axis; the unit cell is outlined as green solid lines.

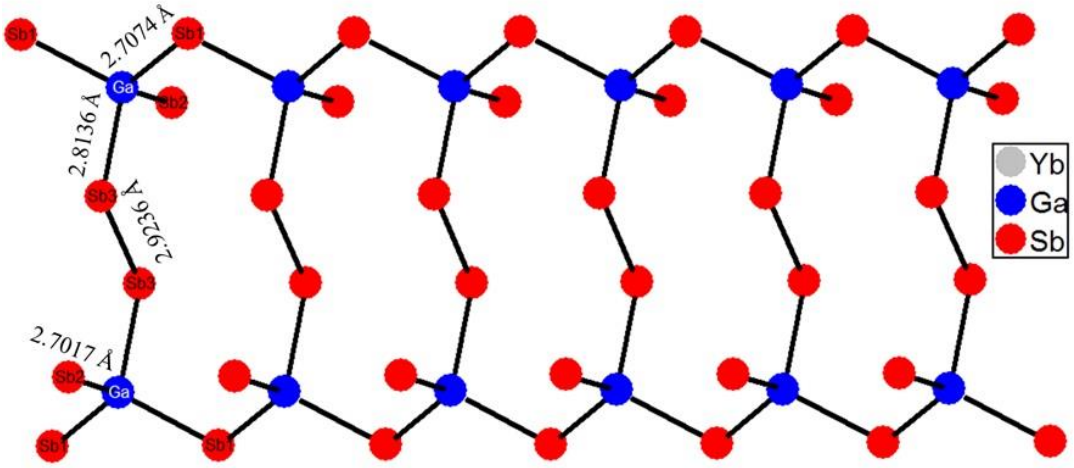

Figure 4.3.3. $1/\infty$ $[Ga_2Sb_6]^{13-}$ double chains with atomic labelling and bond lengths. The ladder type structures of double chains are tetrahedral bridged by Sb-Sb bonding.

However, the magnetic measurements on the selected single crystals of $Yb_5Ga_2Sb_6$ indicate mixed valent behaviour of Yb (discussed below). For a close investigation on the Yb

valence, the coordination environment of three Yb atoms are drawn and shown in Figure 4.3.4 as similar to the previous reports of $Yb_5Al_2Sb_6$ and $Yb_5In_2Sb_6$. The coordination environments of Yb in $Yb_5Ga_2Sb_6$ exactly matches with the compounds $Yb_5Al_2Sb_6$[17] and $Yb_5In_2Sb_6$[6] and all the bonding and structural explanations remain the same in the new compound as well.

The average bond distances between Yb and Sb atoms within the first coordination sphere for all three Yb atoms were calculated and found in the order Yb1-Sb (3.2929 Å) > Yb2-Sb (3.1897 Å) > Yb3-Sb (3.0988 Å). Considering the fact that divalent Yb is larger in size (1.86 Å)[33, 34] compared to trivalent Yb (1.66 Å),[33, 34] Yb1 can be in the divalent state (Wyckoff site 2*a*, 20%), Yb2 in the mixed valent state (Wyckoff site 4*g*, 20% divalent and 20% trivalent) and Yb3 in the trivalent state (Wyckoff site 4*g*, 40%) bearing the ratio of trivalent Yb to divalent Yb as 60:40. Finally, assuming the mixed valent state of ytterbium as per the magnetic studies and crystal structure, the formula for the compound $Yb_5Ga_2Sb_6$ can be described as $(Yb^{3+})_3(Yb^{2+})_2[(Ga^{1-})_2(Sb^{1-})_1(Sb^{2-})_5]$ or alternatively $(Yb^{3+})_3(Yb^{2+})_2[(Ga^{3+})_2(Sb^{3-})_5(Sb^{4-})_1]$. Similar differences in the Yb-Sb bond distances for all three Yb atoms in the $Yb_5Al_2Sb_6$ and $Yb_5In_2Sb_6$ structures were also found.

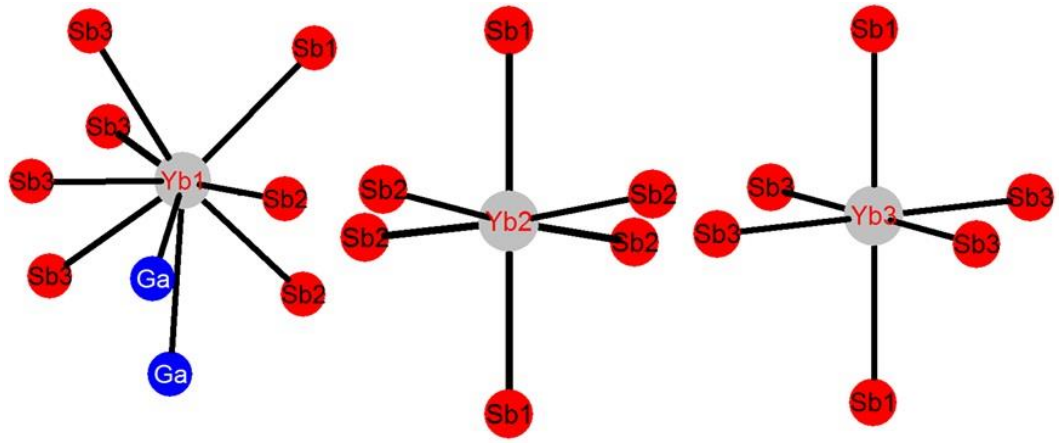

Figure 4.3.4. Coordination environment of Yb1, Yb2, and Yb3 atoms in $Yb_5Ga_2Sb_6$.

4.3.1.3. Physical Properties

4.3.1.3.1. Magnetism

Magnetic susceptibility measurements were performed on polycrystalline sample of $Yb_5Ga_2Sb_6$ obtained from the HFIH method. The temperature dependent molar magnetic susceptibility (χ_m) and inverse susceptibility ($1/\chi_m$) of $Yb_5Ga_2Sb_6$ at an applied field of 1 kOe are shown in Figure 4.3.5. The inverse susceptibility curve above 150 K for $Yb_5Ga_2Sb_6$

obeys CW law, $\chi(T) = C/(T-\theta_p)$,[35, 36] where C is the CW constant ($N_A\mu_{eff}^2/3K_bT$) and θ_p is the Weiss temperature.

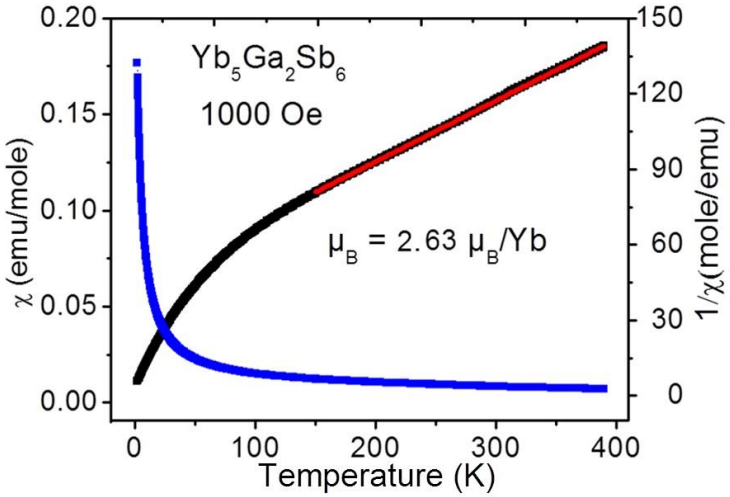

Figure 4.3.5. Temperature dependent magnetic susceptibility (χ_m) and inverse magnetic susceptibility ($1/\chi_m$) of $Yb_5Ga_2Sb_6$.

A fit to the curve above 150 K resulted in an effective magnetic moment (μ_{eff}) of 2.63 μ_B/Yb atom suggesting the existence of mixed valency in Yb atoms of $Yb_5Ga_2Sb_6$. The estimated experimental μ_{eff} value is about 58% of that expected for a free ion Yb^{3+} moment (4.56 μ_B/Yb). Temperature dependent magnetic susceptibility data of $Yb_5Ga_2Sb_6$ shows no magnetic ordering down to 2 K but the susceptibility slightly increases at lower temperature which is normal for *RE* based intermetallics.[37] This lower temperature deviation can be attributed to crystal field contributions and/or to a possible onset of valence fluctuations.

4.3.1.3.2. Electrical Resistivity

The electrical resistivity of polycrystalline $Yb_5Ga_2Sb_6$ sample obtained from the high frequency induction heating is shown in Figure 4.3.6a. Resistivity does not vary much with temperature down to 35 K. Below this temperature, resistivity increases exponentially and starts falling following a maximum at around 14 K and a broad minima at around 10 K. This kind of minima in the resistivity plot is characteristic of the compounds with either a gap/pseudo gap (for semiconductors)[38] or a Kondo lattice (in case of dilute magnetic alloys).[39] The decrease in resistivity is an indication of movement of carriers from the valence to conduction band.[10] After the dip, the resistivity increases steeply with temperature which could be attributed to a significant rise in electron-phonon scattering which lowers the carrier mobility. The exponential of the resistivity data is plotted against the inverse

temperature and the high temperature end was fitted with the Arrhenius equation $\rho = \rho_o \exp(E_g/2kT)$ (Figure 4.3.6b). The fitting gave the band gap (E_g) of 0.36 eV which is comparable with other previously reported compounds in the $RE_5M_2X_6$ family,[16] indicates that $Yb_5Ga_2Sb_6$ can also be considered as a potential candidate for the thermoelectric applications.

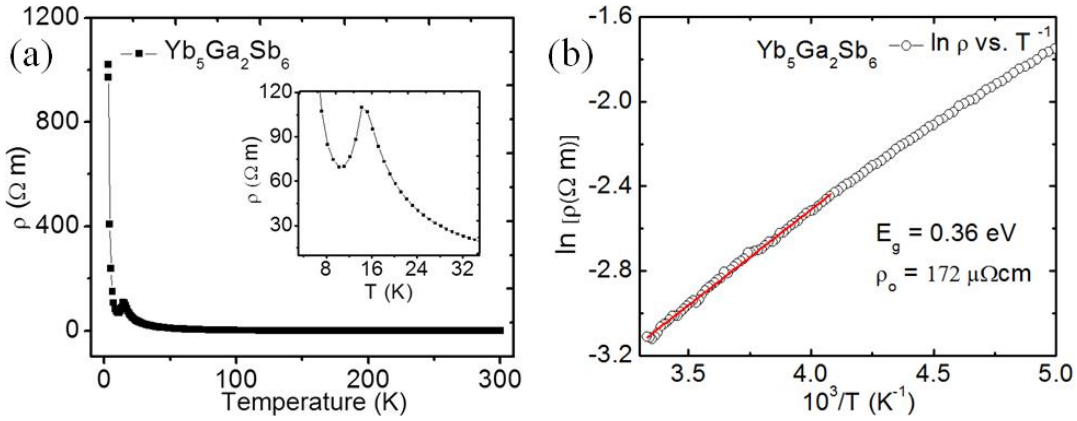

Figure 4.3.6. (a) Resistivity (ρ) measured as a function of temperature. Inset shows that there is a transition at 15 K. (b) Logarithmic resistivity (ln ρ) vs inverse temperature of $Yb_5Ga_2Sb_6$.

4.3.1.3.3. Optical Properties

Optical absorption studies were done on the sample in the IR region (Figure 4.3.7).

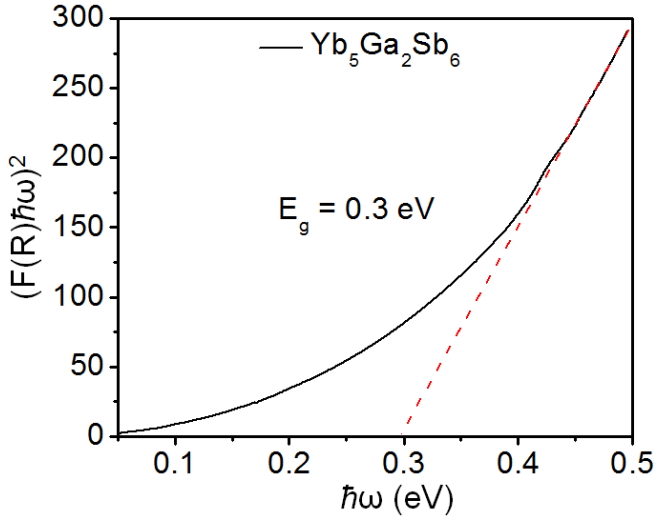

Figure 4.3.7. Optical absorption data for $Yb_5Ga_2Sb_6$ plotted in terms of the Kubelka-Munk function against energy (eV). The red dashed lines show direct band gap of 0.3 eV.

The Kubelka-Munk function $(F(R)\hbar\omega)^2$ was plotted against energy ($\hbar\omega$) and a tangent was drawn at the region near the slope change. The tangent was extrapolated up to the *x*-axis giving rise to an energy band gap of 0.3 eV. This value is very close to the band

gap calculated from the electrical resistivity data (0.36 eV). The energy gap in $Yb_5Ga_2Sb_6$ is slightly shorter than the previously reported compounds $Ca_5Al_2Sb_5$ (0.71 eV), $Ca_5Ga_2Sb_5$ (0.56 eV) and $Ca_5In_2Sb_5$ (0.68 eV).[17]

4.3.1.3.4. Band Structure and Density of States

Understanding the electronic structure of *RE* elements and compounds has been a great challenge in the field of condensed matter physics. Several methods have been developed to understand the above from the theoretical perspective. DFT is one such method which is found to be successful in explaining the crystal structure and the complex electronic structure of *RE* compounds.[40] The major challenge in DFT is the understanding of the complex nature of the *RE* ion. Standard DFT based exchange-correlations functional are not adequate enough to handle the same and one has to go beyond the standard functionals such as LSDA+U, SIC, and DMFT like approaches. In the present work LDA and LDA+U has been used to investigate the electronic structure of $Yb_5Ga_2Sb_6$ and no significant difference was found. The structural parameters of $Yb_5Ga_2Sb_6$ are taken from the experimental results as input for the band structure and density of states calculation. The calculated band structure of $Yb_5Ga_2Sb_6$ including the spin-orbit coupling along the high symmetry directions of the orthorhombic Brillouin zone of the reciprocal space is shown in Figure 4.3.8.

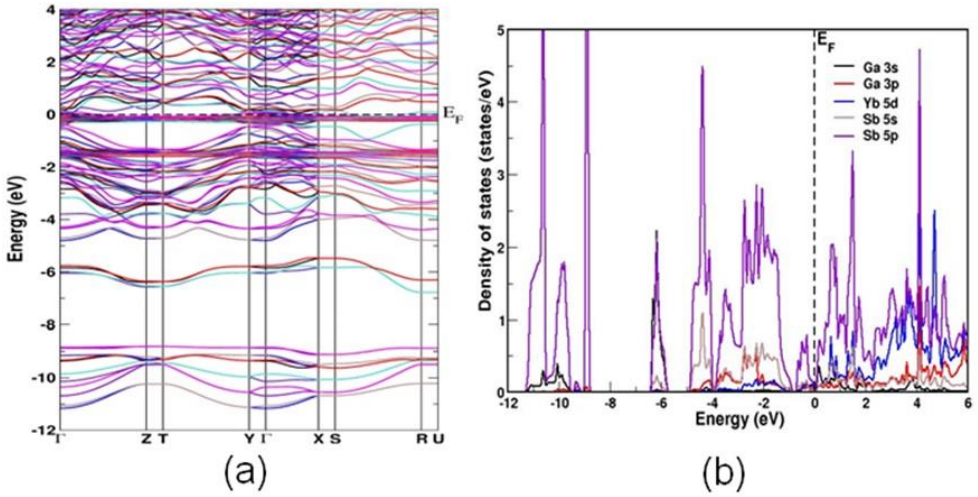

Figure 4.3.8. Calculated band structure (a) and projected density of states (b) of $Yb_5Ga_2Sb_6$ within GGA including spin-orbit coupling.

The band structure of $Yb_5Ga_2Sb_6$ is compared with the isostructural compound $Yb_5Al_2Sb_6$[17] and both looks similar to each other. The striking feature between the two compounds is in the vicinity of the Fermi level, E_F. From Figure 4.3.8, there is a weak

overlap of bands near the Fermi level resulting in a semimetallic behaviour as seen in other Zintl phase compounds. From the band structure the valence band region near -9.0 to -12.0 eV are mainly due to the Sb 5*p* states. The Ga 3*s* and Sb 5*p* states are dominated in the region of -5.5 to 7.0 eV. From 4.5 eV till the Fermi level, the bands are mostly from the Sb 5*p* states. The conduction band is mainly dominated by the Yb 5*d* states. A weak hybridization between the conduction and valence band near the Fermi level was observed, which is contributed mainly from the Sb 5*p* and Yb 5*d* states. From the density of states it can be clearly seen that the compound has a pronounced pseudogap feature at the Fermi level.

4.4. Magnetic and XANES Studies on $RE_5M_2Sb_6$

4.4.1. Results and Discussion

4.4.1.1. Crystal chemistry

As discussed in the previous section, the compounds $Yb_5Ga_2Sb_6$,[41] $Yb_5Al_2Sb_6$[17, 42] and $Yb_5In_2Sb_6$[6] crystallize in the orthorhombic $Ba_5Al_2Bi_6$ structure type having *Pbam* space group.[6] $Eu_5In_2Sb_6$ also holds similar structural motif, but crystallizes in the $Ca_5Ga_2As_6$ type structure.[7] The crystal structures of $Eu_5In_2Sb_6$ and $Yb_5M_2Sb_6$ are compared in Figure 4.4.1. The crystal structure of $Yb_5M_2Sb_6$ along the [001] direction is shown in Figure 4.4.1b, which can be explained as the composition of infinite one dimensional $[X_2Sb_6]^{10-}$ double chains arranged in parallel fashion in the [110] plane resulting in the formation of a stable crystal structure.[6, 17, 42]

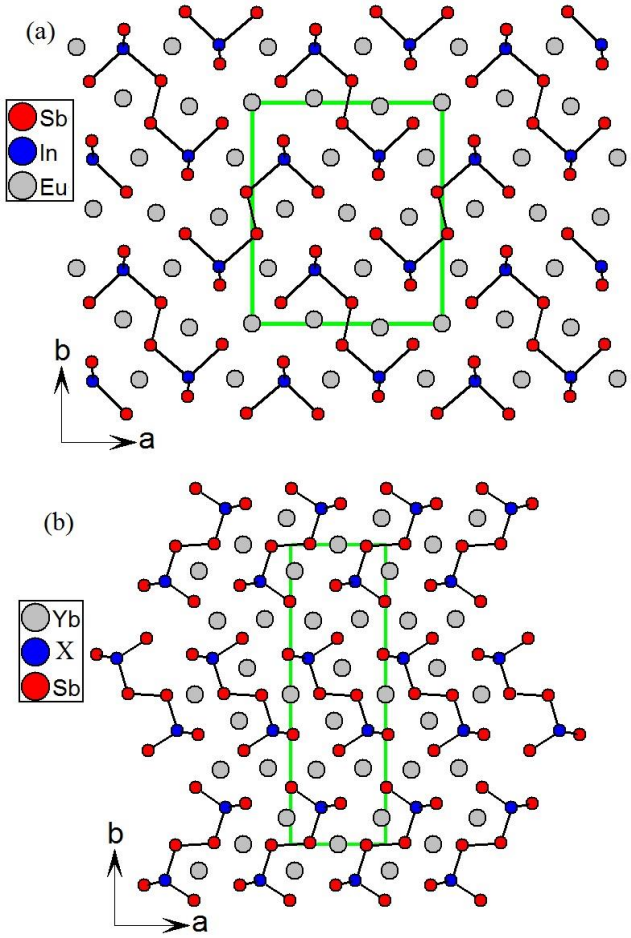

Figure 4.4.1. Crystal Structures off $Eu_5In_2Sb_6$ and $Yb_5M_2Sb_6$ are shown along the c-direction. The unit cells are represented in bright green colour.

The coordination environment of the Eu atoms in $Eu_5In_2Sb_6$ is similar to that of Yb atoms in $Yb_5M_2Sb_6$ (Figure 4.4.2). Eu1/Yb1 is coordinated to two In atoms and stabilized in seven fold coordination with Sb atoms in a capped trigonal prismatic geometry. Eu2 and Eu3 atoms are in distorted octahedral geometries with Sb atoms. Eu3 has different coordination environment from Yb3 atom in $Yb_5M_2Sb_6$. Yb3 in $Yb_5M_2Sb_6$ is surrounded by two Sb1 and four Sb3 atoms, but Eu3 is surrounded by two Sb1, two Sb2 and two Sb3. Both $Ca_5Ga_2As_6$ [8] and $Ba_5Al_2Bi_6$ structure types[43] have the structural difference in the packing pattern of double chains. Details of the crystal structure studies are available in reported papers.[6, 7, 41, 42] $Eu_5In_2Sb_6$ and $Yb_5Ga_2Sb_6$ compounds satisfy the classical Zintl concept and are reported as narrow band gap semiconductors.[7, 41]

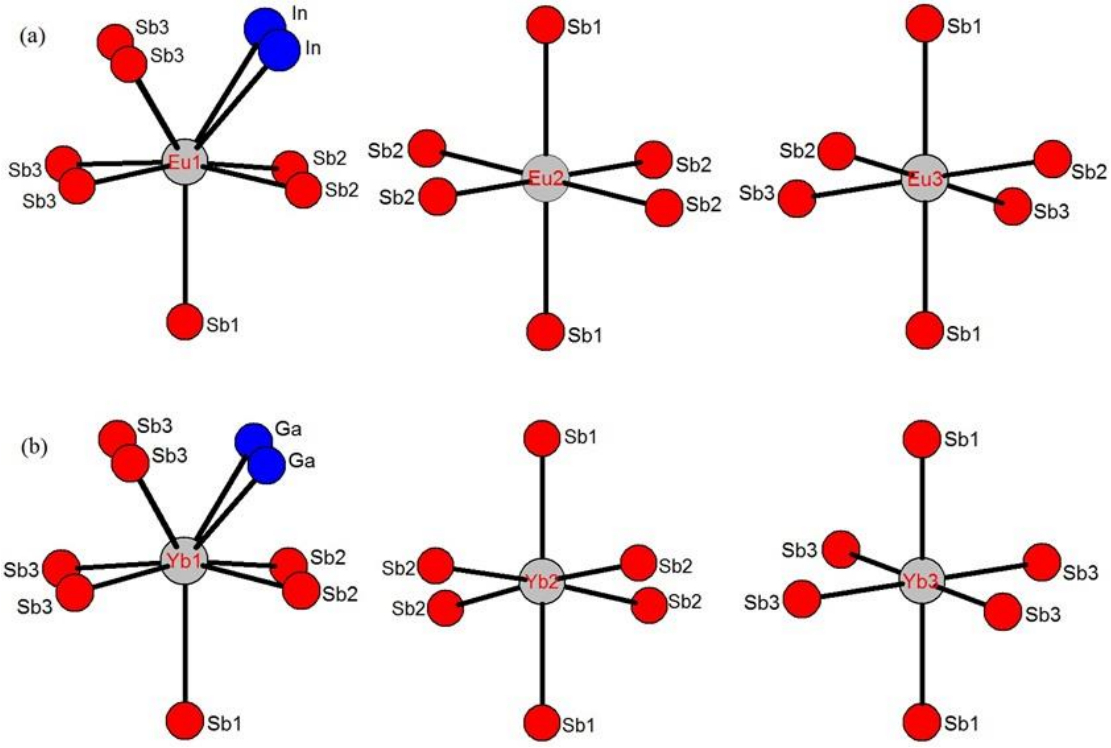

Figure 4.4.2. Coordination sphere of (a) Eu1, Eu2 and Eu3 in $Eu_5In_2Sb_6$ and (b) Yb1, Yb2 and Yb3 in $Yb_5M_2Sb_6$.

Recently, Snyder group reported YbX_2Sb_6 (X = Al, Ga, In) phases as semimetals.[44] Based on the Zintl-Klemm concept the formula for the compounds $Yb_5Al_2Sb_6$ and $Yb_5In_2Sb_6$ have been proposed as $(Yb^{2+})_5[(\{Al/In\}^{3+})_2(Sb_2^{4-})(Sb^{3-})_4$.[6, 17, 42] As explained in previous section, Yb atoms in $Yb_5Ga_2Sb_6$ show mixed valence behaviour and proposed the formula of the compound as $(Yb^{3+})_3(Yb^{2+})_2[(Ga^{3+})_2(Sb^{3-})_5(Sb^{4-})_1]$.[41] One of the best ways to assign

oxidation states is to check the bond distances obtained from the single crystal structure refinement. The theoretical values of the Yb^{2+}-*X* and Yb^{3+}-*X* (*X* = Al, Ga and In) distances calculated from the covalent radii of Yb^{2+} and Yb^{3+} have been taken from the literature[33, 34] and were compared with the ones obtained from the single crystal structure refinement. Table 4.4.1 shows the selected Yb-*X* and Eu-*X* bond distances in the compounds $Yb_5Al_2Sb_6$, $Yb_5Ga_2Sb_6$, $Yb_5In_2Sb_6$ and $Eu_5In_2Sb_6$ and the trend along the group for $Yb_5M_2Sb_6$ (*X* = Al, Ga and In) is shown in Figure 4.4.3.

Table 4.4.1. Selected bond lengths [Å] for Yb-*X* (*X* = Al, Ga and In) in $Yb_5Al_2Sb_6$, $Yb_5Ga_2Sb_6$ and $Yb_5In_2Sb_6$ and Eu-In in $Eu_5In_2Sb_6$ at 296(2) K with estimated standard deviations in parentheses.

Label	Distances (Å)	Label	Distances (Å)
$Yb_5Al_2Sb_6$		**$Yb_5Ga_2Sb_6$**	
Yb1-Al	3.536(2)	Yb1-Ga	3.4968(5)
Yb3-Al	3.634(2)	Yb2-Ga	3.6236(6)
$Yb_5In_2Sb_6$		**$Eu_5In_2Sb_6$**	
Yb1-In	3.5953(10)	Eu1-In	3.6771(11)
Yb2-In	3.6664(10)	Eu3-In	3.8564(9)
Yb3-In	3.7983(9)		

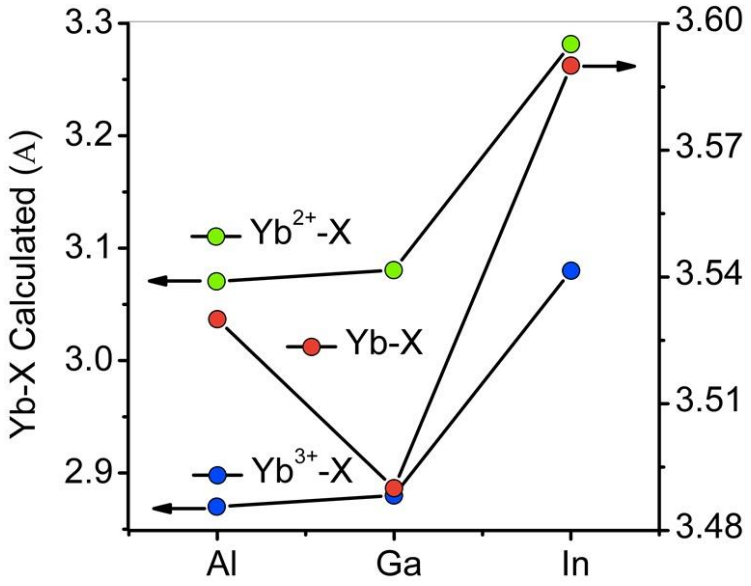

Figure 4.4.3. Comparison of the Yb-*X* distances obtained from the single crystal structure refinement and calculated distances of Yb^{2+}-*X* and Yb^{3+}-*X*.

Considering the fact that divalent Yb is larger in size (1.86 Å) compared to trivalent Yb (1.66 Å),[45, 46] Yb^{2+}-*X* distances are larger than Yb^{3+}-*X*. As expected, in a compound, these

distances are longer or shorter depends on the electronic contributions and geometrical constraints. However, assuming these compounds are crystallizing in the same crystal structure type, the trend should sequentially increase along the group. However, as seen in Figure 4.4.3, there is a sudden drop in the Yb-Ga distance compared to Yb-Al and Yb-In indicating a clear deviation from divalent oxidation states of Yb atoms assuming all terelides generally exist in the trivalent state. The deviation from the divalent Yb in $Yb_5Ga_2Sb_6$ was later confirmed by magnetic and XANES measurements (discussed below).

4.4.1.2. Physical Properties

The temperature dependent molar magnetic susceptibility (χ_m) at various applied fields 100 Oe, 1000 Oe and 5000 Oe and inverse susceptibility ($1/\chi_m$) at an applied field of 1000 Oe for $Eu_5In_2Sb_6$ are shown in Figure 4.4.4.

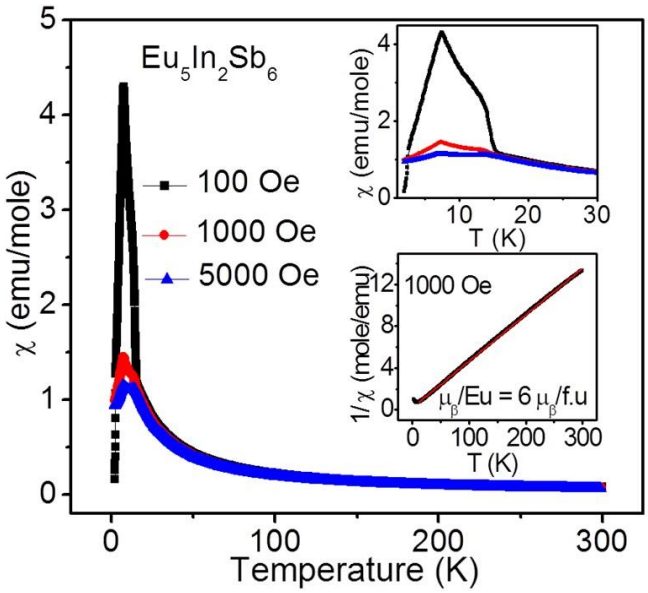

Figure 4.4.4. Temperature dependent magnetic susceptibility (χ_m) of $Eu_5In_2Sb_6$ in the field of 100, 1000 and 5000 Oe. Above inset shows at low temperature region there are two magnetic transitions; ferromagnetic transition at 15 K and antiferromagnetic transition at 7 K. The inset below shows the temperature dependent inverse magnetic susceptibility ($1/\chi_m$).

Magnetic susceptibility data of $Eu_5In_2Sb_6$ shows two consecutive antiferromagnetic ordering at 7.3 and 7.5 K followed by a ferromagnetic ordering at 15 K. The fitting of inverse susceptibility within the range 15-300 K resulted in the effective magnetic moment 6 μ_B/Eu atom, which suggests that Eu atoms may be existing in the mixed valence or intermediate valence states compared to the expected theoretical effective magnetic moment of 7.94 μ_B/Eu atoms for Eu^{2+} ions. Such a low magnetic moment is not unusual for systems with divalent

Eu as it was reported in $EuAu_2Si_2$ (6.7 μ_B),[47] $EuFe_4P_{12}$ (6.2 μ_B)[48] and Eu_2AuGe_3 (7.13 μ_B). However, XANES measurements and BVS calculation corroborating with magnetic measurements confirm that Eu atoms exist in the mixed valence state. The measurements at various applied magnetic field on $Eu_5In_2Sb_6$ clearly indicate a substantial decrease in magnetic susceptibility upon increasing the field. The temperature dependent molar magnetic susceptibility (χ_m) and inverse susceptibility ($1/\chi_m$) at an applied field of 1000 Oe for the compounds $Yb_5M_2Sb_6$ are shown in Figure 4.4.5.

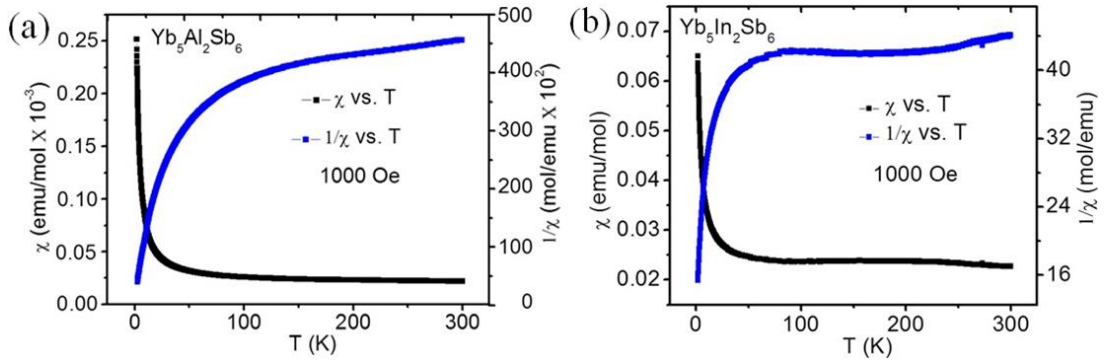

Figure 4.4.5. Temperature dependent magnetic susceptibility (χ_m) and inverse magnetic susceptibility ($1/\chi_m$) of (a) $Yb_5Al_2Sb_6$ and (b) $Yb_5In_2Sb_6$.

Magnetic susceptibility data show that the compounds $Yb_5Al_2Sb_6$ and $Yb_5In_2Sb_6$ are Pauli paramagnets whereas $Yb_5Ga_2Sb_6$ is paramagnetic in nature. The magnetic property of $Yb_5Ga_2Sb_6$ has been reported in previous section. Temperature dependent magnetic susceptibility data of $Yb_5M_2Sb_6$ (M = Al, Ga and In) shows no magnetic ordering down to 2 K but the susceptibility slightly increases at lower temperature, which is normal for *RE* based intermetallics.[6, 17] This lower temperature deviation can be attributed to crystal field contributions and/or to a possible onset of valence fluctuations. The magnetic moment for the compounds $Yb_5Al_2Sb_6$ and $Yb_5In_2Sb_6$ at room temperature calculated as 0.228 μ_B/Yb and 0.286 μ_B/Yb, respectively, clearly suggest Yb atoms are mostly in the divalent states with Pauli paramagnetic nature.

The field dependence of the magnetization $M(H)$ for ground samples of $Eu_5In_2Sb_6$ were measured at 2 K and 300 K are shown in Figure 4.4.6a. The data measured at 300 K exhibits linear behaviour. At 2 K, in $Eu_5In_2Sb_6$ magnetization suddenly increases with the magnetic field, it shows a metamagnetic behaviour, in intermetallic systems,[49, 50] generally the metamagnetic region lies in between a ferromagnetic and an antiferromagnetic region.[51]

This is clearly supporting that magnetic data of $Eu_5In_2Sb_6$ also shows ferromagnetic and antiferromagnetic transitions. $M(H)$ for $Yb_5Ga_2Sb_6$ measured at 300 K exhibit linear behaviour and no signs of saturation up to highest attainable field of 60000 Oe. The magnetization curve taken at 2 K shows a slight field dependent response up to ~ 30000 Oe, and continues to rise slowly up to the highest obtainable field (60000 Oe) without any hint of saturation (Figure 4.4.6c) and $Yb_5M_2Sb_6$ were measured at 2 K and 300 K shown in Figure 4.4.6(b-d). The data measured at 300 K exhibit linear behaviour, but in case of the $Yb_5In_2Sb_6$ compound at zero Oe it started increasing till 1000 Oe and it became linear till its highest field. The magnetization curve taken at 2 K shows a slight field dependent response up to ~ 30000 Oe, continues to rise slowly up to the highest obtainable field (60000 Oe) without any hint of saturation, but it was almost saturated in the case of $Yb_5Al_2Sb_6$ sample.

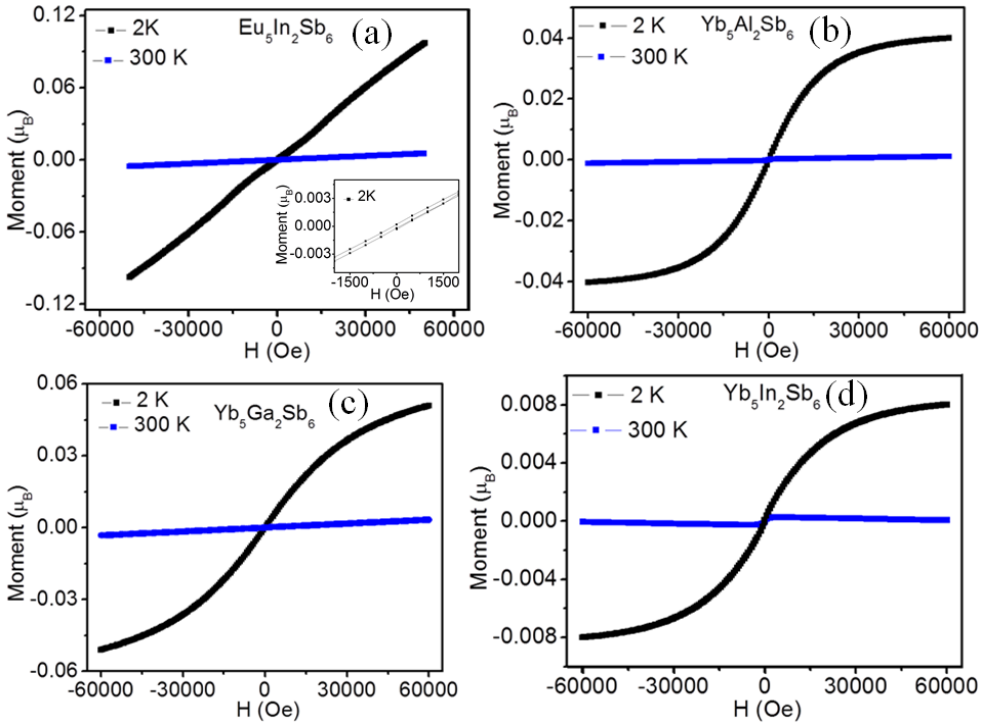

Figure 4.4.6. Magnetization as a function of applied magnetic field at 2 K and 300 K for the polycrystalline sample of (a) $Eu_5In_2Sb_6$, (b) $Yb_5Al_2Sb_6$, (c) $Yb_5Ga_2Sb_6$ and (d) $Yb_5In_2Sb_6$.

The substantial deviation of Eu and Yb magnetic moments from the spin only value for divalent Eu (7.94 μ_B) in $Eu_5In_2Sb_6$ and trivalent Yb (4.56 μ_B) $Yb_5Ga_2Sb_6$ led to the belief that it might be in an intermediate or mixed valence state. To unambiguously establish the actual valence state of Eu and Yb, XANES measurements have been performed at ambient pressure and at room temperature, which is a strong experimental tool in order to firmly

establish the valence state of an element in a compound. A sharp signal at 6973 eV was observed in the Eu-L_3 X-ray absorption spectrum of $Eu_5In_2Sb_5$ (Figure 4.4.7a). This value is characteristic of the $4f^7$ (Eu^{2+}) configuration and arises due to a $2p_{3/2}$ to 5d transition.[52] Another small peak at around 6984 eV corresponding to Eu^{3+} is also observed.[53] Integrating over the respective areas using Lorentzian fitting yields 35% of Eu in trivalent 65% is in divalent state (Figure 4.4.7a) with a magnetic moment of 5.2 μ_B/Eu. The value of the divalent Eu estimated from the XANES analysis is slightly smaller than the value obtained from the magnetic susceptibility data, which predicts 75% of divalent Eu in the system. The intense absorption peak of the spectrum (Figure 4.4.7b) centered at ~8948 eV, which is attributed to trivalent Yb atoms.[54] The spectra also showed the presence of another peak at ~8940 eV, revealing clearly that some divalent Yb ions ($4f^{14}$) are also present.[55] From the XANES measurements, the compound $Yb_5Ga_2Sb_6$ can be classified either as an intermediate valence compound, with all three Yb atoms having a non-integer valence, or heterogeneous mixed-valence compound, in which specific Yb atoms are either exactly 2+ or 3+. Fitting of the data resulted in ~ 64% Yb^{3+} corresponds to an average Yb valence of ~2.91, these values are very close to the values obtained from the magnetic measurements (58% Yb^{3+}).

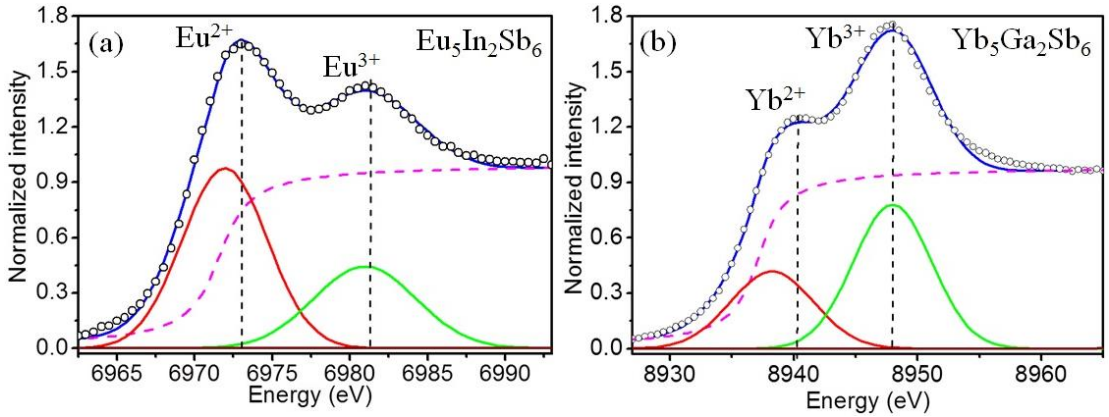

Figure 4.4.7. (a) Eu L_{III} absorption edge spectrum for $Eu_5In_2Sb_6$ and (b) Yb L_{III} absorption edge spectrum for $Yb_5Ga_2Sb_6$. The dotted lines represent the energy at which divalent and trivalent Eu and Yb absorbs.

In order to understand the oxidation states of Eu and Yb in these compounds, BVS calculations from the data obtained from the single crystal structure refinement. The average oxidation state obtained from the BVS calculations for $Eu_5In_2Sb_6$ and $Yb_5Ga_2Sb_6$ are 2.33 and 2.61, respectively. These values indicates 67% of divalent Eu and 33% trivalent Eu in $Eu_5In_2Sb_6$ and 39% of divalent Yb and 61% of trivalent Yb in $Yb_5Ga_2Sb_6$. These values are

in reasonable agreement with magnetic and XANES measurements. The uncertainty in the absolute valence is ~5-10%, arising from correlations between parameters used to represent the edge-step and white line resonances and from systematic errors due to fitting-model dependence.

4.5. Conclusion

Since the compounds $Yb_5Al_2Sb_6$ and $Yb_5In_2Sb_6$ were already reported in the $RE_5M_2X_6$ family within the $Ba_5Al_2Bi_6$ structure type, the existence of the prototype $Yb_5Ga_2Sb_6$ was highly probable. This motivated further to perform the synthesis of $Yb_5Ga_2Sb_6$ using different synthetic techniques. In the first attempt, rod shaped single crystals of $Yb_5Ga_2Sb_6$ were obtained from the metal flux technique using Ga as an active flux. The crystal structure of $Yb_5Ga_2Sb_6$ was studied using the XRD data of a good quality single crystal. Later, this compound was also synthesized by a HFIH as well. The earlier reports proposed that Yb exists in the divalent state based on the Zintl-Klemm concept. However, the magnetic susceptibility measurements on $Yb_5Ga_2Sb_6$ gave an effective magnetic moment of 2.63 μ_B/Yb atom, which suggests Yb is mixed valent with approximately 58 % of Yb^{3+}. Optical measurements and electrical resistivity studies suggest a band gap whereas a pseudogap like feature is seen in the density of states, which is in line with the other compounds in the $RE_5M_2X_6$ family and can be considered as a probable material for the thermoelectric applications.

Although these compounds have been studied for their thermoelectric properties, the chemical properties particularly oxidation state and other physical properties are lessexplored. And the chemical properties in terms of bonding analysis and bond valence sum calculations, which coupled with magnetic and XANES measurements to estimate the oxidation state of Eu and Yb. Among these compounds $Eu_5In_2Sb_6$ and $Yb_5Ga_2Sb_6$ are of mixed/intermediate valence. $Eu_5In_2Sb_6$ shows interesting magnetic properties with two magnetic orderings (around 15 and 7 K), the origin of which calls for further theoretical and experimental investigations.

4.6. References

1. Sevov, S. C., Zintl Phases in Intermetallic Compounds, Principles and Practice: Progress, Westbrook, J.H.; Freisher, R.L.: Eds.; John Wiley & Sons. Ltd., Chichester, England, **2002**, 113-132.
2. Snyder, G. J.; Toberer, E. S., *Nat. Mater.* **2008,** *7*, 105-114.
3. Kim, S. J.; Hu, S. Q.; Uher, C.; Kanatzidis, M. G., *Chem. Mater.* **1999,** *11*, 3154-3159.
4. Kim, S. J.; Kanatzidis, M. G., *Inorg. Chem.* **2001,** *40*, 3781-3785.
5. Clarke, D. R., *Surf. Coat. Technol.* **2003,** *163*, 67-74.
6. Kim, S. J.; Ireland, J. R.; Kannewurf, C. R.; Kanatzidis, M. G., *J. Solid State Chem.* **2000,** *155*, 55-61.
7. Park, S. M.; Choi, E. S.; Kang, W.; Kim, S. J., *J. Mater. Chem.* **2002,** *12*, 1839-1843.
8. Verdier, P.; l'Haridon, P.; Maunaye, M.; Laurent, Y., *Acta Crystallogr. B* **1976,** *32*, 726.
9. Cordier, G.; Sch¨afer, H.; Stelter, M., *Z. Naturforsch. B* **1984,** *39*, 727-732.
10. Toberer, E. S.; Zevalkink, A.; Crisosto, N.; Snyder, G. J., *Adv. Funct. Mater.* **2010,** *20*, 4375-4380.
11. Yan, Y. L.; Wang, Y. X.; Zhang, G. B., *J. Mater. Chem.* **2012,** *22*, 20284-20290.
12. Zevalkink, A.; Swallow, J.; Snyder, G. J., *J. Electron Mater.* **2012,** *41*, 813-818.
13. Johnson, S. I.; Zevalkink, A.; Snyder, G. J., *J. Mater. Chem. A* **2013,** *1*, 4244-4249.
14. Yan, Y. L.; Wang, Y. X., *J. Mater. Chem.* **2011,** *21*, 12497-12502.
15. Zevalkink, A.; Toberer, E. S.; Bleith, T.; Flage-Larsen, E.; Snyder, G. J., *J. Appl. Phys.* **2011,** *110*.
16. Zevalkink, A.; Pomrehn, G. S.; Johnson, S.; Swallow, J.; Gibbs, Z. M.; Snyder, G. J., *Chem. Mater.* **2012,** *24*, 2091-2098.
17. Todorov, I.; Chung, D. Y.; Ye, L. H.; Freeman, A. J.; Kanatzidis, M. G., *Inorg. Chem.* **2009,** *48*, 4768-4776.
18. Fornasini, M. L.; Manfrinetti, P., *Z. Krist-New Cryst. St.* **2009,** *224*, 345-346.
19. SAINT, e., Bruker AXS, Madison, WI, **1999**.
20. Sheldrick, G. M. S., Empirical Absorption Correction Program, University of; Göttingen, G., Germany, **1997**.

21. WinGX. A Windows Program for Crystal Structure Analysis: Farrugia, L. J., *J. Appl. Cryst.* **1999,** *32*, 837-838.

22. Sheldrick, G. M., *Acta Cryst.* **2008,** *A64*, 112-122.

23. SHELXTL 5.10; Bruker Analytical X-ray Systems, I. M., WI, **1997**.

24. Putz, H.; Brandenburg, K. *Diamond-Crystal and Molecular Structure Visualization*, Crystal Impact GbR: Bonn, Germany, 2011.

25. Blaha, P.; Schwarz, K.; Madsen, G. K. H.; Kvasnicka, D.; Luitz, J. *WIEN2k: An Augmented Plane Wave + Local Orbitals Program for Calculating Crystal Properties*, Technical University: Wien, Germany, 2001.

26. Perdew, P.; Burke, K.; Ernzerhof, M., *Phys. Rev. Lett.* **1996,** *77*, 3865-3868.

27. Monkhorst, H. J.; Pack, J. D., *Phys. Rev. B.* **1976,** *13*, 5188-5192.

28. Pauling, L., *J. Am. Chem. Soc.* **1929,** *51*, 1010–1026.

29. Brown, I. D.; Altermatt, D., *Acta Crystallogr. B* **1985,** *41*, 244–247.

30. Naskar, J. P.; Hati, S.; Datta, D., *Acta Crystallogr. B* **1997,** *53*, 885-894.

31. Brown, I. D., *J. Appl. Crystallogr.* **1996,** *29*, 479-480.

32. C.D. Malliakas, C., 2010.

33. Sanderson, R. T., *J. Am. Chem. Soc.* **1983,** *105*, 2259-2261.

34. Allen, F. H.; Kennard, O.; Watson, D. G.; Brammer, L.; Orpen, A. G.; Taylor, R., *J. Am. Chem. Soc.* **1987,** *2*, S1-S19.

35. Smart, J. S. *Effective Field Theories of Magnetism*, Saunders, Philadelphia, PA, 1966.

36. Kittel, C., *Introduction to Solid State Physics*. 7th ed.; John Wiley and Sons: Hoboken, NJ, 1996.

37. Peter, S. C.; Chondroudi, M.; Malliakas, C. D.; Balasubramanian, M.; Kanatzidis, M. G., *J. Am. Chem. Soc.* **2011,** *133*, 13840-13843.

38. Sengupta, K.; Sampathkumaran, E. V.; Nakano, T.; Hedo, M.; Abliz, M.; Fujiwara, N.; Uwatoko, Y.; Rayaprol, S.; Shigetoh, K.; Takabatake, T.; Doert, T.; Jemetio, J. P. F., *Phys. Rev. B* **2004,** *70*.

39. Sampathkumaran, E. V.; Ekino, T.; Ribeiro, R. A.; Sengupta, K.; Nakano, T.; Hedo, M.; Fujiwara, N.; Abliz, M.; Uwatoko, Y.; Rayaprol, S.; Doert, T.; Jernetio, J. P. F., *Physica B* **2005,** *359*, 108-110.

40. Kanchana, V.; Vaitheeswaran, G.; Zhang, X. X.; Ma, Y. M.; Svane, A.; Eriksson, O., *Phys. Rev. B* **2011,** *84*, 205135.

41. Subbarao, U.; Sarkar, S.; Gudelli, V. K.; Kanchana, V.; Vaitheeswaran, G.; Peter, S. C., *Inorg. Chem.* **2013,** *52*, 13631-13638.

42. Fornasini, M. L.; Manfrinetti, P., *Z. Krist-New Cryst. St.* **2009,** *224*, 345-346.

43. Cordier, G.; Schäfer, H.; Stelter, M., In *Z. Naturforsch. B*, 1985; Vol. 40, pp 5-8.

44. Aydemir, U.; Zevalkink, A.; Ormeci, A.; Wang, H.; Ohno, S.; Bux, S.; Snyder, G. J., *Dalton Trans.* **2015,** *44*, 6767-6774.

45. Sanderson, R. T., *J. Am. Chem. Soc.* **1983,** *105*, 2259−2261.

46. Allen, F. H.; Kennard, O.; Watson, D. G.; Brammer, L.; Orpen, A. G.; Taylor, R. J., *Chem. Soc., Perkin Trans.* **1987,** *2*, S1−S19.

47. Felner, I., *J. Phys. Chem. Solids* **1975,** *36*, 1063-1066.

48. Gerard, A.; Grandjean, F.; Hodges, J. A.; Braun, D. J.; Jeitschko, W., *J. Phys. C: Solid State Phys.* **1983,** *16*, 2797-2801.

49. Jacobs, I. S.; Kouvel, J. S.; Lawrence, P. E., *J. Phys. Soc.* **1962,** *17*, 656-658.

50. Doukoure, M.; Gignoux, D., *J. Magn. Magn. Mater.* **1982,** *30*, 111–116.

51. Vinokurova, L. I.; Veselago, V. G.; Ivanor, V. Y.; Rodionov, D. P.; Sagoyan, L. I., *Phys. Mer. Metall.* **1979,** *45*, 49-52.

52. Stockert, O.; Arndt, J.; Faulhaber, E.; Geibel, C.; Jeevan, H. S.; Kirchner, S.; Loewenhaupt, M.; Schmalzl, K.; Schmidt, W.; Si, Q.; Steglich, F., *Nat. Phys.* **2011,** *7*, 119-124.

53. Inoue, T.; Kubozono, Y.; Kashino, S.; Takabayashi, Y.; Fujitaka, K.; Hida, M.; Inoue, M.; Kanbara, T.; Emura, S.; Uruga, T., *Chem. Phys. Lett.* **2000,** *316*, 381−386.

54. Kim, K.-B.; Kim, Y. I.; Chun, H.-G.; Cho, T.-Y.; Jung, J.-S.; Kang, J. G., *Chem. Mater.* **2002,** *14*, 5045−5052.

55. Rao, C. N. R.; Sarma, D. D.; Sarode, P. R.; Sampathkumaran, E. V.; Gupta, L. C.; Vijayaraghavan, R., *Chem. Phys. Lett.* **1980,** *76*, 413-415.

Chapter 5

Ordered Crystal Structures of the Compounds with Mixed Valent Rare Earths

---

Papers published on this work have appeared in

[1] *Cryst. Growth Des.,* **2013**, *13*, 352-359.

[2] *J. Alloy Comp.,* **2014**, *589*, 405–411.

[3] *Inorg. Chem.,* **2014**, *53*, 6615−6623.

[4] *J. Chem. Sci.,* **2014**, *126*, 1605–1613

[5] *Adv. Mat. Phys. Chem.,* **2013**, *3*, 54-59.

[6] *Dalton Trans.,* **2015**, *44*, 5797-5804.

5. 1. Introduction

The main focus of this chapter is to synthesize ordered intermetallic compounds, which is basically aimed to alter the structure and properties of these materials compared to the disordered parent compounds. This chapter also focused to develop new structures or superstructures of the existing ones. The new structures often find a close relation with known compounds, which will be discussed in detail in the respective chapters. In general, all crystalline compounds can be classified as ordered and disordered compounds based on the fact that whether each crystallographic site is occupied solely by a single constituent atom or have mixed positions shared statistically between two atoms respectively. Both of these arrangements are crucial in generating novel ternary and quaternary structure types from the corresponding binaries, which effectively acts as a structural template for those compounds.

Consider two atoms A and B. These two types of atoms should occupy two sites in the lattice namely, I and II. If all the A atoms occupy type I site and the B atoms occupy type II site, the crystal is said to be perfectly ordered. However, it is possible that a few A atoms may occupy type II sites and few B atoms may occupy type I sites. This leads to disordered structure. It is also possible that the location of A and B atoms is completely random in the type I and type II sites, which leads to indistinguishable arrangements of A and B atoms. Then the structure of the compound is said to be totally disordered.

Ordering and disordering factors will play crucial role in tuning their structural and physical properties. The assignment of atoms in disordered compounds is quite difficult as they are statistically distributed. Most of the conventional techniques such as ceramic, arc melting and high frequency induction heating lead into the formation of disordered compounds though these techniques can be used for the synthesis of majority of the compounds within short period of time, so it is difficult to access the metastable phases or the structures that are stable at low temperatures. On the other hand, metal flux technique favoured the formation of the ordered compounds. Metal flux method has not only been proved to be a tremendous tool to grow single crystals of already known polycrystalline compounds for studying detailed physical properties but also have been an effective way to explore completely new phases.[1-7] For example $BaNiSn_3$ structure type have ordered arrangement of atoms in the crystal structure. Whereas this structure type is related to the

disordered $BaAl_4$[8] and its ternary derivative disordered centrosymmetric $CeAl_2Ga_2$ as discussed in Chapter 2.[9]

5.2. Experimental Section

5.2.1. Synthesis

The following reagents were used as purchased from Alfa-Aesar without further purification: Eu, Yb and Sm (in the form of metal pieces cut from metal chunk, 99.99%), Ni, Cu, Ag and Ir (powder, 99.99%), Ge (pieces, 99.999%), Al (Chunk, 99.99%) and Sn and In (shots, 99.99%).

5.2.1.1. Metal flux synthesis

The compounds EuInGe, Yb_2CuGe_6, $Yb_3Cu_4Ge_4$, $Yb_{6.6}Ir_6Sn_{16}$, $Sm_3Ni_5Al_{19}$, $Yb_7Ni_4InGe_{12}$, $EuCu_2Ge_2$ and $Eu_3Ag_2In_9$ were obtained by adding stoichiometric amount in an alumina crucible under an inert nitrogen atmosphere inside a glove-box. The crucible was placed in a 13 mm fused silica tube, which was flame sealed under vacuum of 10^{-4} Torr, to prevent oxidation during heating. The reactants were then heated to designed temperature profiles. The reaction product was isolated from the excess indium flux by heating at 350 ºC and excess aluminium flux by heating at 750 ºC followed by subsequent centrifugation through a coarse frit. Any remaining flux was removed by immersion and sonication in glacial acetic acid for 48 h. The final crystalline product was rinsed with water and dried with acetone. Several crystals, which grow as metallic silver rods were carefully selected for elemental analysis, structure characterization, and the measurements of physical properties.

5.2.1.2. High frequency induction heating

Elemental metals were mixed in the ideal atomic ratio and sealed in tantalum ampoules under argon atmosphere in an arc-melting apparatus. The tantalum ampoules were subsequently placed in a water-cooled sample chamber of an HFIH (Easy Heat induction heating system, Model 7590). It is then rapidly heated by applying respective Amperes current (reaching ca. 1000-1100 ˚C in temperature) and kept at that temperature for 30-60 min. Finally, the reaction was rapidly cooled to room temperature by switching off the power supply. The product could easily be removed from the tantalum tubes. No side-reactions with the crucible material could be detected. EuInGe, Yb_2CuGe_6, $Yb_3Cu_4Ge_4$, $Yb_{6.6}Ir_6Sn_{16}$, $EuCu_2Ge_2$ and $Eu_3T_2In_9$ (T = Cu and Ag) are in polycrystalline form and light grey in colour

and were found to be stable in moist air for several weeks. The weight losses of the final material were found to be less than 1%. The samples obtained from the high frequency induction heating method were used for the resistivity studies.

5.2.1.3. Arc Melting

$Sm_3Ni_5Al_{19}$ was prepared by arc melting in Ar atmosphere. The sample was melted repeatedly (four times) in the same atmosphere to ensure homogeneity. The weight losses of the final material were found to be less than 1%. The sample obtained via arc melting method was used for the magnetic studies.

5.2.2. Elemental analysis

Semi-quantitative microanalyses were performed on the single crystals obtained from the flux techniques using a SEM equipped with Bruker 129 eV EDAX. Data were acquired with an accelerating voltage of 20 kV and in 90 s accumulation time. The EDAX analysis performed on visibly clean surfaces of the single crystals and gave the target atomic composition was in good agreement with the results derived from the refinement of single crystal XRD data.

5.2.3. Powder XRD

Phase identity and purity of the EuInGe, Yb_2CuGe_6, $Yb_3Cu_4Ge_4$, $Yb_{6.6}Ir_6Sn_{16}$, $Sm_3Ni_5Al_{19}$, $Yb_7Ni_4InGe_{12}$, $EuCu_2Ge_2$ and $Eu_3T_2In_9$ sample were determined by powder XRD experiments that were carried out with a Bruker D8 Discover diffractometer using Cu-$K\alpha$ radiation (λ = 1.5406 Å) over the angular range $10^0 \leq 2\theta \leq 90^0$, with a step size of 0.014903^0 at room temperature, calibrated against corundum standards. The experimental powder pattern of EuInGe, Yb_2CuGe_6, $Yb_3Cu_4Ge_4$, $Yb_{6.6}Ir_6Sn_{16}$, $Sm_3Ni_5Al_{19}$ and $Yb_7Ni_4InGe_{12}$ and the XRD pattern simulated from the single-crystal X-ray structure refinement were found to be in good agreement.

5.2.4. Single-Crystal XRD

Suitable single crystal of EuInGe, Yb_2CuGe_6, $Yb_3Cu_4Ge_4$, and $Yb_{6.6}Ir_6Sn_{16}$ using a STOE IPDS 2T (with additional capability of 2θ swing of the detector) diffractometer with graphite-monochromatized Mo $K\alpha$ (λ = 0.71073 Å) radiation. The X-AREA (X-RED and X-SHAPE) package suite[10] was used for the data extraction and integration and to apply empirical and analytical absorption corrections. The crystal structure of EuInGe, Yb_2CuGe_6,

$Yb_3Cu_4Ge_4$ and $Yb_{6.6}Ir_6Sn_{16}$ were refined with the JANA2006[11] package of programs. The unit cell edge length determination was performed with the Peak list 1.06 software part of the X-Area 1.39 suite[10] using a least square refinement algorithm. $Sm_3Ni_5Al_{19}$, $Yb_7Ni_4InGe_{12}$, $EuCu_2Ge_2$ and $Eu_3Ag_2In_9$ were mounted on a thin glass fiber with commercially available super glue. X-ray single crystal structural data was collected on a Bruker Smart CCD diffractometer equipped with a normal focus, 2.4 kW sealed tube X-ray source with graphite monochromatic Mo-$K\alpha$ radiation (λ = 0.7107 Å) operating at 50 kV and 30 mA, with ω scan mode. The software programme SAINT[12] was used for integration of diffraction profiles and absorption correction were made with SADABS programme.[13] The structure was solved by SHELXS 97 and refined by a full matrix least-squares method using SHELXL.

5.2.5. Magnetic Measurements

Magnetic measurements on selected single crystals of EuInGe, Yb_2CuGe_6, $Yb_3Cu_4Ge_4$, $Yb_{6.6}Ir_6Sn_{16}$, $Sm_3Ni_5Al_{19}$, $Yb_7Ni_4InGe_{12}$, $EuCu_2Ge_2$ and $Eu_3T_2In_9$ were carried out on a Quantum Design MPMS-SQUID magnetometer. Temperature dependent magnetic data were collected for field cooled mode (FC) between 2 to 400 K in an applied field (H) of 1000 Oe. Magnetization data were also collected for EuInGe, Yb_2CuGe_6, $Yb_3Cu_4Ge_4$, $Yb_{6.6}Ir_6Sn_{16}$, $Sm_3Ni_5Al_{19}$, $Yb_7Ni_4InGe_{12}$, $EuCu_2Ge_2$ and $Eu_3T_2In_9$ at 2 K and 300 K with field sweeping from -60000 Oe to 60000 Oe.

5.2.6. Electrical Resistivity

The resistivity measurements were performed in 1T field on EuInGe and $Yb_{6.6}Ir_6Sn_{16}$ with a conventional AC four probe setup. Four very thin copper wires were glued to the pellet using a strongly conducting silver epoxy paste. The data were collected in the range form 3-300 K using commercial QD-PPMS. The results were reproducible for several batches.

5.2.7. XANES

XANES experiments of $Yb_{6.6}Ir_6Sn_{16}$, $Yb_7Ni_4InGe_{12}$, $EuCu_2Ge_2$ and $Eu_3T_2In_9$ were performed at the Sector 20 bending magnet beam line (PNC/XSD, 20-BM), of the Advanced Photon Source at the Argonne National Laboratory and Yb_2CuGe_6, $Yb_3Cu_4Ge_4$ were performed at PETRA III, P06 beamline of DESY, Germany. Measurements at the Yb L_{III}-edge were performed in the transmission mode using gas ionization chambers to monitor the

incident and transmitted X-ray intensities. A third ionization chamber was used in conjunction with a copper foil to provide internal calibration for the alignment of the edge positions. Monochromatic X-rays was obtained using a Si [111] double crystal monochromator. The monochromator was calibrated by defining the inflection point (first derivative maxima) of Cu foil as 8980.5 eV. Rh-coated X-ray mirror was utilized to suppress higher-order harmonics. XANES samples were prepared by mixing an appropriate amount of the finely ground $Yb_{6.6}Ir_6Sn_{16}$, $Yb_7Ni_4InGe_{12}$, Yb_2CuGe_6, and $Yb_3Cu_4Ge_4$ with BN. The mixture was pressed to form a self-supporting pellet and the measurements were performed at 300 K. Care was taken to suppress distortion in the data from thickness effects.

5.2.8. Mössbauer Spectroscopy

The ^{151}Eu Mossbauer measurements of EuInGe were carried out in the transmission geometry using standard PC based spectrometer at room temperature using Eu_2O_3 was used as the reference sample at UGC-DAE Indore.

5.2.9. Theoretical calculations

The electronic structure and total energy of the EuInGe, Yb_2CuGe_6 and $Yb_3Cu_4Ge_4$ compounds were calculated with the LMTO method[14] in the full-potential (FP) implementation.[15] The exchange and correlation energy were treated in the LSDA.[16] In the FP-LMTO method, the crystal volume is split into two regions, one with non-overlapping muffin-tin spheres surrounding each atomic nucleus and the other comprised of the interstitial space between the atoms.[15] A double κ *spdf* LMTO basis set is used to describe the valence electrons, i.e. Hankel-functions characterized by decay constants κ are smoothly augmented inside the atomic spheres with numerical radial functions. The basis set of EuInGe was further augmented with local orbitals to describe the semicore states of Eu 5*p* and In 4d and with floating orbitals centered on interstitial positions.[17] The k-point sampling used a regular mesh of 6x10x4 in the $P2_1/c$ structure or 8x8x4 in the *Pnma* structure (corresponding to 84 and 170 k-points in the irreducible wedge of the Brillouin zone, respectively). The atoms were treated in the scalar-relativistic approximation with the spin-orbit interaction added within the atomic spheres. The basis set was further augmented with local orbitals to describe the semi-core states of Yb 5*p* and Ge 3*d*.[15] The *k*-point sampling used a regular mesh of 8x8x8 in the $C2/m$ structure of Yb_2CuGe_6 or 8x8x8 in the *Cmmm*

structure of $Yb_3Cu_4Ge_4$ (which corresponds to 150 and 95 *k*-points in the irreducible wedge of the respective Brillouin zones).

Comparable *k*-point meshes were used for the calculations of the other candidate structures of Yb_2CuGe_6. The atoms were treated in the scalar-relativistic approximation with the spin-orbit interaction added within the atomic spheres.[15] A finite magnetization on the Yb ions was found neither for Yb_2CuGe_6 nor for $Yb_3Cu_4Ge_4$, i.e. when starting the calculations assuming a large magnetic moment on Yb, the iterations towards charge self-consistency lead to a vanishing net spin polarization in the crystal. The inclusion of a Hubbard *U* correlation parameter on the Yb atoms (LSDA+*U*) was further attempted. However this did not change the situation with respect to Yb magnetization for several reasonable choices for the *U* parameter.

5.3. Metal flux Crystal Growth Technique in the Determination of Ordered Superstructure in EuInGe

5.3.1. Introduction

The crystal structure of EuInGe was previously reported within the orthorhombic system.[18] EuInGe was synthesized in a high temperature reaction of the pure elements in equiatomic ratio and the reactions were done within Ta tubes in an inert atmosphere and by the HFIH method. A new type orthorhombic structure with space group *Pnma* was elucidated from the single crystal data, with lattice constants a = 4.921(1) Å, b = 3.986(9) Å and c = 16.004(3) Å. The crystal structure of EuInGe was explained on the basis of the Zintl-Klemm concept[19] with an unusual anionic network. However, during the structure refinement, a large disorder was faced which showed up in the largely unsatisfactory residuals ($R1$ > 10 %), large electron density residuals and high thermal ellipsoid at the indium atomic position. In order to solve those problems, a split atom model was used in the indium position, however creating unacceptable In-In bond distances of 0.8 Å. All these factors and the recent reports on this kind of problems in intermetallic systems,[20] pointed towards a probable superstructure of the EuInGe compound. Hence, to answer the unresolved questions about the structure to produce high quality single crystals of EuInGe using the metal flux technique has been set, with indium as the active flux, and to determine the actual structure of this compound. The crystal structure was studied using single crystal XRD. The stability of the crystal structure and the nature of the chemical bonding in EuInGe were investigated by first-principles density functional calculations. The valence state of europium was determined using ^{151}Eu Mössbauer spectroscopy and magnetic susceptibility measurements. Physical properties such as magnetism and transport measurements are also reported.

5.3.2. Results and Discussion

5.3.2.1. Structure Refinement

Indexing of the first few frames obtained from the diffractometer led to a primitive monoclinic cell. The intensity of the superstructure reflections increased when the exposure time increased to 6 min for better data. This clearly confirms the weak additional peaks in the powder XRD. Initially, the systematic absences were leading to the non-centrosymmetric space group $P2_1$. A combined general and racemic twinning with three BASF parameters were applied for the successful refinement for this non-centrosymmetric space group.

However, the Platon program within WinGx system, ver. 1.70.01.[21] was used to check the additional symmetry, and this lead to space group $P2_1/c$. The structure was solved by direct method and refined using Shelxl-97 (full-matrix least-squares on F^2)[22] with anisotropic atomic displacement parameters for all atoms. As a check for the correct composition, the occupancy parameters were refined in a separate series of least-squares cycles. All sites were fully occupied within two standard uncertainties and in the final cycles the ideal occupancies were assumed again. All bond lengths are within the acceptable range compared to the theoretical values. In addition the superstructure reflections were omitted and refined the substructure in orthorhombic system within the *Pnma* space group. A better residual obtained using a split model did not solve the unacceptable In-In bond distance (0.8164(10) Å). The details of the data collection and complete refinement are shown in Table 5.3.1. The positional parameters and interatomic distances are listed in Table 5.3.2 and 5.3.3. Further information on the structure refinements is available from: Fachinformationszentrum Karlsruhe, D-76344 Eggenstein-Leopoldshafen (Germany), by quoting the Registry No. CSDs–425244 and 425245 for substructure and superstructure, respectively.

5.3.2.2. Reaction Chemistry

Single crystals of EuInGe were grown in indium flux generally as metallic silver rods. SEM image of a typical single crystal of EuInGe is shown in Figure 5.3.1. Reaction by-products were small amounts of recrystallized germanium as well as very small amounts of $EuGe_2$,[23] which due to very different crystal morphology (polygonal shape) could be easily distinguished and removed when necessary. The EuInGe compound also synthesized by direct combination of the reactants in primarily grey polycrystalline form and pieces made up from packed crystals. EuInGe is stable in air and no decomposition was observed for weeks. The elemental analysis of this compound with SEM/EDAX gave the atomic composition 33(1):34(1):33(1) for Eu:In:Ge, in excellent agreement with the results obtained from the single crystal refinement. Single crystals were selected from the reaction mixture and their crystal structure was crystallographically refined. The polycrystalline sample obtained from the high frequency induction furnace method was used for the physical property measurements.

5.3.2.3. Crystal Chemistry

The crystal structure of EuInGe is shown in the Figures 5.3.2a and 5.3.2b as viewed along the *b*-axis and *a*-axis, respectively. Mao et al.[18] proposed that a structural relationship exists between $BaGe_2$ (tetragonal) and EuInGe (orthorhombic *Pnma*) through the intermediate EuInGe ($GdSi_2$, orthorhombic *Imma*).[18] The refinement suggests that EuInGe crystallizes in an ordered monoclinic structure, which can be explained in a similar way as the previously reported orthorhombic structure except that the doubling of the *b*-axis is observed in the crystal obtained from the flux reactions, together with a change in the symmetry from tetragonal ($I4_1/amd$, $ThSi_2$ type structure) to monoclinic ($P2_1/c$ space group and its own type structure).

Table 5.3.1. Crystal data and structure refinement for EuInGe at 293(2) K.

	Substructure	Superstructure
Formula weight	339.37	
Wavelength	0.71073 Å	
Crystal system	Orthorhombic	Monoclinic
Space group, *Z*	*Pnma*, 4	$P2_1/c$, 8
Formula weight	1705	424.22
Unit cell dimensions	*a* = 4.9066(10) Å *b* = 3.9834(8) Å *c* = 15.964(3) Å	*a* = 7.9663(16) Å *b* = 4.9119(10) Å *c* = 16.465(5) Å *β* = 104.03 deg.
Volume	312.02(11) $Å^3$	625.1(3) $Å^3$
Density (calculated)	7.224 g/cm^3	7.213 g/cm^3
Absorption coefficient	36.42 mm^{-1}	36.36 mm^{-1}
F(000)	576	1152
Crystal size	110 x 70 x 60 *μm*	110 x 70 x 60 *μm*
θ range for data collection	2.55 to 31.71°	2.55 to 31.69°
Index ranges	-7<=*h*<=6, -5<=*k*<=5 -23<=*l*<=23	-11<=*h*<=11, -7<=*k*<=6 -24<=*l*<=24
Reflections collected	2601	5641
Refinement method	100%	
Refinement method	Full-matrix least-squares on F^2	
Data / restraints / parameters	585 / 0 / 23	2122 / 0 / 57
Goodness-of-fit	1.114	1.062
Final *R* indices [>2σ(I)]	*R*1 = 0.025, *wR*2 = 0.0496	*R*1 = 0.0467, *wR*2 = 0.113
Largest diff. peak and hole	1.853 and -1.366 e.$Å^{-3}$	9.733 and -4.244 e.$Å^{-3}$

$R = \Sigma||F_o|-|F_c|| / \Sigma|F_o|$, $wR = \{\Sigma[w(|F_o|^2 - |F_c|^2)^2] / \Sigma[w(|F_o|^4)]\}^{1/2}$ and $w=1/(\sigma^2(I)+0.0016I^2)$

Table 5.3.2. Atomic coordinates (x 10^4) and Anisotropic displacement parameters (Å^2 x 10^3) for EuInGe. The anisotropic displacement factor exponent takes the form: $-2\pi^2[h^2a^{*2}U_{11} + ... + 2hka^*b^*U_{12}$. Equivalent isotropic displacement parameters U_{eq} is defined as one third of the trace of the orthogonalized U_{ij} tensor.

	Wyckoff Site	*x*	*y*	*z*	U_{11}	U_{22}	U_{33}	U_{23}	U_{13}	U_{12}	U_{eq}
Substructure											
Eu1	4*c*	191(1)	2500	3925(1)	9(1)	8(1)	8(1)	0	0	0	8(1)
In1	8*d*	5026(1)	1475(2)	7105(1)	7(1)	13(1)	6(1)	-1(1)	0	0	9(1)
Ge1	4*c*	4238(2)	2500	5422(1)	10(1)	7(1)	6(1)	0	1(1)	0	7(1)
Superstructure											
Eu1	4*e*	8215(2)	177(4)	8927(1)	6(1)	5(1)	9(1)	1(1)	0	0	7(1)
Eu2	4*e*	6793(2)	9791(4)	1077(1)	7(1)	12(1)	7(1)	0	-1(1)	-1	9(1)
In1	4*e*	5716(2)	4934(4)	7895(1)	14(1)	8(1)	10(1)	0	1(1)	0	11(1)
In2	4*e*	314(2)	4984(5)	2105(1)	15(1)	9(1)	10(1)	-1(1)	3(1)	0	11(1)
Ge1	4*e*	6001(4)	5765(3)	9581(1)	6(1)	8(1)	6(1)	-6(2)	1(1)	1	6(1)
Ge2	4*e*	9012(4)	4235(3)	424(1)	4(1)	9(1)	6(1)	-3(2)	2(1)	0	6(1)

Table 5.3.3. Interatomic distances (Å) in the structure of EuInGe, calculated with the powder lattice parameters.

Substructure

Eu:	1	Ge	3.1077(9)	In:	1	In	0.8164(14)	Ge:	2	Ge	2.5188(9)	
	2	Ge	3.1265(7)		1	Ge	2.7444(10)		2	In	2.7443(10)	
	2	In	3.2741(8)		2	In	2.7584(7)		2	Eu	3.1265(7)	
	2	In	3.3106(8)		2	In	2.8767(8)		2	Eu	3.5389(8)	
	2	In	3.4297(8)		1	In	3.1670(15)					
	2	Ge	3.5389(8)		1	Eu	3.2741(8)					
	1	In	3.7379(8)		1	Eu	3.3106(8)					
					1	Eu	3.4297(8)					
					1	Eu	3.7379(8)					
					1	Eu	3.7699(9)					

Superstructure

Eu1:	1	Ge2	3.094(3)	Eu2:	1	Ge1	3.103(2)	In1:	1	Ge1	2.760(2)	In2:	1	Ge2	2.736(2)			
	1	Ge2	3.113(2)		1	Ge1	3.118(3)		2	In1	2.882(1)		2	In2	2.879(1)			
	1	Ge1	3.145(3)		1	Ge2	3.158(3)		1	In2	3.163(2)		1	In1	3.163(2)			
	1	In1	3.267(2)		1	In1	3.310(2)		1	Eu2	3.310(2)		1	Eu1	3.298(3)			
	1	In2	3.298(3)		1	In2	3.315(2)		1	Eu1	3.442(3)		1	Eu2	3.306(2)			
	1	In2	3.414(2)		1	Ge1	3.522(3)		1	Eu2	3.726(2)		1	Eu1	3.414(2)			
	1	In1	3.441(3)		1	Ge2	3.557(3)		1	Eu1	3.777(2)		1	Eu1	3.743(2)			
	1	Ge2	3.523(3)		1	In1	3.726(2)		1	Eu2	3.900(2)		1	Eu2	3.865(3)			
	1	Ge1	3.567(3)		1	In2	3.743(3)	Ge1:	1	Ge1	2.465(6)		1	Ge2	2.461(6)			
	1	In2	3.773(2)		1	In2	3.865(3)		1	Ge2	2.575(5)		1	Eu1	3.094(3)			
	1	In1	3.777(2)		1	In1	3.900(2)		1	Eu2	3.102(3)		1	Eu2	3.158(3)			
	1	Eu1	3.965(2)		1	Eu1	3.974(3)		1	Eu1	3.146(3)		1	Eu1	3.523(3)			
									1	Eu2	3.522(3)							

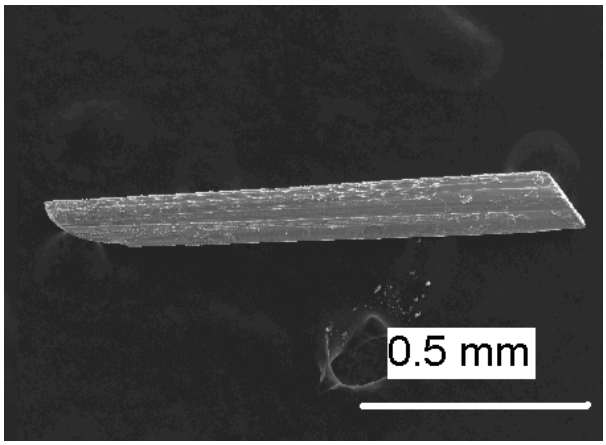

Figure 5.3.1. A typical single crystal of EuInGe grown using the metal flux technique.

Group-subgroup relationships and group analysis can predict a lowering symmetry from orthorhombic *Pnma* to monoclinic $P2_1/c$ (see Figure 5.3.3). The bonds to the Eu atoms were omitted to emphasize the three-dimensional [InGe] framework and its channels. The structure can also be described as an intergrowth of two independent slabs of parallel zig-zag chains of In and Ge atoms that run parallel to the *a* or *b*-axis (Figures 5.3.2c and 5.3.2d) with two Eu atoms residing within the channels formed by the connection of the layers.

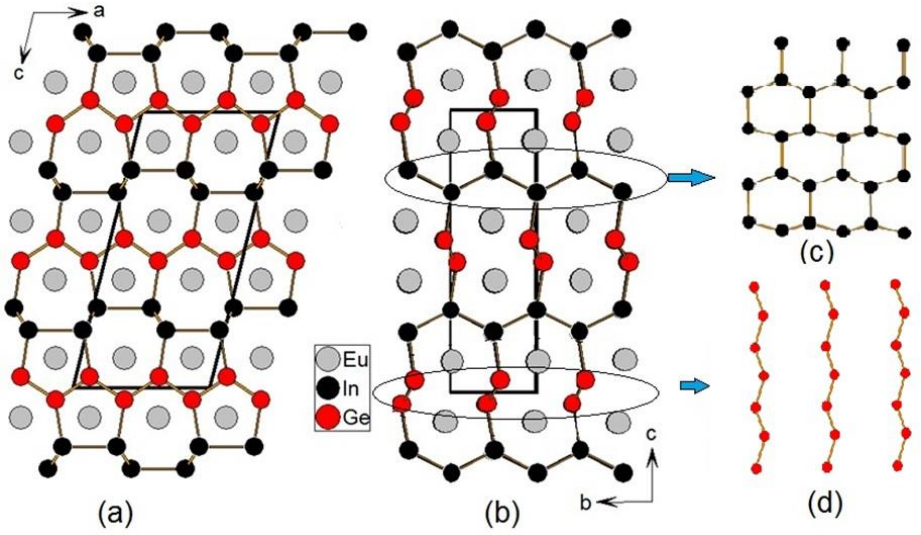

Figure 5.3.2. Crystal structure view of monoclinic EuInGe along [010] and [100] shown in (a) and (b), respectively. (c) Two dimensional zigzag layer of In atom. (d) One dimensional Ge layer.

The refined crystal structure is fully ordered with acceptable bond distances. The nearest Ge-Ge distances are 2.465(6) Å and 2.575(5) Å and comparable to the Ge-Ge distances in $EuGe_2$.[23] The shortest distance between the Eu and Ge atoms is 3.094(3) Å which is common in Eu-Ge based intermetallics.[24] Crystallographically, there are six

different sites in EuInGe, two each of europium, indium and germanium atoms. Both In atoms are four-fold coordinated and have almost tetrahedral geometries, while germanium atoms are tri-fold coordinated (Figure 5.3.4) making this compound of Zintl type Eu^{2+}(4b-In)$^-$ (3b-Ge)$^-$ as explained by Mao et al.[18]

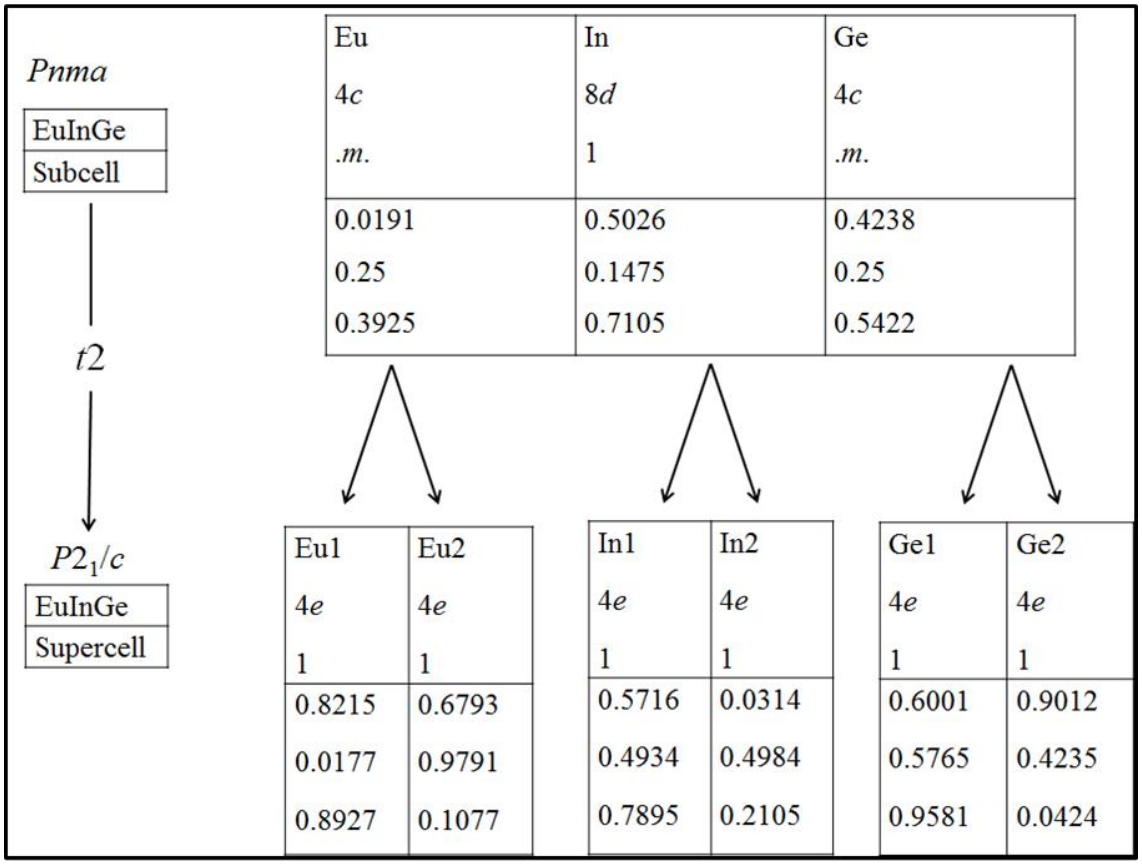

Figure 5.3.3. Group-subgroup scheme of sub-cell and the superstructure of EuInGe. The indices for the *translationengleiche* (*t*) transition and the unit cell transformations are given. The evolution of the atomic parameters is shown at the right.

The magnetic susceptibility and Mössbauer spectroscopic studies also revealed the divalent nature of europium atoms in EuInGe. The coordination environments of all atoms are shown in Figure 5.3.5. Eu1 and Eu2 are located in 15 membered prismatic cages. Although the overall nature of both environments is the same, strong interactions of Eu1-In (3.41-3.44 Å) and weak interactions of Eu2-In (3.86-3.90 Å) lead to cages with different distortions. The coordination environment of In atoms are formed as tetracapped triangular prismatic, composed of 10 atoms of which six are Eu atoms, 3 are In atoms and one is a Ge atom. On the other hand, the coordination environment of Ge atoms is formed as tricapped

triangular prismatic, composed of 9 atoms of which 6 are Eu atoms, one is an In atom and 2 are Ge atoms.

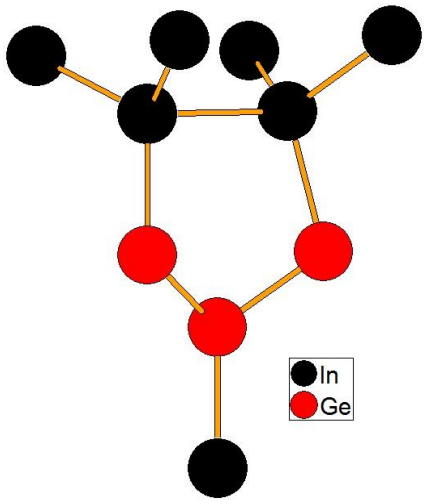

Figure 5.3.4. Tetra-coordinate indium and tri-coordinate germanium in the basic unit of the monoclinic structure of EuInGe.

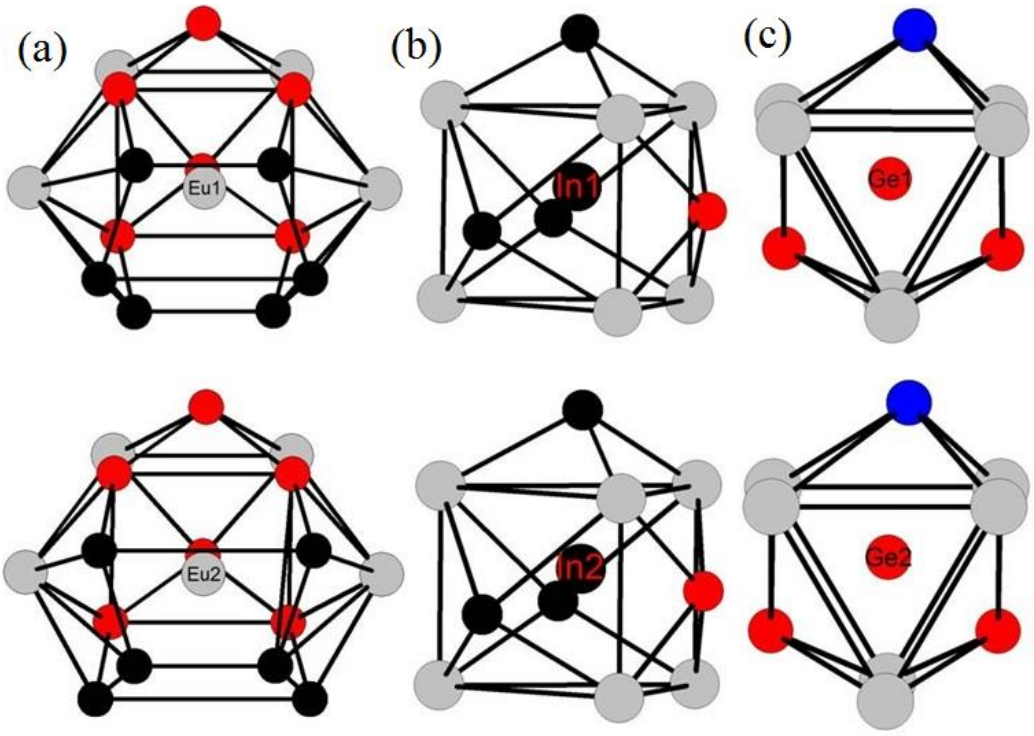

Figure 5.3.5. The local coordination environments of (a) Eu atoms, (b) In atoms and (c) Ge atoms in the monoclinic structure of EuInGe.

5.3.2.4. Mössbauer Spectroscopy

The ^{151}Eu Mössbauer spectrum of EuInGe at room temperature is presented in Figure 5.3.6 together with transmission integral fits. The spectra show one line with an isomer shift

of around –10 mm/s with respect to the Eu_2O_3 source, which indicates divalence of europium in EuInGe consistent with the magnetic susceptibility measurements and the chemical bonding analysis. The experimentally observed line widths are close to the usual line width of 2.3 mm/s of europium.

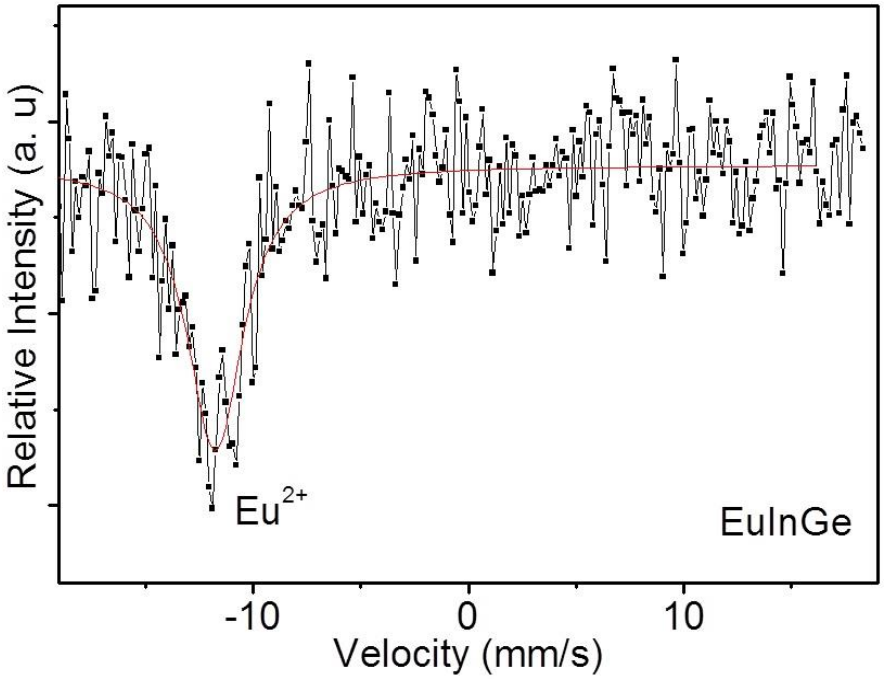

Figure 5.3.6. Experimental and simulated ^{151}Eu Mössbauer spectra of EuInGe at room temperature. The spectrum is measured relative to a Eu_2O_3 source.

5.3.2.5. Physical Properties

Magnetic susceptibility ($\chi = M/H$) was measured as a function of temperature under two different applied fields of H = 100 Oe and 5 kOe. $\chi(T)$ was also measured in the ZFC and FC conditions of the sample. In Figure 5.3.7, a plot of ZFC and FC, $\chi(T)$ measured in a field of 100 Oe is shown. Overall, the features of $\chi(T)$ observed here are in good agreement with those reported by Mao et al.[18] However, on close examination of the profile, signatures of multiple magnetic transitions are observed. As temperature (T) is lowered, χ increases monotonically but undergoes a sudden change below 70 K indicates a ferromagnetic transition. On further lowering of the temperature, more structures are observed in $\chi(T)$ at 44, 25 and 13 K, respectively. To highlight the anomalies in $\chi(T)$, the first derivative of the magnetization (dM/dT) is plotted as an inset in Figure 5.3.7. The temperatures at which anomalies observed are marked as T_1, T_2, T_3 and T_4.

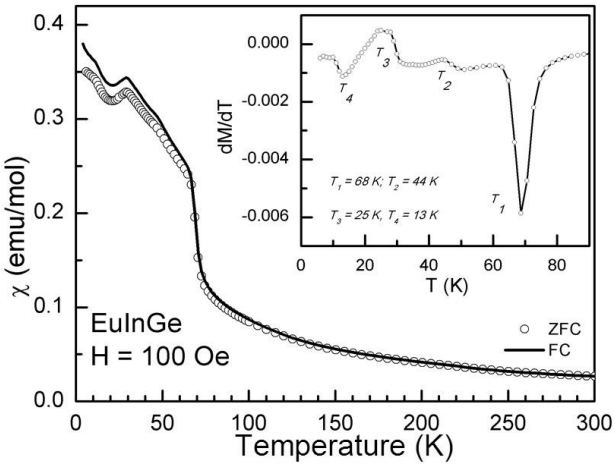

Figure 5.3.7. ZFC and FC Magnetic susceptibility ($\chi = M/H$) for EuInGe measured in a field of 100 Oe. The first derivative of the observed magnetization (M) is plotted as a function of temperature in the inset of the figure, to highlight the multiple magnetic transitions.

In Figure 5.3.8a the molar magnetic susceptibility measured in a field of 5 kOe, in ZFC condition of the sample is plotted as a function of temperature. The inverse susceptibility plot, $\chi^{-1}(T)$, is linear above 100 K corresponding to the CW law. The deviation from CW behaviour is seen below 100 K. The values of the paramagnetic Curie temperature (θ_p) and the effective moment (μ_{eff}) obtained from the linear fit of the $\chi^{-1}(T)$ data in the 150–30 K range, are θ_p = 12 K and μ_{eff} = 7.61 μ_B, respectively. The positive value of θ_p indicates predominant ferromagnetic interactions. The value of μ_{eff} is close to the expected free ion moment for Eu^{2+} of 7.94 μ_B. Several intermetallic compounds exhibit similar values for divalent europium.[25] These values are slightly different from the ones reported by Mao et al.[18] and may be attributed to sample preparation conditions. In order to verify the field induced changes to magnetic susceptibility, shown in Figure 5.3.8b, $\chi(T)$ measured in two different magnetic fields (H = 100 Oe and 5 kOe). Though the essential features are similar in both cases, the low field data is sharper and the anomalies are clearly visible. The ordering temperatures observed in low field data are also seen in 5 kOe. It is interesting to note that above 70 K, the two curves overlap as if the behaviour is field-independent. In Figure 5.3.9a, the isothermal magnetization curves (M vs. H) are shown for EuInGe measured at T = 1.8, 50 and 100 K. The notable observations made here at all three temperatures, is that there is no hysteresis observed and there is no saturation of magnetization.

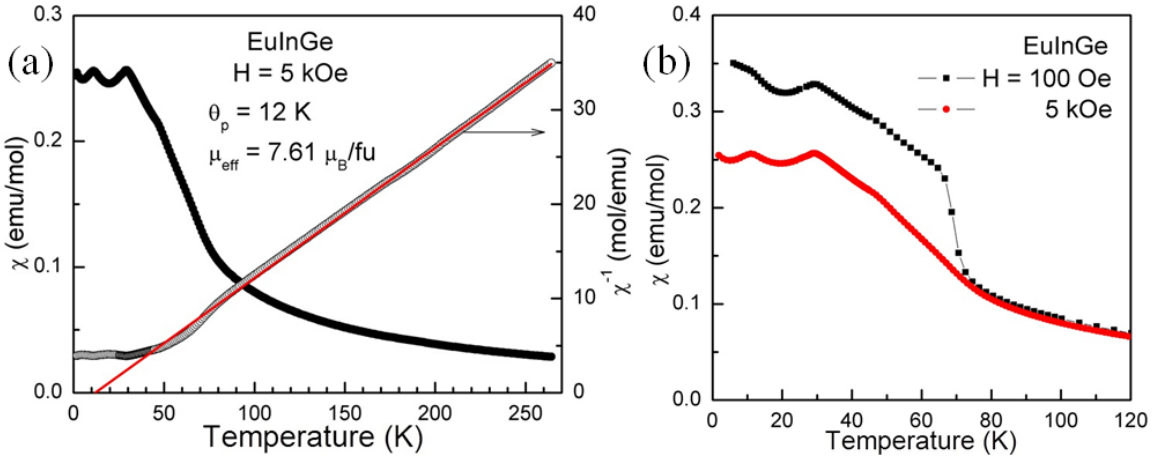

Figure 5.3.8. (a) Magnetic susceptibility and inverse susceptibility of EuInGe measured in a field of 5 kOe. The red line passing through the data points is the linear fit of the $\chi^{-1}(T)$ data exhibiting the CW behaviour. The intercept of this line on *x*-axis marks the paramagnetic Curie temperature (θ_p). (b) Magnetic susceptibility of EuInGe measured in H = 100 Oe and 5kOe is plotted on the same scale to highlight the influence of field on the moment formation.

For initial application of field, M varies linearly with H. However, for T = 1.8 and 50 K, there is slight deviation from this linearity above a field of 10 kOe. This means that the magnetic correlations persist up to 50 K, but less than 100 K. At T = 100 K, M varies linearly with H, indicating the paramagnetic state of the sample. The normal state temperature dependent resistivity of EuInGe is shown in Figure 5.3.9b. The resistivity decreases almost linearly with decreasing temperature, which is typically seen in metallic systems[26] without any long range magnetic ordering.

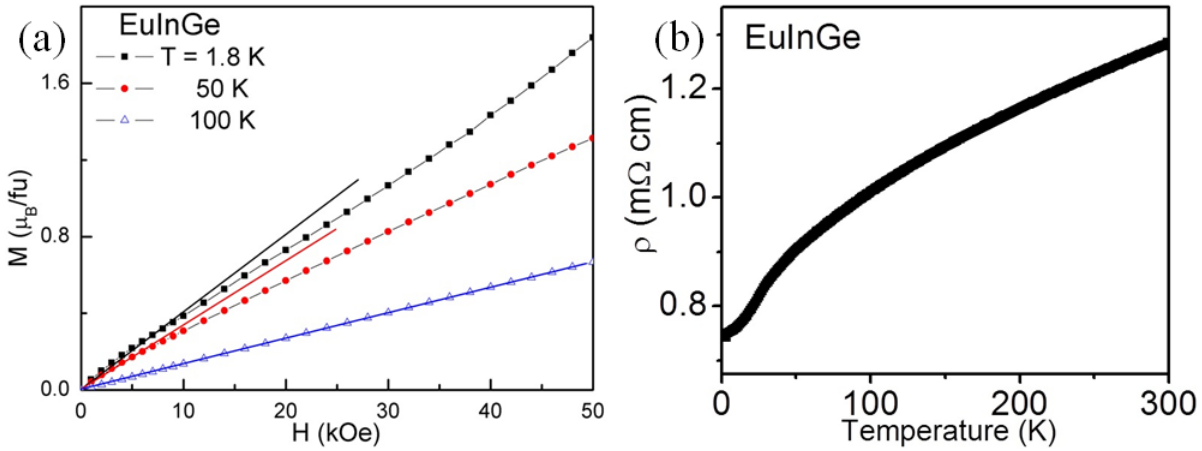

Figure 5.3.9. (a) Isothermal magnetization curves (M vs. H) for EuInGe measured at T = 1.8 K, 50 K and 100 K. The straight thick lines passing through the data points are guide for eyes only, shown to highlight the deviation of the data from linearity, (b) Electrical resistivity (ρ) of EuInGe measured as a function of temperature.

5.3.2.6. Band Structure Calculations

The calculated electronic density of states of EuInGe in the experimental $P2_1/c$ crystal structure of the present work is shown in Figure 5.3.10. A Hubbard parameter of U = 0.5 Ry was used. The density of states reveals that a significant hybridization takes place in EuInGe, with a distinct pseudogap occurring at the Fermi level. The lowest valence bands, from -11 eV to about -7.5 eV relatively to the Fermi level are dominated by the Ge states, in the region from -7.5 eV to -4 eV the In states dominate, while all constituent atoms contribute to the states between -4 eV and the Fermi level. Most notably the Eu *f* states fall in this region. The exact position of the Eu *f* level cannot be predicted accurately within the LSDA+U as it depends on the value adopted for the U parameter. With U = 0, i. e. in the LSDA, the *f*-states fall just below the Fermi level, while for U = 0.5 Ry, the *f*-peak has moved to about -2.5 eV below the Fermi level.

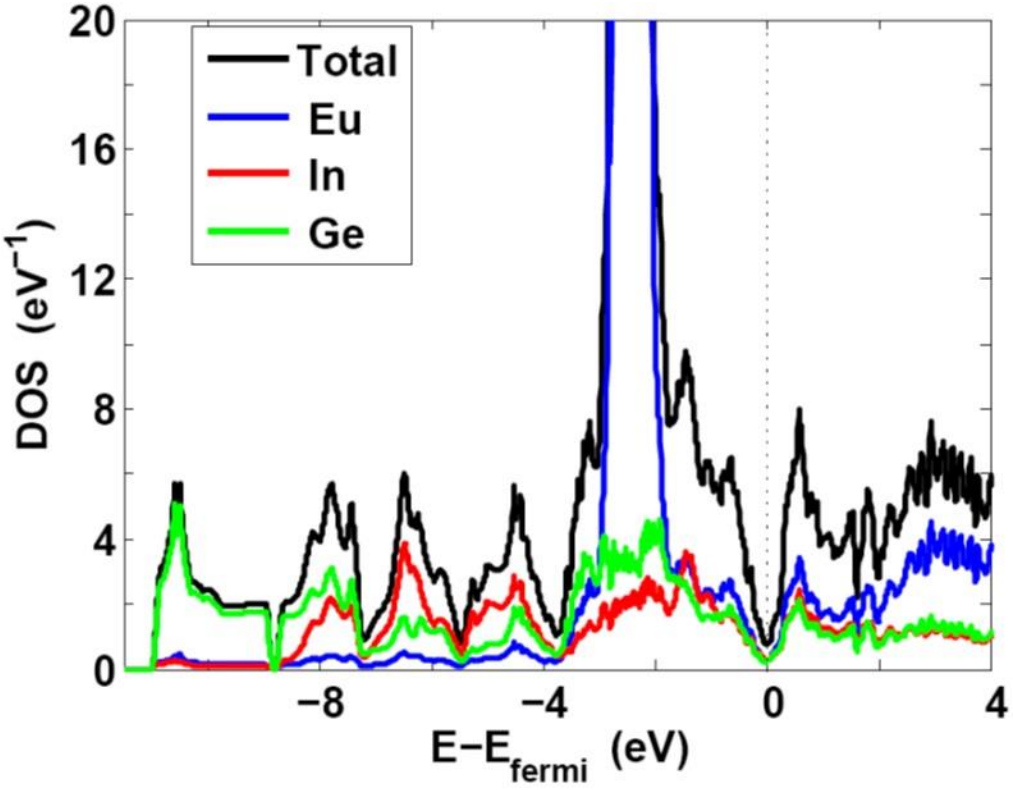

Figure 5.3.10. Density of states of EuInGe in the experimental $P2_1/c$ crystal structure as calculated with the LSDA+U method with U = 0.50 Ry. The Fermi level is marked with a dashed line and the Eu, In and Ge partial contributions are illustrated.

In both cases the *f*-occupation is close to seven corresponding to divalent Eu ions and spin-moments of 7 μ_B per Eu atom, which is consistent with out Magnetic susceptibility and Mössbauer data. The pseudo-gap around the Fermi level is also present in LSDA (i.e. with U

= 0), but less pronounced (not shown). In comparison of the total energy of the crystal with ferromagnetic and antiferromagnetic ordering of the Eu moments the ferromagnetic arrangement was found to be most favorable both in LSDA and LSDA+*U*, by about 0.17 eV per formula unit in LSDA. The energy was also calculated for a EuInGe compound assuming the *Pnma* parent crystal structure with half occupation of the 8*d* positions of In. The energy is in this case 0.40 eV higher per formula unit. By doubling the *Pnma* unit cell along the crystallographic *b*-axis and allowing for different In occupations in the two cells, the energy difference to the $P2_1/c$ structure comes down to 25 meV, still in favor of the $P2_1/c$ structure. These results show that the subcell picture largely is valid, i.e. that the observed $P2_1/c$ structure energetically is close to that of a *Pnma* structure with a double unit cell and rearrangement of the In atoms.

5.4. Crystal Structure of Yb_2CuGe_6 and $Yb_3Cu_4Ge_4$ and the Valency of Ytterbium

5.4.1. Introduction

The Yb-Cu-Ge system has been little explored. Among the four compounds reported in the the equiatomic compound YbCuGe[27] crystallizes in the NdPtSb type structure and has mixed valent Yb atoms and orders ferromagnetically below 8 K.[28] $YbCu_2Ge_2$ adopts the $CeAl_2Ga_2$ structure type[29] and has divalent ytterbium.[30] The other two compounds are Yb_2CuGe_6[31] and $Yb_3Cu_4Ge_4$,[32] but are little known as the crystal structures were investigated only using powder XRD data. Konyk et al. reported that Yb_2CuGe_6 crystallizes in the Ce_2CuGe_6 type structure with the *Amm*2 space group and lattice parameters a = 3.994(1) Å, b = 4.0802(1) Å and c = 21.018(3) Å.[33] Hanel et al. reported that $Yb_3Cu_4Ge_4$ adopts the orthorhombic $Gd_3Cu_4Ge_4$ structure type.[34] $Yb_3Cu_4Ge_4$ orders ferromagnetically at ~7.5 K and features trivalent Yb atoms.[35] The estimated magnetic moments from magnetic susceptibility measurements are 4.1 μ_B/Yb atom for Yb_2CuGe_6[33] and 4.52 μ_B/Yb atom for $Yb_3Cu_4Ge_4$, respectively.[35]

Following the previous investigation of the Yb_4TGe_8 (T = Cr-Ni) class of compounds which show anomalous thermal expansion[36] the synthesize set out to the next compound in the sequence, Yb_4CuGe_8, with the metal flux technique. The attempts did not produce the target compound but led to Yb_2CuGe_6 and $Yb_3Cu_4Ge_4$ instead yielding well shaped single crystals that permitted for the first time the full crystal structure determination of these compounds. In this section, the synthesis of Yb_2CuGe_6 and $Yb_3Cu_4Ge_4$ from indium flux, refinement of their crystal structures and physical characterization are discussed. The electronic structure calculations performed on both compounds revealed similar electronic structures.

5.4.2. Results and Discussion

5.4.2.1. Structure Refinement

Indexing of the first few frames obtained from the diffractometer for Yb_2CuGe_6 suggested an orthorhombic cell, and the systematic extinctions were compatible with the Ce_2CuGe_6 type structure, space group *Amm*2, in agreement with a previously reported study.[12] However, additional reflections observed in reciprocal space and taken into account which lead to a monoclinic structure with La_2AlGe_6 type atomic arrangement.[37] Also, the

refinement was largely unsatisfactory in the Ce_2AuGe_6 type structure, and was marked with relatively high residuals ($R1 > 10$ %). As a check for the correct composition, the occupancy parameters were refined in a separate series of least-squares cycles. All sites were fully occupied within two standard uncertainties and in the final cycles the ideal occupancies were assumed. A successful refinement was achieved in the monoclinic system with *C*2/*m* space group. For $Yb_3Cu_4Ge_4$, the atomic coordinates of $Gd_3Cu_4Ge_4$ were taken as starting parameters and refined within the orthorhombic space group *Immm*. The lattice constants of $Yb_3Cu_4Ge_4$ are arranged in the standard format. The details of the data collection and complete refinement are shown in Table 5.4.1. The positional parameters and interatomic distances are listed in Tables 5.4.2 to 5.4.4. Details of the structure refinements may be obtained from: Fachinformationszentrum Karlsruhe, D-76344 Eggenstein-Leopoldshafen (Germany), by quoting the Registry No's. CSD– 426133 (Yb_2CuGe_6) and CSD– 426132 ($Yb_3Cu_4Ge_4$).

5.4.2.2. Reaction Chemistry

Crystals of Yb_2CuGe_6 and $Yb_3Cu_4Ge_4$ were grown by a metal flux technique using indium as a flux. Both compounds have metallic silver colour and form cube and rod shapes for Yb_2CuGe_6 and $Yb_3Cu_4Ge_4$, respectively. Figure 5.4.1 shows SEM image of a typical crystals of both compounds. Reaction byproducts were small amounts of recrystallized germanium and In flux which tends to wet the surface of the crystals. Both compounds were synthesized by direct combination of the reactants in primarily grey polycrystalline form and pieces made up from packed crystals. Both compounds are stable in air and no decomposition was observed for several weeks.

5.4.2.3. Crystal Structure

5.4.2.3.1. Yb_2CuGe_6

The crystal structure of Yb_2CuGe_6 was first determined from powder XRD[38] to be of Ce_2CuGe_6 type, an ordered derivative of the $SmNiGe_3$ structure type.[39] However, a few additional peaks in the powder XRD of the sample in this work reveal the superstructure of the compound. In the present work, the single crystal XRD refinement revealed a larger unit cell with doubled *a* and *b* lattice parameters, crystallizing in the La_2AlGe_6 structure, which is another ordered derivative of the $SmNiGe_3$ type. The refinement of the structure in the La_2AlGe_6 type is the correct one and is also supported by the theoretical calculations as

discussed below. There are seven crystallographically distinct atomic positions in the Yb_2CuGe_6 structure one for Yb, one for Cu and five for the Ge atoms (Table 5.4.2). The crystal structure of Yb_2CuGe_6 is similar to that of MNiSi$_3$ (M = Sm, Y)[40] and it is shown in Figure 5.4.2.

Table 5.4.1. Crystal data and structure refinement for Yb_2CuGe_6 and $Yb_3Cu_4Ge_4$ at 293(2) K.

Empirical formula	Yb_2CuGe_6	$Yb_3Cu_4Ge_4$
Formula weight	845.16	1063.64
Wavelength	0.71073 Å	
Crystal system	Monoclinic	orthorhombic
Space group	*C*2/*m*	*Immm*
Unit cell dimensions	a = 8.0011(16) Å b = 8.1962(16) Å, β = 100.63(3)° c = 10.682(2) Å	a = 4.1302(8) Å b = 6.5985(13) Å c = 13.691(3) Å
Volume	688.5(2) Å^3	373.11(13) Å^3
Z	4	2
Density (calculated)	8.153 g/cm^3	9.468 g/cm^3
Absorption coefficient	55.575 mm^{-1}	64.078 mm^{-1}
F(000)	1444	908
Crystal size	0.50 x 0.05 x 0.05 mm^3	0.50 x 0.05 x 0.05 mm^3
θ range for data collection	3.59 to 29.02°	2.98 to 29.10°
Index ranges	-10<=h<=10, -11<=k<=11, -14<=l<=13	-5<=h<=5, -9<=k<=9, -18<=l<=18
Reflections collected	2984	1779
Independent reflections	961 [R_{int} = 0.0888]	317 [R_{int} = 0.0648]
Completeness to θ = 29.02°	97.8%	98.4%
Refinement method	Full-matrix least-squares on F^2	
Data / restraints / parameters	961 / 0 / 50	317 / 30 / 23
Goodness-of-fit	1.219	1.411
Final R indices [>2σ(I)]	R_{obs} = 0.0580, wR_{obs} = 0.1448	R_{obs} = 0.0503, wR_{obs} = 0.1367
R indices [all data]	R_{all} = 0.0595, wR_{all} = 0.146	R_{all} = 0.0545, wR_{all} = 0.169
Extinction coefficient	0.0006(2)	0.0109(19)
Largest diff. peak and hole	4.824 and -4.125 e·Å^{-3}	8.514 and -7.097 e·Å^{-3}

$R = \Sigma||F_o|-|F_c|| / \Sigma|F_o|$, w$R = \{\Sigma[w(|F_o|^2 - |F_c|^2)^2] / \Sigma[w(|F_o|^4)]\}^{1/2}$ and calcw=1/[σ^2(Fo^2)+(0.0359P)^2+6.1794P] where P = (Fo^2+2Fc^2)/3

Table 5.4.2. Atomic coordinates (x 10^4) and equivalent isotropic displacement parameters (Å^2 x 10^3) for Yb_2CuGe_6 and $Yb_3Cu_4Ge_4$ at 293(2) K with estimated standard deviations in parentheses. U_{eq} is defined as one third of the trace of the orthogonalized U_{ij} tensor.

Label	Wyckoff site	*x*	*y*	*z*	Occupancy	U_{eq}*
Yb_2CuGe_6						
Yb1	8*j*	843(1)	2497(1)	3370(1)	1	3(1)
Cu	8*j*	8023(4)	0	2129(3)	1	10(1)
Ge1	4*i*	1452(3)	0	5618(2)	1	6(1)
Ge2	4*i*	3590(3)	0	4176(2)	1	8(1)
Ge3	4*i*	5004(3)	0	1162(2)	1	8(1)
Ge4	4*i*	571(3)	0	1168(2)	1	7(1)
Ge5	4*i*	2791(2)	2240(2)	1160(2)	1	8(1)
$Yb_3Cu_4Ge_4$						
Yb1	2*a*	0	0	0	1	3(1)
Yb2	4*j*	5000	0	3706(1)	1	3(1)
Cu	8*l*	0	3093(4)	3299(2)	1	5(1)
Ge1	4*i*	0	0	2166(2)	1	5(1)
Ge2	4*h*	0	1913(4)	5000	1	4(1)

*U_{eq} is defined as one third of the trace of the orthogonalized U_{ij} tensor.

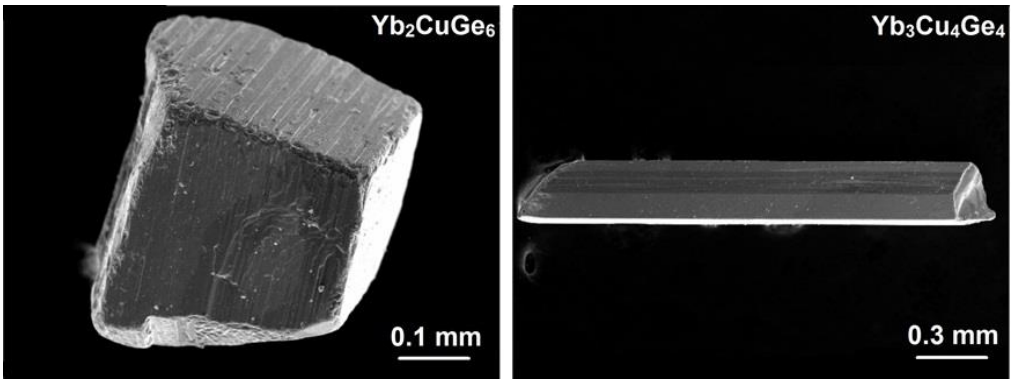

Figure 5.4.1. SEM images of typical single crystals of the compounds Yb_2CuGe_6 and $Yb_3Cu_4Ge_4$.

The bonds to the Yb atoms were omitted in Figure 5.4.2 to emphasize the three-dimensional Cu/Ge framework and its channels. Similar to *M*$NiSi_3$, the structure of Yb_2CuGe_6 contains pseudohexagonal nets formed by Ge and Cu atoms in the *ac*-plane as shown in Figure 5.4.2b. There are two different types of polygermanide fragments, infinite zig-zag chains made up of Ge1 and Ge2 atoms and Ge dimers [Ge3-Ge3, Ge4-Ge4 and Ge5-

Ge5], which are segregated in two areas. The difference between *M*NiSi$_3$ and Yb_2CuGe_6 structures are in the nature and arrangement of the fragments. In Yb_2CuGe_6, the Ge dimers are collinear with the *c*-axis direction compared to *b*-axis in the case of *M*NiSi$_3$ structure. These dimers in Yb_2CuGe_6 are arranged side by side in a rectangular array which extends over the *ab*-plane (Figure 5.4.3).

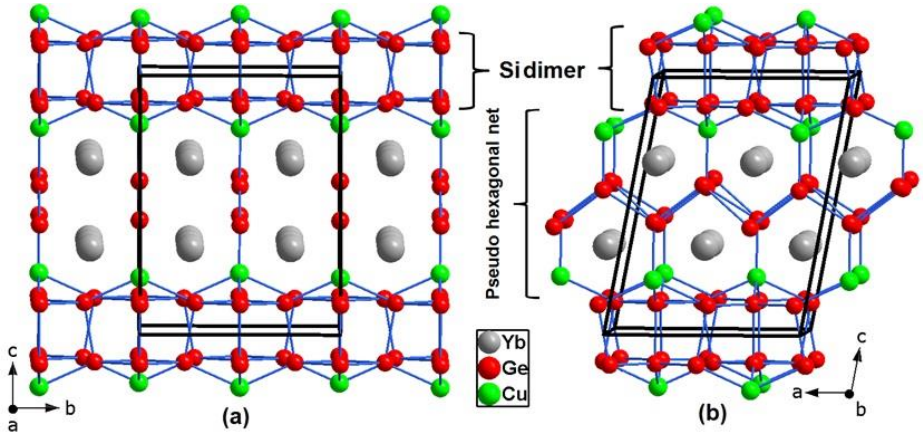

Figure 5.4.2. Crystal structure of monoclinic Yb_2CuGe_6 emphasized along the *a* and *b* axes. The unit cell is marked as solid black lines.

Table 5.4.3. Anisotropic displacement parameters (Å^2 x 10^3) for Yb_2CuGe_6 and $Yb_3Cu_4Ge_4$ at 293(2) K with estimated standard deviations in parentheses.

Label	U_{11}	U_{22}	U_{33}	U_{12}	U_{13}	U_{23}
Yb_2CuGe_6						
Yb1	2(1)	6(1)	1(1)	0(1)	0(1)	0(1)
Cu	6(2)	16(2)	6(2)	0	0(1)	0
Ge1	1(1)	12(2)	4(1)	0	0(1)	0
Ge2	5(1)	10(2)	10(1)	0	4(1)	0
Ge3	6(1)	11(2)	6(1)	0	-1(1)	0
Ge4	8(1)	10(2)	3(1)	0	0(1)	0
Ge5	4(1)	16(1)	2(1)	0(1)	0(1)	0(1)
$Yb_3Cu_4Ge_4$						
Yb1	5(1)	1(1)	3(1)	0	0	0
Yb2	4(1)	3(1)	1(1)	0	0	0
Cu	8(1)	4(1)	5(1)	0	0	1(1)
Ge1	5(1)	6(1)	5(2)	0	0	0
Ge2	4(1)	2(1)	4(1)	0	0	0

The anisotropic displacement factor exponent takes the form: $-2\pi^2[h^2a^{*2}U_{11}+ \ldots +2hka^*b^*U_{12}]$.

Table 5.4.4. Bond lengths [Å] for Yb_2CuGe_6 and $Yb_3Cu_4Ge_4$ at 293(2) K with estimated standard deviations in parentheses. All distances of the first coordination spheres are listed.

Label	Distances	Label	Distances
Yb_2CuGe_6			
Yb1-Ge2	2.9618(18)	Ge1-Cu	2.366(4)
Yb1-Ge2	3.0102(19)	Ge1-Ge1	2.451(5)
Yb1-Ge1	3.0331(19)	Ge1-Ge2	2.504(3)
Yb1-Ge5	3.0673(18)	Ge2-Ge2	2.593(5)
Yb1-Ge1	3.0756(19)	Ge3-Cu	2.446(4)
Yb1-Ge5	3.076(2)	Ge3-Ge3	2.482(5)
Yb1-Ge4	3.0952(19)	Ge3-Ge5	2.550(3)
Yb1-Ge3	3.1048(19)	Ge4-Cu	2.446(4)
Yb1-Ge1	3.1235(18)	Ge4-Ge4	2.494(5)
Yb1-Cu	3.141(2)	Ge4-Ge5	2.556(3)
Yb1-Cu	3.152(2)	Ge5-Ge5	2.472(3)
Yb1-Ge2	3.294(2)	Ge5-Cu	2.481(2)
$Yb_3Cu_4Ge_4$			
Yb1-Ge2	2.9007(19)	Ge1-Yb2	3.5085(13)
Yb1-Ge1	2.965(3)	Cu-Ge2	2.456(3)
Yb1-Cu	3.3573(19)	Cu-Ge1	2.5005(16)
Yb2-Ge1	2.951(2)	Cu-Cu	2.516(5)
Yb2-Cu	2.9565(18)	Cu-Ge	2.564(3)
Yb2-Ge2	2.9994(14)	Ge2-Ge2	2.524(5)

The average Ge-Ge distance of the dimers in the Yb_2CuGe_6 structure is 2.482 Å very close to the elemental Ge. It was observed that the Si-Si distances between dimers in *M*$NiSi_3$ were very short (2.8 Å) (Figure 5.4.3a) compared to the van der Waals distance of 3.8 Å. In comparison to this, there are two types of bond distances between the dimers in Yb_2CuGe_6; short distances (2.550(2) Å for Ge3-Ge5 and 2.556(2) for Ge4-Ge5) and long distances (3.177(2) Å for Ge3-Ge5 and 3.171(2) for Ge4-Ge5), see Figure 5.4.3b. This variable bond distances between the dimers favored the distortion in the network and probably the reason for the Cu vacancy and the formation of compound in the monoclinic system. The polygermanide fragments made up of Ge dimers are capped by copper atoms above and below (Figure 5.4.4). The rectangularly packed Ge atoms are then sandwiched between two layers of Cu atoms. Since the Yb_2CuGe_6 show Cu vacancies, only half of the rectangles are

caped with Cu, compared to all rectangles in *M*$NiSi_3$ with Ni atoms (Figure 5.4.4a). These slabs are connected with Ge-Cu bonds via the infinite zig-zag Ge chains resulting in a three-dimensional tunnel framework with Yb atoms filling the tunnels (Figure 5.4.2).

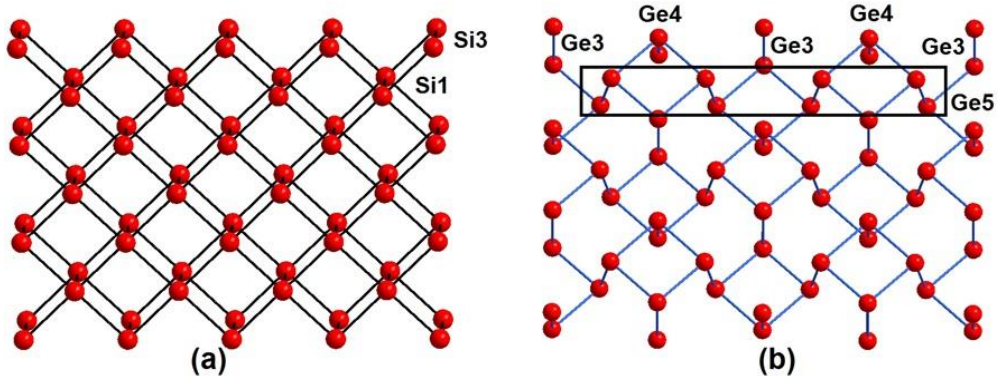

Figure 5.4.3. (a) The polysilicide fragment made up of Si dimers in *M*$NiSi_3$ (*M* = Sm, Y) and the polygermanide fragment made up of Ge dimers in Yb_2CuGe_6.

The infinite zigzag Ge chains are parallel to the *a*-axis with the plane of the zigzag chain being parallel to the crystallographic *ac*-plane. One other notable difference between *M*$NiSi_3$ and Yb_2CuGe_6 structure is the coordination environment of *RE*s (Figure 5.4.5). In *M*$NiSi_3$, the *RE* atoms are arranged in a pocket made of two parallel Ni_2Si_4 hexagonal rings linked by bridging Si atoms via Ni-Si-Si bonds. On the other hand, the hexagonal rings in Yb_2CuGe_6 are not completed due to the vacancy at the copper atom, which results in a huge distortion of the Yb polyhedra. The shortest bonds in the *M*$NiSi_3$ have been selectively removed to show the comparison between the structures. The shortest distance between the Yb and Ge atoms is 2.962(2) Å, comparable to the distances in other ytterbium based transition metal germanides such as YbAgGe,[41] Yb_2IrGe_2[42] and YbMnGe.[43]

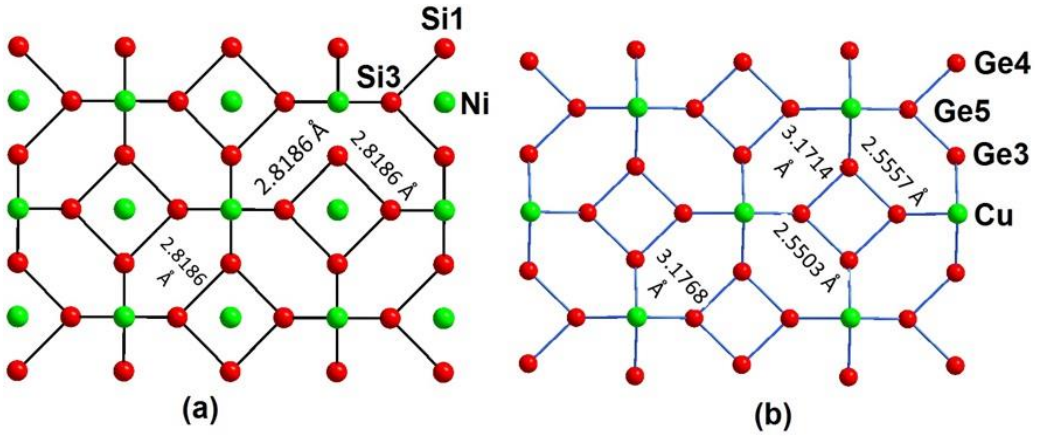

Figure 5.4.4. (a) Ni capped Si dimer fragment in *M*$NiSi_3$ (*M* = Sm, Y) and (b) Cu caped Ge dimer in Yb_2CuGe_6.

The shortest Cu-Ge distance (2.366(4) Å) is found between Cu and Ge4, which is much shorter than the distance between Cu and Ge with 2.446(4) Å. The zig-zag layers contain three different types of Ge-Ge bonds; 2.451(3) Å for Ge1-G1, 2.5042(2) Å for Ge1-G2 and 2.593(3) Å for Ge2-Ge2. The observed shortest Cu-Ge distances in other Yb-Cu-Ge systems are 2.458 Å in YbCuGe,[27] 2.464 Å in $YbCu_2Ge_2$[29] and 2.456(3) Å in $Yb_3Cu_4Ge_4$ (this work).

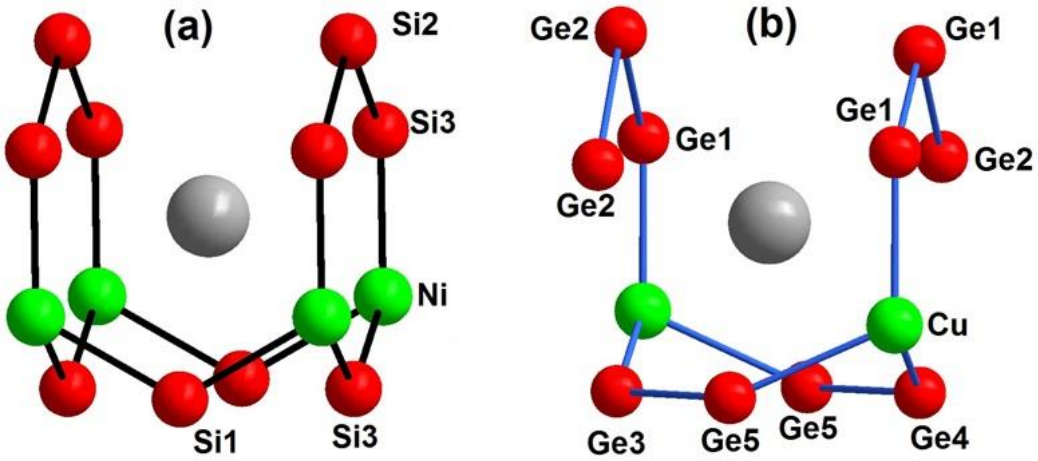

Figure 5.4.5. The local coordination environment of rare earths in the (a) $MNiSi_3$ (M = Sm, Y) and (b) Yb_2CuGe_6 structures.

5.4.2.3.2. $Yb_3Cu_4Ge_4$

Previous powder XRD studies suggested that $Yb_3Cu_4Ge_4$ crystallizes in the $Gd_3Cu_4Ge_4$ type structure.[34] The crystal structure contains two non-equivalent ytterbium, two germanium and one copper crystallographic sites. The $Gd_3Cu_4Ge_4$ type structure has been described previously as an intergrowth of $MgCuAl_2$ type slabs and pairs of columns of germanium centered trigonal RE_6 prisms.[44] In another view (Figure 5.4.6), as explained by Gladyhevskii et al.[45] $Yb_3Cu_4Ge_4$ consists of three trigonal prismatic columns sharing rectangular faces, the prism being centered by copper and germanium atoms. Yb1 is situated in the smaller cage and Yb2 is situated in the larger cage. In this model, the bonds to the Yb atoms were omitted to emphasize the 3D framework and its channels. The average Yb-Cu distances for the two ytterbium sites with Yb1-Cu (3.3573(19) Å) and Yb2-Cu (2.9565(18) Å) are quite different. This finding is similar to other $Yb_3T_4Ge_4$ compounds and was pointed out in the case of $Yb_3Pd_4Ge_4$.[46] Dhar et al. reported trivalent state of Yb atom based on their magnetic measurement.[35] The short Yb-Ge distances for Yb1-Ge (2.9642 Å) and Yb2-Ge

(2.9208 Å) are close and comparable to the Yb-Ge distances in some ytterbium transition metal germanides.[41, 42]

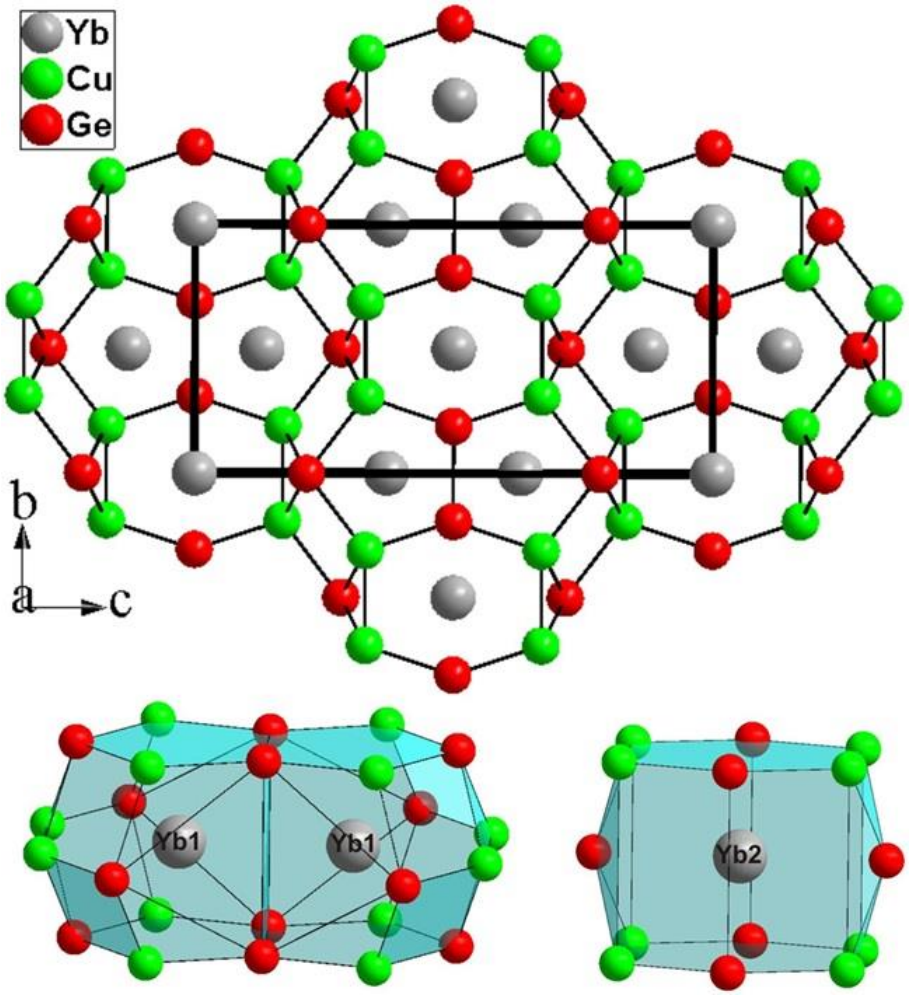

Figure 5.4.6. Crystal structure of $Yb_3Cu_4Ge_4$ and coordination polyhedral of ytterbium atoms. The cage like environments of the two crystallographically different ytterbium positions are outlined.

5.4.2.4. XANES

X-ray absorption measurements at the Yb L_{III}-edge were performed in order to investigate the valence state of the Yb atoms in Yb_2CuGe_6 and $Yb_3Cu_4Ge_4$. The spectra at room temperature for both compounds are given in Figure 5.4.7. Yb_2CuGe_6 shows a broad signal with the main signal centered at 8945 eV and a hump at 8937 eV showing the presence of Yb^{3+} and Yb^{2+}, respectively.[47, 48] Thus, the XANES data corroborate the information on valence states obtained from the magnetic and X-ray photoelectron spectroscopy measurements on the Yb_2CuGe_6 compound.[31] Since the crystal structure of Yb_2CuGe_6 in this work was reported to be Ce_2CuGe_6 type structure having two inequivalent Yb sites,[31] a mixed

valent picture of Yb was proposed. However, the crystal structure obtained in the present work from the single crystal data contains only one crystallographic Yb site, which is indicating that Yb in Yb_2CuGe_6 exists as an intermediate valent ion. XANES data of $Yb_3Cu_4Ge_4$ show a single sharp peak at 8945 eV, which can be attributed to Yb^{3+}. The absence of a broad shoulder below this energy shows that the Yb ions exist as almost pure trivalent, in agreement with the magnetic properties of this compound.[32]

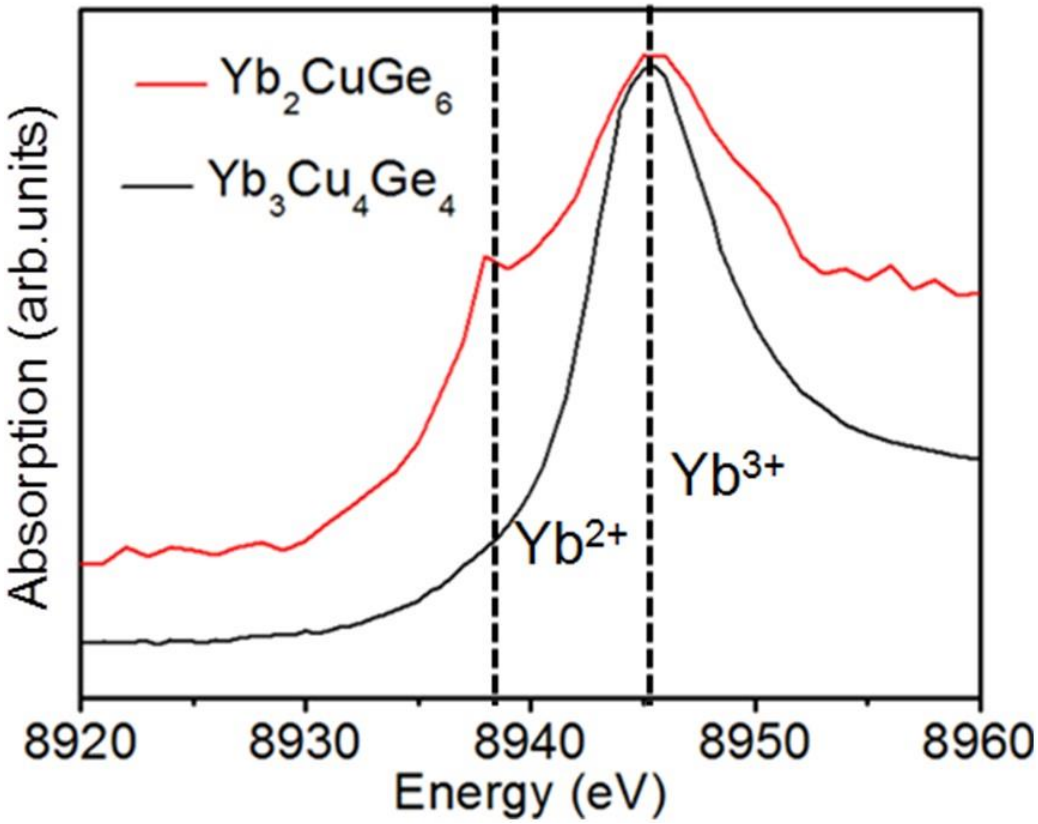

Figure 5.4.7. L_{III} absorption edge spectra of Yb in Yb_2CuGe_6 and $Yb_3Cu_4Ge_4$

5.4.2.5. Calculations

The calculated densities of states of Yb_2CuGe_6 and $Yb_3Cu_4Ge_4$ are shown in Figure 5.4.8. The electronic structures of the two compounds have distinct similarities. Both compounds are predicted to be metallic. The spin-orbit split Yb *f*- states are seen as narrow peaks with the highest $j = 7/2$ component pinning the Fermi level. The Cu *d*- bands are seen to appear below the Yb *f* bands, about 3.5-4 eV below the Fermi level, while the Ge *s* and *p* states are broad and include some hybridization into the Cu and Yb bands. The LDA total energy of Yb_2CuGe_6 was evaluated in the monoclinic *C*2/*m* structure determined from the present experiments and compared to the total energy for the competing structures, the

reported Ce_2CuGe_6 structure as well as the defective $SmNiGe_3$ structure. In the latter case, the atomic coordinates of $SmNiGe_3$ were used, with half occupancy of the Sm sites by Yb. The total energy per formula unit is higher by 44 mRy in the defective $SmNiGe_3$ structure and by 60 mRy in the Ce_2CuGe_6 structure compared to the *C*2/*m* structure, in agreement with the observed structure.

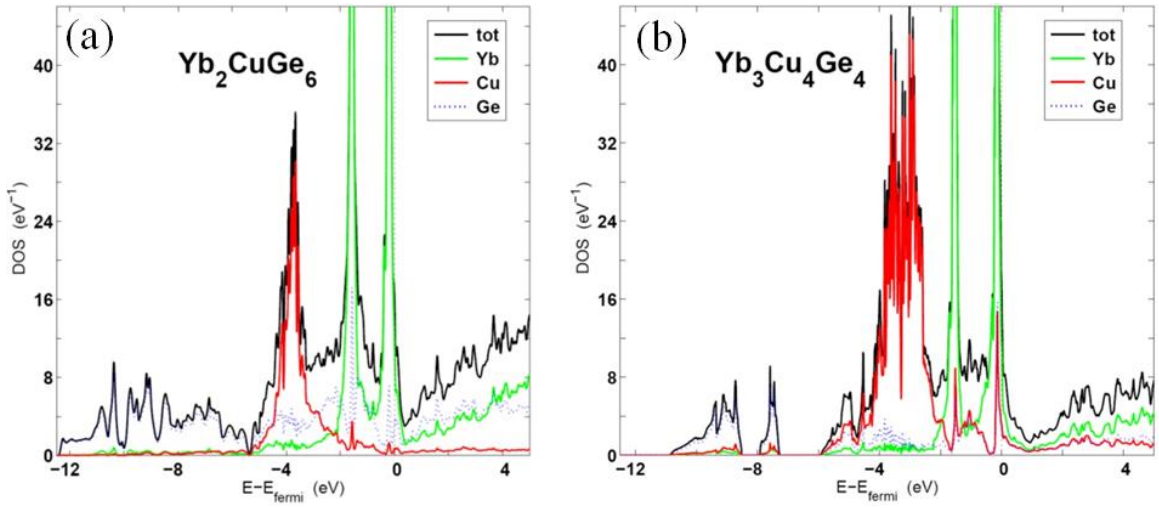

Figure 5.4.8. Electronic density of states for (a) Yb_2CuGe_6 in the *C*2/*m* structure and (b) $Yb_3Cu_4Ge_4$ in the *Immm* structure.

5.5. Flux Growth of $Yb_{6.6}Ir_6Sn_{16}$ Having Mixed Valent Ytterbium

5.5.1. Introduction

Rare earth based iridium stannides are an interesting class of materials because of their structural diversity and unusual physical properties. The compounds reported in this family include: *RE*IrSn (*RE* = La-Pr, Sm, Eu-Tb, Ho-Lu), which crystallize in the ZrNiAl structure type and $P\bar{6}2m$ space group;[49] $CeIr_2Sn_2$, which adopts the tetragonal $CaBe_2Ge_2$ structure type with *P*4/*mmm* space group;[50] $MgCuAl_2$-type $EuIrSn_2$ (*Cmcm* space group);[51] *RE*Ir_xSn_2 (*RE* = La, Nd, Gd) in the $CeNiSi_2$ structure type and *Cmmm* space group;[52] $RE_3Ir_4Sn_{13}$ (*RE* = La-Pr, Sm, Eu, Er-Lu), which adopts the cubic $Yb_3Rh_4Sn_{13}$ structure type ($Pm\bar{3}n$ space group);[53] and $RE_5Ir_4Sn_{10}$ (*RE* = La-Pr) which adopt the $Sc_5Co_4Si_{10}$ structure with *P*4/*mbm* space group.[54] Apart from the above mentioned compounds, Espinosa and Cooper reported the tin-rich family $RE_5T_{5.5}Sn_{18}$ consisting of a *RE* or other metal such as Ca, Sr, or Th with the *T* metals Co, Ru, Rh and Ir.[55] Considerable attention has also been paid to compounds where *T* is a late second and third row transition metal such as Rh, Ir, Ru, which exhibit superconducting and/or interesting magnetic properties.[55] Among them, $Yb_5Ir_{5.5}Sn_{18}$ is the most interesting because of its structural diversity. The early work of Espinosa using powder XRD has pointed to at least five different structures, deriving from compositional variations created by the non-equilibrium conditions during synthesis. The observed phases were primitive cubic, tetragonal, face centered cubic, slightly distorted body centered cubic [Ir_3Sn_7 structure type] and an unidentified phase as well.[56]

The structural diversity of the $Yb_5Ir_{5.5}Sn_{18}$ compound and the continued interest in ytterbium based intermetallic compounds,[57] which is based on the valence flexibility of ytterbium, allowing it to adopt different or mixed oxidation states,[58] motivates the current work. During the investigations of the $Yb_5Ir_{5.5}Sn_{18}$ compound the compound $Yb_{6.6}Ir_6Sn_{16}$ has been discovered.

5.5.2. Results and Discussion

5.5.2.1. Structure Refinement

In the first step, the intense peaks in the powder XRD pattern of $Yb_{6.6}Ir_6Sn_{16}$ were considered and suggested that the compound crystallizes in the $Tb_5Rh_6Sn_{17}$ structure type.[59] The single crystal data of $Yb_{6.6}Ir_6Sn_{16}$ also showed a cubic cell and the systematic extinctions

were compatible with the space group $F\bar{4}3m$. Therefore, the atomic parameters of $Tb_5Rh_6Sn_{17}$ were taken as starting points to refine the structure using JANA2006[44] with anisotropic atomic displacement parameters for all atoms. As a check for the correct composition, the occupancy parameters were refined in a separate series of least-squares cycles. Similar to $Tb_5Rh_6Sn_{17}$, seven crystallographically different positions were found in the $Yb_{6.6}Ir_6Sn_{16}$ structure - two Yb atoms, one Ir atom and four Sn atoms. During isotropic refinement it was observed that the atomic displacement parameters of the Sn3 atoms were anomalously large (109(7) $Å^2x10^3$). Furthermore, the refinement was largely unsatisfactory, giving relatively high residuals (R_1 > 19%) and large electron density residuals (48-20 $eÅ^{-3}$) around the Ir and Sn atoms. The anomalous atomic displacement parameter could not be resolved by subsequent refinement of the occupancy parameters. All these features suggest crystallographic disorder associated with the Ir and Sn atoms. An attempt to mix with Ir and Sn atoms also did not improve the refinement of the structure in cubic $F\bar{4}3m$ space group. To resolve this, the weak reflections (Figure 5.5.1a and 5.5.1b) were also considered and a stable refinement for $Yb_{6.6}Ir_6Sn_{16}$ in the tetragonal space group $P4_2/mnc$ was accomplished. Even in the $P4_2/mnc$ refinement, disorder still exists in the Yb3 site in the form of with partial occupancy and a large isotropic displacement parameter.

The details of the data collection and crystallographic refinement of $Yb_{6.6}Ir_6Sn_{16}$ are given in Table 5.5.1. A list of the atomic positions, the isotropic displacement parameters, the anisotropic displacement parameters and the bond distances are available in the Tables 5.5.2 to 5.5.4.

5.5.2.2. Reaction Chemistry

The tetragonal phase of $Yb_{6.6}Ir_6Sn_{16}$ was synthesized in high yield from a reaction of ytterbium, iridium and tin and excess indium. The truncated cube-shaped single crystals were silver metallic in colour and up to 3 mm x 2 mm x 2 mm in size. They were stable in air and no decomposition was observed even after several months. Attempts to change the amount of tin in the reaction to look for other phases proposed by Espinosa and Cooper also resulted in the $Yb_{6.6}Ir_6Sn_{16}$ tetragonal phase, although extensive studies in this direction were not carried out. An SEM image of a typical polyhedral crystal of $Yb_{6.6}Ir_6Sn_{16}$ grown from the flux synthesis is shown in Figure 5.5.1c. Small amounts of $YbIrIn_2$ and residual In metal were

also found in the reaction mixture. HFIH of a stoichiometric mixture of the elements was also successful in producing the title compound.

Table 5.5.1. Crystal data and structure refinement for $Yb_{6.6}Ir_6Sn_{16}$ at 100(2) K.

Empirical formula	$Yb_{6.6}Ir_6Sn_{16}$
Formula weight	4187.1 g/mol
Wavelength	0.71073 Å
Crystal system	Tetragonal
Space group, Z	$P4_2/nmc$, 2
Unit cell dimensions	$a = b$ = 9.7105(7) Å, c = 13.7183(11) Å
Volume	1293.55(17) $Å^3$
Density (calculated)	10.76 g/cm^3
Absorption coefficient	69.38 mm^{-1}
F(000)	3444
Crystal size	0.080 x 0.061 x 0.046 mm^3
θ range for data collection	2.57 to 29.14°
Index ranges	$-13 \le h \le 13$, $-11 \le k \le 12$, $-18 \le l \le 18$
Reflections collected	9584
Refinement method	Full-matrix least-squares on F^2
Data / restraints / parameters	949 / 0 / 47
Goodness-of-fit	3.11
Final R indices [>2σ(I)]	R_{obs} = 0.0636, wR_{obs} = 0.1499
Largest diff. peak and hole	4.35 and -3.62 e·$Å^{-3}$

$R = \Sigma||F_o|-|F_c|| / \Sigma|F_o|$, $wR = \{\Sigma[w(|F_o|^2 - |F_c|^2)^2] / \Sigma[w(|F_o|^4)]\}^{1/2}$ and $w=1/(\sigma^2(I)+0.0016I^2)$

Table 5.5.2. Atomic coordinates ($x10^4$) and equivalent isotropic displacement parameters ($Å^2x10^3$) for $Yb_{6.6}Ir_6Sn_{16}$ at 100(2) K with estimated standard deviations in parentheses.

Label	*x*	*y*	*z*	Occupancy	U_{eq}*
Yb1	2500	7500	2500	1	6(1)
Yb2	4860(2)	2500	1180(1)	1	2(1)
Yb3	2500	2874(6)	9819(4)	0.393(9)	36(2)
Ir1	7500	2500	88(1)	1	2(1)
Ir2	5088(1)	88(1)	2500	1	2(1)
Sn1	7500	637(2)	1568(2)	1	4(1)
Sn2	5794(2)	4295(2)	9250(1)	1	5(1)
Sn3	2500	1002(2)	2576(2)	1	3(1)

*U_{eq} is defined as one third of the trace of the orthogonalized U_{ij} tensor.

Table 5.5.3. Anisotropic displacement parameters ($Å^2x10^3$) for $Yb_{6.6}Ir_6Sn_{16}$ at 100(2) K with estimated standard deviations in parentheses.

Label	U_{11}	U_{22}	U_{33}	U_{12}	U_{13}	U_{23}
Yb1	5(1)	5(1)	7(1)	0	0	0
Yb2	2(1)	1(1)	3(1)	0	0(1)	0
Yb3	48(4)	23(4)	37(4)	0	0	5(2)
Ir1	2(1)	1(1)	2(1)	0	0	0
Ir2	2(1)	2(1)	2(1)	0(1)	0(1)	0(1)
Sn1	4(1)	5(1)	3(1)	0	0	2(1)
Sn2	4(1)	7(1)	4(1)	2(1)	-2(1)	0(1)
Sn3	2(1)	3(1)	3(1)	0	0	2(1)

The anisotropic displacement factor exponent takes the form: $-2\pi^2[h^2a^{*2}U_{11} + ... + 2hka^*b^*U_{12}]$.

Table 5.5.4. Selected bond lengths [Å] for $Yb_{6.6}Ir_6Sn_{16}$ at 293(2) K with estimated standard deviations in parentheses.

Label	Distance	Label	Distance
Yb1-Sn2 x 8	3.3978(16)	Yb3-Sn3 x 2	3.422(6)
Yb1-Sn3 x 4	3.4024(19)	Ir1-Sn1 x 2	2.720(2)
Yb2-Yb3 x 2	2.979(4)	Ir1-Sn2 x 4	2.6655(19)
Yb2-Ir1	2.9695(15)	Ir2-Sn1 x 2	2.7204(12)
Yb2-Ir2 x 2	2.9681(9)	Ir2-Sn2 x 2	2.6628(14)
Yb2-Sn1 x 3	3.1825(18)	Ir2-Sn3 x 2	2.6676(10)
Yb2-Sn2 x 2	3.2978(18)	Sn2-Sn2	2.913(2)
Yb2-Sn2 x 2	3.231(2)	Sn2-Sn2	3.486(3)
Yb2-Sn3 x 2	3.322(2)	Sn2-Sn2	3.313(3)
Yb3-Yb3	0.727(8)	Sn2-Sn3	3.369(2)
Yb3-Sn1	3.289(6)	Sn2-Sn3	3.431(2)
Yb3-Sn2 x 2	3.454(5)	Sn3-Sn3	2.909(3)

5.5.2.3. Crystal Chemistry

The structure of $Yb_{6.6}Ir_6Sn_{16}$ is composed of a complex 3D $[Ir_6Sn_{16}]$ polyanionic network with cages hosting the Yb atoms, Figure 5.5.2. These polyhedral cages share edges defined by Ir and Sn atoms. Cooper observed five different phases in the Yb-Ir-Sn family: (a) primitive cubic, $P\bar{4}3m$ or $Pm\bar{3}n$ space group (a = 9.709 Å), (b) face centered cubic, $F\bar{4}3m$ space group (a = 13.751 Å), (c) tetragonal (a = 13.757 Å, c = 9.703 Å), (d) a phase

crystallizing in lower symmetry closely related to the Ir_3Sn_7 type structure and (e) an unknown phase.[11]

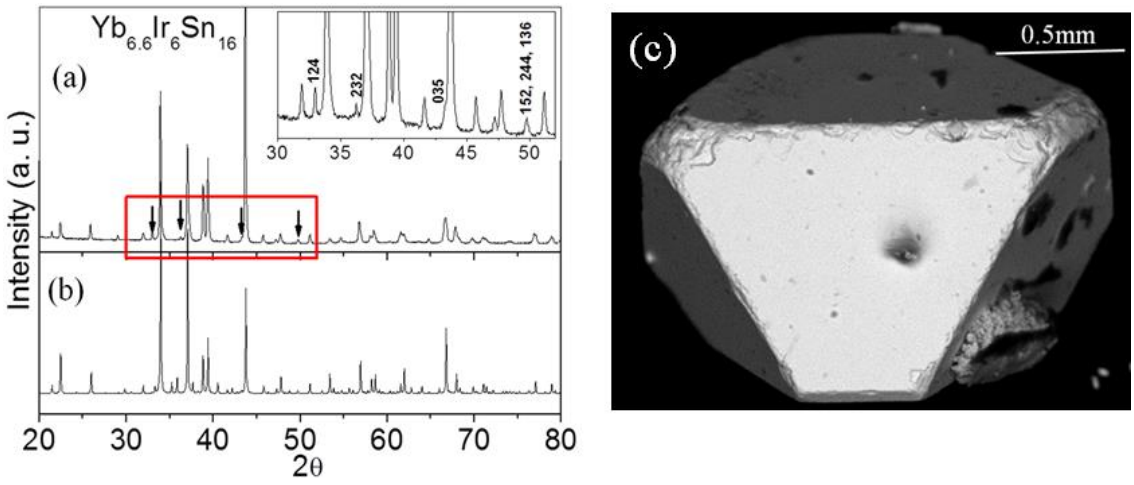

Figure 5.5.1. The experimental powder XRD pattern of $Yb_{6.6}Ir_6Sn_{16}$ (a) compared with the simulated pattern obtained from the single crystal XRD structure refinement (b). Inset is the expanded view marked with *hkl* indices corresponds to weak reflections in the tetragonal structure. (c) SEM image of typical single crystals of $Yb_{6.6}Ir_6Sn_{16}$

In this work, the crystal structure of $Yb_{6.6}Ir_6Sn_{16}$ was refined within the tetragonal system. By considering the fact that the lattice constants of the tetragonal system are related to the cubic lattice constants by a factor of the square root of 2 (9.709 x $\sqrt{2}$ = 13.69 Å), $Yb_{6.6}Ir_6Sn_{16}$ and those reported by Cooper are either closely related or they are one and the same. A schematic representation of the relation between the tetragonal $Yb_{6.6}Ir_6Sn_{16}$ and the cubic model (Cooper reported the composition as $Yb_5Ir_{5.5}Sn_{18}$)[11] is shown in Figure 5.5.3 and the crystal structures in both symmetries along the *c*-axis are shown in Figure 5.5.4. The crystal structure of $Yb_{6.6}Ir_6Sn_{16}$ in the cubic system has seven crystallographically distinct positions. Two Yb atoms occupy the 16*e* and 4*a* Wyckoff sites with point symmetry .3*m* and $\bar{4}3m$, one Ir atom occupies the 24*f* Wyckoff site with point symmetry 2.*mm*, and four Sn atoms occupy 48*h*, 16*e*, 4*c* and 4*d* Wyckoff sites with point symmetries of ..*m*, .3*m*, $\bar{4}3m$ and $\bar{4}3m$, respectively. In the tetragonal compound ($Yb_{6.6}Ir_6Sn_{16}$), three distinct Yb atoms occupy Wyckoff positions 2*a*, 8*g* and 8*g* with point symmetry $\bar{4}m2$, *.m.* and *.m.* One of the 8*g* positions is partially occupied. One Ir and four Sn in the cubic structure rearrange to two Ir atoms occupying the 4*c* and 8*f* Wyckoff sites of point symmetry 2*mm.* and ..2, respectively, and three Sn atoms occupying Wyckoff positions 8*g*, 16*h* and 8*g* of point symmetry *.m.*, 1 and *.m.*, respectively. The full stoichiometry of this structure type is

$Yb_9Ir_6Sn_{16}$. The fact that the single crystal refinement gives only $Yb_{6.6}Ir_6Sn_{16}$ suggests a very large number of Yb3 vacancies in the lattice. The crystal structures in both compounds ($Yb_5Ir_{5.5}Sn_{18}$ and $Yb_{6.6}Ir_6Sn_{16}$) are closely related to each other in terms of the arrangement of atoms.

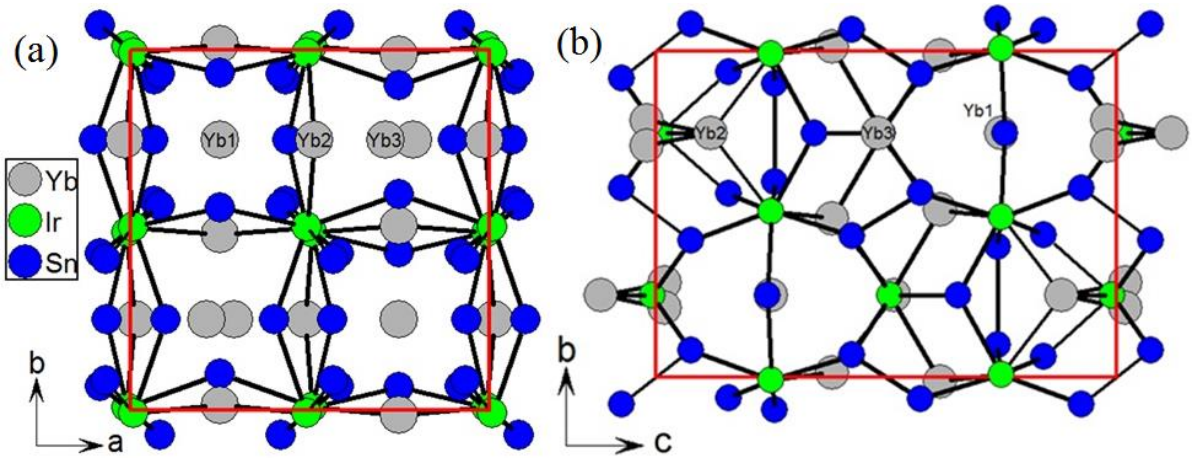

Figure 5.5.2. The crystal structure of $Yb_{6.6}Ir_6Sn_{16}$ as viewed along the *c*-axis (a) and *a*-axis (b). The unit cell outlined with thick red lines.

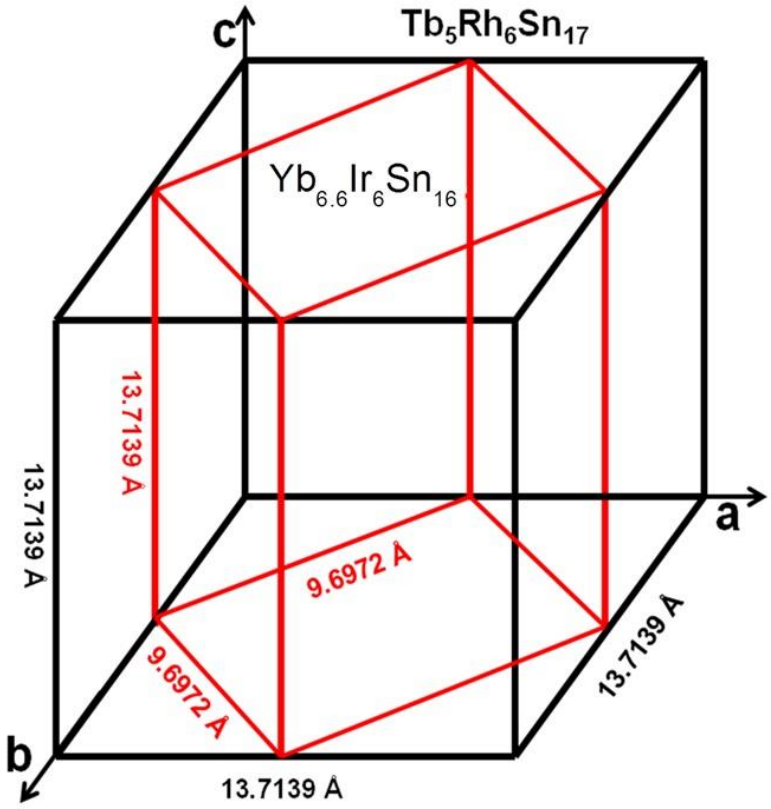

Figure 5.5.3. Relationship between the cubic ($Tb_5Rh_6Sn_{17}$) and tetragonal ($Yb_{6.6}Ir_6Sn_{16}$) unit cells.

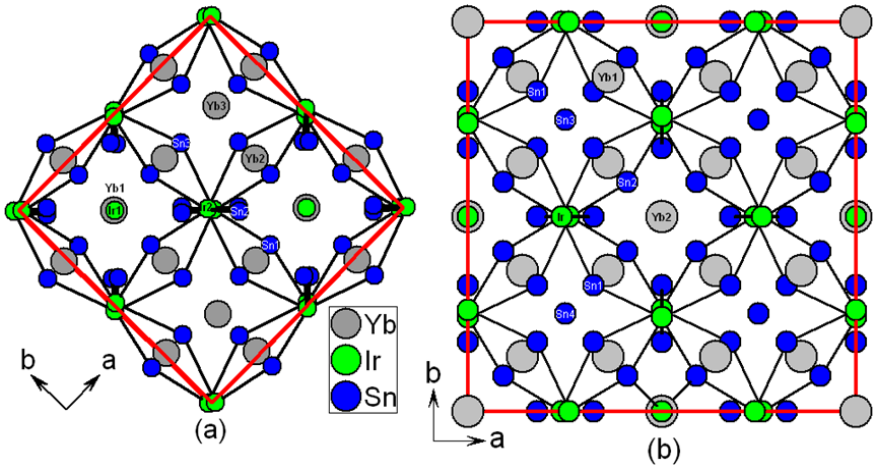

Figure 5.5.4. Structural comparison between tetragonal $Yb_{6.6}Ir_6Sn_{16}$ and reported cubic $Yb_5Ir_{5.5}Sn_{18}$ ($Tb_5Rh_6Sn_{17}$ structure type) compounds.

As shown in Figure 5.5.5, both structures are formed by the interconnection of large cage type structure made up of 14 Ir atoms and 20 Sn atoms. Both compounds contain Ir_4Sn_4 and Ir_6Sn_{12} units connected through the Ir atoms. Some notable differences between the two structures include that the Sn3 atom in the cubic system is instead Yb3 in the tetragonal structure. The Ir atoms split into two atomic sites in the tetragonal system, and a slight distortion in the Ir_4Sn_{12} unit results in the reduction of symmetry from cubic to tetragonal. Ir_4Sn_4 and Ir_4Sn_{12} units are connected through the Ir atoms with two Ir-Sn1 bonds (2.6994 Å and 2.7204(12) Å for $Yb_5Ir_{5.5}Sn_{18}$ and $Yb_{6.6}Ir_6Sn_{16}$, respectively) and two Ir-Sn2 bonds (2.7097 Å and 2.6655(19) Å for $Yb_5Ir_{5.5}Sn_{18}$ and $Yb_{6.6}Ir_6Sn_{16}$, respectively).

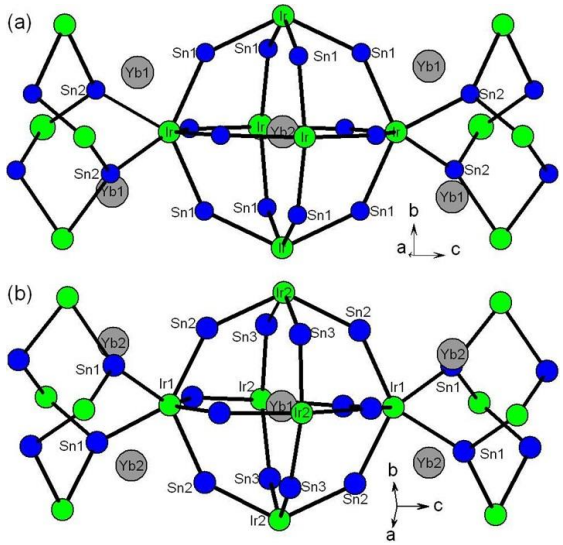

Figure 5.5.5. Structural unit comparison in the compounds (a) reported cubic $Yb_5Ir_{5.5}Sn_{18}$ [11] and (b) tetragonal $Yb_{6.6}Ir_6Sn_{16}$.

The local coordination environments of Yb, Ir and Sn atoms (within the limiting sphere of 4 Å) are presented in Figure 5.5.6.

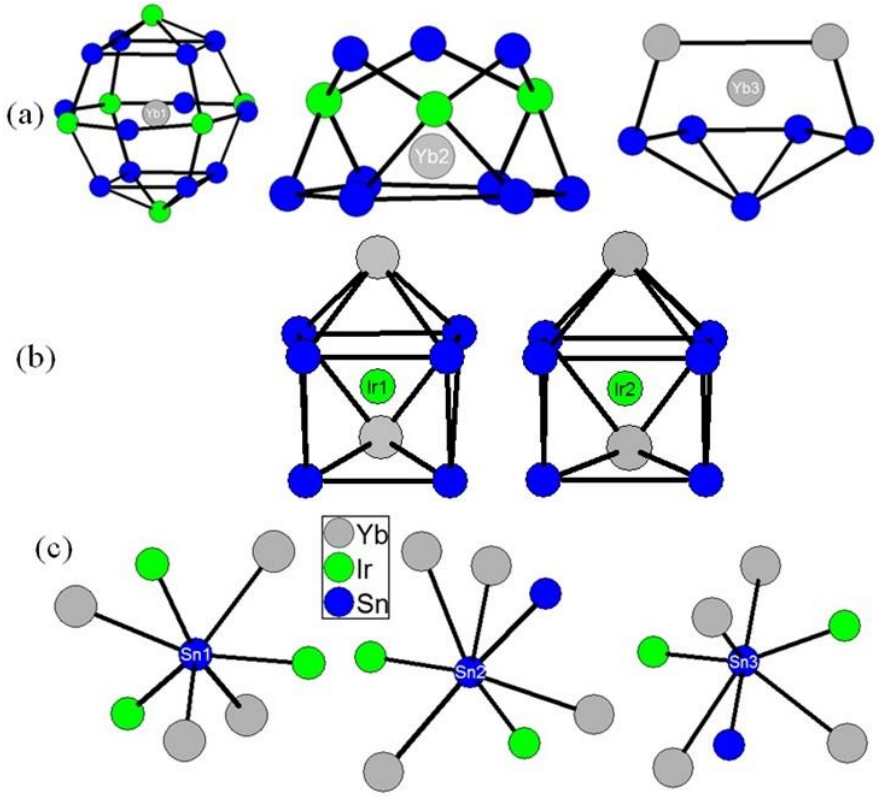

Figure 5.5.6. The coordination environment of (a) Yb, (b) Ir and (c) Sn atoms in the crystal structure of $Yb_{6.6}Ir_6Sn_{16}$.

The Yb1 atom is located at the center of a cage consisting of twelve Sn and six Ir atoms [$Yb[Sn_{12}Ir_6]$], while the Yb2 atom is surrounded by three Ir and nine Sn atoms. The disordered atom Yb3 alternates with vacancies in the lattice and has a coordination environment consisting of seven atoms comprised of two Yb and five Sn atoms. The Yb-Ir bond lengths vary from 2.9681(9) Å to 3.4024(19) Å and Yb-Sn distances are also vary from 3.1825(18) Å to 3.454(5) Å. The shortest Yb-Ir bond distance of 2.9681(9) Å is normal and comparable to that observed in Yb_2IrGe_2 (2.970 Å).[60] Similarly, the shortest Yb-Sn bond distance 3.1825(18) Å is comparable to the distance in $YbBaSn_3$ (3.153 Å).[60] Interestingly, the Yb1 atoms are located in much larger cages than other Yb atoms with corresponding Yb1-Ir and Yb1-Sn average distance of 3.5525Å and 3.4001 Å, respectively, suggest weaker interactions with the Ir and Sn atoms. Both Ir atoms are in the same coordination environment of tricapped triangular prism with a coordination number of nine (Figure

5.5.6b). The Sn atoms form the triangular prism with three Yb capped at three faces. All three Sn atoms are tri-coordinate and have trigonal planar (Figure 5.5.6c). Though the triangular geometry of Sn atom is not common, but it was reported in the $YbBaSn_3$ compound.[61]

5.5.2.4. Magnetism

The molar magnetic susceptibility ($\chi_m = M/H$) of $Yb_{6.6}Ir_6Sn_{16}$ measured in a field of 5 kOe is shown in Figure 5.5.7. With decreasing temperature, χ_m increases and exhibits no magnetic ordering down to 2 K. The behaviour of $\chi_m(T)$ in the temperature range 75-300 K follows the CW law. The inset of Figure 5.5.7 shows the plot of $\chi_m^{-1}(T)$. The straight line passing through the data points is the fit to the CW law with a Weiss constant of -9.5 K. The negative sign indicates predominantly antiferromagnetic interactions. The calculated effective magnetic moment, μ_{eff} is 3.21 μ_B/ Yb ion (or 8.22 μ_B/fu), which is about 70% of the expected value for a free ion Yb^{3+} (calculated as $\mu_{eff} = gJ[\sqrt{J(J+1)}]$, for g = 8/7, J = 7/2, L = 3 and S = ½). Assuming that the Ir and Sn atoms do not possess a magnetic moment, the observed magnetism in this compound suggests the presence of mixed valence Yb atoms.

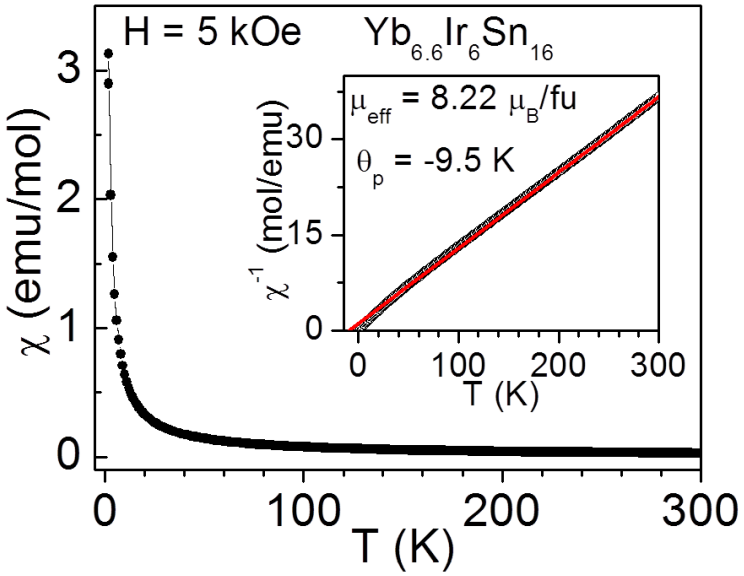

Figure 5.5.7. Magnetic susceptibility ($\chi = M/H$) of $Yb_{6.6}Ir_6Sn_{16}$ measured in a field of 5 kOe is plotted as a function of temperature. The inset exhibits the plot of $\chi^{-1}(T)$. The values of paramagnetic Curie temperature (θ_p) and effective Bohr magneton number (μ_{eff}) calculated from the slope and intercept obtained from the linear region of the $\chi^{-1}(T)$ plot are also shown in the figure. The magnetic susceptibility can be converted to SI units using the conversion factor $4\pi \times 10^{-6}$ m^3/mol; the magnetic field strength in oersted can be converted into SI units using the conversion $(10^3/4\pi)$ A/m.

5.5.2.5. XANES

To further probe the Yb valence state in $Yb_{6.6}Ir_6Sn_{16}$, the X-ray absorption measurements were performed at the Yb L_{III}-edge, at 300 K and ambient pressure (Figure 5.5.8). The main absorption peak (white line resonance) of the spectrum is centered at ~8947.5 eV, which is attributed to trivalent Yb atoms.[61, 62] The spectra also revealed the presence of a weaker feature (shoulder) at ~8939.5 eV, revealing unequivocally that some divalent Yb is also present.[61, 62] Since more than one Yb crystallographic sites are present in $Yb_{6.6}Ir_6Sn_{16,}$ the compound can be classified as either as an intermediate valence compound with all Yb atoms having a non-integer valence or heterogeneous mixed-valence compound, in which specific Yb atoms are either exactly 2+ or 3+.

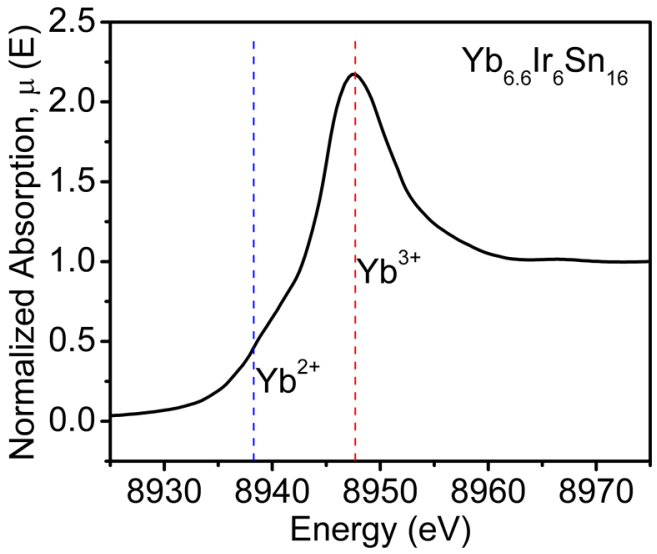

Figure 5.5.8. Yb L_{III} absorption edge spectra in $Yb_{6.6}Ir_6Sn_{16}$ at 300 K.

The relative amounts of the two electronic configurations were estimated by decomposing the normalized Yb XANES into a pair of arc-tangents (representing the edge step) and Lorentzian functions (representing the white line resonance).[63] Fitting of the data with the above technique resulted in ~88% Yb^{3+} and ~12% Yb^{2+} which corresponds to an average Yb valence of ~2.88. Comparison of the real part of the EXAFS Fourier transform suggests the possible presence of ~5% of the Yb^{3+} oxide impurity as well. Due to this oxide impurity, one can believe that the actual intrinsic valence of Yb in the sample is perhaps closer to 2.80. This value is in reasonable agreement with magnetic measurements. The uncertainty in the absolute valence is ~5%, arising from correlations between parameters

used to represent the edge-step and white line resonances and from systematic errors due to fitting-model dependence.

5.5.2.6. Electrical resistivity and heat capacity

The temperature dependent resistivity data of polycrystalline sample of $Yb_{6.6}Ir_6Sn_{16}$ is shown in Figure 5.5.9a. The resistivity decreases with decreasing temperature, typical for metallic systems.[64] The absolute resistivity value of $Yb_{6.6}Ir_6Sn_{16}$ at 303 K is 650 $\mu\Omega$cm, which is typical of a poor metal a feature, which may be related to strong scattering from the Yb site vacancies in the lattice. Temperature dependent heat capacity (C_p) of $Yb_{6.6}Ir_6Sn_{16}$ was measured in the range 1.8 K < T < 30 K using a commercial QD-PPMS. The data were obtained under standard thermal relaxation methods in a zero magnetic field. The temperature-dependent molar specific heat for $Yb_{6.6}Ir_6Sn_{16}$ sample is shown in Figure 5.5.9b. Below 7 K, C_p reaches a minimum and on further reduction in temperature, there is a sudden increase in C_p (which is more clearly seen in the case of C_p/T vs. T^2). Assuming the Debye low temperature approximation, the measured specific heat can be given as:

$$C_p = \gamma T + \beta T^3 \text{ or } C/T = \gamma + \beta T^2 \quad (1)$$

Where, γ is the charge carrier contribution also known as Sommerfeld parameter, and β is the lattice contribution. Owing to the upturn in the plot of C/T *vs.* T^2 at lower temperatures, the electronic specific heat capacity coefficient has been calculated for a higher temperature range ($100<T^2<200$). The γ value (47 mJ $mol^{-1}K^{-2}$) obtained from the fitting is low to rule in any heavy fermion behaviour in $Yb_{6.6}Ir_6Sn_{16}$. In the absence of a non-magnetic counterpart of $Yb_{6.6}Ir_6Sn_{16}$, it was not possible to quantify the magnetic part of the specific heat.

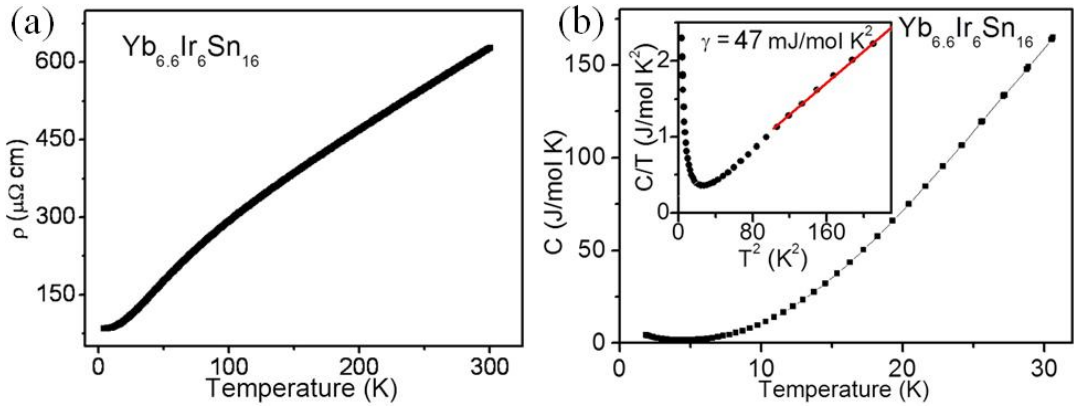

Figure 5.5.9. (a) Resistivity (ρ) measured as a function of temperature at zero applied field and (b) Molar specific heat (C_p) of $Yb_{6.6}Ir_6Sn_{16}$. The top inset shows the plot of C_p/T vs. T^2.

5.6. Crystal Growth, Structure and Magnetic Properties of $Sm_3Ni_5Al_{19}$: A Compound in the $Sm_{2n+m}Ni_{4n+m}Al_{15n+4m}$ Homologous Series

5.6.1. Introduction

During the systematic work on *RE*-Ni-Al phases, $Sm_3Ni_5Al_{19}$ was obtained as large rod shaped single crystals. A few compounds already reported in the Sm-Ni-Al family: Wang et al. reported that the hydrogenation and field cooling lead to an abnormal diamagnetism in SmNiAl and its hydride,[65] Takeshita et al. reported the hydrogenation of *RE*Ni_4Al (*RE* = La, Ce, Pr, Nd, Sm, Gd, Tb, Dy, Ho, Er and Tm) at moderate pressure and ambient temperature.[66] Other compounds reported in the family are $Sm_3Ni_6Al_2$,[67] Sm_2Ni_2Al,[68] SmNiAl[69] $SmNiAl_2$[70] $SmNiAl_4$[71] and $Sm_4Ni_6Al_{23}$[72] only for the their brief XRD studies. The detailed search on different databases including PCD[73] and ICSD[74] suggest that $Sm_3Ni_5Al_{19}$ was not reported. However, Delsante et al. proposed the existence of $Sm_3Ni_5Al_{19}$ by preliminary XRD and EPMA.[75] Apart that, no report about this compound is available in the literature. The compounds in the family $RE_3Ni_5Al_{19}$ with other *RE*s (Y, Gd-Lu) were reported in the past.[75, 76] All these compounds crystallize in the orthorhombic *Cmcm* space group with *RE* atoms in the trivalent state except Yb, which exists in the mixed valent state.

The single crystals of $Sm_3Ni_5Al_{19}$ were obtained from the excess aluminium metal. The crystal structure of $Sm_3Ni_5Al_{19}$ has refined using single crystal XRD data. $Sm_3Ni_5Al_{19}$ is classified as a member in the $RE_{2n+m}Ni_{4n+m}Al_{15n+4m}$ homologous series. The structure relation between $Sm_3Ni_5Al_{19}$ and other members in the homologous series $SmNiAl_4$ and $Sm_4Ni_6Al_{23}$ is explained in detail. After establishing the crystal structure, $Sm_3Ni_5Al_{19}$ was successfully synthesized using arc melting technique as well. The phase purity of these compounds was checked by powder XRD and microstructure analysis. The magnetic susceptibility measurements suggest trivalent Sm with a weak antiferromagnetic ordering at 18 K.

5.6.2. Results and Discussion

5.6.2.1. Reaction Chemistry

The EDAX analyses were performed on visibly clean surfaces of the single crystals (Figure 5.6.1) obtained from the flux method indicated that the atomic composition was close to 3:5:19, which is in good agreement with the composition obtained from the single crystal X-ray data refinement.

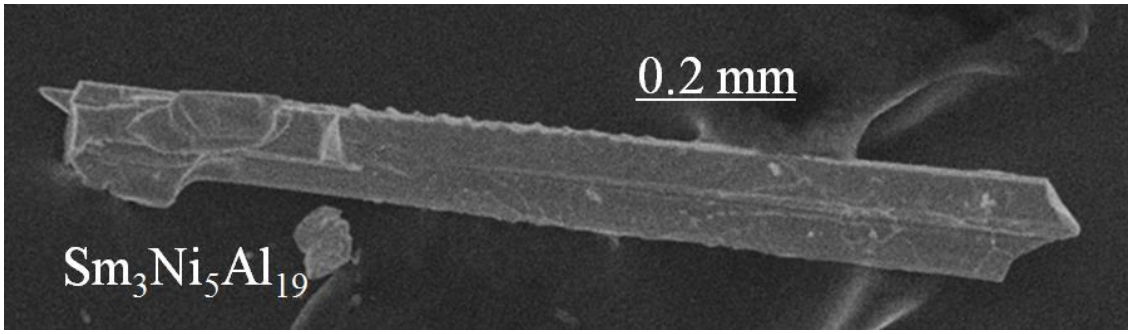

Figure 5.6.1. Typical SEM image of $Sm_3Ni_5Al_{19}$ single crystal grown from the active aluminum flux.

The experimental powder pattern of $Sm_3Ni_5Al_{19}$ was found to be in good agreement with the pattern calculated from the single-crystal X-ray structure refinement with small amount of Ni_2Al_3 phase (Figure 5.6.2).

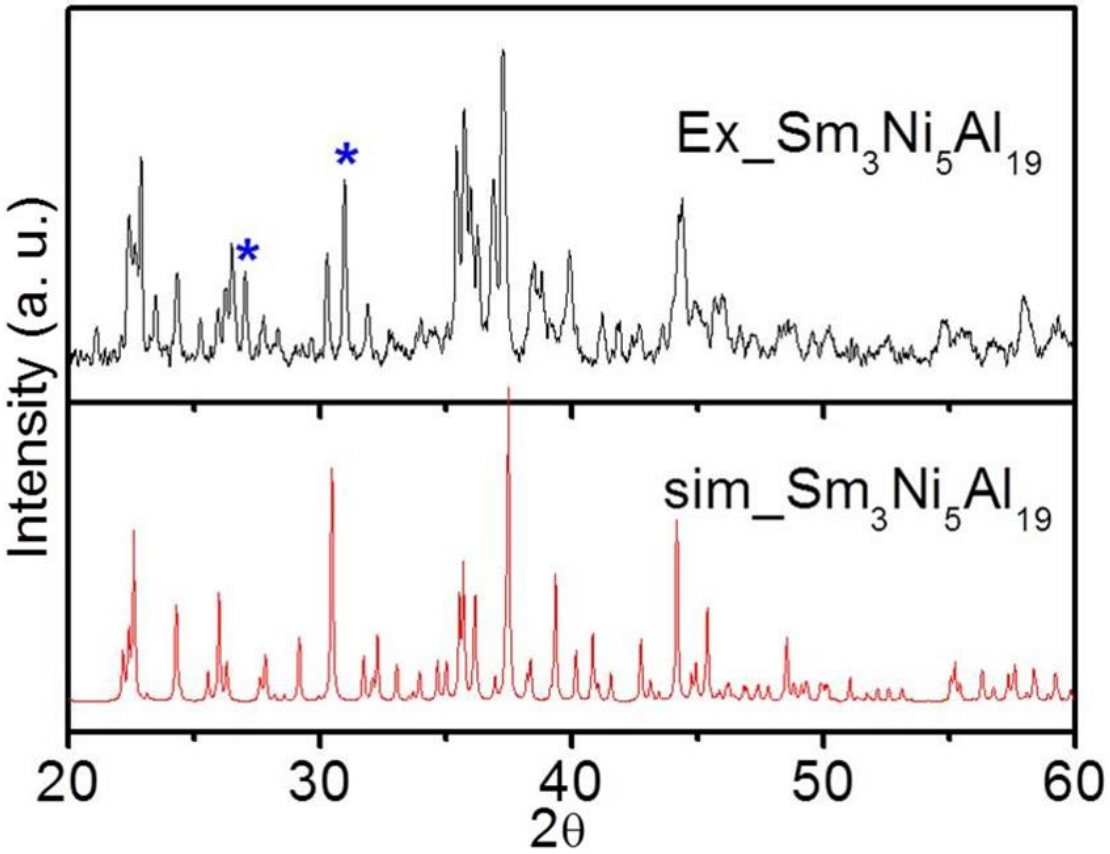

Figure 5.6.2. PXRD comparison of experimental $Sm_3Ni_5Al_{19}$ and simulated $Sm_3Ni_5Al_{19}$ (star marks corresponds to impurity peaks).

5.6.2.2. Structure Refinement

The structure of $Sm_3Ni_5Al_{19}$ was solved by SHELXS 97[77] and refined by a full matrix least-squares method using SHELXL[78] with anisotropic atomic displacement parameters for

all atoms. As a check for the correct composition, the occupancy parameters were refined in a separate series of least-squares cycles. Single crystals of $Sm_3Ni_5Al_{19}$ from different syntheses batches were used for the data collection. The lattice parameters of the $Gd_3Ni_5Al_{19}$ structure were taken at the initial step and the refinement resulted in fifteen crystallographic positions in the $Sm_3Ni_5Al_{19}$ structure; which are two samarium atoms, three nickel atoms and ten aluminium atoms. Among them, samarium atoms occupy 8*f* and 4*c* sites of point symmetry *m*.. and *m*2*m*, respectively, two nickel atoms occupy 8*f* sites (point symmetry *m*..), other nickel atom occupies 4*c* site (point symmetry *m*2*m*), nine aluminium atoms occupy the 8*f* sites (point symmetry *m*..) and one aluminium atom occupies 4*c* site (point symmetry *m*2*m*).

As a check for the correct composition, the occupancy parameters were refined in a separate series of least-squares cycles. All bond lengths are within the acceptable range compared to the theoretical values. Packing diagrams were generated with Diamond software.[79] The data collection and structure refinement for $Sm_3Ni_5Al_{19}$ are listed in Table 5.6.1. The standard atomic positions and isotropic atomic displacement parameters of this compound are collected in Table 5.6.2. The anisotropic displacement parameters and important bond lengths are listed in Tables 5.6.3 and 5.6.4, respectively. Further information on the structure refinements is available from Cambridge Crystallographic Data Centre by quoting the Registry No. CCDC 993911.

5.6.2.3. Crystal Chemistry

The reports on the compounds $RE_3Ni_5Al_{19}$ with rare earths *RE* = Y, Sm, Gd-Lu suggest that this composition is favored by small *RE*s.[75, 76] The absence of Eu in this series is probably due to the large size of divalent Eu atom, which suggests that in addition to size, the valency of *RE* also plays a crucial role in the formation of these compounds. The lattice parameters of all reported compounds in the $RE_3Ni_5Al_{19}$ are listed in Table 5.6.5 and cell volume against the rare earths is plotted in Figure 5.6.3. The decrease in cell volume from Sm to Lu corroborate with the lanthanide contraction and the deviation from the curve with a huge hump for Yb sample indicate the probable mixed valent behaviour of Yb, which is in fact reported by Bauer et al.[76]

$Sm_3Ni_5Al_{19}$ is one representative with largest volume in this family, which crystallizes in the orthorhombic $Gd_3Ni_5Al_{19}$ type structure (space group *Cmcm*) can be

considered as a member of the homologous series $Sm_{2n+m}Ni_{4n+m}Al_{15n+4m}$ (n = 1 and m = 1).[80] The crystal structure of $Sm_3Ni_5Al_{19}$ along the *a*-axis is shown in Figure 5.6.4. The structure can be explained as $nSm_2Ni_4Al_{15}$ slabs are intergrown with $mSmNiAl_4$ slabs along the *b*-axis. $SmNiAl_4$ slab in $Sm_3Ni_5Al_{19}$ is a Sm-centered pentagonal, while $Sm_2Ni_4Al_{15}$ slab contains two Ni-centered trigonal prisms, one Al-centered tetragonal prism and two Sm centered pentagonal prisms. The crystal structure of $Sm_3Ni_5Al_{19}$ can be compared with the other two members in the homologous series $SmNiAl_4$ (n = 0 and m = 1) and $Sm_4Ni_6Al_{23}$ (n = 1 and m = 2) as shown in Figure 5.6.5.

Table 5.6.1. Crystal data and structure refinement for $Sm_3Ni_5Al_{19}$ at 293(2) K.

Empirical formula	$Sm_3Ni_5Al_{19}$
Formula weight	1257.22
Wavelength	0.71073 Å
Crystal system	Orthorhombic
Space group	*Cmcm*
Unit cell dimensions	a = 4.0974(1) Å, b = 16.0172(6) Å c = 27.0774(10) Å
Volume	1777.06(10) $Å^3$
Z	4
Density (calculated)	4.7 g/cm^3
Absorption coefficient	15.85 mm^{-1}
F(000)	2291
Crystal size	0.05 x 0.05 x 0.10 mm^3
θ range for data collection	2.54 to 33.23°
Index ranges	-6<=*h*<=6, -24<=*k*<=23, -32<=*l*<=41
Reflections collected	16247
Independent reflections	1942 [R_{int} = 0.0368]
Completeness to θ = 32.17°	100%
Refinement method	Full-matrix least-squares on F^2
Data / restraints / parameters	1942 / 0 / 86
Goodness-of-fit	1.319
Final *R* indices [>2σ(I)]	R_{obs} = 0.018, wR_{obs} = 0.034
Extinction coefficient	0.004
Largest diff. peak and hole	1.358 and -2.129 e·$Å^{-3}$

$R = \Sigma||F_o|-|F_c|| / \Sigma|F_o|$, $wR = \{\Sigma[w(|F_o|^2 - |F_c|^2)^2] / \Sigma[w(|F_o|^4)]\}^{1/2}$ and calcw=$1/[\sigma^2(Fo^2)+(0.0359P)^2+6.1794P]$ where $P = (Fo^2+2Fc^2)/3$

Table 5.6.2. Atomic coordinates ($x10^4$) and equivalent isotropic displacement parameters ($Å^2x10^3$) for $Sm_3Ni_5Al_{19}$ at 296(2) K with estimated standard deviations in parentheses

Label	Wyckoff site	*x*	*y*	*Z*	Occupancy	U_{eq}*
Sm1	8*f*	0	1659(1)	1352(1)	1	5(1)
Sm2	4*c*	0	3863(2)	2500	1	6(1)
Ni1	8*f*	0	532(4)	5835(2)	1	7(1)
Ni2	8*f*	0	3405(3)	5418(2)	1	5(1)
Ni3	4*c*	0	451(5)	2500	1	61)
Al1	8*f*	0	355(9)	6737(5)	1	9(1)
Al2	8*f*	0	678(9)	304(5)	1	8(1)
Al3	8*f*	0	2084(9)	5883(5)	1	7(1)
Al4	8*f*	0	2242(9)	6932(5)	1	9(1)
Al5	8*f*	0	2344(9)	284(5)	1	7(1)
Al6	8*f*	0	3701(9)	1348(5)	1	9(1)
Al7	8*f*	0	4051(9)	370(5)	1	9(1)
Al8	8*f*	0	5362(9)	1001(5)	1	8(1)
Al9	8*f*	0	5779(9)	2018(5)	1	8(1)
Al10	4*f*	0	1930(12)	2500	1	9(1)

*U_{eq} is defined as one third of the trace of the orthogonalized U_{ij} tensor.

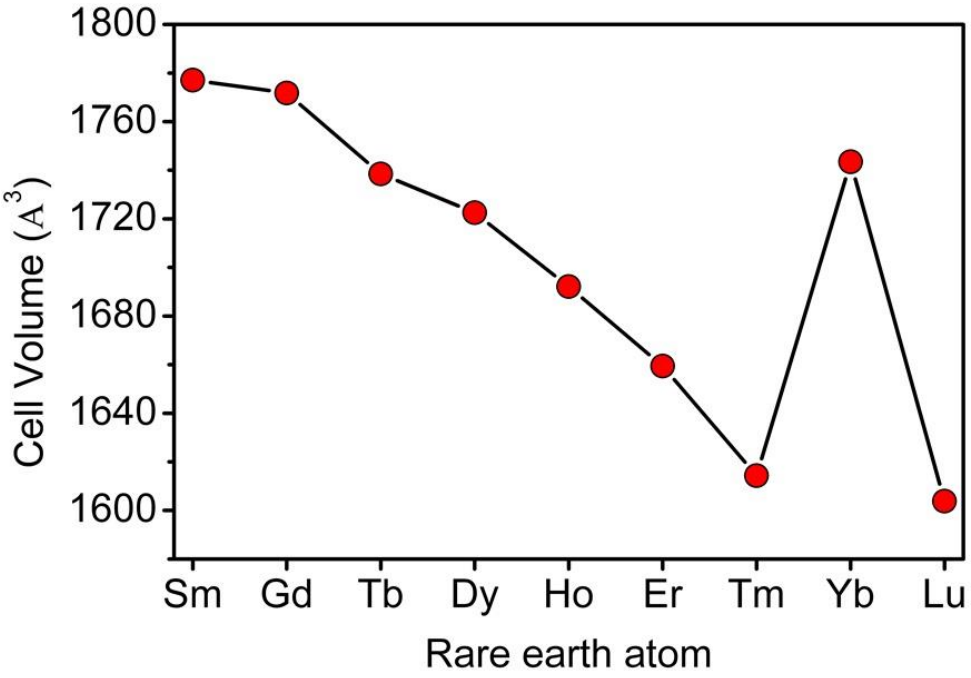

Figure 5.6.3. The cell volume ($Å^3$) of the compounds reported in the $RE_3Ni_5Al_{19}$ (*RE* = Sm, Gd-Lu) plotted against the *RE* atoms.

$SmNiAl_4$ [71] is an orthorhombic system crystallizes in the $YNiAl_4$ [81] type structure with *Cmcm* space group, while, $Sm_4Ni_6Al_{23}$ [72] is a monoclinic system crystallizes in the $Y_4Ni_6Al_{23}$ [82, 83] structure type with space group *C*2/*m*. The compounds with m is odd (m = 1, 3 etc.) adopt orthorhombic structure and m is even (m = 0, 2 etc.) adopt the monoclinic structure. $SmNiAl_4$ contains two $SmNiAl_4$ slabs rotated by 180° with respect to each other. On the other hand $Sm_4Ni_6Al_{23}$ contains two $SmNiAl_4$ and one $Sm_2Ni_4Al_{15}$ slabs intergrown similar in $Sm_3Ni_5Al_{19}$. The bond angles in all three compounds are very close. As an example the Al-Ni-Al bond angle in $SmNiAl_4$ slabs of $SmNiAl_4$, $Sm_3Ni_5Al_{19}$ and $Sm_4Ni_6Al_{23}$ are 113.28°, 110.62° and 114.87°, respectively, and Al-Sm-Al bond angles in trigonal prisms are 46.66°, 49.76° and 49.46° for $SmNiAl_4$, $Sm_3Ni_5Al_{19}$ and $Sm_4Ni_6Al_{23}$, respectively.

Table 5.6.3. Anisotropic displacement parameters ($Å^2x10^3$) for $Sm_3Ni_5Al_{19}$ at 293(2) K with estimated standard deviations in parentheses

Label	U_{11}	U_{22}	U_{33}	U_{12}	U_{13}	U_{23}
Sm1	6(1)	5(1)	5(1)	0	0	0
Sm2	7(1)	6(1)	5(1)	0	0	0
Ni1	8(2)	6(1)	8(1)	0	0	0
Ni2	6(2)	5(2)	5(2)	0	0	0
Ni3	7(3)	6(3)	5(3)	0	0	0
Al1	10(5)	9(1)	7(6)	0	0	1(1)
Al2	9(5)	6(1)	10(1)	0	0	0
Al3	9(5)	6(1)	7(6)	0	0	1(1)
Al4	9(5)	11(6)	8(6)	0	0	2(1)
Al5	7(5)	8(6)	7(6)	0	0	2(1)
Al6	10(6)	8(6)	8(6)	0	0	0
Al7	11(5)	10(6)	6(1)	0	0	-2(1)
Al8	8(5)	7(6)	9(6)	0	0	0
Al9	7(5)	13(6)	5(3)	0	0	1(1)
Al10	12(8)	7(1)	7(1)	0	0	0

The anisotropic displacement factor exponent takes the form: $-2\pi^2 [h^2a^{*2}U_{11} + ... + 2hka^*b^*U_{12}]$.

The local coordination environments of all Sm and Ni atoms in the compounds $SmNiAl_4$, $Sm_3Ni_5Al_{19}$ and $Sm_4Ni_6Al_{23}$ are presented in Figure 5.6.6. Sm and Ni coordination sphere of all three compounds are very similar. Noticeably the coordination sphere of Ni2 and Ni3 are interchanged in $Sm_3Ni_5Al_{19}$ and $Sm_4Ni_6Al_{23}$ if standard atomic coordinates are

taken from the literature. The coordination environments of all Sm atoms are surrounded with 13 aluminium and 2 nickel atoms. The coordination environment of Ni, Ni3 and Ni2 in $SmNiAl_4$, $Sm_3Ni_5Al_{19}$ and $Sm_4Ni_6Al_{23}$, respectively, are similar with seven Al and two Sm neighboring atoms. The coordination environment of Ni1, Ni2 in $Sm_3Ni_5Al_{19}$ and Ni1, Ni3 in $Sm_4Ni_6Al_{23}$ are similar surrounded with ten Al atoms and Ni2 in $Sm_3Ni_5Al_{19}$ and Ni3 in $Sm_4Ni_6Al_{23}$ are similar surrounded with eight Al and two Sm atoms. Such similarity in the coordination environment is also observed for the Al atoms in all three structures.

Table 5.6.4. Selected bond lengths [Å] for $Sm_3Ni_5Al_{19}$ at 293(2) K with estimated standard deviations in parentheses

Label	Distances	Label	Distances
Sm1—Al1	3.3909(15)	Ni2—Al7	2.3751(15)
Sm1—Al2	3.2438(14)	Ni2—Al8	2.5277(15)
Sm1—Al3	3.1403(11)	Ni3—Al1	2.4360(15)
Sm1—Al4	3.1239(11)	Ni3—Al9	2.4847(8)
Sm1—Al5	3.0934(14)	Ni3—Al10	2.370(2)
Sm1—Al8	3.068(1)	Al1—Al6	2.7551(13)
Sm1—Al9	3.0723(11)	Al1—Al9	2.8421(14)
Sm1—Al10	3.1379(4)	Al2—Al2	2.727(3)
Sm1—Ni2	3.2555(2)	Al2—Al5	2.6697(19)
Sm2—Al1	3.1671(11)	Al2—Al7	2.7794(14)
Sm2—Al4	3.1139(11)	Al2—Al8	2.8320(14)
Sm2—Al6	3.1298(14)	Al3—Al4	2.853(2)
Sm2—Al10	3.096(2)	Al3—Al5	2.7683(13)
Sm2—Ni3	3.2655(7)	Al3—Al6	2.7141(13)
Ni1—Al1	2.4568(15)	Al4—Al6	2.9979(15)
Ni1—Al2	2.4143(15)	Al4—Al10	2.8833(14)
Ni1—Al3	2.4893(15)	Al5—Al5	2.6102(17)
Ni1—Al6	2.7619(10)	Al5—Al7	2.745(2)
Ni1—Al7	2.4956(9)	Al6—Al7	2.705(2)
Ni1—Al8	2.5402(9)	Al6—Al8	2.821(2)
Ni2—Al2	2.5394(9)	Al7—Al8	2.707(2)
Ni2—Al3	2.4613(15)	Al8—Al9	2.832(2)
Ni2—Al5	2.5511(15)	Al9—Al9	2.608(3)
Ni2—Al5	2.4025(8)		

The shortest and largest bond distances of Sm-Al in $Sm_3Ni_5Al_{19}$ 3.068(1) Å and 3.391(2) Å, respectively, are comparable with the distances in $SmNiAl_4$ (3.022 Å and 3.358 Å) and in $Sm_4Ni_6Al_{24}$ (3.06 Å and 3.381 Å).[71] Similarly the shortest Sm-Ni bond distance of 3.2555 Å in $Sm_3Ni_5Al_{19}$ also similar in the compounds $SmNiAl_4$ and $Sm_4Ni_6Al_{24}$ with the values 3.209 Å and 3.268 Å, respectively.[71]

Table 5.6.5. The lattice parameters (*a*, *b* and *c*) of all compounds reported in the $RE_3Ni_5Al_{19}$ (*RE* = Sm, Y, Gd-Lu) family

Compound name	*a* (Å)	*b* (Å)	*c* (Å)	reference
$Y_3Ni_5Al_{19}$	4.08	16.04	27.29	[84]
$Sm_3Ni_5Al_{19}$	4.09	16.01	27.07	[75]
$Sm_3Ni_5Al_{19}$	4.0974(1)	16.0172(6)	27.0774(10)	[This work]
$Gd_3Ni_5Al_{19}$	4.08	15.99	27.09	[80]
$Tb_3Ni_5Al_{19}$	4.035	15.91	27.08	[85]
$Dy_3Ni_5Al_{19}$	4.021	15.86	27.01	[85]
$Ho_3Ni_5Al_{19}$	3.991	15.75	26.92	[86]
$Er_3Ni_5Al_{19}$	3.960	15.63	26.81	[86]
$Tm_3Ni_5Al_{19}$	3.92	15.46	26.59	[87]
$Yb_3Ni_5Al_{19}$	4.06	15.90	26.98	[76]
$Lu_3Ni_5Al_{19}$	3.92	15.40	26.54	[87]

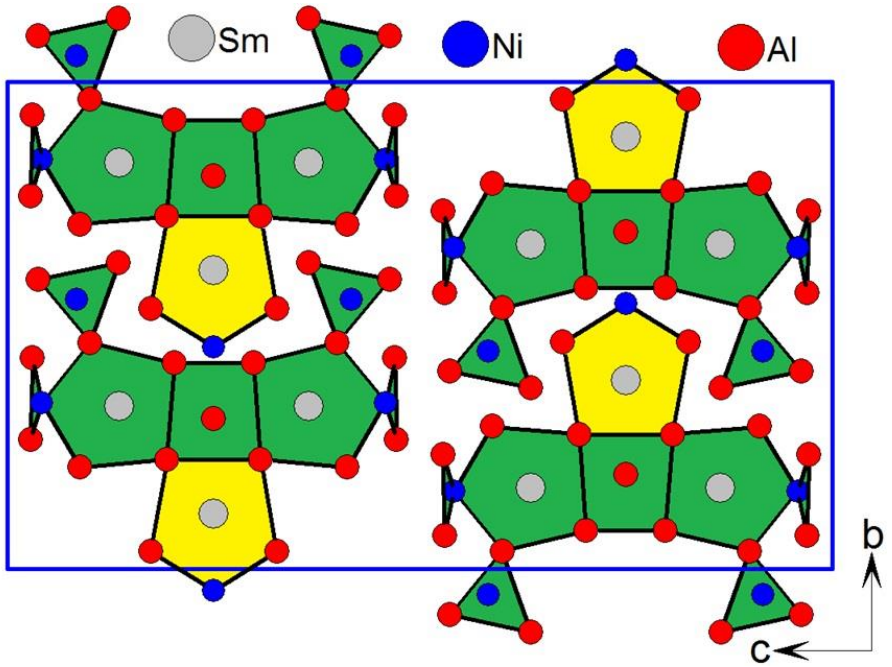

Figure 5.6.4. The crystal structure of $Sm_3Ni_5Al_{19}$ is shown along the *a*-axis. The two slabs $SmNiAl_4$ and $Sm_2Ni_4Al_{15}$ are shaded with yellow and green colours, respectively, intergrown along the *b*-axis.

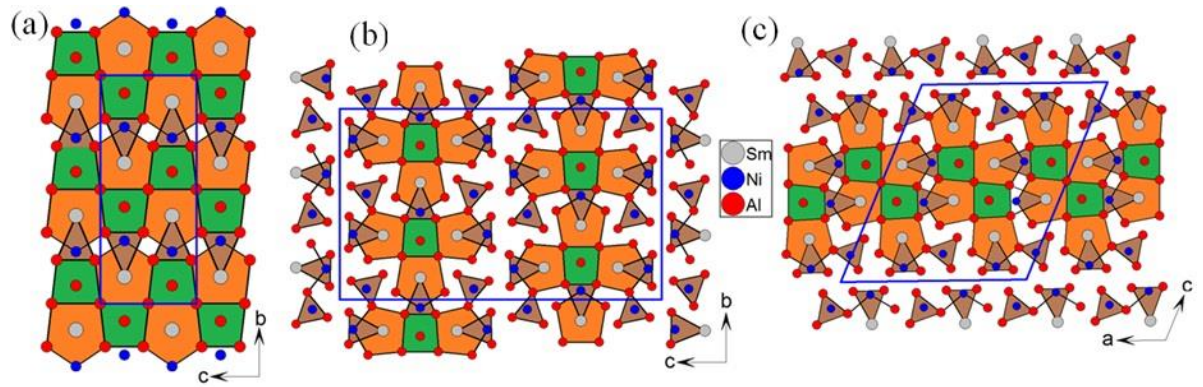

Figure 5.6.5. The crystal structures of (a) $SmNiAl_4$, (b) $Sm_3Ni_5Al_{19}$ and (c) $Sm_4Ni_6Al_{23}$. The pentagonal, tetragonal and trigonal prisms are shaded with orange, green and brown colours. The unit cell is outlined in solid blue line.

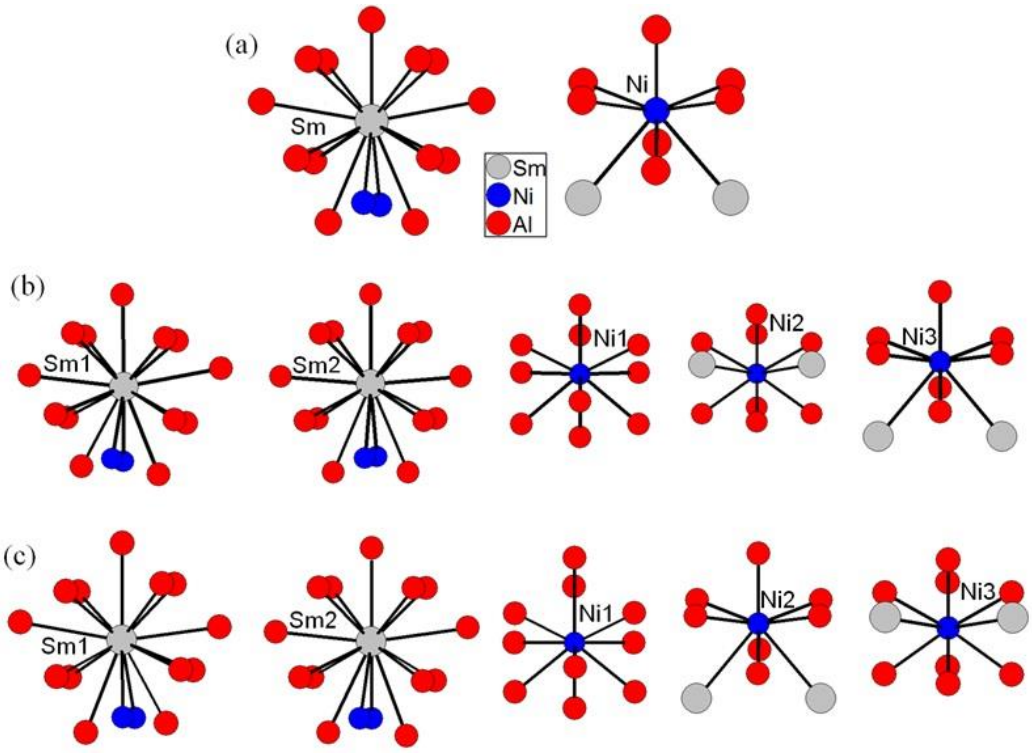

Figure 5.6.6. The coordination sphere of Sm and Ni atoms in (a) $SmNiAl_4$, (b) $Sm_3Ni_5Al_{19}$ and (c) $Sm_4Ni_6Al_{23}$.

5.6.2.4. Magnetic Properties

The temperature dependent magnetic susceptibility and modified inverse molar magnetic susceptibility of $Sm_3Ni_5Al_{19}$ at an applied field of 1000 Oe is shown in Figure 5.6.7a. The temperature dependent molar susceptibility (χ_m) of $Sm_3Ni_5Al_{19}$ obeys modified CW law, $\chi = C/(T-\theta) + \chi_0$ above 150 K with a weak antiferromagnetic ordering at 18 K. A CW fit in the temperature ranges 150-300 K gave the magnetic moments 2.25 μ_B per

formula.[88] The field dependence of the magnetization $M(H)$ for $Sm_3Ni_5Al_{19}$ ground samples were measured at 2 K and 300 K can be seen in Figure 5.6.7b. The data measured at 300 K exhibits linear behaviour and no signs of saturation up to highest attainable field of 60 kG. The magnetization curve taken at 2 K (within the magnetic ordering) shows a slight field dependent response up to ~ 30000 Oe, continues to rise slowly up to the highest obtainable field (60000 Oe).

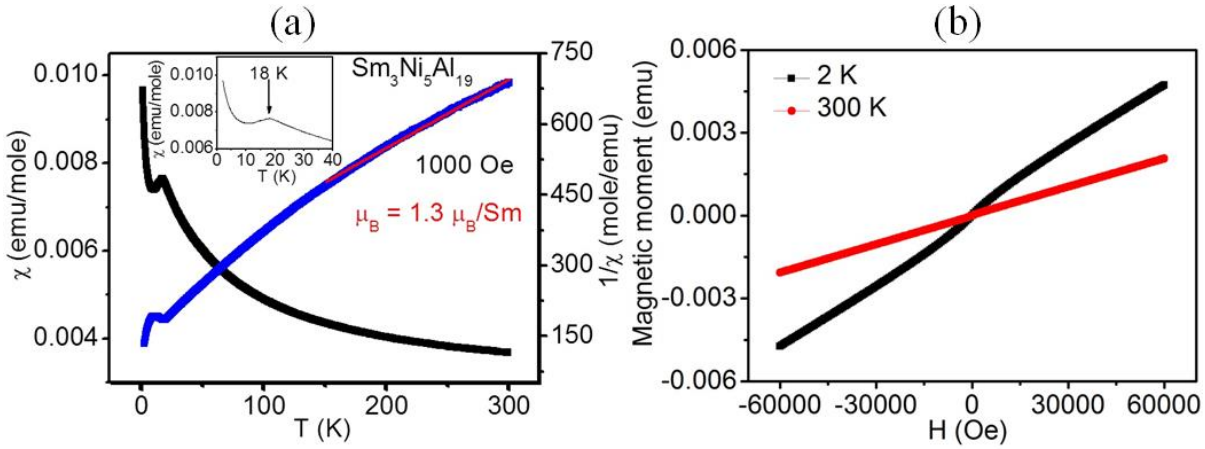

Figure 5.6.7. (a) Temperature dependence of the magnetic susceptibility (χ_m) and modified inverse magnetic susceptibility ($1/\chi_m$) of $Sm_3Ni_5Al_{19}$. The inset show antiferromagnetic like ordering at 18 K. (b) Magnetization as a function of applied magnetic field at 2 K and 300 K for a polycrystalline sample of $Sm_3Ni_5Al_{19}$.

5.7. $Yb_7Ni_4InGe_{12}$: A Quaternary Compound Having Mixed Valent Yb atoms Grown from Indium Flux

5.7.1. Introduction

During the systematic studies on the compounds in the Yb-Ni-Ge family, a new quaternary compound $Yb_7Ni_4InGe_{12}$ was obtained from the reaction run in In flux. There are several compounds reported in the Yb-Ni-Ge family; YbNiGe,[89] $YbNi_{0.25}Ge_{1.25}$,[89] $YbNiGe_2$,[90] $YbNiGe_3$,[89] $YbNi_2Ge_2$,[89] $YbNi_5Ge_3$,[89] $YbNi_{4.4}Ge_{0.6}$,[89] Yb_2NiGe_6,[91] $Yb_2Ni_{15.1}Ge_{1.9}$,[89] $Yb_3Ni_{11}Ge_4$[89] and $Yb_5Ni_4Ge_{10}$.[2] So far only a few quaternary polyindides with an impressive set of diverse structures and compositions have been synthesized using In as active solvent. Chondroudi et al. reported the quaternary compounds $RE_7Co_4InGe_{12}$ (*RE* = Dy, Ho, Yb),[92] which contains mixed-valent Yb and trivalent Dy and Ho. In this family, $Dy_4Ni_2InGe_4$, $Ho_4Ni_2InGe_4$ and $Er_4Ni_2InGe_4$ show antiferromagnetic transitions at low temperature. On other hand, $Tm_4Ni_2InGe_4$ has no magnetic ordering down to the lowest temperature attainable. $Yb_3AuGe_2In_3$ is another example having mixed valent Yb grown from In flux which crystallizes as an ordered variant of the YbAuIn structure.[93] Apart from these interesting compounds several quaternary indides worth mentioning are $REMn_2In_xZn_{20-x}$ (*RE* = Ce-Sm, Gd, Dy, Er, Yb),[94] $REMn_6InSn_5$ (*RE* = Ho, Tm),[95] $Ce_2NiPdIn$,[96] $CeNiX_3In$ (*X* = Al, Ga),[97] $RE_7Ni_{5-x}Ge_{3+x}In_6$ (*RE* = La, ND, Sm)[98] and CeCuAgIn.[99]

$Yb_7Ni_4InGe_{12}$ is a new quaternary compound isostructural to the $RE_7Co_4InGe_{12}$ family, which is closely related to the structure of $Yb_5Ni_4Ge_{10}$.[2] Magnetic susceptibility measurements were performed on the selected single crystals of $Yb_7Ni_4InGe_{12}$ suggests mixed valent behaviour of Yb atoms, which was confirmed by XANES measurement.

5.7.2. Results and Discussion

5.7.2.1. Reaction Chemistry

The new compound $Yb_7Ni_4InGe_{12}$ was discovered in a reaction that was run in indium flux with the ratio of Yb:Ni:Ge:In as 4:2:5:35. In addition to $Yb_7Ni_4InGe_{12}$, single crystals of Yb_2InGe_2[100] and $YbNiIn_2$[101] were also observed in small quantity. The amount of indium taken for the synthesis of these phases played a crucial role. While decreasing the amount of indium from 2.32 g to 1.99 g and then to 1.66 g, the compounds Yb_2InGe_2 and $YbNiIn_2$, respectively, were obtained as major products. Interestingly, in all these reactions indium acts

as reactive flux. On the other hand, as reported, the composition 5:4:10:45 for Yb:Ni:Ge:In favored in the formation of $Yb_5Ni_4Ge_{10}$ without the inclusion of the In atom into structure.[2] The attempts to synthesize the similar composition to $Yb_7Ni_4InGe_{12}$ with other *RE* metals were not successful. HFIH method was also not successful in preparing the pure phase of $Yb_7Ni_4InGe_{12}$. The single crystals of $Yb_7Ni_4InGe_{12}$ are metallic silver in colour and stable in air and no decomposition observed even after several months. A SEM image of typical single crystals of $Yb_7Ni_4InGe_{12}$ is shown in Figure 5.7.1.

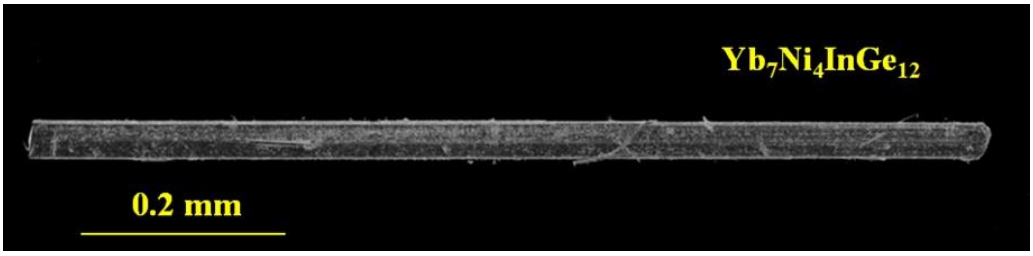

Figure 5.7.1. SEM image of the typical single crystal of $Yb_7Ni_4InGe_{12}$ grown from indium flux.

5.7.2.2. Structure refinement

X-ray single crystal data of $Yb_7Ni_4InGe_{12}$ showed that the compound crystallizes in the primitive tetragonal lattice (*P*4/*m*) within the $Yb_7Co_4InGe_{12}$ type structure and lattice constants are $a = b = 10.291(2)$ Å and $c = 4.1460(8)$ Å. The atomic parameters of the $Yb_7Co_4InGe_{12}$ structure were taken as starting values and the crystal structure of $Yb_7Ni_4InGe_{12}$ was refined using Shelxl-97 (full-matrix least-squares on F^2)[77] with anisotropic atomic displacement parameters for all the atoms. As a check for the correct composition, the occupancy parameters were refined in a separate series of least-squares cycles. This refinement resulted in eight atomic sites fully occupied within two standard uncertainties. All bond lengths are within the acceptable range compared to the expected values.[91] The overall stoichiometry obtained from the refinement is $Yb_7Ni_4InGe_{12}$.

The data collection and structure refinement details for $Yb_7Ni_4InGe_{12}$ are listed in Table 5.7.1. The standard atomic positions and isotopic atomic displacement parameters are listed in Table 5.7.2. The anisotropic displacement parameters and important bond lengths are listed in Tables 5.7.3 and 5.7.4, respectively. Further information on the structure refinements is available from: by quoting the Registry No. CCDC 989027.

Table 5.7.1. Crystal data and structure refinement for $Yb_7Ni_4InGe_{12}$ at 296(2) K.

Empirical formula	$Yb_7Ni_4InGe_{12}$
Formula weight	2432.02
Wavelength	0.71073 Å
Crystal system	Tetragonal
Space group, *Z*	*P*4/*m*, 1
Unit cell dimensions	$a = b = 10.291(2)$ Å, $c = 4.1460(8)$ Å
Volume	439.1(2) $Å^3$
Absorption coefficient	62.44 mm^{-1}
F(000)	1034.4
Crystal size	0.05 x 0.05 x 0.10 mm^3
θ range for data collection	1.98 to 25.00°
Index ranges	-12<=*h*<=11, -11<=*k*<=12, -4<=*l*<=4
Reflections collected	3545
Completeness to $\theta = 30.55°$	100%
Refinement method	Full-matrix least-squares on F^2
Data / restraints / parameters	387/ 0 / 40
Goodness-of-fit	1.170
Final *R* indices [>2σ(I)]	$R_{obs} = 0.042$, $wR_{obs} = 0.108$
Extinction coefficient	0.010792(1)
Largest diff. peak and hole	3.184 and -4.485 e·$Å^{-3}$

$R = \Sigma||F_o|-|F_c|| / \Sigma|F_o|$, $wR = \{\Sigma[w(|F_o|^2 - |F_c|^2)^2] / \Sigma[w(|F_o|^4)]\}^{1/2}$ and calcw=$1/[\sigma^2(Fo^2)+(0.0359P)^2+6.1794P]$ where $P = (Fo^2+2Fc^2)/3$

Table 5.7.2. Atomic coordinates ($x10^4$) and equivalent isotropic displacement parameters ($Å^2x10^3$) for $Yb_7Ni_4InGe_{12}$ at 296(2) K with estimated standard deviations in parentheses.

Label	Wyckoff site	*x*	*y*	*z*	Occupancy	U_{eq}*
Yb1	4*k*	3273(1)	3256(1)	5000	1	6(1)
Yb2	1*a*	0	0	0	1	6(1)
Yb3	2*f*	0	5000	5000	1	8(1)
Ni	4*j*	1194(3)	2800(3)	0	1	6(1)
In	1*c*	5000	5000	0	1	9(1)
Ge1	4*j*	2180(2)	4903(2)	0	1	6(1)
Ge2	4*j*	2878(3)	1134(3)	0	1	20(1)
Ge3	4*k*	673(3)	1929(3)	5000	1	18(1)

*U_{eq} is defined as one third of the trace of the orthogonalized U_{ij} tensor.

Table 5.7.3. Anisotropic displacement parameters ($Å^2x10^3$) for $Yb_7Ni_4InGe_{12}$ at 296(2) K with estimated standard deviations in parentheses.

Label	U_{11}	U_{22}	U_{33}	U_{12}	U_{13}	U_{23}
Yb1	5(1)	5(1)	9(1)	2(1)	0	0
Yb2	5(1)	5(1)	9(1)	0	0	0
Yb3	4(1)	8(1)	11(1)	0	0	0
Ge1	4(1)	3(1)	12(1)	0	0	0
Ni	5(1)	5(1)	10(2)	-1(1)	0	0
In	7(1)	7(1)	15(2)	0	0	0
Ge2	13(1)	11(1)	36(2)	1(1)	0	0
Ge3	30(1)	14(2)	9(2)	-15(1)	0	0

The anisotropic displacement factor exponent takes the form: $-2\pi^2[h^2a^{*2}U_{11} + ... + 2hka^*b^*U_{12}]$.

Table 5.7.4. Selected bond lengths [Å] for $Yb_7Ni_4InGe_{12}$ at 296(2) K with estimated standard deviations in parentheses.

Label	Distances	Label	Distances
Yb1—Ge1	2.9041(19)	Yb3—Ge1	3.056(18)
Yb1—Ge1	3.008(19)	Yb3—Ge2	3.229(2)
Yb1—Ge2	3.039(2)	Yb3—Ge3	3.235(3)
Yb1—Ge3	3.005(3)	Yb3—Ni	3.306(2)
Yb1—Ni	3.017(2)	Ge1—Ni	2.390(4)
Yb1—In	3.267(8)	Ge1—In	2.904(2)
Yb1—Yb1	3.5709(15)	Ge2—Ni	2.396(4)
Yb2—Ge3	2.953(2)	Ge2—Ge1	2.525(4)
Yb2—Ni	3.132(3)	Ge3—Ni	2.3210(19)

5.7.2.3. Crystal chemistry

$Yb_7Ni_4InGe_{12}$ crystallizes in the tetragonal structure of the $Yb_7Co_4InGe_{12}$ type (space group *P*4/*m*). The crystal structure of $Yb_7Ni_4InGe_{12}$ is composed of a complex $[Ni_4InGe_{12}]$ polyanionic network with three different types of one-dimensional channels. These channels are constructed by five, six and eight membered rings propagated along the *c*-axis with different types of ytterbium atoms embedded in them. These three different type channels are interconnected through edge and corner sharing form a three dimensional network. The crystal structure of $Yb_7Ni_4InGe_{12}$ is similar to the compounds crystallize in the $Sc_5Co_4Si_{10}$ type structure.[2] The comparison between $Yb_5Ni_4Ge_{10}$ and $Yb_7Ni_4InGe_{12}$ structures shown in Figure 5.7.2 clearly suggest the atomic arrangements in both compounds are similar. Both compounds crystallize in the tetragonal system, but different space groups; *P*4/*m* for

$Yb_7Ni_4InGe_{12}$ and *P*4/*mbm* for $Yb_5Ni_4Ge_{10}$. In $Yb_7Ni_4InGe_{12}$, the twofold rotation axis with centre of symmetry (2/*m*) and twofold screw axis (2_1) are absent compared to $Yb_5Ni_4Ge_{10}$.

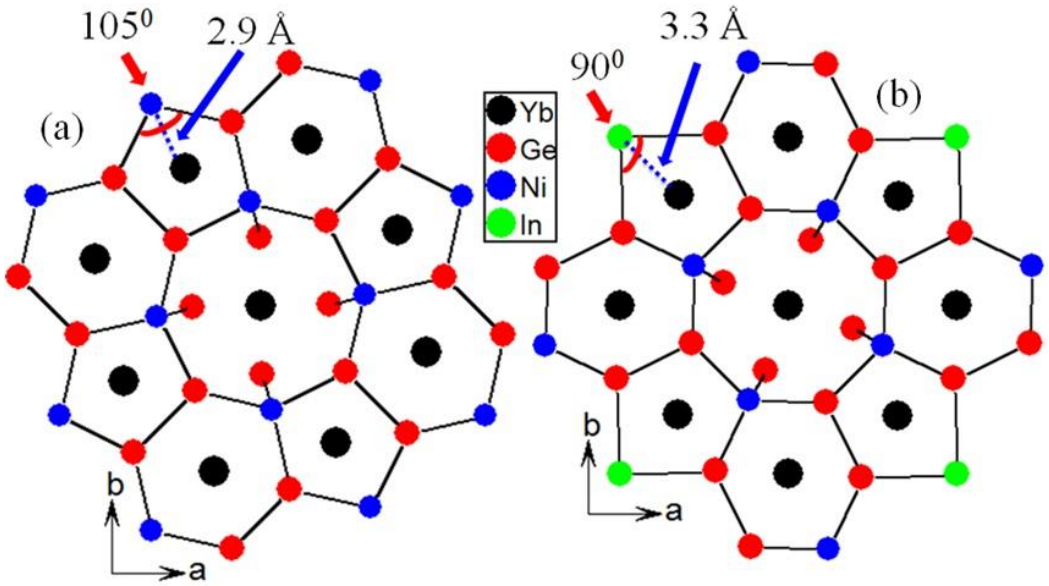

Figure 5.7.2. Crystal structure comparison of (a) $Yb_5Ni_4Ge_{10}$ and (b) $Yb_7Ni_4InGe_{12}$ is viewed in the *ab*-plane. Both structures consist of eight-membered ring with surrounding five and six membered rings.

In both structures, the widest channels in the structure are built from stacked alternating planar octagonal and square rings interconnected via Ni–Ge and Ge–Ge bonds, in which the octagons are defined by alternating four Ni and four Ge atoms, and the square rings are composed of four Ge atoms. In $Yb_5Ni_4Ge_{10}$, Yb1 atoms are sitting in the center of the octagonal rings, where as in $Yb_7Ni_4InGe_{12}$, it is occupied by the Yb3 atom. The Ge-Ge distance in the square ring can be considered as a weak bonding interaction because of the large interatomic distance of 2.9162(3) Å and 2.973(4), respectively for $Yb_5Ni_4Ge_{10}$ and $Yb_7Ni_4InGe_{12}$. The eight membered rings are surrounded by four six membered rings and four five membered rings arranged opposite to each other. However the notable difference is in the distribution of pentagonal and hexagonal rings. As shown in Figure 5.7.3, in the quaternary compound, the four pentagons are shared through edges and one common In corner, while in $Yb_5Ni_4Ge_{10,}$ they are separated by Ni-Ge and Ge-Ge bonds. This difference is reflected in the bond distance and bond angles as well. The bond distances and bond angles in both compounds are close except in five membered rings. In $Yb_7Ni_4InGe_{12}$ bond distance of Yb1-In in five membered channel is 3.3267(1) Å and bond angle of Ge1-In-Ge1 is 90° (marked in Figure 5.7.2b) and $Yb_5Ni_4Ge_{10}$ bond distance of Yb2-Ge1 in five membered ring

is 2.8470(3) Å and bond angle of Ge1-Ni-Ge2 is 105° (marked in Figure 5.7.2a). The hexagons in $Yb_7Ni_4InGe_{12}$ exist as individual unit with a separation of Ni-Ge bonds between them, whereas, in $Yb_5Ni_4Ge_{10}$, they exist as dimers with edge sharing. The hexagonal rings in $Yb_7Ni_4InGe_{12}$ are more distorted with bond angles in the range 113-129° compared 115-121° in the case of ternary compound clearly indicates a reduction of symmetry in the quaternary compound.

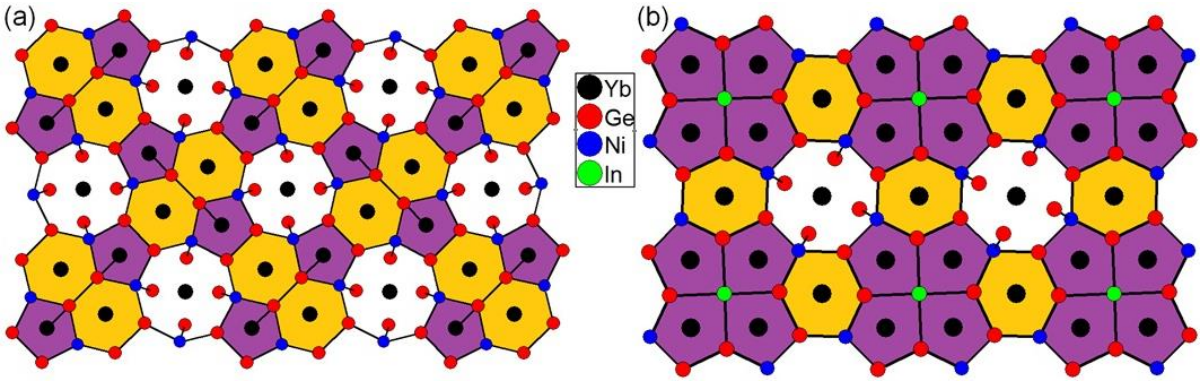

Figure 5.7.3. Comparison of the crystal structures of (a) $Yb_5Ni_4Ge_{10}$ and (b) $Yb_7Ni_4InGe_{12}$ viewed along the *c*-axis

The average Yb-Ni bond distance in the $Yb_7Ni_4InGe_{12}$ crystal structure calculated as 3.151(1) Å, which is close to the atomic radii of Yb-Ni distance (3.124 Å) observed in Yb_2NiGe_6[91] and the calculated distance of 3.110 Å.[102, 103] The average distance obtained for Yb1-Ge and Yb2-Ge bonds are 2.989 Å and 2.953 Å, respectively, smaller than the calculated distances of Yb^{2+}-Ge (3.08 Å)[103] and larger than Yb^{3+}-Ge (2.91 Å)[102, 103] suggest mixed or intermediate valency of Yb atoms in $Yb_7Ni_4InGe_{12}$.[92] A similar mixed valent behaviour was noticed in the prototype compound $Yb_7Co_4InGe_{12}$. However, shorter Yb1-Ge and Yb2-Ge distances (2.904 Å and 2.953 Å) and larger Yb3-Ge distance (3.056 Å) suggest Yb1 and Yb2 are in the trivalent and Yb3 in the divalent oxidation states. Based on these bond analyses it can be speculated that Yb atoms in $Yb_7Ni_4InGe_{12}$ exist as divalent and trivalent valent states. Moreover magnetism data, which will be discussed in the next section, also support the mixed valence behaviour. The overall Yb valency calculated by considering the quantitative atomic contribution taken from the Wyckoff sites as 72% trivalent Yb, which is close to the value of 80% obtained from the magnetic data. The slight increase of the oxidation state of Yb^{3+} observed in the magnetic data perhaps due to the impurity of Yb^{3+} oxide present in the sample. The average bond distance between Yb3 and Ge atoms is

3.173(1) Å, close to the Yb-Ge distance observed in $Yb_7Co_4InGe_{12}$ (3.16 Å) and the calculated value of 3.16 Å.[92]

The local coordination environments of ytterbium, germanium, nickel and indium atoms in the crystal structure of $Yb_7Ni_4InGe_{12}$ are compared in Figures 5.7.4 and 5.7.5 with the coordination environments of the atoms in $Yb_5Ni_4Ge_{10}$. Crystallographically there are three distinct Yb atoms present in both structures.

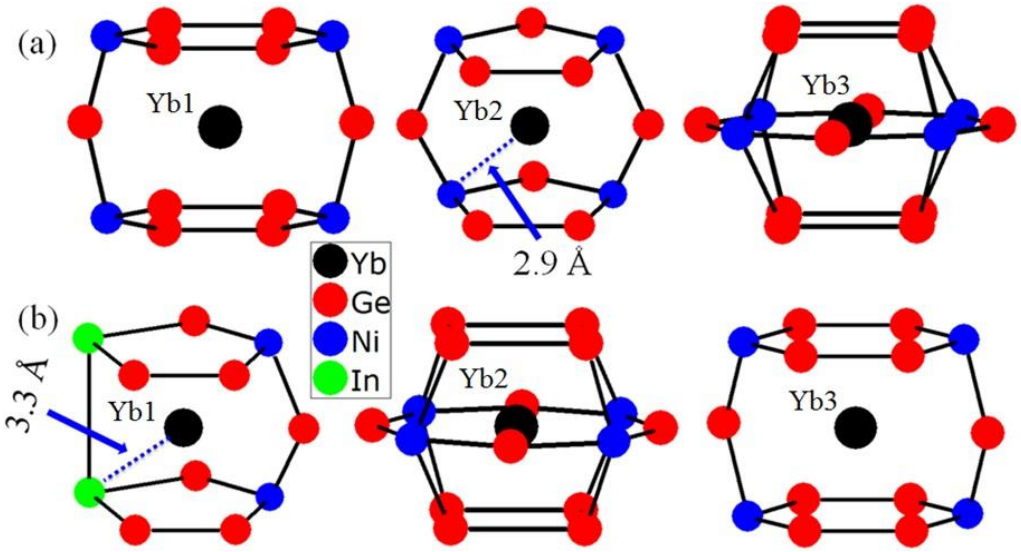

Figure 5.7.4. The coordination sphere of all Yb atoms in in (a) $Yb_5Ni_4Ge_{10}$ and (b) $Yb_7Ni_4InGe_{12}$.

While adopting standard atomic coordinates of the reported $Yb_5Ni_4Ge_{10}$ structure, the coordination sphere of Yb1, Yb2 and Yb3 in $Yb_7Ni_4InGe_{12}$ are closely related to the environment of Yb2, Yb3 and Yb1 in $Yb_5Ni_4Ge_{10}$. The notable difference is between Yb1 in $Yb_7Ni_4InGe_{12}$ and Yb2 in $Yb_5Ni_4Ge_{10}$, which is probably due to the presence of In the environment of Yb1 in $Yb_7Ni_4InGe_{12}$. This overall affects the distortion in the rings and aids the reduction in symmetry. Yb1 atom coordinates with eleven atoms with two pentagonal rings, made up of six Ge, two Ni and two indium atoms. These two pentagonal rings are connected by one Ge atom and host Yb1 atoms at the center. Yb3 atom is surrounded by twelve Ge atoms and four Ni atoms, whereas, the Yb1 atom, located at the hexagonal tunnel, is in contact with 10 Ge atoms and four Ni atoms. The coordination environment of Ni and Ge of both compounds are similar, see Figure 5.7.5.

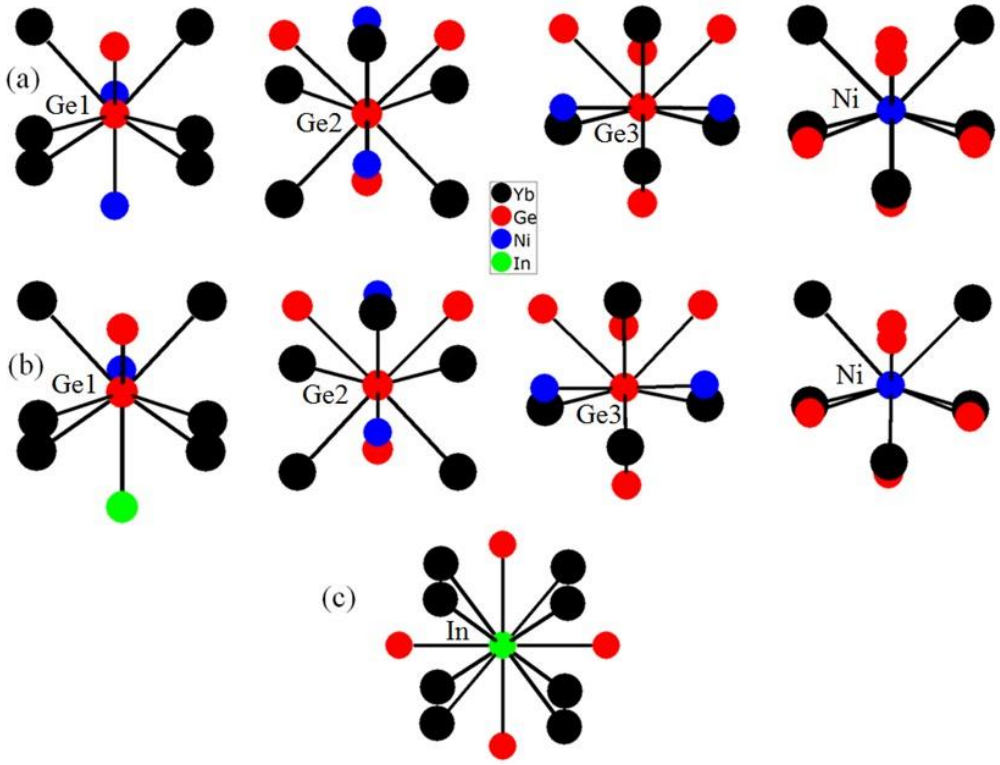

Figure 5.7.5. The coordination sphere of Ge and Ni and In atoms in (a) $Yb_5Ni_4Ge_{10}$ and (b) $Yb_7Ni_4InGe_{12}$ are presented. The coordination environment of In atom in $Yb_7Ni_4InGe_{12}$ is presented in (c).

5.7.2.4. Physical Properties

The temperature dependent molar magnetic susceptibility (χ_m) and inverse susceptibility ($1/\chi_m$) of $Yb_7Ni_4InGe_{12}$ at an applied field of 1000 Oe are shown in Figure 5.7.6a. As it can be clearly seen, a continuous deviation from the linearity observed in the entire temperature range of measurement signalling non-CW type behaviour. In order to explore the possibility of any large diamagnetic signal, the modified CW law was applied to the data. The constant susceptibility term, χ_0, was subtracted from the measured susceptibility data, and the inverse of the resultant (χ-χ_0) vs temperature also resulted in non-linear behaviour. This means that the system exhibits non-CW behaviour and indicates neither a simple paramagnet nor complete magnetic ordering. However, to get the magnetic moment, the high temperature inverse susceptibility data fitted with CW law, $\chi = C/(T-\theta_p)$,[104, 105] where C is the CW constant ($N_A\mu_{eff}^2/3K_bT$) and θ_p is the Weiss temperature.

A fit to the curve above 200 K with an effective magnetic moment of 3.66 μ_B/Yb atom suggest mixed valent or intermediate valent nature of Yb atoms. The magnetic moment

obtained above 200 K is close to value of the prototype compound $Yb_7Co_4InGe_{12}$.[92] The estimated experimental μ_{eff} values calculated above 200 K is about 80% of that expected for a free ion Yb^{3+} moment (4.56 μ_B/Yb). Magnetic susceptibility of $Yb_7Ni_4InGe_{12}$ shows no magnetic ordering down to 2 K but the susceptibility slightly increases at lower temperature with increasing field, which is normal for *RE* based intermetallics.[5] This deviation can be attributed to crystal field contributions, magnetic impurities and/or valence fluctuations.

The field dependence of the magnetization $M(H)$ for ground sample of $Yb_7Ni_4InGe_{12}$ was measured at 2 K and 300 K is shown in Figure 5.7.6b. The data measured at 300 K exhibit linear behaviour up to highest field of 60000 Oe and no show sign of saturation. The magnetization curve taken at 2 K shows a slight field dependent response up to ~ 30000 Oe, continues to rise slowly up to the highest obtainable field 60000 Oe without any hint of saturation.

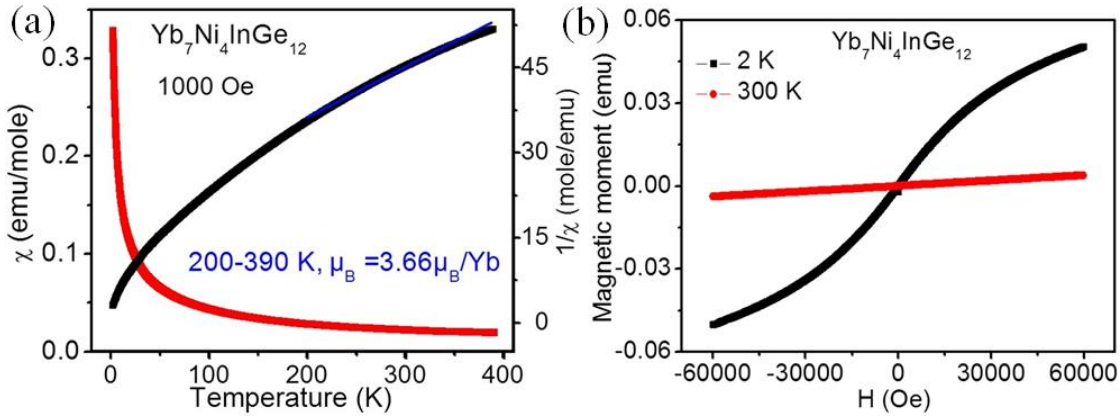

Figure 5.7.6. (a) Temperature dependence of the magnetic susceptibility (χ_m) and inverse susceptibility ($1/\chi_m$) for a polycrystalline sample of $Yb_7Ni_4InGe_{12}$ measured at 1000 Oe applied field, (b) Magnetization as a function of applied magnetic field at 2 K and 300 K for $Yb_7Ni_4InGe_{12}$.

5.7.2.4.1. XANES

X-ray absorption measurements were performed at the Yb L_{III}-edge, at different temperatures (300 K and 18 K) and ambient pressure to probe the Yb valence state in $Yb_7Ni_4InGe_{12}$. The main absorption peak (white line resonance) of the spectrum (Figure 5.7.7) is centered at ~8947.5 eV, which is attributed to trivalent Yb atoms.[62, 106] The spectra also revealed the presence of a weaker feature (shoulder) at ~8939.5 eV, revealing unequivocally that some divalent Yb is also present.[62, 106] From the XANES measurements, the compound $Yb_7Ni_4InGe_{12}$ can be classified as either as an intermediate valence compound

with all three Yb atoms having a non-integer valence or heterogeneous mixed-valence compound, in which specific Yb atoms are either exactly 2+ or 3+. The relative amounts of the two electronic configurations were estimated by decomposing the normalized Yb XANES into a pair of arc-tangents (representing the edge step) and Lorentzian functions (representing the white line resonance).[92] Fitting of the data with the above technique resulted in ~ 73(5)% Yb^{3+} corresponds to an average Yb valence of ~ 2.73. This value is in reasonable agreement with magnetic measurements. The uncertainty in the absolute valence is ~5%, may be arising from correlations between parameters used to represent the edge-step and white line resonances and from systematic errors due to fitting-model dependence. There are no substantial differences in the XANES data measured at 18 K and 300 K confirmed the absence of valence fluctuation in this compound.

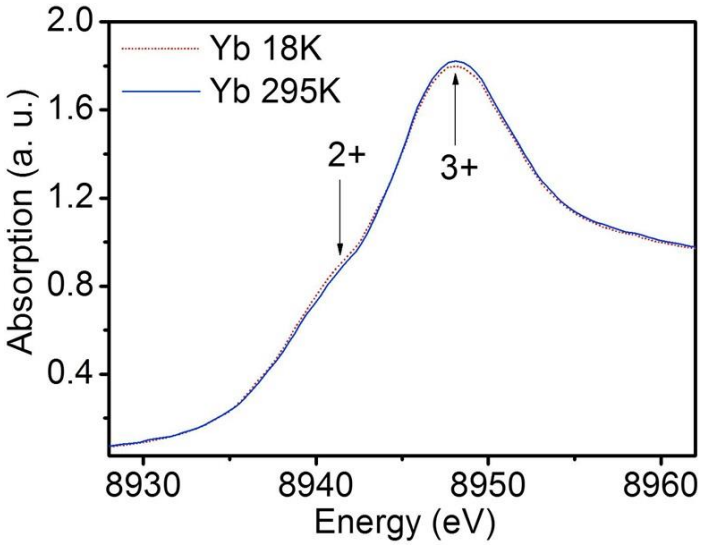

Figure 5.7.7. Yb L_{III} absorption edge spectra taken from a polycrystalline sample of $Yb_7Ni_4InGe_{12}$ at 300 K and 18 K.

5.8. The Structural Evolution of the Compounds $Eu_3T_2In_9$ (T = Cu and Ag) through the Superstructure of $EuCu_2Ge_2$ and their Physical Properties

5.8.1. Introduction

According to the ICSD[107] and PCD,[73] so far $EuAg_4In_8$ is the only compound reported in the Eu-Ag-In system. Sysa et al. reported $EuAg_4In_8$ in the hexagonal system[108] and its tetragonal polymorph reported very recently.[109] During the systematic studies on the Eu-Ag-In system, one more new phase $Eu_3Ag_2In_9$ was discovered. This is fact first indide in the $RE_3T_2X_9$ series although more than 80 ternary compounds were reported, but most of them Al and Ga based compounds. As per ICSD, PCD and other relevant databases, there are no Eu based compounds reported in the $RE_3T_2X_9$ series and $Eu_3Ag_2In_9$ can be considered as the first one in this context. The crystal structure of the $RE_3T_2X_9$ compounds are closely related to the compounds within the families $RETX_3$ and $RE(TX)_4$. Amerioun et al. explained the structural relation between $RE_3T_2X_9$ (La_3Al_{11} type) and $RETX_3$ ($BaAl_4$ type).[110] Preliminary powder XRD measurements suggest that the compounds $RE(Ag,Al)_4$ (RE = Y, Gd, Tb, Dy)[111] and $RECuAl_3$ (RE = Tb, Dy, Ho, Er, Tm, Yb)[112] crystallize in the $CeNi_{2+x}Sb_{2-x}$ structure type,[113] and are closely related to the $BaAl_4$ structure type.

Since a new compound obtained in the Eu-Ag-In family, the research has extended to the Eu-Cu-Ge series. There is only one compound $EuCu_2Ge_2$ reported so far in this series, which crystallizes in the tetragonal crystal system.[114-116] The synthesis was aimed to obtain $Eu_3Cu_2In_9$ using similar synthesis approach, but resulted in the formation of $EuCu_2Ge_2$. Although the divalent nature of Eu atoms in $EuCu_2Ge_2$ via ^{151}Eu Mössbauer spectroscopy and magnetic susceptibility measurements,[117] Banik et al. proposed the mixed valent nature through X-ray absorption spectroscopy studies.[118] Interestingly, the single crystal analysis suggests new structure type in $EuCu_2Ge_2$, which is closely related to the $Eu_3Ag_2In_9$.

5.8.2. Results and Discussion

5.8.2.1. Reaction Chemistry

The single crystals of the compound $Eu_3Ag_2In_9$ were obtained from the reaction that was initially designed to optimize the synthesis of the compounds within the Eu-Ag-Ge family. However, indium acted as the active solvent and resulted in the formation of

$Eu_3Ag_2In_9$. A selected rod shaped grey single crystal of $Eu_3Ag_2In_9$ obtained from the flux reaction is shown in Figure 5.8.1a. After establishing the crystal structure of $Eu_3Ag_2In_9$, the syntheses of $Eu_3Cu_2In_9$ have been attempted using similar synthesis strategies. However, in this case indium acted as the non-active solvent and resulted in the formation of the single crystals of $EuCu_2Ge_2$. SEM image of a typical single crystal of $EuCu_2Ge_2$ is shown in Figure 5.8.1b.

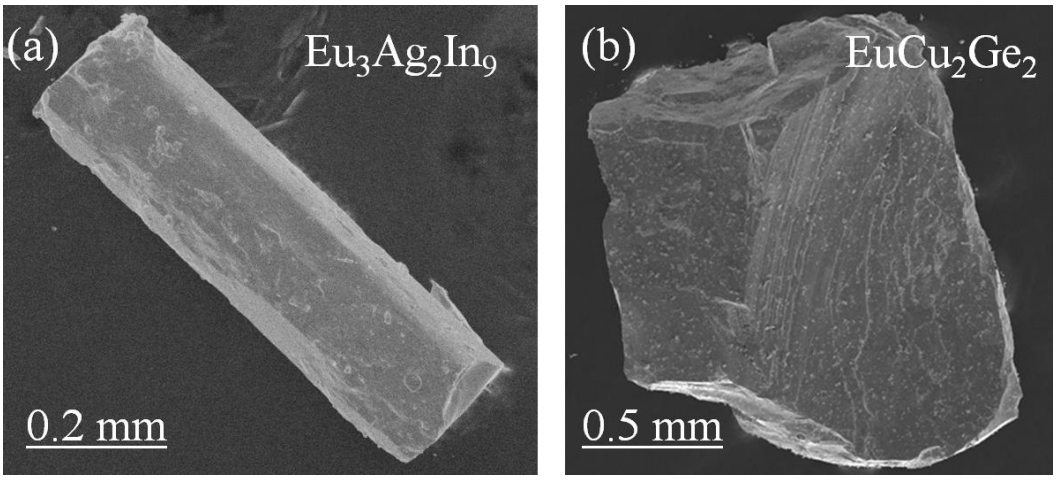

Figure 5.8.1. SEM images of the typical single crystal of (a) $Eu_3Ag_2In_9$ and (b) $EuCu_2Ge_2$ grown from the indium flux.

Both $Eu_3Ag_2In_9$ and $EuCu_2Ge_2$ are stable in air and no decomposition was observed even after several months. Although the synthesis $Eu_3Cu_2In_9$ by metal flux method was not succeeded, the same has been synthesized by HFIH. High quality single crystals were used to collect the XRD data and the structure of $Eu_3Ag_2In_9$ and $EuCu_2Ge_2$. $EuCu_2Ge_2$ was earlier reported in the tetragonal crystal system with the space group of *I*4/*mmm*.[114-116] The simulated powder XRD pattern obtained from the orthorhombic refinement of $EuCu_2Ge_2$ showed additional peaks at 2θ = 27.2° and 44.7° corresponds to the [031] and [035] planes, respectively, which are comparable with the experimental powder XRD pattern confirming the formation of the compound within a new superstructure (Figure 5.8.2).

5.8.2.2. Structure Refinement of $Eu_3Ag_2In_9$ and $EuCu_2Ge_2$

The crystal structure of $Eu_3Ag_2In_9$ and $EuCu_2Ge_2$ were refined using Shelxl-97 (full-matrix least-squares on F^2)[77] with anisotropic atomic displacement parameters for all the atoms. As a check for the correct composition, the occupancy parameters were refined in a separate series of least-squares cycles. The first step of refinement showed that *Immm* space

group and with lattice parameters *a* = 4.8370(1) Å, *b* = 10.6078(3) Å and *c* = 13.9195(4) Å. During the isotropic refinement of $Eu_3Ag_2In_9$, it was noticed with unacceptable highest difference peak and deepest hole is little bit high (>14 and -9 eÅ^3). The refinement residual value (*R*1) also was found to be slightly high (12%). Since the scattering power of Ag and In are very close due to only two electron difference, the refinement of the structure was attempted with Ag and In mixing; however, the refinement parameters could not improve further. To overcome all these problems observed in the refinement for $Eu_3Ag_2In_9$, the data was recollected with long exposure time (60 s) and more number of frames (90). This revised data collection overcame the problems associated with the initial data collection (10 s and within 60 frames). On the other hand, $EuCu_2Ge_2$ was already reported in tetragonal crystal system with the space group of *I*4/*mmm*.[114-116] However, the attempt to refine in tetragonal crystal system by using reported coordinates was unsuccessful, and found the stable refinement in orthorhombic crystal system with the space group of *Immm* and new structure type.

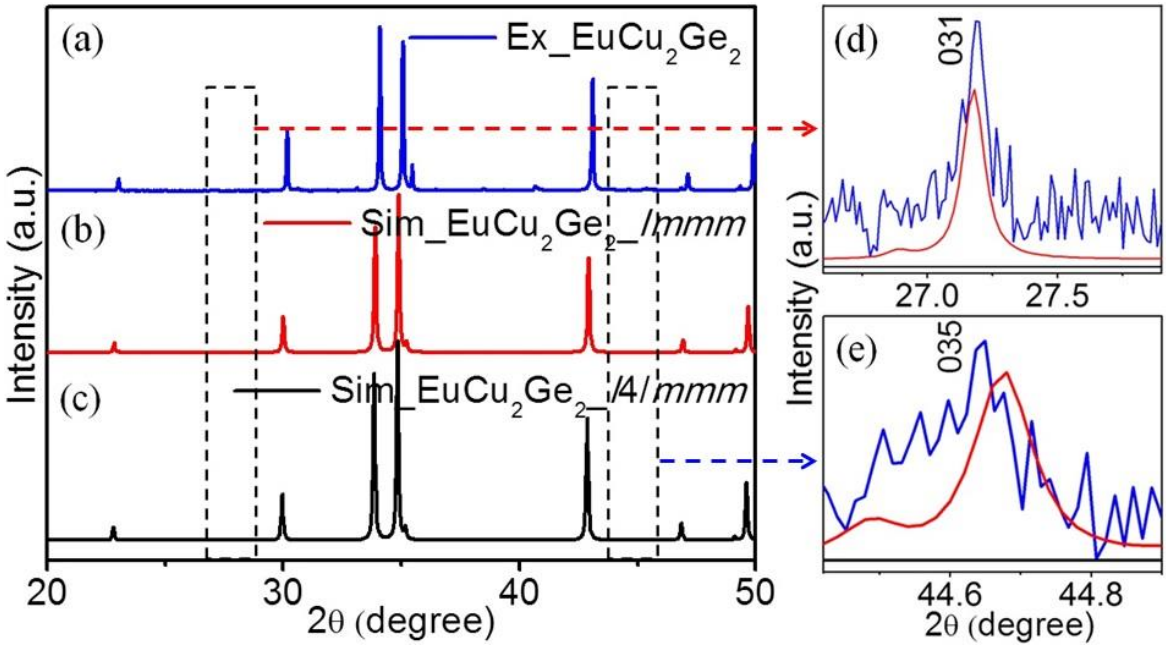

Figure 5.8.2. Comparison of the simulated powder XRD patterns obtained from the single crystal data of tetragonal and orthorhombic systems with experimental pattern for the compound $EuCu_2Ge_2$. (a) Experimental powder XRD (b) simulated pattern obtained from the orthorhombic structure refinement, (c) simulated pattern obtained from the tetragonal crystal system and (d and e) peaks at 2θ = 27.2° and 44.7° corresponds to the superstructure planes [031] and [035].

The details of data collection and structure refinement of $Eu_3Ag_2In_9$ and $EuCu_2Ge_2$ are listed in Table 5.8.1. The standard atomic positions and isotopic atomic displacement parameters of this compound are given in Table 5.8.2. The anisotropic displacement parameters and important bond lengths are listed in Tables 5.8.3 and 5.8.4, respectively. Further information on the structure refinements is available from: by quoting the CCDC Registry No. 1436853 ($Eu_3Ag_2In_9$) and 1436854 ($EuCu_2Ge_2$).

Table 5.8.1. Crystal data and structure refinement for $Eu_3Ag_2In_9$ and $EuCu_2Ge_2$ at 296(2) K

Empirical formula	$Eu_3Ag_2In_9$	$EuCu_2Ge_2$
Formula weight	1705	424.22
Unit cell dimensions	a = 4.8370(1) Å b = 10.6078(3) Å c = 13.9195(4) Å	a = 4.2107(2) Å b = 10.1847(5) Å c = 12.6314(6) Å
Wavelength	0.71073 Å	
Crystal system	Orthorhombic	
Crystal system	*Immm*	
Volume	714.21(3) $Å^3$	541.69(5) $Å^3$
Z	2	6
Density (calculated)	7.9278 g/cm^3	7.803 g/cm^3
Absorption coefficient	29.792 mm^{-1}	44.881 mm^{-1}
F(000)	1447.8	1110
Crystal size	0.1 x 0.05 x 0.05 mm^3	0.1 x 0.05 x 0.05 mm^3
θ range for data collection	2.4 to 35.8°	2.57 to 29°
Index ranges	-7=<h=<7, -17=<k=<12, -22=<l=<22	-5=<h=<5, -13=<k=<13, -17=<l=<16
Reflections collected	6194	2883
Independent reflections	972 [R_{int} = 0.0321]	437 [R_{int} = 0.0563]
Refinement method	100%	
Refinement method	Full-matrix least-squares on F^2	
Data / restraints / parameters	972 / 0 / 28	437 / 0 / 29
Goodness-of-fit	1.177	1.007
Final R indices [>2σ(I)]	R_{obs} = 0.038, wR_{obs} = 0.106	R_{obs} = 0.0694, wR_{obs} = 0.2281
Extinction coefficient	0.000195 (7)	0.0093 (16)
Largest diff. peak and hole	6.886 and -3.899 e·$Å^{-3}$	5.469 and -6.797 e·$Å^{-3}$

$R = \Sigma||F_o|-|F_c|| / \Sigma|F_o|$, $wR = \{\Sigma[w(|F_o|^2 - |F_c|^2)^2] / \Sigma[w(|F_o|^4)]\}^{1/2}$ and calcw=1/[σ^2(Fo^2)+(0.0359P)^2+6.1794P] where P = (Fo^2+2Fc^2)/3

Table 5.8.2. Atomic coordinates ($x10^4$) and equivalent isotropic displacement parameters ($Å^2x10^3$) of $Eu_3Ag_2In_9$ and $EuCu_2Ge_2$ at 296(2) K.

Label	Wyck. site	*x*	*y*	*z*	Occupancy	U_{eq}*
$Eu_3Ag_2In_9$						
Eu1	2*a*	0	0	0	1	14(2)
Eu2	4*i*	0	0	2994(5)	1	15(1)
In1	2*d*	5000	0	5000	1	21(3)
In2	8*l*	0	3653(8)	3497(6)	1	16(1)
In3	8*l*	0	2838(8)	1428(6)	1	16(1)
Ag	4*h*	0	1751(16)	5000	1	25(2)
$EuCu_2Ge_2$						
Eu1	2*a*	0	0	0	1	6(1)
Eu2	4*i*	0	0	3333(1)	1	6(1)
Ge1	4*g*	0	3765(2)	0	1	7(1)
Ge2	8*l*	0	3767(2)	3333(1)	1	7(1)
Cu1	8*l*	0	2500(2)	1668(1)	1	8(1)
Cu2	4*h*	0	2498(2)	5000	1	8(1)

*U_{eq} is defined as one third of the trace of the orthogonalized U_{ij} tensor.

Table 5.8.3. Anisotropic displacement parameters ($Å^2x10^3$) for $Eu_3Ag_2In_9$ and $EuCu_2Ge_2$.

Label	U_{11}	U_{22}	U_{33}	U_{12}	U_{13}	U_{23}
$Eu_3Ag_2In_9$						
Eu1	14(4)	21(5)	8(4)	0	0	0
Eu2	13(3)	19(4)	12(3)	0	0	0
In1	28(8)	20(7)	14(6)	0	0	0
In2	14(3)	17(3)	19(3)	0	0	0
In3	14(3)	17(3)	17(1)	0	0	0
Ag	27(6)	35(7)	13(5)	0	0	0
$EuCu_2Ge_2$						
Eu(1)	5(2)	5(2)	8(2)	0	0	0
Eu(2)	6(2)	3(2)	8(2)	0	0	0
Ge(1)	8(2)	1(2)	12(2)	0	0	0
Ge(2)	8(2)	1(2)	12(2)	0	0	0(1)
Cu(1)	11(2)	1(2)	13(2)	0	0	0(1)
Cu(2)	11(2)	1(2)	13(2)	0	0	0

The anisotropic displacement factor exponent takes the form: $-2\pi^2[h^2a^{*2}U_{11} + ... + 2hka^*b^*U_{12}]$.

Table 5.8.4. Selected bond lengths [Å] for $Eu_3Ag_2In_9$ and $EuCu_2Ge_2$ at 296(2) K with estimated standard deviations in parentheses.

Label	Distances	Label	Distances
$Eu_3Ag_2In_9$		**$EuCu_2Ge_2$**	
Eu1—In2	3.5020(6)	Eu1—Ge2	3.2320(7)
Eu1—In3	3.6078(8)	Eu1—Cu2	3.3048(13)
Eu2—Ag	3.3528(11)	Eu2—Ge1	3.2324(8)
Eu2—In1	3.6931(6)	Eu2—Ge2	3.2304(8)
Eu2—In2	3.4934(7)	Eu2—Cu1	3.3030(13)
Eu2—In3	3.4283(6)	Eu2—Cu2	3.3031(13)
In1—Ag	3.0497(10)	Ge1—Cu1	2.4676(11)
In2—Ag	2.9062(14)	Ge1—Cu2	2.4690(13)
In3—Ag	3.1609(6)	Ge1—Ge1	2.5150(3)
In2—In2	2.8568(17)	Ge2—Cu2	2.4673(14)
In2—In3	2.8919(7)	Ge2—Cu2	2.4694(10)
In2—In3	3.0072(11)	Ge2—Cu1	2.4707(13)
In3—In1	3.0351(8)	Ge2—Ge2	2.5120(2)
		Cu1—Cu2	2.9781(7)
		Cu2—Cu2	2.9759(15)

5.8.2.3. Crystal Chemistry of $Eu_3Ag_2In_9$ and $EuCu_2Ge_2$

The crystal structure of $Eu_3Ag_2In_9$ along [110] plane is shown in Figure 5.8.3. $Eu_3Ag_2In_9$ crystallizes in the body centered orthorhombic crystal system with the structure type of La_3Al_{11} type (space group *Immm*).[119] Crystal structure of $Eu_3Ag_2In_9$ is composed of six membered rings made up of In atoms. $Eu_3Ag_2In_9$ is a building block unit of edge shared six membered In rings and corner shared In_4 atoms along the *a*-axis as shown in Figure 5.8.3. The one dimensional chains of edge shared In_6 rings are further interconnected into another six membered rings forming a three dimensional stable crystal structure along the *a*-axis. The comparison of crystal structure $EuCu_2Ge_2$ in tetragonal and orthorhombic crystal systems are shown along the [011] plane in Figure 5.8.4. Tetragonal system contains only three atomic coordinates, but orthorhombic system is made up of six atomic coordinates. The crystal structure in new type can be explained in a similar way as the previously reported tetragonal structure except that the tripling of the *b*-axis is observed in the crystal obtained from the flux reactions, together with a change in the symmetry from tetragonal (*I*4/*mmm*, $CeAl_2Ga_2$ type structure) to orthorhombic (*Immm* space group and new structure type). The crystal structure of orthorhombic $EuCu_2Ge_2$ along [011] plane is shown in Figure 5.8.4.

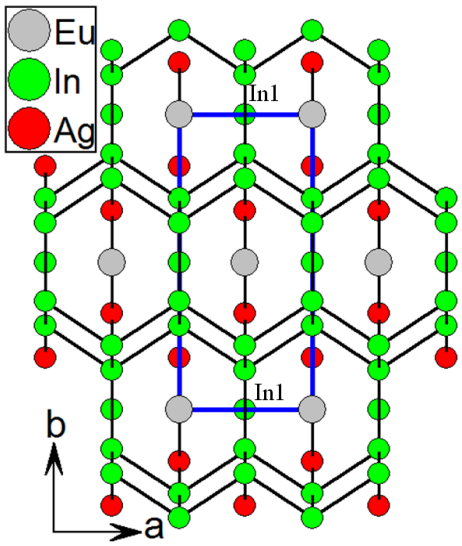

Figure 5.8.3. Crystal structure of $Eu_3Ag_2In_9$ as viewed along the *c*-axis; the unit cell is outlined as blue solid lines.

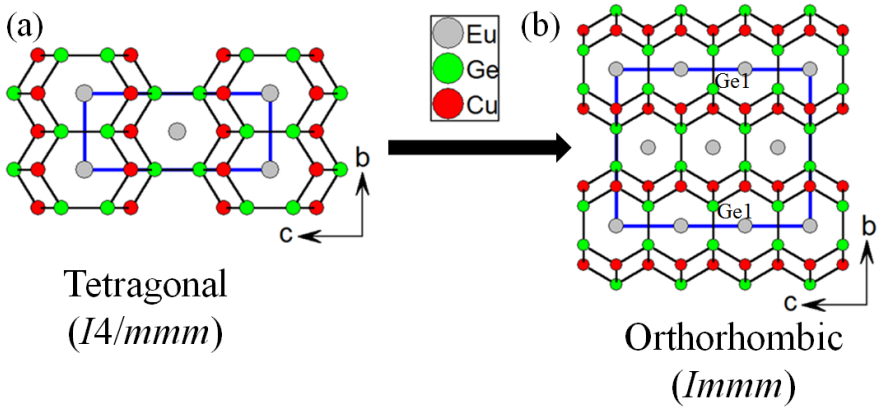

Figure 5.8.4. The crystal structure of $EuCu_2Ge_2$ (a) tetragonal and (b) orthorhombic as viewed in the *bc*-plane. The unit cell is outlined as blue solid lines.

$EuCu_2Ge_2$ crystallizes in the body centered orthorhombic crystal system with a new structure type (space group *Immm*). Both crystal structures of $EuCu_2Ge_2$ are composed of a complex $[CuGe]^{(2+\delta)-}$ polyanionic network in which the Eu ions are embedded. These polyanionic networks are shared through the edges of Cu and Ge atoms along the [011] plane resulting in a three dimensional network. The superstructure of $EuCu_2Ge_2$ contains six crystallographic positions *viz.* two europium atoms occupy 2*a* and 4*i* Wyckoff sites of point symmetry *mmm* and *mm*2, two copper atoms occupy 4*h* and 8*l* Wyckoff sites of point symmetry *m*2*m* and *m*.. and two germanium atoms occupy 4*g* and 8*l*Wyckoff sites of point symmetry *m*2*m* and *m*… Group-subgroup relationships and group analysis can predict a

lowering symmetry from the tetragonal $EuCu_2Ge_2$ (space group of *I*4/*mmm*) to the orthorhombic $EuCu_2Ge_2$ and $Eu_3Ag_2In_9$ (space group of *Immm*), indices for the isomorphic (i) transition (Figure 5.8.5). Interestingly the orthorhombic $EuCu_2Ge_2$ crystal system is very close to the $Eu_3Ag_2In_9$ system except the difference in the atomic coordination of Ge1 in $EuCu_2Ge_2$ and In1 in $Eu_3Ag_2In_9$ as highlighted blue dotted line (see Figure 5.8.5). In both the crystal systems there are six atomic coordinates are present; two Eu atoms, two Ge atoms, two Cu atoms in $EuCu_2Ge_2$ and two Eu atoms, three In atoms, one silver atom in $Eu_3Ag_2In_9$.

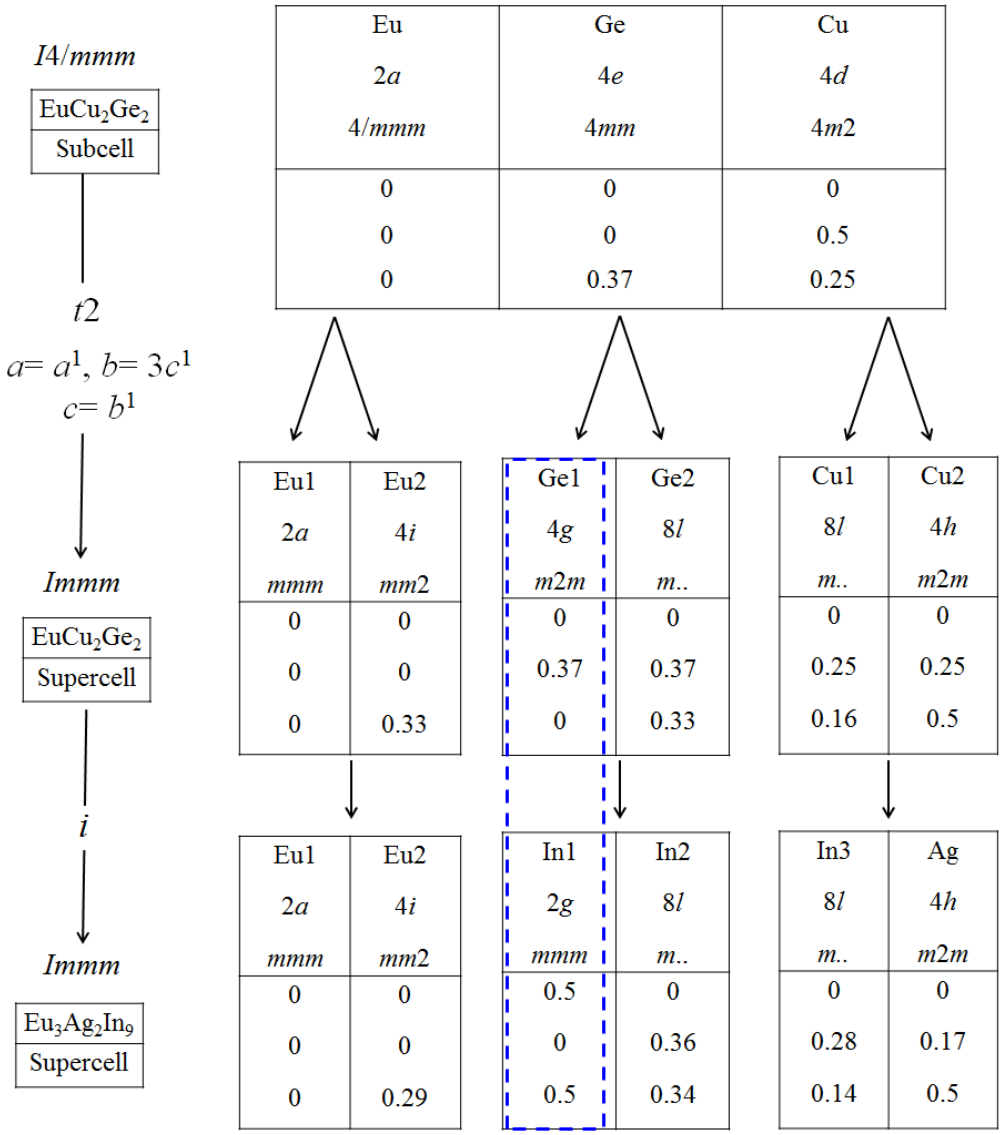

Figure 5.8.5. Group-subgroup scheme of sub- and the super-structures of $EuCu_2Ge_2$. The indices for the *translationengleiche* (*t*) transition, orthorhombic $EuCu_2Ge_2$ to orthorhombic $Eu_3Ag_2In_9$ indicates *isomorphic* (*i*) transition and the unit cell transformations are given. The evolution of the atomic parameters is shown at the right.

The local coordination environments of all atoms in the crystal structures of $Eu_3Ag_2In_9$ and $EuCu_2Ge_2$ are compared in Figures 5.8.6 and 5.8.7. The coordination environment of Eu1 and Eu2 consist of 16 atoms in both crystal structures. In $EuCu_2Ge_2$, both Eu atoms have the coordination environments made up of 8 Cu and 8 Ge atoms. On the other hand, Eu atoms in $Eu_3Ag_2In_9$ are not equivalent with 12 In, 4 Ag around Eu1 atom and 14 In, 2 Ag around Eu2 (Figure 5.8.6). The main difference in the both crystal structure is Ge1 and In1 atomic coordinates as shown in Figure 5.8.7. The coordination environment of Ge1 in $EuCu_2Ge_2$ consisting of 10 atoms with the combination of 5Eu, 5Cu and 1Ge atoms and In1 in $Eu_3Ag_2In_9$ consisting 12 atoms with the combination of 4Eu, 4In and 4Ag atoms. The average bond distances of Ge1-Eu, Ge1-Cu and Ge1-Ge in $EuCu_2Ge_2$ are 3.53 Å, 2.47 Å and 2.51 Å respectively, while In1-Eu, In1-In and In1-Ag in $Eu_3Ag_2In_9$ are 3.69 Å, 3.03 Å and 3.05 Å, respectively. These values are comparable to the reported compounds.[116,114,120]

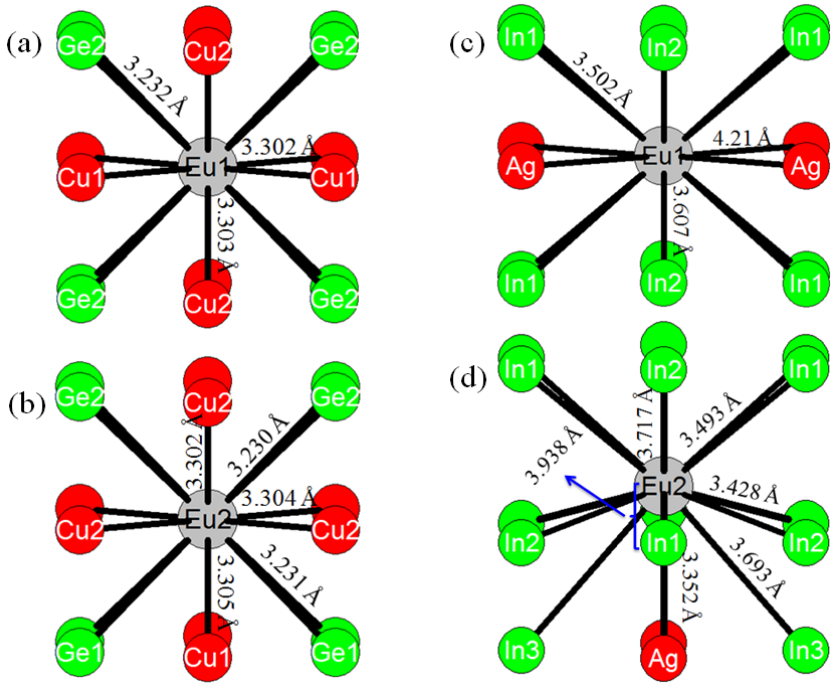

Figure 5.8.6. Coordination spheres of Eu1 and Eu2 atoms in $EuCu_2Ge_2$ (a and b) and $Eu_3Ag_2In_9$ (c and d).

As explained above the coordination environments of all the atoms are comparable in both structures except Ge1 in $EuCu_2Ge_2$ and In1 in $Eu_3Ag_2In_9$, which are respectively occupied at the Wyckoff sites 4*g* and 2*g*. $EuCu_2Ge_2$ can be represented as $Eu_3(CuGe)_{12}$ ($Eu_3Cu_6Ge_6$), while $Eu_3Ag_2In_9$ can be represented as $Eu_3(AgIn)_{11}$ clearly indicates the

deficiency at Ag atom. This deficiency may be originated due to difference in the sizes of atoms. From this anlaysis, it can be concluded that $Eu_3T_2In_9$ is a deficient variant of the new orthorhombic crystal structure of $EuCu_2Ge_2$.

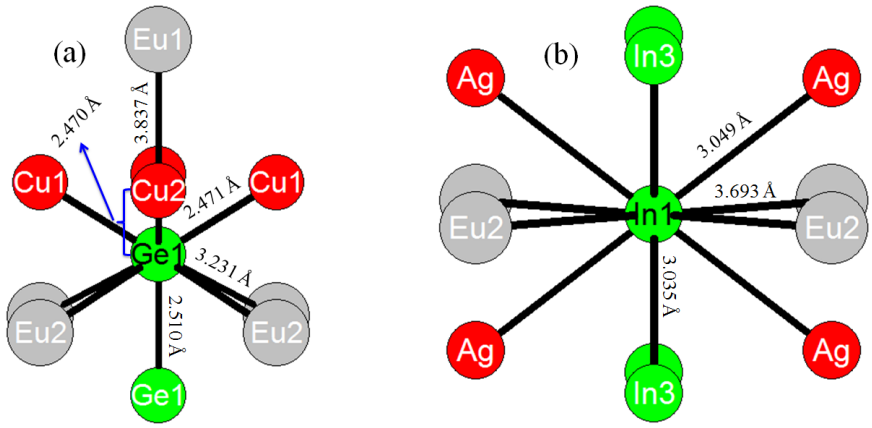

Figure 5.8.7. Coordination spheres of Ge1 in $EuCu_2Ge_2$ (a) and In1 in $Eu_3Ag_2In_9$ (b).

5.8.2.4. Magnetism

The temperature dependent molar magnetic susceptibility (χ_m) and inverse susceptibility ($1/\chi_m$) of $Eu_3T_2In_9$ and $EuCu_2Ge_2$ at an applied field of 1000 Oe are shown in Figure 5.8.8.

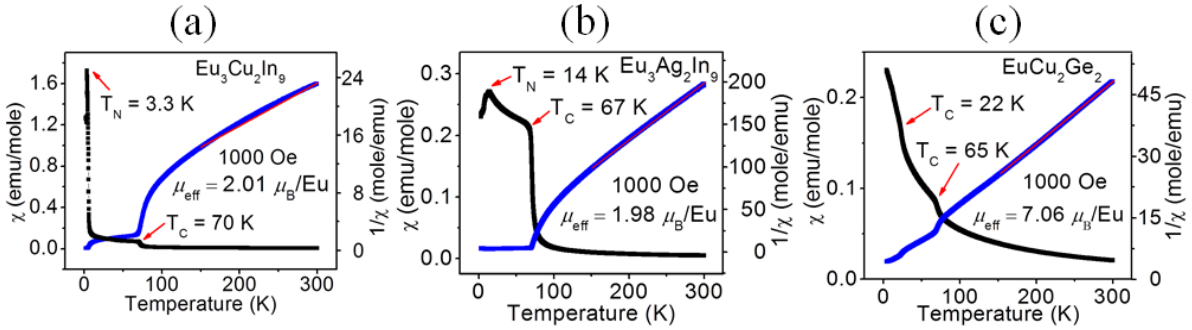

Figure 5.8.8. Temperature dependence of magnetic susceptibility (χ_m) and inverse magnetic susceptibility ($1/\chi_m$) of (a) $Eu_3Cu_2In_9$, (b) $Eu_3Ag_2In_9$ and (c) $EuCu_2Ge_2$ measured at1000 Oe.

The inverse susceptibility curve obeys CW law, $\chi = C/(T-\theta)$, above 150 K with an effective magnetic moment of 2.01 μ_B, 1.98 μ_B and 7.06 μ_B per Eu atom for $Eu_3Cu_2In_9$, $Eu_3Ag_2In_9$ and $EuCu_2Ge_2$ respectively, which suggests the existence of mixed/intermediate valent nature of Eu atoms. The estimated experimental μ_{eff} value is about 25% and 24% for $Eu_3Cu_2In_9$ and $Eu_3Ag_2In_9$, respectively, of that expected for a free ion Eu^{2+} moment (7.96 μ_B/Eu). In the case of $EuCu_2Ge_2$, the calculated magnetic moment 7.06 μ_B/Eu atom can be assigned as 88% divalent (Eu^{2+}) and 12% trivalent (Eu^{3+}) respectively, which is

corroborating with reported literature.[118] Temperature dependent magnetic susceptibility data of $Eu_3T_2In_9$ and $EuCu_2Ge_2$ shows multiple ordering transitions, $Eu_3Cu_2In_9$ shows ferromagnetic ordering at 70 K followed by anti-ferromagnetic transitions at 3.3 K. $Eu_3Ag_2In_9$ also shows similar feature with ferro and anti-ferromagnetic transitions at 67 K and 14 K, respectively. On the other hand $EuCu_2Ge_2$ shows two ferro-magnetic transitions at 65 K and 22 K, respectively.

5.8.2.5. XANES

The mixed/intermediate valent nature of Eu atoms in $Eu_3T_2In_9$ and $EuCu_2Ge_2$ was further confirmed by XANES measurements, which were performed at the Eu L_{III}-edge, at 300 K and ambient pressure. The main absorption peak of the spectrum (Figure 5.8.9) at 6973 eV for $EuCu_2Ge_2$ and broad hump for $Eu_3T_2In_9$ was observed in the Eu L_{III} X-ray absorption spectrum. This value is characteristic of the $4f^7$ (Eu^{2+}) configuration and arises due to a $2p_{3/2}$ to $5d$ transition.[121] Another main absorption peak at around 6982 eV for $Eu_3T_2In_9$ and broad hump for $EuCu_2Ge_2$ was observed which is corresponding to $4f^7$(Eu^{3+}).[122]

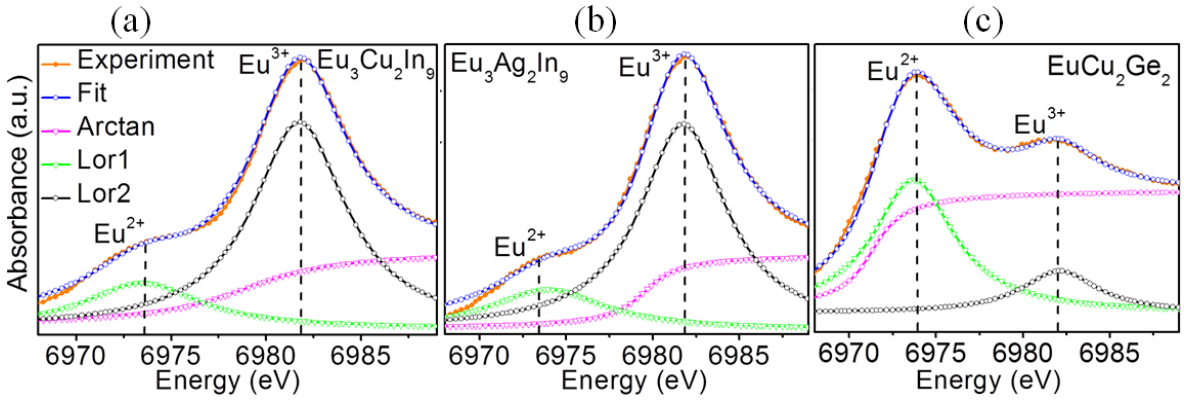

Figure 5.8.9. L_{III} absorption edge spectra of Eu in (a) $Eu_3Cu_2In_9$, (b) $Eu_3Ag_2In_9$ and (c) $EuCu_2Ge_2$.

From the XANES measurements, the compounds $Eu_3T_2In_9$ and $EuCu_2Ge_2$ can be classified as either as an intermediate valence compounds with all two Eu atoms in all compounds having a non-integer valence or heterogeneous mixed-valence compound, in which specific Eu atoms are having either exactly 2+ or 3+ oxidation states. Previous results also support that Eu atoms are exhibiting mixed valence behaviour in $EuCu_2Ge_2$ confirmed by X-ray absorption spectroscopy studies.[118] Integrating over the respective areas using lorentzian fitting yields 22%, 20% and 80% of Eu in divalent state for $Eu_3Cu_2In_9$, $Eu_3Ag_2In_9$

and $EuCu_2Ge_2$ (see Figure 5.8.9a, b and c). Detailed crystallography and physical property studies on these compounds are under process.

5.9. Conclusion

The metal flux technique was successfully applied to produce single crystals of EuInGe, Yb_2CuGe_6, $Yb_3Cu_4Ge_4$, $Yb_{6.6}Ir_6Sn_{16}$, $Sm_3Ni_5Al_{19}$, $Yb_7Ni_4InGe_{12}$, $EuCu_2Ge_2$ and $Eu_3Ag_2In_9$. The flux method proves to be an excellent tool for growing an ordered intermetallic compounds to understand the complex crystal structures. This work resulted in the discovery of a few new structure types. To summarize, EuInGe crystallizes in a new monoclinic structure type with space group $P2_1/c$, $Yb_{6.6}Ir_6Sn_{16}$ crystallizes in a new tetragonal crystal system with the space group $P4_2/nmc$ and $EuCu_2Ge_2$ is a new structure type with space group *Immm.* This work also resulted in the development of new compounds. For examples, $Sm_3Ni_5Al_{19}$ is a new member in the $Sm_{2n+m}Ni_{4n+m}Al_{15n+4m}$ series with n = 1 and m = 1, $Yb_7Ni_4InGe_{12}$ is a new compound adopting the $Yb_7Co_4InGe_{12}$ structure type with the space group of $P4/m$, $Eu_3T_2In_9$ (T = Cu and Ag) are considered as the first Eu and In based new members in the structure type La_3Al_{11} with space group *Immm*. Apart that, the metal flux method also used to understand the absolute crystal structure of a few compounds as discussed in the case of Yb_2CuGe_6, which crystallizes in the ordered monoclinic La_2AlGe_6 structure type with space group $C2/m$ and $Yb_3Cu_4Ge_4$ crystallizes in the orthorhombic $Gd_3Cu_4Ge_4$ structure type with space group *Immm*. Finally, this chapter discussed the structural relationship between the ordered, disordred and superstructures in details For example, Yb_2CuGe_6 can be considerd as the vacant variant of $SmNiGe_3$, $Yb_{6.6}Ir_6Sn_{16}$ is closely related to $Yb_5Ir_{5.5}Sn_{18}$ and $Eu_3T_2In_9$ is the metal deficient variant of the new structure type of $EuCu_2Ge_2$.

Since most of the compounds discovered or synthesized in this chapter are based on the mixed valent *RE*, the valency of *RE* has been studied by XANES and magnetic measurements. The chapter also discusses briefly about the magnetic and transport properties. Every compound discovered displayed not only the unique crystal structures, but also exhibited diverse physical properties. A systematic and more advanced temperature and magnetic field dependent structural and physical property measurements on these compounds will bring out the interesting physical phenomena.

5.10. References

1. Kanatzidis, M. G.; Pöttgen, R.; Jeitschko, W., *Angew. Chem. Int. Edit.* **2005,** *44*, 6996-7023.

2. Peter, S. C.; Rayaprol, S.; Francisco, M. C.; Kanatzidis, M. G., *Eur. J. Inorg. Chem.* **2011**, 3963-3968.

3. Peter, S. C.; Malliakas, C. D.; Kanatzidis, M. G., *Inorg. Chem.* **2013,** *52*, 4909-4915.

4. Peter, S. C.; Kanatzidis, M. G., *Z. Anorg. Allg. Chem.* **2012,** *638*, 287-293.

5. Chondroudi, M.; Peter, S. C.; Malliakas, C. D.; Balasubramanian, M.; Li, Q. A.; Kanatzidis, M. G., *Inorg. Chem.* **2011,** *50*, 1184-1193.

6. Peter, S. C.; Chondroudi, M.; Malliakas, C. D.; Balasubramanian, M.; Kanatzidis, M. G., *J. Am. Chem. Soc.* **2011,** *133*, 13840-13843.

7. Peter, S. C.; Kanatzidis, M. G., *J. Solid State Chem.* **2010,** *183*, 2077-2081.

8. Andress, K. R.; Alberti, E., *Z. Metallkd.* **1935,** *27*, 126-128.

9. Zarechnyuk, O. S.; Krypyakevych, P. I.; Gladyshevskii, E. I., *Sov. Phys. Crystallogr.* **1965,** *9*, 706-708.

10. STOE, C. *X-AREA, IPDS Software*, STOE & Cie GmbH: Darmstadt, 2006.

11. Petříček, V.; Dušek, M.; Palatinus, L., The crystallographic computing system. In *Jana2006*, Praha, Czech Republic, 2006.

12. SAINT 6.02; Bruker AXS Inc.: Madison, Wisconsin, USA, 2000.

13. Sheldrick, G. M., SADABS: Göttingen, Germany, 1997.

14. Andersen, O. K., *Phys. Rev. B* **1975,** *12*, 3060-3083.

15. Methfessel, M.; van Schilfgaarde, M.; Casali, R. A., *Lect. Notes Phys.* **2000,** *535*, 114-147.

16. Vosko, S. H.; Wilk, L.; Nusair, M., *Can. J. Phys.* **1980,** *58*, 1200-1211.

17. Methfessel, M.; Van Schilfgaarde, M.; Casali, R. A., *Lect. Notes Phys.* Springer: Berlin, 2000; Vol. 353, p 114.

18. Mao, J. G.; Goodey, J.; Guloy, A. M., *Inorg. Chem.* **2002,** *41*, 931-937.

19. Corbett, J. D., *Chemistry, Structure and Bonding of Zintl Phases and Ions*. VCH Publishers: New York, 1996; p 139.

20. Peter, S. C.; Chondroudi, M.; Malliakas, C. D.; Balasubramanian, M.; Kanatzidis, M. G., *J. Am. Chem. Soc.* **2011,** *133*, 13840-13843.

21. WinGX *A Windows Program for Crystal Structure Analysis*, *J. Appl. Crystallogr.*: 1999.

22. SHELXTL; 5.10 ed.; Bruker Analytical X-ray Systems, I. M., WI, 1998.

23. Bobev, S.; Bauer, E. D.; Thompson, J. D.; Sarrao, J. L.; Miller, G. J.; Eck, B.; Dronskowski, R., *J. Solid State Chem.* **2004,** *177*, 3545-3552.

24. Wortmann, G.; Nowik, I.; Perscheid, B.; Kaindl, G.; Felner, I., *Phys. Rev. B* **1991,** *43*, 5261-5268.

25. Buschow, K. H. J., *Handbook of Magnetic Materials*. Elsevier: UK, 2009; Vol. 18.

26. He, J.; Ling, G.; Jiao, Z., *Physica B* **2001,** *301*, 196-202.

27. Heying, B.; Rodewald, U. C.; Pöttgen, R.; Katoh, K.; Niide, Y.; Ochiai, A., *Monat. Chem.* **2005,** *136*, 655-661.

28. Kato, H.; Mano, Y.; Nakano, K.; Terui, G.; Niide, Y.; Ochiai, A., *J. Magn. Magn. Mater.* **2004,** *268*, 212-218.

29. Rieger, W.; Parthé, E., *Monat. Chem.* **1969,** *100*, 444.

30. Ghatikar, M. N.; Hatwar, T. K.; Padalia, B. D.; Sampathkumaran, E. V.; Gupta, L. C.; Vijayaraghavan, R., *Phys. Status Solidi B* **1981,** *106*, K89-K93.

31. Szytula, A.; Konyk, M.; Penc, B.; Winiarski, A., *Acta. Phys. Pol. A* **2008,** *113*, 1205-1209.

32. Katoh, K.; Maeda, M.; Matsuda, S.; Ochiai, A., *J. Magn. Magn. Mater.* **2012,** *324*, 2914-2920.

33. Konyk, M. B.; Salamakha, P. S.; Bodak, O. I.; Pecharsky, V. K., *Kristallografiya* **1988,** *33*, 838-840.

34. Hanel, G.; Nowotny, H., *Monat. Chem.* **1970,** *101*, 463-468.

35. Dhar, S. K.; Singh, S.; Bonville, P.; Mazumdar, C.; Manfrinetti, P.; Palenzona, A., *Physica B* **2002,** *312*, 846-847.

36. Peter, S. C.; Chondroudi, M.; Malliakas, C. D.; Balasubramanian, M.; Kanatzidis, M. G., *J. Am. Chem. Soc.* **2011,** *133*, 13840-13843.

37. Zhao, J. T.; Cenzual, K.; Parthé, E., *Acta Crystallogr. C* **1991,** *47*, 1777-1781.

38. Salamakha, P. S.; Konyk, M. B.; Dzyanyi, R.; Sologub, O. L.; Bodak, O. I., *Pol. J. Chem.* **1996,** *70*, 270-274.

39. Bodak, O. I.; Pecharsky, V. K.; Mruz, O. Y.; Zavodnik, V. E.; Vitvitskaya, G. M.; Salamakha, P. S., *Dopov. Akad. Nauk Ukr. RSR (Ser. B)* **1985,** *2*, 36-38.

40. Chen, X. Z.; Small, P.; Sportouch, S.; Zhuravleva, M.; Brazis, P.; Kannewurf, C. R.; Kanatzidis, M. G., *Chem. Mater.* **2000,** *12*, 2520-2522.

41. Pöttgen, R.; Gibson, B.; Kremer, R. K., *Z. Kristallogr.* **1997,** *212*, 58-58.

42. Rodewald, U. C.; Pöttgen, R., *Solid State Sci.* **2003,** *5*, 487-493.

43. Sologub, O.; Salamakha, P.; Bocelli, G.; Otani, S.; Takabatake, T., *J. Alloy Compd.* **2000,** *312*, 196-200.

44. Parthé, E.; Chabot, B., Crystal Structures and Crystal Chemistry of Ternary Rare Earth Transition Metal Borides, Silicides and Homologues. In Handbook on the Physics and Chemistry of Rare Earths. In Elsevier: New York, 1984; Vol. 48.

45. Gladyhevskii, R. E.; Sologub, O. L.; Parthé, E., *J. Alloy Compd.* **1991,** *176*, 329-335.

46. Niepmann, D.; Prots', Y. M.; Pöttgen, R.; Jeitschko, W., *J. Solid State Chem.* **2000,** *154*, 329-337.

47. Rao, C. N. R.; Sarma, D. D.; Sarode, P. R.; Sampathkumaran, E. V.; Gupta, L. C.; Vijayaraghavan, R., *Chem. Phys. Lett.* **1980,** *76*, 413-415.

48. Peter, S. C.; Disseler, S. M.; Svensson, J. N.; Carretta, P.; Graf, M. J., *J. Alloy Compd.* **2012,** *516*, 126-133.

49. Chevalier, B.; Peter, S. C.; Pöttgen, R., *Solid State Sci.* **2006,** *8*, 1000-1008.

50. Selsane, M.; Lebail, M.; Hamdaoui, N.; Kappler, J. P.; Noel, H.; Achard, J. C.; Godart, C., *Physica B* **1990,** *163*, 213-215.

51. Pöttgen, R.; Hoffmann, R. D.; Moller, M. H.; Kotzyba, G.; Kunnen, B.; Rosenhahn, C.; Mosel, B. D., *J. Solid State Chem.* **1999,** *145*, 174-181.

52. Francois, M.; Venturini, G.; Malaman, B.; Roques, B., *J. Less-Common Met.* **1990,** *160*, 197-213.

53. Niepmann, D.; Pöttgen, R.; Poduska, K. M.; DiSalvo, F. J.; Trill, H.; Mosel, B. D., *Z Naturforsch. B* **2001,** *56*, 1-8.

54. Venturini, G.; Malaman, B.; Roques, B., *Mater. Res. Bull.* **1989,** *24*, 1135-1139.

55. Cooper, A. S., *Mat. Res. Bull.* **1980,** *15*, 799-805.

56. Espinosa, G. P., *Mat. Res. Bull.* **1980,** *791-798.*

57. Peter, S. C.; Malliakas, C. D.; Nakotte, H.; Kothapilli, K.; Rayaprol, S.; Schultz, A. J.; Kanatzidis, M. G., *J. Solid State Chem.* **2012,** *187*, 200-207.

58. Stewart, G. R., *Rev. Mod. Phys.* **2001,** *73*, 797.

59. Vandenberg, J. M., *Mater. Res. Bull.* **1980,** *15*, 835-847.

60. Rodewald, U. C.; Pöttgen, R., *Solid State Sci.* **2003,** *5*, 487-493.

61. Rao, C. N. R.; Sarma, D. D.; Sarode, P. R.; Sampathkumaran, E. V.; Gupta, L. C.; Vijayaraghavan, R., *Chem. Phys. Lett.* **1980,** *76*, 413-415.

62. Chondroudi, M.; Peter, S. C.; Malliakas, C. D.; Balasubramanian, M.; Li, Q. A.; Kanatzidis, M. G., *Inorg. Chem.* **2011,** *50*, 1184-1193.

63. Chondroudi, M.; Balasubramanian, M.; Welp, U.; Kwok, W. K.; Kanatzidis, M. G., *Chem. Mater.* **2007,** *19*, 4769-4775.

64. Dremov, R. V.; Koblyuk, N.; Mudryk, Y.; Romaka, L.; Sechovsky, V., *J. Alloy Compd.* **2001,** *317*, 293-296.

65. Wang, Y. T.; Zhang, H.; Shao, H. Y.; Li, X. G.; Zhang, L. F.; Takahashi, S., *Appl. Phys. Lett.* **2006,** *88*, 072505-072508.

66. Takeshita, T.; Malik, S. K.; Wallace, W. E., *J. Solid State Chem.* **1978,** *23*, 271-274.

67. Yartys, V. A.; Parlenko, V. V., *Koord. Khim.* **1992,** *18*, 424-427.

68. Romaka, V. A.; Grin, Y.; Yarmolyuk, Y. P.; Zarechnyuk, O. S.; Skolozdra, R. V., *Phys. Met. Metallogr.* **1982,** *54*, 4-58.

69. Tsvyashchenko, A. V.; Fomicheva, L. N., *J. Less-Common Met.* **1987,** *135*, L9-L12.

70. Bruzzone, G.; Ferretti, M.; Merlo, F.; Olcese, G. L., *Lanthanide Actinide Res.* **1986,** *1*, 153-161.

71. Fornasini, M. L.; Raggio, R.; Borzone, G., *Z. Krist.- New Cryst. St.* **2004,** *219*, 75-76.

72. Fornasini, M. L.; Raggio, R.; Borzone, G., *Z. Krist.- New Cryst. St.* **2004,** *219*, 77-78.

73. Villars, P.; Cenzual, K. ASM International, Materials Park: Ohio, USA, 2011.

74. Bergerhoff, G.; Brown, I. D., International Union of Crystallography. In *In Crystallographic Databases; Allen, F. H. et al., Eds.;* , International Union of Crystallography: Chester, 1987.

75. Delsante, S.; Richter, K. W.; Ipser, H.; Borzone, G., *Z. Anorg. Allg. Chem.* **2009,** *635*, 365-368.

76. Bauer, E. D.; Bobev, S.; Thompson, J. D.; Hundley, M. F.; Sarrao, J. L.; Lobos, A.; Aligia, A. A., *J. Phys.: Condens. Matter* **2004,** *16*, 4025-4032.

77. Sheldrick, G. M., *Acta Crystallogr. A* **2008,** *64*, 112-122.

78. Sheldrick, G. M. 5.10; University of Göttingen: Göttingen, Germany, 1997.

79. Diamond 3.g; Rathausgasse, Bonn, Germany, 2011.

80. Gladyshevskii, R. E.; Cenzual, K.; Parthé, E., *J. Solid State Chem.* **1992,** *100*, 9-15.

81. Rykhal', R. M.; Zarechnyuk, O. S.; Yarmolyuk, Y. P., *Sov. Phys. Crystallogr.* **1972,** *17*, 453-455.

82. Verbovytsky, Y. V.; Mika, T.; Bednars' ka, L.; Kotur, B. Y., *Visn. L'viv. Derzh. Univ. (Ser. Khim.)* **2005**, 46-105.

83. Gladyshevskii, R. E.; Parthé, E., *Acta Crystallogr. C* **1992,** *48*,, 232-236.

84. Rykhal', R. M.; Zarechnyuk, O. S., *Dopov. Akad. Nauk Ukr. RSR (Ser. A)* **1977,** *39*, 375-377.

85. Rykhal', R. M.; Zarechnyuk, O. S.; Mandzin, V. M., *Dopov. Akad. Nauk Ukr. RSR (Ser. A)* **1980,** *6*, 77-82.

86. Zarechnyuk, O. S.; Rykhal', R. M.; Romaka, V. A.; Koval'skaya, O. K.; Sharabura, A. I., *Dopov. Akad. Nauk Ukr. RSR (Ser. A)* **1982,** *1*, 78-87.

87. Rykhal', R. M.; Zarechnyuk, O. S.; Protasov, V. S.; Romaka, V. A., *Dokl. Akad. Nauk Ukr. SSR, Ser. B* **1982,** *3*, 43-45.

88. McCarthy, J. E.; Duffy, J. A.; Detlefs, C.; Cooper, M. J.; Canfield, P. C., *Phys. Rev. B* **2000,** *62*, R6073-R6076.

89. Dzyanyi, R. B.; Bodak, O. I.; Pavlyuk, V. B., *Russ. Metall.* **1995**, 133-135.

90. Salvador, J. R.; Gour, J. R.; Bilc, D.; Mahanti, S. D.; Kanatzidis, M. G., *Inorg. Chem.* **2004,** *43*, 1403-1410.

91. Shigetoh, K.; Hirata, D.; Avila, M. A.; Takabatake, T., *J. Alloy Compd.* **2005,** *403*, 15-18.

92. Chondroudi, M.; Balasubramanian, M.; Welp, U.; Kwok, W. K.; Kanatzidis, M. G., *Chem. Mater.* **2007,** *19*, 4769-4775.

93. Rossi, D.; Ferro, R.; Contardi, V.; Marazza, R., *Z. MetaIlkd.* **1977,** *68*, 493-497.

94. Benbow, E. M.; Latturner, S. E., *J. Solid State Chem.* **2006,** *179*, 3989-3996.

95. Lefevre, C.; Venturini, G.; Malaman, B., *J. Alloy Compd.* **2003,** *358*, 29-35.

96. Gordon, R. A.; Ijiri, Y.; Spencer, C. M.; Disalvo, F. J., *J. Alloy Compd.* **1995,** *224*, 101-107.

97. Poduska, K. M.; DiSalvo, F. J.; Petricek, V., *J. Alloy Compd.* **2000,** *308*, 64-70.

98. Dominyuk, D.; Zaremba, V. I.; Pöttgen, R., *Z. Naturforsch.* **2011,** *66b*, 433-436.

99. Lahiouel, R.; Pierre, J.; Siaud, E.; Murani, A. P., *J. Magn. Magn. Mater.* **1987,** *63-4*, 104-106.

100. Tobash, P. H.; Lins, D.; Bobev, S.; Lima, A.; Hundley, M. F.; Thompson, J. D.; Sarrao, J. L., *Chem. Mater.* **2005,** *17*, 5567-5573.

101. Zaremba, V. I.; Muts, I. R.; Rodewald, U. C.; Hlukhyy, V.; Pöttgen, R., *Z. Anorg. Allg. Chem.* **2004,** *630*, 1903-1907.

102. Allen, F. H.; Kennard, O.; Watson, D. G.; Brammer, L.; Orpen, A. G.; Taylor, R., *J. Chem. Soc.* **1987,** *2*, S1–S19.

103. Sanderson, R. T., *J. Am. Chem. Soc.* **1983,** *105*, 2259–2261.

104. Smart, J. S., *Effective Field Theories of Magnetism*. Philadelphia, Pennsylvania, 1966.

105. Kittel, C., *Introduction to Solid State Physics* 7th ed.; John Wiley & Sons: Hoboken, NJ, 1996; p 426.

106. Rao, C. N. R.; Sarma, D. D.; Sarode, P. R.; Sampathkumaran, E. V.; Gupta, L. C.; Vijayaraghavan, R., *Chem. Phys. Lett.* **1980,** *76*, 413-415.

107. Bergerhoff, G.; Brown, I. D. *International Union of Crystallography*, In Crystallographic Databases: Chester, 1987.

108. Sysa, L. V.; Kalychak, Y. M.; Ctets, I. N.; Galadzhun, Y. V., *Kristallografiya.* **1994,** *39*, 821-824.

109. Subbarao, U.; Sarkar, S.; Peter, S. C., *J. Solid State Chem.* **2015,** *226*, 126-132.

110. Amerioun, S.; Haussermann, U., *Inorg. Chem.* **2003,** *42*, 7782-7788.

111. Kuzma, Y. B.; Stelmakhovich, B. M., *Russ. Metall.* **1990**, 209-211.

112. Kuz'ma, Y. B.; Stel'makhovych, B. M., *Dopov. Akad. Nauk Ukr. RSR (Ser. B)* **1988,** *11*, 38-41.

113. Pecharskii, V. K.; Pankevich, Y. V.; Bodak, O. I., *Dopov. Akad. Nauk Ukr. RSR (Ser. B)* **1982,** *4*, 44-48.

114. Levin, E. M.; Kuzhel, B. S.; Bodak, O. I.; Belan, B. D.; Stets, I. N., *Phys. Status Solidi B* **1990,** *161*, 783-795.

115. Felner, I.; Nowik, I., *J. Phys. Chem. Solids* **1978,** *39*, 763-773.

116. Mayer, I.; Felner, I., *J. Phys. Chem. Solids* **1977,** *38*, 1031-1034.

117. Wang, P.; Stadnik, Z. M.; Zukrowski, J.; Cho, B. K.; Kim, J. Y., *Solid State Commun.* **2010,** *150*, 2168-2173.

118. Banik, S.; Bendounan, A.; Thamizhavel, A.; Arya, A.; Risterucci, P.; Sirotti, F.; Sinha, A. K.; Dhar, S. K.; Deb, S. K., *Phys. Rev. B* **2012,** *86*.

119. Gomes De Mesquita, A. H.; Buschow, K. H. J., *Acta Crystallogr.* **1967,** *22*, 497-501.

120. Belan, B.; Bodak, O.; Gladyshevskii, R.; Soroka, I.; Kuzhel, B.; Protsyk, O.; Stets, I., *J. Alloy Compd.* **2005,** *396*, 212-216.

121. Inoue, T.; Kubozono, Y.; Kashino, S.; Takabayashi, Y.; Fujitaka, K.; Hida, M.; Inoue, M.; Kanbara, T.; Emura, S.; Uruga, T., *Chem. Phys. Lett.* **2000,** *316*, 381−386.

122. Kim, K.-B.; Kim, Y. I.; Chun, H.-G.; Cho, T.-Y.; Jung, J.-S.; Kang, J. G., *Chem. Mater.* **2002,** *14*, 5045−5052.

Chapter 6

Nanofication and Dimensional Reduction Mediated Valence Transition as a Tool towards Air Stable Material

---

Manuscript based on this work is under revision.

6.1. Introduction

Designing nanostructured materials with different morphology is an important tool in the field of nanotechnology as it gives an extra handle to manipulate the materials for unique magnetic, optical, catalytic and transport properties. During the last two decades, considerable interests have grown in the fabrication of low-dimensional materials, such as nanorods,[1] nanowires,[2] nanotubes,[3] nanospheres[4] and nanoplates[5] due to their potential applications in the disciplines of chemistry,[6] physics[7] and medicine.[8, 9] A few notable technological applications of these materials recently developed are solar cell,[10] water splitting,[11] hydrogen generation,[1] catalysis,[12] photodetector,[2] optical transmission,[5] engineered electronic and magnetic phases[13] and drug delivery.[14] However, use of several promising materials having desired chemical and physical properties in potential applications is limited due to their lack of stability in normal conditions. For example, perovskite based materials are proved to be promising with power efficiency of more than 15% in solar cell.[15] Although, these materials showed remarkable ability to convert solar energy to electrical energy, their stability under ambient conditions is still questionable due to their degradation into other chemical species in the presence of oxygen. High temperature YBCO superconductors are another class of materials, in which the origin of the superconductivity was proposed due to the presence of trivalent copper atom. However, it is quite obvious that these materials would not survive in air and aqueous solution due the presence of unstable trivalent copper.[16] The well-known blood pool MRI agents based on iron oxides are also found to be less stable in air.[17]

The oxidation state of an element has significant effect on the Gibbs free energy ($-\Delta G^o$) of a system, which in turn is a direct measure of the stability of a material associated with it. This can be presented either by Latimer diagram or Frost diagram in terms of volts equivalent (nE^o) as $-\Delta G^o/F = nE^o$. Frost diagram is valid for multivalent ionic species in extreme acidic or alkaline medium. The calculated nE^o for three sets of metal family, namely six transition metals, four *p*-block metals and four *RE*s in basic medium and plotted them against corresponding oxidation states assuming that addition of sodium borohydride ($NaBH_4$), which is used as a reducing agent in ethylene glycol (EG) would give rise to alkaline medium. It is apparent from Figure 6.1 that a particular oxidation state is more stable in aqueous medium (higher oxidation states in most of the cases) over others owing to the

advantages in terms of hydration energy. Hence, a material can be stabilized in a given medium by modulating its oxidation state by chemical route keeping in mind that change in oxidation state will inevitably bring changes in the electronic structure of the material, which may give way to discovery of newer properties in addition to the stability of the materials.

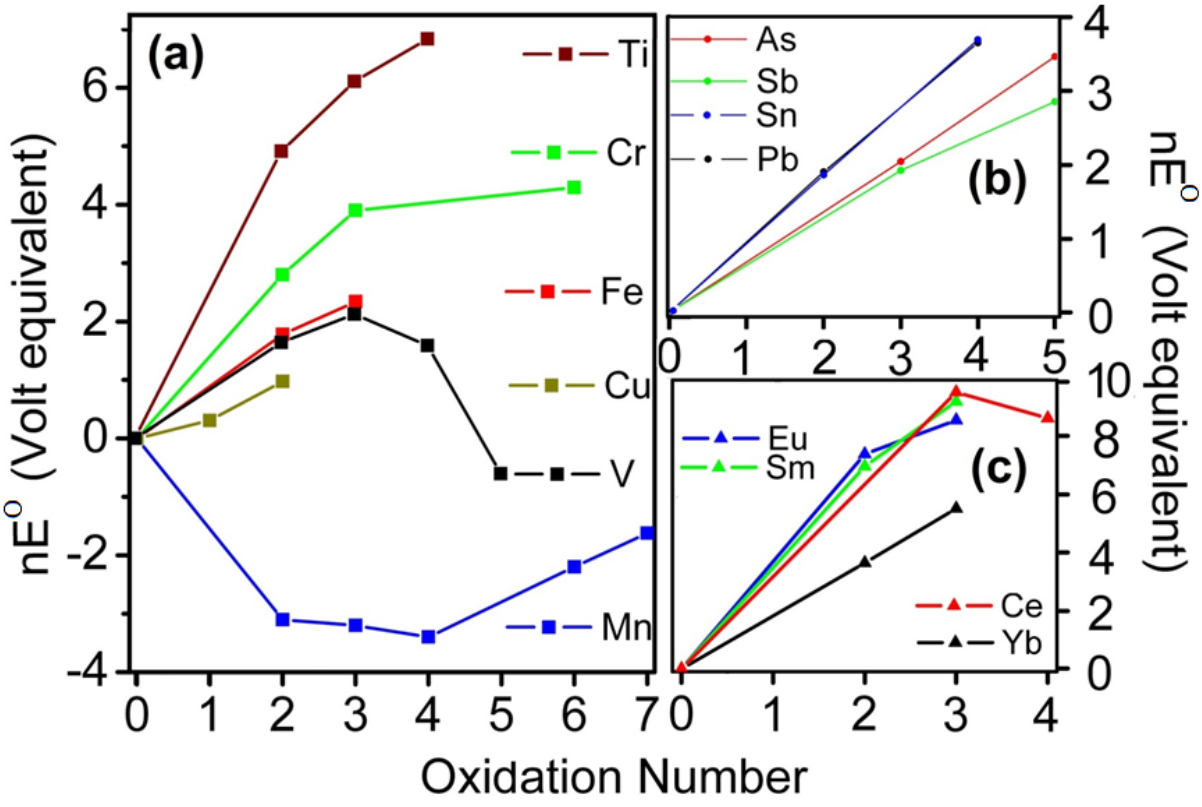

Figure 6.1. Frost diagram on selected elements having the probability of multiple oxidation states; (a) transition metals, (b) p-block metals and (c) *RE* metals

To circumstantiate this proposal, a few selected compounds *RE*Pb_3 (*RE* = Eu and Yb) strategically synthesized in ordered nano-dimension with different size and morphology using solvothermal method. *RE*Pb_3 compounds crystallizing in the ordered cubic $AuCu_3$ structure type, with space group $Pm\bar{3}m$, have been previously synthesized by HFIH.[18] $EuPb_3$[19] is reported as paramagnetic and $YbPb_3$ is reported as diamagnetic.[20] The work has focused only to Eu and Yb compounds as they have the ability to exist in two energetically similar electronic configurations, which may leads into valence transitions towards the higher oxidation and aerial stability.

6.2. Experimental Section

6.2.1. Chemicals

The following materials were used for the synthesis: Ytterbium (III) chloride ($YbCl_3$), lanthanum (III) chloride ($LaCl_3$), europium (III) chloride ($EuCl_3$) and lead (II) acetate trihydrate ($Pb(CH_3COO)_2.3H_2O$) as solid salt precursors, ethylene glycol (EG) as solvent was purchased from Alfa Aesar with purity 99.99%. Polyvinylpyrrolidone (PVP) and Cetyl trimethylammonium bromide (CTAB) as surfactants and $NaBH_4$ as the reducing agent purchased from Sigma Aldrich with more than 98% purity. The ordered compounds have synthesized by the following two methods.

6.2.2. Solvothermal method

Pure phase of *RE*Pb_3 (*RE* = Yb, La and Eu) nanoparticles were synthesized by the solvothermal method in the presence and absence of surfactants and ethylene glycol as solvent. The compounds are represented as $YbPb_3$_None ($YbPb_3$-N), $YbPb_3$_PVP ($YbPb_3$_P), $YbPb_3$_CTAB ($YbPb_3$_C), $EuPb_3$_None ($EuPb_3$_N) and $LaPb_3$_None ($LaPb_3$_N). 0.1 moles of $YbCl_3$ (0.0279 g), $LaCl_3$ (0.0245g), $EuCl_3$ (0.0258) and 0.3 moles of $Pb(CH_3COO)_2.3H_2O$ (0.1138 g) were taken in three different 25 ml teflon lined stainless steel autoclave filled with EG of about 80% (20 ml). $LaPb_3$ was synthesized as controlled material assuming that there is no valence transition expected for La. The surfactants (0.080 g) were added followed by $NaBH_4$ in greater than twice stoichiometric amount into the solution for respected reactions. The autoclave was then immediately sealed and kept for heating at 493 K for four different reaction times 12, 24, 36 and 48 h for $YbPb_3$ and 24 h for $LaPb_3$ and $EuPb_3$. After the reaction was complete, the autoclave was cooled down to the room temperature (300 K) naturally. Black precipitate was then washed thoroughly with ethanol several times by centrifuging at 8000 rpm for 5 min followed by drying under vacuum at 333 K for 8 h. All the characterizations were carried out on dried powder samples.

6.2.3. High Frequency Induction Heating (HFIH)

HFIH method was used for the synthesis of polycrystalline material with large particle size approximately in micron range. *RE* and lead elements were mixed with three different reactions in the ideal 1:3 atomic ratio and sealed in tantalum ampoules under argon atmosphere in an arc-melting apparatus. The tantalum ampoules were subsequently placed in a water-cooled sample chamber of an induction furnace (Easy Heat induction heating system,

Model 7590), first rapidly heated to 160 Amperes (ca. 1100 K) and kept at that temperature for 30 min. Finally, the reaction was rapidly cooled down to room temperature by switching off the power supply. The product could easily be removed from the tantalum tubes and no reaction with the crucible material was observed. The polycrystalline samples of $YbPb_3$ _Bulk ($YbPb_3$_B) and $EuPb_3$_Bulk ($EuPb_3$_B) were stable only for one week, followed by slow decomposition to oxide of ytterbium in $YbPb_3$ and to oxide of lead in $EuPb_3$. They were in polycrystalline form with light grey in colour. The weight losses of the final material were found to be less than 1%. The samples obtained from the HFIH method were used for the bulk property studies.

6.2.4. Characterization

Phase identity and purity of all the compounds were determined by powder XRD experiments with a Bruker D8 Discover diffractometer using Cu-$K\alpha$ radiation (λ = 1.5406 Å) over the angular range $20^{\circ} \leq 2\theta \leq 80^{\circ}$ at 300 K calibrated against corundum standard. The experimental powder patterns of all the compounds and the XRD pattern simulated from the reported data were found to be in good agreement (Figure 6.2).[21]

All stability tests in air were characterized by using powder XRD. Quantitative microanalyses on $YbPb_3$ were performed with a FEI NOVA NANOSEM 600 instrument equipped with an EDAX® instrument. Data were acquired with an accelerating voltage of 20 kV and a 100 s accumulation time. The EDAX analysis was performed using P/B-ZAF standardless method (where, Z = atomic no. correction factor, A = absorption correction factor, F = fluorescence factor, P/B = peak to background model) on selected spots and points. The compositions obtained for the Yb:Pb ratio confirmed the Pb deficiency in nanomaterial compared to the bulk compound. The EDAX spectra of $YbPb_3$ are shown in Figure 6.3. TEM, HRTEM images and SAED patterns were collected using a JEOL 200 TEM instrument. Samples for TEM were prepared by sonicating the nanocrystalline powders in ethanol and dropping a small volume onto a carbon-coated copper grid.

Magnetic measurements were carried out using a Quantum Design MPMS-SQUID magnetometer. Measurements were performed on poly crystalline samples, which were grinded and screened by powder XRD to verify phase identity and purity. Temperature dependent magnetic susceptibility data were collected in the FC from 2 to 300 K in an applied field (H) of 10 and 1000 Oe. Field dependent magnetization data were also collected

for *RE*Pb_3 (*RE* = Yb, La and Eu) nanoparticles at 2 and 300 K with field sweeping from -50 kOe to 50 kOe.

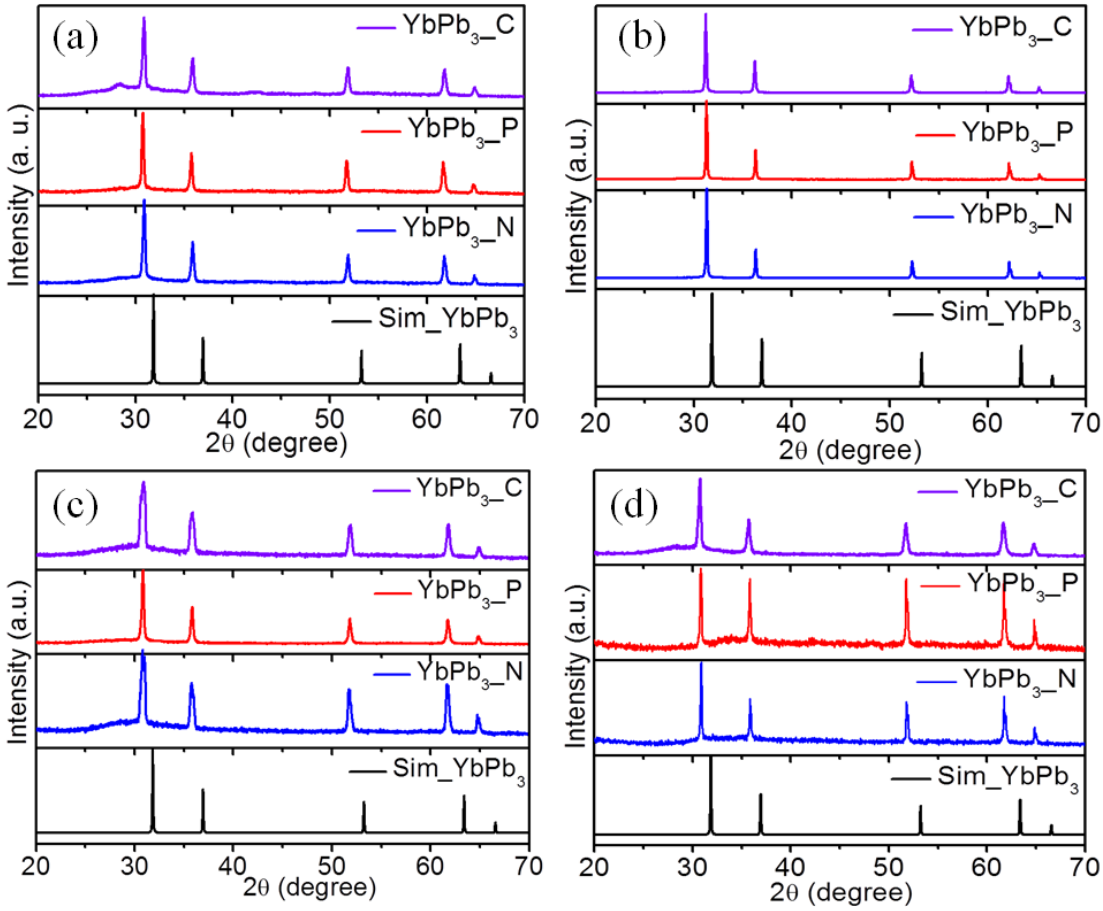

Figure 6.2. Experimental and simulated powder patterns of $YbPb_3$ nanoparticle in the presence and absence of surfactant at 12h, 24h, 36h and 48h.

XANES experiments at 300 K on $YbPb_3$_NB, $YbPb_3$_N, $YbPb_3$_P and $YbPb_3$_C, $EuPb_3$_B and $EuPb_3$_N were performed at PETRA III, P06 beamline of DESY, Germany. Measurements at the Eu and Yb L_{III}-edges and at ambient pressure were performed in transmission mode using gas ionization chambers to monitor the incident and transmitted X-ray intensities. Monochromatic X-rays were obtained using a Si [111] double crystal monochromator, which was calibrated by defining the inflection point (first derivative maxima) of Cu foil as 8980.5 eV. The beam was focused employing a Kirkpatrick–Baez (K–B) mirror optic. A rhodium coated X-ray mirror was used to suppress higher order harmonics. A CCD detector was used to record the transmitted signals. The sample was prepared by mixing an appropriate amount of finely ground powder with cellulose and cold

pressing them to a pellet. TGA of $YbPb_3$_B and $YbPb_3$_N samples were recorded on Perkin-Elmer TGA analyzer. Samples were carried out in Ar and O_2 atmosphere (flow rate 40 mL/min) with the heat rate of 10 K/min within the temperature range 303-1000 K.

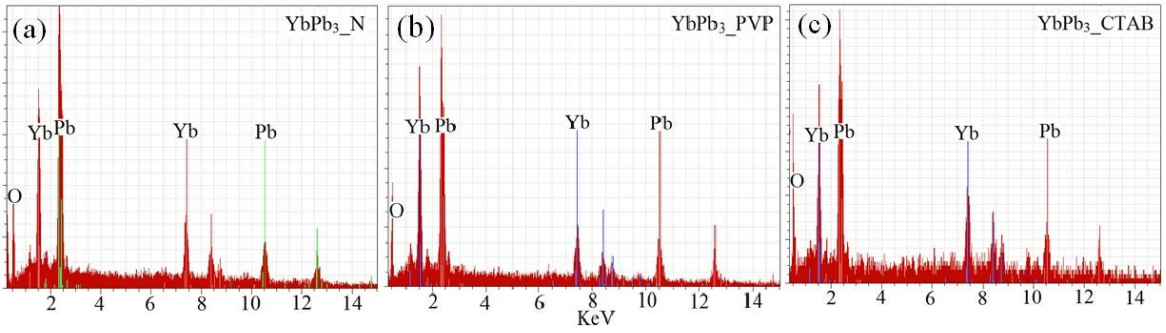

Figure 6.3. Typical EDAX spectrum for $YbPb_3$_None, $YbPb_3$_PVP and $YbPb_3$_CTAB for 24h sample.

The Latimer diagram for each of the element in acidic media was taken from literature.[22] The corresponding reduction potential for each redox pair was calculated using the equation: $E = E^o - 0.059\ pH$,[23] where, E = reduction potential, E^o is standard reduction potential. In extreme acidic conditions, pH = 0, $E_a = E^o$. All the potentials were calculated extreme basic conditions pH =14 using $E_b = E_a - (0.059 \times 14)$.

The microstructural strain in both the bulk and nano samples of $YbPb_3$ from the corresponding PXRD patterns have been calculated using Williamson-Hall (WH) method using the equation $\beta_r = K\lambda/D\cos\theta + 4\eta\tan\theta$.[24, 25] Here, β_r is the resultant broadening after subtracting from the instrumental broadening. The first term ($K\lambda/D\cos\theta$) in the right hand side is from Scherer equation which accounts for broadening owing to crystallite size, while the second term i.e. ($4\eta\tan\theta$) is the measure of broadening arising due to microstructural strain and η is directly proportional to strain. Best fitting parameters were obtained when Lorentzian and Gaussian functions were used for bulk and nano samples respectively. Details of this procedure can be found elsewhere.[26, 27] Linear fitting of $\beta_r\cos\theta$ vs. $4\sin\theta$ curve yielded values of η, which were 5.6×10^{-5} and 5.3×10^{-4} for bulk and nano, respectively.

6.3. Results and Discussions

6.3.1. Reaction Chemistry

REPb_3 compounds crystallize in the ordered cubic $AuCu_3$ structure type with space group $Pm\bar{3}m$ (Figure 6.4). In solvothermal method, pure phase of $YbPb_3$ was obtained by varying different parameters such as time intervals, surfactants and solvents. Since the

standard reduction potentials of Yb^{3+} and Pb^{2+} are -2.19 and -0.13 V,[28] respectively, Pb^{2+} is more easily reduced to Pb^{o} in the solution compared to the reduction of Yb^{3+} to Yb^{0}. The slight shift of all peaks in the powder XRD patterns (Figures 6.2) towards the lower 2θ angle indicates 8% deficiency in Pb content, which was calculated from the rietveld refinement of the XRD pattern and later confirmed by the EDAX measurements (Figure 6.3 and Table 6.1).

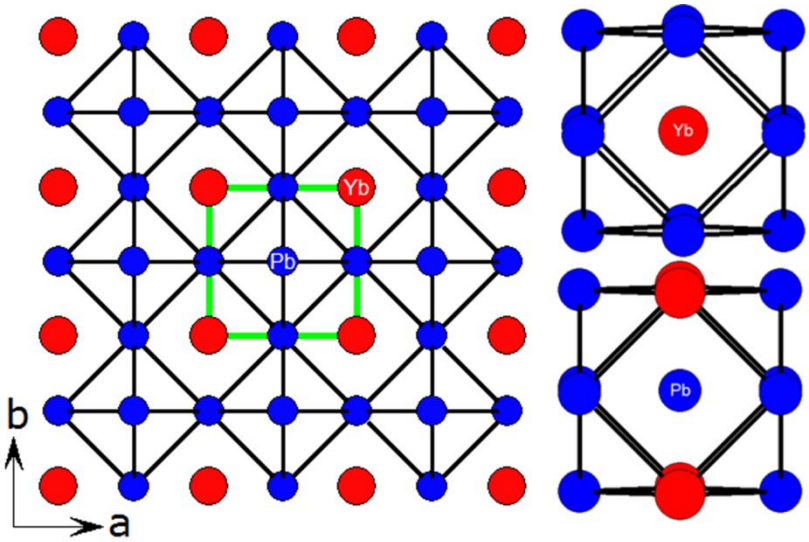

Figure 6.4. The crystal structure of $YbPb_3$ (left side) as viewed along the *c*-axis; the unit cell is outlined as green solid lines and the coordination environment (right side) of Yb and Pb.

Table 6.1: Rietveld refinement composition and EDAX compositions obtained for $YbPb_3$_N 24h sample.

Compound	Rietveld Refinement composition (For 24h sample)		EDAX composition (For 24h sample)	
	Yb	Pb	Yb	Pb
$YbPb_3$_N	27.26	73.88	31.64	68.36

Variation of surfactant is one of the most important parameters in controlling the size and morphology of the nanoparticles.[29-35] There are two distinct cases in the nanofication processes: the first one is the occurrence of magnetism in the nanoparticles with nonmagnetic in their corresponding bulk phases as noticed in several nonmagnetic inorganic oxides ZnO, SnO_2, In_2O_3, HfO_2, CdS, GaN and NbN.[36, 37] The presence of oxygen, sulphur and nitrogen vacancies have been asserted as the cause for the "universal" occurrence of ferromagnetism in these type of nanomaterials, which are diamagnetic in their bulk phases.[36] In the second case, there is switch from one type of magnetic phenomenon to the other as noticed in Mn nanoparticles.[38] The presence of additives or surfactant molecules used during the synthesis

may further affect and sometimes complicate the magnetic properties of the system. Occurrence of ferromagnetic ordering in thiolate modified gold nanoparticles is an ideal example in this context.[39] In fact, $YbPb_3$ is the first *RE* based intermetallic material synthesized as nanomaterial in different morphologies. TEM measurements and SAED patterns on the sample in the absence of surfactant ($YbPb_3$_N) show that nanofication (NF) favoured the formation of spherical nanoparticles. On the other hand, the surfactants CTAB ($YbPb_3$_C) and PVP ($YbPb_3$_P) favour both NF and dimensional reduction (DR) in the formation of rod shaped nanoparticles. In effect, the overall role of the surfactants may be conceived as an indirect scission along a particular direction(s) or plane(s) so that growth occurs in other direction(s). Figure 6.5a shows the representative unit cell of $YbPb_3$. In the absence of surfactants, the growth of nanoparticle on the seed happens along all the planes with equal probability (Figure 6.5b). The particle size measured from the TEM for the sample obtained after 24 h of reaction is about 16 nm (Figures 6.5c and 6.6).

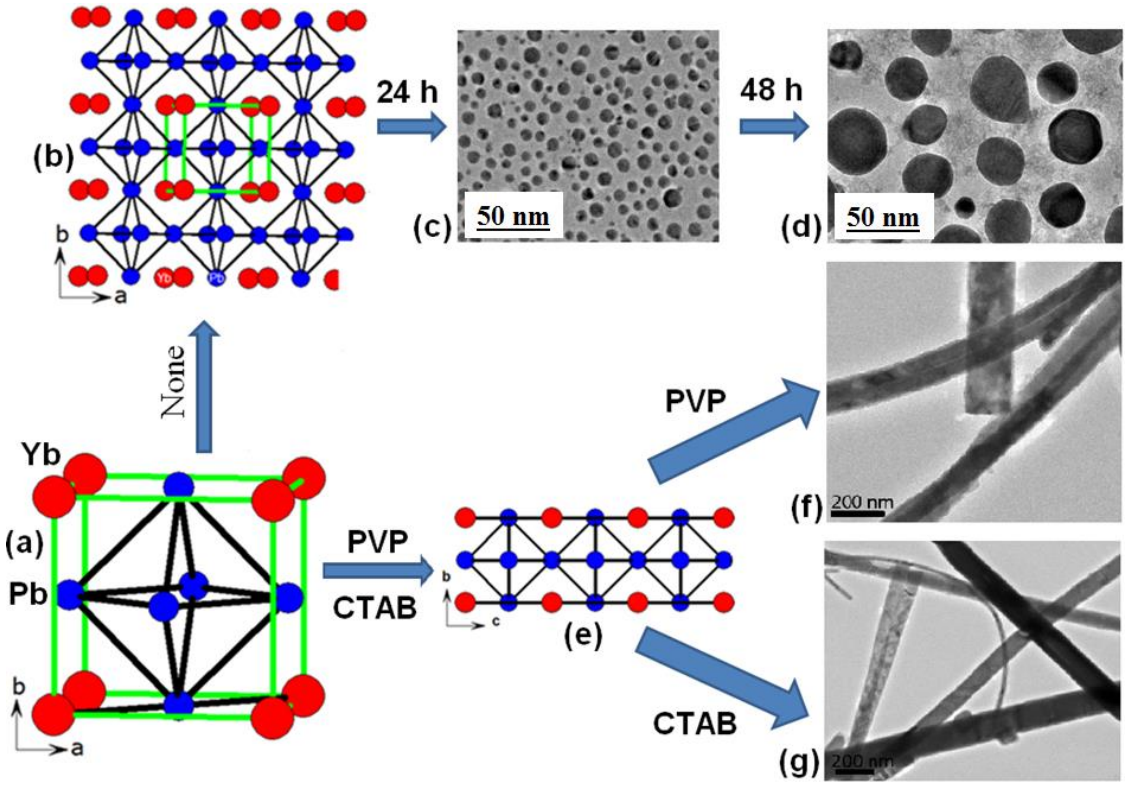

Figure 6.5. Surfactant directed morphological evolution in the formation of $YbPb_3$ nanoparticle. Unit cell of $YbPb_3$, (a) three dimensional structure of $YbPb_3$ in the absence of any surfactant (b) TEM image of spherical nanoparticle without surfactant after 24 h (c) and 48 h (d), surfactant assisted dimensional reduction to one dimension crystal structure of $YbPb_3$ (e) and TEM images of PVP (f) and CTAB (g) assisted growth of nanorods of $YbPb_3$.

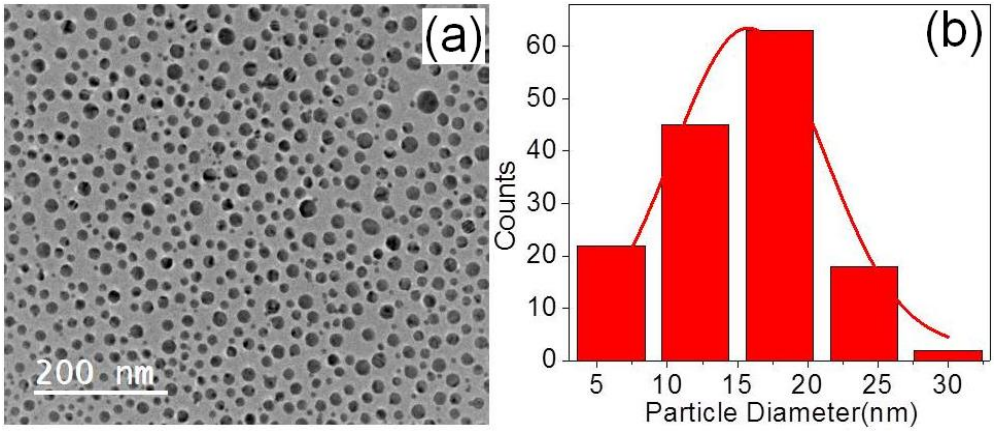

Figure 6.6. TEM image and the corresponding particle size histograms of $YbPb_3$_N for 24h sample.

As the reaction time extends the nucleation and growth continued in all directions resulting in larger particle size (Figure 6.5d). The particle size for the sample obtained after 48 h of reaction is about 45 nm as shown in Figure 6.7. These values are corroborating with the crystallite size obtained using Scherrer formula on the powder XRD data with 24 nm and 51 nm, respectively (Table 6.2).

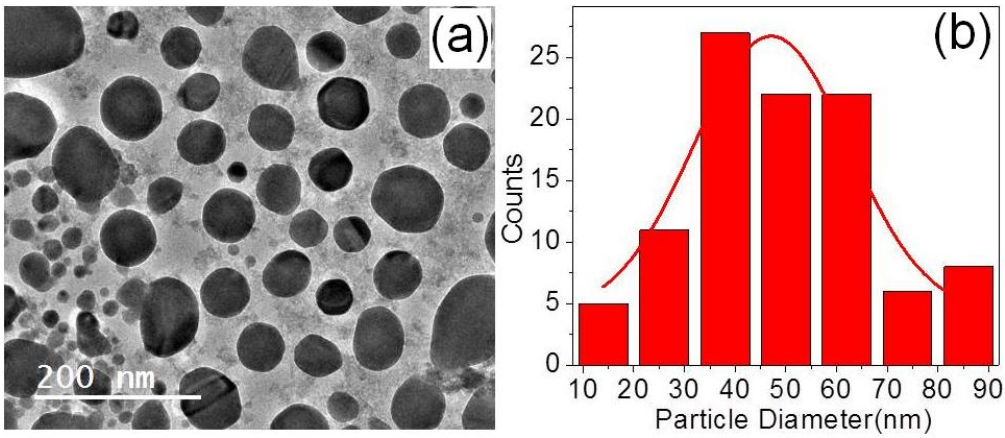

Figure 6.7. TEM image and the corresponding particle size histograms for $YbPb_3$_N for 48 h sample.

Table 6.2: Crystallite size calculated using Scherrer formula on the powder XRD data and EDAX compositions obtained for $YbPb_3$_N, $YbPb_3$_P and $YbPb_3$_C of 24 and 48 h.

Compound	Crystallite size (nm)	
	24 h	48 h
$YbPb_3$_N	24.369	51.72
$YbPb_3$_P	40.85	46.16
$YbPb_3$_C	20.66	27.49

In the presence of surfactants PVP and CTAB, the NF and DR resulted in one dimensional nanorods of around 40 nm and 20 nm width (Figure 6.5e). The nanorods obtained with PVP and CTAB are shown in Figures 6.5f and 6.5g. The mechanism of CTAB-triggered nanorod formation in aqueous solution (a polar solvent) has been reported previously by several groups.[35, 40] A similar mechanism can be proposed for the $YbPb_3$ nanorod formation as EG is highly polar solvent. In polar solvents at high temperature CTAB forms a double layer structure,[41] which acts as a soft template for the nucleation and growth of $YbPb_3$ nanorods in [100] direction, which is also clear from the HRTEM images of rod (Figure 6.8b). Similarly, PVP acts as a surface regulating polymer to control rod like morphology.[42, 43] PVP has a polyvinyl skeleton with polar group (N-C=O), which may preferentially absorb on the faces parallel to the [100] axis direction[42] of the $YbPb_3$ seeds, leading to the growth along [100] direction forming rod like morphology (Figure 6.5f). The HRTEM and SAED pattern for the selected sphere and rod shaped nanocrystals were taken and shown in Figure 6.8.

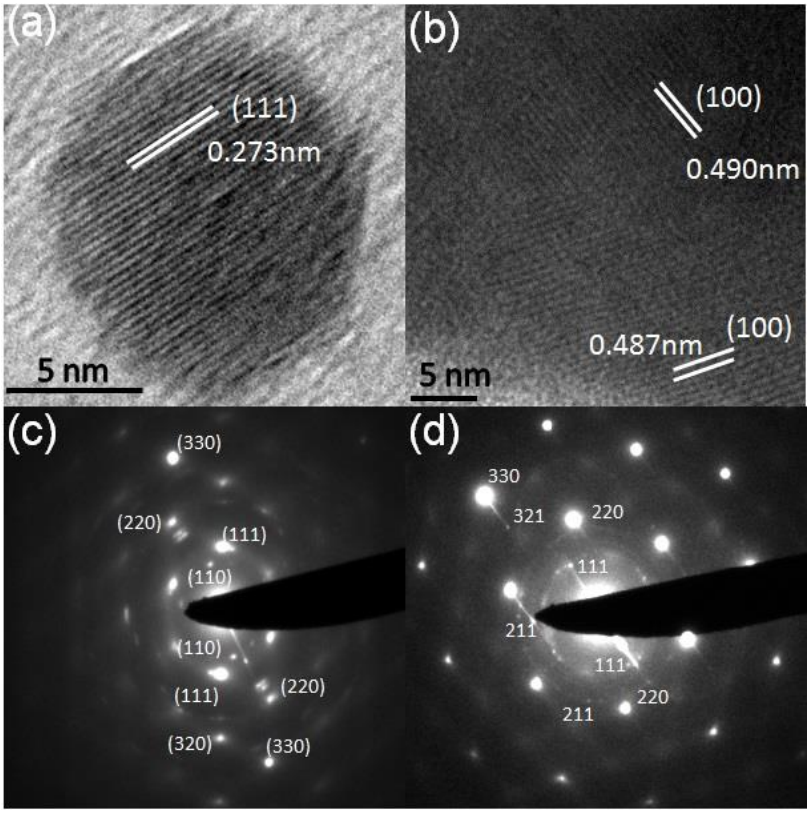

Figure 6.8. HRTEM images for $YbPb_3$_N24 (a) and $YbPb_3$_P24 (b) and the corresponding SAED patterns in (c) and (d).

The intensity ratio of the planes [111] to [200] in the powder XRD pattern has been calculated for the samples synthesized after 24 h and 48 h. As expected, the ratio remains the same for the sample without surfactant, but proportionally increased for the sample with PVP, which suggests that the growth occurs along the [100] direction. This is very well supported by TEM as there is no change in the width of nanorods (~40 nm) in the case of samples with PVP (Figure 6.9a). However, interestingly, this ratio with CTAB remains close for 24 h and 48 h samples, which was further supported by TEM as there is a 5 times enhancement in the width of nanorods from 20 nm for the 24 h sample to ~250 nm for 48 h sample (Figure 6.9b) with a proportional enhancement in the length of the crystals.

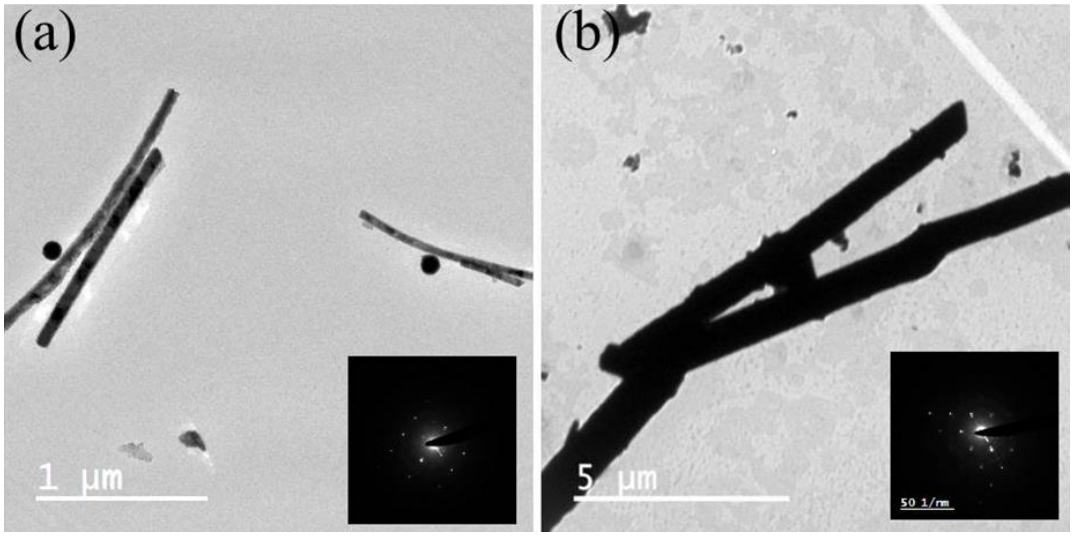

Figure 6.9. TEM images of $YbPb_3$ (48h) synthesized by solvothermal method in the presence of PVP (a) and CTAB (b). Inset figures show corresponding SAED pattern.

HRTEM (Figures 6.8) clearly shows the lattice fringes, suggesting that the crystal growth occurs in a particular direction. In case of spherical sample ($YbPb_3$_N), the d-spacing calculated is 0.273 nm suggests growth occurs along the [111] direction, while in the case of nanorods ($YbPb_3$_P/C), d-spacing is 0.490 nm that confirms the crystal growth along [100] direction. The SAED patterns confirm highly ordered crystalline state and the presence of only one set of diffraction spots in both samples (Figure 6.8c and 6.8d) indicates that unique growth direction as a result of NF and DR (Figure 6.10).

PVP is known to preferentially bind with [110] planes of the polyhedral seeds. It is proposed that these seeds orient along [100] plane, which is more accessible due to the presence of relatively lesser number of additive molecules at high temperature.[44] This

mechanism can also explain the inhibition of lateral growth of the nanorods synthesized at higher reaction time in presence of PVP as a result of selective blocking of [110] planes by the additive. CTAB on the other hand, is known to form double layer miceller tubes which act as a soft template towards the synthesis of rod like morphology.[45] This ability in fact leads to an increase in the width of nanorods as the reaction time increases.

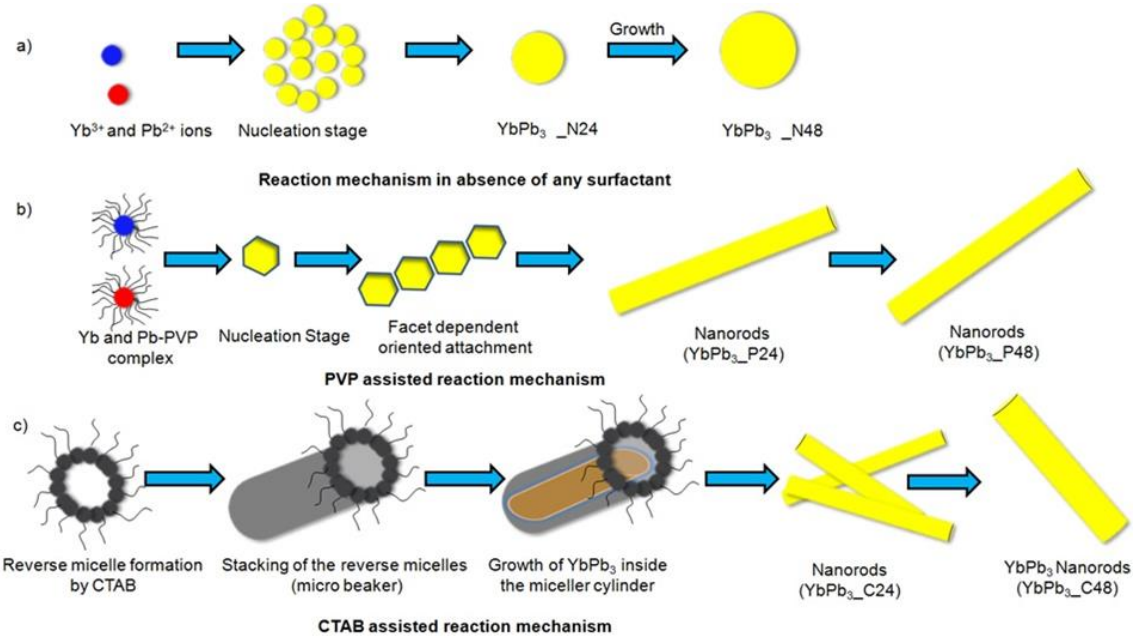

Figure 6.10. Cartoon presentation of the crystal growth at 24 and 48h of (a) $YbPb_3$_N, (b) $YbPb_3$_P and (c) $YbPb_3$_C.

6.3.2. Magnetism

Anticipating valence fluctuations of Yb and surface magnetism as proposed earlier for several *RE* oxides, and performed magnetic measurements on all compounds at an applied field of 1000 Oe (Figure 6.11). The diamagnetic nature of bulk $YbPb_3$ ($YbPb_3$_B) reported earlier[18] was confirmed by magnetic measurements (Figure 6.11a). The negative slope in field dependent magnetization data at room temperature (300 K, inset in Figure 6.11a) and low temperature (2 K, See Figure 6.12), suggest that $YbPb_3$_B is purely diamagnetic with divalent Yb. On the other hand, temperature dependent inverse susceptibility (Figure 6.11b) curve above 100 K for all nanoparticles obey CW law, $\chi(T) = C/(T-\theta_p)$.[46, 47] where C is the CW constant ($N_A\mu_{eff}^2/3K_bT$) and θ_p is the Weiss temperature. A fit to the curve in high temperature range resulted in an effective magnetic moment of 4.98, 4.18 and 3.6 μ_B/Yb atom for $YbPb_3$_N, $YbPb_3$_P and $YbPb_3$_C, respectively, suggesting the

existence of Yb^{3+} in all these materials. These results confirmed the fact that scaling the size from micro to nano-regime triggered the valence fluctuation of nonmagnetic divalent Yb to magnetic trivalent Yb. The estimated experimental μ_{eff} value for $YbPb_3$_N is about 10% more than that of expected for a free ion Yb^{3+} moment (4.56 μ_B/Yb), which can be attributed to other parameters, mostly surface magnetism or deficiency also contributing to the total magnetic moment in addition to trivalent Yb. This is in fact corroborating with 8% of Pb deficiency observed in XRD and EDAX measurements (Table 6.1), but the possible role of surface magnetism cannot be ruled out completely. In addition, the estimated experimental μ_{eff} value for $YbPb_3$_P and $YbPb_3$_C are respectively 9% and 21%, lower than that of expected value of Yb^{3+}can be attributed to crystal field contributions. The transition from Yb^{2+} in bulk material to Yb^{3+} in nanomaterials was also confirmed from the magnetization measurements (Figure 6.11c).

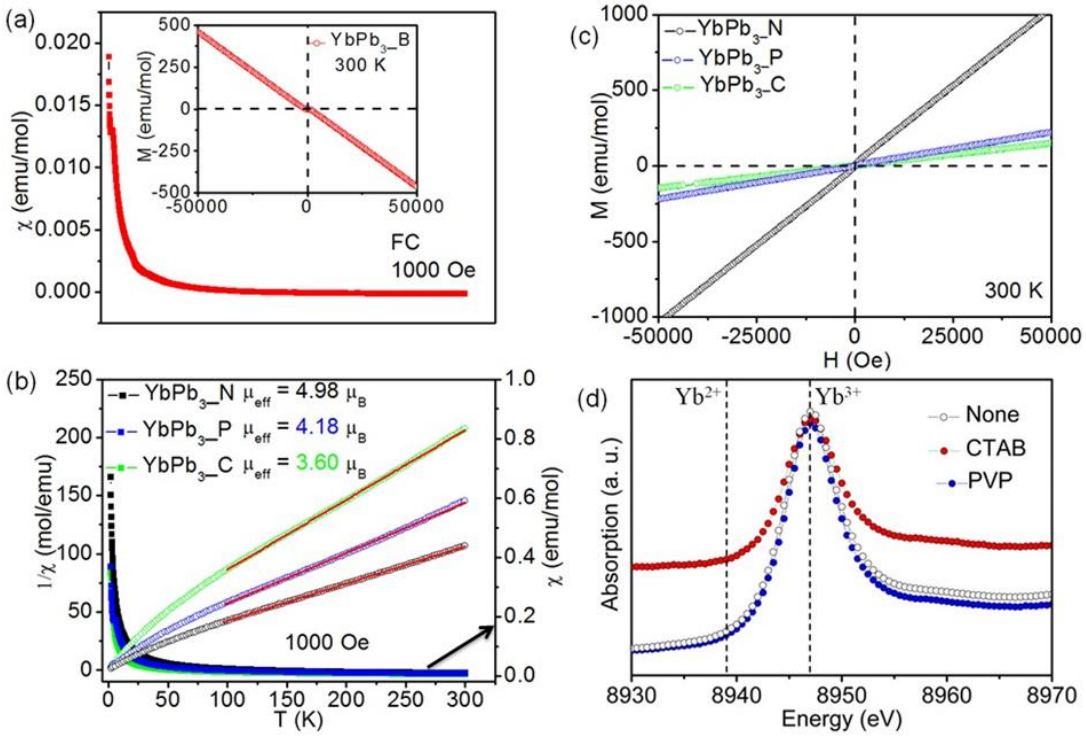

Figure 6.11. (a) Temperature dependent magnetic susceptibility (χ_m) of $YbPb_3$ at 1000 Oe, synthesized in bulk form**.** Inset figure shows the magnetization as a function of applied magnetic field at 300 K for $YbPb_3$ bulk materials. (b) Temperature dependent magnetic susceptibility (χ_m) and inverse susceptibility (1/ χ_m) of $YbPb_3$_N, $YbPb_3$_P and $YbPb_3$_C at 1000 Oe. The CW fitting is shown as red line. The estimated magnetic moment is included in each plot. (c) Magnetization as a function of applied magnetic field at 300 K $YbPb_3$_N, $YbPb_3$_P and $YbPb_3$_C and (d) L_{III} absorption edge spectra of Yb for $YbPb_3$_N, $YbPb_3$_P and $YbPb_3$_C for 24h sample.

It is well understood that the surface spin of the magnetic system will be enhanced with the reduction of dimensionality from bulk to nano scale,[48] which in fact changes the magnetic properties of these materials. In bulk phase, the spins of the sublattices responsible for the bulk magnetic properties are well compensated, whereas NF process not only leaves many uncompensated spins on the surface of the particles, but also favors the valence transition of the Yb atom. In order to prove the actual valence state of Yb in nanomaterials, XANES measurements were performed at the Yb L_{III}-edge at 300 K and ambient pressure (Figure 6.11d). The spectra show only one absorption peak centered at ~8948 eV for all samples attributing to Yb^{3+} atoms[49, 50] and clearly confirms the absence of Yb^{2+} or mixed valence behaviour in all nano samples.

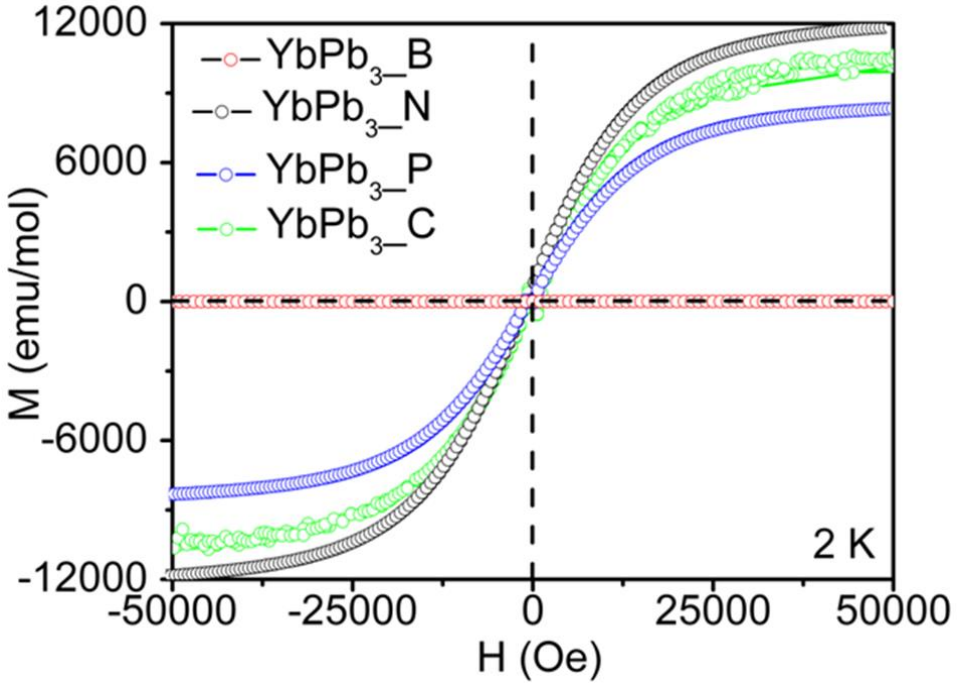

Figure 6.12. Magnetization as a function of applied magnetic field at 2 K for $YbPb_3$ bulk and nano materials (24h).

This valence transition can be triggered by several reasons: the reduction in the size of the particles, surface magnetism and the deficiency at the atomic sites. In case of Yb based nanomaterials, the reduction in dimension leads to reduction in valence state due to loss of nearest neighbours.[51] The enhanced magnetic behaviour of $YbPb_3$_N24 (4.98 μ_B/Yb) can be attributed due to the presence of uncorrelated paramagnetic spins at the surface that undergo a magnetic transition to a collective spin state at low temperatures yielding the large measured magnetization values and related to broken exchange bonds and reduced

coordination numbers at the surface.[52] The presence of surfactants suppresses the paramagnetic behaviour compared to the surfactant free sample probably due to the fact that they compensate the unfulfilled surface spins by donating electrons fully or partially. The reduction can also be directly connected to the particle size and surface area. Nanomagnetism was previously reported in many systems originating from different surface states.[51, 53] As mentioned in the previous section, the particle size of $YbPb_3$_N24 increased from 16 nm to 45 nm in $YbPb_3$_N48. Since the particle size is larger for $YbPb_3$_N48, the surface area to volume ratio becomes smaller and reduces the contribution of surface magnetism (Figure 6.13a). The role of surface magnetism was further proved from the magnetization curve of all samples at 300 K in low magnetic field with the presence of small hysteresis loop (Figure 6.13b).

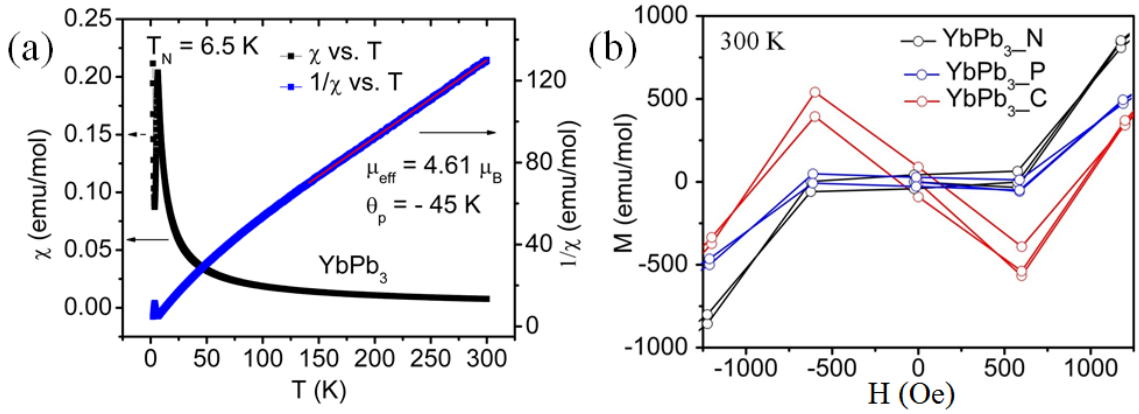

Figure 6.13. (a) Temperature dependent magnetic susceptibility (χ_m) and inverse susceptibility ($1/\chi_m$) of $YbPb_3$_N for 48h sample at an applied field of 1000 Oe. The CW fitting is shown as red line. (b) Magnetization as a function of applied magnetic field at 300 K for $YbPb_3$ nanomaterial's in lower applied magnetic field for 24h sample.

Since La is expected to have only one oxidation state (La^{3+}), and also synthesized $LaPb_3$ both bulk and nano forms (Figure 6.14a). Controlled magnetic measurements with slight enhancement in the magnetic moment (Figure 6.14b) in the susceptibility data confirm the occurrence of some surface contribution towards the enhanced magnetic moment in these nanomaterials. It should be noted that this kind of valence transition also occurs in many oxides due to the deficiencies in O sites, such as $CuFeO_{2+\delta}$.[54] Similarly, $YbPb_3$ nanoparticles also show deficiency at Pb position, which further concludes that the role of deficiency cannot completely be ruled out. Although, could not find the trace of Pb in powder XRD, the magnetic susceptibility measurements at lower field (10 Oe) resulted in demagnetization at

7.2 K (Figure 6.15), which is the superconducting temperature of Pb metal, proving the presence of elemental Pb.[55] However, it should be noticed that the extent of demagnetization for the nanoparticles is higher than bulk suggesting more unreacted Pb in the total system. From the various controlled studies, it can be concluded that the origin of magnetism, via valence transition of Yb, is due to the combined effect of reduction in the size of the particles, surface magnetism and the deficiency at the atomic sites.

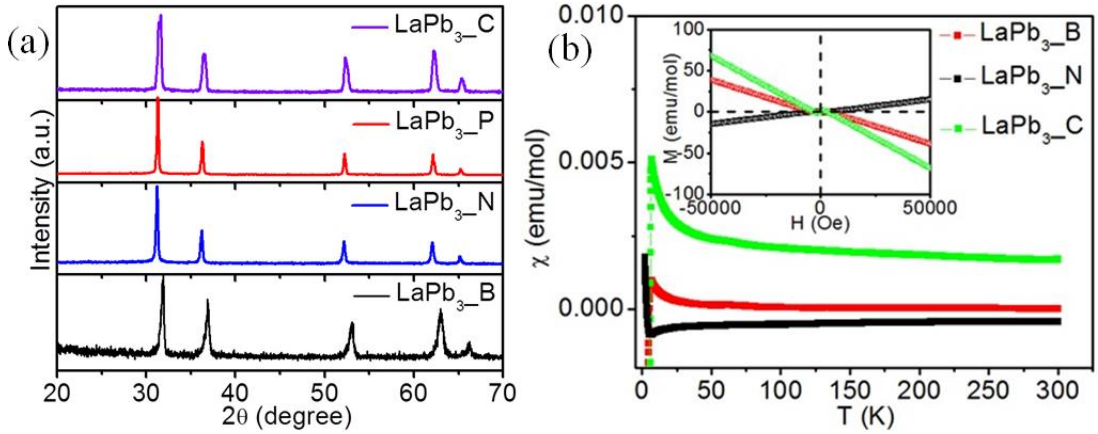

Figure 6.14. (a) Experimental and simulated of $LaPb_3$ nanoparticle in the presence and absence of surfactant at 24 h. (b) Temperature dependent magnetic susceptibility (χ_m) of $LaPb_3$_B, $LaPb_3$_N and $LaPb_3$_C at 1000 Oe, inset figure shows the magnetization as a function of applied magnetic field at 300 K for $LaPb_3$_B, $LaPb_3$_N and $LaPb_3$_C nano materials.

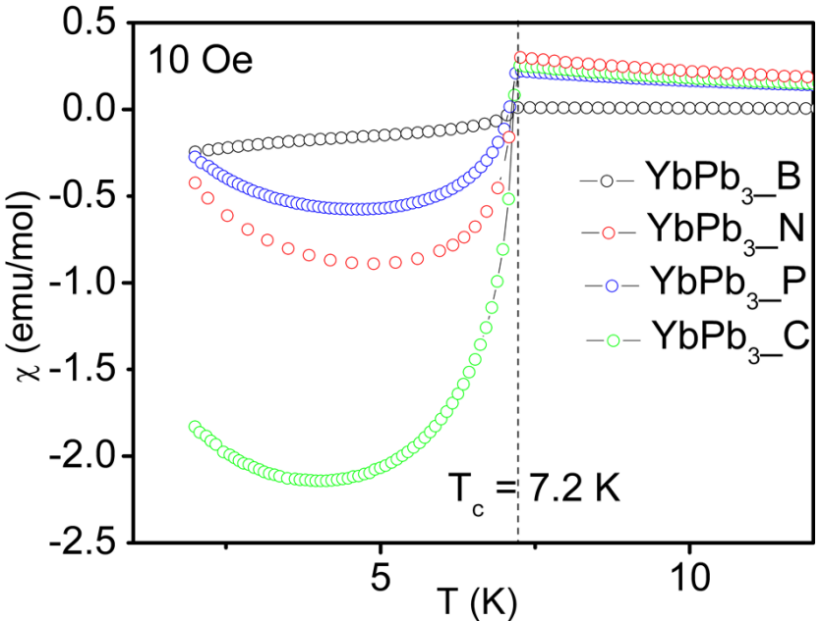

Figure 6.15. Temperature dependence of magnetic susceptibility at 10 Oe magnetic field of $YbPb_3$_P, $YbPb_3$_C, $YbPb_3$_N and $YbPb_3$_B at 24 h.

The reactivity of an atom apparently depends on the oxidation state and size of the ion. Since Yb has the ability to exist in two different oxidation states, their reactivity should also be different. The valence transition of Yb is energetically favourable, but Yb^{2+} is a more stable valence state in comparison to Yb^{3+} because of substantial decrease in strain and higher exchange coupling interaction in Yb^{2+}.[22] However, the non-magnetic Yb^{2+} has ionic radius of 194 pm,[56] which is larger than the magnetic Yb^{3+} having an ionic radius, 174 pm.[56] Due to large size, the reactivity of Yb^{2+} is expected to be more than Yb^{3+}. In other words, the compounds with Yb^{2+} are expected to react more with oxygen compared to the trivalent compounds. In order to check this, PXRD measurements on $YbPb_3$_B (divalent) and $YbPb_3$_N (trivalent) samples were performed over a period of five months. The PXRD of bulk sample contains $YbO_{0.5}$,[57] which shows the oxidization of the sample (Figure 6.16a to 6.16b and 6.17a), but nanomaterials remain stable without any peak corresponding to $YbO_{0.5}$ (Figure 6.16c-d and 6.17b). Surprisingly, the PXRD of nano materials contains peaks at 2θ = 28.6°, 31.9° and 48.7° corresponding to PbO (Figure 6.17b).

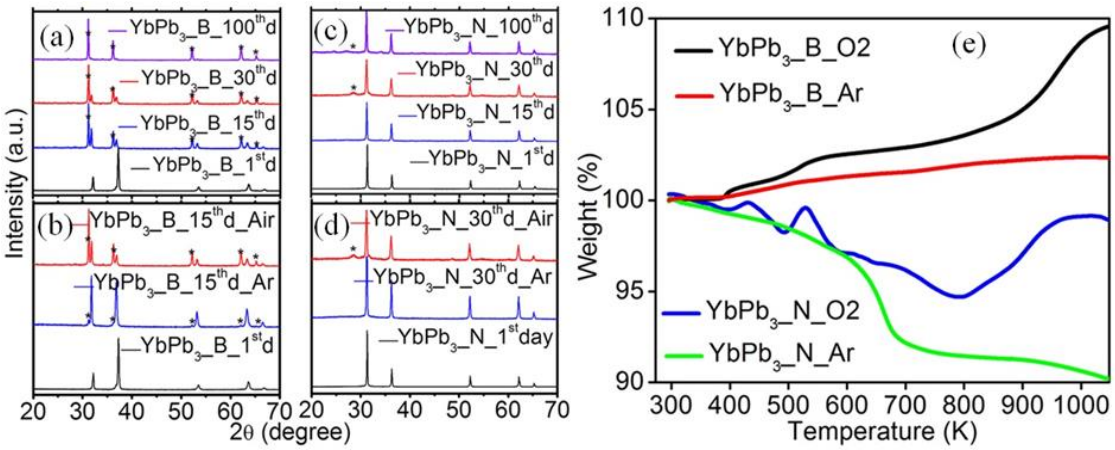

Figure 6.16. PXRD comparison $YbPb_3$_bulk and nano (a) $YbPb_3$_B comparing a period of one month (b) $YbPb_3$_B comparison of Ar and air condition (c) comparison of $YbPb_3$_N a period of one month and (d) $YbPb_3$_N comparison of argon and air condition. (e) Thermogravimetric analysis on $YbPb_3$_B and $YbPb_3$_N in the presence of argon and oxygen atmosphere.

This can be explained as the oxidation of Pb, which was either slowly etched from the system probably due to the strain or unreacted Pb present in the system as observed in the magnetic measurements. In order to understand the leaching of Pb from $YbPb_3$ nanoparticles, and quantified the microstructural strain in both the bulk and nano samples from corresponding PXRD patterns using Williamson-Hall (WH) method (Figure 6.18).[24, 25] The

calculations showed that $YbPb_3$_B has almost 9.5 times strain compared to $YbPb_3$_N. This excessive strain may trigger valence transition from Yb^{2+} to Yb^{3+}, which in turn may give rise to shortening in Yb-Pb bond distances leading to expulsion of Pb from the system. It is widely expected that the surface of the nanoparticles are more prone to the oxidation compared to the bulk materials. However, induced valence transition of Yb in $YbPb_3$ gives more stability towards aerial oxidation. The stability was further checked by TGA in the presence oxygen and argon within the temperature range 303-1000 K (Figure 6.16e).

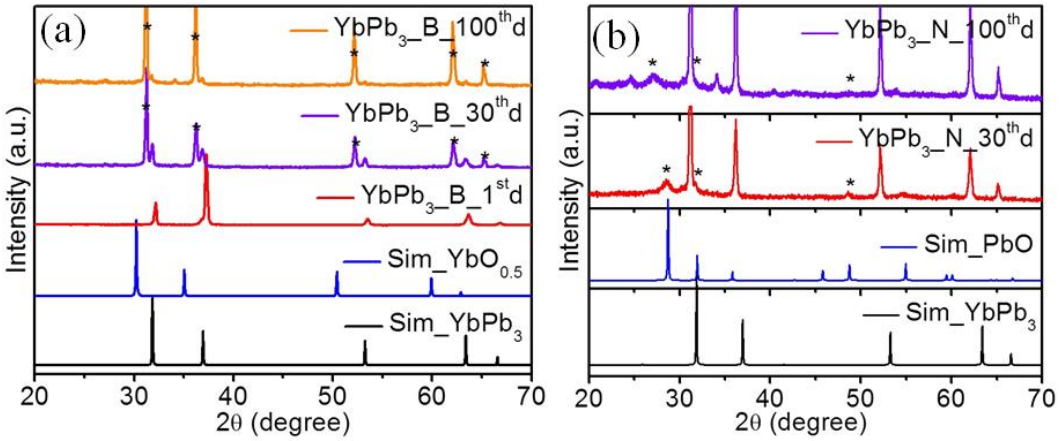

Figure 6.17.(a) Experimental PXRD of $YbPb_3$_B 1st day, 30 th day and 100th day comparison with simulated $YbO_{0.5}$ and $YbPb_3$. (b) Experimental PXRD of $YbPb_3$_N 30th day and 100th day comparison with simulated PbO and $YbPb_3$.

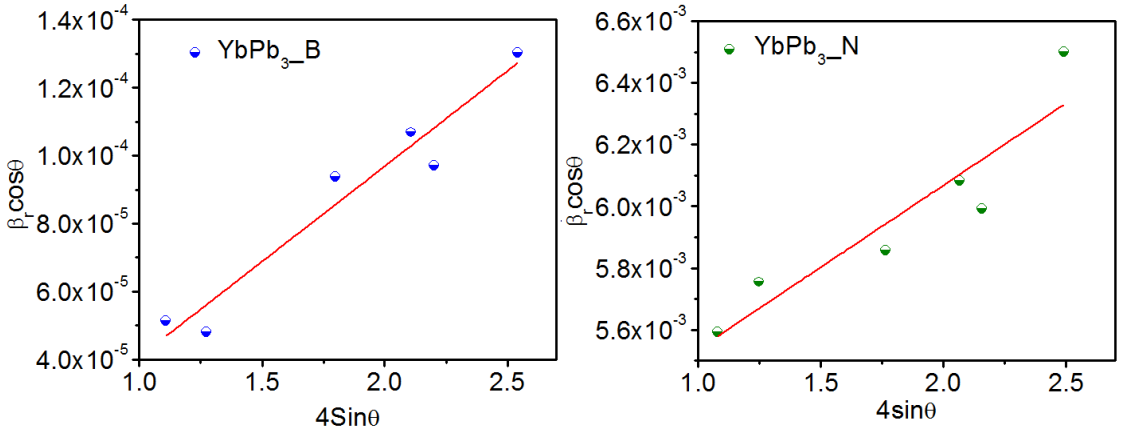

Figure 6.18. Linear fitting of $\beta_r\cos\theta$ vs. $4\sin\theta$ curve obtained from Williamson-Hall (WH) method for the compounds $YbPb_3$_B and $YbPb_3$_N.

In the presence of Ar, $YbPb_3$_B shows negligible difference till 1000 K, but the material started to gain weight with oxygen at 373 K due to the oxidation of Yb. The total weight gain of $YbPb_3$_B in the presence of oxygen during the temperature range 373-900 K

is around 6%. On contrary, the presence of PbO in the PXRD of $YbPb_3$_B after TGA measurements in presence of oxygen at 1073 K is probably due to the oxidation of unreacted or dealloyed Pb (Figure 6.19a). On the other hand the TGA plot for $YbPb_3$_N is completely different as it does not show any weight gain both in oxygen and argon atmosphere and hence rule out the oxidation of Yb. Instead, a weight loss of 8% and 5% in the temperature range 303-800 K in presence of Ar and O_2, respectively, can be attributed to the dealloying of Pb, followed by the formation of PbO and finally decomposition to Pb_2O_3 (Figure 6.19b).

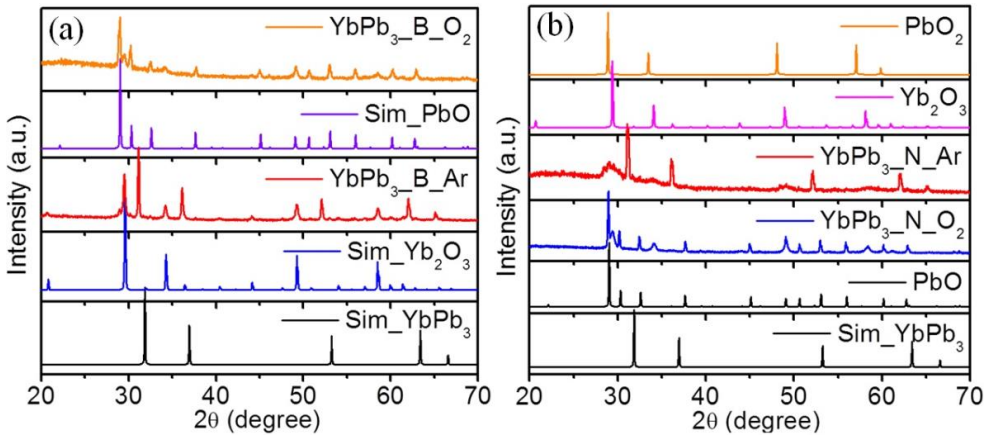

Figure 6.19. PXRD comparison of (a) $YbPb_3$_B and (b) $YbPb_3$_N after TGA measurements at 800 ^{0}C.

However, there is no gain in weight for the sample in the presence of Ar after 800 K confirms no oxidation has occurred. Also noticed that surfactants give extra stability towards the aerial oxidation of the materials as the compounds $YbPb_3$_P and $YbPb_3$_C have not decomposed neither to the oxide of Yb nor Pb over a period of five months (Figure 6.20).

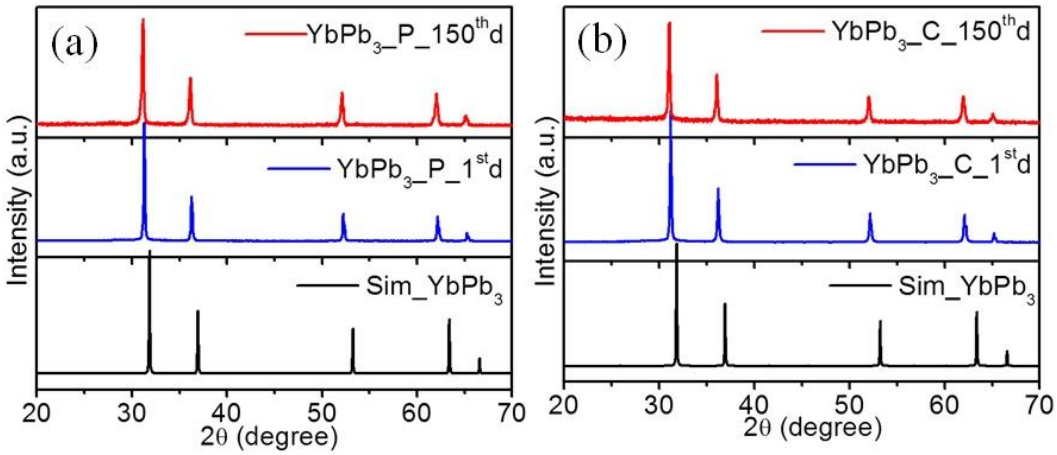

Figure 6.20. PXRD comparison (a) $YbPb_3$_P and (b) $YbPb_3$_C with simulated $YbPb_3$ over a period of 150 d.

XPS spectra of the samples $YbPb_3$_bulk, $YbPb_3$_N, $YbPb_3$_P, $YbPb_3$_C were recorded to know the oxidation state of Yb in the intermetallic $YbPb_3$ compounds. For, $YbPb_3$_bulk compound, both Yb^{3+} and Yb^{2+} are present which may be because of the oxidation of $YbPb_3$_bulk during experimental and/or measurement procedure as $YbPb_3$_bulk is highly sensitive to aerial oxidation. However, all the nano compounds are only in Yb^{3+} states (Figure 6.21a). Even after 150 d, there is almost no shift in binding energy of Yb^{3+} in $YbPb_3$_N nano intermetallic compound, which clearly indicates that there is no change in the co-ordination environment of Yb^{3+} ions even after 150 days. Therefore, $YbPb_3$ in nano-dimension is highly stable without the formation of detectable amount of ytterbium oxide (Figure 6.21b). In order to ascertain hypothesis, the induced valence transition of Yb towards the air stability, and synthesized the prototype compound $EuPb_3$ both in micro ($EuPb_3$_B) and nano ($EuPb_3$_N) crystalline forms (Figure 6.22).

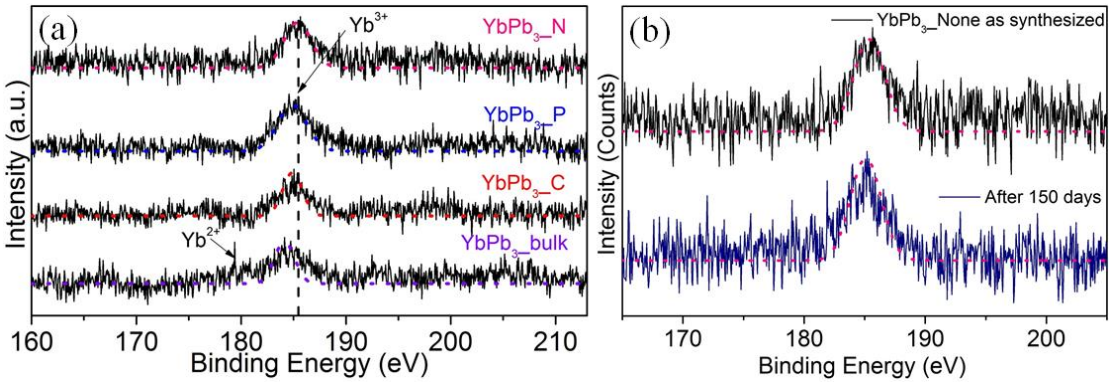

Figure 6.21. (a) XPS spectra of Yb 4*d* in different samples (a) $YbPb_3$_bulk, $YbPb_3$_N, $YbPb_3$_P, $YbPb_3$_C and (b) $YbPb_3$_N sample in different time interval.

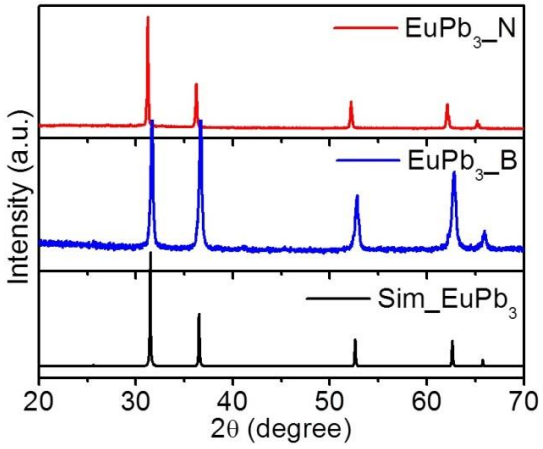

Figure 6.22. PXRD comparison $EuPb_3$_B and $EuPb_3$_N (without surfactant) with simulated $EuPb_3$.

As reported before, Eu is divalent in $EuPb_3$_B and orders antiferromagnetically at 20 K.[19] $EuPb_3$_N obtained is of uniform particle size of around 150 nm as observed in TEM measurement (Figure 6.23). Temperature dependent magnetic susceptibility confirmed that $EuPb_3$_B is paramagnetic with divalent Eu, while $EuPb_3$_N is diamagnetic with trivalent Eu (Figure 6.24a and 6.24b).

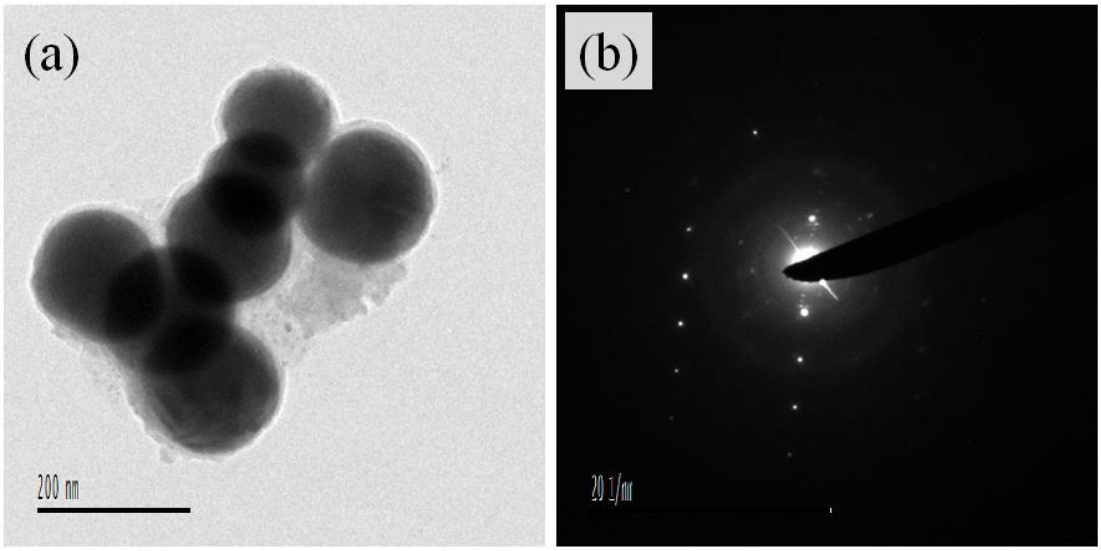

Figure 6.23. TEM image of $EuPb_3$ (a) spherical nanoparticle (b) corresponding ED pattern of without surfactant after 24 h.

The stability of these two forms has been checked in oxygen and argon atmosphere over a period of two months. As expected from hypothesis, $EuPb_3$_B decomposed gradually (Figure 6.24c) and $EuPb_3$_N remains stable (Figure 6.24d). Interestingly, $EuPb_3$_B was decomposed to PbO instead of Eu_2O_3 (Figure 24c), which is probably due to relatively more stable Eu^{2+}. The stability of the samples towards oxygen was further checked over a period of 7 months using XANES measurements and shown in Figure 6.25. The near-edge spectra for $YbPb_3$_B obtained at 300 K and at ambient pressure (Figure 6.25a) showed a main absorption peak (white line resonance) of the spectrum for both spectra is centered at ~8941.5 eV, which is attributed to divalent Yb atoms.[58-60] The spectrum also revealed the presence of a weaker feature at ~8949 eV, indicating that some trivalent Yb is also present.[58-60] However, over a period of time, the low-energy peak originating from the Yb^{2+} ions is gradually decreased, whereas the high-energy one originating from Yb^{3+} is enhanced. The amplified intensity at 8949 eV and concomitant decrease in intensity at 8941 eV implies conversion of Yb^{2+} to Yb^{3+} upon time and almost completely converted after 7 months. A

similar trend was observed for $EuPb_3$_B sample where the complete conversion of divalent Eu to trivalent Eu occurred after 5 months. On the other hand, the nonmaterials $YbPb_3$_N and $EuPb_3$_N showed only one peak corresponds to the trivalent oxidation state of *RE* and no change was observed over a period of seven and 5 months, respectively (Figure 6.25b and 6.25d).

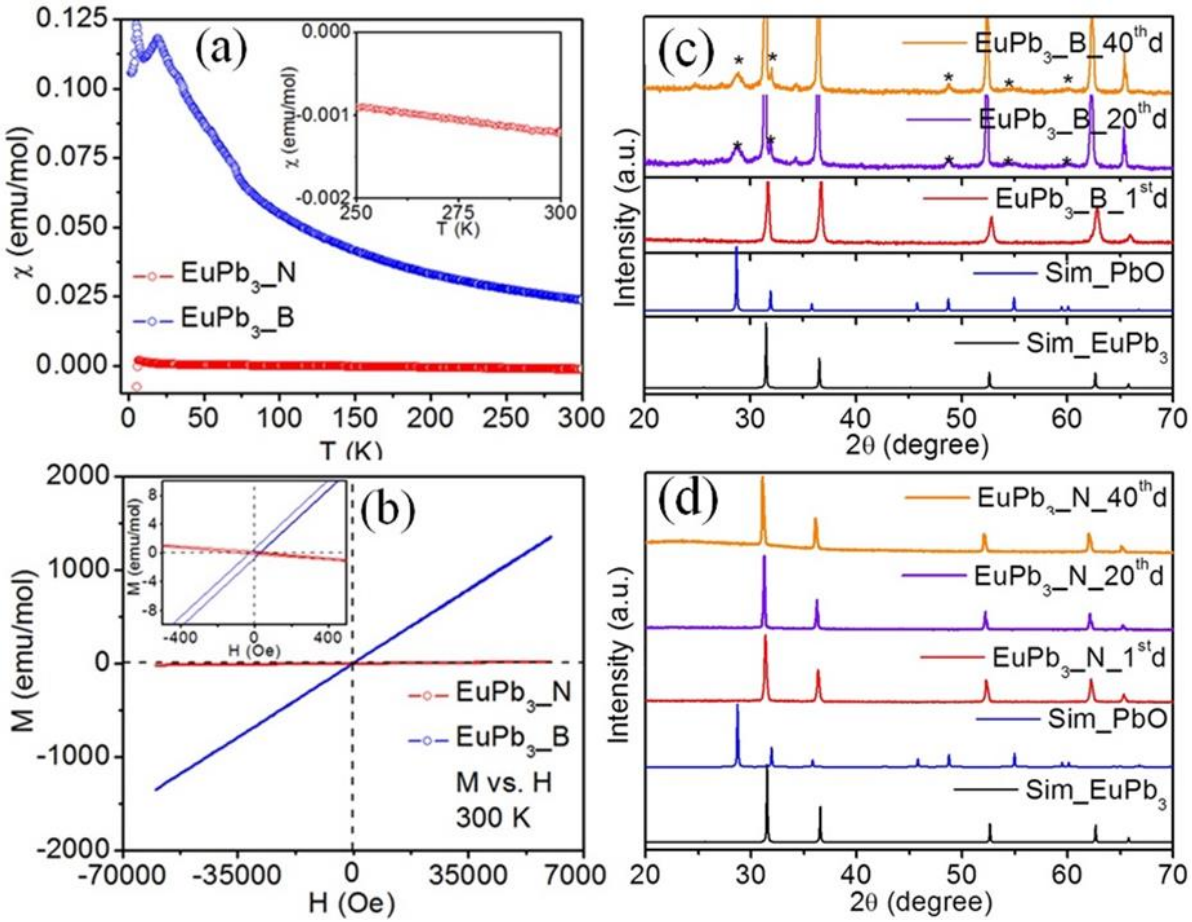

Figure 6.24. a) Temperature dependent magnetic susceptibility (χ_m) of $EuPb_3$ at 10 Oe, synthesized in bulk ($EuPb_3$_B) and nano without surfactant ($EuPb_3$_N)**.** Inset figure shows the susceptibility data of $EuPb_3$_N sample at low temperature to confirm the negative values. (b) Magnetization as a function of applied magnetic field at 300 K for $EuPb_3$_B and $EuPb_3$_N. Insets show the same in the lower field range for better clarity. PXRD comparison $EuPb_3$_bulk and nano comparing a period of 40 d in air (c) $EuPb_3$_B and (d) $EuPb_3$_N.

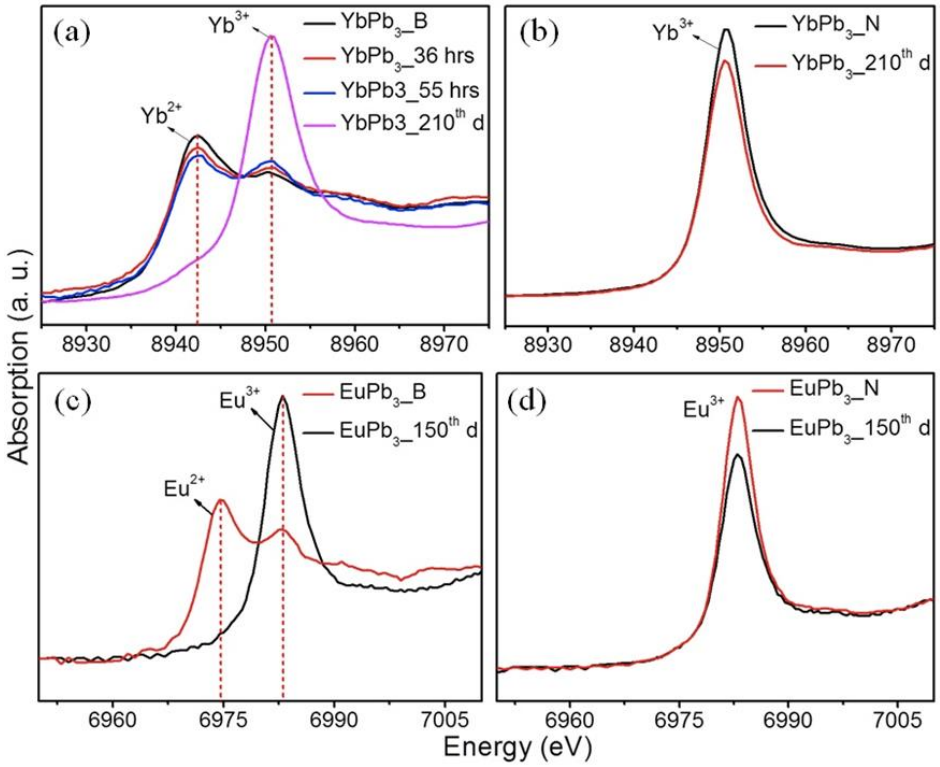

Figure 6.25. Time dependent Yb and Eu L_{III} absorption edge spectra for (a) $YbPb_3$_B, (b) $YbPb_3$_N, (c) $EuPb_3$_B and (d) $EuPb_3$_N samples over a period of seven months.

6.4. Conclusion

In conclusion, the current study shows the development of air stable materials as promising materials for various applications in the field of chemistry, physics, biology and engineering. Although several methods have been employed for this objective, not a single method dealt with chemical transformation of metal in a molecule/compound from its one oxidation state to more stable one. A few metals are known to exists in various oxidation states and compared the stability of each one using standard well-known material has been selected from frost diagram. Among them, a couple of *RE* elements, Eu and Yb, are known to exist in both divalent and trivalent oxidation states and strategically targeted a simple cubic compound of formula *RE*Pb_3 crystallizing in $AuCu_3$ structure type, for the detailed studies. A new and facile synthetic strategy for synthesis of these materials in nano form has been employed. The formation of different morphologies in nanoscale has been assisted with the concepts of nanofication and dimensional reduction in connection with the concept of crystallography. Although various parameters such as particle size, presence of surfactants, and deficiency of metal and surface states could play the crucial roles, controlled studies

confirmed that the valence transition of *RE* metals is responsible for the stability of these materials towards air. This work is expected to give good input on the synthesis of future air stable materials for various scientific and technological applications.

The work has further extended towards their probable energy related applications in fuel cells by using REPd$_3$ (*RE* = Eu and Yb) intermetallic nano material.

6.5. Nano Intermetallic REPd$_3$ (*RE* = Eu and Yb) Compounds for Electrochemical Studies

6.5.1. Introduction

The fast depletion of non-renewable fossil fuels has triggered a huge uncertainty on the sustainability of future energy, which stands primarily on coal. This has inevitably forced the human kind to explore other alternative sources of energy. One of the most promising candidates, at this end, is fuel cell, which efficiently convert chemical energy into electrical energy. However, this process is sluggish in nature due to high activation energy involved in the breaking of bonds in a molecule, which is essentially kinetic in nature and adds up extra input energy in the form of overpotential. A catalyst is an obvious choice to overcome this obstacle by cutting down the activation energy required for a selected reaction. Platinum, owing to its high conductivity and robust stability is regarded as the most formidable catalyst. However, poor abundance in the earth crust and high cost bars its long term and large scale up in the industry. Hence different strategies have been applied, for example, decreasing Pt content by means of forming alloys, bimetallic and intermetallic compounds. There are several advantages of using a second metal. As mentioned, the first and foremost is that it reduces the amount of costly Pt metal. Secondly, in alkaline medium these metals are very effective in adsorbing hydroxyl ions, which help in oxidizing carbon monoxide (CO) molecules adsorbed on the Pt active sites; this effect is known as "ligand effect". It is worthwhile to mention that CO acts as a catalytic poison for Pt by irreversible binding with it. This work, *RE* as the second metal to Pd to synthesize REPd$_3$ compounds and understand their cleansing ability remove the adsorbed CO from the catalytic surface.

6.5.2. Structure analysis

The crystal structures of the REX_3 intermetallic compounds have been reported by Harris and Raynor.[41] They have found Cu_3Au structure types crystallizes in cubic crystal system with the space group of $Pm\bar{3}m$. The PXRD data (Figure 6.26) of the samples REX_3

synthesized by solvothermal processes confirmed the formation of pure phase. Figure 6.26(a-d) shows the combined experimental PXRD patterns of $EuPd_3$, $EuPt_3$, $YbPd_3$ and $YbPt_3$ phases and simulated patterns of the respective compounds.

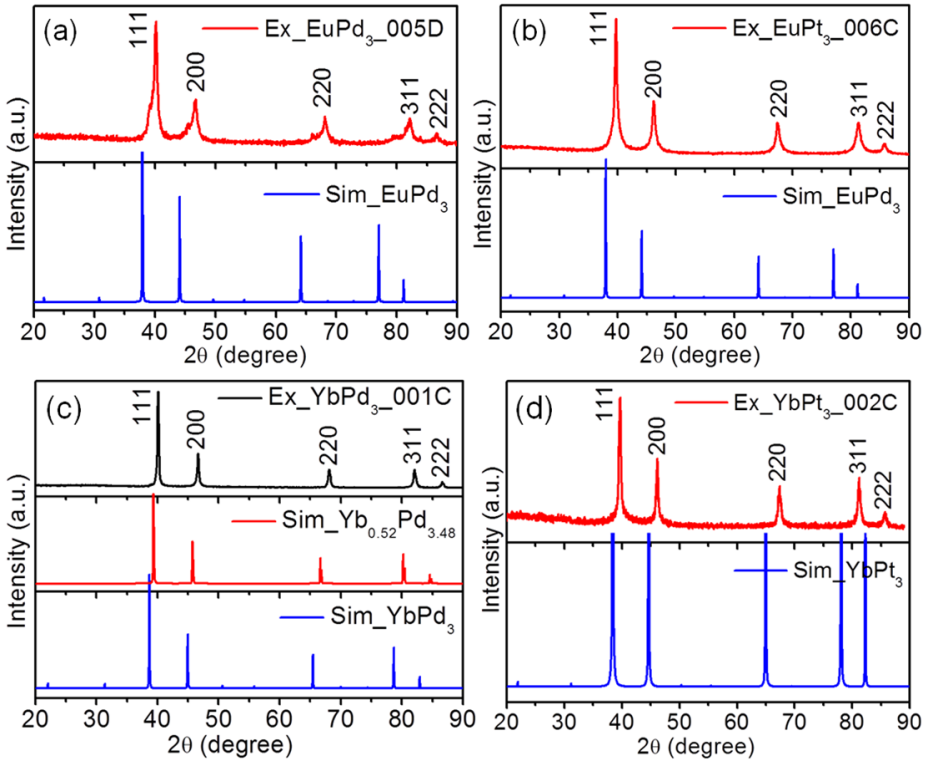

Figure 6.26. (a-d) PXRD comparison of simulated and experimental of REX_3 compounds synthesized by solvothermal method.

6.5.3. TEM Analysis

The TEM images of the synthesised intermetallic nanoparticles give a lot of insight information about the morphology and the size of the particles. Figure 6.27a shows the TEM image of $EuPd_3$ which shows well segregated small black spots from which it can be concluded that the shape of the particles is spherical and the particles are not agglomerated. The particle size in case of $EuPd_3$ was less than 5 nm whereas $EuPt_3$ particles got agglomerated as seen from the dense black region of TEM images (Figure 6.27b). This could be due to the lack of surfactant during the synthesis of this compound. Figure 6.27c shows the TEM image of $YbPd_3$, which also displays that the particles have got aggregated which may be due to the absence of surfactant. $YbPt_3$ on the other hand has well separated particles just like $EuPd_3$ as shown in Figure 6.27d. The size of the particles in this case can be determined and is less than 10 nm. The compounds synthesised in this work are found to be

polycrystalline in nature as can be clearly visualised from the SAED images of these compounds in the inset figures. In these SAED images several concentric circles are easily visible which prove that the sample is polycrystalline in nature if there would have been only bright spots and no circles it would have shown the compound to be single crystalline in nature.

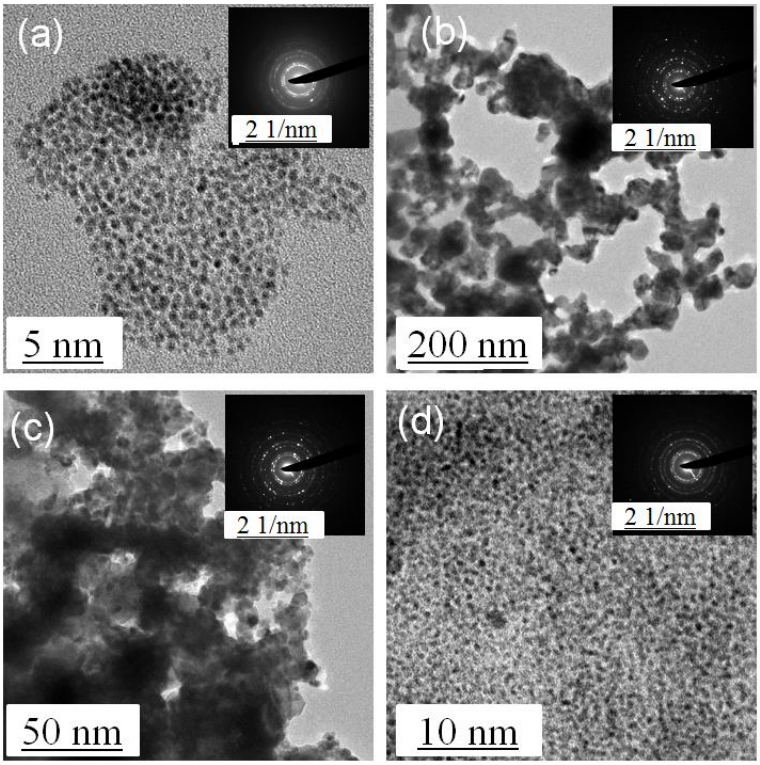

Figure 6.27. TEM images of (a) $EuPd_3$, (b) $EuPt_3$, (c) $YbPd_3$ and (d) $YbPt_3$. Inset shows the corresponding selected area electron diffraction (SAED) patterns.

6.5.4. XANES Analysis

To confirm the oxidation state of europium and ytterbium in REX_3 compounds have performed the XANES measurements at the Eu L_{III}-edge and Yb L_{III}-edge, at 300 K and ambient pressure (Figure 6.28). This is a strong experimental tool in order to firmly establish the valence state of an element in a compound. The spectra shows only one absorption peak centered at 6983 eV for $EuPd_3$ and $EuPt_3$ (Figure 6.28a and 6.28b), at ~8952 eV for $YbPd_3$ and $YbPt_3$ (Figure 6.28c and 6.28d), can be attributed to trivalent Eu and Yb atoms. This value is characteristic of the $4f^6$ (Eu^{2+}) and $4f^{13}$ (Yb^{3+}) configurations, arises due to a $2p_{3/2}$ to $5d$ transition.[61] These results directly corroborate with magnetic susceptibility data, which predicts trivalent Eu and Yb in the system.

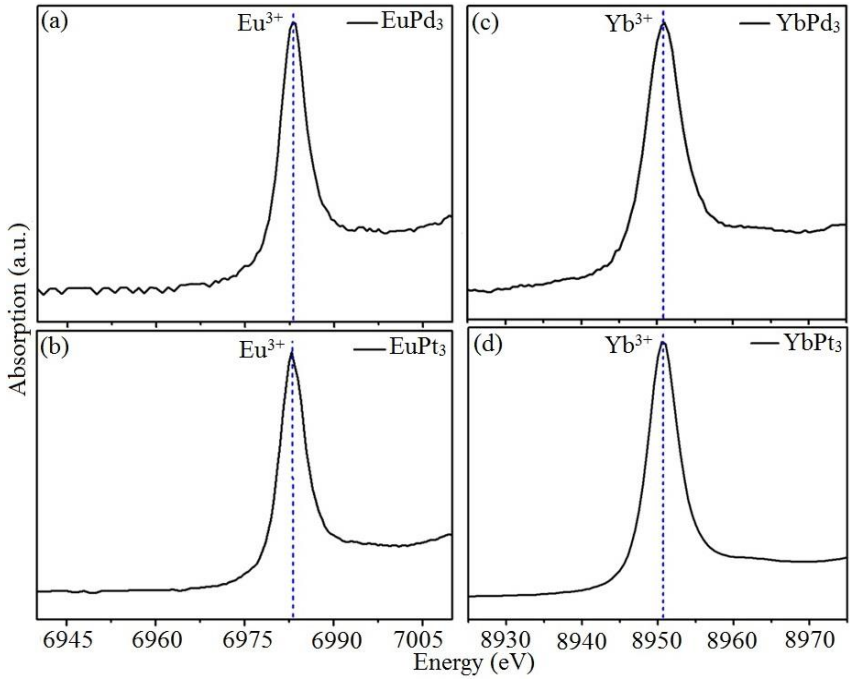

Figure 6.28. X-ray absorption near edge spectroscopy of Eu L_{III} and Yb L_{III}-edge in the REX_3 compounds.

6.5.5. Electrochemical Studies

The electrochemical measurements were performed at room temperature on a CHI 608E electrochemical workstation with three electrode channels. Three electrode set-up consists of a glassy carbon (GC) (having a diameter of 3 mm) as working electrode, platinum wire as counter electrode and Hg/HgO (MMO) (alkaline medium) as reference electrode. All the solutions were purged with nitrogen gas for 30 min prior to the measurement. The catalyst ink was prepared by dispersing 1 mg of catalyst in 200 μL of mixed solvent solution (IPA: H_2O=1:3 v/v). From the prepared catalyst ink 10 μL was dropcasted on GC electrode and dried overnight in air. Before depositing the catalyst, the GC electrode was polished with 0.05 μm alumina slurry, washed several times with distilled water. Commercial Pd/C (20 wt%, Sigma Aldrich) was used for comparison of activity with the $REPd_3$ catalysts. Cyclic voltammetry (CV) measurement was carried out with 0.5M KOH aqueous solution at a scan rate 50 mV/sec.

The activity of the catalysts $EuPd_3$ and $YbPd_3$ and were studied by running cyclic voltametric sweeps in the range -0.85 to 0.2 V in 0.5 M aqueous KOH solution as shown in Figure 6.29a and Figure 6.30a. In the anodic sweep, the peaks correspond to the desorption of hydrogen (-0.8 to -0.6 V) and oxidation of Pd (0.0 to 0.25) are quite prominent. In the

cathode sweep part, the reduction of Pd-O (0 to -0.4 V) and adsorption of hydrogen are also apparent. Since Pd-O reduction peak current is proportional to the exposure of Pd/Pt catalytic surface to OH^- adsorption, the electrochemically active surface area (ECSA) was calculated by the integration of charges from Pd-O reduction region considering the value of 405 $\mu C/cm^2$ for Pd-O reduction.

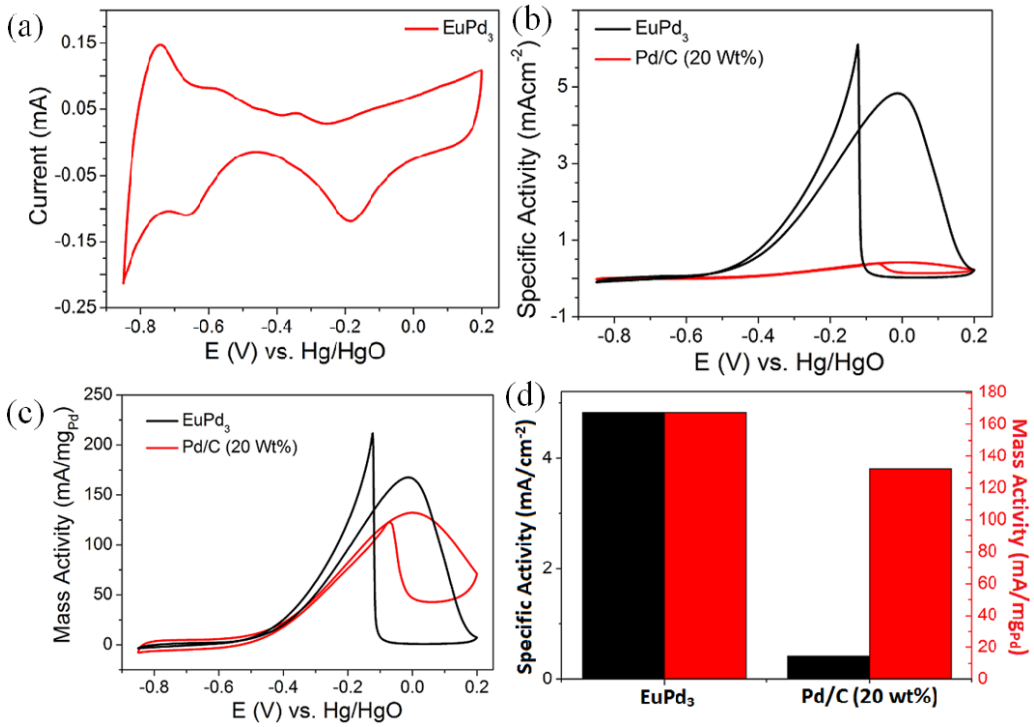

Figure 6.29. (a) Cyclic voltametry curves obtained for $EuPd_3$ electrocatalyst in 0.5M KOH solution at a scan rate of 50 mV/sec. The comparison of the electrocatalytic activities towards ethanol oxidation of the $EuPd_3$ catalyst and commercial Pt/C. (b) CV curves recorded in 0.5M KOH and 1M C_2H_5OH solution at a scan rate of 50 mV s^{-1} (comparison of specific activities), (c) comparison of mass activities in 0.5M KOH and 1M C_2H_5OH solution at a scan rate of 50 mV s^{-1}, (d) Bar graph showing specific and mass activities for ethanol oxidation.

To evaluate electrocatalytic activities of *RE*Pd_3 catalysts towards the electrochemical oxidation of ethanol, the CV measurements were performed in 0.5M KOH + 1M C_2H_5OH solution as shown in Figures 6.29b and Figure 6.30b. The CV data are normalised with respect to the amount of Pd in each composite. In all the cases, the CV curves exhibit two well defined ethanol electro-oxidation peaks. The oxidation peak near 0 V in the forward scan is attributed to the oxidation of ethanol whereas peak near -0.2 V in the reverse scan is primarily associated with the removal of carbonaceous species (such as CO) which are

generated due to the incomplete oxidation of ethanol in the forward scan. Mass activity and bar graph of specific and mass activities for ethanol oxidation shown in figure 6.29c-d and 6.30c- d.

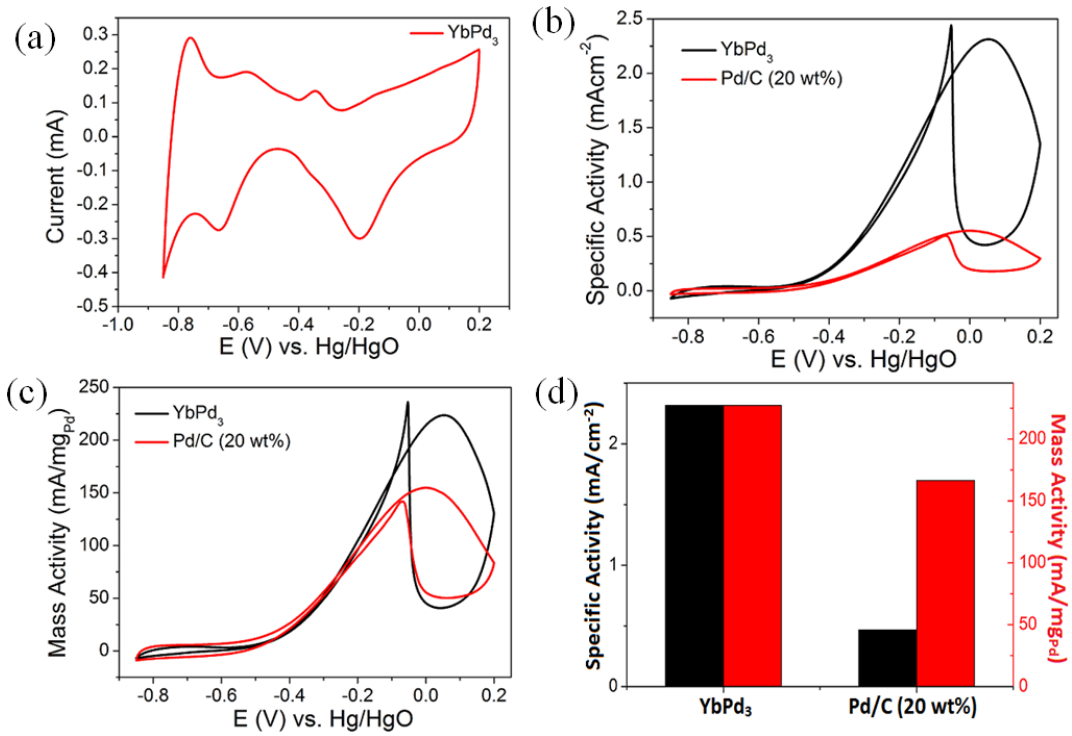

Figure 6.30. (a) Cyclic voltametry curves obtained for $YbPd_3$ electrocatalyst in 0.5M KOH solution at a scan rate of 50 mV/sec. The comparison of the electrocatalytic activities towards ethanol oxidation of the $YbPd_3$ catalyst and commercial Pd/C. (b) CV curves recorded in 0.5M KOH and 1M C_2H_5OH solution at a scan rate of 50 mV s^{-1} (comparison of specific activities), (c) comparison of mass activities in 0.5M KOH and 1M C_2H_5OH solution at a scan rate of 50 mV s^{-1}, (d) Bar graph showing specific and mass activities for ethanol oxidation.

$EuPd_3$ and $YbPd_3$ have been found to show good activity in comparison to its Pt counterparts.[62, 63] A significant increase in surface area normalized current density and mass normalized current density have been observed for the *RE*Pd_3 when compared to Pd/C (20 wt%) for the same loading clearly indicating that *RE* atom plays a very important role in enhancing the EOR activity in case of Pd counterparts.[63, 64] A plausible reason for this could be synergetic interaction of *RE* with Pd.

Based on preliminary studies it has been confirmed that *RE*Pd_3 (*RE* = Eu and Yb) materials are good candidates for fuel cell applications. Detailed studies on these compounds towards fuel cell applications are under progress.

6.6. References

1. Simon, T.; Bouchonville, N.; Berr, M. J.; Vaneski, A.; Adrovic, A.; Volbers, D.; Wyrwich, R.; Doblinger, M.; Susha, A. S.; Rogach, A. L.; Jackel, F.; Stolarczyk, J. K.; Feldmann, J., *Nat. Mater.* **2014,** *13*, 1013-1018.

2. Liu, X.; Gu, L. L.; Zhang, Q. P.; Wu, J. Y.; Long, Y. Z.; Fan, Z. Y., *Nat. Commun.* **2014,** *5*, 4007.

3. Tour, J. M., *Nature* **2014,** *512*, 30-31.

4. Albrecht, M.; Hu, G. H.; Guhr, I. L.; Ulbrich, T. C.; Boneberg, J.; Leiderer, P.; Schatz, G., *Nat. Mater.* **2005,** *4*, 203-206.

5. Yao, J.; Koski, K. J.; Luo, W. D.; Cha, J. J.; Hu, L. B.; Kong, D. S.; Narasimhan, V. K.; Huo, K. F.; Cui, Y., *Nat. Commun.* **2014,** *5*, 5670.

6. Ghosh, T.; Matsumoto, F.; McInnis, J.; Weiss, M.; Abruna, H. D.; DiSalvo, F., *J. Nanopart. Res.* **2009,** *11*, 965-980.

7. Hao, E.; Schatz, G. C.; Hupp, J. T., *J. Fluoresc.* **2004,** *14*, 331-341.

8. Gao, J. H.; Gu, H. W.; Xu, B., *Accounts Chem. Res.* **2009,** *42*, 1097-1107.

9. Jain, P. K.; Huang, X. H.; El-Sayed, I. H.; El-Sayed, M. A., *Accounts Chem. Res.* **2008,** *41*, 1578-1586.

10. Chuang, C. H. M.; Brown, P. R.; Bulovic, V.; Bawendi, M. G., *Nat. Mater.* **2014,** *13*, 796-801.

11. Liao, L. B.; Zhang, Q. H.; Su, Z. H.; Zhao, Z. Z.; Wang, Y. N.; Li, Y.; Lu, X. X.; Wei, D. G.; Feng, G. Y.; Yu, Q. K.; Cai, X. J.; Zhao, J. M.; Ren, Z. F.; Fang, H.; Robles-Hernandez, F.; Baldelli, S.; Bao, J. M., *Nat. Nanotechnol.* **2014,** *9*, 69-73.

12. Cui, C. H.; Gan, L.; Heggen, M.; Rudi, S.; Strasser, P., *Nat. Mater.* **2013,** *12*, 765-771.

13. Liu, J.; Kargarian, M.; Kareev, M.; Gray, B.; Ryan, P. J.; Cruz, A.; Tahir, N.; Chuang, Y. D.; Guo, J. H.; Rondinelli, J. M.; Freeland, J. W.; Fiete, G. A.; Chakhalian, J., *Nat. Commun.* **2013,** *4*, 2714.

14. Mura, S.; Nicolas, J.; Couvreur, P., *Nat. Mater.* **2013,** *12*, 991-1003.

15. Jeon, N. J.; Noh, J. H.; Kim, Y. C.; Yang, W. S.; Ryu, S.; Il Seol, S., *Nat. Mater.* **2014,** *13*, 897-903.

16. Magnuson, M.; Schmitt, T.; Strocov, V. N.; Schlappa, J.; Kalabukhov, A. S.; Duda, L. C., *Sci. Rep.* **2014,** *4*, 7017.

17. Kucheryavy, P.; He, J. B.; John, V. T.; Maharjan, P.; Spinu, L.; Goloverda, G. Z.; Kolesnichenko, V. L., *Langmuir* **2013,** *29*, 710-716.

18. Ebihara, T.; Haga, Y.; Yamamoto, E.; Aoki, Y.; Sato, H.; Dhar, S. K.; Onuki, Y., *J. Phys. Soc. Jpn.* **1997,** *66*, 1842-1843.

19. Aoki, D.; Katayama, Y.; Settai, R.; Suzuki, N.; Sugiyama, K.; Kindo, K.; Harima, H.; Onuki, Y., *J. Phys. Soc. Jpn.* **1998,** *67*, 4251-4259.

20. Baranovskiy, A. E.; Grechnev, G. E.; Mikitik, G. P.; Svechakarev, I. V., *Low Tem. Phys.* **2003,** *29*, 356-358.

21. Borzone, G.; Parodi, N.; Ferro, R.; Gambino, M.; Bros, J. P., *J. Alloy Compd.* **1993,** *201*, 17-22.

22. Barrett, J., *Inorganic Chemistry in Aqueous Solution*. Royal Society of Chemistry: 2003.

23. Rieger, P. H., *Electrochemistry*. Springer Science & Business Media: 1994.

24. Williamson, G. K.; Hall, W. H., *Acta Metall.* **1958,** *1*, 22-31.

25. Burton, A. W.; Ong, K.; Rea, T.; Chan, I. Y., *Micropor. Mesopor. Mat.* **2009,** *117*, 75-90.

26. Zak, A. K.; Abd Majid, W. H.; Abrishami, M. E.; R., Y., *Solid State Sci.* **2011,** *13*, 251-256.

27. Gonçalves, N. S.; Carvalho, J. A.; Lima, Z. M.; Sasaki, J. M., *Mater. Lett.* **2012,** *72*, 36-38.

28. Milazzo, G.; Caroli, S.; Sharma, V. K., *Tables of Standard Electrode Potentials*. Wiley: Chichester, 1978.

29. Sau, T. K.; Rogach, A. L., *Adv. Mater.* **2010,** *22*, 1781-1804.

30. Grzelczak, M.; Perez-Juste, J.; Mulvaney, P.; Liz-Marzan, L. M., *Chem. Soc. Rev.* **2008,** *37*, 1783-1791.

31. Pileni, M. P., *Size and Morphology Control of Nanoparticle Growth in Organized Surfactant Assemblies*. Wiley-VCH: Verlag GmbH, 2007.

32. Sau, T. K.; Murphy, C. J., *J. Am. Chem. Soc.* **2004,** *126*, 8648-8649.

33. Pileni, M. P., *Nat. Mater.* **2003,** *2*, 145-150.

34. Jana, N. R.; Gearheart, L.; Murphy, C. J., *Adv. Mater.* **2001,** *13*, 1389-1393.

35. Ganguli, A. K.; Vaidya, S.; Ganguly, A., *Indian J. Chem. A* **2012,** *51*, 245-251.

36. Sundaresan, A.; Bhargavi, R.; Rangarajan, N.; Siddesh, U.; Rao, C. N. R., *Phys. Rev. B* **2006,** *74*, 161306-161309.

37. Madhu, C.; Sundaresan, A.; Rao, C. N. R., *Phys. Rev. B* **2008,** *77*, 201306-201309.

38. Wei, X. H.; Zhou, R. L.; Lefebvre, W.; He, K.; Le Roy, D.; Skomski, R.; Li, X. Z.; Shield, J. E.; Kramer, M. J.; Chen, S.; Zeng, X. C.; Sellmyer, D. J., *Nano Lett.* **2014,** *14*, 1362-1368.

39. Zhu, M. Z.; Aikens, C. M.; Hendrich, M. P.; Gupta, R.; Qian, H. F.; Schatz, G. C.; Jin, R. C., *J. Am. Chem. Soc.* **2009,** *131*, 2490-2492.

40. Becker, R.; Liedberg, B.; Kall, P. O., *J. Colloid Interf. Sci.* **2010,** *343*, 25-30.

41. Perez-Juste, J.; Pastoriza-Santos, I.; Liz-Marzan, L. M.; Mulvaney, P., *Coordin. Chem. Rev.* **2005,** *249*, 1870-1901.

42. Du, X. W.; Chu, Y.; Xing, S. X.; Dong, L. H., *J. Mater. Sci.* **2009,** *44*, 6273-6279.

43. Tao, A. R.; Habas, S.; Yang, P. D., *Small* **2008,** *4*, 310-325.

44. Giersig, M.; Pastoriza-Santos, I.; Liz-Marzan, L. M., *J. Mater. Chem.* **2004,** *14*, 607-610.

45. Sarkar, S.; Balisetty, L.; Shanbogh, P. P.; Peter, S. C., *J. Catal.* **2014,** *318*, 143-150.

46. Kittel, C., *Introduction to Solid State Physics*. 7th ed. ed.; John Wiley and Sons: Hoboken, NJ, 1996.

47. Smart, J. S., *Effective Field Theories of Magnetism*. Saunders: Philadelphia, PA, 1966.

48. Sundaresan, A.; Rao, C. N. R., *Nano Today* **2009,** *4*, 96-106.

49. Peter, S. C.; Subbarao, U.; Sarkar, S.; Vaitheeswaran, G.; Svane, A.; Kanatzidis, M. G., *J. Alloy Compd.* **2014,** *589*, 405-411.

50. Iyer, A. K.; Peter, S. C., *Eur. J. Inorg. Chem.* **2012,** *2012*, 1790-1794.

51. Rojas, D. P.; Barquin, L. F.; Espeso, J. I.; Fernandez, J. R., *Phys. Rev. B* **2008,** *78*, 094412-094420.

52. Proenca, M. P.; Sousa, C. T.; Pereira, A. M.; Tavares, P. B.; Ventura, J.; Vazquez, M.; Araujo, J. P., *Phys. Chem. Chem. Phys.* **2011,** *13*, 9561-9567.

53. Johansson, B., *Phys. Rev. B* **1979,** *19*, 6615-6619.

54. Hasegawa, M.; Batrashevich, M. I.; Zhao, T. R.; Takei, H.; Goto, T., *Phys. Rev. B* **2001,** *63*, 184437-184443.

55. Eisenstein, J., *Rev. Mod. Phys.* **1954,** *26*, 277-291.

56. Pauling, L., *The Nature of the Chemical Bond*. 3 ed.; Cornel University Press: Ithaca, NY, 1960; p 410.

57. Andreeva, A. F.; Gil'man, I. Y., *Inorg. Mater.* **1978,** *14*, 384-390.

58. Rao, C. N. R.; Sarma, D. D.; Sarode, P. R.; Sampathkumaran, E. V.; Gupta, L. C.; Vijayaraghavan, R., *Chem. Phys. Lett.* **1980,** *76*, 413-415.

59. Hatwar, T. K.; Nayak, R. M.; Padalia, B. D.; Ghatikar, M. N.; Sampathkumaran, E. V.; Gupta, L. C.; Vijayaraghavan, R., *Solid State Commun.* **1980,** *34*, 617-620.

60. Moreschini, L.; Dallera, C.; Joyce, J. J.; Sarrao, J. L.; Bauer, E. D.; Fritsch, V.; Bobev, S.; Carpene, E.; Huotari, S.; Vanko, G.; Monaco, G.; Lacovig, P.; Panaccione, G.; Fondacaro, A.; Paolicelli, G.; Torelli, P.; Grioni, M., *Phys. Rev. B* **2007,** *75*.

61. Inoue, T.; Kubozono, Y.; Kashino, S.; Takabayashi, Y.; Fujitaka, K.; Hida, M.; Inoue, M.; Kanbara, T.; Emura, S.; Uruga, T., *Chem. Phys. Lett.* **2000,** *316*, 381−386.

62. Jiang, L.; Hsu, A.; Chu, D.; Chen, R., *Int. J. Hydrogen Energ.* **2010,** *35*, 365-372.

63. Xu, C. W.; Shen, P. K.; Liu, Y. L., *J. Power Sources* **2007,** *164*, 527-531.

64. Cui, G. F.; Song, S. Q.; Shen, P. K.; Kowal, A.; Bianchini, C., *J. Phys. Chem. C* **2009,** *113*, 15639-15642.

Chapter 7

Size and Morphology Controlled Synthesis of Ordered Nanoparticles in the NiAs Structure type as efficient Catalysts for the Hydrogenation Reactions

---

Papers published on this work have appeared in

[1] *Patent Application number:* WO 2015/011680 A1.

[2] *Manuscript based on this work is under revision.*

7.1. Introduction

The design of good catalysts by controlling the size, shape, composition, crystal structure, surface chemistry and the selection of suitable supports has drawn a great attention of researchers during past two decades. Typical heterogeneous catalysts currently being used are transition metals, bimetallic, alloys or intermetallics.[1] An enhanced activity was often observed for these materials when they are in the low dimensional (nano) due to the large surface area. The catalytic activity of these compounds can be improved further with the aid of suitable support.[2]

Generally, noble metals such as Pd, Pt, Rh and Au and their compounds are extensively studied for the catalytic hydrogenation process.[3] The interesting examples are PdGa,[4] ZnPd,[5] $NaAu_2$[6], CoAl, and FeAl.[7] These compounds contain Pd, Zn, Fe, Na and Co, which are the catalytically active metal atoms, surrounded by catalytically inactive or less active metals like Ga and Al. This peculiar nature of the ordered crystal structure results in the isolation of catalytically active centres, which promotes the selective interaction of substrate molecules to undergo reduction and enhances the selectivity of the reaction in the hydrogenation of alkynes. Since, the thermodynamically stable prototypes for these compounds are not much reported in the bulk form, the scope of selection of the compounds based on these structures is limited. In this regard, the NiAs structure type is very interesting and versatile with a substantial number of bulk prototypes, motivated to choose *M*Sb (*M* = Co and Ni) and *M*Se (*M* = Co and Ni) for the current study.[8]

The Pauli paramagnetic NiSe is a member of the transition metal chalcogenides, which shows very poor metallic behaviour in bulk (2.0 eV)[9] and band gap semiconducting behaviour in its nano form (2.8 eV to 3.6 eV).[10] Because of the valence electronic configuration of Ni ($3d^8 4s^2$) and the small difference in electronegativity between Ni (E_n = 1.9) and Se (E_n = 2.4), they can form a variety of complexes with varied stoichiometry. Apart from NiSe, there are other nickel selenides based semiconductors ($NiSe_2$, Ni_3Se_2) which have been reported for various applications. These semiconductors exhibit interesting electronic[11] and magnetic properties,[12] proposed as Pt-free catalysts for electrochemical H_2 production[13] and have found several applications in the field of materials science, which has attracted considerable attention over the last decades.[14-16] These materials were also proposed as a potential candidate for solar cells [17] as their band gap is wider than bulk nickel sulfide (0.4

eV)[18] and narrower than nickel oxide (3.6 to 4.0 eV).[19, 20] These materials have found applications in the fields of catalysis, optical recording, lithium ion cells, laser materials and energy storage.[21-23] Motivated by these various applications of this class of semiconducting materials, the synthesis of the semiconducting NiSe in nano form has been targeted. NiSe have been previously synthesized in nano form using hydrothermal method.[10, 24] The morphology and size of NiSe have been controlled by varying nickel salt precursors,[25] capping agents, reducing agents, reaction temperature and duration of the reaction.[26] However, none of these materials were subjected to detailed applications except routine optical measurements. This stimulated to focus on the synthesis and application of *M*Sb (*M* = Co and Ni) and *M*Se (*M* = Co and Ni) nanoparticles in detail, especially for the hydrogenation of small organic molecules. *M*Sb as the low cost representative of the whole family due to the reason that they were reported for their interesting properties such as optical, electrical, anti-corroding, anode material for lithium ion battery, and fuel cells but seldom explored as catalysts.[21-23]

Generally, nanomaterials can be synthesized using two synthetic routes; one is solution method such as solvothermal,[27, 28] polyol,[29, 30] microemulsion technique,[31] and microwave assisted reactions[32] and another is mechanical or ball milling method.[33, 34] Both synthetic routes have their own advantages and disadvantages. In case of solution phase synthesis, particle size can be controlled with required morphology. On the other hand, in ball milling method, the morphology cannot be controlled, often leading to particle agglomeration[35] and in some cases, sample can be contaminated as well. However, using milling method, large quantity (industrial scale) of nano material can be produced within short period of time without using any additional reagents like solvent, reducing agent and surfactant. On the other hand, polyol method requires a lot of additional reagents and produce only small quantity of the products over a large period of time.

This chapter discusses the synthesis of *M*Sb (*M* = Co and Ni) and *M*Se (*M* = Co and Ni) ball milling and polyol methods. Though some of these compounds already been synthesized by the co-reduction of metal precursor using sodium borohydride in a high boiling polyol and solvothermal methods,[36] here, the synthesis of these nanoparticles by mechanical milling method has been attempted for the first time. The catalytic activity of selected nanoparticles has checked for the hydrogenation of para-nitroaniline (PNA) to para-

phenyldiamine (PPD) and para-nitrophenol (PNP) to para-aminophenol (PAP) using $NaBH_4$ as the reducing agent. These reactions have been selected for the study because PPD and PAP are two industrially important compounds finding remarkable application in various industries. PPD is a useful chemical in many industrial materials (e.g., polymers, azo dyes, fur dyes, rubber antioxidants, textile fibres and thermoplastics),[37, 38] and PAP is another important intermediate in the preparation of several analgesic and antipyretic drugs such as phenacetin, acetanilide and paracetamol.[39]

7.2. Experimental Section

7.2.1. Synthesis

7.2.1.1. Chemicals

The following materials were used for the synthesis: cobalt (powder, 99.99%), nickel (powder, 99.99%), antimony (shots, 99.99%), selenium (powder, 99.99%), nickel(II)chloride ($NiCl_2$) (99.99%), selenous acid (H_2SeO_3) (99.99%), tetraethylene glycol (TEG) (99+%) as solvent, PVP (all purchased from Alfa Aeser) as surfactant and sodium borohydride ($NaBH_4$) (98%, Sigma Aldrich) as the reducing agent in solution phase reaction. All air sensitive chemicals were handled inside the glove box.

7.2.1.2. Direct Method

The direct method was used for the synthesis of *M*Sb and *M*Se samples in polycrystalline form having larger particle size. Inside the glovebox, under argon atmosphere, metals were mixed in the ideal 1:1 atomic ratio by combining respective weights, and were placed in a 9 mm diameter quartz tube, which was flame-sealed under vacuum of 10^{-3} torr, to prevent oxidation during heating. The tube was then placed in a vertically aligned tube furnace and heated to 960 ^{o}C over the period of 10 h, and kept there isothermally for 72 h. Finally, the system was cooled to room temperature within 10 h. NiSe was found to be stable in moist air for several months. The weight losses of the final grey coloured material were found to be less than 1%. The samples obtained from the direct method were used to produce nanoparticles by planetary ball milling synthesis.

7.2.1.3. Ball Milling Method

Pure compounds of *M*Sb and *M*Se obtained from the direct method was subsequently loaded into a planetary ball miller (Fritsch Planetary Micro Mill Pulverisette-7 premium line)

having two steel bowls of 25 mL capacity with tungsten carbide balls. The tungsten carbide balls of 10, 5, 3 and 1.6 mm diameter were used for the synthesis of NiSe nanoparticle of different sizes and are represented as *MX* (*M* = Co, Ni, *X* = Sb, Se)_BM10, NiSe_BM5, NiSe_BM3 and NiSe_BM1.6, respectively. The milling was performed for a period of 15 min with 2 min break after every 5 min to avoid the overheating of the sample.

7.2.1.4. Polyol Method

Pure phase of NiSe nanoparticles were synthesized by the polyol method with (NiSe_PP) and without (NiSe_PN) the surfactant PVP (mole. wt. = 58000), where tetra ethylene glycol was used as solvent. $NiCl_2$ (0.1 m moles, 25.9 mg) and H_2SeO_3 (0.1 m moles, 25.8 mg) were taken in 25 mL round bottom flask. For the synthesis in the presence of surfactant, PVP was added followed by $NaBH_4$ in greater than twice stoichiometric amount into the solution. The temperature of the solution was slowly increased to 50 °C under constant argon gas purging. Stoichiometric amount of freshly prepared $NaBH_4$-TEG solution was slowly injected into the reaction flask under vigorous magnetic stirring. Upon reduction, the solution was heated to 220 °C and maintained at this temperature for 3 h. The product obtained as black precipitate was washed thoroughly with ethanol several times by centrifuging at 5000 rpm followed by drying under vacuum at 60 °C for 8 h. Similar strategy was used for the synthesis of Ni and Se nanoparticles to perform controlled catalysis reactions.

7.2.1.5. Elemental analysis

Quantitative microanalysis on all the samples were performed with a FEI NOVA NANOSEM 600 instrument equipped with an EDAX® instrument. Data were acquired with an accelerating voltage of 20 kV and a 100 s accumulation time. The EDAX was performed using P/B-ZAF standard less method (where, Z = atomic no. correction factor, A = absorption correction factor, F = fluorescence factor, P/B = peak to background model) on selected spots and points. The average atomic weight obtained from the EDAX measurements are on average 48% and 52% for Ni and Se, respectively suggest that NiSe_PN and NiSe_PP samples are slightly Ni deficient.

7.2.1.6. Powder XRD

Phase identity and purity of the *M*Sb and *M*Se nanoparticles were determined by powder XRD experiments with a Bruker D8 Discover diffractometer using Cu-*Kα* radiation (λ = 1.5406 Å) over the angular range $20^{\circ} \leq 2\theta \leq 70^{\circ}$ at room temperature calibrated against corundum standard. The experimental powder XRD patterns of NiSe and the simulated pattern of reported single-crystal X-ray structure refinement were found to be in good agreement (Figure 7.1 and 7.2). The PXRD pattern of *M*Sb and CoSe nanoparticle synthesized by mechanical milling method (Figure 7.3) are matching with the simulated one obtained from the reported crystallographic data, indicating that the pure phases were obtained within 15 min of milling process.

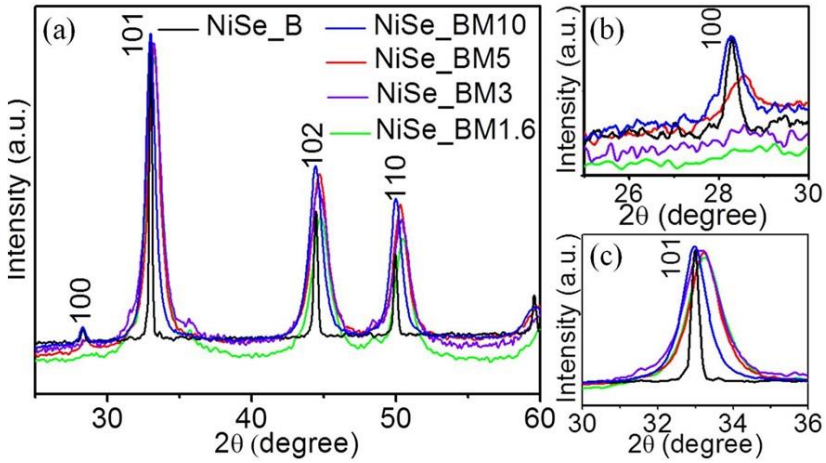

Figure 7.1. PXRD comparison of bulk and nanoparticles of NiSe synthesized by ceramic (high temperature solid state reaction) and ball milling methods, respectively.

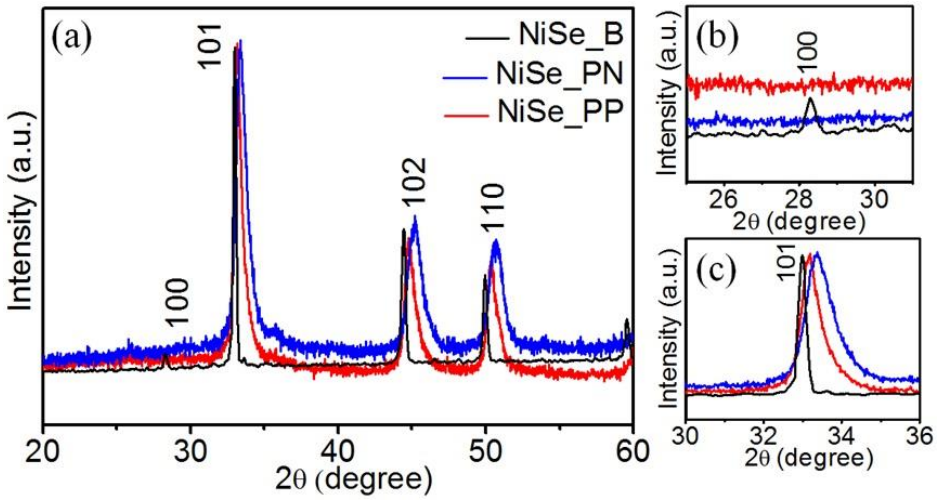

Figure 7.2. PXRD comparisons of bulk and nanoparticles of NiSe synthesized by ceramic and polyol methods, respectively.

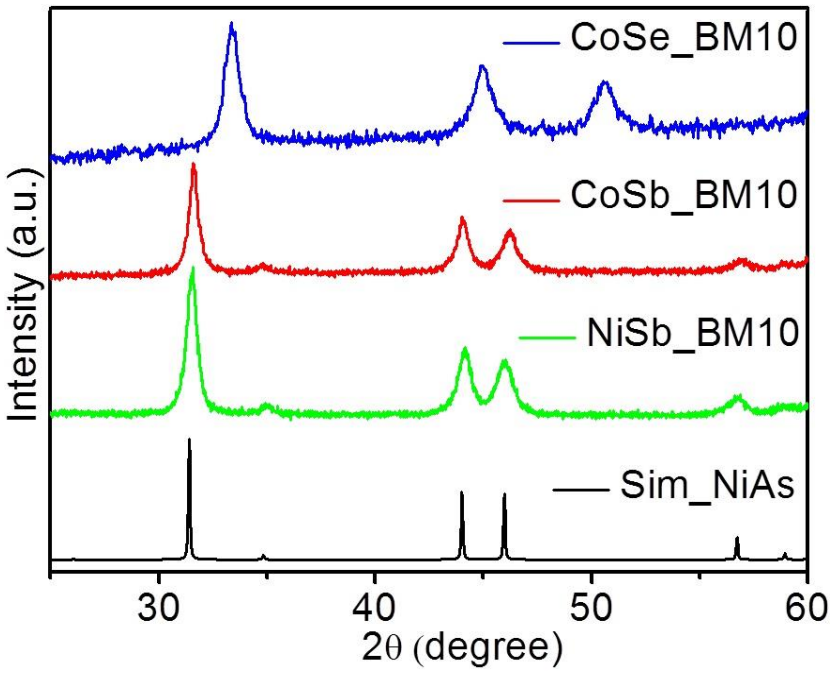

Figure 7.3. PXRD comparison of simulated NiAs and nanoparticles of NiSb_BM10, CoSb_BM10 and CoSe_BM10 synthesized by ball milling methods.

7.2.1.7. TEM

TEM images and SAED patterns were collected using a TECNAI and JEOL 200 kV TEM. The samples were prepared by first sonication of the nano-crystalline powders in ethanol solution and then drop cast onto a holey carbon grid.

7.2.1.8. UV-Vis spectroscopy

Absorption studies were carried out using the Perkin lambda 900 UV-Vis spectrometer. The catalysts used were well dispersed in water for all spectroscopic and catalytic studies. For the catalytic studies of the nanoparticles, the absorbance was measured in the range 210–500 nm at a scan rate of 300 nm/min.

7.2.1.9. Catalytic studies

*M*Sb and *M*Se nanoparticles were dispersed ultrasonically in deionized water. About 0.1 mg of MSb or MSe catalyst was added to 1 mL (1.0×10^{-4} M) aqueous solution of PNA in a quartz cuvette followed by the addition of 1 mL (6×10^{-2} M) freshly prepared $NaBH_4$ solution. The total volume of the solution was made up to 3 mL by adding deionized water and time-dependent absorption spectra were recorded in the UV-Vis spectrophotometer at 25 °C. The hydrogenation of PNP was also carried out under similar conditions.

7.3. Results and Discussions

7.3.1. Structure analysis

The compounds *M*Sb and *M*Se crystallizes in the hexagonal NiAs structure type [40] having space group $P6_3/mmc$ (Figure 7.4).

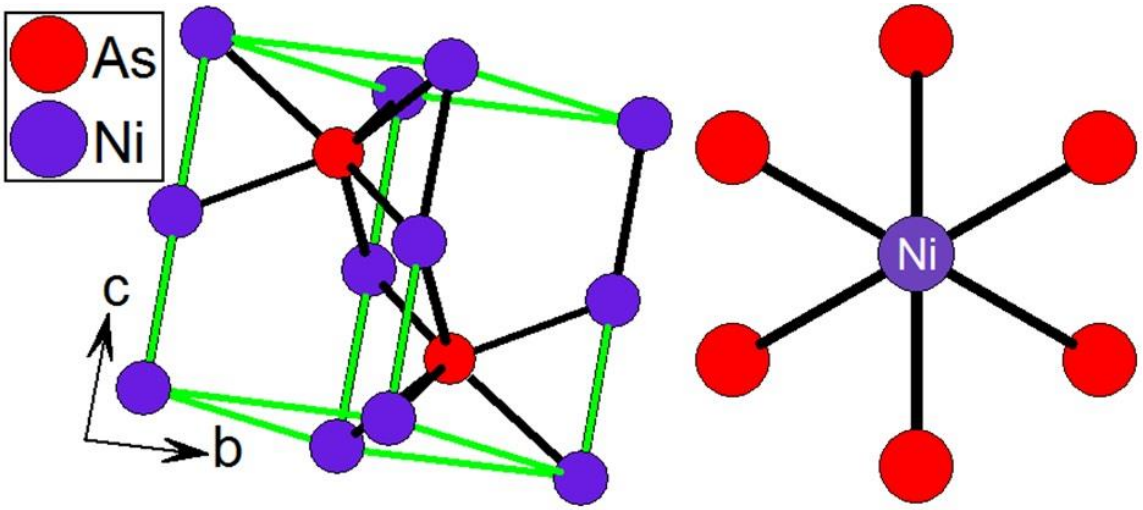

Figure 7.4. Hexagonal closed packing crystal structure of NiAs (left) and the coordination spheres of the Ni atom (right).

The crystal structure of *M*Sb and *M*Se can be described as hexagonal close packed arrangement of selenium/antimony atoms with the nickel/cobalt atoms filling in the octahedral voids. The detailed crystal structure description of the compounds within the NiAs structure type have been reported.[8] NiSe synthesized previously by the solid state reaction in an evacuated quartz ampoule and high pressure technique, which exhibited very poor metallic behaviour.[9] In this chapter NiSe nanoparticles were synthesized by solution and ball milling methods and MSb and CoSe by ball milling method. Since the standard reduction potentials of Ni^{2+} and SeO_3^{2-} are -0.26 V and -0.36 V, respectively,[41] Ni^{2+} is more easily and rapidly reduced to Ni^0 in the solution than Se^{4+} to Se^0. The powder XRD patterns of NiSe synthesized at different reaction conditions (Figure 7.1) are were matching with the simulated one obtained from the reported crystallographic data, indicating that the pure phases were obtained within 15 min of milling process.

In ball milling method, the compounds were obtained in different sizes by varying the size of the milling balls. On the other hand, both particle size and the morphology of NiSe were controlled in the polyol method with and without surfactant represented as NiSe_PP and NiSe_PN, respectively (Figure 7.2). The slight shift of all peaks towards the higher 2θ

angle (Figure 7.1c and 7.2c) and absence or less intense [100] peak at 2θ = 28.5° suggests the probable deficiency in Ni content, which was confirmed by the EDAX measurements (Figure 7.5). The tungsten carbide balls of diameter 10 mm (NiSe_BM10), 5 mm (NiSe_BM5), 3 mm (NiSe_BM3) and 1.6 mm (NiSe_BM1.6) leads to the formation of NiSe with crystallite size 11, 9, 8 and 7 nm, respectively, clearly indicating the crucial role of ball size in controlling the size of the nanoparticles.

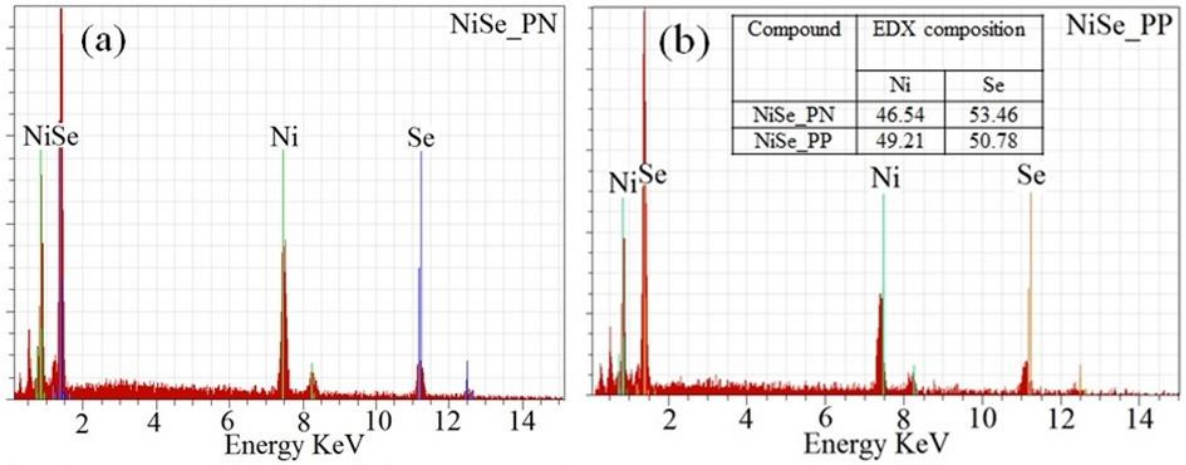

Figure 7.5. Typical EDAX spectra of NiSe_PN and NiSe_PP samples. The average composition obtained from the EDAX measurements shown in the inset table of Figure 7.5b.

The peaks [100], [101], [102], [110], [103] and [202] observed in PXRD confirm the formation of the ordered structure of NiSe.[40] The absence or less intense [100] peak at 2θ = 28.5° (Figure 7.1b and 7.2b) suggests the probable deficiency at Ni position, which is well supported by reported $Ni_{0.85}Se$.[42] As the size of the tungsten carbide balls decreased (NiSe_BM3 and NiSe_BM1.6), the intensity of [100] plane has reduced proportionally or disappeared. Increase in FWHM of [101] plane, represents Ni deficiency and reduction in particle size (Figure 7.1b). Similarly, the absence of [100] plane in the PXRD pattern of the samples NiSe_PN and NiSe_PP (Figures 7.2a and 7.2b) also indicates the Ni deficiency with an expected composition of $Ni_{0.85}Se$.[42] The crystallite size of NiSe_BM10, NiSe_BM5, NiSe_BM3, NiSe_BM1.6 and NiSe_PN, NiSe_PP were calculated by using Scherrer formula and are listed in Table 7.1. The TEM measurements and SAED patterns of sample NiSe_PN confirmed the formation of rectangular uniform nanoparticles (Figure 7.6). On the other hand, the surfactant PVP favours the formation of more or less mono dispersed nano cubes of NiSe_PP (Figure 7.5c). The corresponding SAED reveals highly crystalline nature in both

compounds (Figure 7.5b and 7.5d). However, as expected, the particles were aggregated in the case of samples synthesized by ball milling method (Figure 7.7).[35] The TEM image of NiSe (Figure 7.7) samples milled for 15 min by varying tungsten carbide ball dimension from 10 to 1.6 mm shows the particles are more or less spherical in shape and strongly agglomerated. The average crystallite size of NiSe_BM was found to be around 9 nm (Table 7.1), which is consistent with the crystallite size calculated from the PXRD patterns using the Scherrer formula. In addition, the SAED pattern (inset in Figure 7.7) infers the NiSe_BM are polycrystalline in nature. Previous results suggest that PVP serves as capping agent and stabilizes the formed nanoparticles against agglomeration, but also plays a role in the formation of specific morphology such as cubes or wires.[43]

Table 7.1: The reaction conditions on the synthesis of NiSe nanoparticle by ball milling and crystallite size of NiSe nano particle by ball milling and polyol methods.

Compound	Ball diameter (mm)	No. of balls used	Crystallite Size (nm)
NiSe_BM10	10	10	11
NiSe_BM5	5	80	9
NiSe_BM3	3	100	8
NiSe_BM1.6	1.6	120	7
NiSe_PN	-	-	7
NiSe_PP	-	-	9

IR and XPS studies were used to explain the growth mechanism, it is observed that both the oxygen and nitrogen atoms of the pyrrolidone unit can promote the adsorption of PVP chains on the surface of silver.[44] When PVP was introduced, it is believed that the selective interaction between PVP and various crystallographic planes of *fcc* could greatly reduce the growth rate along the [100] direction or enhance the growth rate along [111] direction. PVP has a polyvinyl skeleton with polar group (N-C=O) indicates the presence of a strong interaction between the surfaces of NiSe nanoparticles and PVP through coordination bonding with the O and N atoms of the pyrrolidone ring.[45] These can efficiently bind with the active sites of Ni, resulting in the shortage of active sites for the hydrogenation. It is well supported that, with isotropic growth in the case of NiSe_PP leads to cube shaped morphology.[43, 46] On the other hand, the absence of surfactant (NiSe-PN) allows the growth in [100] direction, resulting in rectangular morphology.

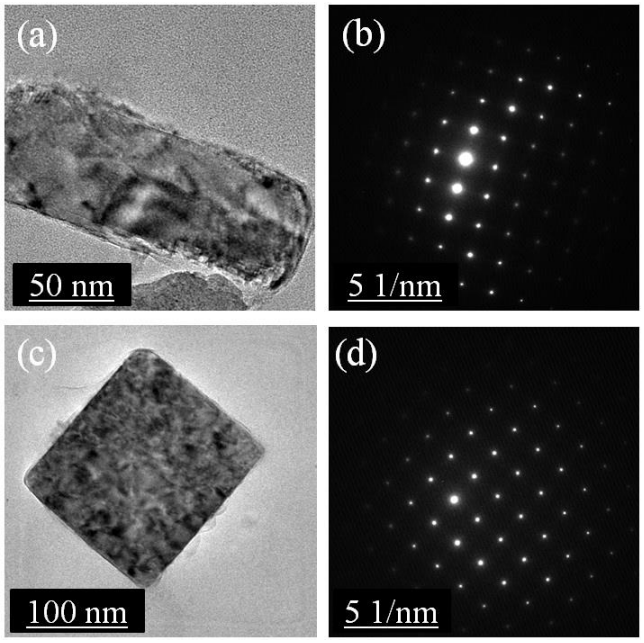

Figure 7.6. (a) TEM images of NiSe_PN nano rectangle, (b) SAED patterns of NiSe_PN, (c) TEM images of NiSe_PP nano cube synthesized by polyol method and (d) SAED patterns of NiSe_PP.

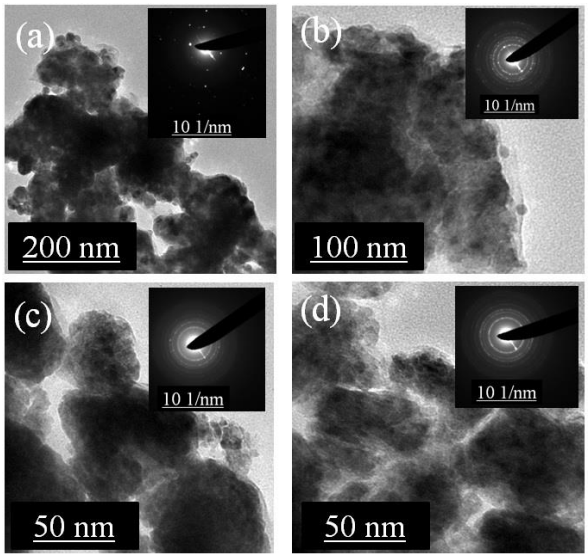

Figure 7.7. TEM images of NiSe nanoparticles synthesized by ball milling method: (a) NiSe_BM10, (b) NiSe_BM5, (c) NiSe_BM3 and (d) NiSe_BM1.6. Inset in each figure represent the SAED pattern of the corresponding sample.

7.3.2. Hydrogenation of PNA and PNP

The reduction of nitro aromatic compounds to the corresponding amines is considered as the important process in controlling environmental pollution.[47, 48] The conventional method of reducing these compounds using sulphides generates substantial environmental

waste. Therefore, catalytic hydrogenation has been considered as an environment friendly method for the large-scale production of many amines from the corresponding aromatic nitro compounds.

In this chapter the catalytic hydrogenation of two aromatic nitro compounds have been selected viz. PNA and PNP reduction using NiSe and *M*Sb nanoparticles as catalysts using $NaBH_4$ as the reducing agent. Since, several noble metals based bimetallic and alloys were used for the hydrogenation of PNA,[30, 49-52] and PNP[53] to confirm the catalytic activity of these materials. The step wise reaction process for both the hydrogenation reactions are represented schematically in Figures 7.8a and 7.8b.

The aqueous solution of PNA is bright yellow in colour (Figure 7.8a), giving an absorption maxima at 380 nm in UV-Vis spectrum. The addition of the aqueous solution of $NaBH_4$ to PNA did not change in colour of the solution (Figure 7.8a) hence the peak at 380 nm remains unchanged in the presence of $NaBH_4$ (Figure 7.9a) and in the absence of the catalyst for a period of 15 min of the reaction time (Figure 7.9b) indicate that the reduction of aromatic nitro group under mild conditions does not occur in the absence of any catalyst.

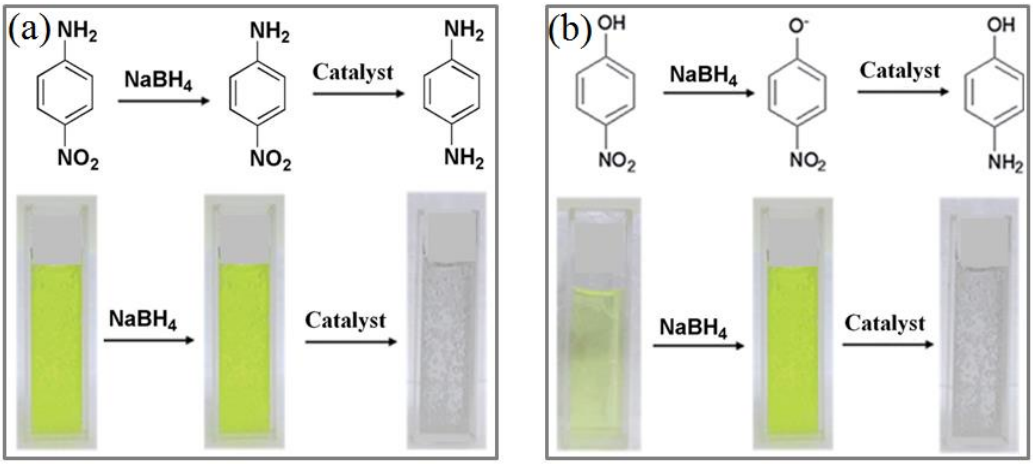

Figure 7.8. The hydrogenation of (a) para nitroaniline to para phenyldiamine, yellow colour and colourless represent PNA and PPD, (b) Pale yellow, intense yellow and colourless represent PNP, para-nitrophenolate and PAP, respectively.

The aqueous solution of PNP is light yellow in colour, which shows absorption maximum at 317 nm under neutral or acidic conditions.[39] The addition of aqueous $NaBH_4$ to PNP cause a change in colour of the solution from light to deep yellow (Figure 7.8b). This colour change can be attributed to an increase in the alkalinity of the solution, which results in the formation of the para-nitrophenolate ion.[39] The absorption maximum of the para-

nitrophenolate ion observed at 400 nm (Figure 7.10a) remains unchanged in the presence of $NaBH_4$, even up to 15 min of the reaction (Figure 7.10b). This also indicates the reduction of PNP to PAP does not occur without the help of catalyst.

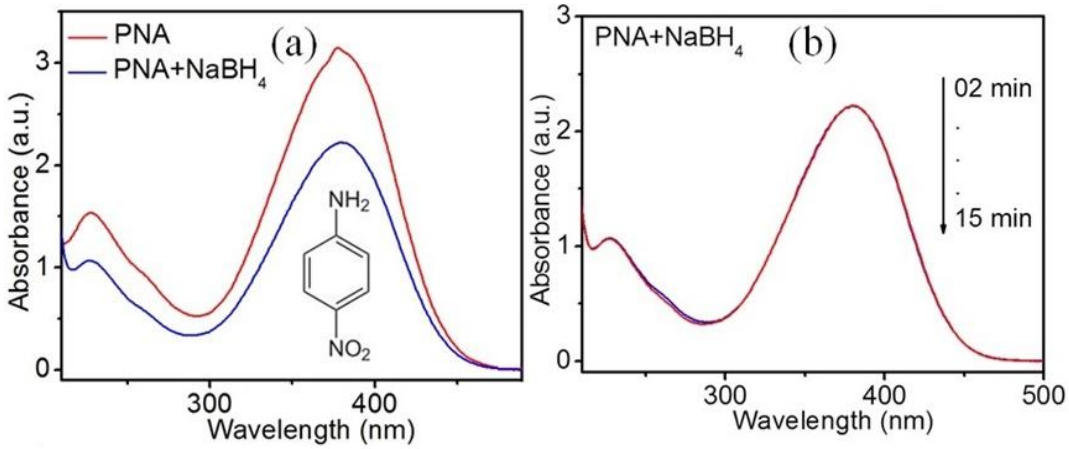

Figure 7.9. UV-Vis absorption spectra for the hydrogenation of PNA (a) in the presence and the absence of $NaBH_4$ and (b) in the absence of catalyst.

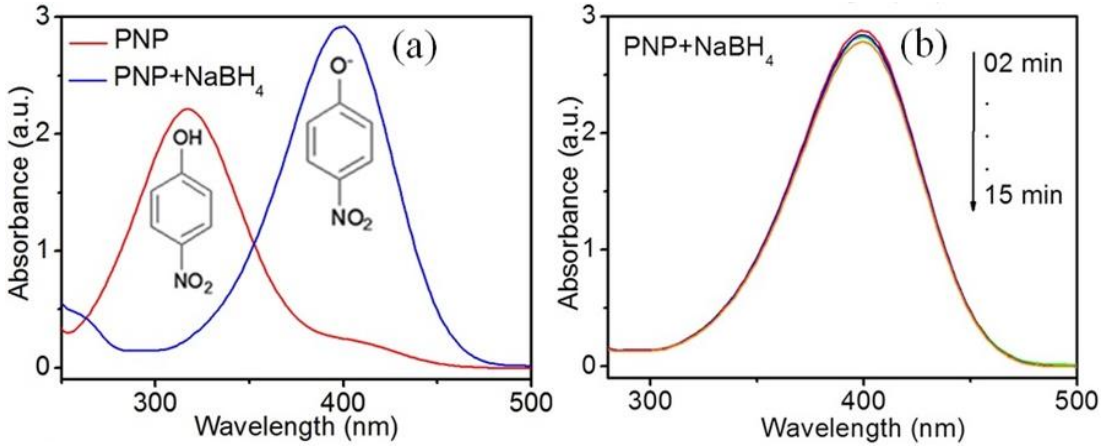

Figure 7.10. UV-Vis absorption spectra for the reduction of PNP (a) in the presence and absence of $NaBH_4$ and (b) in the absence of catalyst for the period of 15 min reaction.

It is well known that reduction of nitro group to amino group by using $NaBH_4$ is a kinetically slow process.[54] In order to check the–catalytic properties of NiSe intermetallic nanoparticles over metal counterparts, and the hydrogenation of PNA and PNP was performed over Ni and Se synthesized by similar method (Figure 7.11). As seen from (Figure 7.11a and 7.11b), the reactions over Ni nanoparticles have not completed even after a period of 60 min and Se nanoparticles (Figure 7.11c and 7.11d) not even initiate the reactions suggest the intermetallics made up of these metals are very essential for the fast hydrogenation of PNA and PNP.

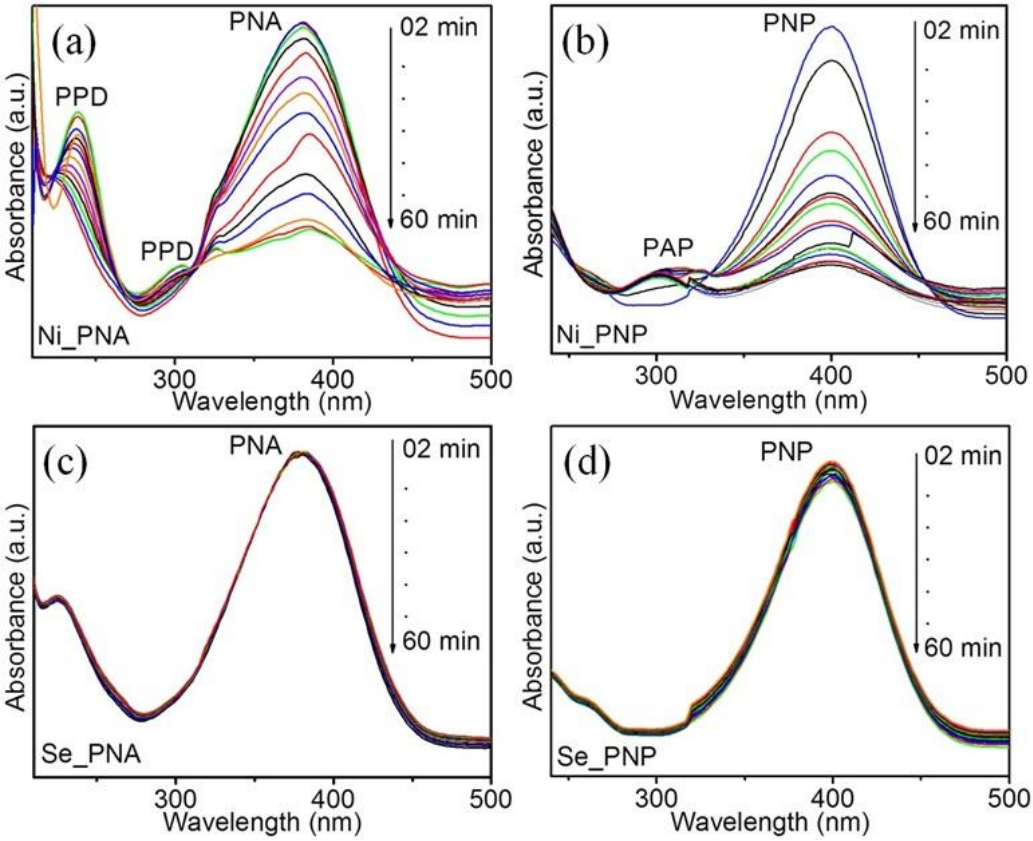

Figure 7.11. UV-Vis absorption spectra for the reduction of PNA and PNP in the presence of (a) and (b) Ni nanoparticles and (c) and (d) Se nano particles, catalyst for the period of till 60 min reaction.

The addition of the NiSe nanoparticles to the solution , changes the colour gradually from yellow to colourless (Figure 7.8a) and two new peaks were observed at 305 and 240 nm in the absorption spectra, which corresponds to formation of PPD.[59] The hydrogenation of these reactions was monitored through UV-Vis absorption spectrometer. The nitro groups of PNA and PNP in aqueous solution shows absorbance maximum (λ_{max}) at 380 and 317 nm respectively, under neutral or acidic condition.[39] In PNP reduction, the addition of $NaBH_4$ enhances the alkalinity of the solution where phenolate ions are predominating with a shift in absorbance maximum to 400 nm, which can be observed by change in the colour intensity of the solution. The intensity of the absorption peak at 380 nm dramatically decreases with a proportional increase of the new peaks at 305 and 240 nm confirming the conversion of PNA to PPD (Figure 7.12 and 7.13). Among the ball milling products, the compound NiSe_BM1.6 is the most active catalyst completing hydrogenation of PNA to PPD within 2 min (with the

highest rate constant k = 5.0 x 10^{-3} sec^{-1}) as compared to the other samples NiSe_BM10 (24 min), NiSe_BM5 (8 min) and NiSe_BM3 (4 min) are shown in Figure 7.12.

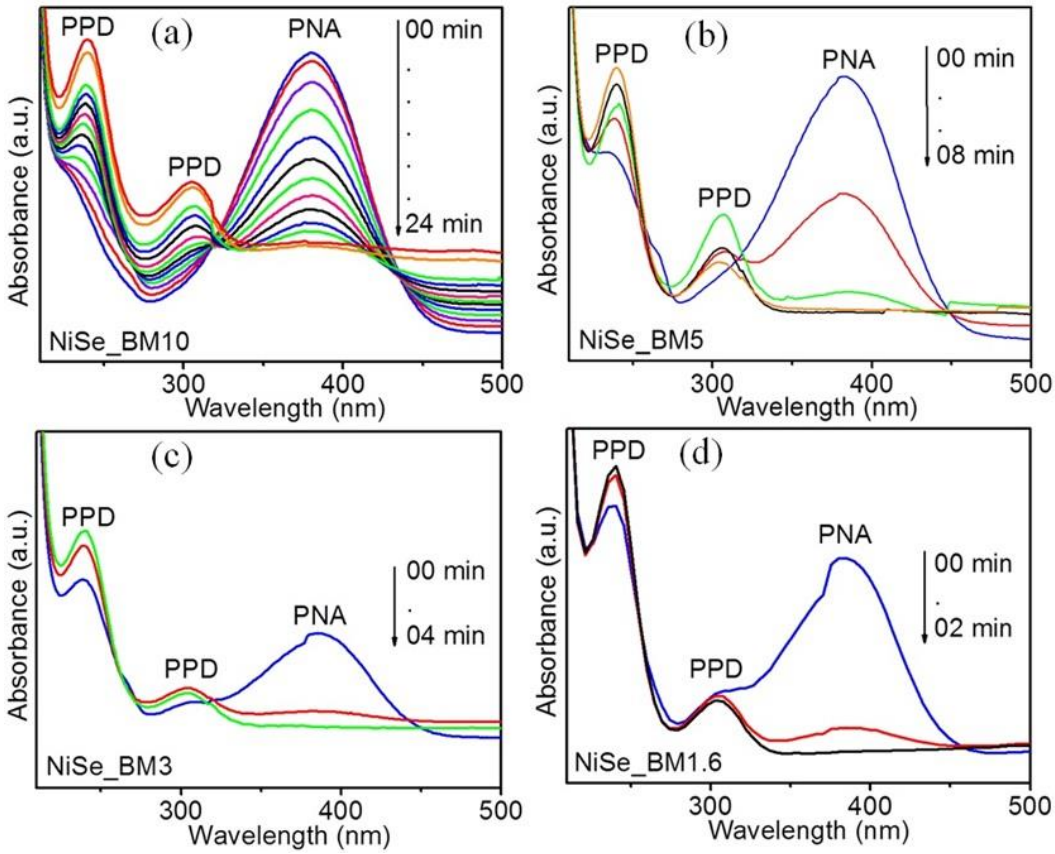

Figure 7.12. UV-Vis absorption spectra for the reduction of PNA to PPD in the presence of NiSe nanoparticle obtained by ball milling method.

The particle size and deficiency of nickel are playing crucial role in the hydrogenation process. It is well known that the reduction of the particle size increases the surface to volume ratio leading to an increase in the number of active sites.[60-62] Also, the creation of deficiency at active site favours enhanced catalytic activity.[63] The catalytic activity of NiSe_PN and NiSe_PP for the hydrogenation of PNA to PPD (Figure 7.13) also studied. NiSe_PN catalyses the reaction faster (6 min reduction time and rate constant k = 4.22 x 10^{-3} sec^{-1}) compared to NiSe_PP (14 min reduction time and rate constant of k = 3.09 x 10^{-3} sec^{-1}), clearly indicates that the presence of surfactant reduces the activity by blocking substrate molecules.

Upon the addition of NiSe catalyst nanoparticles, the colour of the solution changed and the intensity of the absorption peak at 400 nm (corresponding to PNP) gradually

decreased and a new peak was observed at 310 nm, which corresponds to PAP. Similar to the previous reaction, among the samples obtained from the ball milling method, NiSe_BM1.6 shows the highest activity or rate constant compared to other samples (Figure 7.14 and 7.15) with the rate constant of $k = 4.31 \times 10^{-3}$ sec^{-1}.

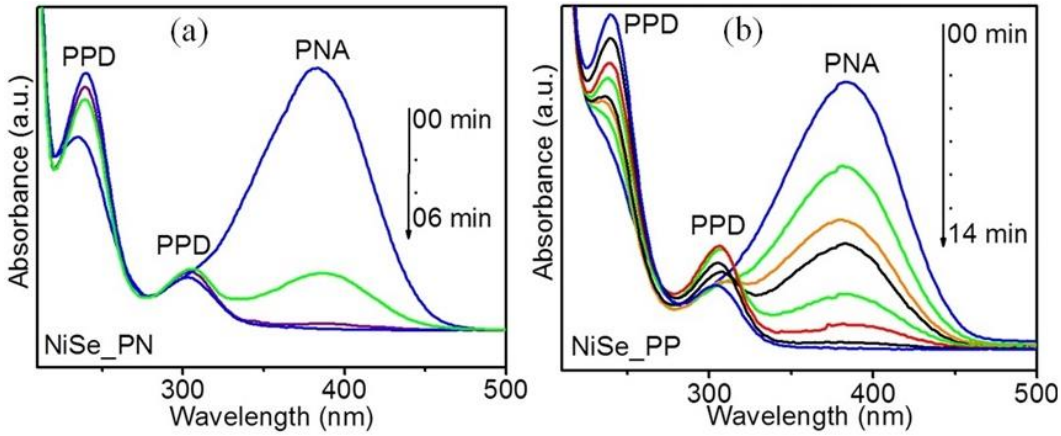

Figure 7.13. UV-Vis absorption spectra for the hydrogenation of PNA to PPD in the presence of NiSe nanoparticle obtained by polyol method.

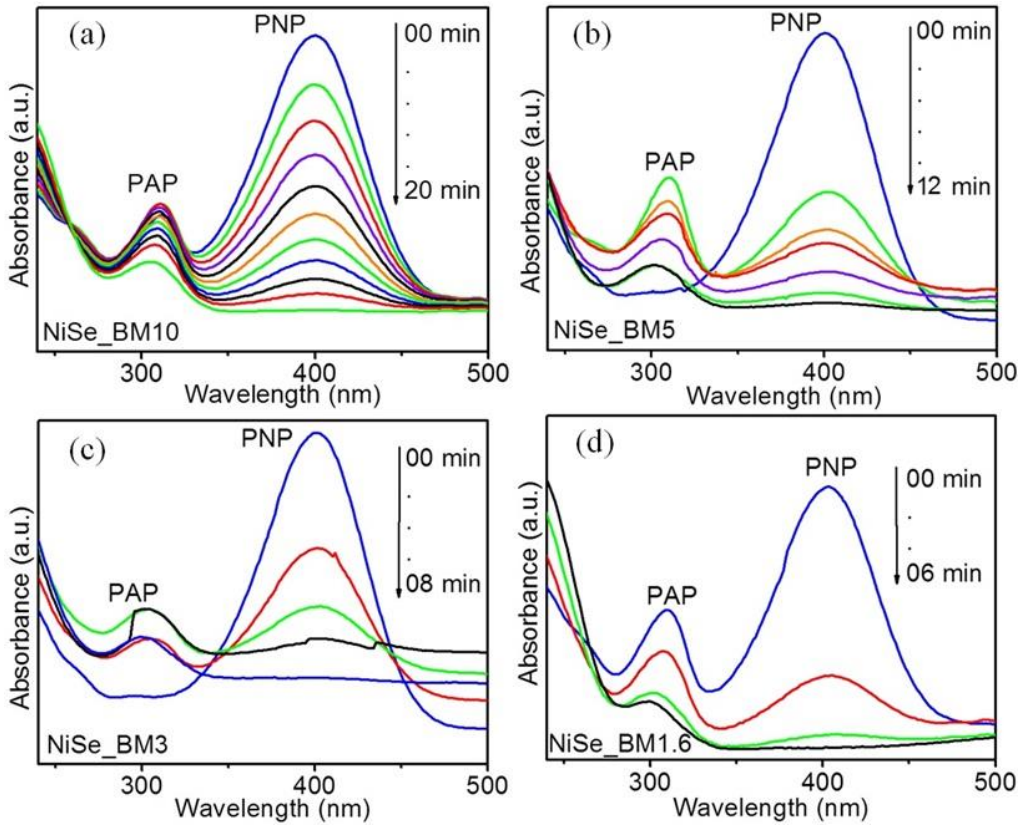

Figure 7.14. UV-Vis absorption spectra for the hydrogenation of PNP to PAP in the presence of NiSe nanoparticle obtained by ball milling method.

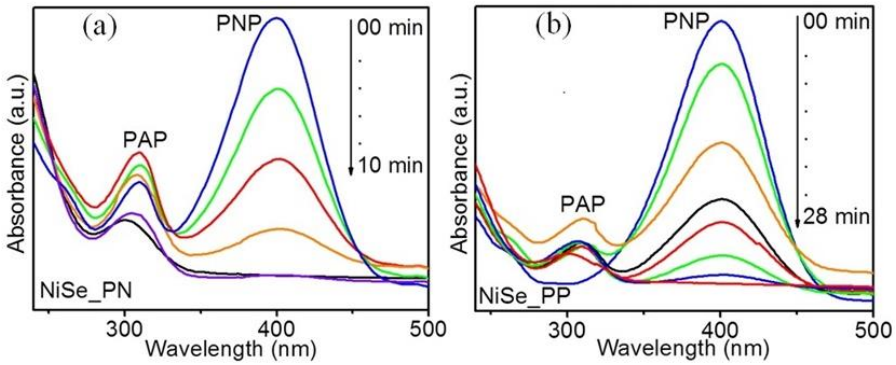

Figure 7.15. UV-Vis absorption spectra for the hydrogenation of PNP to PAP in the presence of NiSe nanoparticle obtained by polyol method.

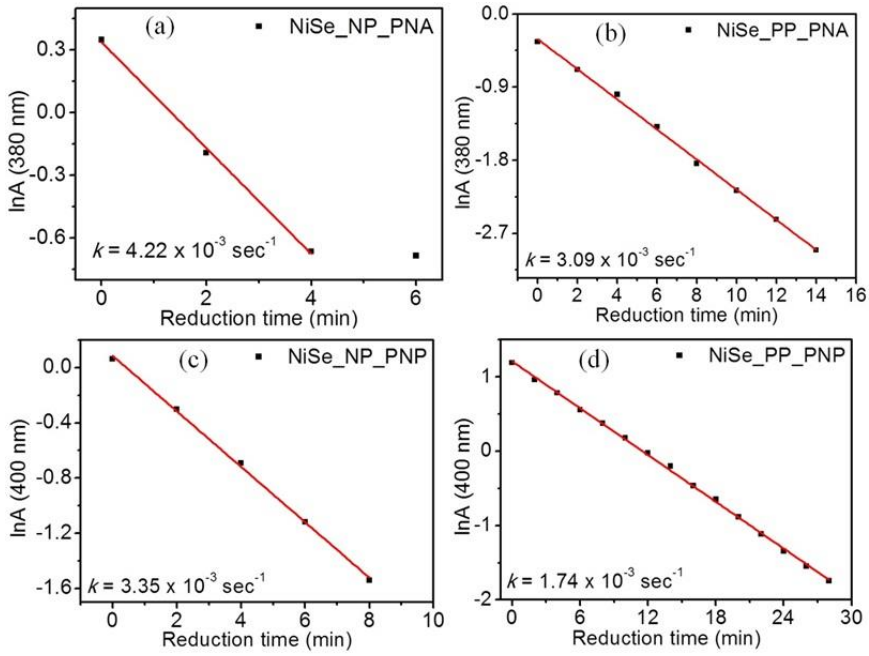

Figure 7.16. The plot of concentration vs reduction time for the hydrogenation of PNA by NiSe_PN (a), NiSe_PP (b) and for the hydrogenation of PNP by NiSe_PN (c), NiSe_PP (d). Other parameters are constant; $NaBH_4$ - 6×10^{-2} M, PNA - 1.0×10^{-4} M, catalyst loading - 0.1 mg/mL and temperature -298 K.

The plot yields a good linear correlation indicating that the reaction follow the pseudo first order kinetics. This can be expressed by the equation $[A_t] = [A_0]e^{-kt}$, where A_t is the absorbance at time t and corresponds to the concentration of the reactant at instant t, A_0 is the initial concentration of the reactant and *k* is the pseudo first order rate constant. The observed rate constants were calculated by linear fit to the logarithmic plot for each reaction. Crystallite size dependent reaction time and rate constants for NiSe_BM10, NiSe_BM5, NiSe_BM3, NiSe_BM1.6 are shown in Figure 7.17, which clearly indicates that smaller

crystallite size favors quicker reactions with corresponding increase in rate constant (Figure 7.17). As expected, NiSe_PN completes hydrogenation within 10 min (k = 3.352 x 10^{-3} sec^{-1}) compared to NiSe_PP which required 30 min to complete the reaction with almost half rate constant of k = 1.74 x 10^{-3} sec^{-1}. This increased catalytic activity is due to the presence of small crystallite size of NiSe_PN and absence of any surfactant. In these studies, the best rate constants were obtained for the compound NiSe_BM1.6 with k = 5.0 x 10^{-3} for the hydrogenation of PNA and k = 4.31 x 10^{-3} for the hydrogenation of PNP. These values are better than the values reported for noble metal catalysts and related compounds (Table 7.2 and 7.3).

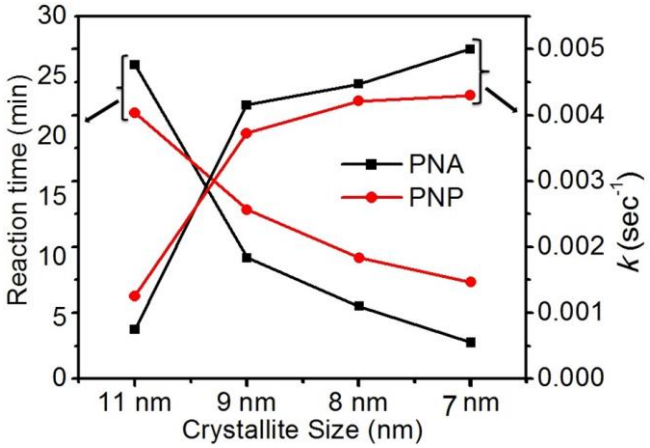

Figure 7.17. Crystallite size dependence on the reaction time and rate constant for the NiSe nanoparticle synthesized by ball milling method.

Table 7.2: Comparison of rate constants obtained for the reduction of para nitrophenol to para aminophenol using various metal and alloy nanoparticles as catalyst.

Compound	Metal loading (mg/mL)	Rate constant (sec^{-1})	Reference
Pt thin film	0.28	1.98 x 10^{-3}	47
$Fe_{33.5}Ni_{66.5}$	0.1	0.95 × 10^{-3}	64
Au	0.18	1.98 x 10^{-3}	65
Pt Pure	4 (μg)	0.13 x 10^{-3}	66
RANEY Ni	4 (μg)	0.14 x 10^{-3}	66
Ni–Pt nanoparticles	4 (μg)	1.94 x 10^{-3}	66
$Ni_{33.8}Co_{66.2}$	0.1	1.22 x 10^{-3}	56

Table 7.3.: Comparison of rate constants obtained for the reduction of para nitroaniline to para phenyldiamine using various metal and alloy nanoparticles as catalyst.

Compound	Metal loading (mg/mL)	Rate constant (sec^{-1})	Reference
Au nanowire	1	3.02 x 10^{-2} & 18.5 x 10^{-2}	67

Similar to NiSe, the use of *M*Sb and CoSe nanoparticle for hydrogenation of PNA and PNP have performed as shown in Figure 7.18. The catalysts CoSb_BM10, NiSb_BM10 and CoSe_BM10 have completed the conversion of PNA to PPD within 16 min, 8 min and 12 min and PNP to PAP within 22 min, 12 min and 28 min, respectively. The compound NiSb_BM10 is the best active catalyst among the ball milling samples favouring, the complete hydrogenation of PNA to PPD in 8 min and PNP to PAP in 12 min. Further detailed studies on these compounds are under progress.

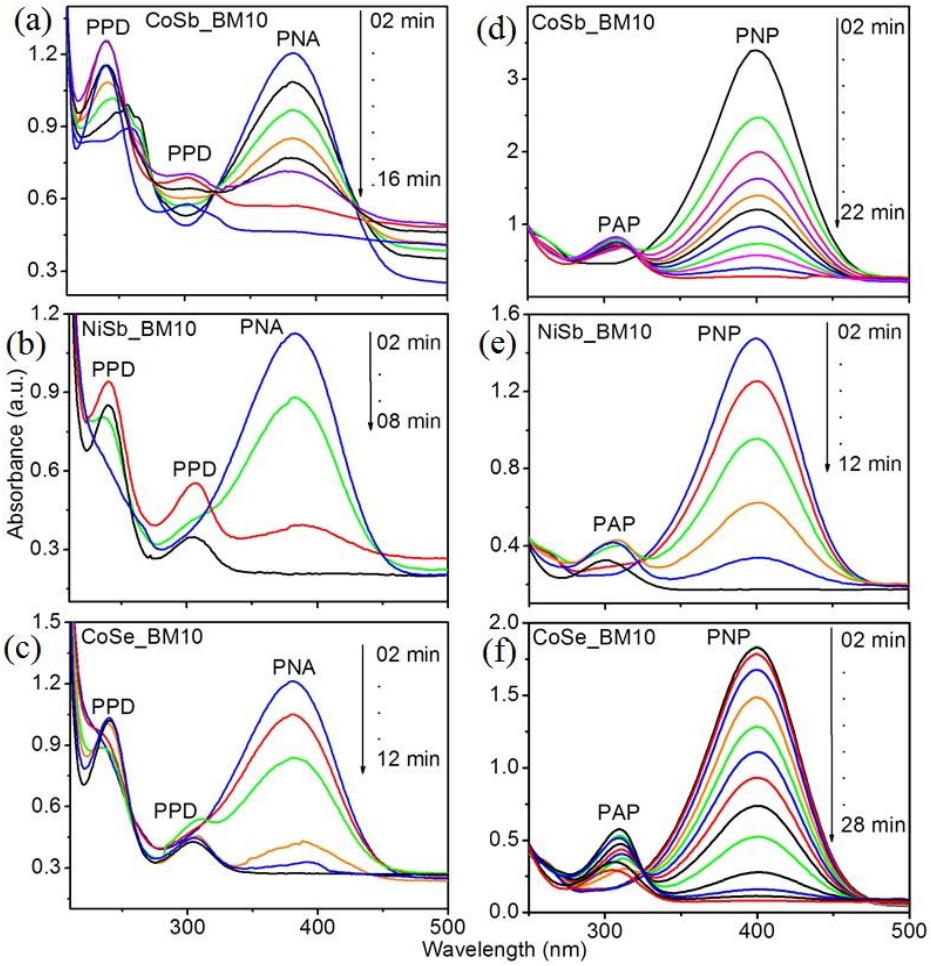

Figure 7.18. UV-Vis absorption spectra for the reduction of PNA to PPD in the presence of (a) CoSb_BM10, (b) NiSb_BM10 and (c) CoSe_BM10; and PNP to PAP in the presence of (d) CoSb_BM10, (e) NiSb_BM10 and (f) CoSe_BM10 nanoparticle obtained by ball milling method.

7.4. Conclusion

This chapter discusses successful synthesis of *M*Sb and *M*Se by ball milling and solution phase methods. *M*Sb and *M*Se nanoparticle are the first materials obtained by ball

milling which can use for the hydrogenation of PNA to PPD and PNP to PAP. The particle size of the NiSe materials was controlled by using different size of tungsten carbide balls in the ball miller and the morphology was controlled by the use of surfactants in the polyol method. These various controlled synthesis methods followed by catalytic activity studies towards the hydrogenation of PNA and PNP suggest that particle size, morphology and the presence of surfactant plays crucial role in the catalytic activity of the nanoparticles. The material NiSe synthesized by ball milling showed slightly better activity compared to the materials synthesized by solution method although the role of the surfactants can be crucial. These catalysts also showed better activity than the reported noble metals and related compounds. Short synthesis time and use of minimal reagents or their absence makes this ball milling method as a facile and efficient synthesis for producing nano materials in large scale. This study can motivate for the development of various low cost metal based nano compounds for the applications not only for hydrogenation but also for several other industrially important reactions.

7.5. References

1. Stamenkovic, V. R.; Mun, B. S.; Arenz, M.; Mayrhofer, K. J. J.; Lucas, C. A.; Wang, G. F.; Ross, P. N.; Markovic, N. M., *Nat. Mater.* **2007,** *6*, 241-247.

2. Ji, X. L.; Lee, K. T.; Holden, R.; Zhang, L.; Zhang, J. J.; Botton, G. A.; Couillard, M.; Nazar, L. F., *Nat. Chem.* **2010,** *2*, 286-293.

3. Studt, F.; Abild-Pedersen, F.; Bligaard, T.; Sorensen, R. Z.; Christensen, C. H.; Norskov, J. K., *Angew. Chem. Int. Edit.* **2008,** *47*, 9299-9302.

4. Armbruster, M.; Kovnir, K.; Behrens, M.; Teschner, D.; Grin, Y.; Schlogl, R., *J. Am. Chem. Soc.* **2010,** *132*, 14745-14747.

5. Luo, Y.; Sun, Y. H.; Schwarz, U.; Armbruster, M., *Chem. Mater.* **2012,** *24*, 3094-3100.

6. Xiao, C. X.; Wang, L. L.; Maligal-Ganesh, R. V.; Smetana, V.; Walen, H.; Thiel, P. A.; Miller, G. J.; Johnson, D. D.; Huang, W. Y., *J. Am. Chem. Soc.* **2013,** *135*, 9592-9595.

7. Armbruster, M.; Kovnir, K.; Friedrich, M.; Teschner, D.; Wowsnick, G.; Hahne, M.; Gille, P.; Szentmiklosi, L.; Feuerbacher, M.; Heggen, M.; Girgsdies, F.; Rosenthal, D.; Schlogl, R.; Grin, Y., *Nat. Mater.* **2012,** *11*, 690-693.

8. Shanbogh, P. P.; Peter, S. C., *Rsc Adv.* **2013,** *3*, 22887-22890.

9. Umeyama, N.; Tokumoto, M.; Yagi, S.; Tomura, M.; Tokiwa, K.; Fujii, T.; Toda, R.; Miyakawa, N.; Ikeda, S. I., *Jpn. J. Appl. Phys.* **2012,** *51*, 053001-053006.

10. Sobhani, A.; Salavati-Niasari, M., *Superlattices Microstruct.* **2014,** *65*, 79-90.

11. Mi, L. W.; Sun, H.; Ding, Q.; Chen, W. H.; Liu, C. T.; Hou, H. W.; Zheng, Z.; Shen, C. Y., *Dalton T.* **2012,** *41*, 12595-12600.

12. Zhuang, Z. B.; Peng, Q.; Zhuang, J.; Wang, X.; Li, Y. D., *Chem. Eur. J.* **2006,** *12*, 211-217.

13. Gao, M. R.; Lin, Z. Y.; Zhuang, T. T.; Jiang, J.; Xu, Y. F.; Zheng, Y. R.; Yu, S. H., *J. Mater. Chem.* **2012,** *22*, 13662-13668.

14. Ribas, X.; Dias, J. C.; Morgado, J.; Wurst, K.; Molins, E.; Ruiz, E.; Almeida, M.; Veciana, J.; Rovira, C., *Chem. Eur. J.* **2004,** *10*, 1691-1704.

15. Matsuura, A. Y.; Watanabe, K.; Kim, C.; Doniach, S.; Shen, Z. X.; Thio, T.; Bennett, J. W., *Phys. Rev. B* **1998,** *58*, 3690-3696.

16. Alivisatos, A. P., *Science* **1996,** *271*, 933-937.

17. Yuan, B. X.; Luan, W. L.; Tu, S. T., *CrystEngComm* **2012,** *14*, 2145-2151.

18. Xu, Y.; Schoonen, M. A., *Am. Mineral.* **2000,** *85*, 543-546.

19. Chakrabarty, S.; Chatterjee, K., *J. Phys. Sci.* **2009,** *13*, 245-250.

20. Wongsaprom, K.; Maensiri, S., *Chiang Mai J. Sci.* **2013,** *40*, 99-108.

21. Mi, L. W.; Ding, Q.; Chen, W. H.; Zheng, Z.; Hou, H. W.; Liu, C. T.; Shen, C. Y., *Rsc Adv.* **2012,** *2*, 6817-6823.

22. Lu, Z. Y.; Chang, Z.; Liu, J. F.; Sun, X. M., *Nano Res.* **2011,** *4*, 658-665.

23. Lai, C. H.; Huang, K. W.; Cheng, J. H.; Lee, C. Y.; Lee, W. F.; Huang, C. T.; Hwang, B. J.; Chen, L. J., *J. Mater. Chem.* **2009,** *19*, 7277-7283.

24. Liu, X. H.; Zhang, N.; Yi, R.; Qiu, G. Z.; Yan, A. G.; Wu, H. Y.; Meng, D. P.; Tang, M. T., *Mater. Sci. Eng., B* **2007,** *140*, 38-43.

25. Salavati-Niasari, M.; Sobhani, A., *Opt. Mater.* **2013,** *35*, 904-909.

26. Sobhani, A.; Salavati-Niasari, M.; Davar, F., *Polyhedron* **2012,** *31*, 210-216.

27. Rajamathi, M.; Seshadri, R., *Curr. Opin. Solid State Mater. Sci.* **2002,** *6*, 337-345.

28. Gu, W.; Deng, X.; Jia, X.; Li, J.; Wang, E., *J. Mater. Chem. A* **2015,** *3*, 8793-8799.

29. He, J. H.; Ichinose, I.; Kunitake, T.; Nakao, A.; Shiraishi, Y.; Toshima, N., *J. Am. Chem. Soc.* **2003,** *125*, 11034-11040.

30. Wu, W.; Lei, M.; Yang, S. L.; Zhou, L.; Liu, L.; Xiao, X. H.; Jiang, C. Z.; Roy, V. A. L., *J. Mater. Chem. A* **2015,** *3*, 3450-3455.

31. Wu, M. L.; Chen, D. H.; Huang, T. C., *Chem. Mater.* **2001,** *13*, 599-606.

32. Truong, T. T.; Liu, Y. Z.; Ren, Y.; Trahey, L.; Sun, Y. G., *Acs Nano* **2012,** *6*, 8067-8077.

33. Chakka, V. M.; Altuncevahir, B.; Jin, Z. Q.; Li, Y.; Liu, J. P., *J. Appl. Phys.* **2006,** *99*, 08E912-08E915.

34. Kim, S.-O.; Manthiram, A., *J. Mater. Chem. A* **2015,** *3*, 2399-2406.

35. Campos, C. E. M.; de Lima, J. C.; Grandi, T. A.; Machado, K. D.; Pizani, P. S.; Hinrichs, R., *Solid State Ionics* **2004,** *168*, 205-210.

36. Wang, M. W.; Zhao, H. L.; He, J. C.; Wang, R. L.; Chen, J. B.; Chen, N., *J. Alloy Compd.* **2009,** *484*, 864-869.

37. Clausen, T.; Schwan-Jonczyk, A.; Lang, G.; Schuh, W.; Liebscher, K. D.; Springob, C.; Franzke, M.; Balzer, W.; Imhoff, S.; Maresch, G.; Bimczok, R., *Hair Preparations*. John Wiley & Sons, Inc.: New York, 2006.

38. Smiley, R. A., *Phenylene and Toluenediamines*. Wiley-VCH: Weinheim, 2002.

39. Pradhan, N.; Pal, A.; Pal, T., *Colloids Surf., A* **2002,** *196*, 247-257.

40. Alsén, N., *Geol. Foeren. Stockholm Foerh.* **1925,** *47*, 19-72.

41. Milazzo, G.; Caroli, S.; Sharma, V. K., *Tables of Standard Electrode Potentials*. Wiley: Chichester, 1978.

42. Komarek, K. L.; Wessely, K., *Monatsh. Chem.* **1972,** *103*, 923-933.

43. Wiley, B.; Sun, Y. G.; Mayers, B.; Xia, Y. N., *Chem. Eur. J.* **2005,** *11*, 454-463.

44. Huang, H. H.; Ni, X. P.; Loy, G. L.; Chew, C. H.; Tan, K. L.; Loh, F. C.; Deng, J. F.; Xu, G. Q., *Langmuir* **1996,** *12*, 909-912.

45. Zhang, Z. T.; Zhao, B.; Hu, L. M., *J. Solid State Chem.* **1996,** *121*, 105-110.

46. Sun, Y. G.; Xia, Y. N., *Science* **2002,** *298*, 2176-2179.

47. Hoseini, S. J.; Rashidi, M.; Bahrami, M., *J. Mater. Chem.* **2011,** *21*, 16170-16176.

48. Dong, Z. P.; Le, X. D.; Liu, Y. S.; Dong, C. X.; Ma, J. T., *J. Mater. Chem. A* **2014,** *2*, 18775-18785.

49. Liu, X. C.; Jin, R. X.; Chen, D. S.; Chen, L.; Xing, S. X.; Xing, H. Z.; Xing, Y.; Su, Z. M., *J. Mater. Chem. A* **2015,** *3*, 4307-4313.

50. Lv, J. J.; Wang, A. J.; Ma, X. H.; Xiang, R. Y.; Chen, J. R.; Feng, J. J., *J. Mater. Chem. A* **2015,** *3*, 290-296.

51. Shen, Y. Y.; Sun, Y.; Zhou, L. N.; Li, Y. J.; Yeung, E. S., *J. Mater. Chem. A* **2014,** *2*, 2977-2984.

52. Song, P.; He, L. L.; Wang, A. J.; Mei, L. P.; Zhong, S. X.; Chen, J. R.; Feng, J. J., *J. Mater. Chem. A* **2015,** *3*, 5321-5327.

53. Xiong, J.; Liu, Y.; Cao, C.; Shen, L.; Wu, W.; Liang, S.; Liang, R.; Wu, L., *J. Mater. Chem. A* **2015,** *3*, 6935-6942.

54. Xie, J.; Zhao, X. B.; Yu, H. M.; Qi, H.; Cao, G. S.; Tu, J. P., *J. Alloy Compd.* **2007,** *441*, 231-235.

55. Sarkar, S.; Balisetty, L.; Shanbogh, P. P.; Peter, S. C., *J. Catal.* **2014,** *318*, 143-150.

56. Wu, K. L.; Wei, X. W.; Zhou, X. M.; Wu, D. H.; Liu, X. W.; Ye, Y.; Wang, Q., *J. Phys. Chem. C* **2011,** *115*, 16268-16274.

57. Huang, J. F.; Vongehr, S.; Tang, S. C.; Meng, X. K., *J. Phys. Chem. C* **2010,** *114*, 15005-15010.

58. Lu, P.; Teranishi, T.; Asakura, K.; Miyake, M.; Toshima, N., *J. Phys. Chem. B* **1999,** *103*, 9673-9682.

59. Reddy, V.; Torati, R. S.; Oh, S.; Kim, C., *Ind. Eng. Chem. Res.* **2013,** *52*, 556-564.

60. Banares, M. A., *Adv. Mater.* **2011,** *23*, 5293-5301.

61. Topsoe, H., *J. Catal.* **2003,** *216*, 155-164.

62. Buurmans, I. L. C.; Weckhuysen, B. M., *Nat. Chem.* **2012,** *4*, 873-886.

63. Wieckowski, A.; Savinova, E. R.; Vayenas, C. G., *Catalysis and Electrocatalysis at Nanoparticle Surfaces*. CRC Press: 2003; p 970.

64. Wu, K. L.; Yu, R.; Li, X. Z.; Wei, X. W., *Micro Nano Lett.* **2012,** *7*, 685-688.

65. Chang, Y. C.; Chen, D. H., *J. Hazard. Mater.* **2009,** *165*, 664-669.

66. Ghosh, S. K.; Mandal, M.; Kundu, S.; Nath, S.; Pal, T., *Appl. Catal., A* **2004,** *268*, 61-66.

67. Chirea, M.; Freitas, A.; Vasile, B. S.; Ghitulica, C.; Pereira, C. M.; Silva, F., *Langmuir* **2011,** *27*, 3906-3913.

Summary and Conclusions

In conclusion, the thesis discussed about the synthesis and crystal growth of several novel ordered bulk and nano intermetallic compounds. One of the biggest challenges in the field of intermetallic chemistry is the synthesis and crystal growth of pure compounds. Since there are difficulties in predicting the chemical bonding nature in these compounds, a systematic synthesis method cannot be employed. Quite often these compounds are synthesized by conventional techniques such as arc melting and high frequency induction furnaces. With the lack of proper single crystal growth, the original structure of the compounds, in most cases, cannot be realized. With this background in mind, several new compounds have been grown by metal flux technique. To be precise, the thesis contributed a total of 37 compounds of which 5 are new structure types (EuInGe, $Yb_{6.6}Ir_6Sn_{16}$, $YbCu_4Ga_8$, $YbCuGa_3$ and $EuCu_2Ge_2$) and 7 are new compounds within known structure types ($Yb_7Ni_4InGe_{12}$, $Yb_5Ga_2Sb_6$, $YbCu_6In_6$, $SmCu_6In_6$, $Sm_3Ni_5Al_{19}$, $Eu_3Cu_2In_9$, $Eu_3Ag_2In_9$). Apart that, the work revisited the synthesis of several other compounds ($EuAg_4In_8$, $Yb_5Co_4Ge_{10}$, Yb_2CuGe_6, $Yb_3Cu_4Ge_4$, *RE*$CuGa_3$ (*RE* = La-Nd, Sm-Gd), $RE_5M_2Sb_6$ (*RE* = Eu, Yb; *M* = Al, In), REX_3 (*RE* = La, Eu, Yb; *X* = Pd, Pt, Pb), NiSb, CoSb and NiSe) for their detailed crystal structure and physical property studies. The work described here extensively used advanced crystallographic tools to understand the crystal structure of novel and revisited compounds. As an interesting example is the discovery of three additional structure types for the members in the family of $RETX_3$ compounds, which include the new monoclinic structure type $YbCuGa_3$ and high temperature phases of $PrCuGa_3$ within the Rb_5Hg_{19} and Cu_3Au structure types, which tallied overall 15 different structure types in this family. Among them $YbCuGa_3$ is the first monoclinic member in this family. The other interesting examples are the discovery of $Sm_3Ni_5Al_{19}$ as a new member in the homologous series $Sm_{2n+m}Ni_{4n+m}Al_{15n+4m}$ (n = 1 and m = 1) and $Eu_3T_2In_9$ as the deficient variant of the new orthorhombic crystal structure of $EuCu_2Ge_2$. CSD/CCDC number of new compounds produced by this work is shown in Appendix 1. All the compounds discovered have been characterized by various techniques and scaled up the synthesis using various techniques.

In the next step, the work devoted to understand the structure-property relationships, which are the fundamental underpinning of solid-state sciences. The pace of the progress in the development of intermetallic compounds should be continued with the synthesis of novel ternary and quaternary or even compounds with more than four

constituents at the ordered positions can lead into the development of novel materials with unique physical properties. One such example is the new compound $Yb_5Ga_2Sb_6$, which was grown by metal flux method. During the work, it was proposed that a probable material for the thermoelectric applications and in fact it was studied by Aydemir et al.[1] during the course of this thesis work. The other example is the development of ordered compounds within the NiAs structure type. The ordered arrangement of active sites in these structures efficiently exploited in the hydrogenation catalysis and fuel cell applications. This work also introduce two chemical processes nanofication and dimensional reduction to chemically convert unstable $REPb_3$ (*RE* = Eu, Yb) to air stable material via valence transition of the *RE* atom. This work may find applications in fabricating future technological devices.

The work also encourages the solid state chemists to use the theoretical tools such as electronic structure and magnetic property calculations to predict novel compounds as reported. The thesis also contributes with the electronic structure calculations of the compounds EuInGe, Yb_2CuGe_6 and $Yb_3Cu_4Ge_4$. The superstructure of EuNiGe, ordered structure in Yb_2CuGe_6 observed in the single crystal XRD were accompanied by these calculations.

In overall, the work described in the thesis contributes to the continued development of intermetallic compounds with diverse structures and unique properties and will be continued in different directions as well. Complex magnetic phases in $EuCuGa_3$ and possible bulk superconductivity are indicated by the preliminary magnetic and electronic transport measurements on $LaCuGa_3$ will be studied with detailed measurements. The enhanced activity proposed in the REX_3 compounds will be extended to oxygen reduction and hydrogen evolution reactions for their applications in the field of fuel cell. The work on the compounds $RE_5X_2Sb_5$ can be extended with the discovery of new compounds as they are considered as the probable thermoelectric materials. The substitution of the metals such as Mn or Zn may improve the thermal conductivity towards better Figure of merit in these compounds.

Reference

1. Aydemir, U.; Zevalkink, A.; Ormeci, A.; Wang, H.; Ohno, S.; Bux, S.; Snyder, G. J., *Dalton T.* **2015,** *44*, 6767-6774.

Appendix 1. CSD/CCDC numbers of the crystal structures obtained the single crystal structure refinement.

Compound Name	CSD/CCDC Number	Compound Name	CSD/CCDC Number
$YbCuGa_3$	425031	$LaCuGa_3$	1047127
$YbCu_6In_6$	424351	$CeCuGa_3$	1047124
$SmCu_6In_6$	424639	$PrCuGa_3$	1047129
$EuAg_4In_8$	1002249	$NdCuGa_3$	1047128
$Yb_5Ga_2Sb_6$	426568	$SmCuGa_3$	1047130
EuInGe (sub)	425244	$EuCuGa_3$	1047125
EuInGe (Super)	425245	$GdCuGa_3$	1047126
Yb_2CuGe_6	426133	$YbCu_4Ga_8$ (Sub)	424999
$Yb_3Cu_4Ge_4$	426132	$YbCu_4Ga_8$ (Super)	425503
$Sm_3Ni_5Al_{19}$	993911	$YbCu_4Ga_8$ (ND)	425502
$Yb_7Ni_4InGe_{12}$	989027	$Eu_3Ag_2In_9$	1436853
$Yb_5Co_4Ge_{10}$	425832	$EuCu_2Ge_2$	1436854

LIST OF PUBLICATIONS

From Thesis

1. **Subbarao, U.;** Rayaprol, S.; Dally, R.; Graf, M. J.; Peter, S. C., Swinging Symmetry, Multiple Structural Phase Transitions and Versatile Physical Properties in *RE*$CuGa_3$ (*RE* = La-Nd, Sm-Gd). *Inorg. Chem.*, **2015**, Press.
2. **Subbarao, U.;** Rajkumar, J.; Chondroudi, M.; Balasubramanian, M.; Kanatzidis, M. G.; Peter, S. C., $Yb_7Ni_4InGe_{12}$: A Quaternary Compound Having Mixed valent Yb atoms Grown from Indium Flux. *Dalton Trans.*, **2015**, *44*, 5797-5804.
3. **Subbarao, U.;** Joseph, B.; Peter, S. C., Magnetic and X-ray Absorption Studies on the $RE_5X_2Sb_6$ (*RE* = Eu, Yb; X = Al, Ga, In) Compounds. *J. Alloy Compd.*, **2016**, *658*, 395-401.
4. **Subbarao, U.;** Sarkar, S.; Peter, S. C., Crystal Structure and Properties of Tetragonal $EuAg_4In_8$ Grown by Metal Flux Technique. *J. Solid State Chem.*, **2015**, *226*, 126–132.
5. Peter, S. C.; **Subbarao, U.;** Sarkar, S.; Vaitheeswaran, G.; Svane, A.; Kanatzidis, M. G., Synthesis, Crystal Structure and Band Structure Calculation of Intermediate Valent Yb_2CuGe_6 and Trivalent $Yb_3Cu_4Ge_4$. *J. Alloy Compd.*, **2014**, *589*, 405–411.
6. Peter, S. C.; **Subbarao, U.;** Rayaprol, S.; Martin, J. B.; Malliakas, C. D.; Kanatzidis, M. G., Flux Growth of $Yb_{6.6}Ir_6Sn_{16}$ Having Mixed-Valent Ytterbium. *Inorg. Chem.*, **2014**, *53*, 6615−6623.
7. **Subbarao, U.;** Aloke, K. G.; Peter, S. C., Crystal Growth, Structure and Magnetic Properties of $Sm_3Ni_5Al_{19}$: A compound in the $Sm_{2n+m}Ni_{4n+m}Al_{15n+4m}$ Homologous Series. *J. Chem. Sci.*, **2014**, *126*, 1605–1613.
8. **Subbarao, U.;** Peter. S. C., Structure and Properties of $SmCu_{6-x}In_{6+x}$ (x = 0, 1, 2). *J. Chem. Science*., **2013**, *125*, 1315–1323.
9. **Subbarao, U.;** Sarkar, S.; Vaitheeswaran, G.; Svane, A.; Peter, S. C., $Yb_5Ga_2Sb_6$: A Mixed Valent and Narrow-Band Gap Material in the $RE_5M_2X_6$ Family. *Inorg. Chem.*, **2013**, *52*, 13631−13638.
10. **Subbarao, U.;** Sebastian, A.; Rayaprol, S.; Yadav, C. S.; Svane, A.; Vaitheeswaran, G.; Peter, S. C., Metal Flux Crystal Growth Technique in the

Determination of Ordered Superstructure in EuInGe. *Cryst. Growth Des.*, **2013,** *13*, 352-359.

11. **Subbarao, U.;** Peter, S. C., Single Crystal X-Ray Diffraction Studies on Magnetic $Yb_5Co_4Ge_{10}$. *Adv. Mat. Phys. Chem.*, **2013**, *3*, 54-59
12. **Subbarao, U.;** Peter, S. C., Crystal Growth and Properties of $YbCuGa_3$: First Monoclinic System in the $RETX_3$ Family. *Cryst. Growth Des.*, **2013**, *13*, 953-959.
13. **Subbarao, U.;** Gutmann, M. J.; Peter, S. C., New Structure Type in the Mixed-Valent Compound $YbCu_4Ga_8$. *Inorg. Chem.*, **2013**, *52*, 2219-2227.
14. **Subbarao, U.;** Peter, S. C., Crystal Structure of $YbCu_6In_6$ and Mixed Valence Behavior of Yb in $YbCu_{6-x}In_{6+x}$ (x = 0, 1, and 2) Solid Solution. *Inorg. Chem.*, **2012**, *51*, 6326-6332.
15. **Subbarao, U.;** Sourav, S. B.; Sarkar, S. Peter, S. C., Nanofication and Dimensional Reduction Mediated Valence Transition as a Tool towards Air Stable Materials. *Communicated.*
16. **Subbarao, U.;** Amshumali, M. K.; Loukya, B.; Datta, R.; Peter, S. C., Size and Morphology Controlled NiSe Nanoparticles as Efficient Catalyst for the Hydrogenation Reactions. *Communicated.*
17. **Subbarao, U.;** Sarma, Ch. S.; Yatish, K.; Rajkumar, J.; Peter, S. C., Synthesis of Nanointermetallic REX_3 (*RE*=Eu and Yb; X=Pd and Pt) for Magnetic and Electrochemical Studies. *Communicated.*
18. **Subbarao, U.;** Sarma, Ch. S.; Vidyanshu, M.; Yatish, K.; Peter, S. C., The Structural Evolution of the Compounds $Eu_3T_2In_9$ (*T*= Cu and Ag) through the Superstructure of $EuCu_2Ge_2$. *Communicated.*
19. **Subbarao, U.;** Dundappa, M.; Graf, M. J.; Peter, S. C., Synthesis, Crystal Structure and Magnetic Properties of $RENiGa_3$ (*RE* = La-Nd, Sm-Gd) Compounds. *Communicated.*

Other Publications

20. Iyer, A. K.; **Subbarao, U.;** Peter, S. C., Structure and Properties of $RELiGe_2$ (*RE* = La-Nd, Sm-Gd, Yb) Compounds. *AIP Conf. Proc.*, **2013**, *1512*, 1010-1011. (AIP-American Institute of Physics).

21. Kalsi, D.; **Subbarao, U.;** Rayaprol, S.; Peter, S. C., Two Polymorphs of $CeRh_{0.5}Ge_{1.5}$ with Possible Spin Glass Behavior. *J. Solid State Chem.*, **2014**, *212*, 73–80.
22. Sarkar, S.; **Subbarao, U.;** Joseph, B.; Peter, S. C., Mixed Valence and Metamagnetism in a Metal Flux Grown Compound $Eu_2Pt_3Si_5$. *J. Solid State Chem.*, **2015**, *225*, 181–186.
23. Jana, R.; **Subbarao, U.;** Peter, S. C., Ultrafast Synthesis of Flower-like Ordered Pd_3Pb Nanocrystals with Superior Electrocatalytic Activities towards Oxidation of Formic Acid and Ethanol. *J. Power Sources*, **2016**, *301*, 160-169.
24. Sorb, Y.; Rajaji, V.; Malavi, P.; **Subbarao, U.;** Halappa, P.; Karmakar, S.; Peter, S. C.; Chandrabhas, N., Pressure induced electronic topological transition in Sb_2S_3. *J. Phys.: Condens. Matt.*, **2015**, Press.
25. **Subbarao, U.;** Sarkar, S.; Peter, S. C., Physical property studies and XANES measurements of Yb*T*In4 (*X*= Pt and Pd) compounds. *Manuscript is under preparation.*
26. **Subbarao, U.;** Dally, R.; Graf, M. J.; Peter, S. C., Magnetism and Magnetic ordering in *RE*$CuGa_3$ *RE* = La-Nd, Sm-Gd) compounds. *Manuscript is under preparation.*
27. **Subbarao, U.;** Peter, S. C., The Role of Indium as Inactive Flux for the Formation of New Intermetallic Ternary Zintal Phase Compound: $Yb_3Ni_3Ge_7$. *Manuscript is under preparation.*
28. **Subbarao, U.;** Sorb, Y.; koushik, P.; Satyanarayana, K. V. V.; Waghmare, U. V.; Chandrabhas, N.; Peter, S. C.; Synthesis, Characterisation and physical properties of Semiconductor to Metal transition nature of Cubic GaSb Semiconductor Material. *Manuscript is under preparation.*

Patents

1. Peter, S. C.; Shanbogh, P. P.; **Subbarao, U.,** A method of synthesizing intermetallic compounds and applications thereof. *Patent Application No: WO2015011680 A1, Year: 01/2015.*

About the Author…

Udumula Subbarao was born in Masaipeta, Kanigiri, Prakasam district, Andhra Pradesh, India. He completed BSc from Sri Nagarjuna Degree College, Acharya Nagarjuna University, Ongole. For his further studies he joined Acharya Nagarjuna University College, Nagarjuna Nagar, Guntur, and obtained the MSc degree in Chemistry. In August 2011, he started working as a PhD student at New Chemistry Unit, JNCASR, Bangalore, under the guidance of Dr. Sebastian C. Peter. His research work at JNCASR was mainly focused on the Investigations of Novel Ordered Bulk and Nano Intermetallic Compounds with Diverse crystal Structures and Versatile Physicochemical Properties. The most important results of this work are presented in this thesis.

usr2010@gmail.com